ISSN 1580-3155

Pages 255–509 ■ Year 2019, Vol. 66, No. 2

Slovensko kemijsko društvo
Slovenian Chemical Society

Acta Chimica Slovenica

2

66/2019

http://acta.chem-soc.si

Acta Chimica Slovenica is indexed in: *Academic Search Complete, Central & Eastern European Academic Source, Chemical Abstracts Plus, Chemical Engineering Collection (India), Chemistry Citation Index Expanded, Current Contents (Physical, Chemical and Earth Sciences), Digitalna knjižnica Slovenije (dLib.si), DOAJ, ISI Alerting Services, PubMed, Science Citation Index Expanded, SciFinder (CAS), Scopus and Web of Science.* Impact factor for 2017 is IF = 1.104.

Izdaja – Published by:
SLOVENSKO KEMIJSKO DRUŠTVO – SLOVENIAN CHEMICAL SOCIETY
Naslov redakcije in uprave – Address of the Editorial Board and Administration
Hajdrihova 19, SI-1000 Ljubljana, Slovenija
Tel.: (+386)-1-476-0252; Fax: (+386)-1-476-0300; E-mail: chem.soc@ki.si

Slovensko kemijsko društvo
Slovenian Chemical Society

Izdajanje sofinancirajo – Financially supported by:
Slovenian Research Agency, Ljubljana, Slovenia
National Institute of Chemistry, Ljubljana, Slovenia
Jožef Stefan Institute, Ljubljana, Slovenia
Faculty of Chemistry and Chemical Technology at University of Ljubljana, Slovenia
Faculty of Chemistry and Chemical Engineering at University of Maribor, Slovenia
Faculty of Pharmacy at University of Ljubljana, Slovenia
University of Nova Gorica, Nova Gorica, Slovenia

Acta Chimica Slovenica izhaja štirikrat letno v elektronski obliki na spletni strani http://*acta.chem-soc.si*. V primeru posvečenih številk izhaja revija tudi v tiskani obliki v omejenem številu izvodov.
Acta Chimica Slovenica appears quarterly in electronic form on the web site *http://acta.chem-soc.si*. In case of dedicated issues, a limited number of printed copies are issued as well.
Transakcijski račun: 02053-0013322846 Bank Account No.: SI56020530013322846-Nova Ljubljanska banka d. d., Trg republike 2, SI-1520 Ljubljana, Slovenia, SWIFT Code: LJBA SI 2X
Oblikovanje ovitka – Design cover: KULT, oblikovalski studio, Simon KAJTNA, s. p. Grafična priprava za tisk: Majanafin, d. o. o.

Graphical Contents

Acta Chimica Slovenica

Year 2019, Vol. 66, No. 2

FEATURE ARTICLE

255–275 Inorganic chemistry

Fluoride in Human Health and Nutrition

Dona Štepec and Maja Ponikvar-Svet

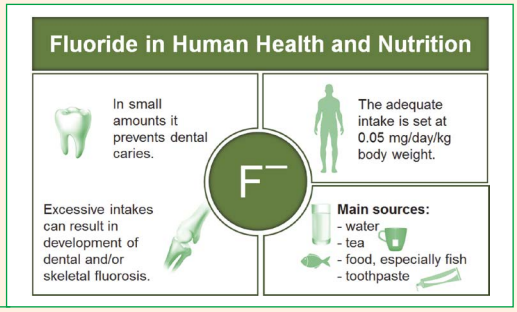

SCIENTIFIC PAPER

276–283 Organic chemistry

Green Synthesis of Bromo Organic Molecules and Investigations on Their Antibacterial Properties: An Experimental and Computational Approach

Naruti Longkumer, Kikoleho Richa, Rituparna Karmaker, Visekhonuo Kuotsu, Aola Supong, Latonglila Jamir, Pranjal Bharali and Upasana Bora Sinha

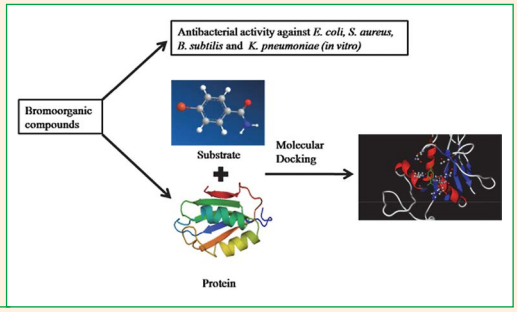

284–293 Analytical chemistry

Electrochemical Degradation of Reactive Blue 21 and Synthetic Textile Effluent by Using $Co_{47.5}/C_{47.5}$-PVC_5 Composite Electrode

Norazzizi Nordin, Mohamad Anis Farith Pisal, Nur Izzatie Hannah Razman and Nur Farhana Jaafar

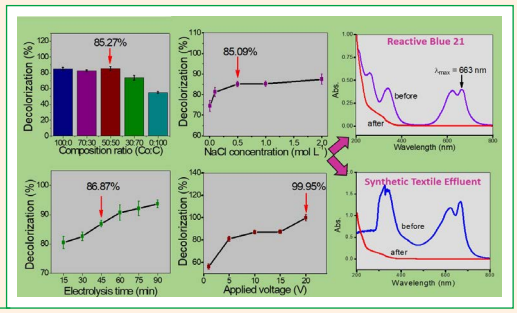

294–307 Organic chemistry

Design, Synthesis, Biological Evaluation and Molecular Docking Studies of Some New Sulfonamides Possessing 1,4-Benzodioxane Nucleus

Misbah Irshad, Muhammad Athar Abbasi, Aziz-Ur-Rehman, Qamar Ali, Muhammad Aslam, Fozia Iram, Muhammad Shahid, Muhammad Ashraf, Muhammad Arif Lodhi and Syed Babar Jamal

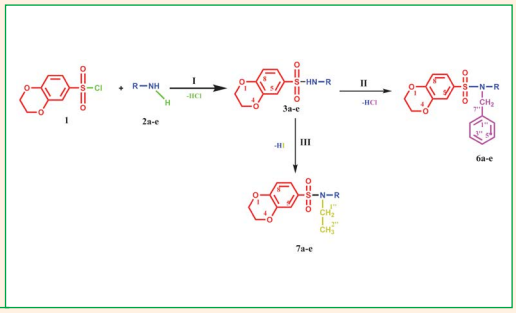

308–314 Inorganic chemistry

Three Chiral Cyanide-Bridged Cr–Cu Complexes: Synthesis, Crystal Structures and Magnetic Properties

Xia Chen, Wen-Long Lan, Xiao-Yun Hao, Yu Liu, Zhen Zhou, Shu-Juan Zhuang, Lu Yang, Qing-Yun Liu, Wei-Jiang Si and Dao-Peng Zhang

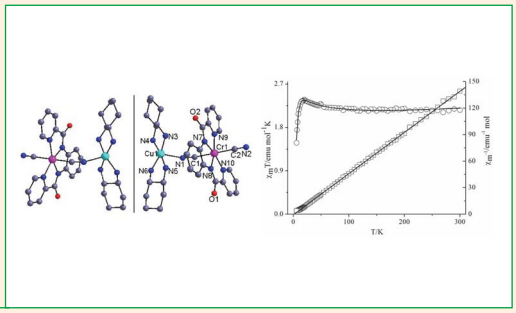

315–325 Chemical, biochemical and environmental engineering

Application of Inverse QSAR/QSPR Analysis for Pesticides Structures Generation

Belgacem Souyei, Abdelkader Hadj Seyd, Faouzi Zaiz and Abdelkrim Rebiai

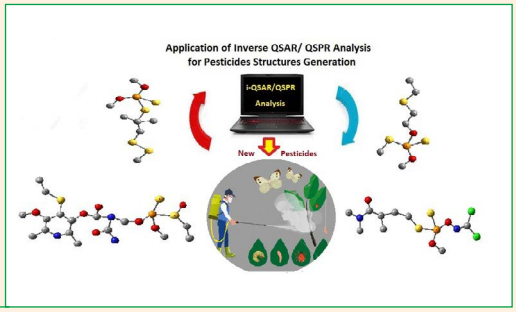

326–336 Chemical, biochemical and environmental engineering

Adsorptive Performance of Soy Bran and Mustard Husk Towards Arsenic (V) Ions from Synthetic Aqueous Solutions

Doina Humelnicu, Laurentiu Valentin Soroaga, Cecilia Arsene, Ionel Humelnicu and Romeo Iulian Olariu

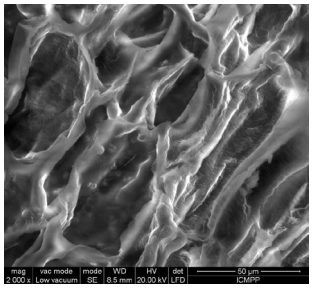

337–343 Chemical, biochemical and environmental engineering

Protein Release from Biodegradable Poly(ε-Caprolactone)-Chitosan Scaffolds Prepared in $scCO_2$

Gregor Kravanja, Maja Globočnik, Mateja, Primožič, Željko Knez and Maja Leitgeb

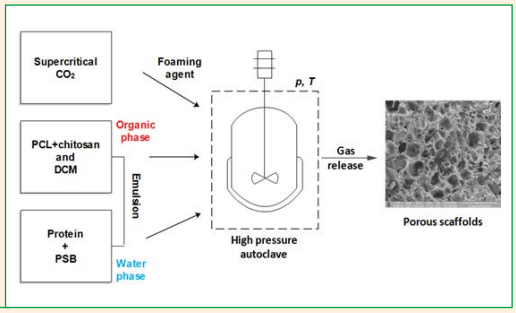

344–350 Organic chemistry

Synthesis and Biological Evaluation of Some Novel S-β-D-Glucosides of 4-Amino-5-alkyl-1,2,4-triazole-3-thiones Derivatives

Anila Rahimi Aghkand, Karim Akbari Dilmaghani, Zahra Dono Ghezelbash and Behvar Asghari

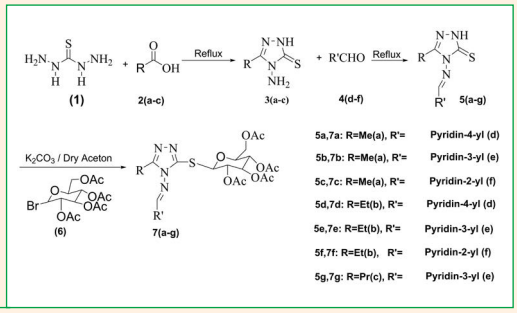

351–359 Applied chemistry

Exploring Bikaverin as Metal Ion Biosensor: A Computational Approach

Zakir Hussain, Haamid Rasool Bhat, Tahira Naqvi3 Malay K. Rana and Masood Ahmad Rizvi

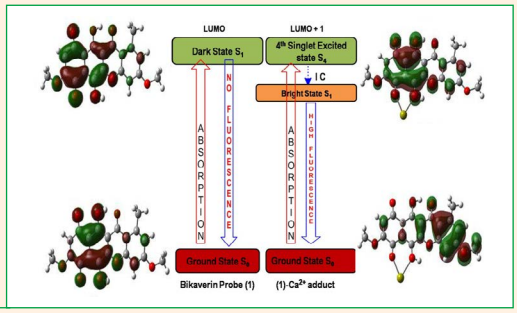

360–366 Inorganic chemistry

Ion-Associated Complex of the Anionic Chelate of Germanium(IV) with Nitro Derivative of the Catechol and the Cation of Monotetrazolium Salt

Kirila Stojnova and Vanya Lekova

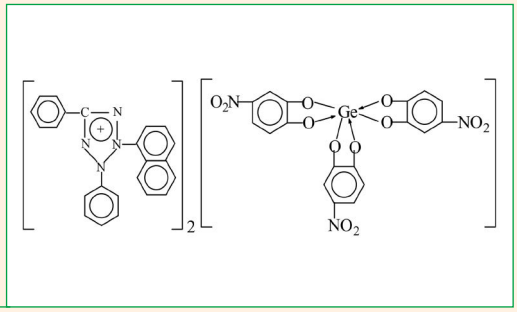

367–377 Chemical, biochemical and environmental engineering

Effect of Microwave-Assisted Extraction on Polyphenols Recovery from Tomato Peel Waste

Marina Tranfić Bakić, Sandra Pedisić, Zoran Zorić, Verica Dragović-Uzelac and Antonela Ninčević Grassino

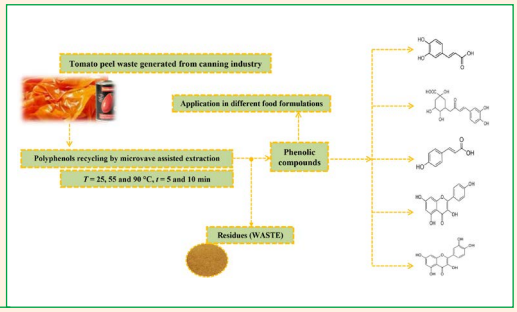

378–387 Inorganic chemistry

Cyclometalated Iridium(III) Complexes Containing 2-Phenylbenzo[d]oxazole Ligand: Synthesis, X-ray Crystal Structures, Properties and DFT Calculations

Xiao-Han Yang, Qian Zhang, Hui Peng, Zi-Cen Zuo, Ding Yuan, Yan Chen, Qin Chen, Guang-Ying Chen, Zhi-Gang Niu and Gao-Nan Li

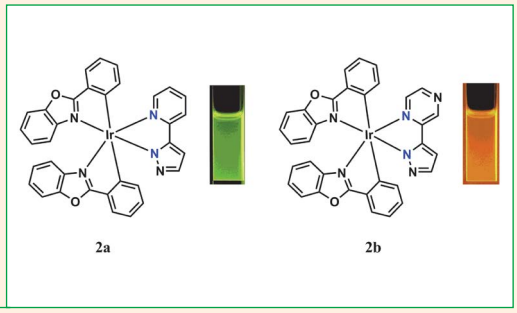

385–394 Analytical chemistry

A Vortex-Assisted Deep Eutectic Solvent-Based Liquid-Liquid Microextraction for the Analysis of Alkyl Gallates in Vegetable Oils

Hasan Çabuk, Yasemin Yılmaz and Elif Yıldız

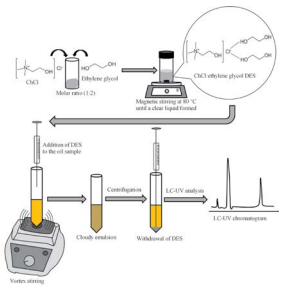

395–401 Physical chemistry

Molecular Dynamics Simulations of p97 Including Covalent, Allosteric and ATP-Competitive Inhibitors

Stefano Rendine, Christian Orrenius, Federico Dapiaggi, Stefano Pieraccini, Ilaria Motto, Roberto D'Alessio, Paola Magnaghi, Antonella Isacchi, Eduard Felder and Maurizio Sironi

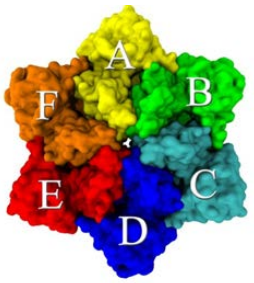

402–413 Chemical, biochemical and environmental engineering

Sandpaper Wastes as Adsorbent for the Removal of Brilliant Green and Malachite Green Dye

Yasemin İşlek Coşkun, Nur Aksuner and Jale Yanik

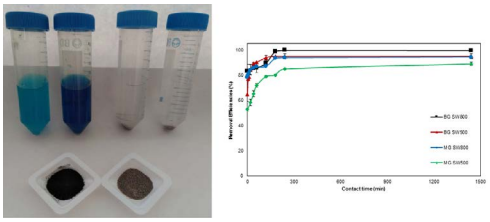

414–420 Inorganic chemistry

Preparation, Structure, Photoluminescent and Semiconductive Properties, and Theoretical Calculation of a Mononuclear Nickel Complex with 3-Hydroxy-2-Methylquinoline-4-Carboxylato Ligand

Xiao-Niu Fang, Jia Li, Xiu-Guang Yi, Qi Luo, Jia-Yi Chen and Yong-Xiu Li

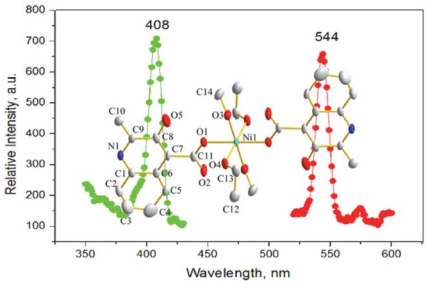

421–426 Organic chemistry

Synthesis and in vivo Anti-inflammatory Evaluation of Piperazine Derivatives Containing 1,4-Benzodioxan Moiety

Zhi-Ping Liu, Chang-Da Gong, Long-Yan Xie, Xiu-Li Du, Yang Li and Jie Qin

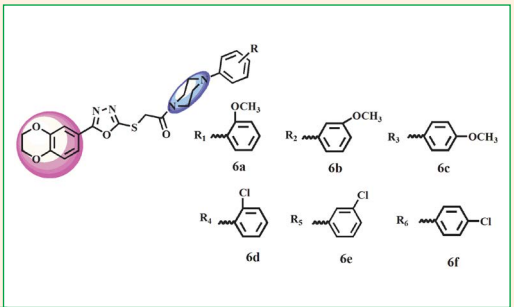

427–434 General chemistry

Growth of Silver Nanoparticles Using Polythiocyanatohydroquinone in Aqueous Solution

Valentina A. Litvin, Boris F. Minaev, Rostislav L. Galagan, Glib V. Baryshnikov and Hans Ågren

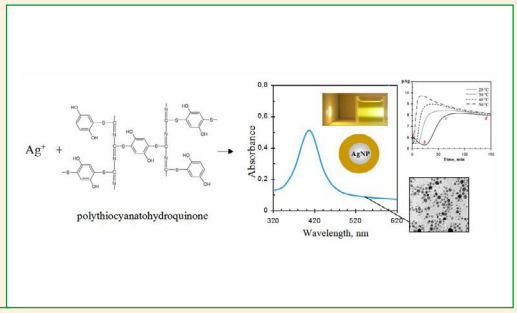

435–442 Physical chemistry

On Topological Indices of *OT* [*m*, *n*] Octagonal Tillings and TiO_2 Nanotubes

Hafiz Usman Afzal and Tahzeeb Fatima

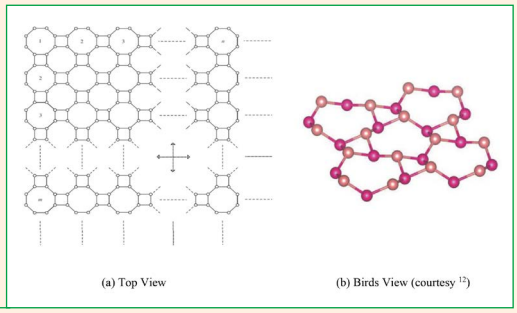

443–454 Chemical, biochemical and environmental engineering

Adsorption Mechanism of Congo Red on Mg–Al-layered Double Hydroxide Nanocompound

Narges Safar Beyranvand, Babak Samiey and Abbas Dadkhah Tehrani

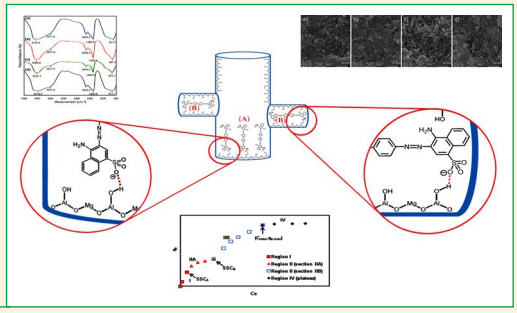

455–465 Materials science

Preparation of Magnetite by Thermally Induced Decomposition of Ferrous Oxalate Dihydrate in the Combined Atmosphere

Josef Kopp, Petr Novak, Josef Kaslik and Jiri Pechousek

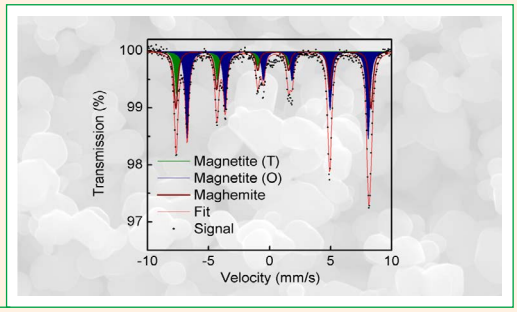

466–472 Materials science

Phase Equilibria in the $MnGa_2Te_4$-$MnIn_2Te_4$ System, Crystal Structure and Physical Properties of $MnGaInTe_4$

Faig Mamedagha Mammadov, Imamaddin Rajabali Amiraslanov, Yegana Rasul Aliyeva, Sadiyar Sultan Ragimov, Leyla Farkhad Mashadiyeva and Mahammad Baba Babanly

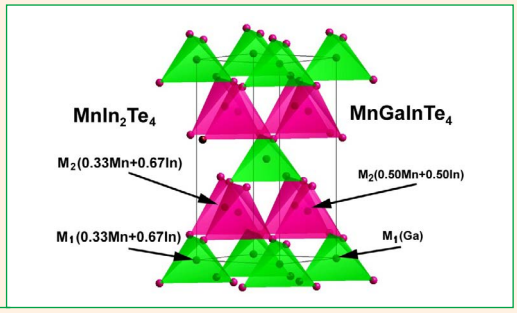

473–483 Chemical, biochemical and environmental engineering

Subcritical Water for Recovery of Polyphenols from Comfrey Root and Biological Activities of Extracts

Jelena Vladic, Natasa Nastic, Tatjana Stanojkovic, Zeljko Zizak, Jelena Cakarevic, Ljiljana Popovic and Senka Vidovic

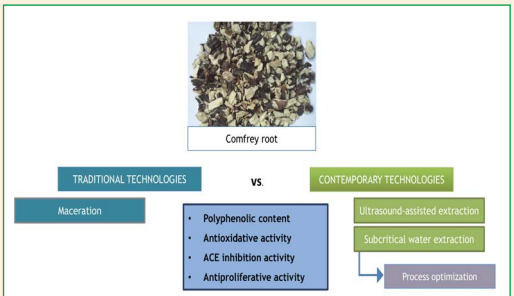

484–489 Inorganic chemistry

Synthesis, Crystal Structure and Antimicrobial Activity of a Linear Trinuclear Nickel(II) Complex with Schiff Base Ligand

Cui-Lin Zhang, Xiao-Yang Qiu, Shu-Juan Liu

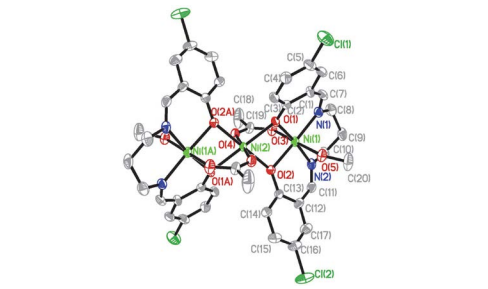

490–500 Organic chemistry

Synthesis, X-Ray Structure Determination and Related Physical Properties of Thiazolidinone Derivative by DFT Quantum Chemical Method

Youcef Megrouss, Fayssal Triki Baara, Nourdine Boukabcha, Abdelkader Chouaih, Antonis Hatzidimitriou, Ayada Djafri, Fodil Hamzaoui

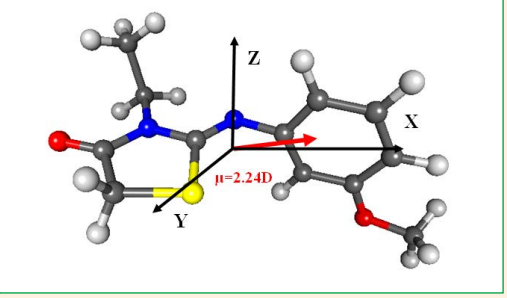

501–509 Biochemistry and molecular biology

Feedback Regulation of Cathepsin C by the Propeptide Dipeptides of Granzymes A and B

Janja Božič and Iztok Dolenc

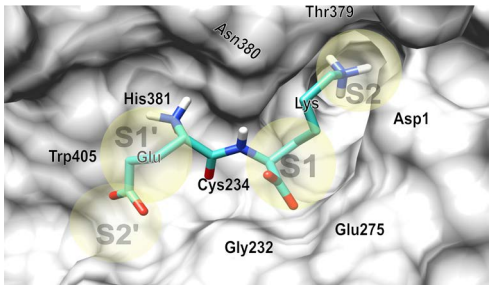

Feature article

Fluoride in Human Health and Nutrition

Dona Štepec[1,2] and Maja Ponikvar-Svet[1,2,*]

[1] *Department of Inorganic Chemistry and Technology, Jožef Stefan Institute, Jamova cesta 39, 1000 Ljubljana, Slovenia*

[2] *Jožef Stefan International Postgraduate School, Jamova cesta 39, 1000 Ljubljana, Slovenia*

** Corresponding author: E-mail: maja.ponikvar-svet@ijs.si*
Tel.: +386 1 477 32 03

Received: 03-13-2019

Abstract

Fluorine is in the form of fluorides ubiquitous in nature and as such an inevitable part of our environment. In small amounts, it is known to have beneficial effects on dental health. On the other hand, excessive chronic intakes can result in adverse effects including the development of dental fluorosis in children and/or skeletal fluorosis in both children and adults. The adequate intake has been set, based on empirical observations, at 0.05 mg/day/kg body weight however, the threshold between beneficial and harmful effects is narrow. Despite numerous studies, knowledge on the fluoride toxicity is still relatively poor. In this review, the role and the effects of fluoride on human health are enlightened. Some of the fluoride controversies are discussed and future research directions suggested.

Keywords: Adequate Intake; Adverse effects; Exposure; Fluoride; Fluorine; Human Health

1. Introduction

Fluorine is chemically most reactive of all the elements and is never or rarely encountered in nature as elemental fluorine. Two extremely rare exceptions where fluorine as gas could be trapped within the crystal of antozonite[1] and villiaumite[2] were recently reported.

In combination with other elements, it comprises 0.065% of the earth's crust, being the thirteenth element in abundance on the planet.[3] A brief note on terminology is in order before proceeding. In this paper, the term fluorine (F) is used to denote the element in any of its forms and fluoride (F^-) to denote the predominant chemical form of inorganic fluoride in which the element is found in nature and to which a fluoride ion selective electrode (ISE) responds.

Fluoride is an inevitable part of the biosphere and human life. The average F contents in soil range from about 100–600 mg/kg[4,5] from which about 0.05–0.5% represents water soluble fluorides.[6,7] Natural waters contain fluoride in varying concentrations, from trace amounts to some mg/l and even toxic concentrations. Waters with high concentrations of fluoride are usually found at the foot of high mountains and in areas with geological deposits of marine origin. The highest fluoride levels have been recorded in the Kenyan lakes Elementaita (1640 mg/l) and Nakuru (2800 mg/l).[8] Fluoride concentrations in ambient air are generally lower than 1 μg/m^3.[9]

The F is released into the air in a form of gaseous or particulate fluorides from natural sources, like dissolution of minerals, volcanoes, marine aerosols, and forest fires[10,11] and from different industrial activities, like phosphate fertilizers and elemental phosphorus production, aluminium smelting, petroleum refining, glass, brick, and ceramic manufacturing.[12]

Combustion of the coal and fuel and controlled fluoridation of drinking-water supplies also contribute to the fluoride dispersion.[13,14] Use of organofluorine compounds serving as pharmaceuticals, agrochemicals, refrigerants, pesticides, surfactants, fire extinguishing agents, fibers, membranes, ozone depletors, and insulating materials is in increase. Over 20% of approved pharmaceutical agents including several of the top drugs and 30–40% of commercially available agrochemicals are organofluorine compounds.[15,16] All these processes and uses result in accumulation of fluoride compounds in soils, surface waters and groundwater reserves, air, and in the living organisms.

The effect of fluoride on humans is a dual one. For over eight decades, it has been recognized that small amounts of fluoride have proven benefits for dental health. This resulted in widespread use of fluorides in public health practices.[17] Continuous exposure to high levels, on the other hand, leads to severe adverse effects in humans, which include the development of dental fluoro-

sis in children or skeletal fluorosis in both, children and adults.[17–20]

The "optimal" (or "adequate") daily intake of fluoride for children between 0.05 and 0.07 mg/kg body weight,[21] that is still accepted worldwide, is based on empirical observations. In Europe, the European Food Safety Authority (EFSA) set, because of proven benefits of small amounts of fluoride on the prevention of caries, the adequate intake (AI) of fluoride from all sources (including non-dietary sources) at 0.05 mg/day/kg body weight for both children and adults.[22]

The primary sources of ingested fluorine for humans are water, beverages and food.[23] In some countries, fluoride is deliberately added to salt[24] or milk[25] or public water supplies.[26,27] Intake with fluoride containing dentifrices, especially in children, should be considered.[28,29] In endemic fluorosis areas intake of fluoride with drinking water[30] or brick tea[31] and coal-burning[32] were reported to result in development of skeletal fluorosis.[33–36]

The adequate intake of fluoride in relation to its beneficial/adverse effects and the main sources of fluoride for humans are graphically depicted in Figure 1.

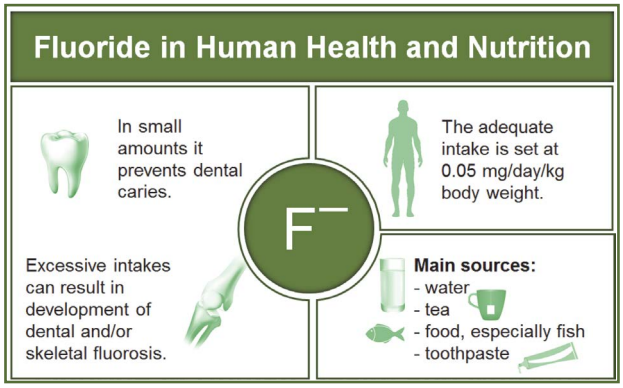

Figure 1: The adequate intake of fluoride in relation to its beneficial/adverse effects and the main sources of fluoride for humans

Fluoride remains a subject of debate, time and time again, especially in view of the current knowledge on its possible adverse effects. The aim of this paper was twofold: first to provide the adequate background information on fluoride, which would assist in understanding its role and effects on humans, and, second, to present some of the analytical problems associated with the determination of fluoride at low levels as present in human and environmental samples. In addition, some of the fluoride controversies related to the intake of fluoride by humans and its impact on health were discussed.

2. Beneficial Effects of Fluoride on Human Health

Fluoride in the body is mainly associated with calcified tissue, i.e. teeth and bone which are its primary targets. Beneficial effects of fluoride on dental health and on the increase of bone mineral content were suggested.

2. 1. Effects on Dental Health

Until the 1980's the paradigm was that, to exert its maximum cariostatic effect, fluoride had to become incorporated into dental enamel during teeth development by forming hydroxyfluorapatite, which is more resistant to ingested acids or to acids generated by oral bacteria from ingested sugars.[37]

The new paradigm, which surprisingly slowly modified fluoride caries research, was introduced in 1981.[38] It explains that fluoride controls caries lesion development predominantly, if not entirely, via its topical effect on de- and re-mineralization processes taking place at the interface between the tooth surface and the oral fluids.[38,39] Thus, topical use of fluoride is recommended, rather than systemic.

Fluoride also interferes with the metabolism of oral microbial cells by a direct inhibition of cellular enzymes (directly or in combination with metals) or enhancing proton permeability of cell membranes in the form of hydrogen fluoride (HF).[40,41]

2. 2. Osteoporosis Treatment

Since the 1960s, fluoride at high dose levels (approximately 20–30 mg/day) has been used to treat age-dependent osteoporosis.[12] Such treatment is currently not recommended. Although it may increase bone mass, the newly formed bone may lack normal structure and strength.[42–44] The effect is more apparent in trabecular bone where volume and thickness is increased but without a concomitant increase in trabecular connectivity resulting in reduced bone quality.[45]

2. 3. Other Functions

No average requirement (AR) of fluoride for the performance of essential physiological functions can be defined, i.e. fluoride is not essential for tooth development and has no known essential function in human growth and development.[22] A statement that "no fluoride deficiency disease has ever been documented for humans"[46] is controversial. An experimental diet completely free of fluoride, capable of provoking fluoride deficiency, is difficult to obtain.[23] It is also difficult to prove that it is free of fluoride, because of methodological and analytical problems in determining fluorine at low levels (see also section Fluorin(d)e analytical methods).[23]

3. Adverse Effects of Fluoride

The terms adverse effects and side effects are often used interchangeably although their meaning is different.

Adverse effects are unintended effects that occur when a medication is administered correctly while a side effect is a secondary unwanted effect that occurs due to drug therapy. Side effects are most often mild in nature and often self resolving but adverse effects can be fatal and need to be reversed or antidote immediately. Adverse effects reduce either by reducing the dose of the medicines or by stopping the administration of the drug altogether.[47,48] There are many fluoride related adverse effects. Their symptoms are nonspecific and are very much similar to the adverse and/or side effects of many other drugs, vitamins, minerals or dietary supplements. We should be therefore not surprised if fluoride related adverse effects are ascribed to other causes than fluoride.

3. 1. Symptoms of Fluoride Toxicity

The toxicity of fluorides is due to the toxicity of the fluoride ion, a direct cellular poison that binds calcium and interferes with the activity of proteolytic and glycolytic enzymes.[49] As such, the toxicity of fluoride depends on the type of compound ingested. Generally, weakly soluble or insoluble salts of inorganic fluorides, such as calcium fluoride, are less toxic than those that are more soluble, such as sodium fluoride.

3. 1. 1. Acute Exposure

Ingested fluoride forms hydrofluoric acid at a pH typical of gastric juice. Acute high oral exposure to fluoride may lead to (with increased seriousness of observed symptoms) nausea, vomiting, abdominal pain, diarrhea, drowsiness, headaches, polyuria and polydipsia, coma, convulsions cardiac arrest, muscle paralysis, carpopedal spasm, spasm of the extremities occurred and death.[50] The most frequently cited range for the certainly lethal dose (CLD) of sodium fluoride is based on a review of case reports prepared by Hodge and Smith.[51] It is set between 32 and 64 mg/kg body weight, which corresponds to 5–10 g of sodium fluoride for a 70 kg person).[52] The probable toxic dose (PTD) for children, defined as the dose of ingested fluoride that should trigger immediate therapeutic intervention and hospitalization, because of the likelihood of serious toxic consequences, is set at 5.0 mg/kg body weight.[51] Contact of liquid HF with the skin can produce severe burns; the gas is corrosive to the eyes and mucous membranes of the respiratory tract.[53] The basis of the treatment of fluoride poisoning is intravenous or intramuscular calcium therapy.[54–56]

3. 1. 2. Chronic Exposure

Development of dental fluorosis in children and/or skeletal fluorosis in both children and adults are the most obvious adverse effects associated with chronic excessive fluoride intakes. Both are an ancient problem because humans settled since ever in areas having high concentrations of fluoride in drinking water.[18] A threshold of 0.03 mg/day/kg body weight has been suggested for the appearance of dental fluorosis however even this intake will result in a certain, although low, level of fluorosis in a population.[39,57]

Enamel fluorosis and primary dentin fluorosis would begin with the lower incisors, which complete mineralization at approximately 2–3 years of age, and end after mineralization of the third molars.[58] Development of dental fluorosis has been controversial at times – on the one hand it is considered as cosmetic and, on the other, as having an adverse effect.[59]

The early symptoms of skeletal fluorosis include stiffness and pain in the joints. In severe cases, the bone structure may change and ligaments may calcify, with resulting impairment of muscles and pain. Constriction of vertebral canal and intervertebral foramen exerts pressure on nerves, blood vessels leading to paralysis and pain.[60]

A review paper in which fluoride has been linked to causing neurodevelopmental harm,[61] has been a subject of debates.[62,63] Recent research however evidenced, that children living in fluorosis prevalent areas have five times higher chances of developing a low intelligence quotient (IQ) than those living in less fluorosis areas[64] and that IQ level was negatively correlated with fluoride concentration level in drinking water.[65] Higher prenatal fluoride exposure was associated with lower scores on tests of cognitive function.[66]

Earlier studies suggested a protective effect of fluoride against Alzheimer's disease. [67,68] This is in contrast to the later studies. The greatest impairments of structure and function may come about through the actions of charged and uncharged Al–F complexes. These complexes may cross the blood brain barrier and accumulate in the brain thus inducing brain neurotoxicity.[69–71]

Many other associations between increased fluoride concentrations in fluoridated drinking water and possible adverse effects were suggested, e.g., decreased total fertility rate in both females and males,[72] diabetes[73] and greater impairment of thyroid function.[74]

3. 2. Mechanisms of Fluoride Toxicity

Fluoride exerts different effects on the cell machinery leading to cell death, apoptosis and/or necrosis both in vivo and in vitro. Necrosis has been observed as a primary mechanism of cell death after a short exposure (≈ 1 h) to fluoride at relatively high concentrations (≈ 100 μm).[75] At relatively lower concentrations (around few mM) different molecular mechanisms lead to fluoride-induced cytotoxicity and eventual apoptotic cell death of different cells from different organs and tissues, e.g. lungs, kidneys, liver, brain, pancreas, thymus, endometrium, bone marrow, hair follicles, erythrocytes, leukemic cells. The molecular mechanisms underlying fluoride-induced apoptosis are

different by nature and include the stimulation of G protein-dependent signaling systems, oxidative stress, ATP depletion, activation of the cell surface death receptors, disruption of outer mitochondria membrane, activation of caspases, alterations in the ratio of anti-apoptotic-apoptotic Bcl-2 proteins, upregulation of p53 expression, expression of apoptosis-related genes, endoplasmic reticulum stress and disturbances in protein synthesis. Reviews on the intracellular molecular mechanisms proven to be responsible for cytotoxicity and development of cell death induced by inorganic fluoride were recently reported.[19,20]

4. Absorption, Metabolism, Distribution and Excretion of Fluoride

In humans, the predominant route of fluoride absorption is via the gastrointestinal tract. Except for occupational exposure or exposure to fluoride by coal or fuel burning, exposure to fluoride by inhalation is negligible.[14,76] Dermal absorption is insignificant except in cases of hydrofluoric acid burns.[77]

When ionic fluoride enters the acidic environment of the stomach lumen, it is largely converted to weak acid hydrogen fluoride with a p*K*a of 3.19.[3] The higher acidity of the stomach speeds up the process of absorption by passive diffusion.[78] The coefficient of permeability of lipid bilayer membranes to HF is 1 million times higher than that of F^-[79] so there is no need for specialized enzymatic systems to be involved.[80] Around 70–75% of fluoride not absorbed from the stomach will be rapidly absorbed from the small intestine in a pH-independent process.[81,82]

Factors like bioavailability, amount of ingested food, emptying the stomach, the presence of the bile salts, concentrations of pepsin and pancreatin all affect the absorption from the stomach. Bioavailability (absorption and utilization) is the most important among them. Bioavailability is a measure of the amount of an administered dose that reaches the blood stream. It is 100%, by definition, when a medication is administered intravenously.

The bioavailability of fluoride from sodium fluoride (NaF) tablets, as used in many caries-prevention programmes, from a fasting stomach, is almost 100%.[83] It is also high from other soluble fluoride compounds that occur naturally or are added to drinking water and yield fluoride ions on dissolution, e.g. KF, Na_2SiF_6, H_2SiF_6.[84] The degree of fluoride absorption is highly affected by the presence of diet containing high contents of calcium and certain other divalent (Mg^{2+}) or trivalent (Al^{3+}, Fe^{3+}) cations with which fluoride can form insoluble or poorly soluble compounds.[85] In studies on adults, this bioavailability was decreased to 50–79% by co-administration of milk or calcium rich products.[86,87] The poor fluoride bioavailability, in the range of 4–24%, observed from food such as bone meal, fish bone meal, canned sardines and chicken bone meal, was ascribed to the high content of calcium in these foods.[88] Fluoride bioavailability from typical meals eaten in different regions of India was found to be low (2–32%).[89]

The halftime for fluoride absorption is approximately 30 minutes and peak plasma concentration usually occurs within 30–60 minutes.[83,87–91] Fluoride is then rapidly distributed in plasma and deposited in bone and other calcified tissues containing approximately 99% of the body's fluoride.[92] The remainder of fluoride is distributed between blood and soft tissues, where a steady-state distribution between extracellular and intracellular fluids is established.[92]

In adults, about 50% of daily fluoride intake is associated with the calcified tissues within 24 hours and the remaining 50% is excreted in urine.[93] This 50:50 distribution is strongly shifted to greater retention in the very early and probably towards greater excretion in the later years of life.[93] In adults, about 40–60%[94] of the daily intake of fluoride is excreted in the urine and in children about 45%.[95] Less than 10% of the daily intake of fluoride is excreted in faeces.[96,97] It was estimated that 1% or less of an ingested dose is excreted in saliva, which returns back to systemic circulation.[98] Sweat provides only a minor route of fluoride excretion.[80]

General features of fluoride metabolism (fluoride flow through the organism) are schematically presented in Figure 2.

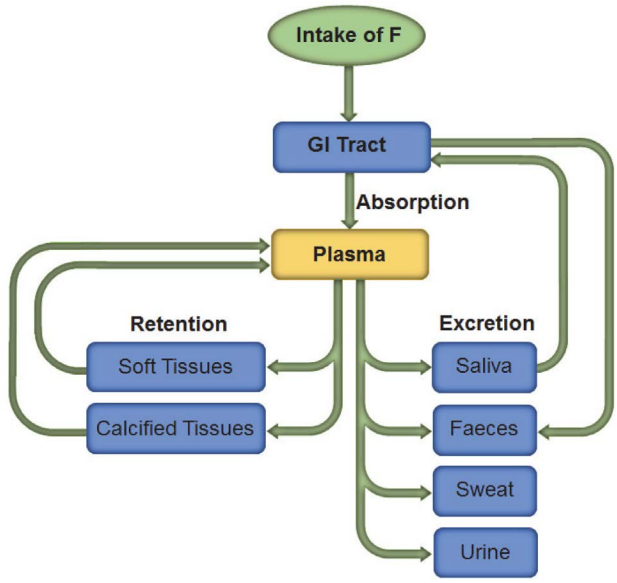

Figure 2: General features of fluoride metabolism

5. Biomarkers of Fluoride Exposure

Identifying and monitoring the human exposure to fluoride is of especial importance in children at the age of risk for development of dental fluorosis and in populations exposed to fluoride, i.e. with tea, via occupational exposure, in areas of the world with endemic fluorosis.

Only absorbed fluoride is involved in the development of fluoride related adverse effects. Identification and monitoring deficient or excessive intakes of biologically available fluoride can be achieved through the use of biomarkers of fluoride exposure.[99]

According to the US National Academy of Sciences (US NAS)[100] definition, accepted for fluoride also by the World Health Organization (WHO),[101] biomarkers are defined in a broad sense to include almost any measurement reflecting an interaction between a biological system and a potential hazard, which may be chemical, physical or biological. The measured response may be functional and physiological, biochemical at the cellular level, or a molecular interaction. For fluoride, several biological fluids and tissues can serve as biomarkers, which can be according to time-perspective classification classified as: (1) contemporary; (2) recent; and (3) historical markers.[101] Extensive information on biomarkers of exposure to fluoride can be found in recent reviews.[102–105] In this section, only a concise information will be presented.

5. 1. Contemporary Markers

The concentrations of fluoride in body fluids (plasma, saliva, urine, milk, sweat) and body tissues (bone surface) were all suggested to assess present or very recent exposure to fluoride. Their fluoride content depends on the intake via water, diet, fluoride supplements and fluoride-containing dentifrices. Fluoride ion does not produce any metabolites, so it is itself the measured indicator.

Both ionic and non-ionic fluoride forms exist in plasma. The ionic fluoride form is of far greater significance when evaluating the effect of fluoride on human's health.[106,107] For less than optimal water fluoride concentrations, the resting ionic fluoride concentrations in plasma ranged from 9.3 to 24.0 ng/ml,[102] however, the data across various age groups enabling to determine the "usual" concentrations are insufficient.[108]

Urine is regarded as the most suitable biomarker for predicting fluoride intake for groups of people, but not the individuals.[109] Using available data it was estimated that the ratio between the excretion and the intake of fluoride is 0.35 and 0.54 in children and adults, respectively above a threshold of total daily intake of 0.5 and 2 mg/day, respectively.[95]

The whole saliva tends to be contaminated by fluoride from the oral environment. Saliva is therefore usually collected from parotid and submandibular/sublingual ducts. Fluoride concentrations in saliva closely follow the plasma concentration but at a lower level. In adults, the ratios of saliva to plasma fluoride concentrations, under resting conditions, varied from 0.32–0.55 for parotid saliva[110] and from 0.61 to 0.88 for submandibular saliva.[98] In the same series of experiments, the ratio for fluoride concentrations in whole saliva and plasma was 1.10.[111] The data on a normal range of fluoride concentrations in ductal saliva as a basis for recommending saliva as a marker of fluoride exposure are however insufficient.[102]

Data on fluoride contents in surface bone, sweat and human milk are rather limited and seem unsuitable for estimating contemporary exposure of humans to fluoride.[102]

5. 2. Recent Markers

In contrast to contemporary markers, whose fluoride concentrations provide a snapshot at a certain point of time and are subject to change due to recent fluoride intake and certain physiological variables, the concentration of fluoride in nails and hair is cumulative. It reflects the average level of intake over a time period taking into account their growth rate. Their major advantage over fluids and tissues as biomarkers for fluoride exposure is that they can easily be obtained in a non-invasive manner. The main issues related to fluoride in nails or hair, as biomarkers seem to be a preparation of the sample for the analysis and high possibility of external contamination. The content of fluoride in fingernails or toenails is about 0.5–5 μg/g[112] and in hair about 0.2–15 μg/g.[113] Extremely higher values in both nails and hair were also reported in populations occupationally exposed to fluoride or populations living in fluoride endemic areas.[112–115]

5. 3. Historical Markers

The main historical biomarkers that could indicate total fluoride body burden are a non-exchangeable inner compartment of bone and dentin.[102,103] Inner bone and dentin both increase with age due to continuous fluoride uptake throughout life.[106,116] In contrast, bulk enamel fluoride concentrations mainly reflect the level of systemic exposure to fluoride during tooth formation.[93] Bone sampling is next to ethical limitations, difficult and invasive. The X-ray screening for increased bone density could be performed, however only when the need for information justifies the radiation dose involved. In addition, bone density might not be related only to fluoride exposure or to bone fluorine content. Thus, teeth in particular third molars or premolars that are commonly extracted have emerged as potential historical biomarkers of exposure to fluoride.

6. Fluorin(d)e Analytical Methods

Fluoride of high concentrations in water or soil and gaseous fluoride emissions, which are all a consequence of natural or anthropogenic activities, represent a threat to vegetation and subsequently entire food chain in many parts of the world. Reliable analytical methods are therefore a prerequisite for the determination of human exposure to fluoride. The goal is to monitor the intake of fluoride and maintain it at adequate levels so that optimal protection against dental caries is achieved, without excessive intake

resulting in the appearance of adverse effects. Basic requirements for accurate and precise determination of fluorine in any type of the sample are: (1) the sample has to be appropriately pre-treated so that the required form can be determined; (2) interfering reactions or ions have to be effectively suppressed; (3) the final concentration of fluorine must be above the detection limit of the method; and (4) the result should be reported together with a measurement uncertainty (MU) evaluated in accordance Guide to the Expression of Uncertainty in Measurement (GUM).117.[117]

6. 1. Forms of Fluorine

As noticed in the Introduction of this paper, the term fluorine (F) is used to denote the element in any of its forms and fluoride (F^-) to denote predominant chemical form inorganic fluoride in which the element is found in nature and to which a fluoride ion selective electrode (ISE) responds. Difference between F and F^- in inorganic compounds, which leads to the amount of bound fluoride was discussed.[118]

In biological samples such as human and animal serum fluorine can be present also in the form of organic fluorine. This represents covalent fluorine that is bound to carbon in all organic fluorine compounds and results from exposure to certain fluorine-containing compounds from natural and/or industrial sources.[119] Classification of different forms of fluorine in biological materials was extensively discussed.[120–122]

6. 2. Sample pre-treatment Procedures

The approach to sample preparation is dependent on the type of matrix and the form of fluorine to be determined. Fluorine in samples can be determined as ionic, total or covalent fluorine.

6. 2. 1. Ionic Fluoride

The concentration of fluoride in water can usually be determined directly without pre-treatment. Dissolution in water prior to fluoride measurement is a valid approach also for determination of soluble fluorides in solid samples. During interpretation of the results it is necessary to consider equilibria between F^- and ions with which fluoride forms soluble or poorly soluble compounds, in relation to the employed analytical technique, e.g. Al^{3+}, Fe^{3+}, Si^{4+}, Sn^{4+}, Zr^{4+}.[85]

Methods for determining gaseous fluorides are generally based on the absorption of gaseous fluorides into a train of absorbing solutions, or collection on a filter with a treated pad and subsequent determination of fluoride.

6. 2. 2. Total Fluorine

Samples containing non-ionic inorganic fluoride and/or organic fluorine have to be decomposed prior to the measurement. Extraction or digestion with acids or mixtures of acids or digestion with alkaline solutions might dissolve the F in the samples only to varying degrees. Results of such studies are difficult or even impossible to compare, especially because there is no certified reference material (CRM) available to support the results of such measurements. Therefore, prior to quantification, samples must undergo a total decomposition to assure release of the inorganic or organic bound F to F^- and bring the solid sample in a water soluble form.

In the classical Willard–Winter[123] distillation procedure introduced in 1933, decomposition of compounds and separation of resulting fluoride from interfering substances take place concurrently. This technique and its modifications[124–126] have provided a wealth of information through the middle decades of the 20th century but, mostly because of its cumbersome procedure, have been replaced by simpler methods, like pyrohydrolysis[127,128] or diffusion methods.[129–131] Commonly used procedures nowadays for total sample decomposition involve oxygen bomb combustion,[132,133] open ashing[134,135] fusion with alkali metal hydroxides or carbonates[136,137] and microwave acid digestion.[138,139]

Reactions proceeding during decomposition of metal fluorides by pyrohydrolysis, oxygen bomb combustion and alkaline carbonate fusion and their related thermochemistry were discussed in our recent papers.[140,141] Calcium and magnesium fluoride, which can be in variable amounts present also in human, animal, vegetation and other environmental samples, were suggested as the most resistant ones to decompose among all the metal fluorides studied.

6. 2. 3. Covalent Fluorine

The basis for determination of organic fluorine in biological materials such as blood serum and soft tissues rely on the determination of total F with respect to F^- using total decomposition methods. As a faster alternative for sample preparation use of sodium biphenyl was described.[142] The method relies on reductive cleavage of the C–F bond, which is the strongest bond in organic chemistry[143,144].

6. 3. Methods for Determination of Fluoride

The methods for determination of F^- range from classical volumetric[123–125] to spectrophotometric[125,126] and fluorometric[145,146] methods. A breakthrough in the analytical chemistry of fluorine was in 1966 when the fluoride ion selective electrode (ISE) was introduced by Frant and Ross[147]. The electrode consists of a single crystal lanthanum fluoride (LaF_3) doped with europium (II) fluoride to improve its conductivity. The electrode is highly selective and covers a wide range of concentrations (1 mol/l to 10^{-5} mol/l). The limit of detection of fluoride ISE is limited by

the solubility of LaF_3 to ≈0.02 mg/l.[148] In our laboratory we developed a multiple known standard addition method for determination of fluoride based on spiking the samples with known amount of fluoride prior to the measurement. In this way the limit of detection (LOD) of ≈0.01 mg/l was achieved.[149]

Various chromatographic methods for fluoride determination include ion chromatography (IC),[150] gas chromatography (GC)[151,152] and high-performance liquid chromatography (HPLC).[153] The main issues related to the use of IC are that fluoride peak tends to overlap with the water negative dip and that monocarboxylic acids interfere because of co-elution with fluoride or only partial resolution. This makes IC suitable for determination of F^- in aqueous samples.[154–157] Use of GC has been reported for determination of fluoride in various kinds of biological matrixes however it is time consuming and requires trained personnel.[158] Use of HPLC with reverse-phase mode columns for determination of fluoride is rarely reported.[153]

Determination of fluorine by atomic absorption spectrometry (AAS), laser-induced breakdown spectroscopy (LIBS), inductively coupled plasma optical emission spectrometry (ICP–OES), or inductively coupled plasma mass spectrometry (ICP–MS) is almost impossible task because of high excitation and ionization potential (17.42 eV) of F and the location of its resonance line in the vacuum ultraviolet range (95 nm).[159] Use of molecular absorption spectrometry (MAS) methods with high-resolution continuum source (HR–CS) to determine fluorine through the absorption of diatomic molecules, such as CaF or GaF was reviewed.[160] Its major limitation is that online coupling with chromatographic separation methods is not possible. Use of mass-shift strategy using tandem inductively coupled plasma quadrupole mass spectrometry (ICP–MS–MS) was reported for the determination of fluorine.[161]

Less frequently used methods for determination of fluorine include polarography,[162] voltammetry,[163] sensors,[164] capillary zone electrophoresis (CZE),[165] near infrared spectroscopy (NIR),[166] ^{19}F-nuclear magnetic resonance (^{19}F-NMR),[167] neutron activation analysis (NAA)[168] and others.

6. 4. Measurement Uncertainty Evaluation

A truly informed decision, based on a measurement result, can only be made with the consideration of the MU.[169] Classically in analytical chemistry, the MU has been expressed as one standard deviation, thus including only random effects. A superior, more comprehensive approach is outlined in the definite document in the field of metrology GUM.[117] In this approach, in addition to random effects, also systematic effects are taken into account and all uncertainty components of each step of analytical procedure are identified, quantified and traceable[169] to the SI units. All these contributors are then combined and the MU is reported as an expanded uncertainty, which corresponds to the 95% level of confidence.[117]

Unfortunately, the only paper reporting procedure for evaluation of the MU according to the GUM for F is on determination of fluoride in water.[170] Recently we suggested a procedure for the MU evaluation for determination of F in solid samples, which must undergo a total decomposition before the measurement.[171] This makes evaluation of the MU much more complex, because: (1) in addition to the uncertainty of the measurement step also uncertainty of the decomposition step must be included; and (2) transformation of the sample from one chemical form to another cannot be traceable to any reference and therefore the highest form of traceability can be achieved by the use of matrix matched CRM.[172]

7. Sources of Oral Exposure to Fluoride

Knowing total fluoride contents contributing to the oral exposure to fluoride, e.g. water and beverages, different food items, dental products and alternatives to water fluoridation, like fluoridated salt or milk and fluoride supplements, can assist in estimating the total daily intake of fluoride and the measure of exposure.

7. 1. Drinking Water

Natural waters aimed also for human consumption contain varying concentrations of fluoride, from trace amounts to some mg/l and even toxic concentrations. Waters with high concentrations of fluoride are usually found at the foot of high mountains and in areas with geological deposits of marine origin. Large variations in natural fluoride contents of drinking water between and within countries can be observed.[173,174]

The WHO, based on earlier documents (from 1984, 1993 and 2004),[77,175,176] set in 2010 the guideline value for fluoride in drinking water, by taking into account drinking water consumption, at 1.5 mg/l.[26] This is in conflict with the WHO recommendation from 1994 according to which the absolute upper limit for fluoride in drinking water is 1.0 mg/l.[99] In the European Union (EU) drinking, water for human consumption may not contain more than 1.5 mg/l.[177] The earlier recommended optimal fluoride concentration for fluoridated water in the US was recently reduced from 0.7–1.2 mg/l to 0.7 mg/l.[178] It has to be pointed out that few subjects in medicine have proved more controversial than fluoridation of public water supplies. The controversy is illustrated by the fact that, while the US Centers for Disease Control and Prevention (CDC) claimed that water fluoridation is one of the ten great public health achievements in the US during the 20th century,[179]– 69% of the population receives fluoridated drinking water[27] – water fluoridation is banned in most of Europe.[173]

Use of bottled water is in increase. In the EU, bottled water exceeding fluoride concentration of 1.5 mg/l shall bear on the label "contains more than 1.5 mg/l of fluoride: not suitable for regular consumption by infants and children under 7 years of age" and a maximum limit of 5 mg/l is set for naturally present fluoride.[180] The concentration of fluoride in bottled water in the US depends on whether fluoride is naturally present or added and on the annual average of maximum daily air temperatures at the location where the bottled water is sold at retail. Thus, the concentrations of fluoride in bottled water packaged in the US and imported water should not exceed 2.4 and 1.4 mg/l, respectively.[181]

7. 2. Tea and Beverages

The tea plant (*Camellia sinensis* L.; family Theacea) (Figure 3) is known to take up fluoride from the soil and accumulate it in the leaves. The total fluorine content of the leaves typically ranges between 50 and 900 mg/kg.[182–186] About 25–100% of fluorine is released during the infusion, thus the infusions may contain about 0.3 to 8.8 mg/l of fluoride, depending also on the amount of dry tea used, the granulation of the tea, the concentration of fluoride in the added water, the presence of milk, duration of infusion, etc.[182–186] Concentrations of fluoride in ready-to-drink tea were reported to range between 0.01 to 4.1 mg/l[187–189] and in one study an extraordinarily high average of 25.7 mg/l of fluoride was reported.[190]

Figure 3: Tea harvesting in Sri Lanka (Photo: M. Ponikvar-Svet)

Concentrations of fluoride in soft drinks, e.g. nectars, juices, juice drinks, ranged between 0.10–2.0 mg/l in Portugal,[191] 0.07–1.14 mg/l in the Canary Islands,[192] 0.02–2.80 mg/l in the US[193] and 0.07–1.42 mg/l in Mexico.[194] Concentrations of fluoride in juices and juices-flavoured drinks for infants and children ranged between 0.01–0.25 mg/l in Poland[195] and 0.11–1.81 mg/l in the US.[196]

Carbonated soft drinks analysed in Europe contained 0.10–0.38 mg/l of fluoride.[191,192] The observed concentrations were higher in the US and Mexico and ranged from 0.02 to 1.28 mg/l[197] and from 0.07 to 1.62 mg/l, respectively.[194]

The range of fluoride concentration in beer available in Europe was 0.067–1.12 mg/l.[198–200] High concentrations, 1.77 and 1.66 mg/l of fluoride, were determined in beer from Ireland and the US, respectively.[194,200] Wide variations in fluoride concentrations found in different studies can be explained either by low natural presence of fluoride or by high presence of fluoride due to naturally occurring or artificially added fluoride in water used in manufacturing process.

Fluoride concentration in bottled wines of the different types from the Canary Islands ranged between 0.03 and 0.70 mg/l[201–203] and from Turkey between 0.02–0.38 mg/l.[204] High concentrations of fluoride between 0.23 to 2.80 mg/l in nineteen California wines apparently resulted from the use of cryolite as a pesticide.[205]

7. 3. Milk and Baby Formulas

The reported concentrations of fluoride in commercially available milk were generally low and did not exceed 0.1 mg/l.[206,207] High concentration of fluoride in pasture or drinking water of livestock might however contribute to fluoride levels in milk of different cattle.[208–210] Reported fluoride concentrations in soya milk varied between 0.01 and 0.964 mg/l.[211–213]

Fluoride concentrations in breast milk are generally low even at very high intakes of fluoride by mothers. The average concentrations range from 0.002 to 0.073 mg/l.[214] Surprisingly high concentrations of fluoride in breast milk were determined in one study conducted in the high altitude (>2000 m). In that study the fluoride contents of breast milk of mothers with dental fluorosis and children with dental fluorosis, in the high altitude ranged between 0.13–0.99 mg/l (average 0.55 mg/l), while breast milk mothers in the control group without dental fluorosis contained 0.001–0.10 mg/l (average 0.006 mg/l).[215] These results suggested that there is more to understand about the factors affecting the level of fluoride in breast milk, such as the effect of altitude.[216]

Concentrations of fluoride between 0.01 and 0.75 mg/l were reported in a review on fluoride concentration in infant formula products reconstituted with fluoride-free water according to the manufacturer's instructions.[217] When formulae were prepared with water of differing fluoride concentrations, the fluoride concentration was found to be a simple linear function of water fluoride concentration.[217]

7.4. Foods

The fluorine contents in different foods and drinks in this paper are illustrated using the data from the USDA National Fluoride Database[218] and the United Kingdom (UK) Fluoride Database.[219,220] The USDA Database[218] is based on the data extracted from reviews of existing scientific literature and unpublished results mainly from the

Table 1: The averages and the ranges of total fluorine contents (w_F) in different food groups on a fresh weight basis listed in the USDA National Fluoride Database[218] and UK Fluoride Database[219,220] analyzed as ready-to-eat items

	USDA Database			UK Database		
	$n_{products}$ [a]	w_F (µg/100g) Average (SD)	Range	$n_{products}$ [a]	w_F (µg/100g) Average (SD)	Range
Fruits, nuts[b]	19	5 (3)	1–12	19	4 (4)	1–19
Fats, oils	6	9 (10)	1–25	8	4 (8)	0–17
Vegetables, spices, herbs[c]	37	17 (15)	1–49	23	7 (6)	1–19
Meat and products	17	24 (14)	4–48	25	7 (7)	2–24
Milk, egg and products[d]	13	12 (13)	1–35	28	7 (13)	1–59
Cereal products	9	27 (18)	6–51	16	31 (21)	4–57
Breakfast cereals	12	44 (19)	17–72	12	26 (30)	4–75
Soups, sauces, gravies	22	39 (34)	1–132	11	14 (21)	1–49
Sweets, snacks	46	33 (26)	1–106	81	15 (19)	1–90
Beverages, water	132	48 (34)	2–204	22	13 (11)	0–45
Tea	25	262 (136)	9–584	3	30 (27)	12–61
Fish, shellfish and products	7	111 (87)	18–210	13	149 (298)	8–1054
Dishes	28	37 (20)	5–84	30	15 (12)	1–51
Infant food and drinks	50	12 (14)	0–67	251	15 (21)	1–120

[a] Number of analyzed items [b] The highest content was not considered (234 µg/100 g of F in raisins) [c] The highest content was not considered (115 µg/100 g of F in french fries, McDonald's) [d] The highest content was not considered (112 µg/100 g of F in cream substitute, powdered)

period between 1977 and 2003. The more recent UK Database[219,220] was generated in a period between 2003 and 2015 through a range of research projects.

These databases arrange food and drink items in different groups, therefore the F contents are difficult to compare. Thus, we re-positioned all food items and drinks from both databases within the same groups. The averages and the ranges of total fluorine contents in these food groups are presented in Table 1.

The presented data compiled from the original databases (Table 1) show a wide variation in fluorine contents within and between individual food groups (see SDs and ranges). The average content of F of all food groups is 2.7-fold higher in the USDA Database than in the UK Database, this is 47 µg/100 g as opposed to 17 µg/100 g. The average content of F in the USDA Database remains 1.9-fold higher than in the UK Database even if tea is taken aside. This can be explained by different levels of fluoride in water used for the preparation of the products requiring water; results obtained using tap water containing 0.71 mg F^-/l are reported in the USDA Database and results reported using tap water containing 0.05–0.13 mg F^-/l were selected from the UK Database. The fluorine contents in individual food groups were, for easier visualization presented also in Figure 4.

The content of fluorine in food is generally below 50 µg/100 g (Figure 4 and Table 1). Exceptions to this include: (1) processed food (breakfast cereals, sweets, snacks, sauces) and beverages which can contain considerable amounts of fluorine if fluoridated water is used during the production process or for their preparation; (2) tea, which can during infusion release high amounts of fluoride accumulated in the leaves; and (3) fish and shellfish which might

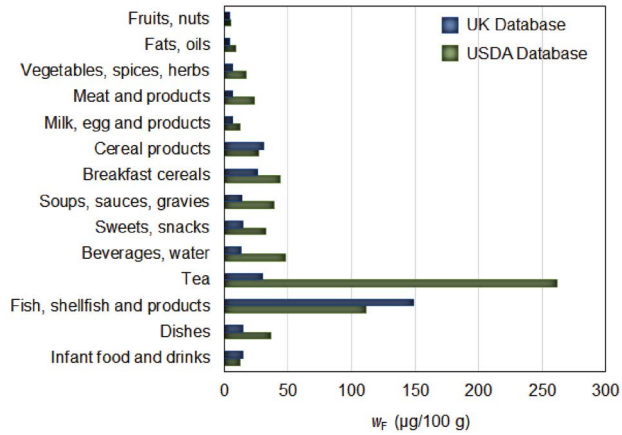

Figure 4: The average contents of fluorine in different food groups on a fresh weight basis listed in the USDA National Fluoride Database[218] and the UK Fluoride Database[219,220] analyzed as ready-to-eat items

contain high fluorine contents, if analyzed samples, due to mechanical deboning, contain bones and exoskeleton remains, where fluoride is accumulated from the sea.

Finally, it is worth mentioning that in addition to these databases many studies reported the contents of total and/or free fluoride in different food items.[221–227] The results of these studies are difficult to compare, because the determined level of fluorine in food is among other influenced by: (1) the locality in which the food is grown; (2) the differences in the amount of fertilizer and pesticides applied or differences in feeding routine; (3) the type of processing the food receives; (4) the amount of water and the fluoride content of water used in their preparation; (5) different sample pre-treatment procedures; and (6) the differences in the analytical procedures. In addition, the re-

sults are not reported according to the Guide to the Expression of Uncertainty in Measurement (GUM).[117117]

7. 5. Fluoride Containing Dental Products

Fluoride containing dental products (toothpaste, rinses and gels) although not considered as a dietary source, can increase the total oral intake of fluoride considerably, especially when used inappropriately. Because of poor control of the swallowing reflex, fluoride ingestion by young children needs to be during the first six years of life carefully controlled and the best balance between risk and efficacy might be achieved by using small amounts of high fluoride toothpaste under close supervision from parents.[28,29] Fluoridated toothpaste (Figure 5) for children usually contains 250 to 500 μg/g of fluoride[228] and for adults from 1000–1500 μg/g of fluoride.[229]

Figure 5: Toothpaste contributes significantly to the daily intake of fluoride especially in children (Photo: M. Ponikvar-Svet)

7. 6. Fluoridated Salt or Milk and Fluoride Supplements

Salt fluoridation which begun in 1956 in Switzerland[24] is practiced as an alternative to water fluoridation. It has been estimated that between 40 million and 280 million people worldwide use fluoridated salt, mainly in European, South American and Central American countries, some Asian countries, including Cambodia and Laos and in Africa, Madagascar. For salt fluoridation, sodium fluoride and potassium fluoride are mostly used at a concentration of 250–300 mg/kg of fluoride.[231,232]

Milk as a relatively cost-effective vehicle for fluoride delivery in the prevention of dental caries was first proposed in the 1950s.[25] As suggested in an update to a Cochrane Review[233] first published in 2005,[234] there is low quality evidence to suggest fluoridated milk may be beneficial to schoolchildren, contributing to a substantial reduction in dental caries in primary teeth.

Systematic reviews[235,236] have shown that there is weak and inconsistent evidence to demonstrate that fluoride supplements administered in the form of tablets, drops, lozenges or chewing gums can effectively prevent caries in primary teeth. However, there is strong evidence that fluoride supplements can prevent caries in permanent teeth. The use of fluoride supplements was associated with a high risk of mild-to-moderate fluorosis. Current recommendations on their use are controversial – on one hand European Academy of Paediatric Dentistry (EAPD) recommends that fluoride tablets and fluoride drops could be considered on an individual basis for children at high risk of caries[237] and, on the other hand, the American Academy of Pediatric Dentistry (AAPD) recommends that fluoride dietary supplements should be considered for children at caries risk who drink fluoride-deficient (less than 0.6 mg/l) water.[238]

8. Daily Intake of Fluoride

Estimating exposure to fluoride, especially in children, is of crucial importance to avoid potential problems associated with too low or too high intakes. The adequate intake (AI) of fluoride from all sources (including non-dietary sources) is because of proven benefits of fluoride on dental health set at 0.05 mg/day/kg body weight for both children and adults.[22] Major contributors to the oral intake of fluoride are drinking water, tea, beverages, foods and fluoride containing dental products.[23] The contribution of inhaled airborne fluoride, or fluoride from the soil, to the total fluoride intake is, under normal conditions, small[23] and is beyond the scope of this paper.

There is a lack of data on the total fluoride intake from dietary and non-dietary sources based on analyses of individual actual diets.[22] The estimates are often based on the estimates of quantities of foods consumed, such as standard food tables or questioners, rather than actual quantities of food consumed.[22] This might result in under or over estimates of actual fluoride intakes because of wide variations in fluoride contents of individual food items.

8. 1. Fluoride Intake in Children

As reported the prevalence of enamel fluorosis is over the last three decades on the rise in the United States (US).[58,239,240] The cases reported include also more cases of moderate-to-severe fluorosis.[58,239–241] One of the possible reasons might be that fluoride appears to be more readily available for consumption nowadays during the critical window when enamel is most susceptible to fluorosis.[240]

Table 2: Estimated intakes of total fluoride from diet and toothpaste for children expressed as averages in mg/day/kg body weight by F^- concentration in water ($\gamma(F^-)_{water}$) and age groups; fluoride intake by breastfed infants is not listed

		mg/day/kg body weight				
Age (yr.)	**$\gamma(F^-)_{water}$ (mg/l)**	**Food (SD)**	**Toothpaste (SD)**	**Total (SD)**	**Note**	**Ref.**
Nonfluoridated water						
2–6	0.08	0.017 (0.009)	NA	NA	a	242
up to 4	0.04	0.006	0.055	0.061	b	243
up to 4	0.04	0.011	NA	0.011	b, c	243
4	0.04–0.07	0.033 (0.012)	0.016 (0.011)	0.050 (0.019)	a	244
4	0.06–0.07	0.033 (0.012)	0.029 (0.016)	0.062 (0.022)	a	244
4.75	0.08–0.015	0.02 (0.01)	NA	NA	b, d	245
5.25	0.08–0.015	0.018 (0.018)	NA	NA	b, d	245
6–7	0.08	0.008 (0.004)	0.023 (0.026)	0.031 (0.025)	a	246
8	0.04–0.07	0.033 (0.012)	0.012 (0.007)	0.048 (0.038)	a	244
8	0.06–0.07	0.030 (0.014)	0.013 (0.006)	0.043 (0.016)	a	244
	Average (SD)	**0.021 (0.011)**	**0.023 (0.015)**	**0.044 (0.018)**		
Fluoridated water						
up to 4	0.64	0.011	0.037	0.048	b	243
up to 4	0.64	0.015	NA	0.015	b,c	243
2–5	0.5–0.7	0.033 (0.013)	0.01 (0.01)	0.043 (0.016)	b	247
2–6	0.6–0.8	0.028	0.036 (0.028)	0.064 (0.035)	a	248
3–4	<0.7	0.02 (0.01)	0.00	0.02	a	249
3–4	0.7–1.2	0.04 (0.01)	0.01	0.05	a	249
4	0.64	0.025 (0.010)	0.046	0.071 (0.036)	b	250
4	0.8–1.0	0.041 (0.026)	0.018	0.059 (0.029)	a	244
4–6	1	0.027 (0.014)	0.030	0.058 (0.042)	b, e	251
4–6	1	0.026 (0.014)	0.028	0.054 (0.034)	b, e	251
6–7	0.47	0.016 (0.005)	0.022	0.038 (0.038)	a	246
6–7	0.82	0.025 (0.014)	0.022	0.047 (0.008)	a	246
8	0.8–1.0	0.041 (0.039)	0.015	0.057 (0.045)	a	244
	Average (SD)	**0.027 (0.010)**	**0.023 (0.013)**	**0.048 (0.017)**		
High fluoridated water						
3–4	>1.2	0.05 (0.03)	0.01 (0.02)	0.07	a	249
4	2.0–3.0	0.362 (0.181)	0.022 (0.014)	0.385 (0.184)	a	244
8	2.0–3.0	0.307 (0.120)	0.019 (0.016)	0.326 (0.128)	a	244
11	5	0.29 (0.10)	0.017	0.307	b,f	30
12	5	0.35 (0.10)	0.017	0.367	b,f	30
12	5	0.36 (0.20)	0.017	0.377	b,f	30
	Average (SD)	**0.287 (0.120)**	**0.017 (0.004)**	**0.305 (0.119)**		

[a] Questionnaire [b] Double plate [c] No tooth brushing as well as non-fluoride-toothpaste user [d] Measured at a baseline and after 6 months [e] Weekly variation [f] The intake from toothpaste was estimated as an average of the intakes reported in refs. 244,249

Estimates for the total fluoride intakes for children from food and toothpaste, by water fluoridation status and the age groups as reported in the last decade are presented in Table 2. The data for breastfed infants, who may receive lower amounts of fluoride than those listed in Table 2, are not included.

Wide variations in the intakes of fluoride within and between studies are evident from Table 2. This can be ascribed to the factors like: (1) considerable differences in the contents of fluoride in different food items; (2) large variation in the quantities consumed; (3) differences between the age groups studied; and (4) differences in the analytical methods used for total fluoride determination.

The average total daily intakes of fluoride in children were estimated using data listed in Table 2 and illustrated in Figure 6.

The estimated average total daily intake of fluoride from all studies in nonfluoridated areas is slightly higher than in fluoridated areas (0.044 and 0.048 mg/kg body weight (Figure 6 and Table 2). Neither of them exceeds the adequate intake of 0.05 mg/day/kg body weight. Review of data (Table 1) reveals that the contribution of fluoride with the toothpaste in nonfluoridated and fluoridated areas is substantial and represents about half of the estimated average total intake and that the estimates for the total daily intake of fluoride in some studies exceed

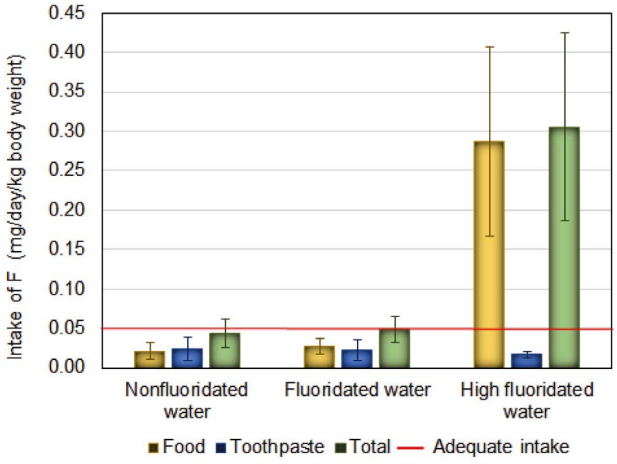

Figure 6: Estimated average total daily intake of fluoride in children from food and toothpaste in areas with nonfluoridated, fluoridated and high fluoridated water

the AI in both nonfluoridated and fluoridated areas.[30,243–251] The average estimated daily intake of fluoride in nonfluoridated areas is higher and in fluoridated areas lower, than that reported with diet and toothpaste a decade ago (0.036 and 0.071 mg/kg body weight in nonfluoridated and fluoridated areas, respectively).[23] Possible explanations for these differences are that the recent research (Table 1) has been more focused on: (1) the actual intakes of fluoride, as determined by duplicate diet technique; (2) the total oral fluoride intake including actual intake of fluoride with the toothpaste; and (3) the use of more accurate and precise analytical methods for total fluorine determination.

A comment has to be put on the average estimated total fluoride intakes of 0.260 mg/kg body weight in areas with fluoride contents in water above 1.2 mg/l.[30,244,249] These intakes extremely exceed the AI and also the upper limit[50] of fluoride daily intake set at 0.10 mg/kg body weight for children up to the age of eight years.

8. 2. Fluoride Intake in Adults

The major source of fluoride intake in adults is diet. The data on the total fluoride intake in adults are of older date before 2007.[23] The average daily total fluoride intake in nonfluoridated areas was then estimated to range from 0.56 to 1.50 mg (average 1.11 mg) (equivalent to 0.008–0.021 (average 0.016) mg/kg body weight for a 70 kg man). The estimated daily intake of fluoride in fluoridated areas was almost 2-fold higher, being 0.91–3.78 (average 2.07) mg, equivalent to 0.013–0.054 (average 0.030) mg/kg body weight for a 70 kg man.[23] The average total daily intake of fluoride estimated in our study conducted in Slovenia, where water is nonfluoridated and fluoride content is generally low was 0.73–2.50 mg (average 1.50 mg) (equivalent to 0.010–0.036 (average 0.021) mg/kg body weight for a 70 kg man). This study is of importance because it is one of the rare studies conducted in adults using duplicate diet technique.[149]

There are exceptions however showing higher fluoride intakes than those listed. Tea can significantly contribute to the total daily intake of fluoride. The content of F^- in tea as determined in our recent study ranged between 0.32 and 3.55 mg/l (average 1.42 mg/l).[163] Figure 7 illustrates average daily intakes of fluoride in adults from food and daily consumption of 1 l of tea. Water with F^- concentration of 1 mg/l was considered for preparing tea infusions in fluoridated areas.

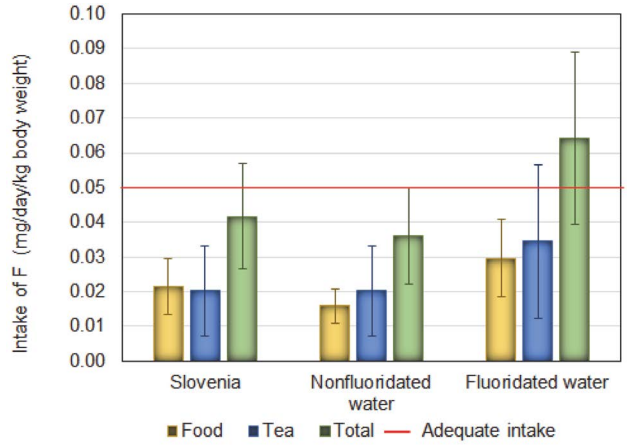

Figure 7: Estimated average total daily intake of fluoride in adults from food and tea in Slovenia and areas with nonfluoridated and fluoridated water

As illustrated in Figure 7, the consumption of tea can significantly contribute to the daily intake of fluoride; the AI for fluoride can be easily exceeded with consumption of higher quantities (≈1 l) of low quality tea. The presented intakes can be however also extremely higher in fluoride endemic areas[13,14] or in southern China, where brick tea-type fluorosis has even become an urgent public health problem.[252,253]

9. Adequate Intake of Fluoride

The basis for setting the adequate intake of fluoride is research by Dean and others. Initial studies conducted in the 1930s and early 1940s were focused on fluoride in water in relation to the appearance of dental fluorosis[254–259] and then turned to fluoride in water in relation to caries.[260,261] A "dose response" relationship between fluoride concentration in water supplies and dental fluorosis was established in the 22 cities study[261] and between fluoride concentration in water supplies and caries in the 21 cities study.[261,262] Reduction in the average number of dental caries per child was nearly maximal in communities having water fluoride concentrations close to 1.0 mg/l. This is how 1.0 mg/l of fluoride became the "optimal" concentra-

tion, i.e. it was associated with a high degree of protection against caries and a low prevalence of the milder forms of enamel fluorosis.

The first conversion of the exposure to fluoride in water supplies to the exposure to fluoride by the intake from water and food was made by McClure.[263] The daily fluoride intake in children at the age between 1 and 12 years ranged from 0.02–0.10 mg/kg body weight (average 0.05 mg/kg body weight).[263] The way on how this information became interpreted as a recommendation was reviewed by Burt[21], who concluded that "Despite its dubious genesis, however, empirical evidence suggests that 0.05–0.07 mg fluoride/kg body weight/day remains a useful upper limit for fluoride intake in children." The beneficial effects of fluoride on the prevention of dental caries were considered as an appropriate indicator for setting the adequate intake also by EFSA. Thus, the AI of fluoride from all sources (including non-dietary sources), was set at 0.05 mg/kg body weight per day for both children and adults, including pregnant and lactating women.[22] At the same time, it was however noted that reliable and representative data on the European population's total fluoride intake are not available (see also section Daily intake of fluoride).[22]

The current guidelines on the AI of fluoride, which are widely used in authoritative advisory recommendations for many decades, have been recently questioned, mainly because: (1) they were established empirically; (2) sources of ingested fluoride have changed; and (3) the prevalence and severity of dental caries and dental fluorosis have changed.[264] As a result, the appropriateness of current guidance was addressed, however, no firm conclusions were made.[265–267]

10. Conclusions – Enough or Too Much Fluoride?

Many health authorities worldwide consider beneficial effects of fluoride on the prevention of dental caries as an appropriate indicator to set the adequate daily intake of fluoride from all sources between 0.05 and 0.07 mg/day/kg body weight. The AI was set based on empirical observations reported by McClure[263] in 1943, when practically the only source of fluoride was fluoride in water. Today next to water, also tea and other beverages, diet, fluoridated food supplements and dental products can significantly contribute to the daily intake of fluoride. Among different food items processed food, fish and shellfish products might contain considerable contents of fluorine.

Excessive chronic intakes of fluoride can result in the development of fluoride related adverse effects. The primary adverse effects associated with chronic, excess fluoride intake are dental and skeletal fluorosis. As reported, the prevalence of enamel fluorosis including more cases of moderate-to-severe fluorosis is in increase.[58,239,240] A threshold as low as 0.03 mg/day/kg body weight has been suggested for the appearance of dental fluorosis, however even this intake will result in a certain, although low, level of fluorosis in a population.[39,57] Other adverse effects related to the toxicity of fluoride for cells of different tissues include, among others, neurodevelopmental disorders, neurotoxicity, decreased total fertility rate and diabetes.

A review of the recent studies showed that the average total daily intake of fluoride with diet and toothpaste in children living in nonfluoridated and fluoridated areas is (0.044 ± 0.026) and (0.048 ± 0.016) mg/kg body weight, respectively. These intakes are high enough to assure optimal protection against dental caries, but on the other hand, also high enough to pose a risk for the development of dental fluorosis. There is a lack of recent studies on the daily intake of fluoride in adults. Earlier reported estimates of the average total daily intake of fluoride are 0.016 and 0.030 mg/kg body weight in nonfluoridated and fluoridated areas, respectively.

Attempts have been made to challenge the guidelines on the AI. However even the most notable ongoing recent study, which started between 1992 and 1995, on the association between fluoride intake, dental caries, and dental fluorosis (Iowa Fluoride Study)[268–274] after years of extensive investigation, came to the following conclusion: "Given the overlap among caries/fluorosis groups in mean fluoride intake and extreme variability in individual fluoride intakes, firmly recommending "optimal" fluoride intake is problematic".[272]

It is therefore not surprising that the guidelines on the AI of fluoride have been recently questioned[264] and addressed.[265–267]

Based on the available literature, current recommendations on fluoride intake and the fact that the majority of fluoride benefits can be ascribed to its topical, rather than systemic, effects, it is hard to say whether the current AI is appropriate, i.e. too low or too high. Knowing this is of crucial importance because the margin between the beneficial and deleterious effects of fluoride appears to be so narrow.

11. Our Research and Future Directions

The majority of the fluoride debate is based on the results of the studies which can be regarded by scepticism. Only a few studies reported the use of certified reference materials (CRMs) as a part of the quality assurance system and only two studies with one being contributed by us reported the results together with the measurement uncertainty (MU) estimated according to the Guide to the Expression of Measurement Uncertainty (GUM).[117,170,171] In addition, in more than eight decades, after McClure[275] published his first study on fluorine contents in different food items, food growing and processing and our eating habits have changed dramatically. This is also evidenced by

meaningful difference between the average contents of F in food consumed in the US and the UK (see Section 7.4.). Thus, more accurate and up to date information on fluoride content in food and possible adverse effects of fluoride in relation to other ions, especially those forming complexes with fluoride are a prerequisite to avoid possible problems related to high intakes.

In our laboratory classical analytics used for determining the composition of bulk material of synthesised compounds containing fluorine[118,276–283] was extended to thermochemical investigations,[118,140,141,280–282,284–287] measurement uncertainty evaluation,[171] determination of fluorine in food[149,183] and environmental samples[7,288,289] and nanomaterials.[290–294]

Principles of thermochemistry were used for the estimation of the entropies of formation of fluorine containing aqueous anions[285] and to discuss ions containing solely fluorine atoms[286] and oxidation potential of fluorine.[287] Possible reactions proceeding during total decomposition of fluorine containing materials by pyrohydrolysis, oxygen bomb combustion and alkaline carbonate fusion were suggested and accompanying thermochemistry discussed. Based on this investigation some of the most resistant fluoride minerals towards the total decomposition were suggested.[140,141]

The importance of evaluating the MU according to the GUM in research laboratories was addressed and a procedure for the MU evaluation for determination of F in vegetation was suggested.[171]

Our study on fluorine contents in total diet samples is important, since it is one of the few studies on the intakes of fluoride from food in adults which is based on duplicate diet technique.[149] There is a number of papers reporting the contents of fluoride in tea infusions (*Camellia sinensis* L.). In our study we extensively investigated contents of total fluorine in tea and its leaching in the form of F^- into the infusion with respect to the type of tea and its manufacturing procedure.[183] As concluded, more attention should be put on consumption of fluoride from food and tea containing beverages.

Our laboratory is devoted also to the environmental issues. In a period of ten years two uncontrolled releases of gaseous fluorides from the industry, which caused damage to the environment and possibly humans via the food chain were identified.[7,289] The first release also initiated a study on the stress syndrome response of nettle (*Urtica dioica* L.) grown in fluoride contaminated substrate to fluoride.[288] Based on these results nettle was suggested as a passive bioindicator for monitoring soil pollution with F^- or for the phytoremediaton by the mechanism of phytoextraction of F^- polluted soils.

We also participated in characterization of upconverting, lanthanide-doped, fluoride nanoparticles, which show a great potential in bioimaging.[290–294]

Fluorine research remains relatively sporadic also because of a lack of sound analytical techniques enabling fast and multielemental analysis of F. Thus the predominate method for F analysis remains fluoride ion selective electrode.

We should be therefore not surprised if a lack of reliable data for F content in different food items and a lack of regulation regarding F content in human and animal diets can be noticed, i.e. the only EU directive related to fluorine in diet addresses the maximum content of F in animal feed.[295–297]

More research and actions regarding: (1) the content of F in different food items; (2) reporting the results in accordance to the GUM; (3) the intakes of fluoride and its possible adverse effects in relation to interaction with other food components should be encouraged to provide support for further development and implementation of legislation concerning fluorine.

Despite all the knowledge we currently have we can conclude that one is currently left with the question "Enough or too much fluoride?". Whether the complex nature of the system precludes there ever being a definite answer, remains to be seen.

Declaration of interest: none.

Funding: This work was supported by the Slovenian Research Agency [ARRS Grant P1-0045, Inorganic Chemistry and Technology].

List of Acronyms

AAPD, American Academy of Pediatric Dentistry; AAS, Atomic Absorption Spectrometry; AI, Adequate Intake; AR, Average Requirement; CDC, Centers for Disease Control and Prevention; CLD, Certainly Lethal Dose; CRM, Certified Reference Material; CZE, Capillary Zone Electrophoresis; EAPD, European Academy of Paediatric Dentistry; EFSA, European Food Safety Authority; EU, European Union; ^{19}F-NMR, ^{19}F-Nuclear Magnetic Resonance; F^-, Fluoride Ion; F, Total Fluorine; GUM, Guide to the Expression of Uncertainty in Measurement; HF, Hydrogen Fluoride; HR-CS, High Resolution-Continuum Source; ICP–OES, Inductively Coupled Plasma Optical Emission Spectrometry; ICP–MS, Inductively Coupled Plasma Mass Spectrometry; ICP–MS–MS, Inductively Coupled Plasma Quadrupole Mass Spectrometry; IQ, Intelligence Quotient; ISE, Ion Selective Electrode; LIBS, Laser-Induced Breakdown Spectroscopy; MAS, Molecular Absorption Spectrometry; MU, Measurement Uncertainty; NAA, Neutron Activation Analysis; NIR, Near Infrared Spectroscopy; PTD, Probable Toxic Dose; SD, Standard Deviation; UK, United Kingdom; US, United States; US NAS, United States National Academy of Sciences; WHO, World Health Organization

Author Biographies

Dona Štepec finished her B.Sc. study (equivalent to M.Sc. after the Bologna reform) in 2013 at the Faculty of

Chemistry and Chemical Technology at the University of Ljubljana. After graduation, she was employed as a researcher at Faculty of Chemistry and Chemical Technology at the University of Ljubljana on the project in collaboration with BIA Separation d.o.o. for a year and a half. Since 2015 she is enrolled in postgraduate study of Ecotechnology at the Jožef Stefan International Postgraduate School. She is a young researcher at the Department of Inorganic Chemistry and Technology at the Jožef Stefan Institute under mentorship of Prof. Dr. Maja Ponikvar-Svet. Her research activities are focused on determination of fluorine in food and environmental samples and evaluation of measurement uncertainty.

Maja Ponikvar-Svet finished her B.Sc. study in 1994 at the Faculty of Chemistry and Chemical Technology at the University of Ljubljana. After being employed at Merck Sharp & Dohme, inovativna zdravila d.o.o., for three years she joined Prof. Dr. Boris Žemva's group at the Jožef Stefan Institute, Department of Inorganic Chemistry and Technology in 1994. She received M.Sc. degree in 2000 and completed her PhD thesis in analytical chemistry in 2002 at the University of Ljubljana under mentorship of Prof. Dr. Boris Pihlar. Her research interests are in analytical chemistry of fluoride, measurement uncertainty and thermochemistry. The majority of her scientific work is devoted to fluoride in inorganic materials, food and environment and thermochemical investigations.

11. References

1. J. Schmedt auf der Günne, M. Mangstl, F. Kraus, *Angew. Chem. Int. Ed.* **2012**, *51*, 7847–7849. **DOI:**10.1002/anie.201203515
2. V. R. Celinski, M. Ditter, F. Kraus, F. Fujara, J. Schmedt auf der Günne, *Chem. Eur. J.* **2016**, *22*, 18388–18393. **DOI:**10.1002/chem.201603402
3. T. A. O'Donnell, in: J. C. Bailar Jr., H. J. Emeléus, R. Nyholm, A. F. Trotman-Dickenson (Eds.): Comprehensive Inorganic Chemistry, 1st Ed., Vol. 5, Pergamon Press, Oxford, England, **1973**, pp. 1009–1106. **DOI:**10.1016/B978-1-4832-8313-5.50019-X
4. A. W. Davison, L. H. Weinstein, in: A. Tressaud (Ed.): Fluorine and the Environment – Atmospheric Chemistry, Emissions, & Lithosphere, Vol. 1, Elsevier, Amsterdam, Netherlands, **2006**, pp. 251–298. **DOI:**10.1016/S1872-0358(06)01008-6
5. E. Álvarez-Ayuso, A. Giménez, J. C. Ballesteros, *J. Hazard. Mater.* **2011**, *192*, 1659–1666. **DOI:**10.1016/j.jhazmat.2011.06.084
6. W. W. Wenzel, W. E. H. Blum, *Soil Sci.* **1992**, *153*, 357–364. **DOI:**10.1097/00010694-199205000-00003
7. A. Koblar, G. Tavčar, M. Ponikvar-Svet, *J. Fluorine Chem.* **2011**, *132*, 755–759. **DOI:**10.1016/j.jfluchem.2011.05.022
8. M. M. Williamson, *East Afr. Med. J.* **1953**, *30*, 217–233.
9. R. J. Thompson, T. B. McMullen, G. B. Morgan, *J. Air Pollut. Control Assoc.* **1971**, *21*, 484–487. **DOI:**10.1080/00022470.1971.10469558
10. R. B. Symonds, W. I. Rose, M. H. Reed, *Nature* **1988**, *334*, 415–418. **DOI:**10.1038/334415a0
11. Agency for Toxic Substances and Disease Registry (ATSDR), Toxicological Profile for Fluorides, Hydrogen Fluoride, and Fluorine, Atlanta, United States, **2003**.
12. World Health Organization (WHO), Environmental Health Criteria 227, Fluorides, World Health Organization, Geneva, Switzerland, **2002**.
13. M. Dessalegne, F. Zewge, *Toxicol. Environ. Chem.* **2013**, *95*, 1056–1068. **DOI:**10.1080/02772248.2013.827685
14. L. Li, K. Luo, Y. Tang, Y. Liu, *Environ. Sci. Pollut. Res.* **2015**, *22*, 2031–2040. **DOI:**10.1007/s11356-014-3485-4
15. Y. Zhou, J. Wang, Z. Gu, S. Wang, W. Zhu, J. L. Aceña, V. A. Soloshonok, K. Izawa, H. Liu, *Chem. Rev.* **2016**, *116*, 422−518.
16. A. M. Thayer, *Chem. Eng. News* **2006**, *84*, 15–24.
17. National Institute of Dental and Craniofacial Research, The story of fluoridation, https://www.nidcr.nih.gov/health-info/fluoride/the-story-of-fluoridation (accessed: November 13, 2018)
18. K. Roholm, Fluorine intoxication, NYT Nordisk Forlag, Copenhagen, Denmark, **1937**.
19. O. Barbier, L. Arreola-Mendoza, L. M. Del Razo, *Chem.-Biol. Interact.* **2010**, *188*, 319–333. **DOI:**10.1016/j.cbi.2010.07.011
20. N. I. Agalakova, G. P. Gusev, *ISRN Cell Biol.* **2012**, 403835, 1–16. **DOI:**10.5402/2012/403835
21. B. A. Burt, *J. Dent. Res.* **1992**, *71*, 1228–1237. **DOI:**10.1177/00220345920710051601
22. European Food Safety Authority Panel on Dietetic Products, Nutrition, and Allergies (EFSA NDA), *EFSA J.* **2013**, *11*, 1–46.
23. M. Ponikvar, in: A. Tressaud, G. Haufe (Eds.): Fluorine and Health, Molecular Imaging, Biomedical Materials and Pharmaceuticals, Elsevier, Amsterdam, Netherlands, **2008**, pp. 487–549.
24. T. M. Marthaler, *Acta Med. Acad.* **2013**, *42*, 140–155. **DOI:**10.5644/ama2006-124.82
25. E. Ziegler, *Schweiz. Med. Wochenschr.* **1953**, *83*, 723–724.
26. World Health Organization (WHO), Inadequate or excess fluoride: A major public health concern, World Health Organization, Geneva, Switzerland, **2010**.
27. Centers for Disease Control and Prevention (CDC), *MMWR Weekly* **2008**, *57*, 737–764.
28. R. P. Ellwood, J. A. Cury, *Eur. Arch. Paediatr. Dent.* **2009**, *10*, 170–176. **DOI:**10.1007/BF03262679
29. American Dental Association Council on Scientific Affairs, *JADA* **2014**, *145*, 190–191. **DOI:**10.14219/jada.2013.47
30. A. Kebede, N. Retta, C. Abuye, S. J. Whiting, M. Kassaw, T. Zeru, M. Tessema, M. Kjellevold, *Int. J. Environ. Res. Public Health* **2016**, *13*, 756. **DOI:**10.3390/ijerph13080756
31. J. Cao, Y. Zhao, J. Liu, R. Xirao, S. Danzeng, Zeguo, S. Zhouma, *Ecotoxicol. Environ. Saf.* **2003**, *56*, 222–227.
32. N. Yang, S. Tang, S. Zhang, W. Huang, P. Chen, Y. Chen, Z. Xi, Y. Yuan, K. Wang, *Minerals* **2017**, *7*, 219. **DOI:**10.3390/min7110219
33. M. Ando, M. Tadano, S. Asanuma, K. Tamura, S. Matsushi-

ma, T. Watanabe, T. Kondo, S. Sakurai,R. Ji, C. Liang, S. Cao, *Environ. Health Perspect.* **1998**, *106*, 239–244. **DOI:**10.1289/ehp.98106239
34. J. Yi, J. Cao, *J. Fluorine Chem.* **2008**, *129*, 76–81. **DOI:**10.1016/j.jfluchem.2007.11.001
35. X. Qin, S. Wang, M. Yu, L. Zhang, X. Li, Z. Zuo, X. Zhang, L. Wang, *J. Environ. Public Health* **2009**, 969764.
36. N. Kakumanu, S. D. Rao, *N. Engl. J. Med.* **2013**, *368*, 1140. **DOI:**10.1056/NEJMicm1200995
37. S. Isaac, F. Brudevold, F. A. Smith, D. E. Gardner, *J. Dent. Res.* **1958**, *37*, 254–263. **DOI:**10.1177/00220345580370020901
38. O. Fejerskov, A. Thylstrup, M. J. Larsen, *Acta Odontol. Scand.* **1981**, *39*, 241–249. **DOI:**10.3109/00016358109162285
39. T. Aoba, O. Fejerskov, *Crit. Rev. Oral. Biol. Med.* **2002**, *13*, 155–170. **DOI:**10.1177/154411130201300206
40. K. Koo, *Adv. Dent. Res.* **2008**, *20*, 17–21. **DOI:**10.1177/154407370802000105
41. R. E. Marquis, S. A. Clock, M. Mota-Meira, *FEMS Microbiol. Rev.* **2003**, *26*, 493– 510. **DOI:**10.1111/j.1574-6976.2003.tb00627.x
42. D. R. Carter, G. S. Beaupre, *J. Bone Miner. Res.* **1990**, *5* (Suppl 1), 177–184. **DOI:**10.1002/jbmr.5650051372
43. B. L. Riggs, S. F. Hodgson, W. M. O'Fallon, E. Y. Chao, H. W. Wahner, J. M. Muhs, S. L. Cedel, L. J. Melton III, *N. Engl. J. Med.* **1990**, *322*, 802–809. **DOI:**10.1056/NEJM199003223221203
44. C. H. Søgaard, L. Mosekilde, A. Richards, L. Mosekilde, *Bone* **1994**, *15*, 393–399. **DOI:**10.1016/8756-3282(94)90815-X
45. J. E. Aaron, M. C. de Vernejoul, J. A. Kanis, *Bone* **1991**, *12*, 307–310. **DOI:**10.1016/8756-3282(91)90015-B
46. S. Peckham, N. Awofeso, *Sci. World J.* **2014**, 293019, 1–10. **DOI:**10.1155/2014/293019
47. S. Lecheny, 'Adverse Event,' Not the Same as 'Side Effect', https://www.pharmacytimes.com/contributor/shelby-leheny-pharmd-candidate-2017/2017/02/adverse-event-not-the-same-as-side-effect, (accessed: November 20, 2018)
48. rachita, Difference Between Side Effects and Adverse Effects, http://www.differencebetween.net/science/health/disease-health/difference-between-side-effects-and-adverse-effects/, (accessed: November 20, 2018)
49. A. F. Danil de Namor, I. Abbas, in: A. Tressaud (Ed.): Fluorine and the Environment, Agrochemicals, Archaeology, Green Chemistry & Water, Vol. 2, Elsevier, Amsterdam, Netherlands, **2006**, pp. 81–119. **DOI:**10.1016/S1872-0358(06)02003-3
50. European Food Safety Authority Panel on Dietetic Products, Nutrition, and Allergies (EFSA NDA), *EFSA J.* **2005**, *192*, 1–65.
51. G. M. Whitford, in: M. A. R. Buzalaf (Ed.): Monographs in Oral Science, Vol. 22, Karger, Basel, Switzerland, **2011**, pp. 66–80.
52. H. C. Hodge, F. A. Smith, in: J. H. Simons (Ed.): Fluorine Chemistry, Academic Press, New York, United States, **1965**, pp. 1–364.
53. National Research Council, Acute Exposure Guidelines Levels for Selected Airborne Chemicals, Vol. 4, The National Academies Press, Washington, D.C., United States, **2004**.
54. D. Peters, R. Miethchen, *J. Fluorine Chem.* **1996**, *79*, 161–165. **DOI:**10.1016/S0022-1139(96)03484-7
55. K. Heard, R. E. Hill, C. B. Cairns, R. C. Dart, *J. Toxicol. Clin. Toxic.* **2001**, *39*, 349–353. **DOI:**10.1081/CLT-100105154
56. J. Ly, R. D. Shin, Fluoride toxicity mechanism, https://emedicine.medscape.com/article/814774-overview, (accessed: November 16, 2018)
57. V. Baelum, O. Fejerskov, F. Manji, M. J. Larsen, *Tandlaegebladet.* **1987**, *91*, 452–456.
58. P. DenBesten, W. Li, in: M. A. R. Buzalaf (Ed.): Monographs in Oral Science, Vol. 22, Karger, Basel, Switzerland, **2011**, pp. 81–96.
59. N. Molina-Frechero, M. Nevarez-Rascón, A. Nevarez-Rascón, R. González-González, M. E. Irigoyen-Camacho, L. Sánchez-Pérez, S. López-Verdin, R. Bologna-Molina, *Int. J. Environ. Res. Public Health* **2017**, *14*, 73. **DOI:**10.3390/ijerph14010073
60. American International Medical University, Fluorosis: Causes, Diagnosis, Management and Prevention, https://www.aimu.us/2017/08/15/fluorosis-causes-diagnosis-management-and-prevention/, (accessed: November 16, 2018)
61. P. Grandjean, P. J. Landrigan, *Lancet Neurol.* **2014**, *13*, 330–338. **DOI:**10.1016/S1474-4422(13)70278-3
62. J. Gelinas, M. Allukian Jr, *Lancet Neurol.* **2014**, *13*, 647–648. **DOI:**10.1016/S1474-4422(14)70119-X
63. P. Grandjean, P. J. Landrigan, *Lancet Neurol.* **2014**, *13*, 648. **DOI:**10.1016/S1474-4422(14)70121-8
64. P. K. Shivaprakash, K. Ohri, H. Noorani, *J. Indian Soc. Pedod. Prev. Dent.* **2011**, *29*, 117–120. **DOI:**10.4103/0970-4388.84683
65. A. Aravind, R. S. Dhanya, A. Narayan, G. Sam, V. J. Adarsh, M. Kiran, *J. Int. Soc. Prev. Community Dent.* **2016**, 6 *(Suppl 3)*, S237–S242. **DOI:**10.4103/2231-0762.197204
66. M. Bashash, D. Thomas, H. Hu, E. A. Martinez-Mier, B. N.. Sanchez, N. Basu, K. E. Peterson, A. S. Ettinger, R. Wright, Z. Zhang, Y. Liu, L. Schnaas, A. Mercado-García, M. M. Téllez-Rojo, M. Hernández-Avila, *Environ. Health Perspect.* **2017**, *125*, 097017-1–097017-12. **DOI:**10.1289/EHP655
67. C. N. Still, P. Kelley, *Neurotoxicology* **1980**, *1*, 125–131.
68. W. F. Forbes, L. M. Hayward, N. Agwani, *Lancet* **1991**, *338*, 1592–1593. **DOI:**10.1016/0140-6736(91)92411-T
69. R. L. Blaylock, *Fluoride* **2004**, *37*, 301–314.
70. I. D. Akinrinade, A. E. Memudua, O. M. Ogundele, *Pathophysiol.* **2015**, *22*, 105–115. **DOI:**10.1016/j.pathophys.2015.03.001
71. K. Hasan, S. Alam, J. Mirkovic, F. Hossain, *Bioinformation* **2018**, *14*, 68–74. **DOI:**10.6026/97320630014068
72. S. C. Freni, *J. Toxicol. Environ. Health Part A* **1994**, *42*, 109–121. **DOI:**10.1080/15287399409531866
73. K. Fluegge, *J. Water Health.* **2016**, *14*, 864–877. **DOI:**10.2166/wh.2016.012
74. Z. Kheradpisheh, M. Mirzaei, A. H. Mahvi, M. Mokhtari, R. Azizi, H. Fallahzadeh, M. H. Ehrampoush, *Sci. Rep.* **2018**, *8*, 1–7. **DOI:**10.1038/s41598-018-20696-4
75. J. Ghosh, J. Das, P. Manna, P.C. Sil, *Toxicol. In Vitro*, **2008**, *22*, 1918–1926. **DOI:**10.1016/j.tiv.2008.09.010

76. World Health Organization (WHO), Air Quality Guidelines for Europe, 2nd Ed., World Health Organization, Geneva, Switzerland, **2000**.
77. World Health Organization (WHO), Environmental Health Criteria 36, Fluorine and Fluorides, World Health Organization, Geneva, Switzerland, **1984**.
78. E. A. Martínez, *J. Evidence-Based Complementary Altern. Med.* **2012**, *17*, 28–32.
79. J. Gutknecht, A. Walter, *Biochim. Biophys. Act*a **1981**, *644*, 153–156. **DOI:**10.1016/0005-2736(81)90071-7
80. G. M. Whitford, The Metabolism and Toxicity of Fluoride, 2nd Ed., Karger, Basel, Switzerland, **1996**.
81. J. Nopakun, H. H. Messer, *Nutr. Res.* **1990**, *10*, 771–779. **DOI:**10.1016/S0271-5317(05)80826-7
82. J. Nopakun, H. H. Messer, V. Voller, *J. Nutr.* **1989**, *119*, 1411–1417. **DOI:**10.1093/jn/119.10.1411
83. J. Ekstrand, M. Ehrnebo, L. O. Boréus, *Clin. Pharmacol. Ther.* **1978**, *23*, 329–337. **DOI:**10.1002/cpt1978233329
84. A. Maguire, F. V. Zohouri, J. C. Mathers, I. N. Steen, P. N. Hindmarch, P. J. Moynihan, *J. Dent. Res.* **2005**, *84*, 989–993. **DOI:**10.1177/154405910508401104
85. F. L. Cerklewski, *Nutr. Res.* **1997**, *17*, 907–929. **DOI:**10.1016/S0271-5317(97)00057-2
86. J. Ekstrand, M. Ehrnebo, *Eur. J. Clin. Pharmacol.* **1979**, *16*, 211–215. **DOI:**10.1007/BF00562063
87. C. J. Spak, J. Ekstrand, D. Zylberstein, *Caries Res.* **1982**, *16*, 249–256. **DOI:**10.1159/000260605
88. K. Trautner, G. Siebert, *Archs. Oral Biol.* **1986**, *31*, 223–228. **DOI:**10.1016/0003-9969(86)90053-1
89. A. Goyal, K. Gauba, A. Tewari, *J. Indian Soc. Pedod. Prev. Dent.* **1998**, *16*, 1–6.
90. K. Trautner, J. Einwag, *J. Dent. Res.* **1989**, *68*, 72–77. **DOI:**10.1177/00220345890680011201
91. E. R. Shulman, M. Vallejo, *Pediatr. Dent.* **1990**, *12*, 237–240.
92. L. S. Kaminsky, M. C. Mahoney, J. Leach, J. Melius, M. J. Miller, *Crit. Rev. Oral Biol. Med.* **1990**, *1*, 261–281. **DOI:**10.1177/10454411900010040501
93. G. M. Whitford, *Adv. Dent. Res.* **1994**, *8*, 5–14. **DOI:**10.1177/08959374940080011001
94. J. Ekstrand, M. Ehrnebo, *J. Occup. Med.* **1983**, *25*, 745–748. **DOI:**10.1097/00043764-198310000-00014
95. A. Villa, M. Anabalon, V. Zohouri, A. Maguire, A. M. Franco, A. Rugg-Gunn, *Caries Res.* **2010**, *44*, 60–68. **DOI:**10.1159/000279325
96. J. Ekstrand, L. I. Hardell, C. J. Spak, *Caries Res.* **1984**, *18*, 87–92. **DOI:**10.1159/000260753
97. J. Ekstrand, E. E. Ziegler, S. E. Nelson, S. J. Fomon, *Adv. Dent. Res.* **1994**, *8*, 175–180. **DOI:**10.1177/08959374940080020701
98. A. Oliveby, F. Lagerlöf, J. Ekstrand, C. Dawes, *J. Dent. Res.* **1989**, *68*, 146–149. **DOI:**10.1177/00220345890680020901
99. World Health Organization (WHO), Report of an Expert Committee on Oral Health Status and Fluoride Use, WHO Technical Report Series 846, World Health Organization, Geneva, Switzerland, **1994**.
100. United States National Research Council (US NRC), Biologic Markers in Reproductive Toxicology, National Academy Press, Washington, D.C., United States, **1989**.
101. World Health Organization (WHO), Biomarkers and Risk Assessment: Concepts and Principles, Environmental Health Criteria 155, World Health Organization, Geneva, Switzerland, **1993**.
102. A. J. Rugg-Gunn, A. E. Villa, M. A. R. Buzalaf, in: M. A. R. Buzalaf (Ed.): Monographs in Oral Science, Vol. 22, Karger, Basel, Switzerland, **2011**, pp. 37–51.
103. J. P. Pessan, M. A. R. Buzalaf, in: M. A. R. Buzalaf (Ed.): Monographs in Oral Science, Vol. 22, Karger, Basel, Switzerland, **2011**, pp. 52–65.
104. A. Mehta, *Indian J. Dent.* **2013**, *4*, 207–210. **DOI:**10.1016/j.ijd.2013.05.002
105. R. C. Agali, S. B. Shintre, *IJSS Rep. Rev.* **2016**, *2*, 49–52.
106. G. M. Whitford, in: G. M. Whitford (Ed.): Monographs in Oral Science, Vol. 16, Karger, Basel, Switzerland, **1996**, pp. 1–9.
107. J. Ekstrand, in: O. Fejerskov, B. A. Burt (Eds.): Fluoride in Dentistry, 2nd Ed., Munksgaard, Copenhagen, Denmark, **1996**, pp. 55–68.
108. D. M. O'Mullane, R. J. Baez, S. Jones, M. A. Lennon, P. E. Petersen, A. J. Rugg-Gunn, H. Whelton, G. M. Whitford, *Community Dent. Health* **2016**, *33*, 69–99.
109. World Health Organization (WHO), Basic Methods for Assessment of Renal Fluoride Excretion in Community Prevention Programmes for Oral Health, World Health Organization, Geneva, Switzerland, **2014**.
110. A. Oliveby, F. Lagerlof, J. Ekstrand, C. Dawes, *Arch. Oral. Biol.* **1989**, *34*, 191–194. **DOI:**10.1016/0003-9969(89)90007-1
111. A. Oliveby, F. Lagerlof, J. Ekstrand, C. Dawes, *Caries Res.* **1989**, *23*, 243–246. **DOI:**10.1159/000261185
112. G. M. Whitford, *Schweiz. Monatsschr. Zahnmed.* **2005**, *115*, 685–689.
113. Z. Kokot, D. Drzewiecki, *Fluoride* **2000**, *33*, 196–204.
114. S. S. Sankhala, R. Harshwal, P. Paliwal, A. Agarwal, *Fluoride* **2014**, *47*, 235–240.
115. N. H. Joshi, C. G. Ajithkrishnan, *Int. J. Trichology.* **2018**, *10*, 71–75. **DOI:**10.4103/ijt.ijt_91_17
116. H. Nakagaki, Y. Koyama, Y. Sakakibara, J. A. Weatherell, C. Robinson, *Arch. Oral. Biol.* **1987**, *32*, 651–654. **DOI:**10.1016/0003-9969(87)90039-2
117. Joint Committee for Guides in Metrology (JCGM), Evaluation of Measurement Data – Guide to the Expression of Uncertainty in Measurement (GUM), **2008**.
118. J. F. Liebman, M. Ponikvar, *Struct. Chem.* **2005**, *16*, 521–528. **DOI:**10.1007/s11224-005-5179-5
119. J. Belisle, *Science* **1981**, *212*, 1509–1510. **DOI:**10.1126/science.7233235
120. D. R. Taves, *Nature* **1968**, *217*, 1050–1051. **DOI:**10.1038/2171050b0
121. P. Venkateswarlu, L. Singer, W. D. Armstrong, *Anal. Biochem.* **1971**, *42*, 350–359. **DOI:**10.1016/0003-2697(71)90047-9
122. P. Venkateswarlu, Adv. Dent. Res. **1994**, *8*, 80–86. **DOI:**10.1177/08959374940080011401
123. H. H. Willard, O. B. Winter, *Ind. Eng. Chem., Anal. Ed.* **1933**, *5*, 7–10. **DOI:**10.1021/ac50081a006

124. G. Pietzka, P. Ehrlich, *Angew. Chem.* **1953**, *65*, 131–134. **DOI:**10.1002/ange.19530650504
125. M. A. Wade, S. S. Yamamura, *Anal. Chem.* **1965**, *37*, 1276–1287. **DOI:**10.1021/ac60229a028
126. L. H. Andersson, B. Gelin, *FOA Rep*. **1967**, *1*, 1–5.
127. M. J. Nardozzi, L. L. Lewis, *Anal. Chem.* **1961**, *33*, 1261–1264. **DOI:**10.1021/ac60177a040
128. R. L. Clements, G. A. Sergeant, P. J. W*ebb, Analyst **1971**, 66, 51–54.* **DOI:**10.1039/an9719600051
129. L. Singer, W. D. Armstrong, *Anal. Chem.* **1954**, *26*, 904–906. **DOI:**10.1021/ac60089a029
130. D. R. Taves, *Talanta* **1968**, *15*, 969–974. **DOI:**10.1016/0039-9140(68)80097-9
131. P. Venkateswarlu, *Anal. Chem.* **1992**, *64*, 346–349. **DOI:**10.1021/ac00028a005
132. J. J. Bailey, *Anal. Chem.* **1961**, *33*, 1760–1762. **DOI:**10.1021/ac60180a040
133. J. Thomas, H. J. Gluskoter, *Anal. Chem.* **1974**, *46*, 1321–1323. **DOI:**10.1021/ac60345a038
134. P. Venkateswarlu, *Anal. Biochem.* **1975**, *68*, 512–521. **DOI:**10.1016/0003-2697(75)90646-6
135. L. Singer, R. H. Ophaug, *Anal. Chem.* **1977**, *49*, 38–40. **DOI:**10.1021/ac50009a018
136. J. Cornog, H. Hopson, *J. Chem. Educ.* **1930**, *7*, 618–623. **DOI:**10.1021/ed007p618
137. R. Bock, A Handbook of Decomposition Methods in Analytical Chemistry, Blackie Group, London, England, **1979**.
138. S. R. Grobler, A. J. Louw, *Caries Res.* **1998**, *32*, 378–384. **DOI:**10.1159/000016474
139. R. A. Rocha, D. Rojas, M. J. Clemente, A. Ruiz, V. Devesa, D. Vélez, *J. Agric. Food Chem.* **2013**, *61*, 10708−10713. **DOI:**10.1021/jf403728r
140. M. Ponikvar, J. F. Liebman, *Struct. Chem.* **2006**, *17*, 75–78. **DOI:**10.1007/s11224-006-9023-3
141. D. Pavlović, M. Ponikvar-Svet, J. F. Liebman, *Struct. Chem.* **2018**, *29*, 1247–1254. **DOI:**10.1007/s11224-018-1148-7
142. P. Venkateswarlu, *J. Dent. Res.* **1990**, *69*, 514–521. **DOI:**10.1177/00220345900690S105
143. D. O'Hagan, *Chem. Soc. Rev.* **2008**, *37*, 308–319. **DOI:**10.1039/B711844A
144. P. Venkateswarlu, *Anal. Chem.* **1982**, *54*, 1132–1137. **DOI:**10.1021/ac00244a028
145. D. R. Taves, *Talanta*, **1968**, *15*, 1015–1023. **DOI:**10.1016/0039-9140(68)80109-2
146. H. B. Li, F. Chen, *Fresenius' Z. Anal. Chem.* **2000**, *368*, 501–504. **DOI:**10.1007/s002160000478
147. M. S. Frant, J. W. Ross Jr., *Science*, **1966**, *154*, 1553–1554. **DOI:**10.1126/science.154.3756.1553
148. Thermo Fisher Scientific, Thermo Scientific Orion Fluoride Ion Selective Electrode, Thermo Fisher Scientific, Waltham, US, **2016**.
149. M. Ponikvar, V. Stibilj, B. Žemva, *Food. Chem.* **2007**, *103*, 369–374. **DOI:**10.1016/j.foodchem.2006.07.032
150. H. Small, T. S. Stevens, W. C. Bauman, *Anal. Chem.* **1975**, *47*, 1801–1809. **DOI:**10.1021/ac60361a017
151. J. Belisle, D. F. Hagen, *Anal. Biochem.* **1978**, *87*, 545–555. **DOI:**10.1016/0003-2697(78)90704-2
152. M. Haldimann, B. Zimmerli, *Anal. Chim. Acta* **1993**, *282*, 589–601. **DOI:**10.1016/0003-2670(93)80124-4
153. J. Musijowski, B. Szostek, M. Koc, M. Trojanowicz, *J. Sep. Sci.* **2010**, *33*, 2636–2644. **DOI:**10.1002/jssc.201000179
154. J. Weiss, S. Reinhard, C. Pohl, C. Saini, L. Narayaran, *J. Chromatogr. A* **1995**, *706*, 81–92. **DOI:**10.1016/0021-9673(94)01162-8
155. T. A. Biemer, N. Asral, A. Sippy, *J. Chromatogr. A* **1997**, *771*, 355–359. **DOI:**10.1016/S0021-9673(97)00066-6
156. V. F. Samanidou, C. K. Zacharis, I. N. Papadoyannis, *J. Liq. Chrom. & Rel. Technol.* **2002**, *25*, 803–818. **DOI:**10.1081/JLC-120003037
157. W. Guo, L. Jin, S. Hu, Q. Guo, *J. Agric. Food Chem.* **2017**, *65*, 3406−3412. **DOI:**10.1021/acs.jafc.7b00535
158. H. W. Kuo, W. G. Chang, Y. S. Huang, J. S. Ali, *Bull. Environ. Contam. Toxicol.* **1999**, *62*, 677–684. **DOI:**10.1007/s001289900927
159. P. Politzer, *J. Am. Chem. Soc.* **1969**, *91*, 6235–6237. **DOI:**10.1021/ja01051a006
160. B. Welz, F. G. Lepria, R. G..O. Araujoa, S. L. C. Ferreira, M. D. Huang, M. Okruss, H. Becker-Ross, *Anal. Chim. Acta* **2009**, *647*, 137–148. **DOI:**10.1016/j.aca.2009.06.029
161. W. Guo, L. Jin, S. Hu, Q. Guo, *J. Agric. Food Chem.* **2017**, *65*, 3406−3412. **DOI:**10.1021/acs.jafc.7b00535
162. L. Guanghan, W. Qiongling, W. Xiaogang, Z. Tong, Y. Xin, *Food Chem.* **1999**, *66*, 519–523. **DOI:**10.1016/S0308-8146(99)00091-6
163. M. Čerňanská, P. Tomčík, Z. Jánošíková, M. Rievaja, D. Bustin, *Talanta* **2011**, *83*, 1472–1475. **DOI:**10.1016/j.talanta.2010.11.026
164. R. Chavali, N. S. K. Gunda, S. Naicker, S. K. Mitra, *Anal. Chem. Res.* **2015**, *6*, 26–31. **DOI:**10.1016/j.ancr.2015.10.003
165. K. Fukushi, Y. Fujita, J. Nonogaki, J. Tsujimoto, T. Hattori, H. Inui, V. P. Beškoski, H. Hotta, M. Hayashi, T. Nakano, *Anal. Bioanal. Chem.* **2018**, *410*, 1825–1831. **DOI:**10.1007/s00216-017-0838-0
166. E. Tamburini, C. Tagliati, T. Bonato, S. Costa, C. Scapoli, P. Pedrini, *Sensors* **2016**, *16*, 1216. **DOI:**10.3390/s16081216
167. D. Deng, P. Deng, X. Wang, X. Hou, *Spectrosc. Lett.* **2009**, *42*, 334–340. **DOI:**10.1080/00387010903185462
168. F. Mostafaei, F. E. McNeill, D. R. Chettle, W. V. Prestwich, *Physiol. Meas.* **2013**, *34*, 1329–1341. **DOI:**10.1088/0967-3334/34/10/1329
169. Joint Committee on Guides for Metrology (JCGM), International Vocabulary of Metrology - Basic and General Concepts and Associated Terms (VIM), **2002**.
170. A. R. Sousa, M. A. Trancoso, *Accred. Qual. Assur.* **2005**, *10*, 430–438. **DOI:**10.1007/s00769-005-0009-4
171. D. Štepec, G. Tavčar, M. Ponikvar-Svet, *J. Fluorine Chem.* **2019**, *217*, 22–28. **DOI:**10.1016/j.jfluchem.2018.08.010
172. International Organization for Standardization (ISO), Guide 35: Reference materials - General and statistical principles for certification, Geneva, Switzerland, **2006**.
173. Scientific Committee on Health and Environmental Risks

(SCHER), Critical review of any new evidence on the hazard profile, health effects, and human exposure to fluoride and the fluoridating agents of drinking water, European Commission, Brussels, Belgium, **2010**.
174. Health and Ecological Criteria Division, Office of Water, Fluoride: Exposure and relative source contribution analysis, U.S. Environmental Protection Agency, Washington, D.C., United States, **2010**.
175. World Health Organization (WHO), Guidelines for drinking-water quality, 2nd Ed., World Health Organization, Geneva, Switzerland, **1993**.
176. World Health Organization (WHO), Fluoride in drinking-water, World Health Organization, Geneva, Switzerland, **2004**.
177. European Commission, *Off. J. Eur. Communities: Legis.* **1998**, *330*, 32–54.
178. United States Public Health Service (USPHE), *Public Health Rep.* **2015**, *130*, 318–331.
179. Centers for Disease Control and Prevention (CDC), *MMWR Weekly* **1999**, *48*, 241–243.
180. European Commission, *Off. J. Eur. Communities: Legis.* **2003**, *126*, 34–39.
181. Food and Drug Administration (FDA), Code of Federal Regulations, https://www.accessdata.fda.gov/scripts/cdrh/cfdocs/cfcfr/CFRSearch.cfm, (accessed: November 14, 2018)
182. K. F. Fung, Z. Q. Zhang, J. W. C. Wong, M. H. Wong, *Environ. Pollut.* **1999**, *104*, 197–205. **DOI:**10.1016/S0269-7491(98)00187-0
183. A. Koblar, G. Tavčar, M. Ponikvar-Svet, *Food Chem.* **2012**, *130*, 286–290. **DOI:**10.1016/j.foodchem.2011.07.037
184. L. Chan, A. Mehra, S. Saikat, P. Lynch, *Food Res. Int.* **2013**, *51*, 564–570. **DOI:**10.1016/j.foodres.2013.01.025
185. C. Peng, H. Cai, X. Zhu, D. Li, Y. Yang, R. Hou, X. Wan, *J. Food Sci.* **2016**, *81*, H235–H239. **DOI:**10.1111/1750-3841.13180
186. D. T. Waugh, W. Potter, H. Limeback, M. Godfrey, *Int. J. Environ. Res. Public Health.* **2016**, *13*, 259. **DOI:**10.3390/ijerph13030259
187. T. Shyu, J. Chen, *J. Food, Agric. Environ.* **2013**, *11*, 178–183.
188. M. P. Whyte, *Am. J. Med.* **2006**, *119*, 189–190. **DOI:**10.1016/j.amjmed.2005.05.028
189. Y. Liu, A. Maguire, G. Tianqui, S. Yanguo, F. V. Zohoori, *Nutr. Health* **2017**, *23*, 25–32. **DOI:**10.1177/0260106016685726
190. S. C. C. Lung, P. K. Hsiao, K. M. Chiang, *J. Expo. Anal. Environ. Epidemiol.* **2003**, *13*, 66–73. **DOI:**10.1038/sj.jea.7500259
191. C. Fojo, M. E. Figueira, C. M. M. Almeida, *Food Addit. Contam., Part A* **2013**, *30*, 705–712.
192. I. Rodríguez, A. Hardisson, S. Paz, C. Rubio, A. J. Gutiérrez, J. R. Jaudenes, A. Burgos, C. Revert, *J. Food Comps. Anal.* **2018**, *72*, 97–103.
193. M. C. Kiritsy, S. M. Levy, J. J. Warren, N. Guha-Chowdhury, J. R. Heilman, T. Marshall T, *J. Am. Dent. Assoc.* **1996**, *127*, 895–902. **DOI:**10.14219/jada.archive.1996.0347
194. M. D. Jiménez-Farfán, J. C. Hernández-Guerrero, J. P. Loyola-Rodríguez, C. Ledesma-Montes, Int. J. Paediatr. Dent. 2004, 14, 260–266. **DOI:**10.1111/j.1365-263X.2004.00564.x
195. J. Opydo-Szymaczek, J. Opydo, *Food Chem. Toxicol.* **2010**, *48*, 2702–2706. **DOI:**10.1016/j.fct.2010.06.043
196. S. Omar, J. Chen, B. Nelson, W. Okumura, W. Zhang, *J. Dent. Child.* **2012**, *81*, 20–26.
197. J. R. Heilman, M. C. Kiritsy, S. M. Levy, J. S. Wefel, *J. Am. Dent. Assoc.* **1999**, *130*, 1593–1599. **DOI:**10.14219/jada.archive.1999.0098
198. M. M. Martin Delgado, A. Hardisson de la Torre, R. Alvarez Marante, *J. Food Comps. Anal.* **1992**, *5*, 172–180.
199. S. Warnakulasuriya, C. Harris, S. Gelbier, J. Keating, T. Peters, *Clin. Chim. Acta* **2002**, *320*, 1–4. **DOI:**10.1016/S0009-8981(02)00043-8
200. I. Rodríguez, J. R. Jaudenes, A. Hardisson, S. Paz, C. Rubio, A. J. Gutiérrez, A. Burgos, C. Revert, *Biol. Trace Elem. Res.* **2018**, *181*, 178–183. **DOI:**10.1007/s12011-017-1191-z
201. M. I. Rodríguez Gómez, A. Hardisson de La Torre, A. Burgos Ojeda, R. Álvarez Marante, L. Díaz-Flores, *Eur. Food Res. Technol.* **2003**, *216*, 145–149. **DOI:**10.1007/s00217-002-0622-y
202. O. B. Martínez, C. Díaz, T. M. Borges, E. Díaz, J. P. Pérez, *Food Addit. Contam.* **1998**, *15*, 893–897. **DOI:**10.1080/02652039809374726
203. S. Paz, J. R. Jaudenes, A. J. Gutiérrez, C. Rubio, A. Hardisson, C. Revert, *Biol. Trace Elem. Res.*, **2017**, *178*, 153–159. **DOI:**10.1007/s12011-016-0910-1
204. N. Ozbek, S. Akman, *LWT Food Sci. Technol.* **2015**, *61*, 112–116.
205. A. W. Burgstahler, M. A. Robinson, *Fluoride* **1997**, *30*, 142–146.
206. C. Liu, L. E. Wyborny, J. T. Chan, *Fluoride* **1995**, *28*, 10–16.
207. M. A. R. Buzalaf, J. P. Pessan, R. Fukushima, A. Dias, H. M. Rosa, *J. Appl. Oral. Sci.* **2006**, *14*, 38–42. **DOI:**10.1590/S1678-77572006000100008
208. O. B. Dirks, J. M. P. A. Jongeling-Eijndhoven, T. D. Flissebaalje, I. Gedalia, *Caries Res.* **1974**, *8*, 181–186. **DOI:**10.1159/000260106
209. P. Gupta, N. Gupta, K. Meena, N. J. Moon, P. Kumar, R. Kaur, *J. Clin. Diagn. Res.* **2015**, 9, 5–7.
210. T. G. Kazi, K. D. Brahman, H. I. Afridi, F. Shah, M. B. Arain, *Environ. Sci. Pollut. Res.* **2018**, *25*, 12909–12914. **DOI:**10.1007/s11356-018-1563-8
211. C. McKnight-Hanes, D. H. Leverett, S. M. Adair, C. P. Shields, *Pediatr. Dent.* **1988**, *10*, 189–194.
212. H. Lal, F. V. Zohoori, N. Omid, V. R. Valentine, A. Maguire, *Br. Dent. J.* **2014**, *217*, E8. **DOI:**10.1038/sj.bdj.2014.736
213. O. Rirattanapong, P. Rirattanapong, *Southeast Asian J. Trop. Med. Public Health* **2016**, *47*, 160–164.
214. National Research Council (NRC), Fluoride in drinking water: a scientific review of EPA's standards, National Academies Press, Washington, D.C., United States, **2006**.
215. H. Poureslami, P. Khazaeli, A. H. Mahvi, K. Poureslami, P. Poureslami, J. Haghani, M. Aghaei, *Fluoride* **2016**, *49*, 485–494.

216. B. Spittle, *Fluoride* **2016**, *49*, 471.
217. P. Cressey, *J. Public Health Dent.* **2010**, *70*, 285–291. **DOI:**10.1111/j.1752-7325.2010.00183.x
218. Nutrient Data Laboratory, Beltsville Human Nutrition Research Center, Agricultural Research Service, of selected beverages and foods, Release 2, Baltimore, United States, **2005**.
219. V. Zohoori, A. Maguire, Database of the Fluoride (F) content of Selected Drinks and Foods in the UK, Newcastle University and Teesside University, United Kingdom, **2015**.
220. F. V. Zohoori, A. Maguire, *Caries Res.* **2016**, *50*, 331–336. **DOI:**10.1159/000445981
221. P. A. San Filippo, G. C. Battistone, *Clin. Chim. Acta* **1971**, *31*, 453–457. **DOI:**10.1016/0009-8981(71)90418-9
222. L. Singer, R. H. Ophaug, B. F. Harland, *Am. J. Clin. Nutr.* **1980**, *33*, 328–332. **DOI:**10.1093/ajcn/33.2.328
223. P. Varo, P. Koivistoinen, *Acta Agric. Scand.* **1980**, *Suppl. 22*, 165–171.
224. D. R. Taves, *Br. J. Nutr.* **1983**, *49*, 295–301. **DOI:**10.1079/BJN19830038
225. L. Singer, R. H. Ophaug, *J. Agric. Food Chem.* **1986**, *34*, 510–513. **DOI:**10.1021/jf00069a035
226. H. Lopez, J. M. Navia, *Caries Res.* **1988**, *22*, 210–216. **DOI:**10.1159/000261108
227. R. W. Dabeka, A. D. McKenzie, *J. AOAC Int.* **1995**, *78*, 897–909.
228. E. Newbrun, *J. Dent. Res.* **1992**, *71*, 1255–1265. **DOI:**10.1177/00220345920710052001
229. G. M. Whitford, *J. Dent. Res.* **1987**, *66*, 1056–1060. **DOI:**10.1177/00220345870660051501
230. H. Pollick, *J. Calif. Dent. Assoc.* **2013**, *41*, 395–404.
231. T. M. Marthaler, P. E. Petersen, *Int. Dent. J.* **2013**, *55*, 351–358. **DOI:**10.1111/j.1875-595X.2005.tb00045.x
232. F. C. Sampaio, S. M. Levy, in: M. A. R. Buzalaf (Ed.): Monographs in Oral Science, Vol. 22, Karger, Basel, Switzerland, **2011**, pp. 133–145.
233. C. A. Yeung, L. Y. Chong, A. M. Glenny, *Cochrane Database Syst. Rev.* **2015**, *3*, CD003876.
234. C. A. Yeung, J. L. Hitchings, T. V. Macfarlane, A. G. Threlfall, M. Tickle, A. M. Glenny, *Aust. Dent. J.* **2005**, *50*, 286–287. **DOI:**10.1111/j.1834-7819.2005.tb00376.x
235. A. I. Ismail, H. Hasson, *J. Am. Dent. Assoc., JADA* **2008**, *139*, 1457–1468. **DOI:**10.14219/jada.archive.2008.0071
236. C. M. Vargas, *J. Evid. Base Dent. Pract.* **2011**, *11*, 18–20. **DOI:**10.1016/j.jebdp.2010.11.022
237. The European Academy of Paediatric Dentistry (EAPD), *Eur. Arch. Paediatr. Dent.* **2009**, *10*, 129–135. **DOI:**10.1007/BF03262673
238. American Academy of Pediatric Dentistry (AAPD), *Ref. Man.* **2014**, *37*, 15–16.
239. D. H. Leverett, *Science* **1982**, *217*, 26–30. **DOI:**10.1126/science.7089534
240. R. G. Rozier, *J. Public Health. Dent.* **1999**, *59*, 239–246. **DOI:**10.1111/j.1752-7325.1999.tb03276.x
241. E. A. Martinez-Mier, K. L. Spencer, B. J. Sanders, J. E. Jones, A. E. Soto-Rojas, A. M. Tomlin, L. A. Vinson, J. A. Weddell, G. J. Eckert, *Community Dent. Oral. Epidemiol.* **2017**, *45*, 251–257. **DOI:**10.1111/cdoe.12283
242. S. M. Levy, J. Eichenberger-Gilmore, J. J. Warren, E. Letuchy, B. Broffitt, T. A. Marshall, T. Burns, M. Willing, K. Janz, J. C. Torner, *Community Dent. Oral Epidemiol.* **2009**, *37*, 416–426. **DOI:**10.1111/j.1600-0528.2009.00478.x
243. A. B. P. Miziara, S. T. Philippi, F. M. Levy, M. A. R. Buzalaf, *Community Dent. Oral Epidemiol.* **2009**, *37*, 305–315. **DOI:**10.1111/j.1600-0528.2009.00477.x
244. F. V. Zohoori, M. A. R. Buzalaf, C. A. B. Cardoso, K. P. K. Olympio, F. M. Levy, L. T. Grizzo, D. F. B. Mangueira, F. C. Sampaio, A. Maguire, *Eur. J. Oral Sci.* **2013**, *121*, 457–464. **DOI:**10.1111/eos.12070
245. O. Ibiyemi, F. V. Zohoori, R. A. Valentine, A. Maguire, *Community Dent. Oral Epidemiol.* **2018**, *46*, 482–491. **DOI:**10.1111/cdoe.12396
246. E. Oganessian, R. Ivancakova, E. Lencova, Z. Broukal, *BMC Public Health* **2011**, *11*, 768–773. **DOI:**10.1186/1471-2458-11-768
247. A. Maguire, F. V. Zohouri, P. N. Hindmarch, J. Hatts, P. J. Moynihan, *Community Dent. Oral Epidemiol.* **2007**, *35*, 479–488. **DOI:**10.1111/j.1600-0528.2006.00366.x
248. P. F. T. Oliveira, J. A. Cury, C. V. Lima, G. C. Vale, M. D. M. Lima, L. F. A. D. Moura, M. S. Moura, *Braz. Oral Res.* **2018**, *32*, e26.
249. L. Abuhaloob, A. Maguire, P. Moynihan, *Int. J. Paediatr. Dent.* **2015**, *25*, 127–135. **DOI:**10.1111/ipd.12108
250. N. Omid, A. Maguire, W. T. O'Hare, F. V. Zohoori, *Community Dent. Oral Epidemiol.* **2017**, *45*, 12–19. **DOI:**10.1111/cdoe.12254
251. C. V. Lima, J. A. Cury, G. C. Vale, M. D. M. Lima, L. D. A. D. Moura, M. S. Moura, *Caries Res.* **2015**, *49*, 640–646. **DOI:**10.1159/000442029
252. Z. Fan, Y. Gao, W. Wang, H. Gong, M. Guo, S. Zhao, X. Liu, B. Yu, D. Sun, *J. Epidemiol.* **2016**, *26*, 57–63. **DOI:**10.2188/jea.JE20150037
253. A. Tressaud, Fluorine, a Paradoxical Element, Progress in Fluorine Science, Vol. 5, Elsevier, Amsterdam, Netherlands, **2019**.
254. H. T. Dean, R. M. Dixon, C. Cohen, *Public Health Rep.* **1935**, *50*, 424–442. **DOI:**10.2307/4581503
255. H. T. Dean, E. Elvove, *Public Health Rep.* **1935**, *50*, 1719–1729. **DOI:**10.2307/4581707
256. H. T. Dean, *J. Am. Med. Assoc.* **1936**, *107*, 1269–1272. **DOI:**10.1001/jama.1936.02770420007002
257. H. T. Dean, E. Elvove, *Am. J. Public Health* **1936**, *26*, 567–575. **DOI:**10.2105/AJPH.26.6.567
258. H. T. Dean, E. Elvove, *Public Health Rep.* **1937**, *52*, 1249–1264. **DOI:**10.2307/4582298
259. H. T. Dean, in: S. M. Gordon (Ed.): Dental Science and Dental Art, Lea and Febiger, Philadelphia, United States, **1938**, pp. 387–414.
260. H. T. Dean, P. Jay, F. A. Arnold Jr., E. Elvove, *Pub. Health Rep.* **1941**, *56*, 761–792. **DOI:**10.2307/4583693
261. H. T. Dean, P. Jay, F. A. Arnold Jr., E. Elvove, *Pub. Health Rep.* **1942**, *57*, 1155–1194. **DOI:**10.2307/4584182

262. H. T. Dean, in: F. R. Moulton (Ed.): Dental caries and fluorine, Science Press, American Association for the Advancement of Science, Washington D.C., US, **1946**, pp. 5–31.
263. F. J. McClure, *Am. J. Dis. Child.* **1943**, *66*, 362–369. **DOI:**10.1001/archpedi.1943.02010220015002
264. A. J. Rugg-Gunn, *Adv. Dent. Res.* **2018**, *29*, 142–143. **DOI:**10.1177/0022034517750588
265. M. A. R. Buzalaf, *Adv. Dent. Res.* **2018**, *29*, 157–166. **DOI:**10.1177/0022034517750850
266. I. Mejàre, *Adv. Dent. Res.* **2018**, *29*, 167–176. **DOI:**10.1177/0022034517750589
267. A. J. Spencer, L. G. Do, U. Mueller, J. Baines, M. Foley, M. A. Peres, *Adv. Dent. Res*. **2018**, *29*, 144–156. **DOI:**10.1177/0022034517750592
268. S. M. Levy, F. J. Kohout, M. C. Kiritsy, J. R. Heilman, W. S. Wefel, *J. Am. Dent. Assoc.* **1995**, *126*, 1625–1632. **DOI:**10.14219/jada.archive.1995.0110
269. S. M. Levy, M. C. Kiritsy, S. L. Slager, J. J. Warren, *J. Public Health. Dent.* **1998**, *58*, 228–233. **DOI:**10.1111/j.1752-7325.1998.tb02998.x
270. S. M. Levy, J. J. Warren, C. S. Davis, H. L. Kirchner, M. J. Kanellis, J. S. Wefel, *J. Public Health Dent.* **2001**, *61*, 70–77. **DOI:**10.1111/j.1752-7325.2001.tb03369.x
271. S. M. Levy, J. J. Warren, B. Broffitt, *J. Public Health. Dent.* **2003**, *63*, 211–220. **DOI:**10.1111/j.1752-7325.2003.tb03502.x
272. J. J. Warren, S. M. Levy, M. J. Kanellis, *J. Public Health Dent.* **2002**, *62*, 109–114. **DOI:**10.1111/j.1752-7325.2002.tb03430.x
273. J. J. Warren, S. M. Levy, B. Broffitt, J. E. Cavanaugh, M. J. Kanellis, K. Weber-Gasparoni, *J. Public Health Dent.* **2009**, *69*, 111–115. **DOI:**10.1111/j.1752-7325.2008.00108.x
274. M. R. Franzman, S. M. Levy, J. J. Warren, B. Broffitt, *Pediatr. Dent.* **2004**, *26*, 87–92.
275. F. J. McClure, Fluorides in food and drinking water, National Institute of Health Bulletin 172, United States Treasury Department, Public Health Service, Washington, D.C., United States, **1939**.
276. B. Sedej, *Talanta*, **1976**, *23*, 335–336. **DOI:**10.1016/0039-9140(76)80209-3
277. M. Ponikvar, B. Sedej, B. Pihlar, B. Žemva, *Anal. Chim. Acta* **2000**, *418*, 113–118. **DOI:**10.1016/S0003-2670(00)00942-9
278. M. Ponikvar, B. Pihlar, B. Žemva, *Talanta* **2002**, *58*, 803–810. **DOI:**10.1016/S0039-9140(02)00371-5
279. M. Ponikvar, B. Pihlar, B. Žemva, *J. Fluorine Chem.* **2003**, *122*, 215–217. **DOI:**10.1016/S0022-1139(03)00090-3
280. M. Ponikvar, B. Žemva, J. F. Liebman, *J. Fluorine Chem.* **2003**, *123*, 217–220. **DOI:**10.1016/S0022-1139(03)00139-8
281. M. Ponikvar, B. Sedej, J. F. Liebman, *Eur. J. Inorg. Chem.* **2004**, 1349–1352. **DOI:**10.1002/ejic.200300632
282. M. Ponikvar, J. F. Liebman, H. D. B. Jenkins, *Eur. J. Inorg. Chem.* **2004**, 3273–3276. **DOI:**10.1002/ejic.200400150
283. P. Benkič, H. D. B. Jenkins, M. Ponikvar-Svet, Z. Mazej, *Eur. J. Inorg. Chem.* **2006**, 1084–1092. **DOI:**10.1002/ejic.200500856
284. M. Ponikvar-Svet, J. F. Liebman, *Struct. Chem.* **2005**, *16*, 587–591. **DOI:**10.1007/s11224-005-6099-0
285. M. Ponikvar-Svet, H. D. B. Jenkins, J. F. Liebman, *Struct. Chem.* **2007**, *18*, 883–889. **DOI:**10.1007/s11224-007-9189-3
286. M. Ponikvar-Svet, K. F. Edwards, J. F. Liebman, *Acta Chim. Slov.* **2013**, *60*, 471–483.
287. M. Ponikvar-Svet, D. N. Zeiger, J. F. Liebman, *Struct. Chem.* **2015**, *26*, 1621–1628. **DOI:**10.1007/s11224-015-0647-z
288. A. Koblar, G. Tavčar, M. Ponikvar-Svet, J. *Fluorine Chem.* **2015**, *172*, 7–12. **DOI:**10.1016/j.jfluchem.2015.01.006
289. D. Štepec, G. Tavčar, M. Ponikvar-Svet, *Environ. Pollut.* **2019**, DOI: **DOI:**10.1016/j.envpol.2019.02.046
290. O. Plohl, B. Majaron, M. Ponikvar-Svet, D. Makovec, D. Lisjak, *Acta Chim. Slov.* **2015**, *62*, 789–795. **DOI:**10.17344/acsi.2015.1508
291. D. Lisjak, O. Plohl, M. Ponikvar-Svet, B. Majaron, *RSC Adv.* **2015**, *5*, 2046–2069.
292. D. Lisjak, O. Plohl, J. Vidmar, B. Majaron, M. Ponikvar-Svet, *Langmuir* **2016**, *32*, 8222–8229. **DOI:**10.1021/acs.langmuir.6b02675
293. O. Plohl, S. Kralj, B. Majaron, E. Fröhlich, M. Ponikvar-Svet, D. Makovec, D. Lisjak, *Dalton Trans.* **2017**, *46*, 6975–6984. **DOI:**10.1039/C7DT00529F

O. Plohl, M. Kraft, J. Kovač, B. Belec, M. Ponikvar-Svet, C. Würth, D. Lisjak, U. Resch-Genger, *Langmuir* **2017**, *33*, 553–560. **DOI:**10.1021/acs.langmuir.6b03907

294. European Commission, *Off. J. Eur. Communities: Legis.* **2002**, *140*, 10–21.
295. European Commission, *Off. J. Eur. Communities: Legis.* **2005**, *318*, 19–24.
296. European Union, *Off. J. Eur. Communities: Legis.* **2015**, *31*, 11–17.

Povzetek

Fluor v obliki fluoridov je v naravi zelo razširjen in zato predstavlja neizogiben del našega okolja. Znano je, da ima fluor v majhnih količinah koristne učinke na zdravje zob. Po drugi strani lahko čezmerni kronični vnos povzroči neželene učinke, vključno z razvojem zobne fluoroze pri otrocih in/ali kostne fluoroze pri otrocih in odraslih. Primeren dnevni vnos fluora, ki temelji na empiričnih raziskavah, je 0,05 mg/dan/kg telesne mase, vendar je prag med koristnimi in škodljivimi učinki ozek. Znanje o strupenosti fluorida je kljub številnim raziskavam še vedno pomanjkljivo. V tem preglednem članku so opisani vloga in učinki fluorida na zdravje ljudi. Podanih je nekaj s fluoridom povezanih kontroverznosti in predlog smernic za bodoče raziskave.

DOI: 10.17344/acsi.2018.4580 *Acta Chim. Slov.* **2019,** *66,* 276–283

Scientific paper

Green Synthesis of Bromo Organic Molecules and Investigations on Their Antibacterial Properties: An Experimental and Computational Approach

Naruti Longkumer,[1] Kikoleho Richa,[1] Rituparna Karmaker,[1] Visekhonuo Kuotsu,[2] Aola Supong,[1] Latonglila Jamir,[2] Pranjal Bharali[2] and Upasana Bora Sinha[1,*]

[1] *Department of Chemistry, Nagaland University, Lumami-798627, Nagaland, India*

[2] *Department of Environmental Science, Nagaland University, Lumami-798627, Nagaland, India*

* *Corresponding author: E-mail: upasanabsinha@gmail.com; Tel: +91-9436006754*

Received: 07-01-2018

Abstract

A simple, environmentally benign methodology has been developed to synthesize some bromoorganic compounds which have potential as antimicrobial agents. The required compounds were obtained through microwave (MW) irradiation, on-water reactions and using cetyltrimethylammonium tribromide (CTMATB) as the bromine source. The high yield of the product could be achieved within short reaction times, thus representing the main attribute of the present synthetic approach. The compounds were evaluated for *in vitro* antibacterial activity against *Escherichia coli, Klebsiella pneumoniae*, *Staphylococcus aureus* and *Bacillus subtilis*. Further, *in silico* studies were carried out to elucidate the interactions of the compounds with the bacterial proteins.

Keywords: Bromo compounds; aqueous conditions; green chemistry; antibacterial activity, *in vitro* studies; molecular docking.

1. Introduction

Bromo derivatives, both naturally occurring as well as synthesised compounds, have been reported to have biological activities, such as feeding deterrent, antimicrobial, anti-diabetic, antioxidant, anti-inflammatory and enzyme inhibition.[1–7] Considering the importance of bromo organic compounds, new methods of their synthesis are always sought and literature enumerates a few reports of the use of quaternary ammonium tribromides (QATBs) under MW irradiation for their synthesis.[8,9] Among the tribromides reported so far, the efficacy and versatility of cetyltrimethylammonium tribromide (CTMATB) has been reported in many important organic transformations.[10–17] Its proven mildness as a brominating reagent and versatility towards various organic substrates added to its compatibility with the aqueous media is what prompted us to choose this reagent for the present study.

In recent years there has been an increasing emphasis on avoiding the use of solvents in organic reactions. It often happens that while many reaction strategies are efficient as well as benign, use of organic solvents in these reactions prevents them from being considered as perfectly green.[18] There is an extensive current debate over the relative "greenness" of the use of various solvent media, but water can undeniably be considered the cleanest solvent available, and the use and release of clean water clearly will have the least impact on the environment. Numerous publications report the combination of water as an environmentally benign solvent for chemical transformations with the use of MW irradiation as an efficient heating method.[19,20] In fact, MW heating has become a broadly accepted non-conventional energy source for performing organic synthesis[21–29] as well as in various aspects of inorganic chemistry and polymer chemistry.[30,31] Microwave heating is preferred in the context of environmentally benign synthesis because it is a more homogenous method and accelerates reaction processes as compared to the traditional heating methods (*e.g.* in an oil bath, heating mantle or hot air oven),[9,25,28,32] hence our choice of MW irradiation and use of water as the solvent medium.

While the presently synthesized compounds are examples of small molecules which are very common, small molecules have found significance as new-age pharmaceutical compounds due to their less challenging manufacturing procedure as compared to larger biologicals. Further, even though bromoorganic compounds have been commonly used as antimicrobial agents,[3–7] there seems to be no reports on the anti-microbial essay of the presently synthesized compounds in the literature. This led us to consider the prospects of such an investigation through experimental and computational approaches.

To explain the promising activity of these compounds, this work includes the molecular docking study of the synthesised compounds within the binding pockets of DNA gyrase subunit B (PDB ID: 1KZN) and dihydrofolate reductase (PDB ID: 3SRW). DNA gyrase is a bacterial protein of the topoisomerase family involved in DNA replication and transcription by catalysing the negative supercoiling of the closed-circular DNA. As this function is essential for DNA replication and transcription, gyrase is really a suitable target for antibacterial agents.[33] Dihydrofolate reductase (DHFR) is an important target in a number of therapeutic areas, including cancer and search for antiinfective compounds where it is used to generate antibacterial, antifungal and antiparasitic agents.[34]

2. Experimental

2. 1. General Chemistry

All the solvents and substrates were purchased from Merck, Spectrochem, Sigma-Aldrich, and S. D. Fine Chem. Hexane and ethyl acetate were distilled before the use in column chromatography, while the substrates were used without further purification. All reactions were monitored by TLC on silica gel HF_{254}. The microwave reactions were carried out in a scientific microwave system CATA 2R (single mode reactor) from Catalyst System (Pune, India). Melting points were determined by digital melting point apparatus. IR spectra were recorded with KBr pellets on a Perkin–Elmer FT-IR (spectrum two). ^{1}H NMR and ^{13}C NMR spectra were recorded on a JEOL ECS-400 using $CDCl_3$ as the solvent and TMS as the internal standard.

2. 1. 1. Procedure for Synthesis of CTMATB

CTMATB was synthesised using a modified version of our method reported earlier.[17] In this procedure, a mixture of 4.89 g (41.07 mmol) of potassium bromide (KBr) and 5.00 g (13.74 mmol) of cetyltrimethylammonium bromide (CTMAB), and 0.057 g (0.53 mmol) of sodium carbonate (Na_2CO_3) were taken in a mortar and 10 mL (88.24 mmol) of 50% H_2O_2 added to the whole. The resultant mixture was grinded thoroughly and then was dissolved in 50 mL of water taken in a 100 mL beaker. The reaction solution was stirred at room temperature for 5 minutes and then 30 mL of 1 M H_2SO_4 was added drop-wise. An exothermic reaction followed and the CTMATB precipitated out. CTMATB formed was filtered using suction pump, washed with water many times till the filtrate contained no trace of acid (tested using litmus paper), and then initially air-dried and finally dried in a vacuum desiccator.

$$\text{CTMAB} \xrightarrow[\text{H}^+/\text{ KBr}]{\text{Na}_2\text{CO}_3\ /\ \text{H}_2\text{O}_2} \text{CTMATB} \qquad (1)$$

The compound was then dried in a vacuum desiccator using anhydrous calcium chloride ($CaCl_2$) as desiccant. The product was obtained as bright yellow micro-crystals which was further recrystallized from methanol. Yield of the product was 5.52 g (96%), m.p. 87–88 °C, m.p. (lit.) 87 or 88 °C.[35]

2. 1. 2. General Procedure for the Synthesis of Compounds 1a–9a.

A homogenous mixture of the reagent CTMATB (2 mmol) and substrate **1–9** (2 mmol) were taken in 1:1 ratio in a 50 mL round bottomed flask equipped with reflux condenser in the microwave reactor. 10 mL H_2O was added to the mixture and stirred thoroughly. The reaction mixture was placed inside the microwave reactor. The reactor was switched on and kept at a controlled power of P-7 which corresponds to 595 W. Reaction temperature was recorded using the flexible temperature probe attached to the microwave reactor, immediately after the completion of the reaction, and was found to be 90 °C. The progress of the reaction was monitored by TLC on silica gel HF_{254} using ethyl acetate–hexane solvent system (volume ratio varied for different substrates). After completion of the reaction, the product was extracted with 10 mL (2×) ethyl acetate and washed with 5 mL (2×) sodium bicarbonate solution. The crude product thus obtained was subjected to column chromatography over a pad of silica gel using ethyl acetate–hexane solvent system (volume ratio varied for different substrates) to obtain the desired products **1a–9a**.

2. 2. Antibacterial Studies

All the synthesized compounds were evaluated for their *in vitro* antibacterial activities against *Escherichia coli* and *Klebsiella pneumonia* as Gram negative bacteria, as well as *Staphylococcus aureus* and *Bacillus subtilis* as Gram positive bacteria. The antimicrobial properties of the synthesised compounds were evaluated by the determination of the zone of inhibition, using agar well diffusion method.[36] Subsequently minimum inhibitory concentrations (MIC) of the compounds were determined by the twofold broth dilution method in nutrient broth. DMSO was used as the control and the tests were performed at 10 mg/mL

concentration using DMSO as the solvent. Streptomycin was used as the standard reagent. Each experiment was performed in triplicate and the average reading was taken.

2. 3. Docking Studies

Molecular docking studies were conducted so as to validate the obtained data and to provide comprehensible evidence for the observed antibacterial activity of all synthesized compounds. In this study, molecular docking simulations were performed using Molegro Virtual Docker (MVD). The pdb file format of enzymes DNA Gyrase B (Pdb id: 1KZN) and dihydrofolate reductase (Pdb id: 3SRW) as receptors were obtained from the RCSB Protein Data Bank and were prepared for molecular docking. All the 3D structure of the ligands was drawn using ChemBioDraw as mol2 file. For molecular docking simulation, water molecules were removed and charges were assigned. By using MVD cavities were predicted and the ligands were docked against the target proteins and 30 independent runs were performed for each ligand.[37–40]

3. Results and Discussion

Cetyltrimethylammonium tribromide (CTMATB), having the molecular formula $C_{19}H_{42}NBr_3$ is a bright orange crystalline solid with sharp melting point at 87–88 °C. However, from thermogravimetric (TG) analysis it was revealed that the compound is stable even up to *ca.* 200 °C. One of the major implications of this property is that the tribromide may be very useful for the appropriate organic transformations at relatively high temperatures as well. It is an obvious fear that tribromides, upon heating, release bromine, which is an environmentally hazardous chemical. However, while investigating their thermal stability by

Table 1. Aqueous microwave bromination of organic substrates with CTMATB[a]

Substrate	Product[b]	Reaction time	Yield[c]
 **1**	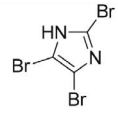 **1a**	4 min	70%
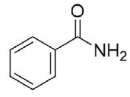 **2**	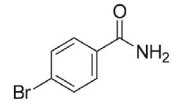 **2a**	5 min	75%
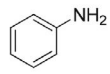 **3**	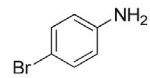 **3a**	4 min	80%
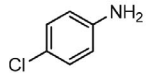 **4**	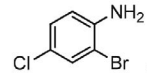 **4a**	4 min	80%
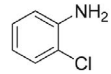 **5**	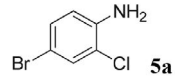 **5a**	5 min	62%
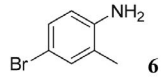 **6**	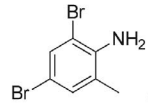 **6a**	2 min	69%
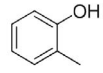 **7**	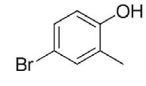 **7a**	3 min	60%
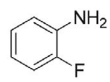 **8**	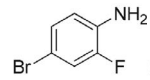 **8a**	5 min	69%
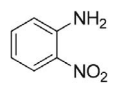 **9**	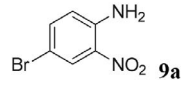 **9a**	4 min	86%

[a] Reactions maintained at 90 °C using controlled power P-7 of the MW reactor; all reactions were monitored by TLC; [b] Confirmed by IR, ^{1}H NMR and ^{13}CNMR; [c] Isolated yields.

TG experiments, it was observed that CTMATB loses Br_2 as the tail fragment at the temperature of 265–267 °C, which is much higher than the temperature at which brominations take place.[17]

In order to determine the efficiency of CTMATB in aqueous condition, different types of organic compounds were used and the reactions were performed under microwave conditions. These reactions, when performed in an oil bath under the same conditions, took longer time. As an example, **3a** took 8 minutes for its formation, while it took 4 minutes using MW reactor, thereby justifying our choice of MW irradiation. The results of the bromination reactions under microwave conditions are presented in Table 1. The products were identified by comparing their melting points and IR absorption spectra with that of authentic samples.[8,9,17,18,41]

The antibacterial activity of the synthesised compounds was tested against *Escherichia coli* and *Klebsiella*

Table 2. Zone of inhibition values (mm) of the synthesised compounds

Compounds (10 mg/mL)	Zone of inhibition (mm)			
	E. coli	*K. pneumoniae*	*S. aureus*	*B. subtilis*
1a	19	12	18	14
2a	24	15	21	18
3a	18	17	19	16
4a	12	10	15	>10
5a	10	>10	12	10
6a	19	15	16	12
7a	12	17	>10	14
8a	16	18	16	>10
9a	19	12	17	14
Streptomycin	32	30	34	30

Table 3. MIC (minimum inhibitory concentration in mg/mL) of the synthesised compounds

Compounds (10 mg/mL)	MIC (mg/ml)			
	E. coli	*K. pneumoniae*	*S. aureus*	*B. subtilis*
1a	0.117	0.468	0.117	0.234
2a	0.058	0.144	0.234	0.117
3a	0.117	0.144	0.117	0.144
4a	0.937	0.937	0.144	0.937
5a	0.937	0.937	0.468	0.937
6a	0.117	0.144	0.144	0.468
7a	0.468	0.117	0.937	0.234
8a	0.144	0.937	0.144	0.937
9a	0.117	0.937	0.144	0.234

Table 4. Docking score of the compounds with 1KZN

Ligand	Moldock score	Rerank score[a]	Interaction[b]	Internal[c]	HBond[d]	LE1[e]	LE3[f]
1a	–64.19	–49.54	–61.17	–3.01	–2.50	–8.02	–6.19
2a	–66.34	–57.59	–76.74	10.40	–2.29	–6.63	–5.76
3a	–56.97	–48.30	–66.03	9.06	–2.58	–7.12	–6.04
4a	–63.30	–52.11	–72.49	9.19	–2.02	–7.03	–5.79
5a	–62.87	–52.41	–72.86	9.99	–1.94	–6.99	–5.82
6a	–62.12	–52.74	–72.86	11.71	–2.08	–6.90	–5.86
7a	–62.72	–55.09	–75.60	12.87	0.00	–5.70	–5.01
8a	–62.50	–50.56	–73.12	10.61	–2.12	–6.25	–5.06
9a	–63.07	–54.09	–72.88	9.81	–3.31	–7.01	–6.01
Streptomycin	–101.15	–29.04	–150.03	48.87	–8.81	–2.53	–0.73

[a] The rerank score is a linear combination of E-inter (steric, Van der Waals, hydrogen bonding, electrostatic) between the ligand and the protein, and E-intra. (torsion, sp2-sp2, hydrogen bonding, Van der Waals, electrostatic) of the ligand weighted by pre-defined coefficients. [b] The total interaction energy between the pose and the protein (kJ/mol). [c] The internal energy of the pose. [d] Hydrogen bonding energy (kJ/mol). [e] Ligand efficiency 1: MolDock score divided by heavy atoms count. [f] Ligand efficiency 3: Rerank score divided by heavy atoms count.

Table 5. Docking score of the compounds with 3SRW

Ligand	Moldock score	Rerank score[a]	Interaction[b]	Internal[c]	HBond[d]	LE1[e]	LE3[f]
1a	−64.94	−49.76	−61.92	−3.02	−4.18	−8.12	−6.22
2a	−62.98	−54.19	−73.36	10.38	−3.19	−6.30	−5.42
3a	−50.44	−41.89	−59.50	9.06	−1.49	−6.30	−5.24
4a	−55.92	−46.30	−65.12	9.19	−1.43	−6.21	−5.14
5a	−55.86	−46.43	−65.85	9.99	−1.78	−6.21	−5.16
6a	−54.38	−46.44	−66.10	11.71	−1.91	−6.04	−5.16
7a	−64.85	−56.88	−78.04	13.19	−8.59	−5.90	−5.17
8a	−61.56	−51.24	−72.18	10.62	−2.38	−6.16	−5.12
9a	−60.34	−49.08	−70.15	9.81	−4.37	−6.70	−5.45
Streptomycin	−134.60	−39.20	−178.12	43.52	−9.39	−3.36	−0.98

[a] The rerank score is a linear combination of E-inter (steric, Van der Waals, hydrogen bonding, electrostatic) between the ligand and the protein, and E-intra. (torsion, sp2-sp2, hydrogen bonding, Van der Waals, electrostatic) of the ligand weighted by pre-defined coefficients. [b] The total interaction energy between the pose and the protein (kJ/mol). [c] The internal energy of the pose. [d] Hydrogen bonding energy (kJ/mol). [e] Ligand efficiency 1: MolDock score divided by heavy atoms count. [f] Ligand efficiency 3: Rerank score divided by heavy atoms count.

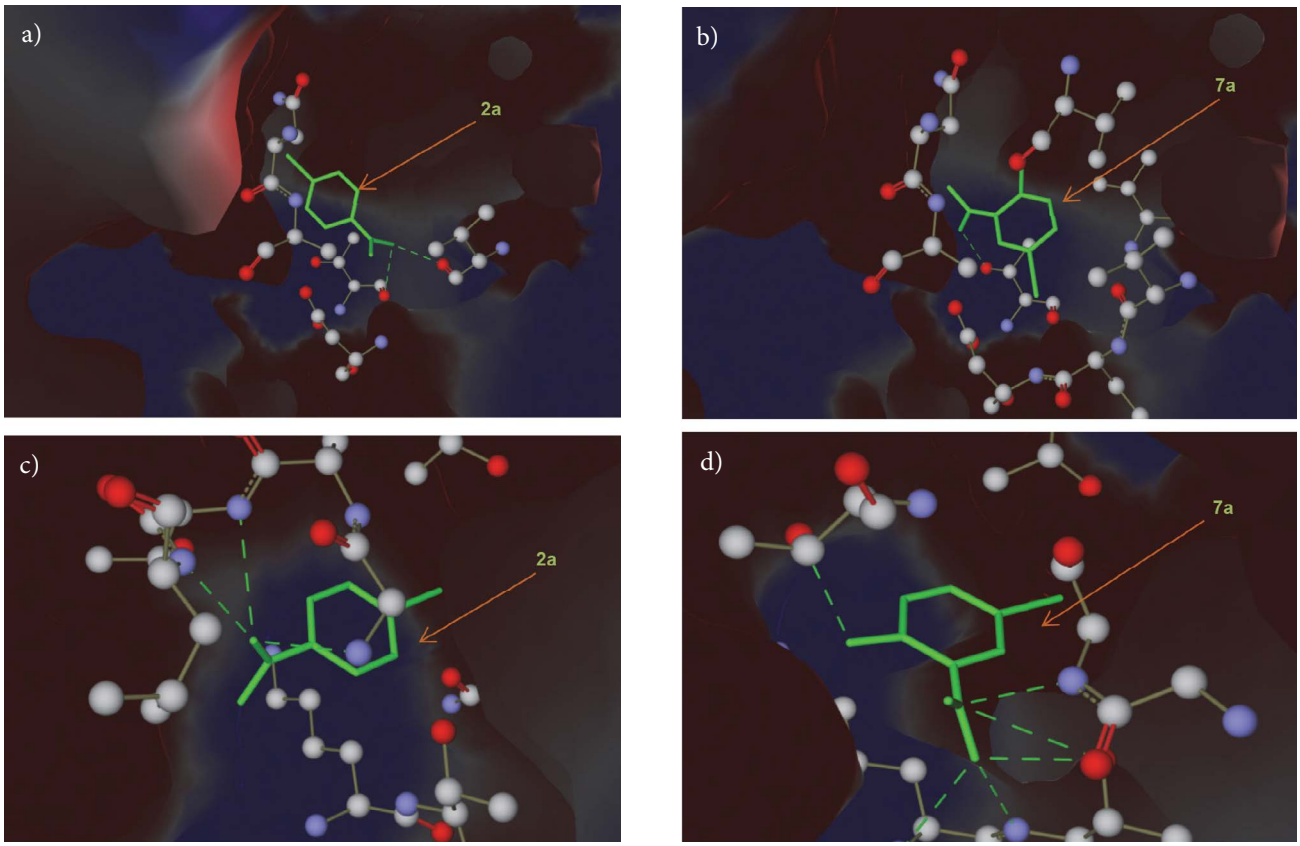

Figure 1. Molecular interaction of the compounds **2a** and **7a** at the active pockets of the protein 1KZN (a and b) and 3SRW(c and d) (green dotted lines indicate the mode of interaction with the protein).

pneumonia as Gram negative bacteria, as well as *Staphylococcus aureus* and *Bacillus subtilis* as Gram positive bacteria. The results of the primary screening are shown in Table 2. The investigation of the screening revealed that the compounds tested showed varying degree of activity against all the investigated microorganisms. Almost all the compounds showed moderate to potent activity against the strains. Subsequently, minimum inhibitory concentrations (MIC) of the compounds were determined to quantify the antibacterial potency of the compounds. The results of the MIC values of antibacterial activity are given in Table 3. Compound **2a** showed a better activity against *E. coli* with a MIC of 0.058 mg/mL and compounds **4a** and **5a** have lesser effectiveness against the bacterial strains. In comparison, compound **2a** showed the best activity indicating its promising broad spectrum of antibacterial property.

Docking studies were performed on known target proteins to understand the antibacterial mechanisms of bromo compounds using Molegro virtual docker (MVD). The proteins used as target were DNA gyrase B (Pdb id: 1KZN) from *Escherichia coli* and dihydrofolate reductase (Pdb id: 3SRW) from *Staphylococcus aureus.* The best pose of each compound were selected for ligand–protein interaction energy analysis as shown in Tables 4 and 5. The interaction energies of **2a** and **7a** were –76.74 kJ/mol and –75.60 kJ/mol as compared to streptomycin with –150.03 kJ/mol. This indicates that **2a** and **7a** also have a favourable ligand–protein interaction energy at the binding cavity of 1KZN. Similarly, the interaction energies of **2a** and **7a** were –73.36 kJ/mol and –78.04 kJ/mol as compared to streptomycin with –178.12 kJ/mol. This indicates that **2a** and **7a** also have a favourable ligand–protein interaction energy at the binding cavity of 3SRW. The snapshots of ligand–protein interaction depicting the binding mode of the best poses are shown in Fig. 1a, b, c and d. In this study, the molecular interaction analysis as shown in Table 6 established a common molecular interaction with Val71 and Thr165. Similarly, in Table 7, a common interaction with Thr122 and Asp121 in the compounds and streptomycin was established.

Table 6. Molecular interaction analysis of the compounds with the active site of 1KZN

Compound	Interaction (Protein···Ligand)	Interaction Energy (kJ/mol)	Interaction distance (Å)	Hybridisation (Protein)	Hybridisation (Ligand)
1a	Asp73(OD1)···N(4)	–2.5	2.785	sp^3(A)	sp^2(D)
2a	Val71(O)···N(8)	–2.409	2.589	sp^2(A)	sp^2(D)
	Thr165(O)···N(8)	–2.209	2.901	sp^2(A)	sp^2(D)
3a	Thr165(O)···N(6)	–2.5	2.928	sp^2(A)	sp^3(D)
	Val71(O)···N(6)	–2.5	2.815	sp^2(A)	sp^3(D)
4a	Val71(O)···N(0)	–2.5	2.676	sp^2(A)	sp^3(D)
5a	Val71(O)···N(0)	–2.5	2.663	sp^2(A)	sp^3(D)
6a	Val71(O)···N(0)	–2.5	2.683	sp^2(A)	sp^3(D)
7a	Thr165(OG1)···O(14)	–2.423	3.115	sp^3(B)	sp^2(A)
8a	Val71(O)···N(0)	–2.5	3.020	sp^2(A)	sp^3(D)
9a	Val167(N)···O(0)	–0.922	3.217	sp^2(D)	sp^3(B)
	Val71(O)···O(0)	–2.5	2.672	sp^2(A)	sp^3(B)
Streptomycin	Asn46(ND2)···N(36)	–2.5	2.866	sp^2(D)	sp^2(A)
	Asn46(ND2)···O(11)	–1.937	2.532	sp^2(D)	sp^3(B)
	Asp49(OD1)···N(38)	–0.377	3.524	sp^3(A)	sp^2(D)
	Asp49(OD1)···N(39)	–1.968	2.880	sp^3(A)	sp^2(D)
	Asn46(O)···N(39)	–1.153	3.396	sp^2(A)	sp^2(D)
	Asn46(O)···O(20)	–2.44	3.111	sp^3(A)	sp^3(B)
	Asp73(OD1)···O(20)	–2.5	2.676	sp^3(A)	sp^3(B)
	Thr165(OG1)···O(14)	–0.464	3.507	sp^3(B)	sp^3(A)
	Thr165(O)···O(35)	–0.335	3.009	sp^2(A)	sp^3(B)
	Val71(O)···O(35)	–2.5	2.621	sp^2(A)	sp^3(B)
	Val167(N)···O(35)	–0.890	3.112	sp^2(D)	sp^3(B)

(A): Acceptor (D): Donor (B): Both donor and acceptor

4. Conclusion

To conclude, microwave assisted aqueous reactions for the bromination of organic compounds as an attractive protocol due to its eco-friendly, efficient and economic nature are presented. The use of a CTMATB in the bromination reactions which is less toxic compared to using molecular bromine makes the process more environmentally benign. The antimicrobial study of these novel bromoorganic derivatives against Gram positive and Gram negative species showed that synthetic mimics of naturally occurring bromoorganic compounds can be of promise against drug-resistant bacteria. Docking studies revealed that both streptomycin and the synthesized compounds have a common interaction at the active sites of the protein and further studies on these compounds might increase their potency thereby enhancing their anti bacterial activity. Thus, this study adopts significance in view of simple molecules that are potent and easy to synthesize. Further studies on derivatives involving synthetic mimics of naturally occurring moieties would provide a lead in the development of novel bromoorganic-based antimicrobial compounds.

5. Acknowledgement

The authors N. Longkumer and K. Richa are thankful to the UGC Non-NET fellowship and UGC Project

Table 7. Molecular interaction analysis of the compounds with the active site of 3SRW

Compound	Interaction (Protein...Ligand)	Interaction Energy (kJ/mol)	Interaction distance (Å)	Hybridisation (Protein)	Hybridistion (Ligand)
1a	Gln96(N)···N(1)	–0.042	3.480	sp^2(D)	sp^2(A)
	Thr97(N)···N(1)	–2.210	3.157	sp^2(D)	sp^2(A)
	Thr97(OG1)···N(1)	–2.225	3.148	sp^3(B)	sp^2(A)
2a	Gly95(N)···O(7)	–0.175	2.944	sp^2(D)	sp^2
	Thr95(N)···O(7)	–0.510	3.223	sp^2(D)	sp^2
	Leu98(N)···O(7)	–2.5	3.027	sp^2(D)	sp^2
3a	Thr122(OG1)···N(6)	–2.5	2.867	sp^3(B)	sp^3(D)
	Asp121(OD1)···N(6)	–2.5	3.052	sp^3(A)	sp^3(D)
4a	Thr122(OG1)···N(0)	–2.5	2.883	sp^3(B)	sp^3(D)
5a	Thr122(OG1)···N(0)	–2.5	2.971	sp^3(B)	sp^3(D)
6a	Thr122(OG1)···N(0)	–2.5	2.956	sp^3(B)	sp^3(D)
7a	Thr97(OG1)···N(0)	–1.813	2.882	sp^3(B)	sp^3(D)
	Gly95(N)···N(13)	–2.208	2.932	sp^2(D)	sp^3(A)
	Thr47(OG1)···N(13)	–0.699	3.460	sp^3(B)	sp^3(A)
	Thr47(OG1)···O(14)	–2.5	2.813	sp^3(B)	sp^2(A)
	Thr47(N)···O(14)	–2.5	2.713	sp^2(D)	sp^2(A)
	Lys46(N)···O(14)	–0.280	3.402	sp^2(D)	sp^2(A)
8a	Thr122(OG1)···N(0)	–2.5	2.815	sp^3(B)	sp^3(D)
9a	Thr97(N)···O(0)	–0.673	3.110	sp^2(D)	sp^3(B)
	Gly95(N)···O(0)	–1.197	2.639	sp^2(D)	sp^3(B)
	Leu98(N)···O(0)	–2.5	2.746	sp^2(D)	sp^3(B)
Streptomycin	Ala8(N)···O(35)	–0.660	3.225	sp^2(D)	sp^3(B)
	Ala8(O)···O(34)	–1.812	2.517	sp^2(A)	sp^3(B)
	Gln20(O)···O(10)	–0.676	2.601	sp^2(A)	sp^3(B)
	Ser50(OG)···O(12)	–2.5	2.702	sp^3(B)	sp^3(B)
	Ser50 (OG)···O(22)	–2.5	2.607	sp^3(B)	sp^2(A)
	Thr47(OG1)···N(39)	–2.5	2.775	sp^3(B)	sp^2(D)
	Thr122(OG1)···N(3)	–2.5	3.085	sp^3(B)	sp^2(A)
	Thr122(OG1)···O(11)	–2.5	2.772	sp^3(B)	sp^2(B)
	Asp121(OD1)···N(2)	–2.5	3.053	sp^3(A)	sp^2(D)
	Asp121(OD1)···N (0)	–2.5	2.817	sp^3(A)	sp^2(D)
	Asn19(OD1)···N(2)	–2.093	3.181	sp^2(A)	sp^2(D)

(A): Acceptor (D): Donor (B): Both donor and acceptor

(UGC MRP No.43-192/2014), respectively, for financial support. We also acknowledge the BIF center, Nagaland University, Lumami for extending the facilities.

6. References

1. I. Saikia, A. J. Borah, P. Phukan, *Chem. Rev*. **2016**, *116*, 6837–7042. **DOI:**10.1021/acs.chemrev.5b00400
2. L. Xiukun, L. Ming, *J. Ocean Univ. China* 2012, *11*, 533–538. **DOI:**10.1007/s11802-012-2109-1
3. P. Rajasulochana, P. Krishnamoorthy, R. Dhamotharan, *IJPBS* **2012**, *3*, 173–186.
4. M. M. Rathore, V. V. Parhate, P. R. Rajput, *IJRPBS* **2013**, *4*, 59–62.
5. K. B. Oh, J. H. Lee, S. C. Chung, J. Shin, H. J. Shin, H. J. Kim, H. S. Leeb, *Bioorg. Med. Chem. Lett.* **2008**, *18*, 104–108. **DOI:**10.1016/j.bmcl.2007.11.003
6. T. S. Bante, V. V. Parhate, P. R. Rajput, *IJCPS* **2015**, *4,* 218–220. **DOI:**10.15416/ijcp.2015.4.3.218
7. S. G. Patil, P. S. Utale, S. D. Thakur, S. V. Pande, *Der Pharma Chem.* **2011**, *3*, 189–196.
8. A. Kumar, A. Jamir, L. Jamir, D. Sinha, U. B. Sinha, *Org. Commun*. **2011**, *4*, 1–8.
9. A. Kumar, B. Alimenla, L. Jamir, D. Sinha, U. B. Sinha, *Org. Commun*. **2012**, *5*, 64–69.
10. G. Bose, P. M. B. Barua, M. K. Chaudhuri, D. Kalita, A. T. Khan, *Chem. Lett.* **2001**, *4*, 290–291. **DOI:**10.1246/cl.2001.290
11. G. Kar, A. K. Saikia, U. Bora, S. K. Dehury, M. K Chaudhuri, *Tetrahedron Lett.* **2003**, *44*, 4503–4505. **DOI:**10.1016/S0040-4039(03)01015-3
12. J. Rabai, I. Kapovits, B. Tanacs, J. Tamas, *Synthesis* **1990**, 847–849. **DOI:**10.1055/s-1990-27033
13. S. Kajigaeshi, K. Murakawa, S. Fujisaki, T. Kakinami, *Bull. Chem. Soc. Jpn.* **1989**, *62*, 3376–3377. **DOI:**10.1246/bcsj.62.3376
14. M. H. Ali, S. Stricklin, *Synth. Commun.* **2006**, *36*, 1779–1786. **DOI:**10.1080/00397910600619044

15. E. Mondal, P. R. Sahu, G. Bose, A. T. Khan, *Tetrahedron Lett.* **2002**, *43*, 2843–2846. **DOI:**10.1016/S0040-4039(02)00345-3
16. E. Mondal, G. Bose, A. T. Khan, *Synlett* **2001**, *6*, 785–786. **DOI:**10.1055/s-2001-14579
17. U. B. Sinha, *J. Applicable Chem.* **2012**, *1*, 137–142.
18. A. Bernard, A. Kumar, L. Jamir, D. Sinha, U. B. Sinha, *Acta Chim. Slov.* **2009**, *56*, 457–461.
19. D. Dallinger, C. O. Kappe, *Chem. Rev*. **2007**, *107*, 2563–2591. **DOI:**10.1021/cr0509410
20. P. R. Likhar, G. N. Reddy, M. R. Reddy, *Res Chem. Intermed*. **2016**, *42*, 5991–5991. **DOI:**10.1007/s11164-015-2419-1
21. A. Srinivas, M. Sunitha, K. Raju, B. Ravinder, S. Anusha, T, Rajasri, P. Swapna, D. Sushmitha, D. Swaroopa, G. Nikitha, C. G. Rao, *Acta Chim. Slov.* **2017**, *64*, 319–331. **DOI:**10.17344/acsi.2016.3153
22. V. Sharma, P. K. Jaiswal, D. K. Yadav, M. Saran, J. Prikhodko, M. Mathur, A. K. Swami, I. V. Mashevskaya, S. Chaudhary, *Acta Chim. Slov.* **2017**, *64*, 988–1004. **DOI:** 10.17344/acsi.2017.3709
23. R. Gedye, F. Smith, K. Westaway, H. Ali, L. Baldisera, L. Laberge, J. Rousell, *Tetrahedron Lett*. **1986**, *27*, 279–282; **DOI:**10.1016/S0040-4039(00)83996-9
24. A. de la Hoz, A. D. Ortiz, A. Moreno, *Chem. Soc. Rev.* **2005**, *34*, 164–178. **DOI:**10.1039/B411438H
25. M. Francavilla, S. Intini, L. Luchetti, R. Luque, *Green Chem.* **2016**, *18*, 5971–5977. **DOI:**10.1039/C6GC02072K
26. J. Peng, F. Shi, Y. Gu, Y. Deng, *Green Chem.* **2003**, *5*, 224–226. **DOI:**10.1039/b211239f
27. J. McNulty, P. Das, P. McLeod, *Chem. Eur. J.* **2010**, *16*, 6756–6760. **DOI:**10.1002/chem.201000438
28. R. S. Varma, *Green Chem.* **1999**, *1*, 43–55. **DOI:**10.1039/a808223e
29. J. D. Moseley, C. O. Kappe, *Green Chem.* **2011**, *13*, 794–806. **DOI:**10.1039/c0gc00823k
30. S. A. Galema, *Chem. Soc. Rev.* **1997**, *26*, 233–238. **DOI:**10.1039/cs9972600233
31. H. E. Blackwell, *Org. Biomol. Chem.* **2003**, *1*, 1251–1255. **DOI:**10.1039/b301432k
32. P. Lidstrom, J. Tiemey, B. Wathey, J. Westman, *Tetrahedron* **2001**, *57*, 9225–9283. **DOI:**10.1016/S0040-4020(01)00906-1
33. D. Lafitte, V. Lamour, P. O. Tsvetkov, A. A. Makarov, M. Klich, P. Deprez, D. Moras, C. Briand, R. Gilli, *Biochemistry* **2002**, *41*, 7217–7223. **DOI:**10.1021/bi0159837
34. X. Li, M. Hilgers, M. Cunningham, Z. Chen, M. Trzoss, J. Zhang, L. Kohnen, T. Lam, C. Creighton, G. C. Kedar, K. Nelson, B. Kwan, M. Stidham, V. Brown-Driver, K. J. Shaw, J. Finn, *Bioorganic Med. Chem. Lett.* **2011**, *21*, 5171–5176. **DOI:**10.1016/j.bmcl.2011.07.059
35. U. Bora, M. K. Chaudhuri, D. Dey, S. S. Dhar, *Pure Appl. Chem.* **2001**, *73*, 93–102. **DOI:**10.1351/pac200173010093
36. P. Bharali, J.P. Saikia, A. Ray, B.K. Konwar, *Colloids Surf. B.* **2013**, *103*, 502–509. **DOI:**10.1016/j.colsurfb.2012.10.064
37. C. S. Mizuno, A. G. Chittiboyina, F. H. Shah, A. Patny, T. W. Kurtz, H. A. Pershadsingh, R. C. Speth, V. T. Karamyan, P. B. Carvalho, M. A. Avery, *J. Med. Chem.* **2010**, *53*, 1076–1085. **DOI:**10.1021/jm901272d
38. D. Pathak, N. Chadha, O. Silakari, *J. Mol. Grap. Modl.* **2016**, *70*, 85–93. **DOI:**10.1016/j.jmgm.2016.09.013
39. B. M. Vinoda, Y. D. Bodke, M. Vinuth, M. A. Sindhe, T. Venkatesh, S. Telkar, *Org. Chem. Curr. Res.* **2016**, *5*, 163. **DOI:**10.4172/2161-0401.1000163
40. M. Madhuri, C. Prasad, V. R. Avupati, *Int. J. Comp. Appl.* **2014**, *95*, 0975–8887. **DOI:**10.5120/16597-6403
41. V. Kavala, S. Naik, B. K. Patel, *J. Org. Chem.* **2005**, *70*, 4267–4271. **DOI:**10.1021/jo050059u

Povzetek

Razvili smo enostavno in okolju prijazno metodologijo za sintezo nekaterih brhttps://doi.org/10.1021/jo050059ustavljale potencialne antimikrobne učinkovine. Zaželjene spojine smo pripravili s pomočjo mikrovalovnega obsevanja v reakcijah »na vodi« ter z uporabo cetiltrimetilamonijevega tribromida (CTMATB) kot vira broma. Visoki izkoristki reakcij, ki smo jih dobili že pri kratkih reakcijskih časih, so glavni atributi predstavljenega sinteznega pristopa. Spojinam smo določil *in vitro* antibakterijsko aktivnost proti *Escherichia coli, Klebsiella pneumoniae*, *Staphylococcus aureus* in *Bacillus subtilis*. Dodatno so *in silico* študije razložile interakcije med raziskovanimi spojinami in bakterijskimi proteini.

DOI: 10.17344/acsi.2018.4705 *Acta Chim. Slov.* **2019,** *66,* 284–293

Scientific paper

Electrochemical Degradation of Reactive Blue 21 and Synthetic Textile Effluent by Using $Co_{47.5}/C_{47.5}$-PVC_5 Composite Electrode

Norazzizi Nordin,[1,*] Mohamad Anis Farith Pisal,[1] Nur Izzatie Hannah Razman[2] and Nur Farhana Jaafar[1]

[1] *School of Chemical Sciences, Universiti Sains Malaysia, 11800 Gelugor, Pulau Pinang, Malaysia.*

[2] *Centre of Foundation Studies, Universiti Teknologi MARA, Selangor Branch, Dengkil Campus, 43800 Dengkil, Selangor, Malaysia.*

** Corresponding author: E-mail: azzizi@usm.my (+604 653 4030)*

Received: 11-09-2018

Abstract

In this study, cobalt/graphite-polyvinyl chloride ($Co_{47.5}/C_{47.5}$–PVC_5) composite electrode was fabricated by mechanical alloying technique. The fabricated electrode and graphite rod were used as anode and cathode, respectively, in the decolourisation of aqueous C. I. Reactive Blue 21 (RB21) and synthetic textile effluent, containing a mixture of azo and anthraquinone dyes. The fabricated electrode showed high efficiency in the decolorisation of aqueous RB21 (99.95%) and synthetic textile effluent. This is further confirmed by the high reduction percentage (>75%) of COD and BOD_5 for both treated samples. The elemental composition study by using FESEM-EDX showed no significant changes in the composition of elements (C, Co and Cl) in the freshly fabricated electrode and after electrolysis of synthetic textile effluent. This showed that the fabricated electrode has a high mechanical strength and strong binding ability between C and Co due to the use of PVC as a binder.

Keywords: Composite electrode; decolorisation; electrochemical technique; C. I. Reactive Blue 21; synthetic textile effluent

1. Introduction

Synthetic dyes are among the most widely used pollutants in various industries, including textiles, paper, food and cosmetics. In line with the increase in usage by various industries, more than 100000 synthetic dyes with different structures are synthesised and more than 0.7 million tonnes of dyestuffs are produced throughout the year.[1] Synthetic dyes are categorised into several groups, depending on their applications (dyeing method) such as reactive dyes, basic dyes, acid dyes, vat dyes, mordant dyes, and disperse dyes. It also depends on their chemical structure, such as azo dyes, anthraquionone dyes, triphenylmethane dyes, and phthalocyanine dyes.[2]

In the textile industry, only 60%–90% of the dyes used are fixed to textile fibre while the other 10%–40% may remain unfixed to the fibre and will be released into the effluent.[3] This has an adverse effect on aquatic ecosystems due to the presence of synthetic dyes even in small quantities (<1 mg L^{-1}). They can be seen with the naked eye and have negatively affected the aesthetic quality and transparency of lakes, rivers, and others.[4] This in turn resulted in the destruction of aquatic ecosystems and the formation of dead deoxygenated zones in seas and oceans.[5] Therefore, the treatment of dye containing effluents is very important to reduce the negative effects on aquatic life.

Various strategies were reported on the treatment of textile effluents. They are classified into biological methods (enzymes and microorganisms), physical methods (filtration, flocculation, and adsorption), and oxidation methods (advanced oxidation and chemical oxidation).[6,7] However, today the use of electrochemical oxidation technique in textile wastewater treatment is getting more attention as this method does not involve the use of additional chemicals.[8,9] Previous studies have shown that this technique provided high efficiency in the removal of organic and inorganic pollutants from the effluents.[10,11,12] According to Najafpoor et al., this technique requires simple equipment, easy implementation, and on-site treatment in less space.[13]

In the electrochemical treatment of industrial effluents, anode plays an important role as it acts as a site for electrochemical reactions. The material for electrode fabrication plays a major role in determining the efficiency and reactivity of the prepared electrode in an electrochemical reaction. Various electrodes were used in the treatment of synthetic dyes and textile industrial effluents, such as Pt,[14–16] boron-doped diamond (BDD),[17–19] and dimensionally stable anodes (DSA).[20–22] In the current study, metal/graphite composite electrodes were prepared by mixing two different material (metal and graphite) powders with polyvinyl chloride (PVC). It is expected that the electrode performance in the electrochemical reaction will increase as the existence of two different materials in an electrode provides better synergistic effects and active bifunctional catalyst.[4]

The main objective of this study is to investigate the efficiency of $Co_{47.5}/C_{47.5}$-PVC_5 composite electrode in the decolourisation of aqueous RB21 and synthetic textile effluents. The effect of electrolysis conditions was also examined in the current study by investigating the effect of metal:-graphite ratio in the prepared electrode, supporting electrolyte concentration, applied voltage, and electrolysis time on RB21 decolourisation. The surface characterisation of the prepared composite electrode was also performed in this study by using FESEM, EDX, and gas sorption analyser.

2. Experimental

2. 1. Chemicals

All the chemicals used were of analytical research (AR) grade. Tin (Sn), copper (Cu), cobalt (Co), and aluminium (Al) powder with 99.9% purity were purchased from Aldrich. Sodium chloride (NaCl) solution, which acts as a supporting electrolyte in the electrolysis process, was purchased from R & M Chemicals. In this study, C. I. Reactive Blue 21 (RB21), C. I. Reactive Blue 19 (RB19), C. I. Reactive Violet 5 (RV5), and C. I. Reactive Red 198 (RR198) (Figure 1) were used as synthetic dyes and purchased from Dylon. Besides, polyvinyl chloride (PVC) and graphite powder (C) were obtained from BDH Ltd. whereas tetrahydrofuran (THF) was obtained from Systerm.

2. 2. Preparation of Metal/Graphite-PVC Composite Electrode

The anode was prepared by mixing 0.475 g of metal powder (Sn, Cu, Al, or Co) with 0.475 g of graphite (C) powder (M:C is 50:50 (wt. %), in which M = metal) and 0.05 g of PVC as a binder by using a mechanical alloying technique (MAT).[4] The ratio of metal and C powders to PVC was 95:5 PVC (wt. %). Then, 4 mL of THF was used to dissolve the PVC. The mixture was stirred until homogenous and oven dried at 100 °C for 2 h. The mixture was placed in a stainless-steel mould of 1 cm diameter and pressed at 10^4 kg cm^{-2}. The pellet obtained (approximately 1.5 g) was then connected to a silver wire with silver conducting paint (Sigma-Aldrich) and sealed in a glass rod. Subsequently, epoxy resin (Devcon) was applied to cover the silver wire connecting surface. The metal/graphite-PVC composite electrode was used in the decolourisation of RB21 solution.

2. 3. Preparation of Aqueous RB21 and Synthetic Textile Effluent

In this study, two types of samples were used, namely aqueous RB21 and synthetic textile effluent. The RB21

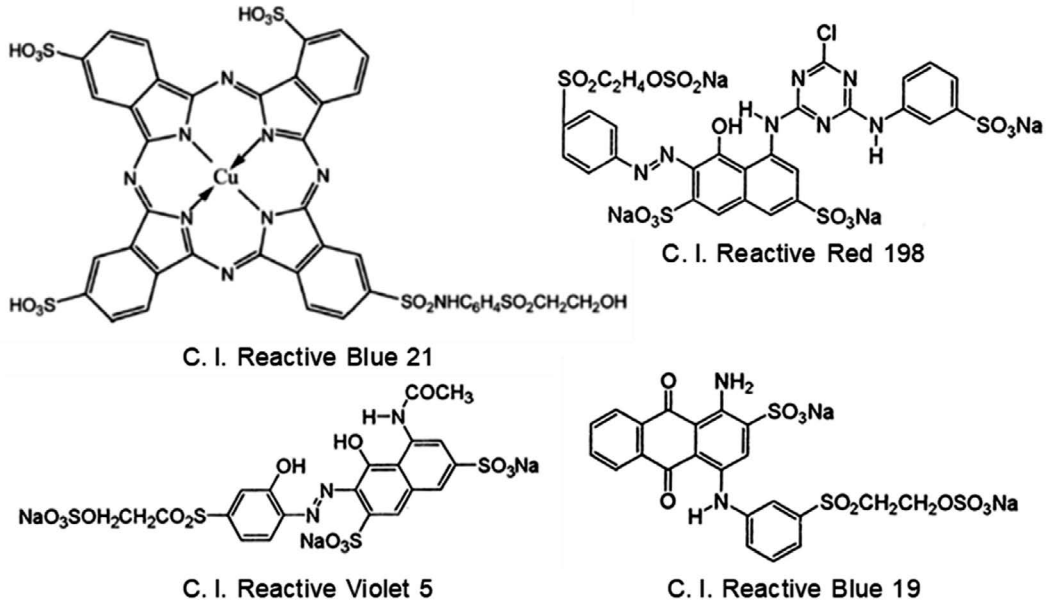

Figure 1. Structures of RB21, RB19, RV5, and RR198.

solution was prepared by dissolving a certain amount of RB21 in deionised water. Synthetic textile effluent was prepared by dissolving equal amount of RB21, RB19, RV5, and RR198 in tap water along with the other chemical additives, as described by Verma et al.[23]

2. 4. Decolourisation of Aqueous RB21 and Synthetic Textile Effluent

The electrolysis of aqueous RB21 was performed by using a two-electrode system, which consisted of an anode (metal/graphite-PVC composite electrode) and a cathode (graphite rod electrode), with NaCl solution as a supporting electrolyte. Prior to electrolysis, both anode and cathode were rinsed with distilled water and a small amount of acetone. A direct current (DC) power supply (TTi PSU Bench CPX 400) and stirrer hotplate with magnetic bar were used throughout the electrolysis process. The electrochemical cell used was a simple and undivided cell made of Pyrex glass with a capacity of 250 mL. The electrodes were placed vertically and parallel to each other in the electrochemical cell, with a constant gap between electrodes at approximately 20 mm. The electrolysis of synthetic textile effluent was carried out by using similar procedures, as described above. The same anode from the previous electrolysis of aqueous RB21 was used in the electrolysis of synthetic textile effluent.

2. 5. Optimisation of Electrolysis Parameters for the Decolourisation of Aqueous RB21

Optimisation of electrolysis parameters was carried out by optimising the ratio of metal and C in the prepared electrode, supporting electrolyte concentration, electrolysis time and applied voltage. For the optimisation of metal and C ratio in the prepared electrode, the ratio and mass of metal, C, and PVC are summarised in Table 1. The procedure for preparation of anodes is similar as mentioned in Section 2.2.

2. 6. Instrumentation

To observe the decolourisation level of aqueous RB21 and synthetic textile effluent, the sample solution was characterised by using an UV-Vis (Perkin Elmer Lambda 35) spectrometer in the range of 200–900 nm by using 10 mm quartz cuvettes. The surface properties of the electrode were determined by using gas sorption analyser (ASAP 2020 V4.010). Brunauer-Emmett-Teller (BET) method was used to determine the surface area of the electrode. BJH model was used to calculate the pore size. Surface morphology of the electrode was observed by using Field Emission Scanning Electron Microscope (FESEM) (Leo Supra 50 VP). The elemental composition of prepared electrode was determined by using Energy Dispersive X-ray (EDX) spectrometer. The size and shape of the particles were observed by using a transmission electron microscopy (TEM) (Philips CM12-12796) with an accelerating voltage of 100 kV. Samples were prepared on carbon-coated copper grids covered with a polyvinyl formal polymer by adding a drop onto the grid and evaporating the solvent (ethanol) in ambient condition.

2. 7. Analytical Measurement

Decolourisation of aqueous RB21 was determined based on the original concentration of RB21 (c_i) and RB21 concentration after electrolysis process (c_t) by measuring absorbance at the wavelength of 624 nm in the Vis region of RB21. Measurement of RB21 absorbance was performed by using UV-Vis spectrophotometer. Decolourisation was calculated in percentage (%) as in the following equation:

$$\text{Decolourisation (\%)} = \left(\frac{C_i - C_t}{c_i}\right) \times 100\% \quad (1)$$

The absorbance versus RB21 concentrations graph in the range of 10 to 110 mg L^{-1} is a linear graph referring to the following equation:

$$\text{Absorbance} = 0.015c + 0.033 \ (R^2 = 0.996) \quad (2)$$

Where c represents the concentration of RB21 solution in mg L^{-1} unit.

2. 8. Reduction of COD and BOD_5

Chemical Oxygen Demand (COD) and Biochemical Oxygen Demand (BOD_5) were performed on an aqueous RB21 and synthetic textile effluent before and after electrolysis by using the prepared electrode. Standard methods

Table 1. The composition ratio and mass of Co, C, and PVC for the preparation of Co/C-PVC electrodes.

Electrode	Co:C ratio (%)	Mass of Co (g)	Mass of C (g)	Mass of PVC (g)
$Co_{95.0}/C_{0.0}$–PVC_5	100:0	0.950	–	0.05
$Co_{66.5}/C_{28.5}$– PVC_5	70:30	0.665	0.285	0.05
$Co_{47.5}/C_{47.5}$– PVC_5	50:50	0.475	0.475	0.05
$Co_{28.5}/C_{66.5}$– PVC_5	30:70	0.285	0.665	0.05
$Co_{0.0}/C_{95.0}$– PVC_5	0:100	–	0.950	0.05

508B and 507 were used for the COD and BOD_5 analyses, respectively, as described by the American Public Health Association (APHA 1981).[24]

2. 9. Statistical Analysis

The data were expressed as mean ± standard error (SE) with at least three times replication. The statistical analysis was carried out by using Statistical Package for Social Sciences (SPSS) Version 17.0 with one-way ANOVA. The data obtained were considered as statistically significant when the value of $p < 0.05$.

3. Results and Discussion

3. 1. Preliminary Experiment

Four types of metal/graphite-PVC composite electrodes were prepared and used in the preliminary experiment to investigate the efficiency of the prepared electrodes in the decolourisation of RB21 solution. This was to identify the best metal-graphite mixture that could give a maximum decolourisation of aqueous RB21. The results in Figure 2 show that maximum decolourisation percentage

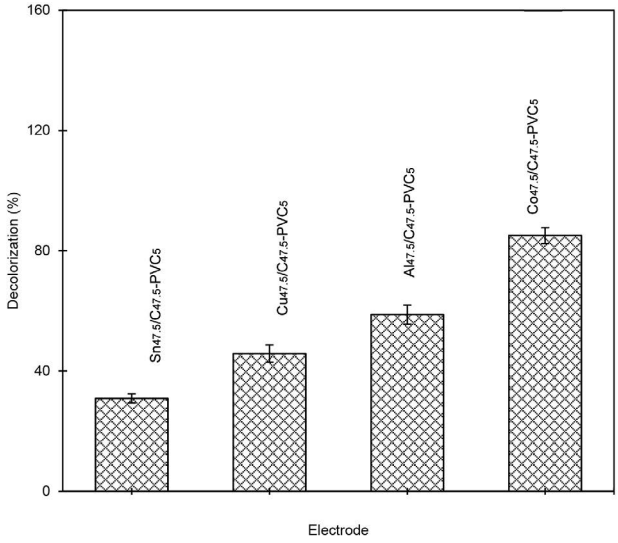

Figure 2. Decolourisation percentage of aqueous RB21 after electrolysis by using different types of metal/graphite-PVC composite electrodes. $[RB21]_o$ = 50 mg L^{-1}; [NaCl] = 1.0 mol L^{-1}; E = 5 V; I = 0.62 A; t = 15 min.

(85.09%) of RB21 is obtained by using $Co_{47.5}/C_{47.5}$-PVC_5 electrode compared to other metal/graphite-PVC composite electrodes. This showed that the mixture of Co and C in the $Co_{47.5}/C_{47.5}$-PVC_5 electrode showed the best synergistic effect with a maximum decolourisation percentage as compared to other electrodes. Therefore, this electrode will be used in the optimisation of electrolysis parameters for the decolourisation of aqueous RB21.

3. 2. Optimisation of Electrolysis Parameters for the Decolourisation of Aqueous RB21

Figure 3a shows the percentage of decolourisation on RB21 by using Co/C-PVC electrodes with different Co:C ratios (100:0, 70:30, 50:50, 30:70, 0:100). The electrode with a composition ratio of 50:50 (known as $Co_{47.5}/C_{47.5}$-PVC_5 electrode) exhibited the highest percentage of decolourisation, which was 85.27% as compared to other electrodes. This showed that the ratio of Co and C in the electrode provided better efficiency for RB21 removal. The composition ratio of 100:0 and 70:30 (known as $Co_{95.0}/C_{0.0}$-PVC_5 and $Co_{66.5}/C_{25.5}$-PVC_5 electrodes, respectively) gave almost equal percentage of decolourisation (84.8% and 82.5%, respectively) as the decolourisation percentage obtained for 50:50 ratio. However, the use of more Co powder in both electrodes can increase the operating costs. Therefore, the electrode with a 50:50 ratio ($Co_{47.5}$ / $C_{47.5}$-PVC_5 electrode) was considered as an optimum electrode based on the highest RB21 decolourisation percentage achieved in this study with less Co used in the preparation of the electrode.

Figure 3b shows the effect of the supporting electrolyte concentration on the decolourisation of RB21 solution. The supporting electrolyte (NaCl solution) was added in the electrochemical system to modify the electrochemical conductivity and facilitate the electrical current flow.[4,25] The presence of chloride ions from the addition of NaCl can lead to active oxidant formations, such as chlorine, hypochlorous acid, and/or hypochlorite, depending on the pH (Equations 3–5). These active oxidants are beneficial in the oxidation of organic pollutants at the anode or/and in bulk solution (Equation 6).[8]

$$2\,Cl^- \rightarrow Cl_2 + 2\,e^- \quad (3)$$

$$Cl_2 + H_2O \rightarrow HOCl + H^+ + Cl^- \quad (4)$$

$$HOCl \rightarrow H^+ + OCl^- \quad (5)$$

$$\text{Organics} + OCl^- \rightarrow \text{intermediates} \rightarrow CO_2 + Cl^- + H_2O \quad (6)$$

As shown in Figure 3b, the percentage of decolourisation increased from 74.57% to 87.45% with the concentration of NaCl from 0.01 mol L^{-1} to 2.0 mol L^{-1}, respectively, after 15 min of electrolysis. Plus, electrolysis by using 0.5 mol L^{-1} and 2.0 mol L^{-1} NaCl resulted in almost equal percentage of decolourisation (85.09% and 85.27%, respectively). In addition, application of higher concentration of electrolyte (in this case 1.0 mol L^{-1} and above) resulted in electrode damage and heat production.

As shown in Equations 3–6, the increased NaCl concentration has increased the electrogenerated OCl^- anions. This electrode corrosion was also due to the presence of OCl^- ions in the electrolysis solution. This was reported

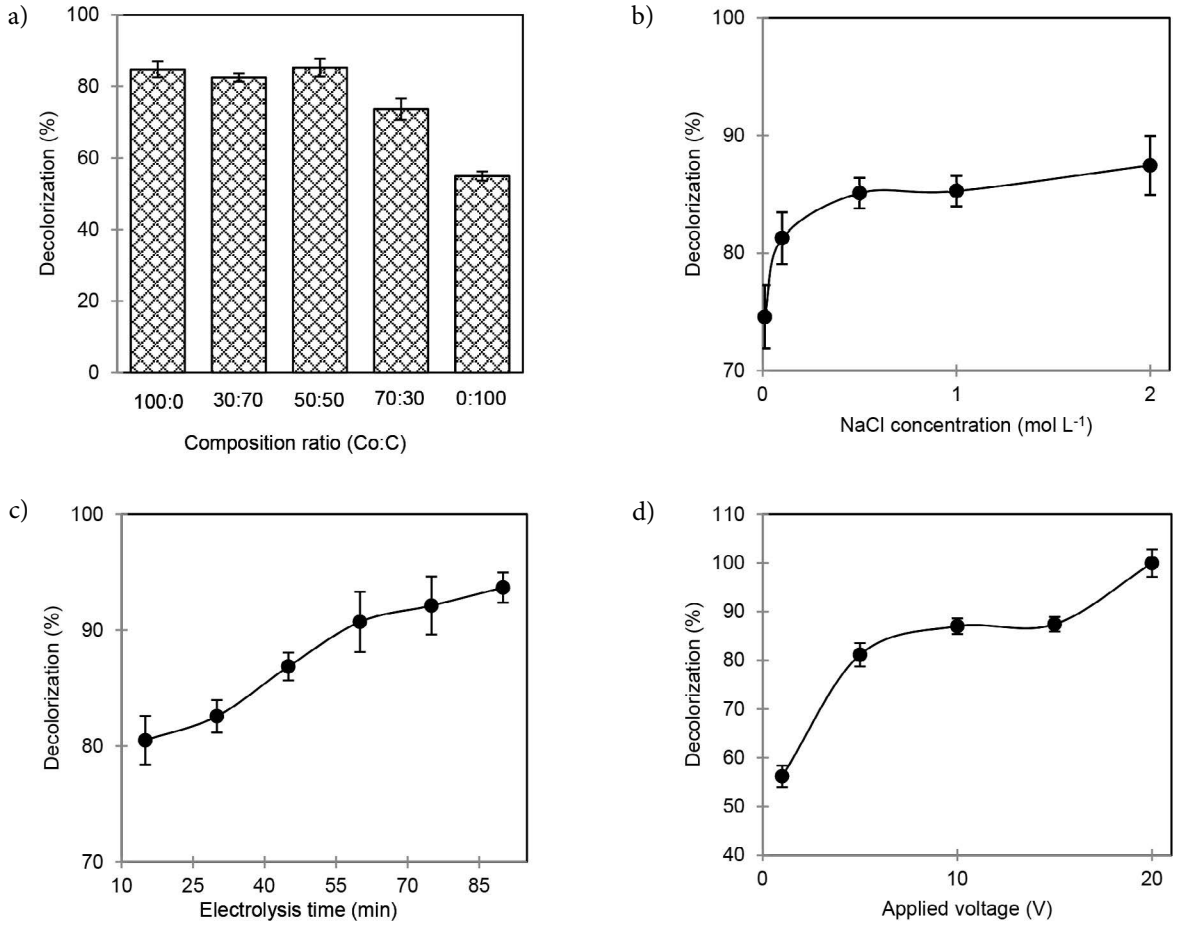

Figure 3. Decolourisation percentage of aqueous RB21 by using different (a) Co:C ratio in the prepared electrode ($[RB21]_o$ = 50 mg L^{-1}; [NaCl] = 1.0 mol L^{-1}; E = 5 V; I = 0.62 A; t = 15 min); (b) NaCl concentration ($[RB21]_o$ = 50 mg L^{-1}; I = 0.02–1.12 A (for 0.01 – 2.0 mol L^{-1} NaCl); E = 5 V; t = 15 min; anode = $Co_{47.5}/C_{47.5}$-PVC_5); (c) electrolysis time ($[RB21]_o$ = 50 mg L^{-1}; [NaCl] = 0.5 mol L^{-1}; E = 5 V; I = 0.36 A; anode = $Co_{47.5}/C_{47.5}$-PVC_5); (d) applied voltage ($[RB21]_o$ = 50 mg L^{-1}; [NaCl] = 0.5 mol L^{-1}; t = 45 min; I = 0.06–0.93 A (for 1–20 V); anode = $Co_{47.5}/C_{47.5}$–PVC_5).

by several researchers in previous studies.[26–28] According to Galvan-Martinez et al.,[26] OCl^- ions are corrosive to some elements. This resulted in the corrosion of $Co_{47.5}/C_{47.5}$-PVC_5 electrode surface after electrolysis of RB21 by using NaCl electrolytes. Therefore, 0.5 mol L^{-1} was considered as an optimum concentration of NaCl for the decolourisation of RB21 with 85.09% of RB21 decolourisation percentage.

The effect of electrolysis time on the decolourisation percentage of RB21 was investigated in the range of 15 min to 90 min. The increase in electrolysis time from this study showed an increased decolourisation percentage of up to 93.67% (Figure 3c). Due to the increase in generation of OCl^- ions in the bulk solution resulting from the longer electrolysis time, better RB21 decolourisation efficiency was obtained as compared to a shorter electrolysis time. Electrolysis by using 60 min to 90 min leads to the electrode damage and corrosion of anode materials into the bulk solution. Due to the anode corrosion, precipitate was formed at the end of the electrolysis process and mixed with the electrolysis product. At 45 min, the electrode showed its ability to decolourise the aqueous RB21 without the formation of precipitate at the end of the electrolysis. Therefore, 45 min was considered as an optimum electrolysis time, with 86.87% of RB21 decolourisation percentage.

The decolourisation efficiency was significantly affected by the applied voltage which was studied in the range of 1 V to 20 V. In Figure 3d, increasing the applied voltage from 1 V to 20 V increased the percentage of RB21 decolourisation after 45 min of electrolysis from 56.20% to 99.95%, respectively. Again, this was due to the increased generation of OCl^- species by the application of high value of applied voltage. Therefore, 20 V of applied voltage was considered as an optimum value of applied voltage based on the complete decolourisation of RB21 obtained in Figure 3d.

3. 3. Decolourisation of Aqueous RB21

Figure 4 shows the UV–Vis spectra obtained for 50 mg L^{-1} of RB21 in 0.5 mol L^{-1} NaCl by using the optimum electrolysis parameters as obtained in the previous Section

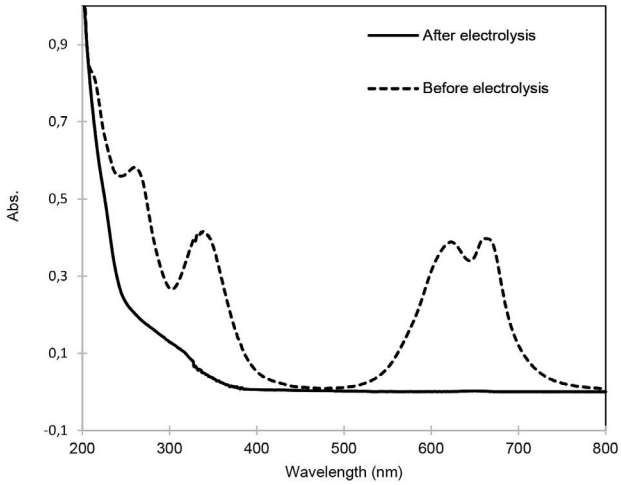

Figure 4. UV–Vis spectra of aqueous RB21 before and after electrochemical treatment by using $Co_{47.5}C_{47.5}$-PVC composite electrode. ($[RB21]_o$ = 50 mg L^{-1}; [NaCl] = 0.5 mol L^{-1}; t = 45 min; E = 20 V; I = 0.93 A).

(3.2). The initial spectra (0 min) showed the appearance of three peaks at the wavelength of 339 nm in the UV region, and 624 nm and 663 nm in the visible region. The peak at 663 nm exhibited maximum absorption and was selected for subsequent study.[29,30] The spectra obtained after 45 min of electrolysis showed the disappearance of all peaks after the electrolysis process. This suggested that the complex structure of RB21 was completely destroyed by the electrochemical process, and a colourless solution was produced after the electrolysis.

3. 4. Decolourisation of Synthetic Textile Effluent

Optimum electrolysis conditions obtained in Section 3.2 were also applied in the decolourisation of synthetic textile effluent. This was to determine the efficiency of $Co_{47.5}/C_{47.5}$-PVC_5 electrode in the degradation of various types of structurally different dyes and other pollutants. Figure 5 shows the UV-Vis spectra obtained for synthetic textile effluent before and after electrolysis. For untreated effluents (0 min), three peaks were observed at the wavelengths of 337 nm in the UV region, and 626 nm and 667 nm in the visible region. After 45 min of electrolysis with an applied voltage of 20 V in the presence of 0.5 mol L^{-1} of NaCl as a supporting electrolyte, the previous peaks completely disappeared. The colour of dyes mixture solution changes from blackish blue to colourless solution at the end of the electrolysis. It proved that the electrochemical treatment by using $Co_{47.5}/C_{47.5}$-PVC_5 electrode was able to degrade the pollutants contained in the effluent.

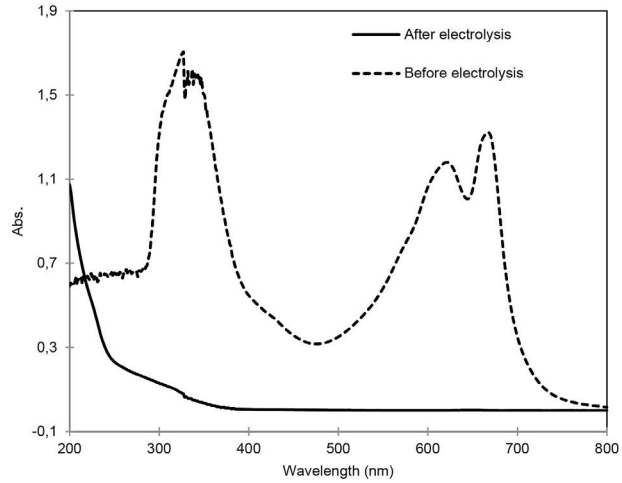

Figure 5. UV–Vis spectra for synthetic textile effluent before and after electrochemical treatment by using $Co_{47.5}/C_{47.5}$-PVC_5 electrode. ([NaCl] = 0.5 mol L^{-1}; t = 45 min; E = 20 V; I = 0.93 A).

3. 5. Reduction of COD and BOD_5

The results for COD and BOD_5 analyses of treated and untreated aqueous RB21 and synthetic textile effluent are summarised in Table 2. In addition to the colour removal, the electrochemical treatment by using the $Co_{47.5}/C_{47.5}$-PVC_5 electrode could also significantly reduce the COD and BOD_5 (Table 2). Table 2 also shows that the removal percentages of COD and BOD_5 for the synthetic textile effluents were lower than for the RB21 solution. This was due to the presence of more organic and inorganic compounds in synthetic textile effluents that created more challenging conditions for the COD and BOD_5 removal, resulting in lower COD and BOD_5 removal percentage than for the aqueous RB21.

Table 2. COD, BOD_5, and pH of untreated and treated 50 mg L^{-1} RB21 solution and synthetic textile effluent by using $Co_{47.5}/C_{47.5}$-PVC_5 electrode. ([NaCl] = 0.5 mol L^{-1}, E = 20 V, t = 45 min).

Sample	Analysis	Untreated	Treated	Removal (%)
RB21 solution	COD (mg L^{-1})	182.4 ± 7.1	15.5 ± 8.5	91.5 ± 6.0
	BOD_5 (mg L^{-1})	56.8 ± 6.7	10.7 ± 8.3	81.2 ± 5.7
	pH	6.6	6.3	–
Synthetic textile effluent	COD (mg L^{-1})	753.0 ± 5.5	89.8 ± 5.0	88.1 ± 6.2
	BOD_5 (mg L^{-1})	81.6 ± 4.2	19.1 ± 7.9	76.6 ± 4.8
	pH	12.3	11.9	–

According to Chatzisymeon et al.,[31] two mechanisms are involved in oxidation of pollutants by an electrochemical technique, namely direct anodic oxidation and indirect anodic oxidation. For direct anodic oxidation, pollutants are absorbed on anodic surfaces and destroyed by anodic electron transfer reactions. Indirect anodic oxidation involves the use of electrogenerated oxidants, such as Cl_2, OCl^-, $OH^\bullet$, O_3 and H_2O_2.[31,32] The effect of NaCl presence on mineralisation of RB21 and synthetic textile effluent can be explained by referring to the following equations (Equations 7–10).

$$H_2O + M + Cl^- \rightarrow M[ClOH^\bullet] + H^+ + 2\,e^- \quad (7)$$

$$R + M[ClOH^\bullet] \rightarrow M + RO + H^+ + Cl^- \quad (8)$$

$$H_2O + M[ClOH^\bullet] + Cl^- \rightarrow M + O_2 + \\ + Cl_2 + 3\,H^+ + 4\,e^- \quad (9)$$

$$H_2O + Cl^- \rightarrow HOCl + H^+ + 2\,e^- \quad (10)$$

In the presence of NaCl, anodic water discharge resulted in the formation of chlorohydroxyl ($ClOH^\bullet$) radicals on the anode surface (M) (Equation 7) which then oxidized the organic matter (R) (Equation 8). Furthermore, molecular O_2 and free Cl_2 can be formed by the reaction between H_2O and $ClOH^\bullet$ radicals on the anode surface (Equation 9). Then, the resulting Cl^- ions will react with water to form OCl^- ions (Equation 10). The presence of large amount of electrogenerated OCl^- ions in the bulk electrolysis provided better mineralisation efficiency (COD and BOD_5 reduction) as these electrogenerated species are beneficial in the degradation of organic pollutants in both samples.[32]

3. 6. Characterisation of $Co_{47.5}/C_{47.5}$-PVC_5 Electrode

Figure 6 shows the FESEM micrograph obtained from the morphological study of freshly prepared $Co_{47.5}/C_{47.5}$-PVC_5 composite electrode and after electrolysis of synthetic textile effluent by using 20 V applied voltage and 45 min electrolysis. Figure 6a shows the distribution of Co and C in the electrode can be seen clearly and are mixed quite well. However, the surface of the electrode slightly changes after electrolysis of RB21 solution in Figure 6b.

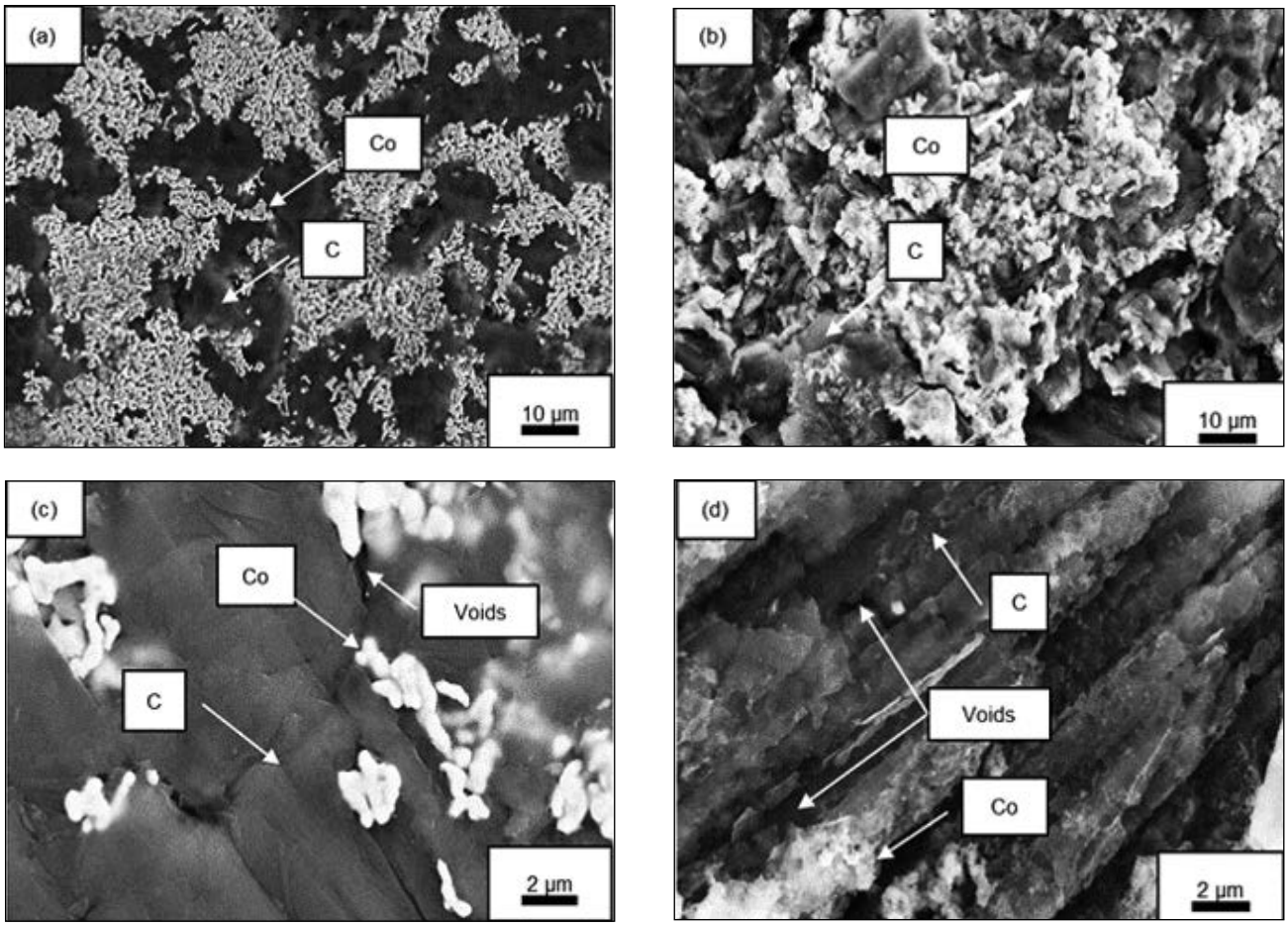

Figure 6. FESEM micrograph of $Co_{47.5}/C_{47.5}$-PVC_5 electrode (a and c) fresh and (b and d) after electrolysis of synthetic textile effluent by using (a and b) 1000x and (c and d) 5000x magnification. ($[RB21]_o$ = 50 mg L^{-1}; [NaCl] = 0.5 mol L^{-1}; t = 45 min; E = 20 V).

This is due to the degradation of the pollutant that occurred on the surface of the electrode. FESEM micrograph in Figure 6d shows a significant change in the surface of the electrode as compared to the freshly prepared electrode in Figure 6c. The surface of the electrode was no longer smooth as compared to the freshly prepared electrode.

In addition, the surface of the prepared electrode showed the existence of voids that were not filled by the element and PVC. The presence of voids in the surface was very important as it increased the porosity characteristic of the electrode for a better electrochemical reaction.[33] Figure 6c and 6d show the presence of voids in the surface of each electrode before and after electrolysis, respectively. The presence of voids in the electrode surface after electrolysis showed that this electrode can be used for further electrolysis process without reducing its efficiency. TEM micrograph of freshly fabricated $Co_{47.5}/C_{47.5}$-PVC_5 powder in Figure 7 indicated that the mixture formed agglomerate of different shapes. The Co particles can be identified due to their almost regular shape while the C was formed in an irregular shape as demonstrated in Figure 7.

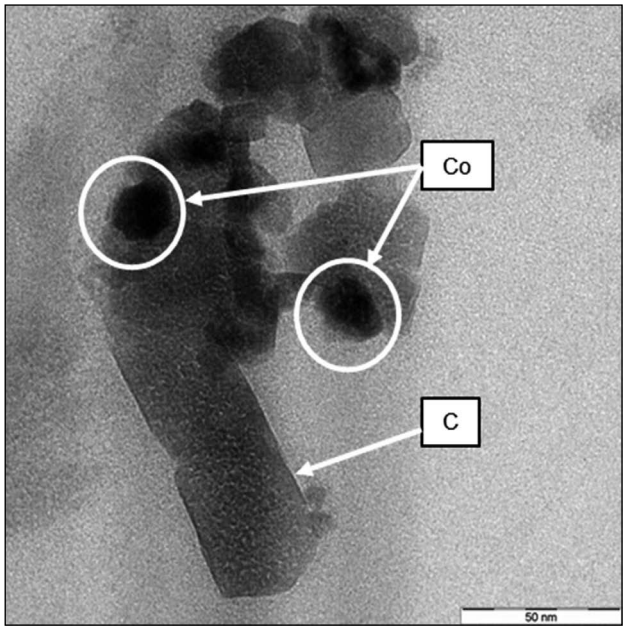

Figure 7. TEM micrograph of fresh $Co_{47.5}/C_{47.5}$-PVC_5 powder by using 100,000x magnification.

The elemental composition of $Co_{47.5}/C_{47.5}$-PVC_5 electrode was determined by using the EDX analysis and the results are presented in Table 3. The results obtained proved that the prepared electrode contained C, Co, and Cl. The presence of Cl elements was due to the use of PVC as a binder in the fabricated electrode. The composition of C for both samples (fresh and after electrolysis) was higher as compared to the Co due to the presence of polymeric carbon chain in PVC. Additionally, no significant changes were indicated by the weight percentage of each element in the fresh electrode and after the electrolysis of synthetic textile effluent. The difference in weight percentage may occur if the precipitate resulted after the electrolysis of synthetic textile effluent. The resulting precipitation was due to the corrosion of anode materials. However, no precipitate was obtained after the electrolysis of synthetic textile effluent. It can be concluded that PVC acts as a good binder agent between C and Co elements inside the electrode.

The surface area and pore size of fresh $Co_{47.5}/C_{47.5}$-PVC_5 powder and after electrolysis of synthetic textile effluent were analysed by using Brunauer-Emmett-Teller (BET) method. The surface area of fresh $Co_{47.5}/C_{47.5}$-PVC_5 and after electrolysis was 2.45 $m^2 g^{-1}$ and 6.89 $m^2 g^{-1}$, while the pore size was 12.53 to 9.19 nm, respectively. The increased surface area and reduced pore size of the $Co_{47.5}/C_{47.5}$-PVC_5 powder after electrolysis were due to the adsorption of compounds on a solid surface. However, no significant difference was shown by the results obtained from the surface area and pore size of $Co_{47.5}/C_{47.5}$-PVC_5 powder ($p > 0.05$). The results obtained were consistent with the observations made based on the FESEM micrographs. The pore sizes obtained from this study for freshly prepared $Co_{47.5}/C_{47.5}$-PVC_5 and after electrolysis of synthetic textile effluent were referred to A mesopore type, as mentioned by Chen et al.[34]

4. Conclusions

The Co/C-PVC electrode with a composition ratio of 50:50 (known as the $Co_{47.5}/C_{47.5}$-PVC_5) was considered to be the best metal/graphite-PVC composite electrode because it gives the highest decolourisation percentage of aqueous RB21. Optimum electrolysis conditions for the decolourisation of aqueous RB21 by using $Co_{47.5}/C_{47.5}$-

Table 3. Elemental composition of $Co_{47.5}/C_{47.5}$-PVC_5 electrode before and after electrolysis of RB21 solution. ($[RB21]_o$ = 50 mg L^{-1}; [NaCl] = 0.5 mol L^{-1}; t = 45 min; E = 20 V).

Element	Before electrolysis		After electrolysis	
	Weight (%)	Atomic (%)	Weight (%)	Atomic (%)
C	77.37	93.96	75.25	91.38
Co	19.96	4.94	21.23	6.25
Cl	2.67	1.10	3.52	2.37

PVC_5 composite electrode was by using 20 V of applied voltage for 45 min of electrolysis time in the presence of 0.5 mol L^{-1} NaCl solution as a supporting electrolyte. Under the optimum electrolysis conditions, 99.95% of RB21 decolourisation percentage was achieved. The $Co_{47.5}/C_{47.5}$-PVC_5 composite electrode also showed high efficiency in the decolourisation of synthetic textile effluent by using similar optimum electrolysis conditions as mentioned above. This was further confirmed by COD and BOD_5 analyses, in which a high percentage of decolourisation was achieved for COD and BOD_5 analyses of RB21 solution and synthetic dye effluent. The electrode surface characterisation by using FESEM showed no significant changes in the presence of void on the electrode surface before and after RB21 electrolysis. The presence of voids on the electrode surface after electrolysis showed that this electrode can be used for further electrolysis process without reducing its efficiency. The results obtained for elemental composition by using EDX showed no significant changes in the composition of C, Co, and Cl elements in the prepared electrode before and after electrolysis of RB21 solution. This showed a good bonding between C and Co by using PVC as a binding agent.

5. Aknowledgements

The funding from Universiti Sains Malaysia through short-term grants (304-PKIMIA/6315104) and Universiti Teknologi MARA through LESTARI grant (600-IRMI/MyRA 5/3/LESTARI (075/2017)) are gratefully acknowledged.

6. Conflict of Interest

The authors declare no conflict of interest.

7. References

1. A. R. Tehrani-Bagha, K. Holmberg, *Materials* **2013**, *6*, 580–608. **DOI:**10.3390/ma6020580
2. N. Ž. Šekuljica, N. Ž. Prlainović, A. B. Stefanović, M. G. Žuža, D. Z. Čičkarić, D. Ž. Mijin, Z. D. Knežević-Jugović, *Sci. World J.* **2015**, *2015*, 1–12. **DOI:**10.1155/2015/371625
3. V. Lopez-Grimau, M. C. Gutierrez, *Chemosphere* **2006**, *62*, 106–112. **DOI:**10.1016/j.chemosphere.2005.03.076
4. N. Nordin, S. F. Mohd Amir, M. R. Yusop, M. R. Othman, *Acta Chim. Slov.* **2015**, *62*, 642–651. **DOI:**10.17344/acsi.2014.1264
5. S. Wijetunga, X. F. Li, C. Jian, *J. Hazard. Mater.* **2010**, *177*, 792–798. **DOI:**10.1016/j.jhazmat.2009.12.103
6. C. R. Holkar, A. J. Jadhav, D. V. Pinjari, N. M. Mahamuni, A. B. Pandit, *J. Environ. Manage.* **2016**, *182*, 351–366. **DOI:**10.1016/j.jenvman.2016.07.090
7. T. Robinson, G. McMullan, R. Marchant, P. Nigam, *Bioresour. Technol.* **2001**. *77*, 247–255. **DOI:**10.1016/S0960-8524(00)00080-8
8. C. A. Martinez-Huitle, E. Brillas, *Appl. Catal. B-Environ.* **2009**, *87*, 105–145. **DOI:**10.1016/j.apcatb.2008.09.017
9. M. Riera-Torres, M. C. Gutierrez, *Chem. Eng. J.* **2010,** *156*, 114–120. **DOI:**10.1016/j.cej.2009.10.006
10. F. Orts, A. I. del Río, J. Molina, J. Bonastre, F. Cases, *J. Electroanal. Chem.* **2018**, 808, 387–394. **DOI:**10.1016/j.jelechem.2017.06.051
11. J. Luo, Y. B. Wang, D. Cao, K. Xiao, T. Guo, X. Zhao, *Chem. Eng. J.* **2018**, *343*, 69–77. **DOI:**10.1016/j.cej.2018.02.120
12. Z. H. Mussa, F. F. Al-Qaim, M. R. Othman, M. P. Abdullah, J. Latip, Z. Zakria, *J. Taiwan Inst. Chem. Eng.* **2017**, *72*, 37–44. **DOI:**10.1016/j.jtice.2016.12.031
13. A. A. Najafpoor, M. Davoudi, E. R. Salmani, *J. Env. Health Sci. Eng.* **2017**, *15*, 1–11. **DOI:**10.1186/s40201-017-0273-3
14. M. Jović, D. Stanković, D. Manojlović, I. Anđelković, A. Milić, B. Dojčinović, G. Roglić, *Int. J. Electrochem. Sci.* **2013**, *8*, 168–183.
15. M. A. Hasnat, J. A. Safwan, M. S. Islam, Z. Rahman, M. R. Karim, T. J. Pirzada, A. J. Samed, M. M. Rahman, *J. Ind. Eng. Chem.* **2015**, *21*, 787–791. **DOI:**10.1016/j.jiec.2014.04.013
16. N. Nordin, S. F. Mohd Amir, Riyanto, M. R. Othman, *Int. J. Electrochem. Sci.* **2013**, *8*, 11403–11415.
17. R. Salazar, M. S. Ureta-Zanartu, C. Gonzalez-Vargas, C. D. N. Brito, C. A. Martinez-Huitle, *Chemosphere* **2018**, *198,* 21–29. **DOI:**10.1016/j.chemosphere.2017.12.092
18. S. Alcocer, A. Picos, A. R. Uribe, T. Pérez, J. M. Peralta-Hernández, *Chemosphere* **2018,** *205*, 682–689. **DOI:**10.1016/j.chemosphere.2018.04.155
19. U. Morales, C. J. Escudero, M. J. Rivero, I. Ortiz, J. M. Rocha, J. M. Peralta-Hernández, *J. Electroanal. Chem.* **2018**, *808*, 180–188. **DOI:**10.1016/j.jelechem.2017.12.014
20. D. Rajkumar, B. J. Song, J. G. Kim, *Dyes Pigm.* **2007**, *72*, 1–7. **DOI:**10.1016/j.dyepig.2005.07.015
21. R. E. Palma-Goyes, J. Silva-Agredo, J. Vazquez-Arenas, I. Romero-Ibarra, R. A. Torres-Palma, *J. Env. Chem. Eng.* **2018**, *6*, 3010–3017. **DOI:**10.1016/j.jece.2018.04.035
22. M. R. Cruz-Díaz, E. P. Rivero, F. A. Rodríguez, R. Domínguez-Bautista, *Electrochim. Acta.* **2018**, *260*, 726–737. **DOI:**10.1016/j.electacta.2017.12.025
23. A. K. Verma, P. Bhunia, R. R. Dash, R. D. Tyagi, R. Y. Surampalli, T. C. Zhang, *Clean (Weinh).* **2015**, *43*, 767–774. **DOI:**10.1002/clen.201400256
24. APHA, AWWA, WPCF, Standard Methods for the Examination of Water and Effluents, American Public Health Association, Washington DC, USA, **1981**, 525–535.
25. I. A. Sengil, M. Ozacar, *J. Hazard. Mater.* **2009**, *16*, 1369–1376. **DOI:**10.1016/j.jhazmat.2008.04.100
26. R. Galvan-Martinez, M. A. Baltazar, E. Mejia, M. Salaza, A. Contreras, R. Orozco-Cruz, *Int. J. Electrochem. Sci.* **2018**, *13*, 9561–9573. **DOI:**10.20964/2018.10.04
27. S. H. Oliveira, M. A. G. A. Lima, F. P. França, M. R. S. Vieira, P. Silva, S. L. U. Filho, *Int. J. Biol. Macromol.* **2016**, *88*, 27–35. **DOI:**10.1016/j.ijbiomac.2016.03.033

28. X. Y. Huang, Y. Shen, X. Wei, M. Haapasalo, *J. Endod.* **2017**, *43*, 1847–1851. **DOI:**10.1016/j.joen.2017.06.033
29. H. Shakoor, M. Ibrahim, M. Usman, M. Adrees, M.A. Mehmood, F. Abbas, N. Rasool, U. Rashid, *J. Dispersion. Sci. Technol.* **2016**, *37*, 144–154. **DOI:**10.1080/01932691.2015.1035387
30. M. C. Silva, A. D. Corrêa, M. T. S. P. Amorim, P. Parpot, J. A. Torres, P. M. B. Chagas, *J. Mol. Catal. B: Enzym.* **2012**, *77*, 9–14. **DOI:**10.1016/j.molcatb.2011.12.006
31. E. Chatzisymeon, N. P. Xekoukoulotakis, A. Coz, N. Kalogerakis, D. Mantzavinos, *J. Hazard. Mater.* **2006**, *137*, 998–1007. **DOI:**10.1016/j.jhazmat.2006.03.032
32. S. Raghu, C. A. Basha, *J. Hazard. Mater.* **2007**, *139*, 382–390. **DOI:**10.1016/j.jhazmat.2006.06.082
33. N. Nordin, M. R. Othman, *Sains Malays.* **2014**, *43*, 1761–1768. **DOI:**10.17576/jsm-2014-4312-10
34. S. Chen, J. Zhang, C. Zhang, Q. Yue, Y. Li, C. Li, *Desalination* **2010**, *252*, 149–156. **DOI:**10.1016/j.desal.2009.10.010

Povzetek

V tej raziskavi smo s tehniko mehanske tvorbe zlitin izdelali kompozitno elektrodo iz kobalta/grafita in polivinilklorida ($Co_{47,5}/C_{47,5}$-PVC_5). Novo elektrodo smo uporabili kot anodo, grafitno paličko pa kot katodo za razbarvanje vodne raztopine C. I. Reactive Blue 21 (RB21) in sintetične tekstilne odpadne vode, ki je vsebovala zmes azo in antrakinonskih barvil. Novoizdelana elektroda je pokazala visoko učinkovitost za razbarvanje RB21 v vodni raztopini (99,95%) in sintetične tekstilne odpadne vode. To smo še nadalje potrdili z visokim deležem zmanjšanja (>75%) KPK in BPK_5 pri obeh obdelanih vzorcih. Elementna sestava (C, Co in Cl), določena s FESEM-EDX, ni bila bistveno različna med sveže izdelano elektrodo in po elektrolizi sintetične tekstilne odpadne vode. To je potrdilo visoko mehansko trdnost novoizdelane elektrode in visoko stopnjo vezave med C in Co zaradi uporabe PVC kot veziva.

DOI: 10.17344/acsi.2018.4714 *Acta Chim. Slov.* **2019,** *66,* 294–307

Scientific paper

Design, Synthesis, Biological Evaluation and Molecular Docking Studies of Some New Sulfonamides Possessing 1,4-Benzodioxane Nucleus

Misbah Irshad,[1,*] Muhammad Athar Abbasi,[2] Aziz-Ur-Rehman,[2] Qamar Ali,[1] Muhammad Aslam,[1] Fozia Iram,[3] Muhammad Shahid,[4] Muhammad Ashraf,[5] Muhammad Arif Lodhi[6] and Syed Babar Jamal[7]

[1] *Department of Chemistry, Division of Science & Technology, University of Education, Lahore-54770, Pakistan.*

[2] *Department of Chemistry, Government College University, Lahore-54000, Pakistan.*

[3] *Department of Chemistry, Lahore College for Women University, Lahore-75500, Pakistan*

[4] *Department of Biochemistry, University of Agriculture, Faisalabad-38040, Pakistan.*

[5] *Department of Pharmacy; The Islamia University of Bahawalpur, Bahawalpur-63100, Pakistan.*

[6] *Department of Biochemistry, Abdul Wali Khan University, Mardan-23200, Pakistan.*

[7] *Department of Bioinformatics, Islamic International University, Islamabad, Pakistan.*

** Corresponding author: E-mail: misbahchatha@hotmail.com; misbahirshad@ue.edu.pk*
Tel: (+92)-42-99262232

Received: 09-10-2018

Abstract

In the current research work we have reported a series of *N*-aryl-2,3-dihydrobenzo[1,4]dioxine-6-sulfonamides **3** and their *N*-substituted derivatives **6** and **7**, obtained from **3** with benzyl chloride and ethyl iodide, respectively. The synthesis was accomplished as a multistep sequence. The structural confirmations were established by ^{1}H NMR, IR and EIMS spectral techniques. Butyrylcholinesterase (BChE), acetylcholinesterase (AChE) and lipoxygenase (LOX) enzymes were used in this study. It was observed that most of the compounds prepared exhibit a moderate activity against BChE and AChE but promisingly good activity against lipoxygenase. Among the parent sulfonamides **3a**, **3b**, **3c** and **3e** showed the proficient antimicrobial activities, while from the derivatives **6a**, **6c**, **7a**, **7b** and **7c** were found active against the selected panel of bacterial and fungal species. Hemolytic activity was also conducted to check their therapeutic utility. All the compounds were computationally docked against LOX, BChE and AChE enzymes.

Keywords: 2,3-Dihydrobenzo[1,4]dioxine-6-sulfonyl chloride; lipoxygenase enzyme; antimicrobial and hemolytic activities; molecular docking.

1. Introduction

The very first prepared antimicrobial agents were sulfonamides, which are bacteriostatic agents and active against Gram negative and Gram positive bacteria. Basically, sulfonamides contain a benzene ring with sulfonyl and amino group at *para* position and have general formula Ar SO_2NHR. The nature of Arl and R varies from simple hydrogen to aliphatic carboaromatic, heterocyclic, OH, NH_2 or sugar scaffolds. SAR studies revealed that the liberated NH_2 group of sulfonamides is responsible for their activity. Low activity was observed in the case of attached substituents at *ortho* and *meta* positions.[1–5] Sulfonamides restrain folic acid in bacteria which facilitates the production of bacterial DNA and RNA. Dihydropteroic acid is precursor of folic acid. Dihydropteroate synthase is responsible for the transformation of dihydropteroate diphosphate and *P*-aminobenzoic acid into dihydropteroic

acid; on the other hand, sulfonamides hinder this enzyme.[6,7] These sulfonamide drugs can be classified as oral (absorbed and unabsorbed) and topical. Depending on the action absorbable sulfonamides can be short-, intermediate- and long-acting. Their absorption takes place through stomach and small intestine.[8] Commonly these sulfa drugs are synthesized by treating substituted sulfonyl chloride with suitable amine compounds. Sulfonamides are used to cure membrane infections, enteritis, ulcerative colitis and for skin treatments. In agriculture sulfonamides have antiherbicidal and antifungal uses. They have wide applications as antiobesity,[9] anticancer, antiviral,[3] protease inhibitors,[10] diuretic,[11,12] hypoglycemic,[13] antithyroid,[14] antitumor,[15–17] anti-neuropathic pain,[18] antibacterial,[19,20] cyclooxygenase[21] and carbonic anhydrase inhibitory agents.[22]

Compounds containing a 1,4-benzodioxane skeleton display wider range of biological activities,[23] such as anticancer,[24,25] immunosuppressive,[26] antiinflammatory,[27] antibacterial[28] and some others.[29,30]

Additionally, interaction modes of the synthesized compounds were examined by molecular docking approach. The purpose of docking methodologies was to forecast the ligand and target complex and to align the molecular database (designed inhibitors) on the basis of binding affinity to that of target. The MOE-Dock was used for docking of all the synthesized inhibitors with the binding site of target enzymes. The eventual objective of molecular docking was to get ligands with better characteristics displaying good inhibition potential.[31] This research work is a productive effort to bring in close proximity the pharmacologically significant moieties. Keeping continuity in connection with the research work on sulfonamide molecules,[32] the different *N*-substituted sulfonamides derived from 1,4-benzodioxine-6-sulfonyl chloride were synthesized. It was aimed that the new drugs bearing sulfamoyl functionality would have striking activity and be able to cope with the challenges.

2. Experimental

2. 1. General

2,3-Dihydrobenzo[1,4]dioxine-6-sulfonyl chloride, different aryl amines and the other electrophilic reagents were purchased from local suppliers of chemicals. All the solvents were used after distillation and purification. Griffin and George melting point instrument was employed to record melting points of the target compounds. The open capillary tube was used and melting points are reported uncorrected. The TLC was utilized to check the purity and reaction progress. TLC plates were finished from pre-coated silica gel G-25-UV_{254}. The gradient solvent systems of ethyl acetate ($C_4H_8O_2$) and *n*-hexane (C_6H_{14}) were applied. The detection was carried out at 254 nm and TLC plates were developed by ceric sulphate reagent. On a Jasco-320-A spectrophotometer the IR spectra were recorded. The pellet of a sample was made with KBr and functional group stretchings are reported in wave numbers (cm^{-1}). NMR spectra were recorded on Bruker spectrometers. The deutrated methanol and chloroform were used as the solvents. The operating frequencies thus utilized were 300 and 400 MHz and chemical shifts are given in ppm. On a JMS-HX-110 spectrometer the mass spectra (EIMS) were measured with a data system.

2. 2. Synthesis

2. 2. 1. General Procedure for the Synthesis of *N*-Aryl-2,3-dihydrobenzo[1,4]dioxine-6-sulfonamides (3a–e) in Aqueous Medium

0.85 mmol of various substituted aryl amines **2a–e** were dispensed in 50 mL of distilled water contained in a 250 mL round-bottom flask. The pH of the reacting medium was maintained at 9.0–10.0. The aqueous solution of Na_2CO_3 was added drop wise at 25 °C. Subsequently 0.85 mmol (0.20 g) of 2,3-dihydrobenzo[1,4]dioxine-6-sulfonyl chloride (**1**) was added slowly to the reaction mass over 10–15 min. The reaction mixture was kept on stirring at RT till the TLC confirmation indicated the completion of the reaction. The workup was done by slowly adding conc. aq. HCl (2 mL) and dropping pH to 2.0. The title compounds **3a–e** were collected as solid precipitates on filtration and washed with immense volume of distilled water.

***N*-(2,3-Dimethylphenyl)-2,3-dihydrobenzo[1,4]dioxine-6-sulfonamide (3a)**

White solid; yield: 80% (217.7 mg); m.p. 102–104 °C; molecular formula: $C_{16}H_{17}NO_4S$; molecular weight: 319 g/mol; HR-MS: $[M]^+$ 319.3772 (Calcd. for $C_{16}H_{17}NO_4S$; 319.3854); IR (KBr, cm^{-1}): ν_{max} stretching: 3419 (N-H), 3026 (C-H Ar ring), 2914 (CH_2), 1613 (C=C Ar ring), 1325 (SO_2),1125 (C-O-C of ether); ^{1}H NMR (400 MHz,C-DCl_3): δ (ppm) 1.99 (s, 3H, CH_3-2"), 2.27 (s, 3H, CH_3-1"), 4.24–4.27 (m, 4H, CH_2-2, CH_2-3), 6.73 (brd, J = 7.6 Hz, 1H, H-4'), 6.78 (t, J = 7.6 Hz, 1H, H-5'), 6.80 (d, J = 8.0 Hz, 1H, H-6'), 6.95 (d, J = 8.4 Hz, 1H, H-8), 7.18 (dd, J_1 = 8.4 Hz, J_2 = 2.0 Hz, 1H, H-7), 7.25 (d, J = 2.0 Hz, 1H, H-5); EIMS: *m/z* 319 $[M]^+$, 255 $[M\text{-}SO_2]^+$, 214 $[C_6H_3C_2H_4O\text{-}_2SO_2NH]^+$, 199 $[C_6H_3C_2H_4O_2SO_2]^+$, 135 $[C_6H_3C_2H_4O_2]^+$, 107 $[C_6H_3O_2]^+$, 105 $[C_6H_3(CH_3)_2]^+$, 90 $[C_6H_3CH_3]^+$, 79 $[C_4H(CH_3)_2]^+$, 75 $[C_6H_3]^+$, 64 $[C_4HCH_3]^+$.

***N*-(2,4-Dimethylphenyl)-2,3-dihydrobenzo[1,4]dioxine-6-sulfonamide (3b)**

White solid; yield: 89% (242.2 mg); m.p. 108–110 °C; molecular formula: $C_{16}H_{17}NO_4S$; molecular weight: 319 g/mol; HR-MS: $[M]^+$ 319.3772 (Calcd. for $C_{16}H_{17}NO_4S$; 319.3854); IR (KBr, cm^{-1}): ν_{max} stretching: 3435 (N-H), 3021 (C-H Ar ring), 2917 (-CH_2-), 1615 (C=C Ar ring), 1324 (-SO_2-), 1140 (C-O-C of ether); ^{1}H NMR (400 MHz, $CDCl_3$): δ (ppm) 1.99 (s, 3H, CH_3-2"), 2.24 (s, 3H, CH_3-1"), 4.24–4.26 (m, 4H, CH_2-2, CH_2-3), 6.80 (s, 1H, H-3'),

6.84 (d, J = 8.0 Hz, 1H, H-5'), 6.92 (d, J = 8.4 Hz, 1H, H-6'), 7.12 (d, J = 8.0 Hz, 1H, H-8), 7.17 (dd, J_1= 8.4 Hz, J_2 = 2.0 Hz, 1H, H-7), 7.26 (d, J = 2.0 Hz, 1H, H-5); EIMS: *m/z* 319 $[M]^+$, 255 $[M\text{-}SO_2]^+$, 214 $[C_6H_3C_2H_4O_2SO_2NH]^+$, 199 $[C_6H_3C_2H_4O_2SO_2]^+$, 135 $[C_6H_3C_2H_4O_2]^+$, 107 $[C_6H_3O_2]^+$, 105 $[C_6H_3(CH_3)_2]^+$, 90 $[C_6H_3CH_3]^+$, 79 $[C_4H(CH_3)_2]^+$, 75 $[C_6H_3]^+$, 64 $[C_4HCH_3]^+$.

_N_-(2,5-Dimethylphenyl)-2,3-dihydrobenzo[1,4]dioxine-6-sulfonamide (3c)

White solid; yield: 82% (223.1 mg); m.p. 124–126 °C; molecular formula: $C_{16}H_{17}NO_4S$; molecular weight: 319 g/mol; HR-MS: $[M]^+$ 319.3772 (Calcd. for $C_{16}H_{17}NO_4S$; 319.3854); IR (KBr, cm^{-1}): ν_{max} stretching: 3415 (N-H), 3024 (C-H Ar ring), 2912 (-CH_2-), 1619 (C=C Ar ring), 1325 (-SO_2-), 1122 (C-O-C of ether); ^{1}H NMR (300 MHz, CD_3OD): δ (ppm) 1.96 (s, 3H, CH_3-2"), 2.20 (s, 3H, CH_3-1"), 4.22–4.30 (m, 4H, CH_2-2, CH_2-3), 6.85 (d, J = 7.6 Hz, 1H, H-4'), 6.89 (d, J = 7.5 Hz, 1H, H-3'), 6.91 (s, 1H, H-6'), 6.99 (d, J = 8.1 Hz, 1H, H-8), 7.09 (d, J = 2.1 Hz, 1H, H-5), 7.13 (dd, J_1 = 7.8 Hz, J_2 = 2.1 Hz, 1H, H-7); EIMS: *m/z* 319 $[M]^+$, 255 $[M\text{-}SO_2]^+$, 214 $[C_6H_3C_2H_4O_2SO_2NH]^+$, 199 $[C_6H_3C_2H_4O_2SO_2]^+$, 135 $[C_6H_3C_2H_4O_2]^+$, 107 $[C_6H_3O_2]^+$, 105 $[C_6H_3(CH_3)_2]^+$, 90 $[C_6H_3CH_3]^+$, 79 $[C_4H(CH_3)_2]^+$, 75 $[C_6H_3]^+$, 64 $[C_4HCH_3]^+$.

_N_-(2,6-Dimethylphenyl)-2,3-dihydrobenzo[1,4]dioxine-6-sulfonamide (3d)

White solid; yield: 71% (193.2 mg); m.p. 151–153 °C; molecular formula: $C_{16}H_{17}NO_4S$; molecular weight: 319 g/mol; HR-MS: $[M]^+$ 319.3772 (Calcd. for $C_{16}H_{17}NO_4S$; 319.3854); IR (KBr, cm^{-1}): ν_{max} stretching: 3410 (N-H), 3045 (C-H Ar ring), 2909 (-CH_2-), 1614 (C=C), 1326 (-SO_2-), 1125 (C-O-C of ether); ^{1}H NMR (300 MHz, $CDCl_3$): δ (ppm) 2.02 (s, 6H, CH_3-1", CH_3-2"), 4.25–4.30 (m, 4H, CH_2-2, CH_2-3), 6.93 (brd, J = 7.8 Hz, 1H, H-4'), 7.01 (d, J = 8.4 Hz, 2H, H-3', H-5'), 7.03 (d, J = 8.4 Hz, 1H, H-8), 7.38 (d, J = 2.4 Hz, 1H, H-5), 7.48 (dd, J_1 = 8.4 Hz, J_2 = 2.4 Hz, 1H, H-7); EIMS: *m/z* 319 $[M]^+$, 255 $[M\text{-}SO_2]^+$, 214 $[C_6H_3C_2H_4O_2SO_2NH]^+$, 199 $[C_6H_3C_2H_4O_2SO_2]^+$, 135 $[C_6H_3C_2H_4O_2]^+$, 107 $[C_6H_3O_2]^+$, 105 $[C_6H_3(CH_3)_2]^+$, 90 $[C_6H_3CH_3]^+$, 79 $[C_4H(CH_3)_2]^+$, 75 $[C_6H_3]^+$, 64 $[C_4HCH_3]^+$.

_N_-(3,4-Dimethylphenyl)-2,3-dihydrobenzo[1,4]dioxine-6-sulfonamide (3e)

White solid; yield: 86% (234.0 mg); m.p. 124–126 °C; molecular formula: $C_{16}H_{17}NO_4S$; molecular weight: 319 g/mol; HR-MS: $[M]^+$ 319.3772 (Calcd. for $C_{16}H_{17}NO_4S$; 319.3854); IR (KBr, cm^{-1}): ν_{max} stretching: 3422 (N-H), 3018 (C-H Ar ring), 2919 (-CH_2-), 1615 (C=C Ar ring), 1323 (-SO_2), 1118 (C-O-C of ether); ^{1}H NMR (400 MHz,$CDCl_3$): δ (ppm) 2.15 (s, 6H, CH_3-1", CH_3-2"), 4.23–4.25 (m, 4H, CH_2-2, CH_2-3), 6.76 (d, J = 7.6 Hz, 1H, H-5'), 6.81 (s, 1H, H-2'), 6.84 (d, J = 8.0 Hz, 1H, H-6'), 6.96 (d, J = 8.0 Hz, 1H, H-8), 7.22 (dd, J_1 = 8.4 Hz, J_2 = 2.0 Hz, 1H, H-7), 7.28 (d, J = 2.0 Hz, 1H, H-5); EIMS: *m/z* 319 $[M]^+$, 255 $[M\text{-}SO_2]^+$, 214 $[C_6H_3C_2H_4O_2SO_2NH]^+$, 199 $[C_6H_3C_2H_4O_2SO_2]^+$, 135 $[C_6H_3C_2H_4O_2]^+$, 107 $[C_6H_3O_2]^+$, 105 $[C_6H_3(CH_3)_2]^+$, 90 $[C_6H_3CH_3]^+$, 79 $[C_4H(CH_3)_2]^+$, 75 $[C_6H_3]^+$, 64 $[C_4HCH_3]^+$.

2. 2. 2. General Procedure for the Synthesis of Compounds 6a–e and 7a–e

0.40 mmol (0.01 g) of lithum hydride was added to a solution containing of 0.1 g of compounds **3a–e** in 25 mL of aprotic solvent (DMF) and kept in round-bottom flask at 25 °C. On complete addition, the reaction mixture was stirred for half an hour. The benzyl chloride (**4**) and ethyl iodide (**5**) were added into the reaction mixture to establish **6a–e** and **7a–e** series, respectively. The stirring lasted for 1–2 h. The monitoring of the reaction completion was done by TLC. The reaction contents were quenched with cold distilled water after ensuring the complete conversion of the reactants. The corresponding *N*-benzyl/ethyl derivatives of *N*-aryl-2,3-dihydrobenzo[1,4]dioxine-6-sulfonamides **6a–e** and **7a–e** were obtained as solid precipitates on filtration. The subsequent washing with distilled water and drying yielded our target molecules. The greasy and sticky compounds were isolated through solvent extraction by using chloroform.

***N*-Benzyl-*N*-(2,3-dimethylphenyl)-2,3-dihydrobenzo[1,4]dioxine-6-sulfonamide (6a)**

Yellow sticky solid; yield: 86% (110.3 mg); molecular formula: $C_{23}H_{23}NO_4S$; molecular weight: 409 g/mol; HR-MS: $[M]^+$ 409.4991 (Calcd. for $C_{23}H_{23}NO_4S$; 409.5187); IR (KBr, cm^{-1}): ν_{max} stretching: 3416 (N-H), 3015 (C-H Ar ring), 2918 (-CH_2-), 1617 (C=C Ar ring), 1329 (-SO_2-), 1135 (C-O-C of ether); ^{1}H NMR (400 MHz, CD_3OD): δ (ppm) 2.00 (s, 3H, CH_3-2'"), 2.06 (s, 3H, CH_3-1'"), 4.25–4.29 (m, 4H, CH_2-2, CH_2-3), 4.63 (s, 2H, CH_2-7"), 6.81 (d, J = 7.6 Hz, 1H, H-4'), 6.87–6.95 (m, 5H, H-2" to H-6"), 7.02 (d, J = 7.2 Hz, 1H, H-6'), 7.10 (t, J = 7.6 Hz, 1H, H-5'), 7.31 (d, J = 8.4 Hz, 1H, H-8), 7.34 (d, J = 2.0 Hz, 1H, H-5), 7.38 (dd, J_1 = 8.4 Hz, J_2 = 2.0 Hz, 1H, H-7); EIMS: *m/z* 409 $[M]^+$, 345 $[M\text{-}SO_2]^+$, 304 $[C_6H_3C_2H_4O_2SO_2NCH_2C_6H_5]^+$, 199 $[C_6H_3C_2H_4O_2SO_2]^+$, 135 $[C_6H_3C_2H_4O_2]^+$, 107 $[C_6H_3O_2]^+$,105 $[C_6H_3(CH_3)_2]^+$, 91 $[C_7H_7]^+$, 90 $[C_6H_3CH_3]^+$, 79 $[C_4H(CH_3)_2]^+$, 75 $[C_6H_3]^+$, 65 $[C_5H_5]^+$, 64 $[C_4HCH_3]^+$.

***N*-Benzyl-*N*-(2,4-dimethylphenyl)-2,3-dihydrobenzo[1,4]dioxine-6-sulfonamide (6b)**

Light grey sticky solid; yield: 78% (100.0 mg); molecular formula: $C_{23}H_{23}NO_4S$; molecular weight: 409 g/mol; HR-MS: $[M]^+$ 409.4991 (Calcd. for $C_{23}H_{23}NO_4S$; 409.5187); IR (KBr, cm^{-1}): ν_{max} stretching: 3423 (N-H), 3067 (C-H Ar ring), 2932 (-CH_2-), 1617 (C=C Ar ring), 1326 (-SO_2), 1145 (C-O-C of ether); ^{1}H NMR (300 MHz,CD_3OD): δ (ppm) 1.90 (s, 3H, CH_3-2'"), 2.22 (s, 3H,

CH_3-1'''), 4.19 (s, 2H, CH_2-7''), 4.32–4.34 (m, 4H, CH_2-2, CH_2-3), 6.55 (d, *J* = 8.1 Hz, 1H, H-5'), 6.86 (d, *J* = 7.8 Hz, 1H, H-6'), 6.90 (s, 1H, H-3'), 6.92–7.01 (m, 5H, H-2'' to H-6''), 7.10 (d, *J* = 8.1 Hz, 1H, H-8), 7.17 (d, *J* = 2.1 Hz, 1H, H-5), 7.19 (dd, J_1 = 8.1 Hz, J_2 = 2.1Hz, 1H, H-7); EIMS: *m/z* 409 $[M]^+$, 345 $[M\text{-}SO_2]^+$, 304 $[C_6H_3C_2H_4O_2SO_2N\text{-}CH_2C_6H_5]^+$, 199 $[C_6H_3C_2H_4O_2SO_2]^+$, 135 $[C_6H_3C_2H_4O_2]^+$, 107 $[C_6H_3O_2]^+$,105 $[C_6H_3(CH_3)_2]^+$, 91 $[C_7H_7]^+$, 90 $[C_6H_3CH_3]^+$, 79 $[C_4H(CH_3)_2]^+$, 75 $[C_6H_3]^+$, 65 $[C_5H_5]^+$, 64 $[C_4HCH_3]^+$.

N-Benzyl-N-(2,5-dimethylphenyl)-2,3-dihydrobenzo [1,4]dioxine-6-sulfonamide (6c)

Yellow sticky solid; yield: 76% (97.4 mg); molecular formula: $C_{23}H_{23}NO_4S$; molecular weight: 409 g/mol; HR-MS: $[M]^+$ 409.4991 (Calcd. for $C_{23}H_{23}NO_4S$; 409.5187); IR (KBr, cm^{-1}): ν_{max} stretching: 3431 (N-H), 3041 (C-H Ar ring), 2922 (-CH_2-), 1612 (C=C Ar ring), 1328 (-SO_2-), 1131 (C-O-C of ether); ^{1}H NMR (300 MHz, CD_3OD): δ (ppm) 1.89 (s, 3H, CH_3-2'''), 2.14 (s, 3H, CH_3-1'''), 4.30–4.36 (m, 4H, CH_2-2, CH_2-3), 4.56 (s, 2H, CH_2-7''), 6.95 (dd, J_1 = 8.4 Hz, J_2 = 2.1 Hz, 1H, H-4'), 7.00 (d, *J* = 8.4 Hz, 1H, H-3'), 7.03 (s, 1H, H-6'), 7.09–7.20 (m, 5H, H-2'' to H-6''), 7.56 (d, *J* = 8.4 Hz, 1H, H-8), 7.62 (d, *J* = 2.1 Hz, 1H, H-5), 7.71 (dd, J_1 = 8.4 Hz, J_2 = 2.4 Hz, 1H, H-7); EIMS: *m/z* 409 $[M]^+$, 345 $[M\text{-}SO_2]^+$, 304 $[C_6H_3C_2H_4O_2SO_2N\text{-}CH_2C_6H_5]^+$, 199 $[C_6H_3C_2H_4O_2SO_2]^+$, 135 $[C_6H_3C_2H_4O_2]^+$, 107 $[C_6H_3O_2]^+$,105 $[C_6H_3(CH_3)_2]^+$, 91 $[C_7H_7]^+$, 90 $[C_6H_3CH_3]^+$, 79 $[C_4H(CH_3)_2]^+$, 75 $[C_6H_3]^+$, 65 $[C_5H_5]^+$, 64 $[C_4HCH_3]^+$.

N-Benzyl-N-(2,6-dimethylphenyl)-2,3-dihydrobenzo [1,4]dioxine-6-sulfonamide (6d)

Creamy white crystalline solid; yield: 72% (92.3 mg); m.p. 156–158 °C; molecular formula: $C_{23}H_{23}NO_4S$; molecular weight: 409 g/mol; HR-MS: $[M]^+$ 409.4991 (Calcd. for $C_{23}H_{23}NO_4S$; 409.5187); IR (KBr, cm^{-1}): ν_{max} stretching: 3422 (N-H), 3013 (C-H Ar ring), 2927 (-CH_2-), 1643 (C=C Ar ring), 1325 (-SO_2-), 1126 (C-O-C of ether); ^{1}H NMR (400 MHz, CD_3OD): δ (ppm) 2.68 (s, 6H, CH_3-1''', CH_3-2'''), 4.23–4.33 (m, 4H, CH_2-2, CH_2-3), 4.61 (s, 2H, CH_2-7''), 6.14–6.94 (m, 5H, H-2'' to H-6''), 6.96 (brd, *J* = 8.8 Hz, 2H, H-3', H-5'), 7.01 (brd, *J* = 8.8 Hz, 1H, H-4'), 7.27 (d, *J* = 8.0 Hz, 1H, H-8), 7.32 (d, *J* = 2.0 Hz, 1H, H-5), 7.58 (dd, J_1 = 8.4 Hz, J_2 = 2.0 Hz, 1H, H-7), EIMS: *m/z* 409 $[M]^+$, 345 $[M\text{-}SO_2]^+$, 304 $[C_6H_3C_2H_4O_2SO_2NCH_2C_6H_5]^+$, 199 $[C_6H_3C_2H_4O_2SO_2]^+$, 135 $[C_6H_3C_2H_4O_2]^+$, 107 $[C_6H_3O_2]^+$,105 $[C_6H_3(CH_3)_2]^+$, 91 $[C_7H_7]^+$, 90 $[C_6H_3CH_3]^+$, 79 $[C_4H(CH_3)_2]^+$, 75 $[C_6H_3]^+$, 65 $[C_5H_5]^+$, 64 $[C_4HCH_3]^+$.

N-Benzyl-N-(3,4-dimethylphenyl)-2,3-dihydrobenzo[1,4]dioxine-6-sulfonamide (6e)

White solid; yield: 90% (115.4 mg); m.p. 118–120 °C; molecular formula: $C_{23}H_{23}NO_4S$; molecular weight: 409 g/mol; HR-MS: $[M]^+$ 409.4991 (Calcd. for $C_{23}H_{23}NO_4S$; 409.5187); IR (KBr, cm^{-1}): ν_{max} stretching: 3416 (N-H), 3055 (C-H Ar ring), 2943 (-CH_2-), 1622 (C=C Ar ring), 1322 (-SO_2), 1134 (C-O-C of ether); ^{1}H NMR (400 MHz,$CDCl_3$): δ (ppm) 2.10 (s, 3H, CH_3-2'''), 2.14 (s, 3H, CH_3-1'''), 4.28–4.31 (m, 4H, CH_2-2, CH_2-3), 4.65 (s, 2H, CH_2-7''), 6.66 (d, *J* = 7.2 Hz, 1H, H-5'), 6.78 (s, 1H, H-2'), 6.81 (d, *J* = 7.2 Hz, 1H, H-6'), 6.88–6.90 (m, 5H, H-2'' to H-6''), 6.92 (d, *J* = 8.4 Hz, 1H, H-8), 7.12 (dd, J_1 = 8.4 Hz, J_2 = 2.0 Hz, 1H, H-7), 7.21 (d, *J* = 2.0 Hz, 1H, H-5); EIMS: *m/z* 409 $[M]^+$, 345 $[M\text{-}SO_2]^+$, 304 $[C_6H_3C_2H_4O_2SO_2N\text{-}CH_2C_6H_5]^+$, 199 $[C_6H_3C_2H_4O_2SO_2]^+$, 135 $[C_6H_3C_2H_4O_2]^+$, 107 $[C_6H_3O_2]^+$,105 $[C_6H_3(CH_3)_2]^+$, 91 $[C_7H_7]^+$, 90 $[C_6H_3CH_3]^+$, 79 $[C_4H(CH_3)_2]^+$, 75 $[C_6H_3]^+$, 65 $[C_5H_5]^+$, 64 $[C_4HCH_3]^+$.

N-(2,3-Dimethylphenyl)-N-ethyl-2,3-dihydrobenzo[1,4]dioxine-6-sulfonamide (7a)

Yellow sticky solid; yield: 82 % (89.2 mg); molecular formula: $C_{18}H_{21}NO_4S$; molecular weight: 347 g/mol; HR-MS: $[M]^+$ 347.4302 (Calcd. for $C_{18}H_{21}NO_4S$;347.4587); IR (KBr, cm^{-1}): ν_{max} stretching: 3435 (N-H), 3032 (C-H Ar ring), 2929 (-CH_2-), 1625 (C=C Ar ring), 1320 (-SO_2), 1123 (C-O-C of ether); ^{1}H NMR (400 MHz, CD_3OD): δ (ppm) 0.96 (t, *J* = 7.2 Hz, 3H, CH_3-2''), 2.00 (s, 3H, CH_3-2'''), 2.06 (s, 3H, CH_3-1'''), 3.63 (q, *J* = 7.2 Hz, 2H, CH_2-1''), 4.20–4.29 (m, 4H, CH_2-2, CH_2-3), 6.81 (d, *J* = 7.6 Hz, 1H, H-4'), 6.93 (t, *J* = 7.6 Hz, 1H, H-5'), 7.02 (d, *J* = 7.2 Hz, 1H, H-6'), 7.21 (d, *J* = 8.0 Hz, 1H, H-8), 7.63 (d, *J* = 2.4 Hz, 1H, H-5), 7.75 (dd, J_1 = 8.0 Hz, J_2 = 2.0 Hz, 1H, H-7); EIMS: *m/z* 347 $[M]^+$, 283 $[M\text{-}SO_2]^+$, 268 $[C_6H_3C_2H_4O_2NCH\text{-}_2C_6H_3(CH_3)_2]^+$, 242 $[C_6H_3C_2H_4O_2SO_2NC_2H_5]^+$, 240 $[C_6H_3O_2NCH_2C_6H_3(CH_3)_2]^+$, 227 $[C_6H_3C_2H_4O_2SO_2NCH_2]^+$, 199 $[C_6H_3C_2H_4O_2SO_2]^+$, 135 $[C_6H_3C_2H_4O_2]^+$, 107 $[C_6H_3O_2]^+$, 105 $[C_6H_3(CH_3)_2]^+$, 90 $[C_6H_3CH_3]^+$, 79 $[C_4H(CH_3)_2]^+$, 75 $[C_6H_3]^+$, 64 $[C_4HCH_3]^+$.

N-(2,4-Dimethylphenyl)-N-ethyl-2,3-dihydrobenzo[1,4]dioxine-6-sulfonamide (7b)

Greenish brown sticky solid; yield: 73% (79.4 mg); molecular formula: $C_{18}H_{21}NO_4S$; molecular weight: 347 g/mol; HR-MS: $[M]^+$ 347.4302 (Calcd. for $C_{18}H_{21}NO_4S$; 347.4587); IR (KBr, cm^{-1}): ν_{max} stretching: 3430 (N-H), 3044 (C-H Ar ring), 2918 (-CH_2-), 1629 (C=C Ar ring), 1328 (-SO_2-), 1120 (C-O-C of ether); ^{1}H NMR (400 MHz, CD_3OD): δ (ppm) 1.00 (t, *J* = 7.2 Hz, 2H, CH_3-2''), 2.20 (s, 3H, CH_3-2'''), 2.27 (s, 3H, CH_3-1'''), 3.77 (q, *J* = 7.6 Hz, 2H, CH_2-1''), 4.28–4.33 (m, 4H, CH_2-2, CH_2-3), 6.48 (s, 1H, H-3'), 6.50 (d, *J* = 7.6Hz, 1H, H-5'), 6.90 (d, *J* =7.6 Hz, 1H, H-6'), 6.97 (d, *J* = 8.0 Hz, 1H, H-8), 7.10 (d, *J* = 2.4 Hz, 1H, H-5), 7.12 (dd, J_1 = 8.2 Hz, J_2 = 2.0 Hz, 1H, H-7); EIMS: *m/z* 347 $[M]^+$, 283 $[M\text{-}SO_2]^+$, 268 $[C_6H_3C_2H_4O_2NCH\text{-}_2C_6H_3(CH_3)_2]^+$, 242 $[C_6H_3C_2H_4O_2SO_2NC_2H_5]^+$, 240 $[C_6H_3O_2NCH_2C_6H_3(CH_3)_2]^+$, 227 $[C_6H_3C_2H_4O_2SO_2NCH_2]^+$, 199 $[C_6H_3C_2H_4O_2SO_2]^+$, 135 $[C_6H_3C_2H_4O_2]^+$, 107 $[C_6H_3O_2]^+$, 105 $[C_6H_3(CH_3)_2]^+$, 90 $[C_6H_3CH_3]^+$, 79 $[C_4H(CH_3)_2]^+$, 75 $[C_6H_3]^+$, 64 $[C_4HCH_3]^+$.

***N*-(2,5-Dimethylphenyl)-*N*-ethyl-2,3-dihydrobenzo [1,4]dioxine-6-sulfonamide (7c)**

Light yellow sticky solid; yield: 69% (75.1 mg); molecular formula: $C_{18}H_{21}NO_4S$; molecular weight: 347 g/mol; HR-MS: $[M]^+$ 347.4302 (Calcd. for $C_{18}H_{21}NO_4S$; 347.4587); IR (KBr, cm^{-1}): ν_{max} stretching: 3438 (N-H), 3021 (C-H Ar ring), 2927 (-CH_2-), 1618 (C=C Ar ring), 1326 (-SO_2-), 1129 (C-O-C of ether); ^{1}H NMR (500 MHz, CD_3OD): δ (ppm) 0.99 (t, *J* =7.0 Hz, 3H, CH_3-2"); 2.16 (s, 3H, CH_3-2'"), 2.27 (s, 3H, CH_3-1'"), 3.60 (q, *J* = 7.5 Hz, 2H, CH_2-1"), 4.28–4.34 (m, 4H, CH_2-2, CH_2-3), 6.39 (s, 1H, H-6'), 6.99 (d, *J* = 8.5 Hz, 1H, H-3'), 7.04 (dd, *J* = 2.0, 8.0 Hz, 1H, H-4'), 7.09 (d, *J* = 2.5 Hz, 1H, H-5), 7.13 (dd, J_1 = 8.5 Hz, J_2 = 2.0 Hz, 1H, H-7), 7.16 (d, *J* = 7.5 Hz, 1H, H-8); EIMS: *m/z* 347 $[M]^+$, 283 $[M\text{-}SO_2]^+$, 268 $[C_6H_3C_2H_4O_2NCH_2C_6H_3(CH_3)_2]^+$, 242 $[C_6H_3C_2H_4O_2SO_2NC_2H_5]^+$, 240 $[C_6H_3O_2NCH_2C_6H_3(CH_3)_2]^+$, 227 $[C_6H_3C_2H_4O_2SO_2NCH_2]^+$, 199 $[C_6H_3C_2H_4O_2SO_2]^+$, 135 $[C_6H_3C_2H_4O_2]^+$, 107 $[C_6H_3O_2]^+$, 105 $[C_6H_3(CH_3)_2]^+$, 90 $[C_6H_3CH_3]^+$, 79 $[C_4H(CH_3)_2]^+$, 75 $[C_6H_3]^+$, 64 $[C_4HCH_3]^+$.

***N*-(2,6-Dimethylphenyl)-*N*-ethyl-2,3-dihydrobenzo [1,4]dioxine-6-sulfonamide (7d)**

White solid; yield: 78% (84.9 mg); m.p; 109–111 °C; molecular formula: $C_{18}H_{21}NO_4S$; molecular weight: 347 g/mol; HR-MS: $[M]^+$ 347.4302 (Calcd. for $C_{18}H_{21}NO_4S$; 347.4587); IR (KBr, cm^{-1}): ν_{max} stretching: 3445 (N-H), 3017 (C-H Ar ring), 2921 (-CH_2-), 1612 (C=C Ar ring), 1325 (-SO_2), 1134 (C-O-C of ether); ^{1}H NMR (300 MHz, CD_3OD): δ (ppm) 1.07 (t, *J* = 7.2 Hz, 3H, CH_3-2"), 2.06 (s, 6H, CH_3-1'", CH_3-2'"), 3.56 (q, *J* = 7.2 Hz, 2H, CH_2-1"), 4.28–4.32 (m, 4H, CH_2-2, CH_2-3), 6.99 (d, *J* = 8.4 Hz, 2H, H-3', H-5'), 7.02 (d, *J* = 8.4 Hz, 1H, H-4'), 7.06 (d, *J* = 8.4 Hz, 1H, H-8), 7.12 (d, *J* = 2.1 Hz, 1H, H-5), 7.24 (dd, J_1 = 8.4 Hz, J_2 = 2.1 Hz, 1H, H-7); EIMS: *m/z* 347 $[M]^+$, 283 $[M\text{-}SO_2]^+$, 268 $[C_6H_3C_2H_4O_2NCH_2C_6H_3(CH_3)_2]^+$, 242 $[C_6H_3C_2H_4O_2SO_2NC_2H_5]^+$, 240 $[C_6H_3O_2NCH_2C_6H_3(CH_3)_2]^+$, 227 $[C_6H_3C_2H_4O_2SO_2NCH_2]^+$, 199 $[C_6H_3C_2H_4O_2SO_2]^+$, 135 $[C_6H_3C_2H_4O_2]^+$, 107 $[C_6H_3O_2]^+$, 105 $[C_6H_3(CH_3)_2]^+$, 90 $[C_6H_3CH_3]^+$, 79 $[C_4H(CH_3)_2]^+$, 75 $[C_6H_3]^+$, 64 $[C_4HCH_3]^+$.

***N*-(3,4-Dimethylphenyl)-*N*-ethyl-2,3-dihydrobenzo [1,4]dioxine-6-sulfonamide (7e)**

Yellowish brown sticky solid; yield: 86% (93.6 mg); molecular formula: $C_{18}H_{21}NO_4S$; molecular weight: 347 g/mol; HR-MS: $[M]^+$ 347.4302 (Calcd. for $C_{18}H_{21}NO_4S$; 347.4587); IR (KBr, cm^{-1}): ν_{max} stretching: 3432 (N-H), 3017 (C-H Ar ring), 2923 (-CH_2-), 1612 (C=C Ar ring), 1325 (-SO_2-), 1134 (C-O-C of ether); ^{1}H NMR (400 MHz, CD_3OD): δ (ppm) 1.02 (t, *J* = 7.2 Hz, 3H, CH_3-2"), 2.19 (s, 3H, CH_3-2'"), 2.24 (s, 3H, CH_3-1'"), 3.55 (q, *J* = 7.2 Hz, 2H, CH_2-1"), 4.26–4.36 (m, 4H, CH_2-2, CH_2-3), 6.62 (d, *J* = 8.4 Hz, 1H, H-5'), 6.71 (dd, J_1 = 8.0 Hz, J_2 = 2.0 Hz, 1H, H-6'), 6.81 (d, *J* = 2.0 Hz, 1H, H-2'), 6.94 (d, *J* = 8.4 Hz, 1H, H-8), 7.01 (d, *J* = 2.0 Hz, 1H, H-5), 7.06 (dd, J_1 = 8.4 Hz, J_2 = 2.4 Hz, 1H, H-7); EIMS: *m/z* 347 $[M]^+$, 283 $[M\text{-}SO_2]^+$, 268 $[C_6H_3C_2H_4O_2NCH_2C_6H_3(CH_3)_2]^+$, 242 $[C_6H_3C_2H_4O_2SO_2NC_2H_5]^+$, 240 $[C_6H_3O_2NCH_2C_6H_3(CH_3)_2]^+$, 227 $[C_6H_3C_2H_4O_2SO_2NCH_2]^+$, 199 $[C_6H_3C_2H_4O_2SO_2]^+$, 135 $[C_6H_3C_2H_4O_2]^+$, 107 $[C_6H_3O_2]^+$, 105 $[C_6H_3(CH_3)_2]^+$, 90 $[C_6H_3CH_3]^+$, 79 $[C_4H(CH_3)_2]^+$, 75 $[C_6H_3]^+$, 64 $[C_4HCH_3]^+$.

2. 3. Enzyme Inhibition Studies

2. 3. 1. Cholinesterase Assay

The BChE and AChE inhibition activities were assayed in concurrence with the reported method after making minor changes.[33] Overall total volume of 100 µL was pertained to reaction mixture; made by mixing 60 µL of Na_2HPO_4 buffer (pH 7.7), 10 µL of each test sample and the enzyme. The sample and buffer strength was kept at 0.5 mM per well. BChE was added 0.5 unit per well and a quantity of 0.005 units was made constant for AChE in each well. After mixing the contents, the reading was recorded at 405 nm. Before this, incubation of 10 min at 37 °C was ensured. On adding 10 µL of both substrate (0.5 mM per well) and DTNB (0.5 mM per well) the reaction was allowed to start. The substrates for BChE and AChE were butyrylthiocholine chloride and acetylthiocholine iodide, respectively. Again the incubation was done for 15 min at 37 °C. Later on, the absorbance was measured at 405 nm. The instrument used was 96-well plate reader Synergy HT, Biotek, USA. 0.5 mM per well of Eserine was exploited as the positive control. The experiments were carried out in triplicate. The % inhibition was calculated as:

$$\text{Inhibition (\%)} = \frac{Control - Test}{Control} \times 100 \qquad (1)$$

Here, total enzyme activity without inhibitor is described as control, whereas test corresponds to its activity in the presence of our synthesized molecules. EZ–Fit Enzyme Kinetics software was employed to determine IC_{50} values. The software was provided by Perrella Scientific Inc. Amherst, USA.

2. 3. 2. Lipoxygenase Assay

For lipoxygenase assay the total volume of the mixture was maintained at 200 µL. It contained 150 µL of 100 mM Na_3PO_4 buffer having pH 8.0, 10 µL of 0.5 mM per well of the test compound and 15 µL of the enzyme. The lipoxygenase was added in 600 units in each well. After mixing and pre-incubation (10 min; 25 °C) the contents were pre-read at 234 nm. On adding 25 µL of substrate solution the reaction was initiated. The absorbance was measured at 234 nm using 96-well plate reader Synergy HT, Biotek, USA. Baicalein was used as the positive control having 0.5 mM per well in the assay. The % inhibition and rest of calculation was executed by the same method as described above.[34–36]

2. 3. 3. Statistical Analysis

All experimental measurements were recorded three folds. The statistical analysis was achieved by Microsoft Excel 2010.

2. 4. Antimicrobial Activity

2. 4. 1. Microbial Strains

A set of microorganisms were used to conduct antimicrobial activity. All the synthesized compounds were tested against fungal, Gram negative and Gram positive bacterial strains. In this study *Bacillus subtilis* (*B. subtilis*) JS 2004 and *Staphylococcus aureus* (*S. aureus*) API Staph TAC 6736152 were used as Gram positive bacteria, whereas *Pasteurella multocida* (*P. multocida*) and *Escherichia coli* (*E. coli*) ATCC 25922 were among Gram negative bacteria. The four pathogenic fungi: *Microsporum canis (M. canis)*, *Candida albicans (C. albican)*, *Aspergillus flavus* (*A. flavus*) and *Fusarium solani* (*F. solani*) were also the constituents of the assay. All the pure strains were provided by CMS department of UAF, Faisalabad. The Department of microbiology checked their purity and confirmed their identification. In nutrient agar (NA, Oxoid) bacterial strains were cultured overnight at 37 °C. For fungal strains Potato Dextrose Agar (PDA, Oxoid) was chosen and subjected to culture at 28 °C overnight.[37]

2. 4. 2. Disc Diffusion Method

Disc diffusion method was used to determine antimicrobial activity of synthesized compounds. Suspension of tested microorganisms (100 μL) comprised 10^7 colony-forming units (CFU)/mL of bacterial cells. They were expanded on NA medium. The suspension with 10^6 spores/mL of fungi were expended on PDA medium. The solution of compound was applied to saturate filter discs. Sample free discs were used for negative control. For the comparison of sensitivity of strain/isolate in the analyzed microbial species, positive reference used for fungi and bacteria were Flumequine (30 μg/disk) (Oxoid, UK) and Amoxycillin (30 μg/dish) (Oxoid, UK), respectively. After keeping it at 4 °C for 2 hours, plates were incubated for 24 hours at 28 °C for fungal strains and for 18 hours at 37 °C for bacteria. Antimicrobial activity was assessed by calculating the diameter (mm of growth) of inhibition zones using zone reader. Later on it was compared with the controls.[37]

2. 4. 3. Hemolytic Activity

To study the hemolytic activity of the compounds 3 mL of fresh blood of heparinized human was collected. After consent the bovine from volunteers of the Department of Clinical Medicine and Surgery, University of Agriculture, Faisalabad, Pakistan was bleeded. Centrifugation of blood was done at 1000 × *g* for 5 min. Plasma was discarded. 5 mL of chilled (4 °C) sterile isotonic Phosphate Buffered Saline (PBS) with pH 7.4 was used to wash the cells. This task was performed for three times. For each assay erythrocytes were maintained 10^8 cells per mL. 100 μL of each compound was taken and mixed with 10^8 cells/mL of human separately. The incubation of samples was done at 37 °C for 35 min. After incubation these samples were settled for 10 min and later on kept on agitation. The samples were placed on ice for 5 min immediately after incubation then centrifuged at 1000 × *g* for 5 min. From each tube 100 μL of supernatant was taken and then diluted with chilled (4 °C) PBS 10 times. As the positive control, Triton X-100 (0.1% v/v) was used; while phosphate buffer saline (PBS) acted as the negative control. The μQuant's life science instrument licensed by Biotek, USA was used to record the absorbance. The absorbance was taken at 576 nm. The % RBCs lysis for each sample was measured.[38,39]

2. 5. Molecular Docking

The structures of all the synthesized inhibitors were constructed using MOE-Builder tool. The default parameters of MOE-Dock program were used for the molecular docking of the ligands. Ligands were allowed to be flexible in order to find the accurate conformations of the ligands and to obtain minimum energy structures. At the end of docking, the best conformations of the ligands were analyzed for their binding interactions.[40]

3. Results and Discussion

3. 1. Chemistry

We report herein the synthesis of a series of heterocyclic compounds containing 1,4-benzodioxane nucleus. The precursor molecules *N*-aryl-2,3-dihydrobenzo[1,4]dioxine-6-sulfonamide **3a**–**e**, were prepared by condensing 1,4-benzodioxane-6-sulfonyl chloride (**1**) and aryl amines **2a**–**e** in basic aqueous medium. Two series of *N*-substituted derivatives (**6a**–**e** and **7a**–**e**) were formed by the reactions of **3a**–**e** with two different electrophiles. The substitution reactions yielded *N*-benzyl (**6a**–**e**) or *N*-ethyl (**7a**–**e**) derivatives of *N*-aryl-2,3-dihydrobenzo[1,4]dioxine-6-sulfonamides as represented in Scheme 1. The derivatives **6a**–**e** and **7a**–**e** were obtained in DMF as the solvent and with LiH as the base and activator. The reaction products were obtained within 30 to 70 min of stirring at room temperature. By adding cold distilled water along with vigorous shaking of the reaction mixtures, the products were precipitated; isolation through filtration yielded pure solid targets. On the other hand, some sticky and greasy compounds were recovered through solvent extraction method using chloroform as the extracting solvent. Here the description of the parent compound **3a** is given as an example for elaborating the spectral data. **3a** was synthesized as a white powder with good yield (80%) and m.p. was recorded as 102–104 °C. High Resolution Mass Spectrome-

try (HR-MS) showed $M^{\cdot+}$ (molecular ion peak) at *m/z* 319.3772. Therefore, molecular formula of the compound was established as $C_{16}H_{17}NO_4S$. The total number of protons was confirmed from ^1H NMR spectrum. The IR spectrum of **3a** confirmed the presence of different functionalities. Like the absorption bands were observed at 3419

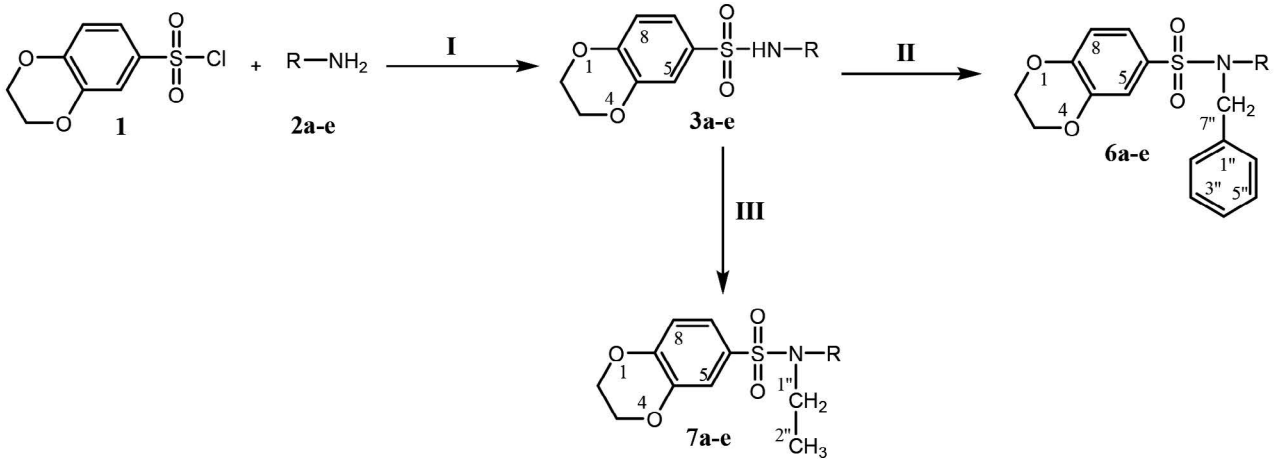

Reagents and conditions: (I) Na_2CO_3 (aq), pH 9–10, stir, 3–4h, rt, (II) $C_6H_5CH_2Cl$ (**4**), DMF, LiH, stir, 4–5 h, rt (III) CH_3CH_2I (**5**), DMF, LiH, stir, 4–5 h, rt

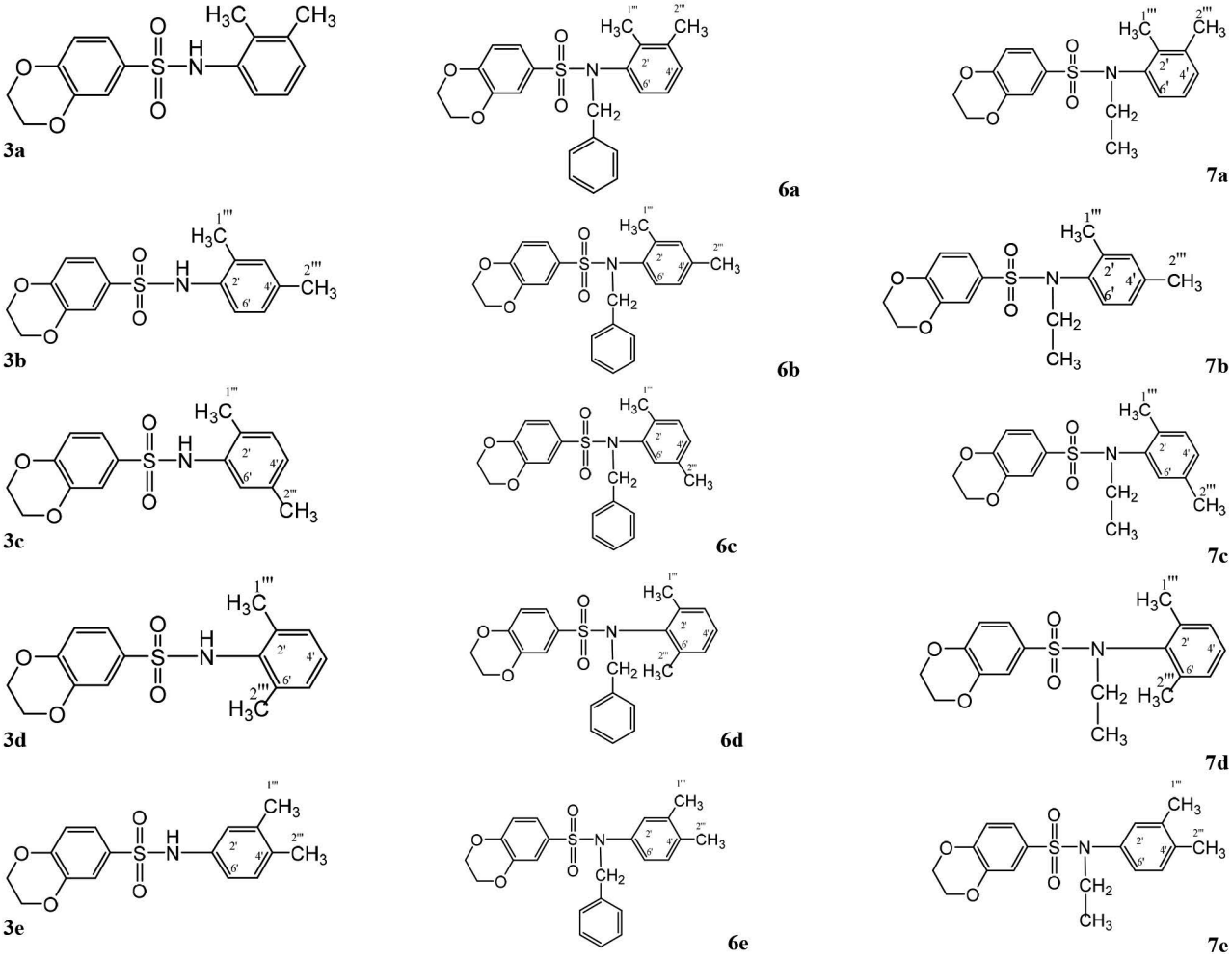

Scheme 1. Synthetic scheme and sulfonamide compounds bearing benzodioxane nucleus.

cm^{-1} for N-H stretching of sulfamoyl group and at 3026 cm^{-1} for aromatic C-H stretching. A peak at 1613 cm^{-1} depicted the presence of C=C stretching of Arl ring. A stretching band at 1325 cm^{-1} confirmed the SO_2 stretching of sulfonyl group in the molecule. A characteristic band at 1125 cm^{-1} was assigned to C-O-C stretching of ether, respectively. The EI-MS gave characteristic peaks at *m/z* 199 and 90. These were attributed to the formation of

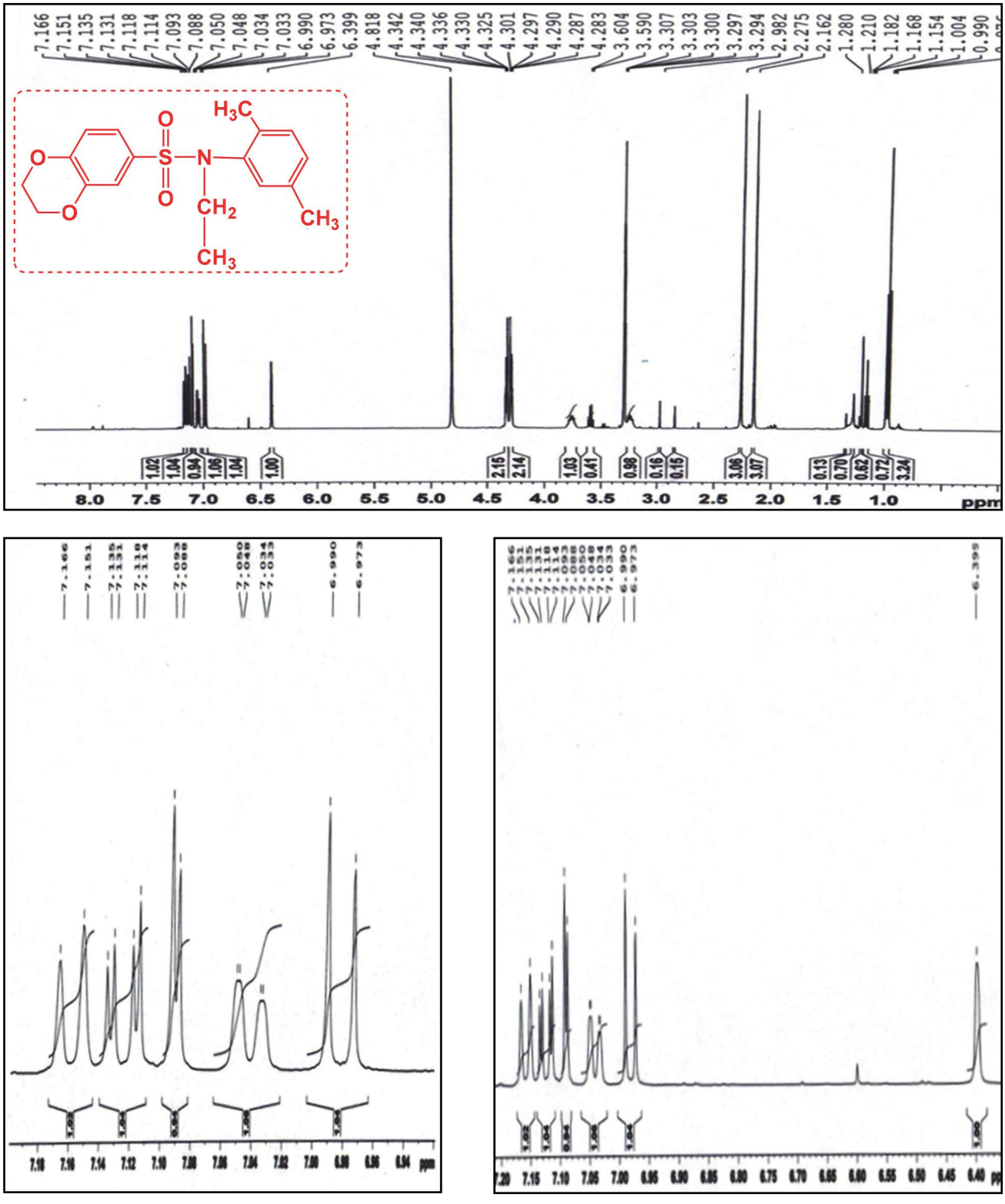

Figure 1a. ^{1}H NMR spectrum of *N*-(2,5-dimethylphenyl)-*N*-ethyl-2,3-dihydrobenzo[1,4]dioxine-6-sulfonamide **7c** (aromatic region)

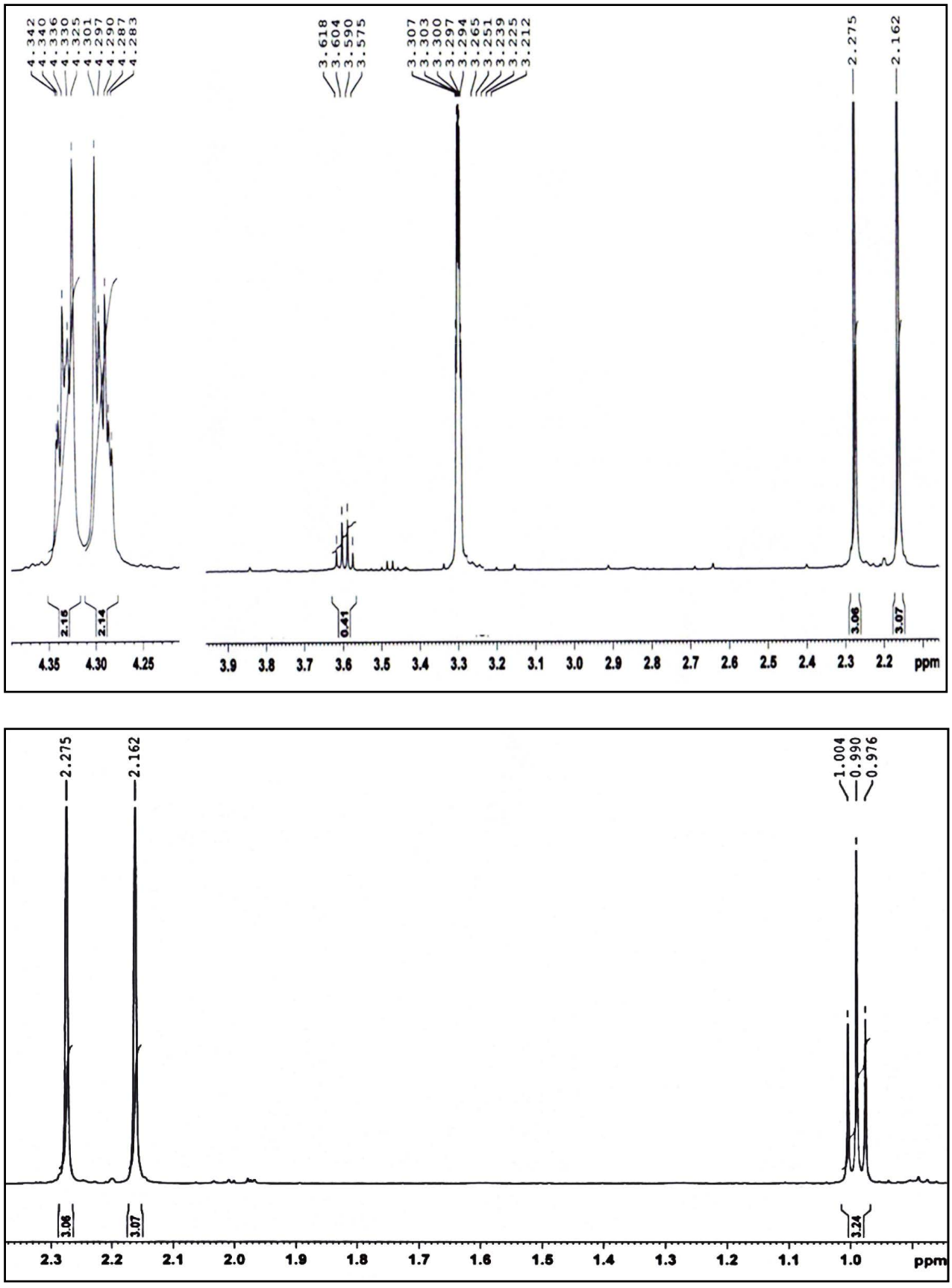

Figure 1b. ^{1}H NMR spectrum of *N*-(2,5-dimethylphenyl)-*N*-ethyl-2,3-dihydrobenzo[1,4]dioxine-6-sulfonamide **7c** (aliphatic region)

$C_6H_3C_2H_4O_2SO_2^+$ and $C_6H_3CH_3^+$ cations, respectively. In the aromatic region of the ^{1}H NMR spectrum signals appeared at δ 7.25 as doublet (small coupling constant) confirming H-5, doublet of doublet at chemical shift of 7.18 showed presence of H-7 and another doublet at δ 6.95 (large coupling constant) indicated H-8 of phenyl ring attached to the sulfonyl group. Whereas three aromatic signals at δ 6.80 (brd), 6.78 (t) and 6.73 (brd) were assigned to the benzene ring of 2,3-dimethylphenyl group. In the shielded, upfield and aliphatic region of the spectrum three distinct signals appeared. The multiplet ranging from 4.24–4.27 (CH_2-2, CH_2-3), singlet at 2.27 (CH_3-1") and relatively higher upfield singlet at 1.99 (CH_3-2") indicated the presence of 1,4-dioxane nucleus and two methyl groups attached to the second and third position of aniline in the molecule. The structure of **3a** was established as (2,3-di-

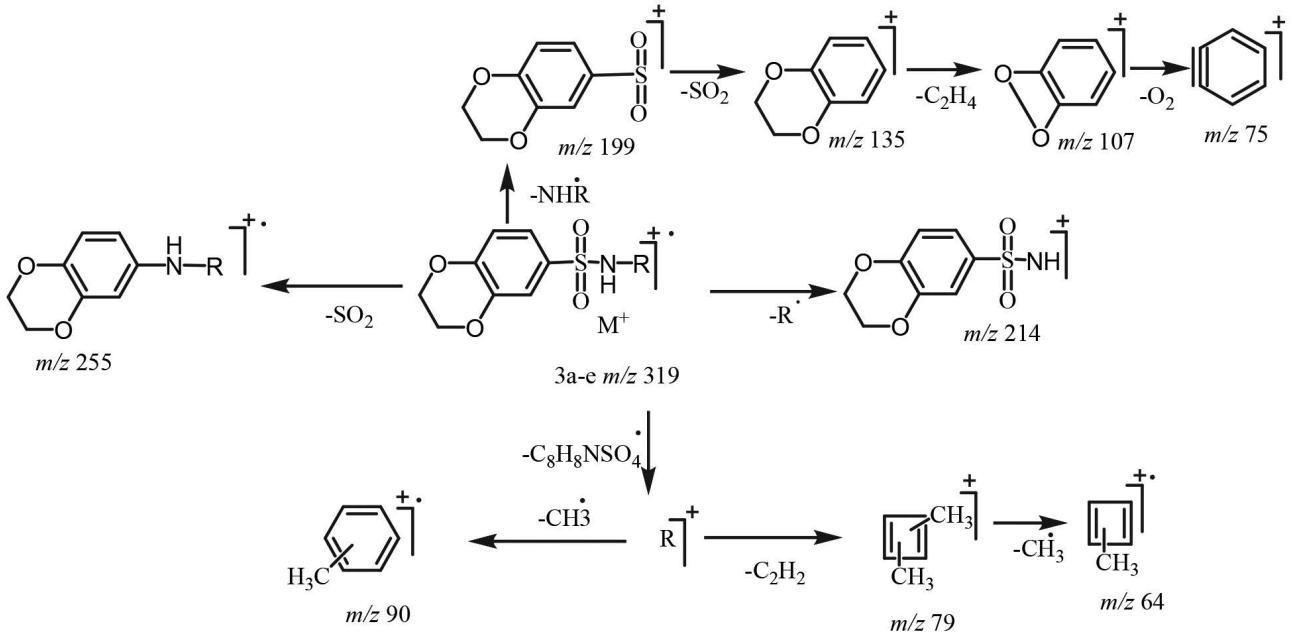

Figure 2. Mass fragmentation pattern of *N*-aryl-2,3-dihydrobenzo[1,4]dioxine-6-sulfonamides **3a**–**e**

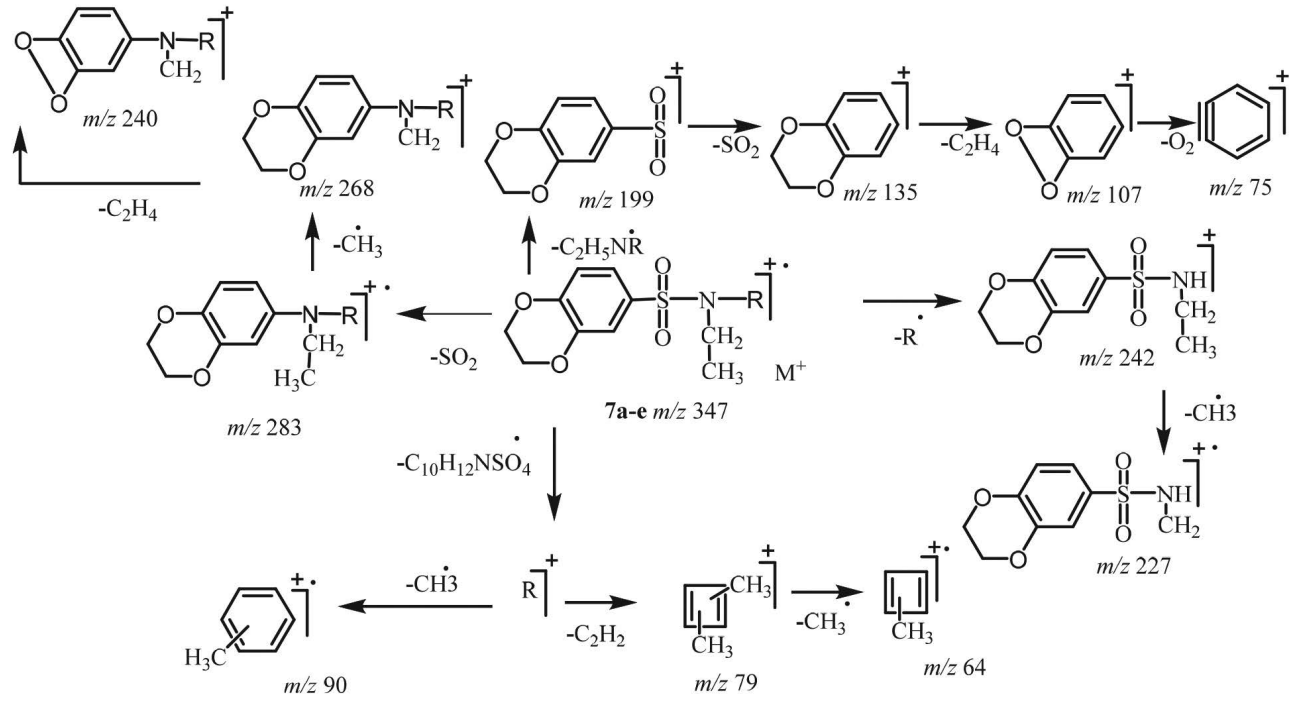

Figure 3. Mass fragmentation pattern of *N*-ethyl-*N*-(dimethylphenyl)-2,3-dihydrobenzo[1,4]dioxine-6-sulfonamide **7a**–**e**

methylphenyl)-2,3-dihydrobenzo[1,4]dioxine-6-sulfonamide on these collective confirmations. The structures of other derivatives were also ascertained on the similar pattern. The ^{1}H NMR spectrum of molecule **7c** is shown in Figure 1. The mass fragmentation pattern of parent sulfonamides **3a–e** and their *N*-ethyl derivatives **7a–e** are provided in Figures 2 and 3.

3. 2. Enzyme Inhibition

The screening of all the synthesized compounds against butyrylcholinesterase enzyme revealed that only three compounds showed better activity; *N*-(2,3-dimethylphenyl)-2,3-dihydrobenzo[1,4]dioxine-6-sulfonamide (**3a**), *N*-benzyl-(2,5-dimethylphenyl)-2,3-dihydro- benzo[1,4]dioxine-6-sulfonamide (**6c**) and *N*-ethyl-(2,4-dimethylphenyl)-2,3 -dihydro- benzo[1,4]dioxine-6-sulfonamide (**7b**) having IC_{50} values of 374.11 ± 0.01, 387.51 ± 0.48 and 353.13 ± 0.86 μmol/L respectively, relative to eserine, a reference standard with IC_{50} value of 0.85 ± 0.0001 μmol/L (Table 1). The activity of these compounds was most probably due to the presence of methyl groups at different positions of phenyl ring in **3a**, benzyl group in **6c** along with alkyl groups and an additional ethyl group for **7b** attached to the nitrogen of sulfonamide. The screening against acetylcholinesterase enzyme of all the synthesized compounds showed that only four compounds were moderately active against it; *i.e.* *N*-(3,4dimethylphenyl)-2,3-dihydrobenzo[1,4]dioxine-6-sulfonamide (**3e**), *N*-benzyl-*N*-(2,4-dimethylphenyl)-2,3-dihydrobenzo[1,4] dioxine-6-sulfonamide (**6b**), *N*-ethyl-*N*-(2,4-dimethylphenyl)-2,3-dihy-drobenzo[1,4]dioxine-6-sulfonamide (**7b**) and *N*-ethyl-*N*-(2,6-dimethylphenyl) -2,3-dihydrobenzo[1,4]dioxine-6-sulfonamide (**7d**) having IC_{50} values ranging from 178.51 ± 0.14 to 364.27 ± 0.54 μmol/L. The relative reference standard was eserine, with IC_{50} value of 0.04 ± 0.0001 μmol/L. The % inhibition associated with these compounds arrayed from 59.91 ± 0.96 to 76.56 ± 0.19 μmol/L respectively. The proficient activity was observed for **7b** and **7d**; this was most likely due to the occurrence of *N*-ethyl group in these compounds in comparison to the other series members. Against lipoxygenase enzyme, all the synthesized compounds showed beneficially good activity but the most active were *N*-(2,6-dimethylphenyl)-2,3-dihydrobenzo[1,4]dioxine-6-sulfonamide (**3d**), *N*-(2,4-dimethylphenyl)-2,3-dihydrobenzo [1,4]dioxine-6-sulfonamide (**3b**), *N*-benzyl-*N*-(2,6-dimethylphenyl)-2,3-dihydrobenzo [1,4] dioxine-6-sulfonamide (**6d**) and *N*-(3,4-dimethylphenyl)-2,3-dihydrobenzo[1,4]dioxine-6-sulfonamide (**3e**) having IC_{50} values of 34.21 ± 0.12, 64.21 ± 0.05, 84.61 ± 0.11 and 87.61 ± 0.14 μmol/L respectively, relative to baicalein, a reference standard with IC_{50}

Table 1. Enzyme inhibition studies of the synthesized compounds.

Compound	BChE			AChE			LOX		
	Conc./well (mM)	Inhibition (%)	IC_{50} μM	Conc. (mM)	Inhibition (%)	IC_{50} (μmol.)	Conc./well (mM)	Inhibition (%)	IC_{50} μM
3a	0.5	59.98 ± 0.45	374.11 ± 0.07	0.5	34.68 ± 0.68	–	0.5	81.34 ± 0.33	89.25 ± 0.17
3b	0.5	36.56 ± 0.66	–	0.5	18.34 ± 0.25	–	0.5	89.11 ± 0.22	64.21 ± 0.05
3c	0.5	36.44 ± 0.22	–	0.5	16.91 ± 0.11	–	0.5	88.45 ± 0.82	92.25 ± 0.11
3d	0.5	29.12 ± 0.55	–	0.5	30.39 ± 0.85	–	0.5	96.86 ± 0.36	34.21 ± 0.12
3e	0.5	56.85 ± 0.91	>400	0.5	59.91 ± 0.96	302.11 ± 0.14	0.5	82.22 ± 0.67	87.61 ± 0.14
6a	0.5	32.32 ± 0.19	>500	0.5	4.37 ± 0.15	>500	0.5	1.04 ± 0.22	–
6b	0.5	54.10 ± 0.17	>500	0.5	76.56 ± 0.19	267.17 ± 0.21	0.25	35.55 ± 0.35	–
6c	0.5	58.72 ± 0.13	387.51 ± 0.48	0.5	64.77 ± 0.36	364.27 ± 0.54	0.25	43.01 ± 0.64	–
6d	0.5	43.41 ± 0.82	–	0.5	15.85 ± 0.55	–	0.5	82.11 ± 0.14	84.61 ± 0.11
6e	0.5	46.26 ± 0.62	–	0.5	46.99 ± 0.38	–	0.5	63.26 ± 0.55	238.71 ± 0.14
7a	0.5	28.85 ± 0.14	>500	0.5	1.97 ± 0.25	>500	0.5	13.79 ± 0.15	–
7b	0.5	67.69 ± 0.18	353.13 ± 0.86	0.5	73.08 ± 0.76	223.1 ± 0.18	0.25	53.44 ± 0.66	>400
7c	0.5	54.09 ± 0.15	>500	0.5	46.67 ± 0.23	>500	0.5	5.21 ± 0.11	–
7d	0.5	42.65 ± 0.61	–	0.5	70.52 ± 0.61	178.51 ± 0.14	0.5	48.46 ± 0.19	–
7e	0.5	42.03 ± 0.58	–	0.5	32.36 ± 0.14	–	0.5	43.84 ± 0.19	–
Control	**Eserine**	82.82 ± 1.09	0.85 ± 0.0001	**Eserine**	91.29 ± 1.17	0.04 ± 0.0001	**Baicalein**	93.79 ± 1.27	**22.4 ± 1.3**

Note: IC_{50} values (concentration at which there is 50% enzyme inhibition) of compounds were calculated using EZ–Fit Enzyme kinetics software (Perella Scientific Inc. Amherst, USA). LOX = Lipoxygenase. AChE = Acetyl cholinesterase. BChE = Butyryl cholinesterase.

value of 22.4 ± 1.3 μmol/L. The proficient activity of first and second compounds was most probably due to the occurrence of two alkyl groups, one at the second position and the other one at the sixth and fourth positions of aniline ring, respectively. In **3e** these two alkyl groups were situated at the third and fourth positions and resulted in less inhibition in comparison to **3d** and **3b**. For **6d** the credibly was due to the presence of two alkyl groups at the second and sixth position of aniline ring along with benzyl group attached to the nitrogen of sulfonamide. From the activity of molecules against LOX it might be concluded that free nitrogen of sulfamoyl group could be more effective in blocking the active site of enzyme; instead when we substitute it with ethyl or benzyl groups. All the parent compounds **3a**–**e** can be further utilized for the synthesis of new derivatives with other different electrophiles to enhance their biological, antimicrobial and other activities.

3. 3. Antimicrobial Activity

The *in vitro* antimicrobial properties of the parent compounds **3** and their derivatives were tested. Against the selected panel of both bacterial and fungal species parent compounds **3a**, **3b**, **3c** and **3e** exhibited moderate antimicrobial activity; and **3c** showed only antibacterial activity as is evident from Table 2. Regarding these parent sulfonamides **3**, the compound **3e** showed relatively higher activity but lower than that of the standard compound. Among the derivatives of **6a**–**e** series **6a** and **6c** have shown both the antibacterial and antifungal activities; and **6a** demonstrated higher activities in contrast to the other series members. **7a**, **7b** and**7c** are the members of **7a**–**e** series which were active against both bacterial and fungal strains; among these **7b** exhibited relatively better results against both microbes. The remaining compounds possess very low or no activity against the assessed microorganisms. The highest hemolytic activity was shown by **3b** (92%) but lower than the positive control (Triton-X-100). The lowest hemolytic activity was shown by **7b** and **7c** (2.1% and 0.7%, respectively) but higher than the negative controls (PBS). Overall it can be concluded here that **7b** and **7c** were the better members overall from all these compounds and ligands; because they have displayed better antimicrobial potential and less hemolytic activity. On the basis of the presented results we may assume that the synthesized sulfonamides may be suitable leads for further improvement to address different targets.

Table 2. Antibacterial and antifungal studies on synthesized compounds.

Compound	Antibacterial activity				Hemolytic activity	Antifungal activity			
	Staphylococcsa ureus	*Bacillus subtilis*	*Pasturella multocida*	*Escherichia coli*	(Mean) % ± S.D.	*Candida albicans*	*Microsporum canis*	*Aspergillus flavus*	*Fusarium solani*
	Zone of inhibition (mm)						Zone of inhibition (mm)		
3a	14	14	16	16	71.847 ± 0.093	14	14	16	16
3b	16	16	12	14	91.721 ± 1.121	16	16	12	14
3c	14	14	12	14	88.162 ± 0.278	–	–	–	–
3d	–	–	–	–	88.328 ± 3.122	–	–	–	–
3e	18	16	14	14	86.918 ± 0.226	19	16	14	14
6a	16	12	14	16	91.684 ± 3.221	16	18	14	14
6b	-	-	-	-	88.372 ± 0.192	–	–	–	–
6c	14	16	12	14	73.814 ± 0.464	13	18	11	12
6d	–	–	–	–	81.770 ± 3.060	–	–	–	–
6e	–	–	–	–	88.481 ± 0.309	–	–	–	–
7a	14	14	16	12	71.472 ± 0.087	16	14	18	16
7b	16	18	14	14	2.186 ± 0.124	19	17	18	16
7c	16	14	14	16	0.743 ± 0.062	17	12	15	18
7d	–	–	–	–	72.372 ± 0.526	–	–	–	–
7e	–	–	–	–	91.668 ± 5.508	–	–	–	–
Streptomycin	30	8	28	30	Flumequine	29	27	26	31
PBS					0.00 ± 0.0				
Triton(toxicity)					100 ± 0.0				

4. Molecular Docking

The results obtained from *in silico* approach were also favoring the fact that the synthesized sulfonamides have shown good interactions with the target site. The interaction analysis has shown that in every compound the sulfonamide group is contributing to the interactions. The interactions of compounds **3b** and **7d** with the active site of lipoxygenase (LOX) and acetylcholinesterase (AChE) are shown in Figures 4 and 5, respectively.

The interaction analysis of compound **7d** against acetylcholinesterase depicted that the residues of the binding pocket interacted with two functionalities of the compound. Tyr121 developed links with the one oxygen of SO_2 group in sulfonamide moiety and Ser122 interacted with the one oxygen atom (at fourth position) of 1,4-dioxane ring (Figure 5). Whereas in compound **3b** His518 has developed interactions with oxygen of sulfamoyl group and His513 has interacted with oxygen of the dioxane functionality (Figure 4).

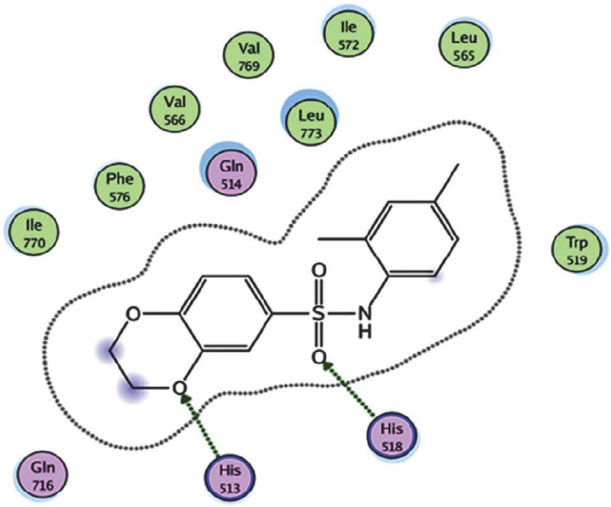

Figure 4: 2D interaction of *N*-(2,4-dimethylphenyl)-2,3-dihydrobenzo[1,4]dioxine-6-sulfonamide (**3b**) against lipoxygenase.

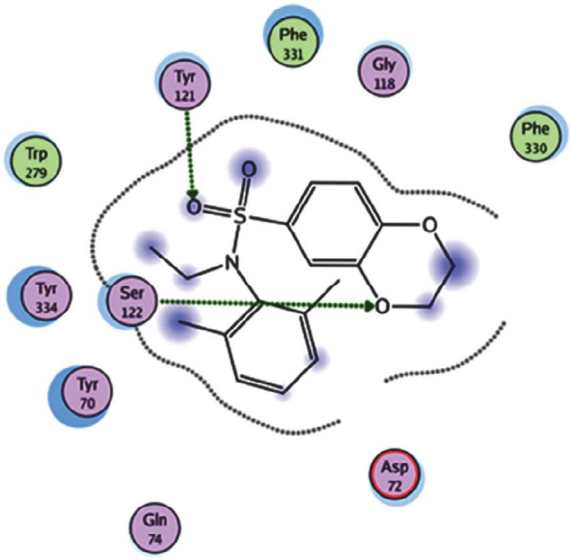

Figure 5: 2D image of compound *N*-(2,6-dimethylphenyl)-*N*-ethyl-2,3-dihydro- benzo[1,4]dioxine-6-sulfonamide (**7d**) against acetylcholinesterase.

5. Conclusion

A new series of sulfonamides bearing 1,4-benzodioxane ring systems were synthesized. These were characterized by IR, ^{1}H NMR and EIMS. All the compounds were screened for their antibacterial and antifungal activity by disc diffusion method. Compounds **3e**, **7b** and **7c** exhibited good antimicrobial activity among all the synthesized compounds but lower than that of the standard drug streptomycin. Compound **7b** was better inhibitor against BchE and **7d** for AchE, while **3d** exhibited good inhibition potential against LOX. Most of the synthesized compounds exhibited an overall bearable toxicity level and could be utilized as possible therapeutic entrants after making structural modifications.

6. Acknowledgements

The authors extend their appreciation to the Higher Education Commission of Pakistan for financial support.

Conflict of Interest:

Authors declare no conflict of interest.

7. References

1. C. T. Supuran, *Expert Opin. Drug Discov.* **2017**, *12*, 61–88. **DOI:**10.1080/17460441.2017.1253677.
2. F. Carta, C. T. Supuran, A. Scozzafava, *Future Med. Chem.* **2014**, *6,* 1149–1165. **DOI:**0.4155/fmc.14.68.
3. A. Scozzafava, T. Owa, A. Mastrolorenzo, C. T. Supuran, *Curr. Med. Chem*. **2003**, *10*, 925–953. **DOI:**10.2174/0929867033457647.
4. C. Capasso, C. T. Supuran, *J. Enzym. Inhib. Med. Chem*. **2014**, *29*, 379–387. **DOI:**10.3109/14756366.2013.787422.
5. F. Carta, A. Scozzafava, C. T. Supuran, *Expert Opin. Ther. Pat.* **2012**, *22*, 747–758. **DOI:**10.1517/13543776.2012.698264.
6. C. Capasso, C. T. Supuran, *J. Enzym. Inhib. Med. Chem*. **2015**, *30*, 325–332. **DOI:**10.3109/14756366.2014.910202.
7. C. Capasso, C. T. Supuran, *Expert Opin. Ther. Targets.* **2015**, *19*, 1689–1704. **DOI:**10.1517/14728222.2014.991312.
8. V. M. Varagic, M. P. Milosevic, Farmakologija, Elitmedica, *Beograd*. **2009**, 622–627.
9. A. Scozzafava, C. T. Supuran, F. Carta, *Expert Opin. Ther. Pat.* **2013**, *23*, 725–735. **DOI:**10.1517/13543776.2013.790957.

10. A. Casini, A. Scozzafava, C. T. Supuran, *Expert Opin. Ther. Pat.* **2002**, *12*, 1307–1327. **DOI:**10.1517/13543776.12.2.217.
11. F. Carta, C. T. Supuran, *Expert Opin. Ther. Pat.* **2013**, *23*, 681–691. **DOI:**10.1517/13543776.2013.780598.
12. C. T. Supuran, *J. Enzym. Inhib. Med. Chem.* **2016**, *31*, 345–360. **DOI:**10.3109/14756366.2015.1122001.
13. A. E. Boyd, *Diabetes.* **1988**, *37*, 847–850. **DOI:**10.2337/diab.37.7.847.
14. T. H. Maren, *Annu. Rev. Pharmacol. Toxicol.* **1976**, *16*, 309–327. **DOI:**10.1146/annurev.pa.16.040176.001521.
15. C. T. Supuran, *Metabolites*. **2017**, *7*, 48–61. **DOI:**10.3390/metabo7040056.
16. F. Abbate, J. Y. Winum, B. V. L. Potter, A. Casini, J. L. Montero, A. Scozzafava, C. T. Supuran, *Bioorg. Med. Chem. Lett*. **2004**, *14*, 231–234. **DOI:**10.1016/j.bmcl.2004.07.087.
17. L. Puccetti, G. Fasolis, D. Vullo, Z. H. Chohan, A. Scozzafava, C. T. Supuran, *Bioorg. Med. Chem. Lett.* **2005**, *15*, 3096–3101. **DOI:**10.1016/j.bmcl.2005.04.055.
18. F. Carta, L. D. C. Mannelli, M. Pinard, C. Ghelardini, A. Scozzafava, R. McKenna, C. T. Supuran, *Bioorg. Med. Chem.* **2015**, *23*, 1828–1840. **DOI:**10.1016/j.bmc.2015.02.027.
19. H. Nikoofard, M. Sargolzaei, F. Faridbod, *Acta. Chim. Slov*. **2017**, *64*, 842–848. **DOI:**10.17344/acsi.2017.3357.
20. M. A. Abbasi, G. Hussain, Aziz-ur-Rehman, S. Z. Siddiqui, S. A. A. Shah, M. A. Lodhi, F. A. Khan, M. Ashraf, Qurat-ul-Ain, I. Ahmad, R. Malik, M. Shahid, Z. Mushtaq, *Acta. Chim. Slov*. **2017**, *64*, 159–169. **DOI:**10.17344/acsi.2016.2986
21. A. Weber, A. Casini, A. Heine, D. Kuhn, C. T. Suparan, A. Scozzafava, G. Kelebe, *J. Med. Chem*. **2004**, *47*, 550–557. **DOI:**10.1021/jm030912m.
22. C. T. Suparan, F. Brigani, S. Tilli, W. R. Chegwidden, A. Scozzafava, *Bioorg. Med. Chem.***2001**, *9*, 703–714. **DOI:**10.1016/S0968-0896(00)00288-1.
23. M. A. R. Matos, C. C. S. Sousa, V. M. F. Morais, *J. Phys. Chem. A*. **2008**, *112*, 7961–7968.
24. Y. Luo, S. Zhang, K. M. Qiu, Z. J. Liu, Y. S. Yang, J. Fu, W. Q. Zhong, H. L. Zhu, *Bioorg. Med. Chem. Lett.* **2013**, *23*, 1091–1095. **DOI:**10.1016/j.bmcl.2012.12.010.
25. J. Sun, Y. S. Yang, W. Li, Y. B. Zhang, X. L. Wang, J. F. Tang, H. L. Zhu, *Bioorg. Med. Chem. Lett*. **2011**, *21*, 6116–6121. **DOI:**10.1016/j.bmcl.2011.08.039.
26. J. Sun, N. Cao, X. M. Zhang, Y. S. Yang, Y. B. Zhang, X. M. Wang, H. L. Zhu, *Bioorg. Med. Chem*. **2011**, *19*, 4895–4902. **DOI:**10.1016/j.bmc.2011.06.061.
27. Y. Harrak, G. Rosell, G. Daidone, S. Plescia, D. Schillaci, M. D. Pujol, *Bioorg. Med. Chem*. **2007**, *15*, 4876–4890. **DOI:**10.1016/j.bmc.2007.04.050.
28. Y. Aiba, D. Hasegawa, T. Marunouchi, K. Nagasawa, H. Uchiro, S. Kobayashi, *Bioorg. Med. Chem. Lett*. **2001**, *11*, 2783–2786. **DOI:**10.1016/S0960-894X(01)00561-3.
29. M. Z. Xu, W. S. Lee, J. M. Han, H.W. Oh, D.S. Park, G.R. Tian, T.S. Jeong, H.Y. Park, *Bioorg. Med. Chem.* **2006**, *14*, 7826–7834. **DOI:**10.1016/j.bmc.2006.07.063.
30. M. T. Vazquez, G. Rosell, M. D. Pujol, *Eur. J. Med. Chem*. **1997**, *32*, 529–534. **DOI:**10.1016/S0223-5234(97)84016-0.
31. I. A. Guedes, C. S. Magalhaes, L. E. Dardenne, *Biophys. Rev*. **2014**, *6*, 75–87. **DOI:**10.1007/s12551-013-0130-2.
32. M. Irshad, M. A. Abbasi, Aziz-ur-Rehman, S. Z. Siddiqui, M. S. Ali, M. Ashraf, T. Ismail, I. Ahmad, S. Hassan, M. A. Lodhi, S. B. Jamal, *Pak. J. Pharm. Sci.* **2016**, *29*, 1913–1925.
33. G. L. Ellman, K. D. Courtney, V. Andres, R. M. Featherstone, *Bio. Pharm*. **1961**, *7*, 88–95. **DOI:**10.1016/0006-2952(61)90145-9.
34. A. L. Tappel, *Arch. Biochem. Biophys.* **1953**, *44*, 378–395.
35. S. Baylac, P. Racine, *Int. J. Aromather*. **2003,** *13*, 138–142. **DOI:**10.1016/S0962-4562(03)00083-3.
36. A. T. Evans, *Biochem. Pharmacol.* **1987**, *36*, 2035–2037. **DOI:**10.1016/0006-2952(87)90505-3.
37. M. Kaspady, V. K. Narayanaswamy, M. Raju, G. K. Rao, *Lett. Drug Des. Discov*. **2009**, *6*, 21–28. **DOI:**10.2174/157018009787158481.
38. P. Sharma, J. D. Sharma, *J. Ethnopharmacol.* **2001**, *74*, 239–243. **DOI:**10.1016/S0378-8741(00)00370-6.
39. W. A. Powell, C. M. Catranis, C. A. Maynard, *Lett. Appl. Microbiol.* **2000**, *31*, 163–168. **DOI:**10.1046/j.1365-2672.2000.00782.x.
40. M. J. Bostro, J. R. Greenwood, J. Gottfries, *Mol. Graph. Model.* **2003**, *21*, 449–462. **DOI:**10.1016/S1093-3263(02)00204-8.

Povzetek

V predstavljenem raziskovalnem delu poročamo o seriji *N*-aril-2,3-dihidrobenzo[1,4]dioksin-6-sulfonamidov **3** in njihovih novih *N*-substituiranih derivatih **6** in **7**, ki smo jih iz **3** pripravili z benzil kloridom oz. etil jodidom. Sintezo smo izvedli v več stopnjah. Strukture produktov smo določili z ^{1}H NMR, IR in EIMS spektroskopskimi tehnikami. Kot encime smo v študiji uporabili butirilholinesterazo (BChE), acetilholinesterazo (AChE) in lipoksigenazo (LOX). Ugotovili smo, da večina spojin izkazuje zmerno aktivnost proti BChE in AChE in obetavno dobro aktivnost proti lipoksigenazi. Med matičnimi sulfonamidi so **3a**, **3b**, **3c** in **3e** izkazali najbolj učinkovite antimikrobne aktivnosti, po drugi strani pa so derivati **6a**, **6c**, **7a**, **7b** in **7c** izkazali dobro aktivnosti proti izbranim bakterijam in glivam. Hemolitsko aktivnost smo določili, da bi ugotovili morebitno terapevtsko uporabnost pripravljenih spojin. Vse spojine smo tudi računsko sidrali v encime LOX, BChE in AChE.

DOI: 10.17344/acsi.2018.4790 *Acta Chim. Slov.* **2019,** *66,* 308–314

Scientific paper

Three Chiral Cyanide-Bridged Cr–Cu Complexes: Synthesis, Crystal Structures and Magnetic Properties

Xia Chen,[1,+] Wen-Long Lan,[1,+] Xiao-Yun Hao,[1] Yu Liu,[1] Zhen Zhou,[1] Shu-Juan Zhuang,[1] Lu Yang,[1] Qing-Yun Liu,[2] Wei-Jiang Si[1,*] and Dao-Peng Zhang[1,*]

[1] *College of Chemical and Chemical Engineering, Shandong University of Technology, Zibo 255049, PR China*

[2] *College of Chemical and Environmental Engineering, Shandong University of Science and Technology, Qingdao 266510, PR China*

* *Corresponding author: E-mail: siweijiang@sdut.edu.cn, dpzhang73@126.com*

[+] *These two authors contributed equally.*

Received: 12-05-2018

Abstract

Two *trans*-dicyanidochromium(III)-containing building blocks and one chiral copper(II) compound have been employed to assemble cyanide-bridged heterometallic complexes, resulting in three chiral cyanide-bridged Cr(III)–Cu(II) complexes, $\{[Cu(L^1)_2Cr(L^3)(CN)_2]ClO_4\}_2 \cdot CH_3OH \cdot H_2O$ (**1a**, L^1 = (*S*,*S*)-1,2-diaminocyclohexane, H_2L^3 =1,2-bis(pyridine-2-carboxamido)benzene), $\{[Cu(L^2)_2Cr(L^2)(CN)_2]ClO_4\}_2 \cdot CH_3OH \cdot H_2O$ (**1b**, L^2 = (*R*,*R*)-1,2-diaminocyclohexane) $\{[Cu(L^3)_2Cr(L^4)(CN)_2][Cr(L^4)(CN)_2]\} \cdot CH_3OH \cdot 2H_2O$ (**2**), (H_2L^4 = 1,2-bis(pyridine-2-carboxamido)-4-chlorobenzene). All the three complexes have been characterized by elemental analysis, IR spectroscopy and X-ray structure determination. Single-crystal X-ray diffraction analysis shows that the two enantiomeric complexes **1a**, **1b** and the complex **2** belong to cyanide-bridged cationic binuclear structure type with ClO_4^- or the anionic cyanide building block as balance anion for complexes **1a**, **1b** or **2**, respectively. Investigation of the magnetic properties of the complexes **1a** and **2** reveals the weak ferromagnetic coupling between the neighboring Cr(III) and Cu(II) ions through the bridging cyanide group.

Keywords: Chiral; cyanide-bridged; heterobimetallic; crystal structure; magnetic property

1. Introduction

Molecular-based magnetic materials have attracted widespread attention in the past few decades due to their potential applications in high-density information storage and quantum tunneling effects.[1–4] During the process of the synthesis of the new magnetic complexes, the choice of magnetic spin carriers, bridging bonds and coordination ligands plays a very important role on the structure and the functional property of the target magnetic complexes. Among which, as one of the well-known magnetic transfer groups, cyanide groups usually exhibit unique advantages when assembling bimetallic or even trimetallic cyanide-bridged magnetic complexes.[5–16] Although there are many combinations of different magnetic carriers for cyanide-bridged complexes, the Cr^{III}-Cu^{II} system still receives much attention and many cyanide-bridged Cr^{III}-Cu^{II} complexes with interesting magnetic properties such as single-molecule magnets, single-chain magnets, spin crossover magnets and photo switchable magnets have been reported.[17–20] Compared with the cyanide-bridged heterometallic Fe^{III}-M (M = Cu(II), Ni(II), Mn(II), Mn(III), et al.) complexes,[21–27] the cyanide-bridged heterometallic Cr^{III}-M complexes are still limited due to the shortage of stable and suitable cyanidochromate(III) building blocks.[28–32]

In recent years, in order to clearly clarify the magnetic structure correlation in low-dimensional magnetic systems and to prepare interesting low-dimensional molecular magnetic materials, a series of cyanide precursors containing the larger equatorial in-plane ligands and two *trans*-cyanide groups have been designed.[33–38] Studies have shown that these types of cyanide-containing precursors were good choices for assembling cyanide bridged bimetallic magnetic complexes with different structures, such as multinuclear, nanomolecular and one-dimension-

al chains, and interesting magnetic properties. On the other hand, in the research field of functional molecular magnetic materials, the design and synthesis of chiral magnetic materials are of great significance for the basic research of magnetic induction second harmonic generation (MSHG) and magnetic chiral dichroism (MCHD) and their possible applications in a variety of new technologies. It is known that the chirality can be reasonably introduced into the cyanide bridging system by coordinating the paramagnetic metal ions (Ni^{2+}, Cu^{2+}, $Mn^{2+/3+}$, etc) with a chiral auxiliary ligand (chiral amine, chiral Schiff base, etc.).[39–46] In order to find new chiral molecular magnetic complexes and further enrich the low-dimensional cyanide bridged *trans*-dicyano-based compounds, we investigated the reactions of *trans*-dicyanidochromium(III) precursors with chiral organic amine copper compounds (Scheme 1) and obtained three new cyanide-bridged chiral Cr(III)-Cu(II) complexes, including the two enantiomeric complexes $\{[Cu(L^1/L^2)_2Cr(L^3)(CN)_2]ClO_4\}_2 \cdot CH_3OH \cdot H_2O$ (**1a**, **1b**), and $\{[Cu(L^2)_2Cr(L^4)(CN)_2][Cr(L^4)(CN)_2]\} \cdot CH_3OH \cdot 2H_2O$ (**2**). This paper will mainly concern the synthesis, crystal structures and magnetic properties for the above three complexes.

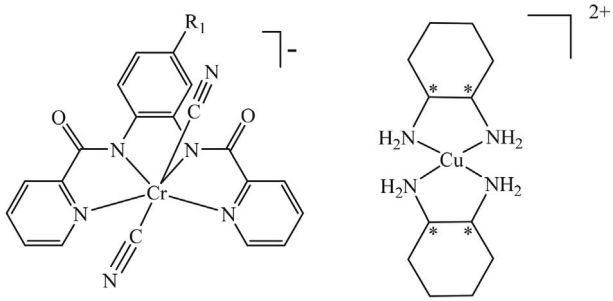

trans-$[Cr^{III}(L^3/L^4)(CN)_2]^-$
[L^3, R_1 = H; L^4, R_1 = Cl]

$[Cu(L^1/L^2)]^{2+}$

Scheme 1. The starting materials used for synthesizing the three complexes.

2. Experimental

Elemental analyses of carbon, hydrogen, and nitrogen were carried out with an Elementary Vario El. The infrared spectroscopy on KBr pellets was performed on a Magna-IR 750 spectrophotometer in the 4000–400cm^{-1} region. Variable-temperature magnetic susceptibilities for the reported complexes were performed on a Quantum Design MPMS SQUID magnetometer. The experimental susceptibilities were corrected for the diamagnetism of the constituent atoms (Pascal's tables).

2. 1. General Procedures and Materials

All the reactions were carried out under an air atmosphere and all chemicals and solvents used were reagent grade without further purification. $K[Cr^{III}(L^3)(CN)_2]$ [H_2L^3 = 1,2-bis(pyridine-2-carboxamido)benzene] was synthesized as described in literature.[47] The synthesis of another cyanide precursor is similar to that for $K[Cr^{III}(L^3)(CN)_2]$, except that the 1,2-diamino-4-chlorobenzene was used to replace 1,2-diaminobenzene during the preparation process. The two chiral 1,2-diaminocyclohexane were from the J&K Scientific LTD.

Caution! KCN is hypertoxic and hazardous. Perchlorate salts of metal complexes with organic ligands are potentially explosive. These chemicals should be handled in small quantities with great care.

2. 2. Preparation of the Complexes 1a, 1b and 2

All three complexes were prepared using similar procedure. Therefore, a representative method for preparation of the complex **1a** is described herein.

Complex **1a** was prepared by the following procedures: The acetonitrile solution (10 mL) formed *in situ* by $[Cu(ClO_4)_2] \cdot 6H_2O$ (36.5 mg, 0.1 mmol) and L^1 (22.8 mg, 0.2 mmol) was added slowly to a solution containing $K[Cr(L^3)(CN)_2]$ (91.6 mg, 0.20 mmol) dissolved in a mixture of methanol and water (8 mL: 2 mL). The mixture was stirred only for one minute at room temperature and filtered at once to remove any insoluble material, and then the filtrate was allowed to evaporate slowly without disturbance for about one week. The dark-orange crystals generated suitable for X-ray diffraction were collected by filtration, washed with cool methanol, and dried in air. Yield: 44.3 mg, 53.1%. Anal. Calcd. for $C_{65}H_{86}Cl_2Cr_2Cu_2N_{20}O_{14}$: C, 46.65; H, 5.18; N, 16.74. Found: C, 46.87; H, 5.26; N, 16.59. Main IR bands (cm^{-1}): 3330, 3295(s, nN-H), 2160, 2130 (s, nC°N), 1100 (vs, nCl=O).

Complex **1b**: Yield: 42.7 mg, 51.2%. Anal. Calcd. for $C_{65}H_{86}Cl_2Cr_2Cu_2N_{20}O_{14}$: C, 46.65; H, 5.18; N, 16.74. Found: C, 46.89; H, 5.25; N, 16.61. Main IR bands (cm^{-1}): 3330, 3296(s, nN-H), 2160, 2130 (s, nC°N), 1100 (vs, nCl=O).

Complex **2**: Yield: 69.8 mg, 55.1%. Anal. Calcd. for $C_{53}H_{56}Cl_2Cr_2CuN_{16}O_7$: C, 50.22; H, 4.45; N, 17.68. Found: C, 50.33; H, 4.59; N, 17.51. Main IR bands (cm^{-1}): 3332, 3294(s, nN-H), 2158, 2127 (s, nC°N).

2. 3. X-ray Data Collection and Structure Refinement

Crystal data of three complexes were collected by using single-crystals with suitable dimensions on an Oxford Diffraction Gemini E diffractometer with Mo*Kα* radiation (λ = 0.71073 Å) at room temperature, and the collected frames were integrated by using the preliminary cell-orientation matrix. The structures of these three complexes were solved by direct method and expanded using Fourier difference techniques with the SHELXTL-97 program package.[48] All non-hydrogen atoms were readily located

Table 1. Crystallographic data and structure refinement summary for the three complexes.

	1a	1b	2
Empirical formula	$C_{65}H_{86}Cl_2Cr_2\ Cu_2N_{20}O_{14}$	$C_{65}H_{86}Cl_2Cr_2\ Cu_2N_{20}O_{14}$	$C_{53}H_{56}Cl_2Cr_2\ CuN_{16}O_7$
Formula weight	1673.52	1673.52	1267.58
Temperature (K)	293	293	293
Crystal system	Monoclinic	Monoclinic	Triclinic
Space group	$P2_1$	$P2_1$	$P1$
a/Å	13.9564(9)	13.934(10)	10.8564(14)
b/Å	12.2866(8)	12.259(8)	12.040(2)
c/Å	22.6709(14)	22.648(15)	13.8215(17)
α/deg	90	90	114.89(1)
β/deg	91.03(0)	90.88(1)	91.40(1)
γ/deg	90	90	105.46(1)
F(000)	1736.0	1736.0	653.0
Reflections collected/unique	19548/11239	19286/10871	11422/8226
Data/restraints/parameters	11239/2/948	10871/1/948	8226/3/750
Goodness-of-fit on F^2	1.028	1.031	0.995
R_1[I>2σ(I)]	0.0535	0.0545	0.0769
wR_2 (all data)	0.1475	0.1536	0.2233
Largest diff. peak/ hole (e/Å^3)	0.622/–0.296	0.513/–0.334	0.778/–0.347

and refined anisotropically. In ligand L^4 in complex **2** chlorine atoms Cl1 and Cl2 were refined as disordered over two positions with 0.80:0.20 and 0.50:0.50 occupancy ratios, respectively. Hydrogen atoms were assigned isotropic displacement coefficients U(H) = 1.2U(C) or 1.5U(C) and their coordinates were allowed to ride on their respective carbon atoms or nitrogen atoms using SHELXL-97 except of the solvent H atoms. For the latter, they were refined isotropically with fixed U values and the DFIX command was used to rationalize the bond parameter. CCDC 1861738–1861740 for these three complexes contain the supplementary crystallographic data for this paper, which can be obtained free of charge from the Cambridge Crystallographic Data Centre via www.ccdc.cam.ac.uk/data_request/cif. Details of the crystal parameters, data collection, and refinement of complexes **1**-**2** are summarized in Table 1.

3. Results and Discussion

3. 1. Synthesis and General Characterization

The recent works have proved that *trans*-dicyanometallates are good building blocks for synthesizing cyanide-bridged magnetic complexes.[33–38] The relatively large planar pyridinecarboxamide ligand at the equatorial position can not only effectively lower the dimensionality of the resulted complex, but also weaken the supramolecular intermolecular magnetic interactions. With this in mind and also for the purpose of the preparation of chiral magnetic complexes, we investigated the reactions of *trans*-dicyanidochromium(III) with chiral amine copper(II) compounds and obtained three new chiral cyanide-bridged Cr(III)-Cu(II) complexes. The different balance anions, i.e. ClO_4^- for complexes **1a**, **1b** and the cyanometallate for complexes **2** indicate that the structure of the cyanide precursor has some effects on the structure of the cyanide-bridged complex formed.

The three cyanide-bridged complexes have been characterized by IR spectroscopy. In the IR spectra of **1a** and **1b**, two sharp peaks due to the cyanide-stretching vibration were observed at about 2125–2130 and 2155–2160 cm^{-1}, respectively, indicating the presence of bridging and non-bridging cyanide ligands in these complexes. The strong broad peak centered at about 1100 cm^{-1} for these two complexes is attributed to the free ClO_4^- anion. To confirm the optical activity and enantiomeric nature, the circular dichroism (CD) spectrum were measured in KBr pellets for complexes **1**–**2**. The CD spectrum of **1a** and **1b** exhibit positive and negative Cotton effect at the same wavelengths (Figure. 1).

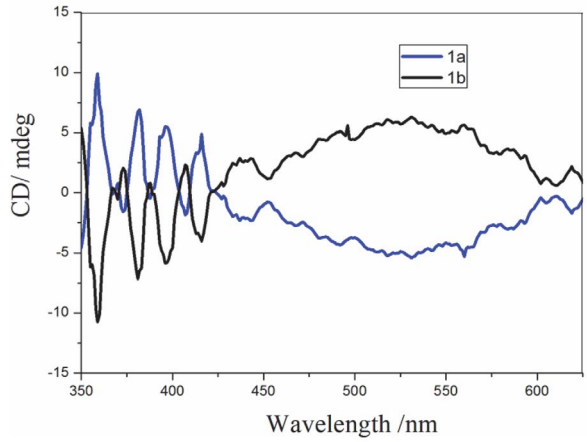

Figure 1. CD spectra of **1a** (*S* isomer, black) and **1b** (*R* isomer, blue) in KBr pellets.

3. 2. Crystal structures of complexes 1a, 1b and 2

Some important structural parameters for complexes **1a**, **1b** and **2** are collected in Table 2. The perspective view of the enantiomeric structure of complexes **1a** and **1b** is demonstrated in Figure 2. The cell packing diagram of the complex **1a** is given in Figure 3, which is similar to that for the complex **1b**. For the complex **2**, its cationic binuclear structure and the cell packing diagram are shown in Figures 4 and 5, respectively.

Table 2. Selected bond lengths (Å) and angles (°) for complexes **1a**, **1b** and **2**.

	1a	1b	2
Cu1–N1	2.346(8)	2.344(6)	2.324(12)
Cu1–N3	2.049(8)	2.029(6)	2.028(9)
Cu1–N4	1.993(8)	2.012(6)	2.022(10)
Cu1–N5	2.062(8)	1.992(7)	1.983(11)
Cu1–N6	2.001(7)	2.000(6)	2.022(11)
Cr1–C1	2.078(11)	2.121(9)	2.103(11)
Cr1–C2	2.048(12)	2.058(8)	2.068(11)
Cr1–N7	1.984(8)	1.967(6)	1.971(9)
Cr1–N8	1.976(7)	1.971(6)	2.123(10)
Cr1–N9	2.063(7)	2.083(6)	1.972(9)
Cr1–N10	2.070(8)	2.093(6)	2.098(9)
Cu1–N1–C1	139.0(9)	141.7(7)	159.2(10)
Cr1–C1–N1	165.7(10)	165.6(7)	172.7(11)
Cr1–C2–N2	176.7(11)	178.8(7)	175.2(12)

The complexes **1a** and **1b** as a pair of enantiomer, containing Cr_2Cu_2 unit in the unit cell with a dimer structure, crystallize in monoclinic cell setting with the non-central space group $P2_1$, while complex **2** crystallizes in triclinic cell setting with the non-central space group $P1$. All the three complexes are with the similar cationic cyanide-bridged binuclear structure and the different balance anion, i.e. the free ClO_4^- for complexes **1a**, **1b** and the free cyanide building block for complex **2**. The distances between the O atom of the ClO_4^- ion and the Cu(II) ion is about 3.273 Å, indicating the existed weak interaction. In

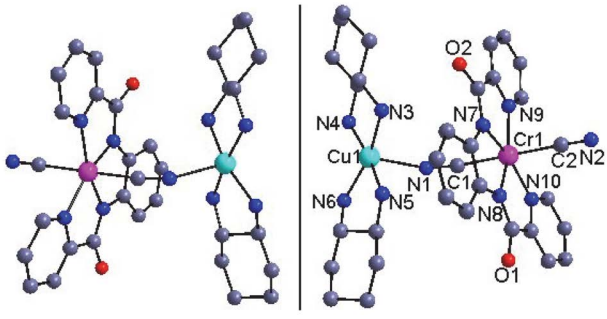

Figure 2. The perspective view of the enantiomeric structure of complexes **1a** and **1b**. All the H atoms, the balanced anion and the solvent molecules have been omitted for clarity.

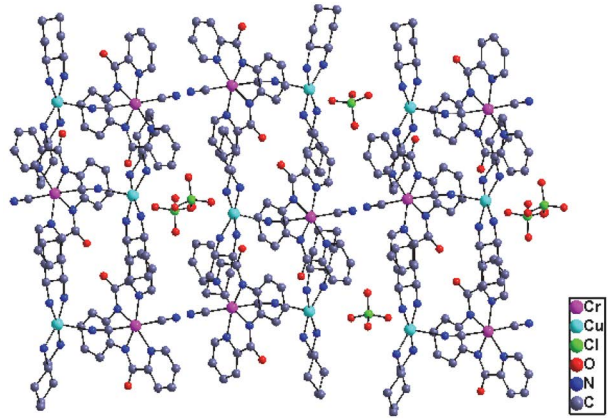

Figure 3. The cell packing diagram along *c* axis of the complex **1a**. All the H atoms and the solvent molecules have been omitted for clarity.

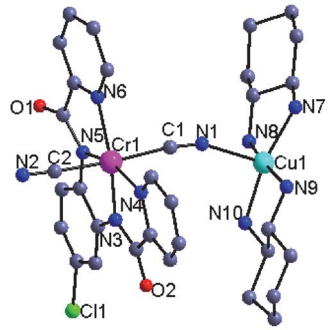

Figure 4. Perspective view of the cationic structure of the complex **2**. All the H atoms, the balanced anion and the solvent molecules have been omitted for clarity.

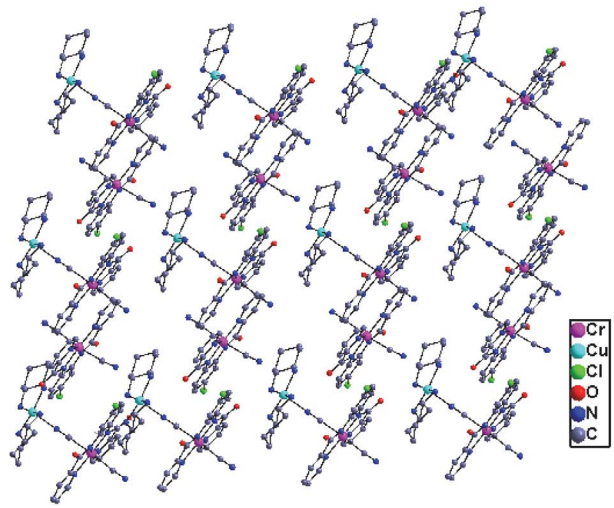

Figure 5. The cell packing diagram along *b* axis of the complex **2**. All the H atoms and the solvent molecules have been omitted for clarity.

all the reported complexes, each cyanide-containing building block acting as a monodentate ligand through one of its two *trans* cyanide groups connects the Cu(II) ion with the other cyanide group as terminal. The Cr(III) ion

is six-coordinates with four equatorial nitrogen atoms from the pyridinecarboxamide ligand and two carbon atoms from the two cyanide groups with a *trans* position, so that forming a slightly distorted octahedral geometry, which can be proven by the bond parameters around the Cr(III) ion (Table 2). The Cr–C≡N bond angles in these three complexes are in a comparatively narrow range of 165.6(7)°–178.8(7)°, showing almost the linear conformation for these three atoms.

The Cu atom in complexes **1a**, **1b** and **2** is five-coordinated by a N_5 unit, in which four N atoms come from the two chiral amine ligands and the additional one N atom from the bridging cyanide group. The Cu atom is only out of the plane formed by four N atoms 0.16(2), 0.17(4) and 0.058(2) Å toward to the fifth coordinated $N_{cyanido}$ atom in these three complexes, indicating that these five atoms are almost located in a plane. The average Cu–N_{amine} bond lengths in complexes **1a**, **1b** and **2** are 2.009, 2.008 and 2.014 Å, respectively, obviously shorter than the Cu–$N_{cyanido}$ bond length with the values of 2.346, 2.344 and 2.324 Å, clearly showing the markedly distorted square pyramid surrounding of the Cu(II) ion. Additionally, it should be pointed out that there exists conspicuous difference for the C≡N–Cu bond angles in these three complexes. The C≡N–Cu bond angle in complexes **1a** and **1b** are only 139.0(9)°, 141.7(7)°, respectively, while the corresponding angle in the complexes **2** is obviously larger than those in complexes **1a** and **1b** with value 159.2(10)°. The intramolecular Cr(III)-Cu(II) separation through bridging cyanide group are 5.076, 5.098 and 5.412 Å for these three complexes, which are obviously shorter than the shortest intermolecular metal–metal distance with the values of 6.519, 7.543, 8.108 and 7.511 Å in the three complexes, respectively.

3. 3. The Magnetic Properties of Complexes

Figure 6 shows the temperature dependences of magnetic susceptibility of complexes **1a** and **2** measured in the temperature range of 2–300 K in the applied field of 2000 Oe. The room temperature c_mT values are 2.13 and 4.09 emu K mol^{-1} for these two complexes, respectively, which are slightly lower than the spin only value of 2.25 emu K mol^{-1} for one uncoupled Cu(II) (S = 1/2) ion and one Cr(III) (S = 3/2) ion in complex **1a** and 4.125 emu K mol^{-1} for one uncoupled Cu(II) (S = 1/2) ion and two Cr(III) (S = 3/2) ion in complex **2** based on g = 2.00. With the temperature decreasing, the c_mT values increases gradually and attains the value of 2.37 and 6.76 emu K mol^{-1} about 15 K, then decreases sharply to 1.51 and 4.51 emu K mol^{-1} at 2 K, which indicated the characteristic of ferromagnetic coupling between the cyanide-bridged Cr(III)-Cu(II) center. The magnetic susceptibility for these two complexes conforms well to Curie-Weiss law in the range 2–300 K and give the positive Weiss constant q = 1.38 K and Curie constant C = 2.15 emu K mol^{-1} for complex **1a** and q = 7.01 K and Curie constant C = 4.15 emu K mol^{-1} for complex **2**, further proves the ferromagnetic coupled Cr(III)-Cu(II) through the cyanide bridge.

On the basis of the binuclear model, the magnetic susceptibility of complex **1a** can be fitted accordingly by the following expression (1) derived from the isotropic exchange spin Hamilton $\hat{H} = -2J\hat{S}_{Cu}\hat{S}_{Cr}$. For complex **2**, its magnetic susceptibility has been analyzed based-on also the binuclear model but by introducing the additional isolated Cr(III) ion with the expression (2).

$$\chi_m = \frac{Ng^2\beta^2}{kT}\cdot\frac{2+10\exp(4J/kT)}{3+5\exp(4J/kT)} \quad (1)$$

$$\chi_m = \frac{Ng^2\beta^2}{kT}\cdot\frac{2+10\exp(4J/kT)}{3+5\exp(4J/kT)} + \frac{Ng^2\beta^2}{3kT}S_{Cr}(S_{Cr}+1) \quad (2)$$

By using the above model, the susceptibilities over the temperature range of 2–300 K for these two complexes were simulated, giving the best-fit parameters J = 0.74(2) cm^{-1}, g = 2.01(2), $R = \Sigma(c_{obsd}T - c_{cald}T)^2/\Sigma(c_{obsd}T)^2$ = 2.30 × 10^{-5} for **1a** and J = 2.37(2), g = 2.01(8), R = 3.21 × 10^{-5} for **2**, respectively, which can further proven the weak ferro-

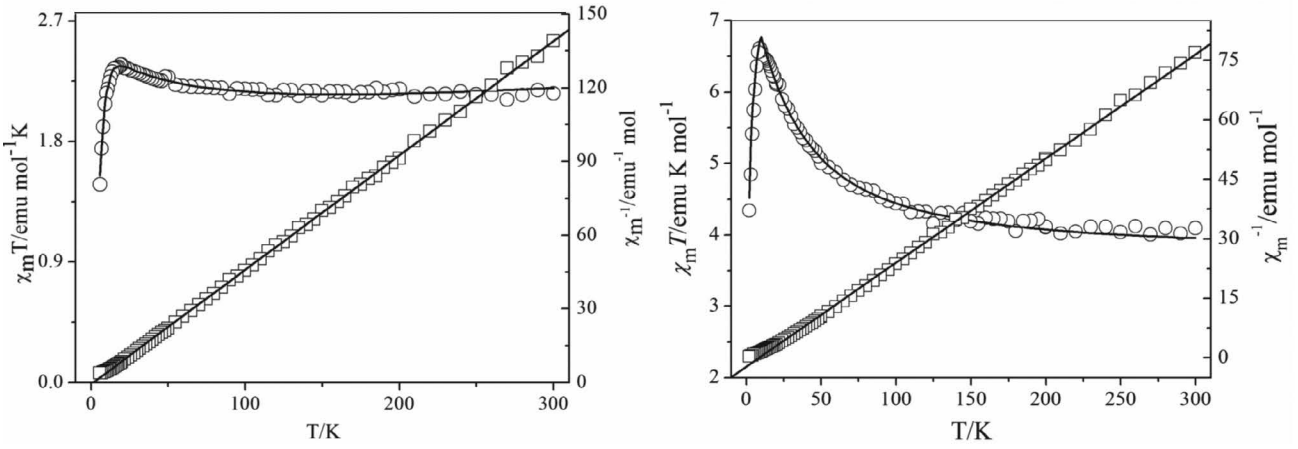

Figure 6. The c_mT and c_m^{-1} *vs T* curves for complexes **1a** (left) and **2** (right).

magnetic coupling between the Cr(III) ion and Cu(II) ion through the bridging cyanide group.

4. Conclusion

In summary, three new chiral cyanide-bridged heterobimetallic complexes, in which two of them are a pair of enantiomers, have been designed and successfully synthesized based on the chiral amine copper(II) compounds and the *trans*-dicyanidochromium(III)-containing building blocks. All the three complexes present the similar cationic cyanide-bridged binuclear structure but with different balanced anion, giving the information that the cyanide precursors with slight structural difference still have some influence on the forming of the target complexes. Investigation over the magnetic properties of the reported complexes reveals that the ferromagnetic coupling between the cyanide-bridged Cr(III)-Cu(II) center.

5. Acknowledgement

This work was supported by the Natural Science Foundation of China (21671121) and the Natural Science Foundation of Shandong Province (ZR2018BB002).

6. References

1. P. Zhang, Y. N. Guo, J. Tang, *Coord. Chem. Rev.* **2013**, *257*, 1728–1763. **DOI:**10.1016/j.ccr.2013.01.012
2. Z. S. Yao, S. Q. Wu, Y. Kitagawa, S. Q. Su, Y. G. Huang, G. L. Li, Z. H. Ni, H. Nojiri, Y. Shiota, K. Yoshizawa, S. Kang, S. Kanegawa, O. Sato, *Angew. Chem. Int. Ed.* **2017**, *56*, 717–721. **DOI:**10.1002/anie.201606165
3. O. Sato, *Nat. Chem.* **2016**, *8*, 644–656. **DOI:**10.1038/nchem.2547
4. R. J. Wei, Q. Huo, J. Tao, R. B. Huang, L. S. Zheng, *Angew. Chem. Int. Ed.* **2011**, *50*, 8940–8943. **DOI:**10.1002/anie.201103648
5. L. M. C. Beltran, J. R. Long, *Acc. Chem. Res.* **2005**, *38*, 325–334. **DOI:**10.1021/ar040158e
6. S. Wang, X. H. Ding, Y. L. Li, W. Huang, *Coord. Chem. Rev.* **2012**, *256*, 439–464. **DOI:**10.1016/j.ccr.2011.10.029
7. Y. H. Li, W. R. He, X. H. Ding, S. Wang, L. F. Cui, W. Huang, *Coord. Chem. Rev.* **2012**, *256*, 2795–2815. **DOI:**10.1016/j.ccr.2012.09.014
8. M. Shatruk, C. Avendano, K. R. Dunbar, *Prog. Inorg. Chem.* **2009**, *56*, 155–334. **DOI:**10.1002/9780470440124.ch3
9. J. H. Lim, J. H. Yoon, S. Y. Choi, D. W. Ryu, E. K. Koh, C. S. Hong, *Inorg. Chem.* **2011**, *50*, 1749–1757. **DOI:**10.1021/ic102179n
10. H. Miyasaka, A. Saitoh, S. Abe, *Coord. Chem. Rev.* **2007**, *251*, 2622–2664. **DOI:**10.1016/j.ccr.2007.07.028
11. Q. L. Wang, H. Southerland, J. R. Li, A. V. Prosvirin, H. Zhao, K. R. Dunbar, *Angew. Chem. Int. Ed.* **2012**, *51*, 9321–9324. **DOI:**10.1002/anie.201203309
12. J. G. DaSilva, J. S. Miller, *Inorg. Chem.* **2013**, *52*, 1418–1423. **DOI:**10.1021/ic302148s
13. J. W. Shi, W. L. Wen,Y. Zhou, C. C. Xue, Q. Y. Liu, D. P. Zhang, *J. Chem. Sci.* **2018**, *130*, 19–27. **DOI:**10.1007/s12039-018-1420-9
14. I. Y. Yoo, D. W. Ryu, J. H. Yoon, A. R. Sohn, K. S. Lim, B. K. Cho, E. K. Koh, C. S. Hong, *Dalton Trans.* **2012**, *41*, 1776–1785. **DOI:**10.1039/C1DT11293G
15. E. Pardo, M. Verdaguer, P. Herson, H. Rousselière, J. Cano, M. Julve, F. Lloret, R. Lescouězec, *Inorg. Chem.* **2011**, *50*, 6250–6262. **DOI:**10.1021/ic200616p
16. J. W. Shi, C. C. Xue, L. Q. Kong, D. P. Zhang, *Acta Chim. Slov.* **2017**, *64*, 215–220. **DOI:**10.17344/acsi.2016.3132
17. M. Ferbinteanu, H. Miyasaka, W. Wernsdorfer, K. Nakata, K. Sugiura, M. Yamashita, C. Coulon, R. Clérac, *J. Am. Chem. Soc.* **2005**, *127*, 3090–3099. **DOI:**10.1021/ja0468123
18. X. Chen, S. Q. Wu, A. L. Cui, H. Z. Kou, *Chem. Commun.* **2014**, *50*, 2120–2122. **DOI:**10.1039/c3cc48117d
19. D. P. Zhang, L. F. Zhang, Y. T. Chen, H. L. Wang, Z. H. Ni, W. Wernsdorfer, J. Z. Jiang, *Chem. Commun.* **2010**, *46*, 3550–3552. **DOI:**10.1039/b926710g
20. T. D. Harris, M. V. Bennett, R. Clérac, J. R. Long, *J. Am. Chem. Soc.* **2010**, *132*, 3980–3988. **DOI:**10.1021/ja910963x
21. H. R. Wen, C. F. Wang, *Inorg. Chem.* **2006**, *45*, 8942–8949. **DOI:**10.1021/ic060928d
22. J. I. Kim, H. S. Yoo, E. K. Kho, H. C. Kim, C. S. Hong, *Inorg. Chem.* **2007**, *46*, 8481–8483. **DOI:**10.1021/ic701361a
23. H. Y. Kwak, D. W. Ryu, J. W. Lee, J. H. Yoon, H. C. Kim, *Inorg. Chem.* **2010**, *49*, 4632–4642. **DOI:**10.1021/ic100301q
24. S. Huh, K. T. Youm, Y. J. Park, A. J. Lough, M. Ohba, *Bull. Korean Chem. Soc.* **2006**, *26*, 1031–1032.
25. F. L. Yang, J. Tao, R. B. Huang, L. S. Zheng, *Inorg. Chem.* **2011**, *50*, 911–917. **DOI:**10.1021/ic101490a
26. M. Andruh, J. P. Costes, C. Diaz, S. Gao, *Inorg. Chem.* **2009**, *48*, 3342–3359. **DOI:**10.1021/ic801027q
27. L. Catala, T. Cacoin, J. P. Boilot, T. Mallah, *Adv. Mater.* **2003**, *15*, 826–829. **DOI:**10.1002/adma.200304696
28. H. Z. Kou, S. Gao, B. Q. Ma, D. Z. Liao, *Inorg. Chem. Commun.* **2000**, 713–714. **DOI:**10.1039/b001005g
29. X. P. Shen, H. B. Zhou, Q. Zhang, Y. Xu, H. Zhou, *Eur. J. Inorg. Chem.* **2012**, *31*, 5050–5057. **DOI:**10.1002/ejic.201200480
30. Y. Pei, Y. Journaux, O. Kahn, *Inorg. Chem.* **1989**, *28*, 100–103. **DOI:**10.1021/ic00300a023
31. J. J. Sokol, M. P. Shores, J. R. Long, *Inorg. Chem.* **2002**, *41*, 3052–3054. **DOI:**10.1021/ic0255499
32. M. X. Yao, Q. Zheng, X. M. Cai, Y. Z. Li, J. L. Zuo, *Inorg. Chem.* **2012**, *51*, 2140–2149. **DOI:**10.1021/ic201982d
33. C. Pichon, T. Senapati, R. Ababei, C. Mathonière, R. Clérac, *Inorg. Chem.* **2012**, *51*, 3796–3812. **DOI:**10.1021/ic2027708
34. D. P. Zhang, Z. D. Zhao, P. Wang, Z. H. Ni, *CrystEngComm.* **2013**, *15*, 2504–2511. **DOI:**10.1039/c3ce27064e
35. D. P. Zhang, W. J. Si, P. Wang, X. Chen, J. Z. Jiang, *Inorg. Chem.* **2014**, *53*, 3494–3502. **DOI:**10.1021/ic4029386

36. J. W. Shi, W. L. Lan, Y. J. Ren, Q. Y. Liu, H. Liu, Y. H. Dong, D. P. Zhang, *J. Solid State Chem.* **2018**, *260*, 59–66. **DOI:**10.1016/j.jssc.2018.01.017
37. J. W. Shi, Q. G. Meng, C. C. Xue, Q. Y. Liu, D. P. Zhang, *Transit. Metal Chem.* **2018**, *43*, 45–52. **DOI:**10.1007/s11243-017-0192-2
38. H. Y. Zhang, L. Q. Kong, D. P. Zhang, *J. Struct. Chem.* **2015**, *56*, 1533–1539. **DOI:**10.1134/S0022476615080119
39. T. Shiga, G. N. Newton, J. S. Mathieson, T. Tetsuka, M. Nihei, L. Cronin, H. Oshio, *Dalton Trans.* **2010**, *39*, 4730–4733. **DOI:**10.1039/b925399h
40. J. Ru, F. Gao, T. Wu, M. X. Yao, Y. Z. Li, J. L. Zuo, *Dalton Trans.* **2014**, *43*, 933–936. **DOI:**10.1039/C3DT52951G
41. D. P. Zhang, Y. Z. Bian, J. Qin, P. Wang, X. Chen, *Dalton Trans.* **2014**, *43*, 945–949. **DOI:**10.1039/C3DT52996G
42. D. P. Zhang, S. P. Zhuo, H. Y. Zhang, P. Wang, J. Z. Jiang, *Dalton Trans.* **2015**, *44*, 4655–4664. **DOI:**10.1039/C4DT03274H
43. D. P. Zhang, H. Y. Zhang, *Polyhedron* **2015**, *100*, 36–42. **DOI:**10.1016/j.poly.2015.07.024
44. M. Gruselle, C. Train, K. Boubekeur, P. Gredin, N. Ovanesyan, *Coord. Chem. Rev.* **2006**, *250*, 2491–2500. **DOI:**10.1016/j.ccr.2006.03.020
45. O. Sereda, J. Ribas, H. Stoeckli-Evans, *Inorg. Chem.* **2008**, *47*, 5107–5113. **DOI:**10.1021/ic702234y
46. A. Biswas, A. Jana, S. Sarkar, H. A. Sparkes, Judith A.K. Howard, N. Aliaga-Alcalde, S. Mohanta, *Polyhedron* **2014**, *74*, 57–66. **DOI:**10.1016/j.poly.2014.02.037
47. M. Ray, R. Mukherjee, J. F. Richardson, R. M. Buchanan, *J. Chem. Soc. Dalton Trans.* **1993**, 2451–2457. **DOI:**10.1039/dt9930002451
48. Sheldrick G. M. (1997) SHELXTL97, Program for the Refinement of Crystal Structure, University of Göttingen, Germany.

Povzetek

Tri heterokovinske Cr(III)–Cu(II) komplekse z mostovnim cianido ligandom s formulami $\{[Cu(L^1)_2Cr(L^3)(CN)_2]ClO_4\}_2 \cdot CH_3OH \cdot H_2O$ (**1a**, L^1 = (*S*,*S*)-1,2-diaminocikloheksan, H_2L^3 =1,2-bis(piridin-2-karboksamido)benzen), $\{[Cu(L^2)_2Cr(L^2)(CN)_2]ClO_4\}_2 \cdot CH_3OH \cdot H_2O$ (**1b**, L^2 = (*R*,*R*)-1,2-diaminocikloheksan) $\{[Cu(L^3)_2Cr(L^4)(CN)_2][Cr(L^4)(CN)_2]\} \cdot CH_3OH{\cdot}2H_2O$ (**2**), (H_2L^4 = 1,2-bis(piridin-2-karboksamido)-4-klorobenzen) smo pripravili s kombiniranjem *trans*-dicianidokromovega(III) strukturnega motiva in kiralnega bakrovega(II) kompleksa. Vse tri komplekse smo karakterizirali z elementno analizo, IR spektroskopijo in rentgensko strukturno analizo. Monokristalna rentgenska analiza razkrije, da oba enantiomerna kompleksa **1a** in **1b** ter kompleks **2** sodijo med s cianidnim mostom povezane kationske dvojedrne zvrsti s prisotnim ClO_4^- ali cianidnim anion. Magnetne lastnosti kompleksov **1a** in **2** kažejo šibko feromagnetno sklopitev med sosednjima Cr(III) in Cu(II) ionoma preko mostovnega cianido liganda.

Scientific paper

Application of Inverse QSAR/QSPR Analysis for Pesticides Structures Generation

Belgacem Souyei,[1,2] Abdelkader Hadj Seyd,[3,*] Faouzi Zaiz[4] and Abdelkrim Rebiai[5]

[1] *Faculty of Applied Sciences, University of Kasdi Merbah-Ouargla, 30000, Algeria*

[2] *Chemistry Department, Echahid Hamma Lakhdar University of El Oued.*

[3] *Faculty of Renewable Energy, Hydrocarbons, Earth and Universe Sciences, University of Kasdi Merbah- Ouargla*

[4] *Informatics department, Echahid Hamma Lakhdar University of El Oued.*

[5] *VTRS Laboratory, University of El Oued, P.O. Box 789, 39000, El-Oued, Algeria.*

** Corresponding author: E-mail: seydtg@gmail.com*
Tel: +213 662 726024

Received: 10-16-2018

Abstract

The present work has focused on the application of the inverse-QSAR/QSPR problem for generating new structures of pesticides; this is in view of its extremely important and widespread use in several areas, particularly the agricultural field. For this reason, we implemented a methodology containing nine detailed successive steps that include a quantitative structure–activity/property relationship (QSAR/QSPR) study performed to develop a model that relate**s** the structures of 190 pesticides compounds to their n-octanol–water partition coefficients (**$logk_{ow}$**). We used the unique atomic signatures which represent the structures and acts as independent variables while the property (**$logk_{ow}$**) as the dependent variable. The model was constructed using 130 molecules as training set, and predictive ability tested using 60 compounds. Modeling of **$logk_{ow}$** of these compounds as a function of the signatures descriptors was established by multiple linear regression (MLR) using (LOO) cross-validation. As a result, a QSAR/QSPR equation with 14 atomic signatures was hereby obtained with a R^2 = 0.659273, Q^2 = 0.65617 and $RMSE_{training}$= 0.930192, s = 1.37297 for the training set and in leave-one-out (LOO) cross-validation experiment set value, q^2 = 0.605676, $RMSE_{LOO}$ = 1.0936 respectively. In addition to all of the above, new structures have been generated for a range of pesticides that can be included as future search topics.

Keywords: Atomic Signatures; I-QSPR algorithm; multiple linear regression (MLR); n-Octanol–water partition coefficients; pesticides.

1. Introduction

Pesticides are a large group of substances used to kill insects. These substances are mainly used to control pests that infest cultivated plants and crops or to eliminate disease-carrying insects in specific areas.[1] The definition of pesticides according to Food Agriculture Organization of the United Nations (FAO 1989), a pesticide is any substance or mixture of substances intended for preventing, destroying, or controlling any pest including vectors of human or animal diseases, unwanted species of plants or animals causing harm during, or otherwise interfering with, the production, processing, storage, or marketing of food, agricultural commodities, wood and wood products, or animal feedstuffs, or which may be administered to animals for the control of insects, arachnids or other pests in or on their bodies.[2]

Pesticides and agrochemicals, in general, became an important component of worldwide agriculture systems during the last century, allowing for a noticeable increase in crop yields and food production.[3]

Poisoning from pesticides is a global public health problem and accounts for nearly 300,000 deaths worldwide every year.[4]

Pesticides have numerous beneficial effects. These include the protection of crop, preservation of food and ma-

terials and prevention of vector-borne diseases. For example pesticides may be used in the prevention of malaria, which kills up to 1 million children per year,[5] and for preventing other vector-borne diseases such as dengue, leishmaniosis and Japanese encephalitis. Sorption, volatilization, solubility in water, hydrolysis or oxidation, photo degradation and biodegradation are some of the important factors dealing with the fate of OPPs in the environment.[6] Pesticides vary by source, structure and usage, for example, we find Botanical Ps and Neonicotinoid pesticides. Botanical Ps are naturally occurring chemical compounds extracted or derived from plants to manage field and storage crop pests.[7] The BPs can easily degrade in the environment, and they are easily available, less toxic to human and non-targeted organisms and are compatible with different human cultures.[8,9] Studies have shown that, plants are very good source of crop protectants against pests.[10,11]

Neonicotinoid pesticides were first introduced in the mid-1990s and since then their use has grown rapidly so that they have become the most widely used class of insecticides in the world, with the majority being used as seed coatings.[12] As for the distribution of pesticides, it is concluded that lipophilicity is the chief determinant of pesticide distribution in sediment/water systems.[13] Accordingly lipophilicity $\mathbf{k_{ow}}$ (n-octanol–water partition coefficients) is a physico-chemical property that characterizes the ability of a chemical compound to dissolve in fats (lipids) and non-polar solvents.[13] Lipophilicity plays an important role in the development of drugs and pesticides, since this parameter affects the pharmacokinetic and pharmacodynamic behavior of a biologically active substance.[15,16] According to IUPAC, lipophilicity reflects the affinity of a molecule or a fragment thereof with a lipophilic medium.[17]

Due to the importance of lipophilicity parameter $\mathbf{k_{ow}}$ in the distribution of these compounds (pesticides) between the water and organic phases in the organism, numerous studies report $\mathbf{k_{ow}}$ values for ionisable compounds.[18–20]

However, most of them determined a single $\mathbf{k_{ow}}$ value, reflecting the lipophilicity of the neutral species only**.** Lipophilicity is expressed by the octanol–water partition coefficient ($\mathbf{k_{ow}}$), estimates the solubility in both aqueous and organic phases.[21] The values of $\mathbf{k_{ow}}$ generated using these various methods may vary by several orders of magnitude hence $\mathbf{k_{ow}}$ is usually expressed in the logarithmic form (**log-$\mathbf{k_{ow}}$**).[22] Given all the above mentioned importance of the **log$\mathbf{k_{ow}}$**, it is necessary to study the shape and characteristics of the relationship between this important property of (**log-$\mathbf{k_{ow}}$**) and the molecular structure of these compounds.

The aim of this work is the application of the Inverse-quantitative structure-property relationship (I-QSPR) study. This method is based on a nine-step methodology. The first is a selection of database compound. The second is the generation of the 2D structures, while the third step is the QSPR analysis after translation of the database compounds into unique atomic signatures. In the fourth one, we construct constraint equations, specifically the graphicality and consistency equations, which facilitate the reconstruction of the solution compounds directly from the signatures. Fifth, we solve constraint equations while the sixth step is the database solutions checking. The seventh, eighth and ninth steps are respectively, keeping solutions with desired range, new structures generating, and finally, the database focused.

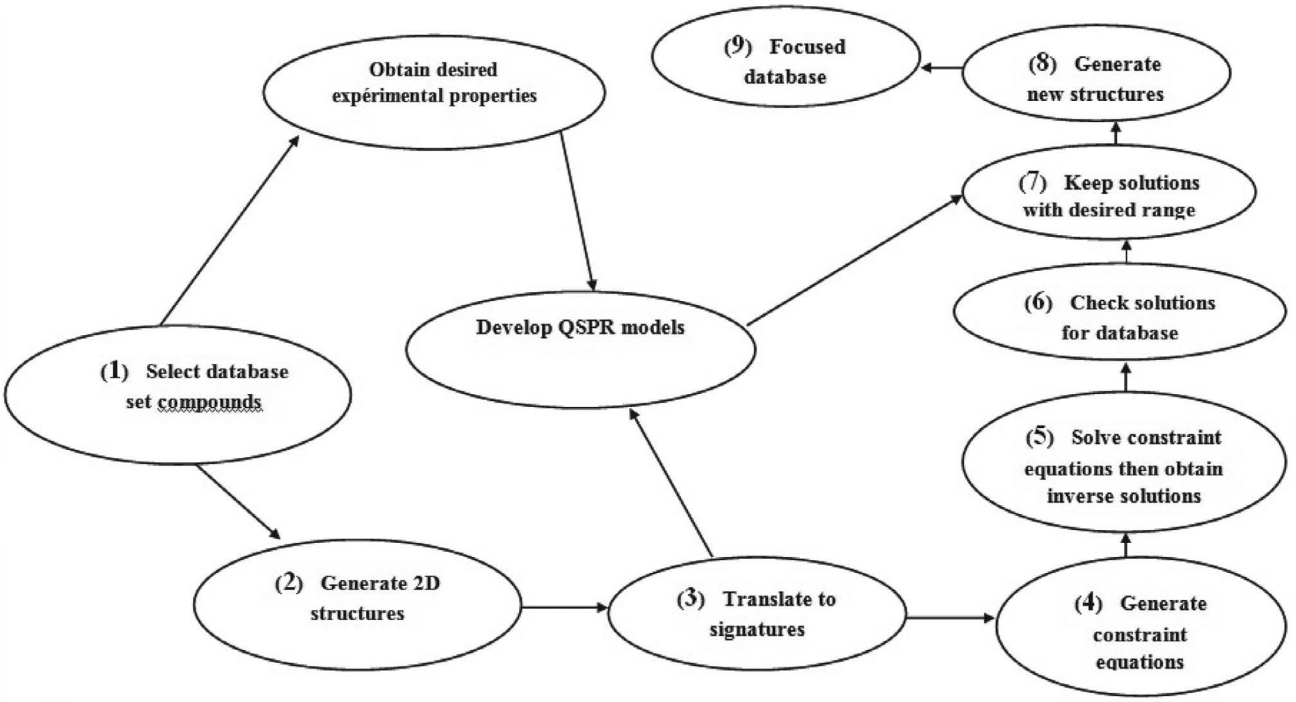

Figure 1. Outline of the I-QSPR Algorithm.[24]

As for important uses of the QSPR analysis step is to develop a QSPR model that relates the structures of 190 pesticides compounds to their n-octanol–water partition coefficients using multiple linear regression technique and to generate new pesticides structures with novel physico-chemical and QSAR properties.

2. Methodology

Inverse-QSAR/QSPR is known as the technical uses values for the independent variables of a particular compound in the QSAR /QSPR to solve for the activity /property of that compound (the dependent variable). In contrast, the goal of the inverse-QSAR/QSPR problem is to determine values for the independent variables given a desired activity /property.[23]

An inverse-QSPR(I-QSPR) problem is a signature-based CAMD (Computer Aided Molecular Design) algorithm that identifies compounds possessing a certain performance (or property) of interest predicted using a developed QSPR model.[24] The I-QSPR technique is interchangeable with the molecular signature descriptor CAMD algorithm.

To achieve the I- QSPR algorithm in our study, we provided the steps detailed in **Figure 1** below, which explains how this algorithm is performed in nine fundamental stages:

(1) The selection of database compounds ; (2) Generation of the 2D structures; (3) Translation of the database compounds into signatures in addition to QSPR analysis; (4) Generation of constraint equations ; (5) Constraint equations solving then inverse solutions obtaining;(6) Check solutions for database; (7)Store solutions within desired range ; (8) New structure generation;(9) Focused database.

2. 1. Step 1: Selection of Database Compounds

In this work the database contains 190 compounds (Pesticides) of different classes, which have an important role in human life. The corresponding experimental data (*n*-octanol/water partition coefficients $\mathbf{logk_{ow}}$) are obtained from the literature (www.chemspider.com chemical structures and www.pubchem.com).

2. 2. Step 2 : Generation of the 2D Structures

We have developed a code that allows us to calculate the atomic signatures of molecules after generating 2D structures.

2. 3. Step 3 : Translation of the Database Compounds into Signatures in Addition to QSPR Analysis

The structural representation of the studied compounds is of great importance for describing, circulating and explaining the significant structural information depending on their characteristics. Based on this representation, the extent to which this structure is related to the activity /physochemical properties of the studied molecule. The structural information of a molecule is evaluated by entities called molecular descriptors. The descriptor which is distinctive and in accordance with the applicable conditions to this technique (I-QSPR) is called signature.[25,26]

a) Signature

The signature is a fragment based descriptor that encodes the local topology of an atom in a molecule.[27] Degeneracy, when using signature, is controlled by the height of the signature, which represents the level of branching in a structure. Signature at height-1 or height-2 has lower degeneracy than height-0, and shows high correlation ability for atomic signatures of a molecule to its corresponding property of interest.[28]

b) Definition of the Atomic Signature

Signature, which has its origins in structural elucidation studies of Faulon, [29] is based on the molecular graph of a molecule, $\mathbf{G} = (\mathbf{V_G}, \mathbf{E_G})$, where the elements in $\mathbf{V_G}$ denote the atoms in the molecule, and the edges of $\mathbf{E_G}$ correspond to the bonds between those atoms. We define an atomic signature, $^{\mathbf{h}}\boldsymbol{\sigma}_{\mathbf{G}}\mathbf{(x)}$, as the canonical sub-graph of **G** consisting of all atoms a distance **h** from the root **x**.[29]

Once a signature height is specified, the molecular signature of each of the N compounds identified in step 1 is calculated using an in-house translator program.

c) Definition of the Molecular Signature Descriptors

Descriptors encoding significant structural information are used to present the physicochemical characteristics of compounds to build the relationship between structure and property in this study. The molecular descriptor used in this project was the molecular descriptor called signature because of its success to address the I-QSAR problem. The success of signature is threefold, First, signature performs the QSAR analysis as well as conventional molecular descriptors.[30,31] Second, signature has a lower degeneracy than other molecular descriptors and can be controlled by the user by a variable termed height. The molecular signature for a compound is the sum of each atomic signature multiplied by the occurrence vector of that atomic signature in the given compound and it can be calculated using the following equation.[32]

$$^{h}\sigma(\mathrm{G}) = \sum_{x \in V_G} {}^{h}\sigma_{G}(x) = {}^{h}\alpha_{G} \quad \sum^{h} \qquad (1)$$

Where the elements of $\mathrm{V_G}$ (matrix of the vertices) are the atoms (X), $\sum^{h} i$ is the basis set of all atomic signatures of height $\boldsymbol{h}$ and $^{\mathbf{h}}\boldsymbol{\alpha}_{\mathbf{G}}$ is the vector of occurrence number of atomic h-signatures of the graph **G**. Example of molecular signatures for Ethephon is given in **Figure2**.

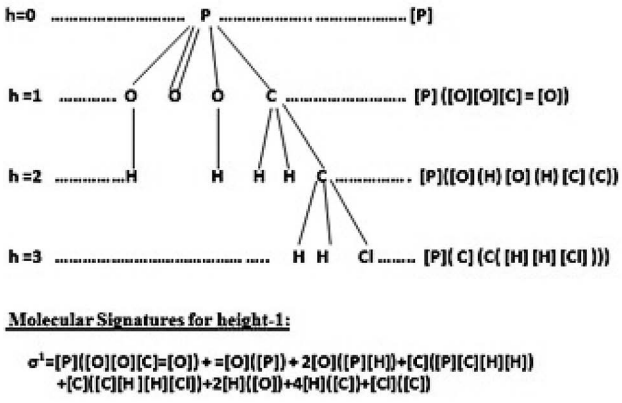

Figure 2. Illustration of the atomic and molecular signatures of Ethephon ($C_2H_6ClO_3P$)

d) QSAR/QSPR analysis:

The QSPR analysis was performed according to the organizational chart below:

Quantitative structure-activity / property relationship (QSAR/QSPR) as an important area of chemometrics has been the subject of a series of investigations.[32,33] The main aim of (QSAR/QSPR) studies is to establish an empirical rule or function relating the structural descriptors of compounds under investigation to properties. This rule or function is then utilized to predict the same properties of the compounds not involved in the training set from their structural descriptors.

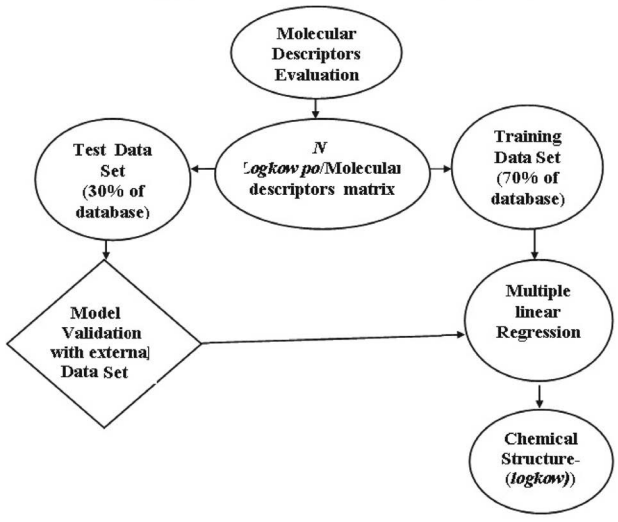

Figure 3: The Steps of QSPR proposed methodology

2. 4. Step 4: Generation of Constraint Equations

In this step, we constructed the constraint equations, which serve in the construction of new compounds by reconnecting atomic signatures into molecular signatures with desired properties determined by the QSPR equation.[34] Constraint Equations are generated from the atomic signature database. Graphicality Equation is developed from the height 0 atomic signatures, and is a necessary condition for a connected graph.[35]

2. 5. Step 5: Solve Constraint Equations

Since the space of solutions is infinite we limit the range that these solutions (independent variables) can take, based on their range in the original training set, minimum and maximum value (per atomic signatures) provides the additional constraints necessary to solve the system. Due to the large number of equations, we have used the min/max values in the Particle Swarm Optimization algorithm called PSO. This algorithm seems to satisfy the constraint equations in a step-wise manner such that the iterations involving those variables which occur in the equations go from least to most iterations.

2. 6. Step 6: Check Solutions for Database

Since the constraint equations are derived from the number of used compounds, this number should represent solutions to the constraint equations, these are evaluated according to the bonding of the atoms within the molecule.

2. 7. Step 7 : Keep Solutions With Desired Range

In this step the solutions must be scored for fitness relative to a desired property value. The solutions which have the desired fitness are kept, while the unsuitable atomic signature must be removed from the solution. It is at this stage where various heuristics can be applied to focus the solution space based on expert knowledge or other means.[26]

2. 8. Step 8: Generate New Structures

The molecular Signatures (solutions) which emerge from Step 7 are the molecular signatures from which structure generation will occur. Structure generation is performed using an algorithm developed by Faulon and Coworkers,[36] which is based on an earlier isomer enumeration algorithm developed by Faulon (**Appendix 1** in supplementary files). In this step we have selected suitable structures after various filters to remove those undesirable candidate structures.

2. 9. Step 9: Focused Database

The structures which have survived until this point become part of the focused database. These are the high-quality structures which are worthy of further investigation. It is here where experiments run on a select num-

ber of compounds to verify the predictions of the algorithm would be employed. Often, the results of the experimentation can be used to refine the QSPRs and the focused database itself.[26]

3. Results and Discussion

3. 1. Atomic Signatures Calculation

As the first step in our I-QSPR analysis, is the translation of the 2D molecular structures into atomic signatures illustrated in **Table 1** bellow.

Table 1. The unique height-1 atomic signatures used in the QSPR analysis.

Variable	Height-1Atomic Signature	Occurrence [Min, max]
X_2	[H]([N])	[0,5]
X_5	**[O](=[C])**	[0,3]
X_6	**[C]([C] [H] [H] H])**	[0,5]
X_8	[S]([P] [C])	[0,3]
X_9	**[O]([P][C])**	[0,4]
X_{11}	[C] ([O] [H] [H] [H])	[0, 4]
X_{12}	**[H] ([C])**	[0,29]
X_{14}	**p[C] ([N] p[C] p[C])**	[0,4]
X_{18}	p[C] (p[C] p[C] [C])	[0,5]
X_{19}	**[Cl] ([C])**	[0,4]
X_{20}	**p[C] (p[C] p[C] [H])**	[0,10]
X_{21}	**[H](p[C])**	[0,11]
X_{23}	pC(p[N] p[N] [N])	[0,3]
X_{24}	**p[N] (p[C] p[C])**	[0,3]
X_{33}	[O] (p[C] [C])	[0,3]
X_{35}	[O] (=[S])	[0,4]
X_{37}	C(N] H] H] H])	[0,4]
X_{39}	[N] ([C] [C] [C])	[0,3]
X_{43}	[C](p[C][H][H][H])	[0,4]
X_{44}	**[pN] (pC] pN])**	[0,4]
X_{49}	[C]([C] H] [H]S])	[0,3]
X_{52}	**p[C](p[C]p[C]Cl])**	[0,5]
X_{53}	**[Cl](p[C])**	[0,5]
X_{57}	p[C]([pC] p[C][O])	[0,3]
X_{64}	[C]([O][C][H][H])	[0,4]
X_{74}	**[C]([C][C][H][H])**	[0,7]
X_{75}	**[F] ([C])**	[0,6]
X_{89}	[H] ([O])	[0,3]
X_{104}	[H](=[C])	[0,3]

The QSPR analysis was calculated on the basis of a descriptor matrix. The descriptor matrix for the height -1 atomic signature contained 190 rows and 253 columns, one column for the $\mathbf{logk_{ow}}$ and 252 columns for the unique atomic signatures. The QSPR equation, however, was only calculated on the basis of 29 atomic signatures, hereby removing 223 atomic signatures, in order to perform the LOOCV.[37] For performing the forward stepping MLR 223 unique atomic signatures removed and we leaved 29 with occurrence numbers greater than or equal to 3 in order to perform the LOOCV analysis. The most significant atomic signatures were then added one at a time, on the basis of the R^2 and Q^2 values were calculated for each step resulting in **Figure 4**, which depicts the R^2 and Q^2 values as function of the number of independent variables, i.e. atomic signatures.

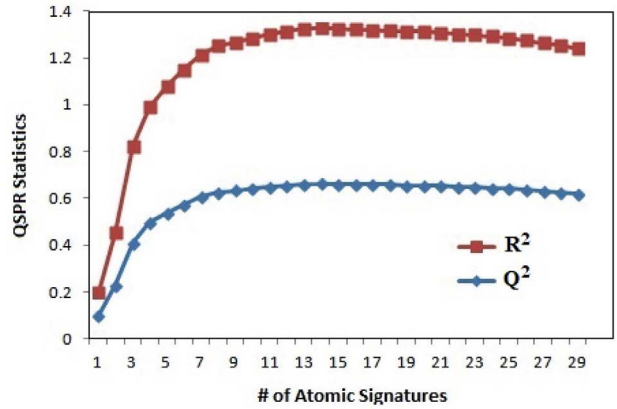

Figure 4. Impact of pesticides height-1 atomic Signatures on the QSPR statistics, which is plotted as function of the number of independent variables

QSPR statistics consists in analyzing the improvement of the correlation with the increase of the number of variables of the model. The representation of the values of R^2 and Q^2 as a function of the number of descriptors (Fig.4) brings out an asymptotic behavior, the model is considered optimal when the improvement of the correlation becomes maximal, that is to say representing the better compromise between correlation and parameterization.

The calculations were terminated at **14** atomic signatures, thus the 15th atomic signature was insignificant. Statistically QSPR model using **MLR** was obtained, the QSPR equation was chosen on the basis of the best predicting model, i.e. highest Q^2 value. A QSPR equation with **14** atomic signatures was hereby obtained with a $\mathbf{R^2}$ **= 0.659273,** $\mathbf{Q^2}$ **=0.65617** and $\mathbf{RMSE_{training}}$ **= 0.930192, s = 1.37297** for the training set, and in leave-one-out (LOO) cross-validation experiment set value, $\mathbf{q^2}$ **= 0.605676**, $\mathbf{RMSE_{LOO}}$ **= 1.0936** respectively. Where R^2 represents the determination coefficient, Q^2: square validation coefficient, s: standard deviation, RMSE: the root square error.

3. 2. The model Equation

The model equation can be written as fellow:

$\mathbf{logk_{ow}}$ = - 0.167497 + 0.444669 * $\mathbf{X_{52}}$ + 0.417366 * $\mathbf{X_6}$ + 0.785521 * $\mathbf{X_{20}}$ + 0.461849 * $\mathbf{X_{75}}$ + 0.0716288 * $\mathbf{X_{12}}$ - 0.419674 * $\mathbf{X_5}$ - 0.409265 * $\mathbf{X_{21}}$ + 0.528737 * $\mathbf{X_{19}}$ - 0.220096 * $\mathbf{X_{44}}$ + 0.251859 * $\mathbf{X_{74}}$ + 0.365269 * $\mathbf{X_9}$ + 0.226272 * $\mathbf{X_{14}}$ + 0.445708 * $\mathbf{X_{53}}$ + 0.0357723 * $\mathbf{X_{24}}$

The **14** atomic signatures included in the QSPR equation are marked with bold in **Table 1.** Statistical results and significance of this final model, illustrate that the positive high value coefficient is for atomic signature $\mathbf{X_{20}}$. It was also suggested from this model that the atomic signature $\mathbf{X_{24}}$ was necessary contributor to $\mathbf{logk_{ow}}$, the atomic signature $\mathbf{X_5}$ was assigned as an effective variable on $\mathbf{logk_{ow}}$, but with a negative coefficient. Using the QSPR equation to predict the $\mathbf{logk_{ow}}$ of the pesticides in the same training set and plotting these values against the experimental data, resulted in **Figure 5.**

The plot shows the predicted $\mathbf{logk_{ow}}$ values based on the model equation which is validated to be statistically significant by the leave-one-out cross-validation versus experimental ones. Obviously, the predicted $\mathbf{logk_{ow}}$ values are in a good agreement with experimental ones. The 14-parameters of model provide a high statistical quality: $\mathbf{R^2 = 0{,}66}$ and $\mathbf{Q^2 = 0.65}$, and this shows that the condition of predictability according to the consideration of R. Veerasamy,[37] and A. Golbraikh,[38] is satisfied.

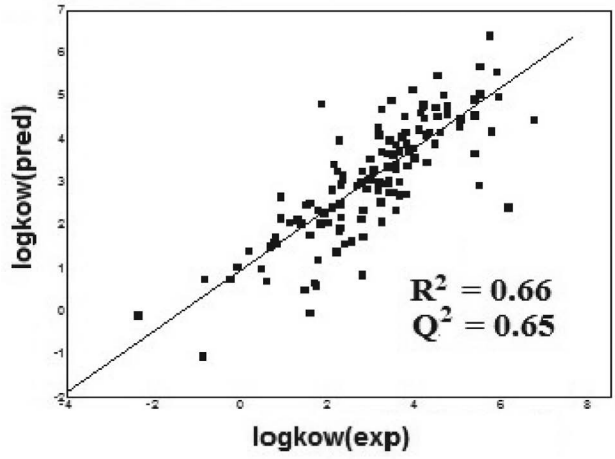

Figure 5: The experimental- versus predicted values for the QSPR equation based on the $\mathbf{logk_{ow}}$ with 29 height-1 atomic Signatures (***logKow(Pred)=0.909412+0.704451.logKow(exp))***

3. 3. The Constraint Equations

The following constraint equations are written in the order of the smallest parameters number to the greatest, thus in the order they were solved: (i) Consistency equations which ensure the alignment of atoms in the construction of molecular signatures. (ii) Graphicality equation which represents the valence of each atom. To solve these equations, a method developed by Weis and Visco.[28] was adopted, and because of the wide database and the large number of constraint equations, we have used a program based on PSO algorithm.

3. 4. Generating of new Pesticides Structures

Base on the inverse solutions obtained from solving the system of constraint equations, new structures can be constructed from molecular signatures. It is worth mentioning that for the same molecular signature there are multiple structures.

Solving the constraint equations (**Table 2**) a total number of 5500 solutions (new molecular signatures) which will be a new structures. Since it would be difficult to examine over 5500 structures, the newly generated structures were refined according to the different chemical

Table 2. Constraint equations

N°	Constraint equation
Eq.1	$\mathbf{Mod(+X_{217},2) = 0}$
Eq.2	$\mathbf{Mod(+X_{242},2) = 0}$
Eq.3	$\mathbf{+X_{44}+X_{169} = 2}$
Eq.4	$\mathbf{-X_{45}+_{X48} = 0}$
Eq.5	$\mathbf{-X_{91}+X_{92} = 0}$
Eq.6	$\mathbf{-2X_{136}+X_{137} = 0}$
Eq.7	$\mathbf{-X_{138}+X_{139} = 0}$
Eq.8	$\mathbf{-X_{144}+X_{145} = 0}$
Eq.9	$\mathbf{-X_{191}+X_{193} = 0}$
Eq.10	$\mathbf{Mod(+X_{213}+X_{215},2) = 0}$
Eq.11	$\mathbf{-X_{243}+X_{244} = 0}$
Eq.12	$\mathbf{-X_{41}+X_{42}-X_{63} = 0}$
Eq.13	$\mathbf{-X_{70}+X_{72}-X_{185} = 0}$
Eq.14	$\mathbf{-X_{70}+X_{73}-X_{185} = 0}$
Eq.15	$\mathbf{-X_{93}+X_{95}+X_{159} = 0}$
Eq.16	$\mathbf{-X_{113}+X_{114}-X_{208} = 0}$
Eq.17	$\mathbf{-X_{173}+2X_{174}-X_{175} = 0}$
Eq.18	$\mathbf{-X_{206}+X_{207}+X_{209} = 0}$
Eq.19	$\mathbf{-X_{52}+X_{53}-X_{119}-X_{187} = 0}$
Eq.20	$\mathbf{-X_{88}+X_{89}-X_{153}-X_{195} = 0}$

N°	Constraint equation
Eq.21	$-X_{149}+X_{150}+X_{226}+X_{250} = 0$
Eq.22	$-X_{168}+X_{169}-X_{186}-X_{246} = 0$
Eq.23	$-X_{121}+2X_{122}-X_{123}-X_{234}-X_{235} = 0$
Eq.24	$-X_{151}+X_{152}+X_{170}-X_{176}-X_{252} = 0$
Eq.25	$-X_{1}+X_{3}+X_{160}-X_{172}+X_{188}-X_{205} = 0$
Eq.26	$-X_{20}+X_{21}-X_{47}-X_{58}-X_{123}-X_{175} = 0$
Eq.27	$-X_{50}+X_{51}-X_{116}-X_{144}-X_{170}-X_{188} = 0$
Eq.28	$-X_{62}+X_{63}+X_{198}-X_{199}-X_{212}-X_{247} = 0$
Eq.29	$-X_{101}+X_{104}-X_{150}-2X_{155}-X_{165}-X_{226} = 0$
Eq.30	$-3X_{71}+X_{75}-X_{133}-3X_{167}-2X_{219}-X_{220}-2X_{239} = 0$
Eq.31	$-X_{109}+X_{112}-X_{142}-X_{207}-X_{215}-X_{250}+X_{251} = 0$
Eq.32	$-X_{3}+X_{7}-X_{59}-X_{96}-X_{134}-X_{152}-X_{160}-X_{232} = 0$
Eq.33	$-X_{17}+X_{19}-2X_{80}-3X_{103}-X_{115}-3X_{117}-2X_{133}-X_{245} = 0$
Eq.34	$-X_{32}+X_{33}-X_{57}+2X_{85}+X_{93}+X_{118}-X_{124}+X_{195} = 0$
Eq.35	$-X_{3}+X_{8}-X_{50}-X_{59}-2X_{96}+X_{146}-X_{170}-3X_{232}+X_{241} = 0$
Eq.36	$-X_{27}+X_{28}-X_{67}+X_{120}+X_{146}-X_{218}+X_{230}+2X_{236}+2X_{240} = 0$
Eq.37	$\mathbf{Mod}(+X_{60}+X_{62}+X_{140}+X_{141}+X_{184}+X_{185}+X_{201}+X_{202}+X_{238},2)= 0$
Eq.38	$-2X_{34}+X_{35}-2X_{38}-2X_{95}-2X_{120}-2X_{159}-2X_{223}-X_{224}-2X_{230}-2X_{240}-2X_{241} = 0$
Eq.39	$-X_{4}+X_{5}-X_{30}-X_{56}-X_{61}-X_{65}-X_{66}-X_{82}-X_{163}-X_{171}-X_{177}-X_{222} = 0$
Eq. 40	$-X_{31}+2X_{34}-2X_{36}+X_{38}-X_{83}-X_{84}+X_{95}+X_{99}+2X_{107}+X_{120}-2X_{132}-X_{221} =0$
Eq.41	$-X_{1}+X_{2}-X_{25}-X_{31}-2X_{46}-X_{69}-X_{79}-X_{83}-X_{162}-X_{184}-2X_{202}-2X_{205}-2X_{221}-X_{238} =0$
Eq.42	$-X_{13}+X_{14}+X_{23}-X_{25}-X_{46}+X_{55}-X_{70}-X_{76}-X_{77}-X_{83}-X_{132}-X_{140}-2X_{162}+X_{234}-X_{238} = 0$
Eq.43	$-X_{3}+X_{9}-2X_{50}-2X_{59}-X_{96}-3X_{116}+X_{118}-3X_{134}-2X_{144}-2X_{152}+X_{153}-2X_{160}-X_{170}-2X_{188}+2X_{231}+X_{251} = 0$
Eq.44	$-2X_{23}+2X_{24}-2X_{27}-X_{32}+X_{44}+2X_{45}-2X_{47}-X_{55}-X_{58}-X_{94}-X_{119}-2X_{124}-2X_{125}-2X_{126}+X_{169}-2X_{187}-X_{218}-X_{234}-X_{235} = 0$
Eq.45	$-X_{40}+X_{41}-X_{105}+X_{149}-X_{177}+2X_{178}-X_{181}-X_{182}-X_{183}-X_{192}+X_{193}-X_{196}-X_{197}+X_{198}-X_{210}-X_{216}+X_{217}-X_{228}-2X_{248}-X_{249} = 0$
Eq.46	$-X_{76}-X_{77}+3X_{78}-X_{79}-X_{141}+X_{142}+X_{150}+X_{165}-2X_{166}-X_{180}+X_{194}-X_{199}+2X_{200}-X_{201}+X_{207}-X_{208}+X_{209}-X_{211}-X_{212}-2X_{214}+X_{215}+X_{250} = 0$
Eq.47	$+2X_{14}+2X_{18}+2X_{20}+X_{32}+2X_{42}+2X_{52}+X_{55}+2X_{57}+X_{58}+2X_{67}+3X_{86}+2X_{91}+X_{94}+X_{119}+X_{121}+X_{123}+X_{126}+2X_{138}+2X_{145}+X_{173}+X_{175}+X_{218} = 2$
Eq.48	$-X_{18}+X_{22}+X_{43}+X_{61}+X_{71}+X_{81}+X_{82}+2X_{87}-X_{94}-X_{121}-X_{125}+X_{127}+2X_{130}+X_{131}+X_{147}+X_{148}+X_{157}+3X_{161}+X_{164}-X_{173}+X_{179}+X_{197}-X_{235}= 0$
Eq.49	$-X_{8}+X_{10}-X_{28}-X_{38}+X_{49}+X_{54}+X_{66}+X_{81}+X_{97}-X_{99}+X_{103}+X_{108}-2X_{111}+X_{133}+2X_{156}-X_{159}+X_{179}+X_{182}+X_{196}-X_{206}+X_{210}-2X_{223}-2X_{224}-X_{230}+X_{237}-X_{241}-X_{242}+X_{243}= 0$
Eq.50	$-X_{100}+2X_{101}-X_{102}-X_{108}+2X_{109}-X_{110}-X_{135}+X_{136}+X_{142}-X_{143}-X_{154}+X_{155}-X_{164}+X_{165}-X_{181}-X_{189}+2X_{190}-X_{192}+2X_{194}+X_{200}-2X_{204}+X_{209}+X_{213}-X_{222}-X_{225}+X_{226}-X_{227}-X_{228}-2X_{229}-X_{245} = 0$
Eq. 51	$-X_{9}+X_{11}+X_{15}-2X_{16}-X_{33}+X_{56}+X_{64}+X_{65}+2X_{68}+X_{82}+X_{87}-X_{88}+X_{90}+X_{106}-X_{112}\ X_{114}+X_{115}+X_{135}+X_{147}+X_{148}+2X_{158}+X_{161}+X_{167}+X_{189}-X_{191}+X_{196}+X_{219}+X_{220}+X_{228}+X_{246}+X_{252} = 0$
Eq.52	$-X_{1}+X_{4}-2X_{13}+X_{15}-X_{25}+X_{26}+X_{29}+2X_{30}-X_{31}.X_{36}+X_{37}-3X_{39}+X_{40}+X_{54}+X_{56}-2X_{60}+X_{61}+X_{66}-2X_{69}-X_{76}-X_{79}-2X_{84}+2X_{105}-2X_{113}+X_{127}+X_{129}-X_{140}-X_{166}+X_{171}-2X_{172}+X_{176}+X_{177}-2X_{180}-X_{184}+X_{189}-X_{201}+2X_{203}+X_{210}-X_{211}-X_{212}+X_{222}+X_{225}+2X_{227}+X_{233}+X_{243}-2X_{247}+X_{249} = 0$
Eq.53	$-3X_{6}-3X_{10}-3X_{11}+X_{12}-2X_{15}-2X_{17}-2X_{22}-2X_{26}-X_{29}-3X_{37}-X_{40}-3X_{43}-2X_{49}-2X_{54}-2X_{64}-2X_{74}-X_{80}-2X_{81}-X_{90}-X_{97}-X_{98}-X_{100}-2X_{102}-3X_{110}-X_{115}-2X_{127}-X_{130}-X_{131}-X_{135}-X_{148}-2X_{151}-2X_{156}-X_{158}-2X_{168}-X_{171}-2X_{176}-X_{179}-X_{181}-2X_{183}-X_{186}-2X_{203}-X_{204}-X_{220}-X_{225}-X_{239}-X_{246}-2X_{249}-X_{252} = 0$
Eq.54	$+X_{4}+X_{6}+X_{17}+X_{22}+X_{26}+2X_{29}+X_{49}+X_{64}+X_{65}+2X_{68}+2X_{74}+X_{80}+X_{87}+2X_{90}+2X_{97}+3X_{98}+X_{100}+X_{102}+3X_{106}+X_{108}+X_{115}+X_{117}+4X_{128}+2X_{129}+X_{130}+2X_{131}+3X_{143}+2X_{147}+X_{148}+X_{151}+2X_{154}+3X_{157}+X_{158}+2X_{163}+X_{164}+X_{168}+X_{179}+X_{182}+X_{183}+2X_{186}+X_{192}+X_{197}+2X_{216}+X_{219}+X_{220}+X_{229}+3X_{233}+3X_{237}+X_{239}+X_{245}+X_{246}+X_{248}+X_{252} = 2$
Eq.55	$\mathbf{Mod}(X_{1}-X_{2}+2X_{3}+X_{4}-X_{5}+2X_{6}-X_{7}+X_{8}+X_{9}+2X_{10}+2X_{11}-X_{12}+X_{13}+X_{14}+2X_{15}+X_{16}+2X_{17}+X_{18}-X_{19}+X20-X_{21}+2X_{22}+X_{23}+X_{24}+X_{25}+2X_{26}+X_{27}+X_{28}+2X_{29}+X_{30}+X_{31}+X_{32}+X_{33}+2X_{34}-X_{35}+X_{36}+2X_{37}+2X_{38}+X_{39}+X_{40}+X_{41}+X_{42}+2X_{43}+X_{44}+X_{45}+X_{46}+X_{47}-X_{48}+2X_{49}+2X_{50}-X_{51}+X_{52}X_{53}+2X_{54}+X_{55}+X_{56}+X_{57}+X_{58}+2X_{59}+X_{60}+X_{61}+X_{62}+X_{63}+2X_{64}+X_{65}+X_{66}+X_{67}+2X_{68}+X_{69}+X_{70}+2X_{71}-X_{72}-X_{73}+2X_{74}-X_{75}+X_{76}+X_{77}+X_{78}+X_{79}+2X_{80}+2X_{81}+X_{82}+X_{83}+X_{84}+X_{85}+X_{86}+2X_{87}+X_{88}-1X_{89}+2X_{90}+X_{91}-X_{92}+X_{93}+X_{94}+2X_{95}+2X_{96}+2X_{97}+2X_{98}+X_{99}+X_{100}+X_{101}+2X_{102}+2X_{103}-X_{104}+X_{105}+2X_{106}+X_{107}+X_{108}+X_{109}+2X_{110}+X_{111}+X_{112}+X_{113}+X_{114}+2X_{115}+2X_{116}+2X_{117}+X_{118}+X_{119}+2X_{120}+X_{121}+X_{122}+X_{123}+X_{124}+X_{125}+X_{126}+2X_{127}+2X_{128}+X_{129}+2X_{130}+2X_{131}+X_{132}+2X_{133}+2X_{134}+X_{135}+X_{136}-X_{137}+X_{138}-X_{139}+X_{140}+X_{141}+X_{142}+2X_{143}+2X_{144}+X_{145}+X_{146}+2X_{147}+2X_{148}+X_{149}+X_{150}+2X_{151}+2X_{152}+X_{153}+X_{154}+X_{155}+2X_{156}+2X_{157}+2X_{158}+2X_{159}+2X_{160}+2X_{161}+X_{162}+X_{163}+X_{164}+X_{165}+X_{166}+2X_{167}+2X_{168}+X_{169}+2X_{170}+X_{171}+X_{172}+X_{173}+X_{174}+X_{175}+2X_{176}+X_{177}+X_{178}+2X_{179}+X_{180}+X_{181}+X_{182}+2X_{183}+X_{184}+X_{185}+2X_{186}+X_{187}+2X_{188}+X_{189}+X_{190}+X_{191}+X_{192}+X_{193}+X_{194}+X_{195}+X_{196}+X_{197}+X_{198}+X_{199}+X_{200}+X_{201}+X_{202}+2X_{203}+X_{204}+X_{205}+X_{206}+X_{207}+X_{208}+X_{209}+X_{210}+X_{211}+X_{212}+X_{213}+X_{214}+X_{215}+X_{216}+X_{217}+X_{218}+2X_{219}+2X_{220}+X_{221}+X_{222}+2X_{223}+X_{224}+X_{225}+X_{226}+X_{227}+X_{228}+X_{229}+2X_{230}+X_{231}+2X_{232}+2X_{233}+X_{234}+X_{235}+X_{236}+2X_{237}+X_{238}+2X_{239}+2X_{240}+2X_{241}+X_{242}+X_{243}-X_{244}+X_{245}+2X_{246}+X_{247}+X_{248}+2X_{249}+X_{250}+X_{251}+2X_{252},2) = 0$

Table 3. Example of a solved molecular Signature, note that only atomic Signatures with occurrence numbers greater than 0 are depicted.

Molecular Signature no. 1	X_6	X_8	X_9	X_{10}	X_{11}	X_{12}	X_{49}	X_{50}	X_{51}	X_{64}
	1	1	2	1	1	15	1	1	1	1

Table 4. Values of $logk_{ow}$ of the 20 new structures calculated by I-QSPR theory and those predicted by Hyperchem software with other QSAR properties simulated by molecular mechanic MM^+ and semi-empirical PM3 calculations.

Formula	3D Structure [a]	$logk_{ow}$ [b]	$logk_{ow}$ [c]	Surface area	Volume	Refractivity	Mass	MM+ (KJ/mol)	PM3 (KJ/mol)
$C_7H_{17}O_2PS_4$	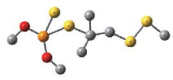	2.93	2.62	536.71	760.29	76.60	292.42	22.67	−2641.14
$C_6H_{15}O_2PS_3$	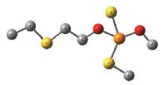	2.17	2.61	531.90	730.74	64.50	246.34	24.518	−2302.97
$C_7H_{15}N_2O_4PS_3$	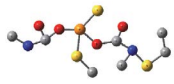	6.05	2.19	580.95	882.26	77.57	318.36	146.488	−2905.23
$C_8H_{17}N_2O_4PS_3$	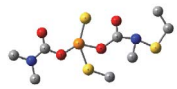	6.74	2.20	577.82	882.76	81.80	332.39	131.31	−3174.98
$C_9H_{17}Cl_2N_2O_3PS_2$	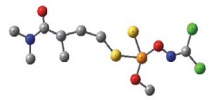	6.30	2.19	564.48	874.47	77.39	353.22	26.47	−2922.12
$C_7H_{18}NO_2PS_2$	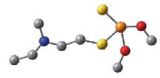	1.87	1.36	573.67	483.36	65.30	243.32	54.01	−2703.03
$C_5H_{12}NO_5PS$	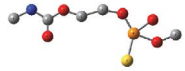	2.65	2.61	451.91	657.32	52.07	229.19	21.28	−2288.44
$C_7H_{16}NO_4PS$	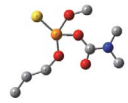	4.56	2.20	510.26	729.30	59.29	241.24	19.674	−2737
$C_6H_{14}OS_2$	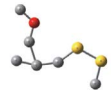	1.46	1.88	410.80	566.15	47.31	166.30	-0.46	−1997.52
$C_9H_{19}N_2O_4PS_4$	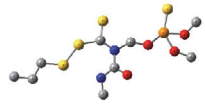	6.00	2.20	651.1	992.59	95.46	378.47	32.8	−3488
$C_{13}H_{23}N_4O_5PS_2$	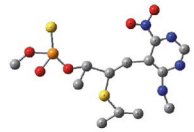	3.34	2.61	600.25	1074.63	106.29	366.51	44.67	−4527.12
$C_6H_{16}NO_2PS_2$	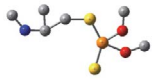	1.55	2.61	606.55	978.56	81.77	347.45	31.30	3549.116
$C_9H_{22}N_3O_3PS_3$	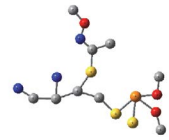	5.02	2.62	651.7	982.59	95.42	346.48	32.8	−3458
$C_6H_{14}NO_3PS_4$	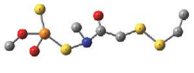	4.71	2.19	499.29	791.32	73.09	307.40	14.102	2539.87

Formula	3D Structure [a]	$logk_{ow}$ [b]	$logk_{ow}$ [c]	Surface area	Volume	Refractivity	Mass	MM+ (KJ/mol)	PM3 (KJ/mol)
$C_{10}H_{15}N_2O_4PS_2$	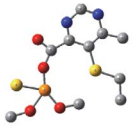	5.2	2.20	488.23	853.74	76.81	322.33	27.922	–3329.07
$C_6H_{16}NO_5PS_2$	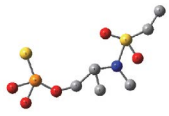	4.27	2.61	493.77	731.	63.56	277.23	49.9	–2743.26
$C_{16}H_{26}N_3O_7PS_3$	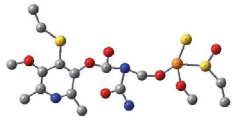	8.66	1.47	693	1249	115.85	499.5	46.36	–5356.36
$C_8H_{18}N_3O_2PS_3$	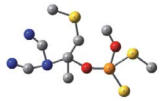	2.59	2.61	506.16	858.53	74.30	315.40	43.37	–3075.79
$C_8H_{20}NO_3PS_2$	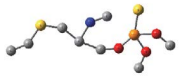	1.51	1.46	543.54	803.91	70.45	273.35	26.001	–3074.00
$C_5H_{15}N_2O_4PS$	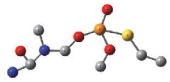	5 .52	2 .20	492.04	72.69	57.54	242.23	40.15	–26.21

[a]: Carbon (C); : Chlorine (Cl) ; : Nitrogen (N); : Oxygen (O); : Phosphorus; : Sulfur (S); (the H atoms are hidden)
[b]: logkow predicted by Hyperchem software ; [c]: logkow calculated by I-QSPR theory

structures of all existing pesticides. All newly generated structures were passed through the ChemSpider, PUB Chem and LookChem (structure search) which are reliable database to identify commercially available compounds. After all these steps, a set of 20 samples was selected (Appendix 2 in supplementary files) according to their **$logk_{ow}$**, which is close to the average value of the database of the 190 pesticides studied (**$logk_{ow}$ = 2.94**).

The 20 identified compounds became part of the focused database. In order to assess the diversity level among the newly generated structures, they were compared to the training set structures.In addition to the work done, we compared the values of the **$logk_{ow}$** predicted by our model to those calculated by Hyperchem software (ver. 8), it was concluded that the values for the two results (Table 4) are close in most cases.

4. Conclusion

The high interest in pesticides and their uses in diverse fields, especially in agriculture, requires us to study these pesticides extensively and in depth . This is done by identification and focus on the characteristics including the physico-chemical properties, then the attempt to establish new chemical structures.

The identification of new pesticides with desired properties was done by developing an inverse-quantitative structure-property relationship on the basis of octanol-water partition coefficient (**$logk_{ow}$**).

We processed a database of 190 pesticide compounds, after developing molecular signatures calculated from atomic signatures. And in order to perform LOOCV. Only 29 atomic signatures from out of 252 are used as independent variables and **$logk_{ow}$** as a dependent variable in the QSPR realization, then the resolution of the constraint equations to the number of 55 by a computation code developed for this purpose, based on the successful PSO method to find 5500 solutions which represent new structures.

Based on the goal of the inverse-QSPR method was to predict, if any, novel compounds structures possessing a **$logk_{ow}$** values are close to those in the training set. There were 20 new compounds classified as pesticides.

We have presented and studied these new structures that do not yet exist in the databases of chemical compounds based on our search of reliable databases for this purpose.

This work indicates that the inverse-QSPR method can be used as a reliable approach to generate new compound structures, since, on the one hand, the coefficient of determination R^2 of the model is greater than 60%, and on the other hand, the predicted results are close to the values calculated by other software such as Hyprchem. This research is envisaged to serve as a base for further studies.

5. Acknowledgments

We thank **Dr. Labbi Yacine**, from Electrical Engineering Department, Echahid Hamma Lakhdar University of El Oued for assisting in the numerical analysis and calculating method.

6. References

1. A. Sharma, P. J. Gadi , V. P. Reddy, *Science of The Total Environment*, **2018**, *643*, 1522–1532. **DOI:**10.1016/j.scitotenv.2018.06.312
2. S. Knillmanna, P. Orlinskiyabc, O. Kaskea, K. Foita, M. Liessad, *Science of The Total Environment*, **2018**, *630*, 1619–1627. **DOI:**10.1016/j.scitotenv.2018.02.056
3. R. Münze, P. Orlinskiy, R. Gunold, A. Paschke, O. Kaske, M. A. Beketov, M. Hundt, C. Bauer, G. Schüürmann, M. Möder, M. Liess, *Science of The Total Environment*, **2015**, *537*, 69–80. **DOI:**10.1016/j.scitotenv.2015.07.012
4. A. Sabarwal, K. Kumar, R. P. Singh, *Environmental Toxicology and Pharmacology*, **2018**, *63*, 103–114. **DOI:**10.1016/j.etap.2018.08.018
5. V. Sujitha, K. Murugan, D. Dinesh, A. Pandiyan, R. Aruliah, J.Hwang, K. Kalimuthu, C. Panneerselvam, A. Higuchi, A. T. Aziz, S. Kumar, A. A. Alarfaj, B. Vaseeharan, A. Canale, G. Benelli, *Aquatic Toxicology*, **2017**, *188*, 100–108 **DOI:**10.1016/j.aquatox.2017.04.015
6. K. V. Ragnarsdottir, *Journal of the Geological Society*, **2000**, *157*, 859–876. **DOI:**10.1144/jgs.157.4.859
7. N. E. El-Wakeil, *Gesunde Pflanzen*, **2013**, *65*, 125–149 **DOI:**10.1007/s10343-013-0308-3
8. E. V. R. Campos, P. L. F.Proença, J. L. Oliveira, M. Bakshi, P. C. Abhilash, L. F. Fraceto, *Ecological Indicators*, (in press), Available online 27 April **2018. DOI:**10.1016/j.ecolind.2018.04.038
9. Y. Huang, L. Li , J. Liu, W. Lin, *Algal Research*, **2014**, *4*, 62–69. **DOI:**10.1016/j.algal.2013.08.001
10. M. L. Umpiérrez, J. Paullier, M. Porrini, M. Garrido, E. Santos, C. Rossini, *Industrial Crops and Products*, **2017**, *109*, 686–692. **DOI:**10.1016/j.indcrop.2017.09.025
11. B. I. Murray, *Pest Management Sci*. **2008**, *64*, 8–11. **DOI:**10.1002/ps.1470
12. R. Potts, M. R. Clarke, S. E. Oldfield, K. L. Wood, N. H. de Ibarra, J. E. Cresswell, *Journal of Insect Physiology,* **2018**, *104*, 33–39. **DOI:**10.1016/j.jinsphys.2017.11.006.
13. O. Ogbeide, A. Chukwuka, I. Tongo, L. Ezemonye, *Journal of Environmental Management*, **2018**, *217*, 23–37. **DOI:**10.1016/j.jenvman.2018.03.065
14. M. Kah, C. D. Brown, *Chemosphere*, **2008,** *10*,1401–1408, https: //doi.org/10.1016/j. chemosphere. 2008.04.074.
15. F. Tsopelas, C.Giaginis, A. Tsantili-Kakoulidou, *Expert Opinion on Drug Discovery*, **2017**, *12*, 885–896. **DOI:**10.1080/17460441.2017.1344210
16. C. Vraka, L. Nics, K. Wagner, M. Hacker, W. Wadsak, M. Mitterhauser, *Nuclear Medicine and Biology*. **2017**, *50*, 1–10. **DOI:**10.1016/j.nucmedbio.2017.03.003
17. V. S. Talismanov, S. V. Popkov, O. G. Karmanova, S.S. Zykova, A. P., Chernobrovkina, *J. Pharm. Sci. & Res.* **2017**, *9*, 2372–2375.
18. E. Benfenati, G. Gini, N. Piclin, A. Roncaglioni, M. R. Varı, *Chemosphere*, **2003**, *53*, 1155–1164. **DOI:**10.1016/S0045-6535(03)00609-X
19. R. N. Waterhouse, *Molecular Imaging & Biology*, **2003**, *5*, 376–389. **DOI:** 0.1016/ j.mibio. 2003.09.014
20. A. Finizio, M. Vighi, D. Sandroni, *Chemosphere*, **1997**, *34*, 131–161. **DOI:**10.1016/S0045-6535(96)00355-4
21. S. G. Machatha, S. H. Yalkowsky, *Int. J. Pharm*, **2005**, *294*, 185–192. **DOI:**10.1016/j.ijpharm.2005.01.023
22. Y. P. Chin, W. J Weber, T. C. Voice, *Water Research*, **1986**, *20*, 1443–1450. **DOI:**10.1016/0043-1354(86)90144-2
23. T. Ferrari, A. Lombardo, E. Benfenati, *Science of The Total Environment*, **2018**, *638*, 1158–1165. **DOI:**10.1016/j.scitotenv.2018.05.072
24. C. J. Churchwell, M. D. Rintoul, S. Martin, D. P. Jr Visco, A. Kotu, R. Slarson, L. O. Sillerud, D. C. Brown, J. L. Faulon, *J Mol Graph Model*, **2004**, *22*, 263–273. **DOI:**10.1016/j.jmgm.2003.10.002
25. J. L. Faulon, D. P. Jr.Visco, R. S.Pophale, *J. Chem. Inf. Comput*. Sci. **2003,** *43*, 707–720. **DOI:**10.1021/ci020345w
26. T. Miyao, H. Kaneko, K. Funatsu, *J Chem Inf Model*. **2016**, *56*, 286–299. **DOI:**10.1021/acs.jcim.5b00628
27. T. Miyao, M. Arakawa, K. Funatsu, *Mol Inform*. **2010**, *29*, 111–125. **DOI:**10.1002/minf.200900038
28. C. D. Weis, D. P. Visco, *Computers & Chemical Engineering*, **2010**, *34*, 1018–1029. **DOI:**10.1016/j.compchemeng.2009.10.017
29. J. L. Faulon, *J. Chem. Info. Comput. Sci*. **1994**, *34*, 1204–1218. **DOI:**10.1021/ci00021a031
30. V. A. Dev, N. G. Chemmangattuvalappil, M. R. Eden, *Computer Aided Chemical Engineering*, **2014**, *33*, 151–156.
31. N. Brown, B. McKay, J. Gasteiger, *J. Comput. Aided Mol. Des*. **2006**, *20*, 333–341. **DOI:**10.1007/s10822-006-9063-1
32. C. Hansch, R. M. Muir, T. Fujita, P. P. Maloney, F. Geiger, M. Streich, *j. Am. Chem. Soc*. **1963**, *85*, 2817–2825. **DOI:**10.1021/ja00901a033
33. E. X. Esposito, A. J. Hopfinger, J. D. Madura, *Methods. Mol. Biol*. **2004**, *275*, 131–214. **DOI:**10.1385/1-59259-802-1:131
34. W. M. Brown, S. Martin, M. D. Rintoul, J. L. Faulon, *J. Chem. Inf. Model*., **2006**, *46*, 826–835. **DOI:**10.1021/ci0504521
35. P. Donald, J. R. Visco, R. S. Pophale, M. D. Rintoul, and J. L. Faulon, *Journal of Molecular Graphics and Modelling*, **2002**, *20*, 429–438.
36. J. L. Faulon, C. J. Churchwell, D. P. Jr. Visco, *J. Chem. Inf. Comput. Sci.* **2003**, *43*, 721–734. **DOI:**10.1021/ci020346o
37. R. Veerasamy, H. Rajak, A.Jain, S. Sivadasan, C. P. Varghese, R.K. Agrawal , *International Journal of Drug Design and Discovery* . **2011**, *2*, 511–519
38. A. Golbraikh, A. Tropsha, *J. Mol. Graphics Mod*. **2002**, *20*, 269–276. **DOI:**10.1016/S1093-3263(01)00123-1

Povzetek

Predstavljena raziskava preučuje uporabo inverznega-QSAR/QSPR pristopa za generiranje novih struktur pesticidov, kar je izredno pomembno v luči njihove široke uporabe, še posebej na področju kmetijstva. S tem namenom smo uporabili metodologijo devetih zaporednih korakov, ki vključujejo kvantitativno študijo relacije med strukturo in aktivnostjo/lastnostmi (QSAR/QSPR) s ciljem razviti model, ki povezuje strukturo 190 pesticidov z njihovim porazdelitvenim koeficientov za sistem n-oktanol-voda ($logk_{ow}$). Uporabili smo enolične atomske deskriptorje, ki predstavljajo strukture in nastopajo kot neodvisne spremenljivke, medtem kot je vrednost $logk_{ow}$ odvisna spremenljivka. Model smo razvili na učenju z nizom 130 molekul, njegovo sposobnost napovedovanja pa smo preverili na ostalih 60 komponentah. Modeliranje $logk_{ow}$ vrednosti teh komponent kot funkcije deskriptorjev smo izvedli z večkratno linearno regresijo (MLR) z uporabo pristopa izpusti-enega (LOO) navzkrižne validacije. Rezultat je QSAR/QSPR enačba s 14 atomskimi deskriptorji z $R^2 = 0.659273$, $Q^2 = 0.65617$ in $RMSE_{training} = 0.930192$, $s = 1.37297$ za niz na katerem smo model učili ter $q^2 = 0.605676$, $RMSE_{LOO} = 1.0936$ s pristopom izpusti-enega (LOO) navzkrižne validacije na testiranem nizu. Generirali smo tudi nove strukture pesticidov, ki bi bili lahko vključeni v nadaljnje študije.

DOI: 10.17344/acsi.2018.4821 *Acta Chim. Slov.* **2019,** *66,* 326–336

Scientific paper

Adsorptive Performance of Soy Bran and Mustard Husk Towards Arsenic (V) Ions from Synthetic Aqueous Solutions

Doina Humelnicu,[1,*] Laurentiu Valentin Soroaga,[1] Cecilia Arsene,[1] Ionel Humelnicu[1] and Romeo Iulian Olariu[1,2,*]

[1] *Alexandru Ioan Cuza" University of Iasi, Faculty of Chemistry, Bld. Carol I, nr. 11, Iasi, 700506, Romania*

[2] *Alexandru Ioan Cuza" University of Iasi, CERNESIM, Bd. Carol I, nr. 11, Iasi, 700506, Romania*

** Corresponding author: E-mail: doinah@uaic.ro, oromeo@uaic.ro, phone: +40232201136*

Received: 10-29-2018

Abstract

Recently, there is growing attention on the use of low-cost sorbents in the depollution of contaminated waters. As a consequence, the present work investigates the potential of soy bran and mustard husk as possible sorbent for the removal of arsenic(V) from residual water. Effects of various operating parameters such as: contact time, pH, initial arsenic concentration, pH, sorbent dose, temperature were investigated to determine the removal efficiency of arsenic(V). Thermodynamic parameters that characterize the process indicated that the adsorption is spontaneous and endothermic. The values for the separation factor, R_L were less than one which confirms that the adsorption process was favorable. Equilibrium data fitted well to the Langmuir model with a higher adsorption capacity of soy bran (74.07 mg g^{-1}) towards arsenic(V) ions than mustard husk (65.79 mg g^{-1}). It was found that the pseudo-second order kinetic model was the best applicable model to describe the adsorption kinetic data.

Keywords: Adsorption; arsenic; isotherm; soy bran; mustard husk

1. Introduction

Arsenic is an element that reaches into the environment from a variety of natural sources (volcanic emission, minerals) and anthropogenic activities (mining activities, burning of fossil fuels and the use of arsenical pesticides which have a longer residence time and also an increased capacity of accumulation.[1–4]

Also, by erosion, decomposition and due to the action atmospheric factors, arsenic can be released into groundwaters and surface waters.[5,6]

Stable inorganic arsenic species in water include arsenic acid anions ($H_2AsO_4^-$, H_3AsO_4,$HAsO_4^{2-}$ şi AsO_4^{3-}). Arsenious acid is also stable in water as H_3AsO_3 and $H_2AsO_3^-$ in moderately reducing conditions (< 200 mV).[7]

Inorganic arsenic in oxidation states +V (arsenate) and +III (arsenite) is found in a variety of mineral in natural waters. Chemical arsenic behavior is related to the ease transformations between +III and +V oxidation states. The oxidation state affects the toxicity of arsenic compounds. The toxicity of different arsenic species decreases in the order arsenite > arsenate > monomethylarsonate > dimethylarsinate).[8,9]

There is clear evidence that chronic exposure to inorganic arsenic increases the risk of cancer.[10] Studies have shown that inhalation of arsenic leads to an increased risk of lung cancer whereas the ingestion of arsenic has been associated with an increased possibility of skin cancer and cancer of the bladder, liver and lungs.[11,12]

Because of that in 2006 the World Health Organization (WHO) has decided to change the maximum admissible concentration of arsenic from 0.05 mg/L to 0.01 mg/L in drinking water.[13]

In order to eliminate arsenic from water has been used various methods: *i) precipitation/co-precipitation,* (method that allows the removal of arsenic up to 0.05 mg/L and in some cases even less than 0.01 mg/L)[14,15]; *ii) membrane filtration* (that may remove a variety of contaminants from water but for arsenic compounds this method can reduce their concentration up to 0.05 mg/L.[16] Howev-

er, this method presents some disadvantages, such as low efficiency, large amounts of waste and high cost, as well[16]; *iii) ion exchange* (method that are nowadays frequently used in the treatment of containing arsenic groundwater and drinking water because of its of high efficacy advantage.[1,13,14,16–21] By using this method the level of the arsenic compounds in water is less than 0.01 mg/L.

By adsorption, the contaminants are concentrated at the sorbent surface. Nature of the adsorption process could be explained based on two theories: one physical and one chemical.

Physical theory, the most widespread theory is the so-called potential theory or concentrated layer theory according to which the reaction between atoms that are found on the surface of the solid (adsorbent) and adsorbed molecules is determined by the van der Waals forces of attraction. Chemical theory of the adsorption admits the existence of a single monomolecular layer on the surface of the solid (adsorbent); adsorption forces act only on a very short distance which not exceeding the diameter of a molecule.[22]

Thus, the adsorbent material must fulfill certain conditions such as: a type of particle size, high adsorption capacity, high selectivity, and high degree of adsorption, water strong physical connection, and low price.

In recent times, more attention is paid to cheap biomass such as powdered eggshell,[23] pine leaves,[24] rice husk.[25]

These biomasses appear to be a possible alternative for heavy metals removal due to their economic and environmental characteristics, the chemical composition, availability, low price, and high efficiency in removal of heavy metals from dilute solutions.

Recently, the need for an economical method for the removal of pollutants from contaminated waters involves researches on low cost sorbents such as agricultural waste by-products. In this regard, various type of agricultural waste by-products such as palm oil fruit shell,[26] coffee grains,[27] fir tree sawdust,[28] rose petals,[29] rice husk,[30] cellulose dust[31] etc. have been investigated for the removal of the pollutants from the wastewaters.

The agricultural by-products may be different parts of plant, such as bark, stem, leaves, root, flower, fruit biomass, husk, hull, shell and may contain compounds such as cellulose, lignin, hemi-cellulose. These compounds have potential functional groups such as hydroxyl, carboxyl, amino, amido and alkoxy with a great affinity for the metal ions.[32]

The aim of the present study is to analyse the sorption capacity of mustard husk soy bran as low cost agricultural by-products towards arsenic(V) ions from the residual waters in different experimental conditions. During this study, effect of some parameters such as the dose of adsorbent, pH, temperature, initial metal concentration and contact time were studied. Moreover, various isotherm and kinetic models were used to explain the adsorption process.

2. Materials and Methods

All chemicals were of analytical reagent grade and no further purification was carried out. The agricultural by-products used in these adsorption experiments were soy bran and mustard husk resulting from the milling and baking. Sorbents were collected from a local mill, ground, were prepared and characterized as shown by Humelnicu and colab.[33]

The stock solution containing the arsenic(V) was prepared from $Na_2HAsO_4\ 7H_2O$ (Sigma-Aldrich). The adsorption experiments were performed in a batch system by stirring at 350 rpm a suspension that contained arsenic(V) ions solution and the sorbent. The pH values were in range 2 and 10, the initial concentration of the solution varied from 50 to 350 mg L^{-1}, at a temperature between of 25 °C – 45 °C, and the sorbent dose varied from 1.5 to 4 g L^{-1}. The pH of the solution was adjusted with NaOH or HNO_3 0.1 M solution and measured with a HANNA pH/temperature meter HI 991001.

After the equilibrium has been reached the supernatant was used for arsenic quantification by using Hydride Generation-Atomic Absorption Spectrometry (HG-AAS). HG-AAS is powerful analytical techniques that provide information of the level of concentrations of As with low interferences and a lower LOQ because the analyte is separated from the sample matrix before the quantification.[34,35] Experiments were conducted on a High Resolution Continuous Source Spectrometer ContrAA 700 (Analytik Jena).

The amount of arsenic adsorbed per unit mass by the sorbent under equilibrium conditions was calculated by the equation (1).

$$q = \frac{(C_0 - C_e)\cdot V}{m},\ (\text{mg As/g sorbent}) \qquad (1)$$

where: C_0 is initial concentration of solution, (mg L^{-1}), C_e is equilibrium As(V) concentration (mg L^{-1}), V is volume of solution (L), and m is sorbent mass (g).

The distribution coefficient, K_d, is defined as the ratio of the concentration of arsenic retained in the sorbent and the one in the solution at equilibrium being calculated with equation (2).

$$K_d = \frac{(C_0 - C_e)}{C_e}\cdot\frac{V}{m} \quad (mL\cdot g^{-1}) \qquad (2)$$

where C_0, C_e,V and m have the same meaning as in Eq (1).

The adsorption capacities of the two adsorbent were analyzed through the use of Langmuir, Freundlich, Temkin and Flory-Huggins models. The kinetics of arsenic adsorption on the soy bran and mustard husk were analyzed by using pseudo first-order, pseudo second-order, and intra-particle diffusion kinetic models.

Desorption experiments were carried out in batch system by using the sorbent loaded with arsenic immediately after the adsorption processes.

Four common eluents have been tested, namely: NaOH, $NaHCO_3$, HCl and HNO_3 0.01 M. The sorbent loaded with As and eluent solution was kept in contact for 24 hours.

The following abbreviations have been used: M-mustard husk, S-soy bran, As-M- mustard husk after As(V) adsorption and As-S-soy bran after As(V) adsorption, respectively.

3. Results and Discussion

3. 1. pH Effect on the Adsorption Process

pH is one of the most important factor that influences the chemistry of arsenic in aqueous solution and surface of the adsorbents. The effect of pH on the adsorption process of As on the mustard husk and soy bran was investigated in the range of values between 2–10. Figure 1 illustrates the effect of pH on As(V) adsorption on the studied adsorbents. The amount of retained As(V) increased slightly with increasing pH and reached a maximum value at pH 6, after that decreased slightly. Consequently, in further experiments pH 6 value was selected as an optimum pH condition.

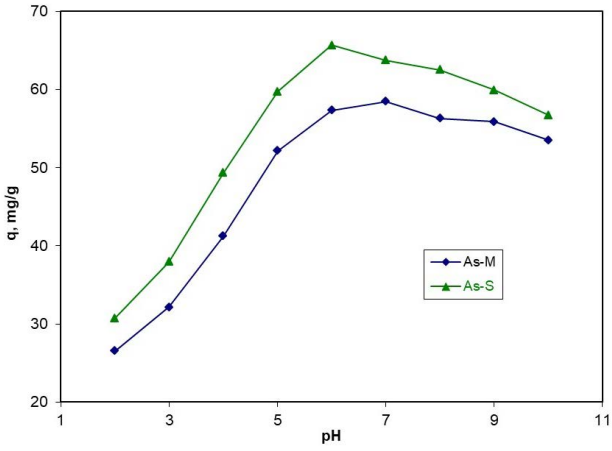

Figure 1. pH dependence of arsenic(V) adsorption on mustard husk and soy bran.

The possible centers on the surface of the sorbents that could be responsible for the adsorption include -OH and -COOH functional groups.[36] Mamindy-Pajany et al.[37] denotes that in according to the arsenic speciation, $H_2AsO_4^-$ is predominant for pH values between 2 and 5, whereas $HAsO_4^{2-}$ is predominant for pH values between 7 and 10. On the other hand, at higher pH condition active centers were not protonated and were both neutral and anionic by releasing H^+ ions ($-COO^-$, $-O^-$) which leads to a less adsorption.

3. 2. Effect of Sorbent Dosage

The adsorption process is efficient if it requires a small amount of sorbent. Effect of sorbent dosage on As(V) adsorption was investigated by changing the sorbent dose from 1.5 to 4 g L^{-1} with the initial metal concentration 250 mg L^{-1} at pH 6.0, temperature of 25 °C and contact time 60 min. Figure 2 shows that the adsorption capacity increases with the increase of adsorbent dose from 1.5 to 3.5 g L^{-1} followed by a slightly decrease. Increase of the adsorption capacity was due to the greater availability of the exchangeable sites or surface area at the higher concentrations of the adsorbent.

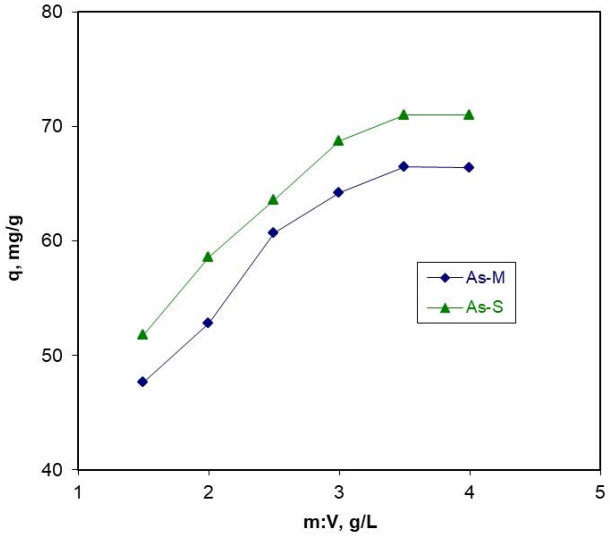

Figure 2. Effect of sorbent dosage on the adsorption process of As(V) on the mustard husk and soy bran.

From the experimental results it was found that the adsorption process has higher efficiency in the case of soy bran as adsorbent in comparison with mustard husk.

3. 3. Effect of Contact Time on the Adsorption Process of As(V)

Influence of the contact time on the adsorption process of As(V) ions on the two sorbents has been studied for a period time between 15 to 180 minutes, all the other parameters being kept constant. In these studies the As ions concentration have been varied from 50 mg L^{-1} to 250 mg L^{-1}. The obtained results are depicted in Figure 3.

The results indicate that the amount of the retained ions increases with the increasing of the contact time and the equilibrium is reached after about 75 minutes. From Figures 3 on can conclude that the adsorption of As is more effective on soy bran as adsorbent.

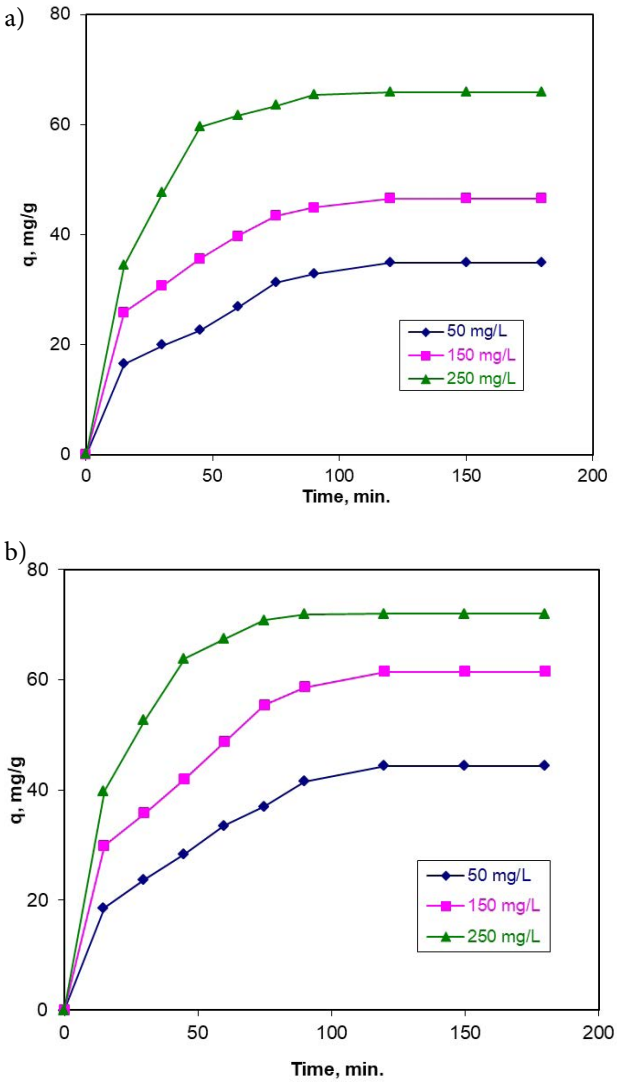

Figure 3. Contact time dependence of adsorption process of As(V) on: a) mustard husk, b) soy bran.

3. 4. Effect of As(V) Initial Concentration on the Adsorption Process

The effect of the initial concentration of the As(V) solution on the adsorption has been investigated, too. The initial concentration was varied from 25 to 350 mg L^{-1}, all other parameters have been maintained constant. Figure 4 shows that the adsorption capacity increases with the increasing of the initial concentration of As(V). Thus, for mustard husk adsorption capacity increases form 31.25 to 59.47 mg g^{-1} and for soy bran from 36.98 to 70.39 mg g^{-1}. In both cases after 250 mg L^{-1} as initial As(V) concentration the adsorption capacities decrease. These results are in good agreement with Asif and Chen[25] that explained this variation due to a raise in the driving force of the concentration gradient and low concentration, the driving force of adsorbent is reduced due to low concentration gradient. In the diluted solutions the mobility of ions is high, and for this reason, the interaction of As(V) ions with the adsorbents was amplified.

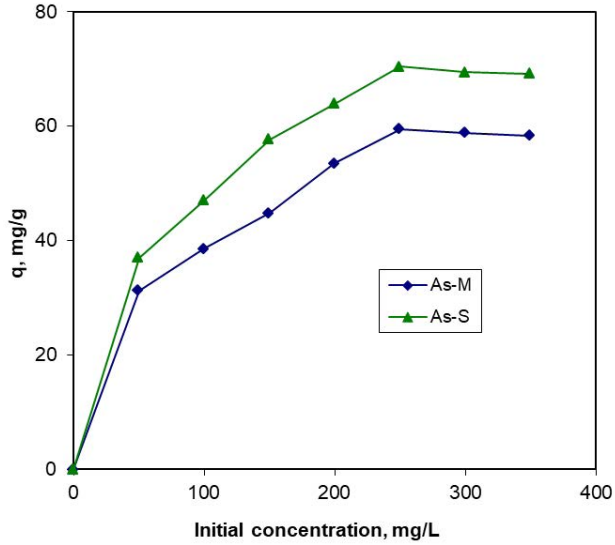

Figure 4. Effect of initial concentration of As(V) on the adsorption process on mustard husk and soy bran.

3. 5. Effect of the Temperature on the Adsorption of As(V)

The effect of temperature on the adsorption process of the As(V) on the mustard husk and soy bran was investigated from the range of 25–45 °C. All the other parameters have been kept constant and the results are depicted in Figure 5.

Figure 5 indicated that with the increasing of the temperature adsorption capacity of the adsorbents increase due to the increasing of the attractive forces between adsorbents surface and arsenic ions that is typical for the adsorption of most metal ions from their solutions

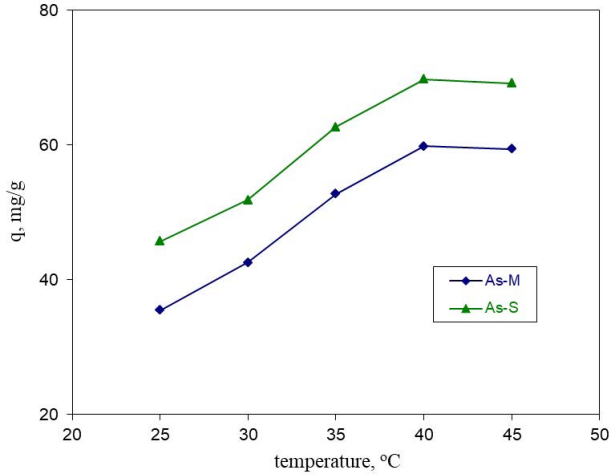

Figure 5. Effect of temperature on the adsorption process of As(V) on the mustard husk and soy bran.

onto natural materials.[38,39] Rate of the adsorbate's molecules distribution along the external layer, as well as in the internal pores of the adsorbent increases with the increasing of temperature.

3. 6. Thermodynamic Parameters

Determination of the thermodynamic parameters: enthalpy (ΔH^o), entropy (ΔS^o), and free Gibbs energy (ΔG^o), was based on experiments performed in a batch system, at temperatures between 25–45 °C.

For this reason equations (3) and (4) have been applied.

$$\ln K_d = \frac{\Delta S^0}{R} - \frac{\Delta H^0}{RT} \quad (3)$$

$$\Delta G^0 = \Delta H^0 - T\Delta S^0 \quad (4)$$

where: K_d is distribution coefficient for adsorption that was calculated with the equation (2).

ΔH^o and ΔS^o values have been estimated from the slope and intercept of the plot of $\ln K_d$ *versus* 1/T (Figure 6). The obtained results are presented in Table 1.

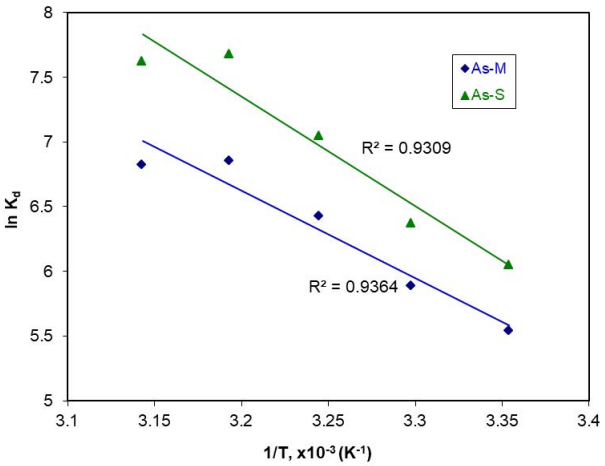

Figure 6. Plot of lnKd function of 1/T.

The data from Table 1 reveal that ΔH^o and ΔS^o have positive values which indicates the sorbent's affinity for arsenic (V) ions and the adsorption is an endothermic process. The positive values of entropy suggest an increase in the disorder degree in the system. The spontaneity of the adsorption process is confirmed by the negative value of Gibbs energy. This parameter values decrease with the increasing of temperature which indicates the efficiency of adsorption at higher temperature.

The activation energy of the adsorption process (E_a) was obtained from the slope of plotting ln(1–θ) *vs.* 1/T, where sorbent surface coverage (θ) was calculated using the equation (Eq. 5):

$$\theta = \left(1 - \frac{C}{C_0}\right) \quad (5)$$

C, C_0 are final and initial concentration of arsenic in aqueous solution (mg/L).

According to the modified Arrhenius equation,[40] the plot of ln(1–θ) *vs.* 1/T gives a straight line with the slope E_a/R. Activation energy values were calculated from the slope of plot and have values of 59.38 kJ mol^{-1} and 31.97 kJ mol^{-1} for mustard husk and soy bran, respectively. The positive values of E_a were consistent with the positive values of ΔH^o and confirm once again the endothermic nature of the adsorption process.

3. 7. Kinetic Models

In order to obtain information on the mechanism of adsorption of arsenic on soy bran and mustard husk three different models were applied, that is: the pseudo-first order model (Eq. 6), pseudo-second order model (Eq. 7) and the intraparticle diffusion model (Eq. 8).[41–43] A relatively high correlation coefficients value indicates that the model successfully describes the kinetics of arsenic adsorption.

$$\log(q_e - q_t) = \log q_e - \frac{k_1}{2.303}t \quad (6)$$

$$\frac{1}{q_t} = \frac{1}{k_2 q_e^2} + \frac{1}{q_e}t \quad (7)$$

$$q_t = k_{id}t^{1/2} + C_d \quad (8)$$

where: q_t and q_e and are the amounts of arsenic adsorbed (mg g^{-1}) at time t and at equilibrium, respectively, k_1 is the rate constant of pseudo-first order kinetic (min^{-1}), k_2 is the rate constant of pseudo-second order kinetic (g mg^{-1} min^{-1}), and k_{id} is the intra-particle diffusion rate constant (mg

Table 1. Thermodynamic parameters for the adsorption of arsenic (V) on mustard husk and soy bran.

Sorbent	ΔH^o, kJ mol^{-1}	ΔS^o, J mol^{-1} K^{-1}	ΔG^o, kJ mol^{-1}				
			25 °C	30 °C	35 °C	40 °C	45 °C
Mustard husk	56.04	234.39	–13.84	–15.01	–16.18	–17.35	–18.52
Soy bran	70.36	286.27	–14.98	–16.41	–17.84	–19.27	–20.70

g^{-1} $min^{-0.5}$). The plot of $\log(q_e - q_t)$ *vs.* time (Figure 7) give a linear relationship from which k_1 and q_e can be determined from the slope and intercept, respectively.

The plot of (t/q_t) *vs.* time (Figure 8) gives a linear relationship from which q_e and k_2 can be determined from the slope and intercept of the plot, respectively.

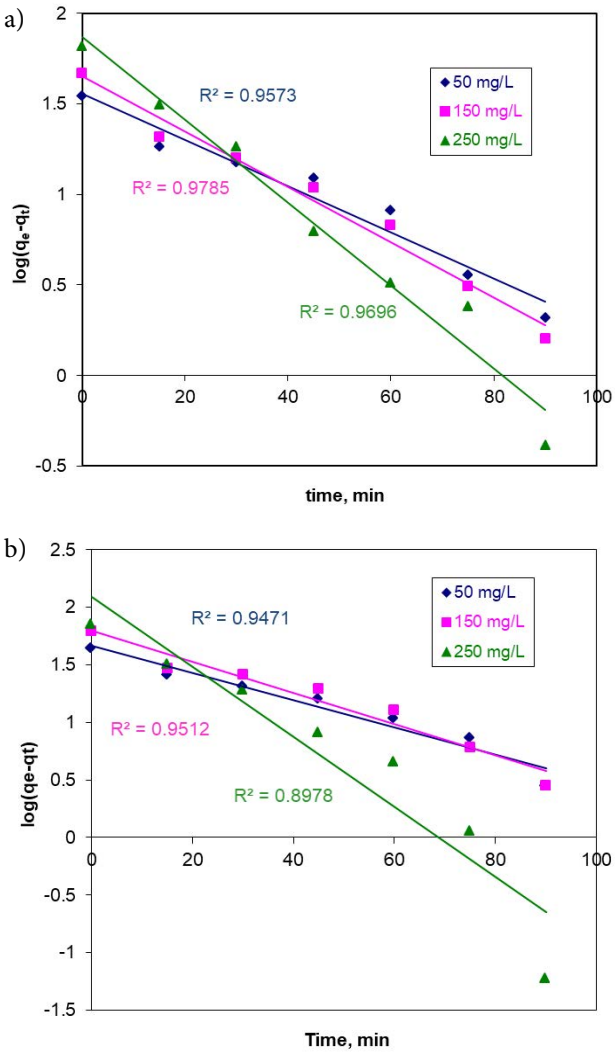

Figure 7. The pseudo-first order kinetics of arsenic (V) adsorption on mustard husk (a) and soy bran (b).

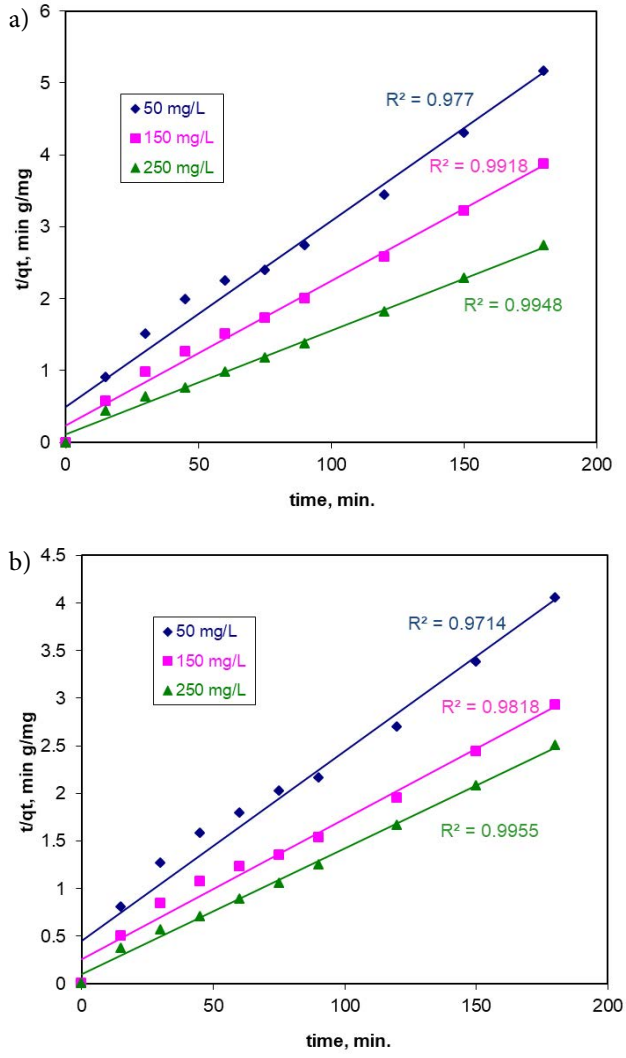

Figure 8. The pseudo-second order kinetics of arsenic (V) adsorption on mustard husk (a) and soy bran (b).

Table 2. Kinetic parameters for the adsorption of arsenic on mustard husk and soy bran.

Model	Initial concentration, mg/L					
	50		150		250	
	Mustard husk	Soy bran	Mustard husk	Soy bran	Mustard husk	Soy bran
Pseudo-first order						
$q_{e,\,exp}$ (mg g^{-1})	34.86	44.39	46.52	61.43	65.79	71.94
$q_{e,\,calc}$ (mg g^{-1})	35.70	46.08	44.66	62.23	73.63	122.71
k_1 (min^{-1})	$2.92 \cdot 10^{-2}$	$2.7 \cdot 10^{-2}$	$3.52 \cdot 10^{-2}$	$3.1 \cdot 10^{-2}$	$5.25 \cdot 10^{-2}$	$7.0 \cdot 10^{-2}$
R^2	0.957	0.947	0.979	0.951	0.969	0.898
Pseudo-second order						
$q_{e,\,exp}$ (mg g^{-1})	34.86	44.39	46.52	61.43	65.79	71.94
$q_{e,\,calc}$ (mg g^{-1})	38.76	50.0	49.75	67.56	69.44	75.75
k_2(g mg^{-1} min^{-1})	$1.35 \cdot 10^{-3}$	$8.88 \cdot 10^{-4}$	$1.71 \cdot 10^{-3}$	$8.6 \cdot 10^{-4}$	$1.78 \cdot 10^{-3}$	$1.77 \cdot 10^{-3}$
R^2	0.977	0.971	0.992	0.918	0.995	0.995

An intra-particle diffusion model was used to predict the rate controlling step but in this case a non-linear relationship has been obtained. The pseudo-first-order and pseudo-second-order rate constants determined are listed in Table 2 along with the corresponding correlation coefficients. From these results it can be seen that the values of correlation coefficient decreases from pseudo second-order to pseudo first-order.

3. 8. Adsorption Isotherms

It is well known that the adsorption isotherms express the interaction between the adsorbent and adsorbate in the adsorption processes. In order to study the adsorption of arsenic ions on the two sorbents, Langmuir, Freundlich, Temkin and Flory-Huggins adsorption models have been used.

Langmuir isotherm characterizes a monolayer adsorption on a surface with a finite number of identical centers which are homogeneously distributed on the surface of the sorbent. In our study a linearized Langmuir isotherm form (Eq. 9) has been used:[44]

$$\frac{C_e}{q_e} = \frac{1}{K_L \cdot q_m} + \frac{C_e}{q_m} \quad (9)$$

where: q_e represents the amount of adsorbed arsenic per sorbent unit (mg g^{-1}); C_e is arsenic ion concentration at equilibrium (mg L^{-1}); q_m is a parameter that express the maximum adsorption capacity (mg g^{-1}) corresponding to monolayer coverage; K_L is constantly referring to the adsorption energy (g L^{-1}).

K_L and q_m parameters values were calculated from the intercept and the slope of the plot C_e/q_e *vs.* C_e (Figure 9).

An important characteristic of Langmuir isotherms can be expressed by the dimensionless constant (Eq.10) called equilibrium parameter or separation factor.

$$R_L = \frac{1}{1 + K_L C_0} \quad (10)$$

where: K_L is the Langmuir constant, C_0 is the initial concentration of As(V) ions (mg L^{-1}). For a favorable adsorption process R_L value must be between 0 and 1. In our study R_L obtained values were less than one (Table 3) which indicates that the arsenic(V) adsorption process was favorable.

The Freundlich isotherm is based on the multilayer adsorption that means a heterogeneous surface of the sorbent and a non-uniform distribution of heat of adsorption.[45]

A logarithmic form of this model (Eq. 11) was applied in our study:

$$\log q_e = \log K_F + \frac{1}{n} \log C_e \quad (11)$$

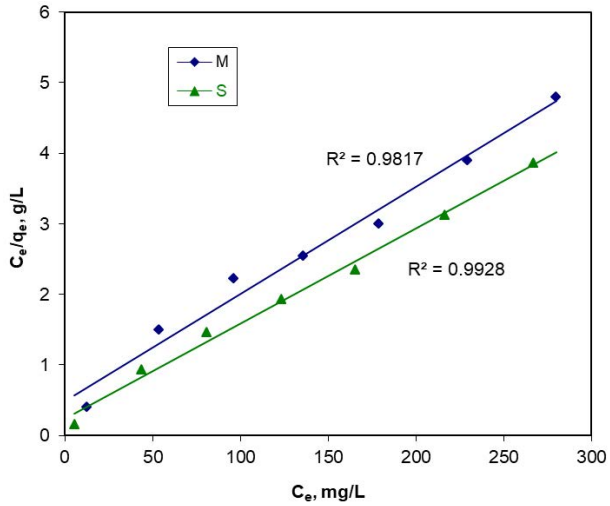

Figure 9. Langmuir isotherms for the arsenic(V) adsorption on mustard husk and soy bran.

In the above equation, q_e and C_e have the same meaning as in Eq (9); K_F ($mg^{(1-1/n)} L^{1/n} g^{-1/n}$) and n are Freundlich constants that indicate the relative adsorption capacity of the sorbent, and the adsorption intensity, respectively.

The slope and intercept of Freundlich model (Figure 10) have been used to calculate K_F and factor n. A value for 1/n less than 1 indicates a normal isotherm while 1/n > 1 suggests a cooperative adsorption. In the case of arsenic adsorption on both mustard husk and soy bran 1/n values are 0.233 and 0.179, respectively, indicating a normal isotherm adsorption.

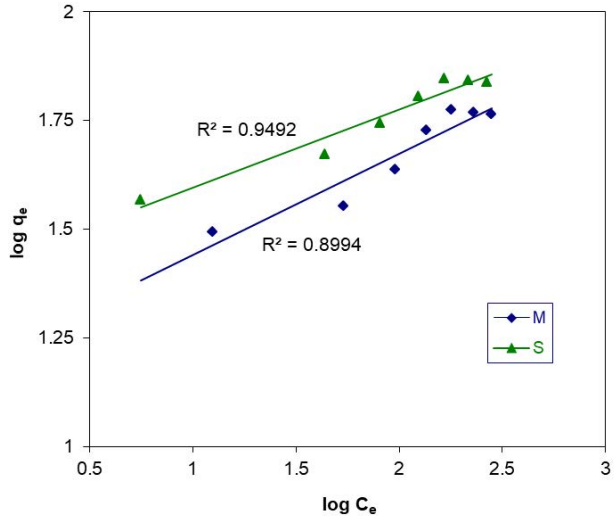

Figure 10. Freundlich isotherms for the arsenic (V) adosrption on mustard husk and soy bran.

The third adsorption isotherm model used in the present work was the Temkin model. In this case, the main assumption is that the heat of adsorption decreases linearly with coverage due to sorbent-sorbate interactions.[46] The

linear Temkin isotherm equation (Eq. 12) used in our study was:

$$q_e = B \ln A + B \ln C_e \quad (12)$$

where: A is the equilibrium constant (L g^{-1}) corresponding to the maximum binding energy and constant B (J mol^{-1}) is correlated to the heat of adsorption as follows:

$$B = RT / b_T \quad (13)$$

where: b_T is the Temkin isotherm energy constant (J mol^{-1}) and R is the universal gas constant (8.3146 J mol^{-1} K^{-1}). The Temkin isotherm plots for both sorbents are presented in Figure 11 and the isotherm parameters extracted are listed in Table 3.

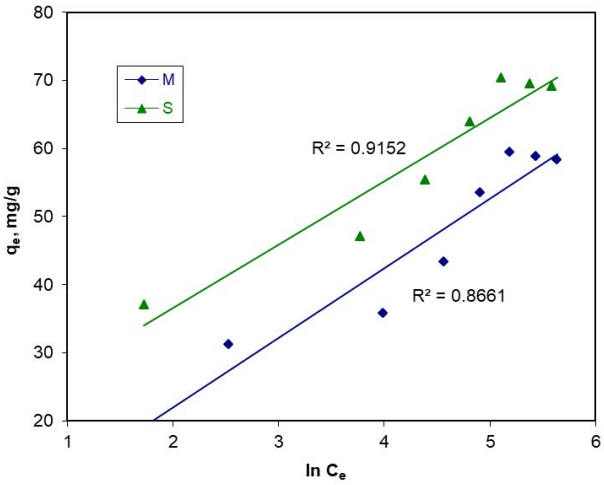

Figure 11. Temkin isotherms for the adsorption of arsenic (V) on mustard husk and soy bran.

For a most comprehensive characterization of the arsenic (V) adsorption process was used the fourth adsorption model, Flory-Huggins, in order to calculate the surface coverage of sorbent by sorbate.[47]

$$\log \frac{\theta}{C_0} = \log K_{FH} + n \log(1-\theta) \quad (14)$$

where θ represents surface coverage and was calculated by Eq. (5), K_{FH} is equilibrium constant of the adsorption process. The parameters of equation (14) were calculated from the slope and intercept of the plot logθ/C_0 *vs.* log(1–*θ) that is depicted in Figure 12 and* are presented in Table 3.

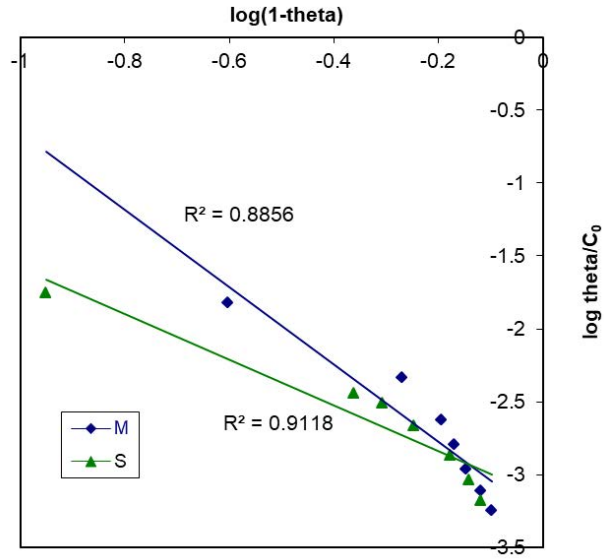

Figure 12. Flory-Huggins isotherms for the arsenic adsorption on mustard husk and soy bran.

Considering all extracted parameters for all four adsorption isotherm models (see Table 3) it can be concluded that for the arsenic (V) adsorption on the mustard husk and soy bran the best fit shows the Langmuir isotherm model. In addition, between the two analyzed materials, in terms of adsorption capacity the best candidate seems to be soy bran than of the mustard husk for arsenic (V). The efficiency of the two studied sorbents, soy bran and mustard husk, on the arsenic (V) was highlighted by a comparison with the results from the literature for other sorbents (Table 4). As can be observed the adsorption capacity of the investigated sorbents for the arsenic (V) is higher compared with some other sorbents and its low cost and abundance make it as possible materials for the use in residual waters decontamination.

The fact that in the sorption stage there are a series of processes that can affect the morphology of the adsorbent materials is pointed out by the images obtained by using a Electronic Scanning Microscope, SEM Quanta 250. Images presents the morphology of sorbens samples (Figure 13)

Table 3. Parameters for the adsorption models.

Sorbent	Langmuir				Freundlich			Flory-Huggins			Temkin		
	q_m, (mg g^{-1})	K_L (L g^{-1})	R^2	R_L	K_F	n	R^2	K_{FH}	n	R^2	A	b_T	R^2
Mustard husk	65.79	0.032	0.982	0.111	16.15	4.29	0.899	$1.99 \cdot 10^3$	1.565	0.886	1.158	242.21	0.866
Soy bran	74.07	0.058	0.993	0.065	26.09	5.56	0.949	$1.29 \cdot 10^3$	2.647	0.911	0.648	265.57	0.915

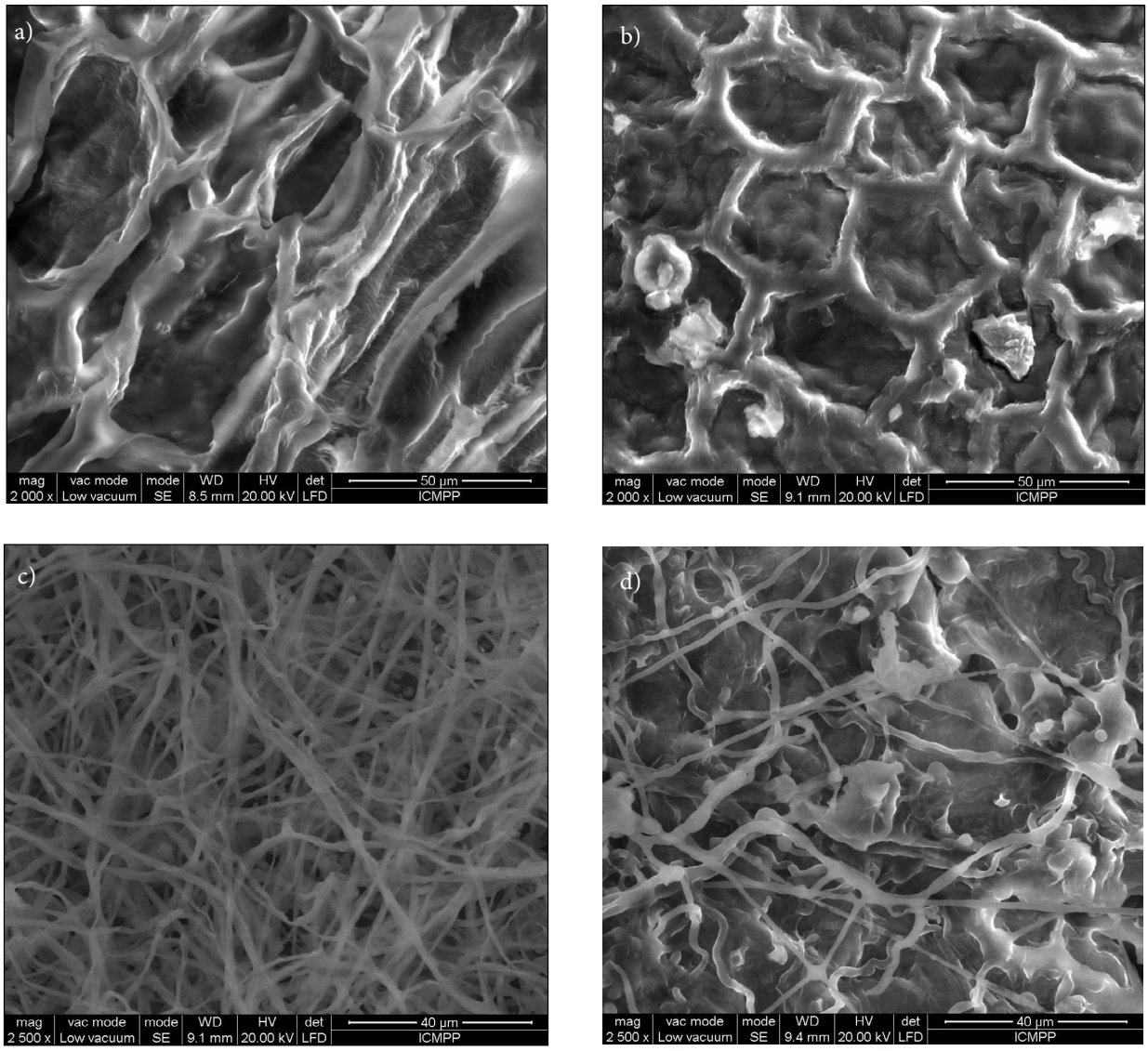

Figure 13. SEM images of the mustard husk and soy bran before (a, c) and after (b, d) adsorption experiments.

Table 4. Comparison of maximum adsorption capacity of different sorbents towards arsenic (V).

Sorbent	q_m (mg g^{-1})	Reference
Rice polish	0.15	48
Rice husk	0.225	25
Coconut shell carbon	2.40	49
Pine leaves	3.27	24
Tea fungal biomass	4.95	48
Polymeric alginate beads	8.33	50
Coconut coir pith	13.75	51
Withania frutescens	16.88	52
Calami rhizoma	22.04	52
Orange juice residue	67.43	53
Mustard husk	65.79	This work
Soy bran	74.07	This work

before and after adsorption processes with enlarge X2500, scale 40 µm.

3. 9. Desorption Results

Once the sorbent is used, it needs to be regenerated. Desorption processes are important from two points of view: first, to recover metal ion and its subsequent use in industrial and secondly, in the regeneration of sorbent for new use processes.

The amount of As released from the sorbent was determined by HG-AAS and the percentage of arsenic desorbed was calculated with equation Eq. 15:

$$desorbed\ ion\ \% = \frac{amount_{des}}{amount_{ads}} \cdot 100 \qquad (15)$$

where: $amount_{des}$ is the amount of desorbed arsenic and $amount_{ads}$ is the amount of arsenic adsorbed by the sorbent. The results of desorption experiments reveal that the best regeneration eluent may be aqueous solution of NaOH 0.01 M, 87.95% for mustard husk and 90.67% for soy bran, respectively.

4. Conclusions

The adsorption of arsenic (V) ions on mustard husk and soy bran was studied as a function of contact time, initial arsenic ion concentration, pH, sorbent mass and temperature, the conclusion being that the sorption capacity of the soy bran was higher than that of mustard husk.

The thermodynamic parameters indicate that adsorption of arsenic (V) ions on mustard husk and soy bran is a spontaneous ($\Delta G^o < 0$) and endothermic ($\Delta H^o > 0$) process.

This study indicates that arsenic (V) adsorption is better described by Langmuir isotherm model and the kinetic of the process obeys the pseudo second-order model.

The results obtained in desorption studies showed that, in order to recover arsenic (V) ions a 0.01 M NaOH solution may be used.

This study reveals the potential of using mustard husk and soy bran as excellent low-cost adsorbent for the removal of arsenic (V) from aqueous solutions.

5. References

1. B. K. Mandal, K. T. Suzuki, *Talanta* **2002**, *58,* 201–235. **DOI:**10.1016/S0039-9140(02)00268-0
2. J. Matschullat, *Sci. Total Environ*. **2000**, *249*, 297–312. **DOI:**10.1016/S0048-9697(99)00524-0
3. J. O. Nriagu, J. M. Azcue, Arsenic: historical perspectives. In: Nriagu JO, Ed. Arsenic in the environment. Part I: Cycling and characterization. New York: John Wiley and Sons Inc, 1990, pp. 1–15.
4. A. K. Sharma, J. C. Tjell, J. J. Sloth, P. E. Holm, *Appl. Geochem*. **2014**, 41, 11–33. **DOI:**10.1016/j.apgeochem.2013.11.012
5. M. Dinesh, C. U. Pittman, *J. Hazard. Mater*. **2007**, 142, 2–53. **DOI:**10.1016/j.jhazmat.2007.01.006
6. E. T. Mackenzie, R. J. Lantzy, V. Paterson, *J. Int. Assoc. Math. Geol.* **1979**, 6, 99–142. **DOI:**10.1007/BF01028961
7. N. N. Greenwood, A. Earnshaw, Chemistry of Elements. Pergamon Press, Oxford, **1984**, pp. 547–596.
8. Agency for Toxic Substances and Disease Registry, Toxicological Profile for Arsenic, US Public Health Service; US Department of Health and Human Services, Atlanta, **1993**.
9. Environmental Protection Agency, Integrated Risk Information System on Arsenic **1995**.
10. C. K. Jain, I. Ali, *Water Res*. **2000**, *34*, 4304–4312. **DOI:**10.1016/S0043-1354(00)00182-2
11. World Health Organisation, Environmental health criteria, arsenic. Geneva, **2001**.
12. J. C. Ng, J. Wang, A. Shraim, *Chemosphere* **2003**, *52*, 1353–1359. **DOI:**10.1016/S0045-6535(03)00470-3
13. Y. Jeong, M. Fan, S. Singh, C. L. Chuang, B. Saha, J. H. van Leeuwen, *Chem. Eng. Proc*. **2007**, *46*, 1030–1039. **DOI:**10.1016/j.cep.2007.05.004
14. M. C. Ciardelli, H. Xu, N. Sahai, *Water Res.* **2008**, *42*, 625–624. **DOI:**10.1016/j.watres.2007.08.011
15. A. Pinisakul, C. Polpraser, P. Porkplan, J. Satayarirod, *Water Sci. Technol* **2002**, *46*, 247–254. **DOI:**10.2166/wst.2002.0250
16. A. Bodalo, J. L. Gomez, E. Gomez, A. M. Hidalgo, A. Aleman, *Desalination* **2005,** *180*, 277–284. **DOI:**10.1016/j.desal.2005.02.008
17. H. Guo, D. Stuben, Z. Berner, *Coll. Interf. Sci*. **2007**, 315, 47–53. **DOI:**10.1016/j.jcis.2007.06.035
18. V. Lenoble, Ph.D Thesis, Laboratoire des Sciences de l'Eau et de l'Environnement, Faculté des Sciences, Limoges, France, **2003**.
19. P. Mondal, C.B. Majumder, B. Mohanty, *J. Hazard. Mater*. **2008**, *150*, 695–702. **DOI:**10.1016/j.jhazmat.2007.05.040
20. M. Streat, K. Hellgardt, N. L. R. Newton, *Proc. Safety Environm. Prot*. **2008**, *86*, 11–20. **DOI:**10.1016/j.psep.2007.10.008
21. M. Peter, *Ultrapure Water* **2005**, *22*, 42–43. **DOI:**10.1016/S0015-1882(06)70888-6
22. A. Negrea, L. Lupa, P. Negrea, M. Ciopec, C. Muntean, *Buletinul AGIR* **2009**, *2–3*, 44–49.
23. I. A. Oke, N.O. Olarinoye, S. R. A. Adewusi, *Adsorption* **2008**, *18*, 73–83. **DOI:**10.1007/s10450-007-9047-z
24. U. Shafique, A. Ijaz, M. Salman, W. Zaman, N. Jamil, R. Rehma, A. Javaid, *J. Taiwan Inst. Chem. Eng.* **2012**, *43*, 256–263. **DOI:**10.1016/j.jtice.2011.10.006
25. Z. Asif, Z. Chen, *Appl. Water Sci.* **2015**, 1–10. **DOI:**10.1007/s13201-015-0323-x
26. M. A. Hossain, H. H. Ngo, W. S. Guo, T. V. Nguyen, *Biores. Technol*. **2012**, *113*, 97–101. **DOI:**10.1016/j.biortech.2011.11.111
27. F. Cerino-Cordova, P. Diaz-Flores, R. Garcia-Reyes, E. Soto-Regalado, R. Gomez-Gonzalez, M. Garza-Gonzalez, E. Bustamante, *Int. J. Environ. Sci. Technol*. **2013**, 1–12. **DOI:**10.1007/s13762-013-0198-z
28. B. Nagy, A. Maicaneanu, C. Indolean, S. Burca, L. Silaghi-Dumitrescu, C. Majdik, Acta Chim. Slov. **2013**, 60, 263–73.
29. Q. Manzoor, R. Nadeem, M. Iqbal, R. Saeed, T. M. Ansari, *Biores Technol*, **2013**, *132*, 446–452. **DOI:**10.1016/j.biortech.2013.01.156
30. D. Yadav, M. Kapur, P. Kumar, M. K. Mondal, *Process. Saf. Environ*., **2015**, *94*, 402–409 **DOI:**10.1016/j.psep.2014.09.005
31. *S. H. S. Pajaie, S. Archin, G. Asadpour, Civil Eng. J.* **2018,** *4,* 620–634. **DOI:**10.28991/cej-0309121
32. S. Kamel, H. Abou-Yousef, M. Yousef, M. El-Sakhawy, Carbohydrate Polym. **2012**, *88*, 250–256. **DOI:**10.1016/j.carbpol.2011.11.090
33. D. Humelnicu, M. Ignat, F. Doroftei, *Environm. Monit. Assess*. **2015,** *187*, 187–198. **DOI:**10.1007/s10661-015-4454-1
34. H. M. Anawar, *Talanta* **2012**, *88*, 30–42. **DOI:**10.1016/j.talanta.2011.11.068
35. A. N. Anthemidis, G.A. Zachariadis, J.A. Stratis, *Anal. Chim. Acta* **2005**, *547*, 237–242. **DOI:**10.1016/j.aca.2005.05.039

36. L. C. Ajjabi, L. Chouba, *J. Environ. Manag.* **2009**, *90*, 3485–3489. **DOI:**10.1016/j.jenvman.2009.06.001
37. Y. Mamindy-Pajany, C. Hurel, N. Marmier, M. Roméo, *C.R. Chimie* **2009**, *12*, 876–881. **DOI:**10.1016/j.crci.2008.10.012
38. K. H. Chong, B. Volesky, *Biotech. Bioeng.* **1995**, *47*, 451–460. **DOI:**10.1002/bit.260470406
39. U. Kumar, *Sci. Res. Essay* **2006**, *1*, 33–37. **DOI:**10.5958/j.0974-4487.11.1.001
40. C. S. Sundaram, N. Viswanathan, S. Meenakshi, *J. Hazard. Mater*. **2008**, *155*, 206–215. **DOI:**10.1016/j.jhazmat.2007.11.048
41. S. Lagergren, *KSvenska Vetenskapsakad Handl* **1898**, *24*, 1–39.
42. G. McKay, Y. S. Ho, *Process Biochem.* **1999**, *34*, 451–465. **DOI:**10.1016/S0032-9592(98)00112-5
43. W. J. Jr. Weber, J. C. Morris, *J. Sanit. Eng. Div. ASCE*, **1963**, *89*, 31–59.
44. I. Langmuir, *J. Am. Chem. Soc.* **1916**, *38*, 2221–2295. **DOI:**10.1021/ja02268a002
45. H. Freundlich, *Phys. Chem. Soc.* **1906**, *40*, 1361–1368.
46. M. Temkin, *Zh. Fiz. Khim.* **1941**, *15*, 296–332. **DOI:**10.2307/40085313
47. K. Vijayaraghavan, T. V. N. Padmesh, K. Palanivelu, M. Velan, *J. Hazard. Mater.* **2006**, *B133*, 304–308. **DOI:**10.1016/j.jhazmat.2005.10.016
48. D. Ranjan, M. Talat, S. H. Hasan, *J. Hazard. Mater.* **2009**, *166*, 1050–1059. **DOI:**10.1016/j.jhazmat.2008.12.013
49. L. Lorenzen, J. S. J van Deventer, W. M. Landi, *Miner. Eng.* **1995**, *8*, 557–569. **DOI:**10.1016/0892-6875(95)00017-K
50. T. Dewangan, A. Tiwari, A. K. Bajpai, *Toxicol. Environ. Chem.* **2009**, *91*, 1055–1067. **DOI:**10.1080/02772240802585012
51. T. S. Anirudhan, M. R. Unnithan, *Chemosphere* **2007**, *66*, 60–66. **DOI:**10.1016/j.chemosphere.2006.05.031
52. M. Chiban, G. Carja, G. Lehutu, F. Sinan, *Arabian J. Chem.* **2016**, *9*, S988–S999. **DOI:**10.1016/j.arabjc.2011.10.002
53. K. N. Ghimire, K. Inoue, K. Makino, T. Miyajima, *Sep. Sci. Technol.* **2002,** *37*, 2785–2799. **DOI:**10.1081/SS-120005466

Povzetek

V zadnjem času je velika pozornost namenjena uporabi cenovno ugodnih adsorbentov za čiščenje kontaminiranih voda. S namenom smo preverili potencial sojinih lupin in gorčičnih luščin za odstranjevanje arzena (V) iz odpadnih voda. Preučili smo vpliv procesnih parametrov kot so kontaktni čas, pH vrednost, začetna koncentracija arzena, količina adsorbenta in temperatura na odstranjevanje arzena (V). Termodinamski parametri so pokazali, da je proces pod preučevanimi pogoji spontan in endotermen. Separacijski faktor je bil manjši kot ena kar kaže, da je adsorpcija ugodna. Adsorpcijsko ravnotežje lahko dobro opišemo z Langmuirjevo izotermo z maksimalno kapaciteto vezave arzenovih (V) ionov na sojine lupine 74.07 mg g^{-1} in na gorčične luščine 65.79 mg g^{-1}. Kinetiko lahko opišemo z reakcijo psevdo-prvega reda.

Scientific paper

Protein Release from Biodegradable Poly(ε-Caprolactone)-Chitosan Scaffolds Prepared in $scCO_2$

Gregor Kravanja,[1] Maja Globočnik,[1] Mateja, Primožič,[1] Željko Knez[1,2] and Maja Leitgeb[1,2,*]

[1] *University of Maribor; Faculty of Chemistry and Chemical Engineering; Laboratory of separation processes and product design; Smetanova ul. 17; 2000 Maribor; Slovenia*

[2] *University of Maribor, Faculty of Medicine, Taborska ulica 8, 2000 Maribor*

* *Corresponding author: E-mail: E-mail: maja.leitgeb@um.si, Telephone: +386 2 2294 462*

Received: 10-29-2018

Abstract

To study the release patterns of protein bovine serum albumin (BSA), porous poly(ε-caprolactone)-chitosan scaffolds with entrapped BSA were fabricated by using supercritical CO_2 for its potential use in tissue engineering applications. An emulsion, consisting of a polymer-solvent solution and buffer protein solution was saturated with $scCO_2$ at 12 MPa and 37 °C and then rapidly depressurized through a release valve causing bubble nucleation and precipitation of the composite material. The controlled total protein release from biodegradable poly(ε-caprolactone) with 5% chitosan (w/w) scaffolds was assessed by Bradford protein assay. After 16 to 20 days of protein release testing, 58.8% of the protein was released from composite with PCL (M_w = 10,000 g/mol) and 43.9% from composite with PCL (M_w = 60,000 g/mol). Preliminary studies for characterization of the prepared composite biomaterials using FTIR spectra, ESEM photo analysis and DSC analysis have been carried out.

Keywords: Protein release; PCL polymer; chitosan; scaffold; supercritical CO_2

1. Introduction

Biodegradable porous polymer scaffolds are often required for reconstruction or regeneration of organ function in tissue engineering applications, alone or in combination with a bioactive agent. They mimic the extracellular matrix (ECM), so they must provide a sustainable template for cell attachment, proliferation, and differentiation. Biocompatibility, absorbability, appropriate mechanical strength, and porous structure are some of the basic requirements of scaffolds. Biodegradability is a very convenient feature of polyesters, and that is why they are so promising and extensively utilized, since ceramic and metal implants require a second surgical operation, to remove them from the body.[1–3] Furthermore, in bone tissue engineering, the material should form an osteoconductive structural support for the newly formed bone and consist of interconnected pores, which have an important role in supporting cell penetration, new tissue ingrowth, nutrient diffusion, and neovascularization.[4–6]

Poly(glycolic acid), poly(lactic acid), poly(hydroxyl butyrate), poly(ε-caprolactone) (PCL) and their copolymers are the most frequently used synthetic biodegradable polymers in tissue engineering. PCL is highly appealing because of its physical-chemical and mechanical characteristics. It has been broadly investigated on account of its soft- and hard-tissue compatibility. Its low melting point (ca. 60 °C) allows easy processing. Its non-toxic degradation products are easily metabolized or secreted from the body. PCL is approved by the Food and Drug Administration (FDA) for use in biomedical applications. However, as with other biodegradable polyesters, its use could be limited by some drawbacks. The absence of cell recognition sites on the surface of scaffolds can lead to poor cell affinity and adhesion. Its hydrophobicity can prevent the cells from penetrating into the porous structure. Neutral charge distribution can cause a lack of interaction with the ECM. Acidic degradation products are formed during hydrolysis of PCL and could possibly cause side effects. It has a very

slow degradation rate, due to high crystallinity. Therefore, PCL is often mixed with natural polymers to enhance its bioactivity.[1,5,7] Chitosan (CS) is a linear polysaccharide. Its numerous good features, such as biocompatibility, biodegradability, non-antigenicity, non-toxicity, antibacterial properties, and bio-adherence have induced its use in biomedical areas. When combined with PCL, hydrophilic chitosan can modulate the hydrophobicity of PCL, which increases the biocompatibility, cellular affinity, wettability and permeability of matrices.[6,7]

Tissue engineering applications require scaffolds with high surface area to volume ratios. This is crucial for effective cell seeding onto the biomaterial support and for efficient nutrient acquisition, so that rapid proliferation and sufficient physiological activity can be achieved. Porous polyester scaffolds can be formed by many techniques, each of which results in different biomaterial characteristics, therefore, the most convenient method may depend on the application.[8] In the last two decades, there has been significant progress in using $scCO_2$ for polymer foaming. This is a non-toxic, non-flammable, chemically inert and environmentally safe gas.[9] Furthermore, it is inexpensive and offers a useful alternative to organic solvents that can be potentially harmful to cells. CO_2, dissolved in the polymer, decreases the viscosity, acts as a plasticizer and allows processing at lower temperatures. This foaming technique enables control of the size and distribution of pores by selecting suitable processing conditions, like temperature, depressurization rate and solubilisation pressure (gas concentration in the polymer). Good solubility of CO_2 in polymers can be additionally influenced by temperature, pressure and weak interactions with functional groups of polymers.[5,10]

With the ability to control the morphology of the composite, supercritical fluid technology has also overcome the problem of incorporating biologically active species into polymeric composites without a change in activity. The combination of gas-like viscosity and liquid-like density makes $scCO_2$ an ideal medium for making polymer-based materials containing bioactive species. Interaction of $scCO_2$ with amorphous polymers leads to depression of the glass transition temperature (T_g); under these conditions, the polymer is plasticized, which significantly lowers the viscosity and allows incorporation of insoluble bioactive particles into the polymer. Additionally, no solvent residues remain in the material after processing.[11,12]

To create new composite material scaffolds with specific physical-chemical properties PCL (M_w = 10,000 and 60,000 g/mol) was mixed with 5% chitosan (w/w) and further, bovine serum albumin (BSA) was incorporated. We have used BSA as a model protein for preliminary studies of controlled release from prepared porous scaffolds. Measurement of total protein release was performed by Bradford protein assay. As a prior characterization of the prepared material, FTIR, ESEM and DSC analysis on clean PCL and CS and their composites were performed.

2. Experimental

2. 1. Materials

Bovine serum albumin (BSA) (CAS: 9048-46-8) was provided by Sigma-Aldrich. Dimethyl chloride (CAS: 75-09-2), was purchased from Fluka Analytical. Poly(ε-caprolactone) (PCL) of molar weight 10,000 g/mol (CAS: 24980-41-4) and of 60,000 g/mol (CAS: 24980-41-4) and chitosan (CAS: 9012-76-4) were purchased from Sigma-Aldrich. The polymers were delivered as powders and were used without further purification. Moisture content in the polymers, determined gravimetrically by means of an HB43-S Compact Halogen Moisture Analyzer, was lower than 0.10 wt. % for each polymer. CO_2 (99.998%) was supplied by Messer (Slovenia).

2. 2. Scaffold Preparation in $scCO_2$

Before processing with $scCO_2$, an emulsion consisting of a water (aqueous) phase and an organic composite solution phase was prepared by sonicating the immiscible phases.

The water phase consisted of 20 mg BSA dissolved in 200 μL of phosphate buffer at pH 7.4. The organic phase consisted of 500 mg PCL + CS mixture dissolved in 1 mL of dimethyl chloride. Prior to supercritical processing, the emulsion was pipetted into the small cylindrical mold and then immediately placed into a high-pressure view equilibrium cell made of stainless steel (Sitec AG, Zurich, CH) (Figure 1).[13] The high-pressure cell was pressurized to 12 MPa with CO_2 by a high-pressure pump (NWA PM-101). The pressure inside the cell was measured by an electronic pressure gauge (WIKA Alexander Wiegand GmbH & Co. KG, Alexander-Wiegand-Straße, Klingenberg, Germany). The temperature of the cell was kept constant using a heating jacket and was observed using calibrated thermocouple immersed in the cell. The pressure deviation was ± 0.01 MPa and the total temperature deviation was 0.1 °C. When the CO_2 reached the desired working pressure, a stable 20 mL/h flow-rate of CO_2 was produced through the pressure cell by a syringe pump manufactured by ISCO (Lincoln, NE) to fully extract the dimethyl chloride. The emulsion consisting of BSA and a biodegradable polymer was saturated with $scCO_2$ for 18 h to easily incorporate insoluble bioactive particles into the polymer by lowering the glass transition temperature (T_g) and eliminating all solvent residues from the material. In the last step, the high pressure cell was rapidly depressurized at a controlled depressurization rate of 0.1 MPa/s by opening the release valve in order to create a microporous composite scaffold. After the depressurization step, the composite scaffold was removed from the mold and sectioned into three parts for further protein release studies. Prior to material characterization, additional scaffolds were prepared without incorporating BSA protein.

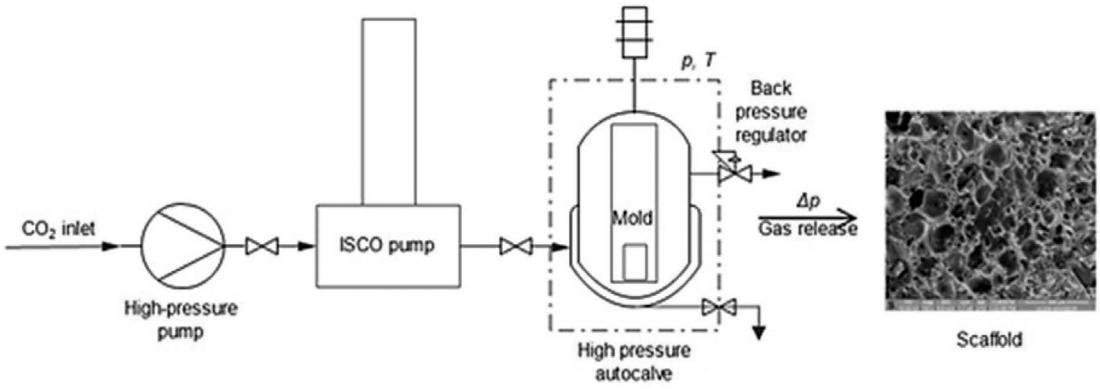

Figure 1. Diagram of the system used to generate biodegradable scaffolds with $scCO_2$.

2. 3. Characterization of Prepared Scaffolds

The porosity of the prepared scaffolds was measured with a graduated cylinder.[1,14] It was calculated as given in the equation (1):

$$\text{Porosity}\ (\%) = \frac{(w_2 - w_3 - w_s)/\rho_e}{(w_1 - w_3)/\rho_e} \times 100 \qquad (1)$$

where w_1 is the weight of graduated cylinder filled with ethanol, w_2 the weight of the graduated cylinder, ethanol and scaffold, w_3 the weight of the graduated cylinder and ethanol after removing the scaffold, w_s the weight of the scaffold and p_e the density of absolute ethanol used in the analysis.

2. 3. 1. DSC Analysis

Differential scanning calorimetry (HP DSC 1, Mettler Toledo) was performed on pure PCL (M_w = 10 000, 60 000 g/mol) and on the prepared porous scaffolds to confirm the composition of PCL and CS and to define the percentage of crystallinity. Samples were placed in sealed aluminium pans. Measurements were held at ambient pressure at a temperature range from 25 °C to 600 °C with a temperature rate of 10 °C/min.

Based on the DSC curves, the melting temperature (T_m), heat of fusion (ΔH_m) and crystallinity of the samples were determined. The crystallinity of the PCL fracture (X_c) in the samples was calculated with equation (2) [15]:

$$X_c = \frac{\Delta H_m}{\Delta H_m^\circ \cdot w} \times 100 \qquad (2)$$

where ΔH_m is the specific melting enthalpy of the sample, ΔH_m° is the melting enthalpy of 100% crystalline poly (ε-caprolactone) (76.9 J/g), and w is the weight fraction of PCL in the blend.[16]

2. 3. 2. FTIR Spectra and ESEM Analysis

The FTIR spectra were recorded on a Fourier Transform infrared instrument (Bruker Platinum-ATR) equipped with OPUS Optik GmBH software in the range from 400 to 4400 cm^{-1} of wavelength.

Pores size for the resulting composite scaffolds generated in $scCO_2$ were determined using environmental scanning electron microscopy (ESEM) Quanta 200 3D (FEI Company, Hillsboro, OR), which allows observation of translation and non-sample without prior preparation (polymer materials, biological and medical samples).

2. 4. Protein Release Studies

Each of the porous PCL-CS composites incorporated with BSA was divided into three smaller units of 50 mg, to verify the uniformity of protein release. Each section was placed into 2 mL microcentrifuge tubes, containing 1 mL of phosphate buffer (PBS) with pH 7.4. In order to simulate the conditions in the human body, the tubes were incubated at 37 °C. The amount of the released BSA was determined by the Bradford method.[17] First measurement was performed after 3 hours and second after 24 hours from the start of the study. Then, Bradford assay was repeated every few days. After each measurement, fresh PBS was added to the microcentrifuges containing parts of the composites.

3. Results and Discussion

Results for the characterization of prepared composite material using FTIR spectra, ESEM photo analysis, DSC analysis and finally protein release studies are presented in the following subsections.

3. 1. DSC Analysis

DSC analysis was performed on two pure PCLs with different molar masses (M_w = 10,000 and 60,000 g/mol) and on porous scaffolds after processing with CO_2 to confirm the composition formation of the mixture between PCL and CS. As seen in Table 1, the melting point of both composites was lower than the melting point of pure PCL.

Table 1. Melting temperatures and specific melting enthalpies of the samples.

Material	T_m (°C)	ΔH_m (J/g)
PCL 10,000	67.58	71.31
PCL 10,000 + 5% CS	62.88	65.17
PCL 60,000	73.04	66.62
PCL 60,000 + 5% CS	66.23	55.04

That coincides with the previously published results by She et al.[18], where the melting point of the composites was decreasing with the increase of the amount of CS in the mixture. PCL 10,000 based composite material has a higher crystallinity (89.2%) than the PCL 60,000 based composite (75.3%). Degradation of materials was observed at a temperature of approximately 420 °C, and a slight decrease in decomposition temperature of the composites can be obtained, compared to pure PCL.

3. 2. FTIR Analysis

The FTIR analysis for raw materials, pure PCL, CS, and other obtained composites was made. Figure 2 shows the spectra of raw materials, PCL (M_w = 10,000 g/mol), CS and the composite material. Figure 3 shows the spectra of pure PCL (M_w = 60,000 g/mol), CS and their composite. The characteristic peak of pure PCL that corresponds C=O stretching vibration of the carbonyl group in ester is at 1732 cm^{-1} for PCL (M_w = 10,000 g/mol) and at 1734 cm^{-1} for PCL (M_w = 60,000 g/mol). The spectra of pure CS shows a broad peak for the O-H stretch at 3408 cm^{-1}. The peak at 1656 cm^{-1} represents N-H stretching. Another peak for 1° amine in CS at 1076 cm^{-1} represents the C-N stretch. C=O stretching vibrations were detected in both composites, at 1735 cm^{-1} for the composite with PCL (M_w = 10,000 g/mol) and at 1734 cm^{-1} for the composite with PCL (M_w = 60,000 g/mol). In the blend of PCL and CS, interactions between the carbonyl groups of PCL and the hydroxyl and amine groups of CS can occur, which leads to the formation of ester and amide bonds. However, there are no major absorptions shifts of the characteristic functional groups to be seen when the spectra of pure PCL is compared to the spectra of the composites. This could indicate that no molecular interactions occurred between functional groups, a finding which corresponds to results from the previous studies.[19] Peaks in the range from 2850 cm^{-1} to 3000 cm^{-1} represent alkyl (sp^3 hybridization of C atoms) stretching vibrations in pure materials and in the composites. This could indicate that no molecular interactions occurred between functional groups, a finding that corresponds to results of Neves et al.[7] who have constructed composite materials by blending CS and PCL to make 3D fiber-mesh scaffolds for articular cartilage tissue repair. On the contrary, spectra in Wu et al.[19], where composites were made with layer-by-layer assembly technique, show

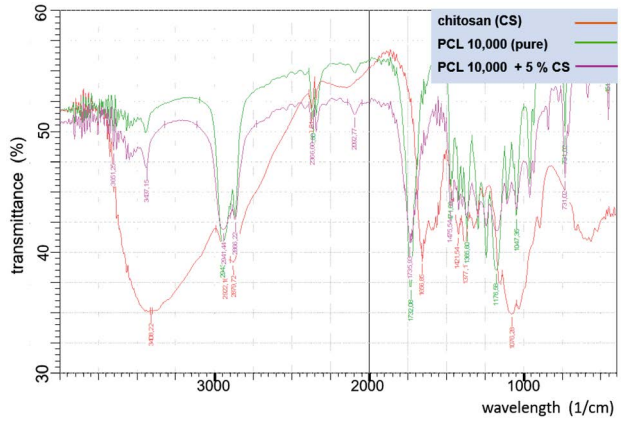

Figure 2. The FTIR spectra of raw materials (PCL (M_w = 10,000 g/mol) and CS) and the composite material.

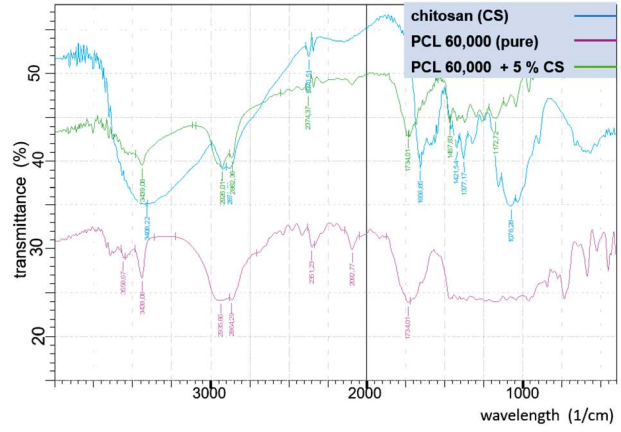

Figure 3. The FTIR spectra of raw materials (PCL (Mw = 60,000 g/mol) and CS) and the composite material.

some new strong peaks when spectrum of pure CS is compared to blend (PCL+CS). FTIR of PCL and CS composites, prepared by She et al.[18], have confirmed that the intensity of characteristic peaks increases with increase of CS content.

3. 3. ESEM Analysis and Porosity

Figure 4 (a and b) shows an ESEM micrograph of PCL-CS scaffolds foamed with $scCO_2$ at 12 MPa and 37 °C. ESEM analysis showed that resulting porous scaffolds have a closed cell structure, which enables better isolating properties because of its greater stiffness and toughness and lower permeability. The diameters of the pores vary from 50 to 130 μm when PCL 10,000 + 5% CS is used; and from 40 to 140 μm when PCL 60,000 + 5% CS is used, so they are considered to be macropores (Table 2).

For the pore growth period, a constant moderate depressurisation rate of 0.1 MPa/s was selected. At quicker depressurization rates more pores could be generated but with undesired smaller pore sizes.[20] Similarly, the lowest possible operating pressure of 12 MPa was used in order to

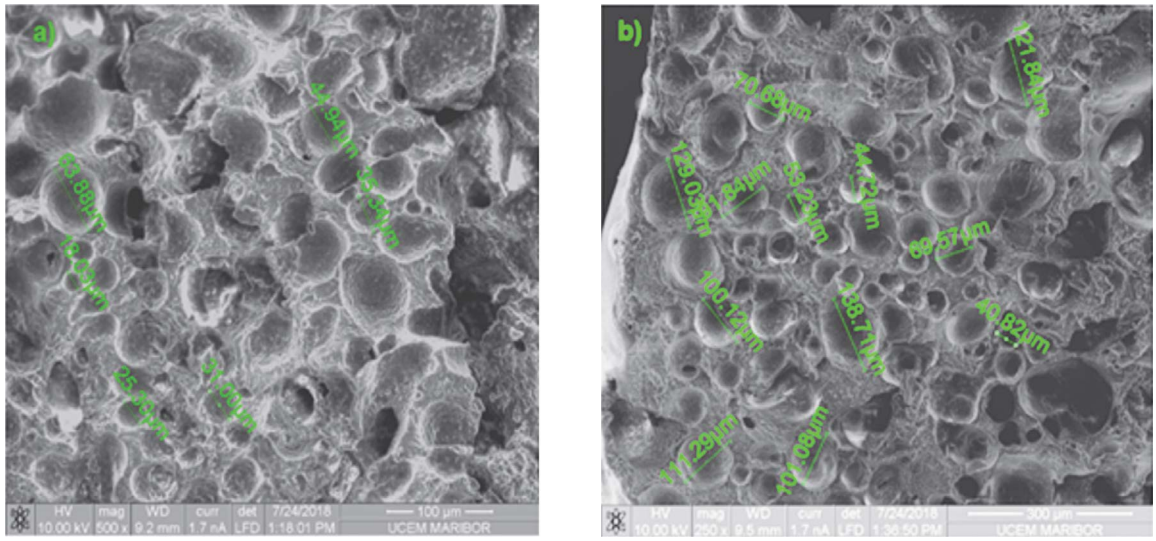

Figure 4. Environmental scanning electronic microscope image of a) PCL 10,000 + 5% CS and b) PCL 60,000 + 5% CS scaffolds.

Table 2. Preparation of biodegradable composite material at an applied pressure of 15 MPa and a temperature of 37 °C.

Composite	Molar mass (g/mol)	Depressurization rate (MPa/s)	Pore size interval (μm)	Porosity (%)
PCL 10,000 + 5% CS	10,000	0.1	50–130	80.1
PCL 60,000 + 5% CS	60,000	0.1	40–140	75.1

achieve the melting behavior of a polymer PCL in contact with $scCO_2$ at 37 °C. At selected supercritical conditions, PCL undergoes to partial or complete melting at 37 °C which is well below its melting point at ambient pressure.[21] Increasing pressure above the selected one results in higher rate of dissolved gas in biomaterial matrix that creates more nuclei and decreases the number of suitable pore sizes for tissue engineering.[22]

Porosity was calculated from. and was in both composites relatively high, above 75%. Biomaterials with a porosity greater than 70% and a size of pores around 100 μm are required to allow vascularization and tissue ingrowth.[23] Additionally, used supercritical foaming method generated high porous biomaterial scaffolds without toxic organic residuals and a waste of the materials.[24] Supercritical foaming method can be easily combined with other scaffold fabrication techniques like salt leaching, breath figure method and thermal induced phase method to obtain better pore interconnectivity and higher porosity.[25]

3. 4. Protein Release Monitoring

Total protein release monitoring was assessed for the PCL 10,000 + 5% CS and PCL 60,000 + 5% CS scaffolds by dividing each of them into three equal parts. The influence of molecular mass of PCL and time of protein release from composite polymers on total concentration of released BSA was studied. As presented in Figure 5, BSA loaded scaffolds showed two-stage release profiles. Larger concentrations of protein were released in the first few days from both investigated scaffolds, and then release of protein was constant, since the total protein concentration linearly increased with increase in release time. The main share of the protein from PCL–based scaffolds was released within the first 16 days. After that time, concentrations of protein in PBS solutions were zero or negligibly small, regardless of the tested composite. Higher total protein release was observed for the scaffold PCL 10,000 + 5% CS compared to the scaffold PCL 60,000 + 5% CS. This can be related to scaffold porosity, which is approximately 5% higher in the

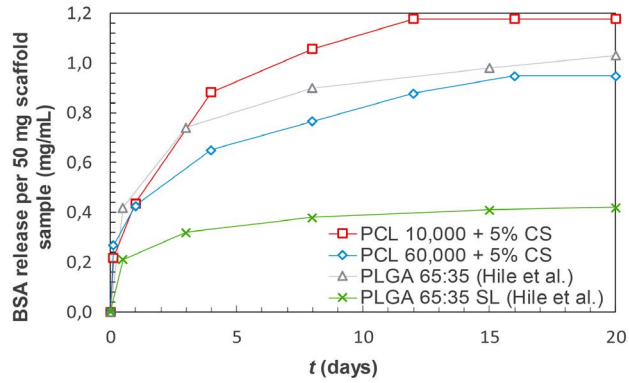

Figure 5. Total concentration of released BSA from PCL 10,000 + 5% CS and PCL 60,000 + 5% CS scaffolds vs. time of release, compared to the literature data.[21]

case of PCL 10,000 + 5% CS. With high porosity, the lightly trapped BSA in the micropores can be easily released.[26] Similar controlled release protein patterns were observed when BSA and basic fibroblast growth factor (bFGF) was encapsulated in poly(lactic-co-glycolic) acid (PLGA 65:35) generated in $scCO_2$.[27] The overall release rates from the scaffolds foamed with CO_2 were up to twice as high compared to release patterns of PLGA 65:35 by the salt leaching method. This can be related to protein loss due to the distilled water required for salt leaching.[28]

The BSA release was normalized to the initial protein entrapped in the scaffold, as shown in Figure 6. At the beginning, the release of proteins follows the same curve for both tested scaffolds and after 4 days of protein release, the PCL 10,000 + 5% CS shows better release profile, which

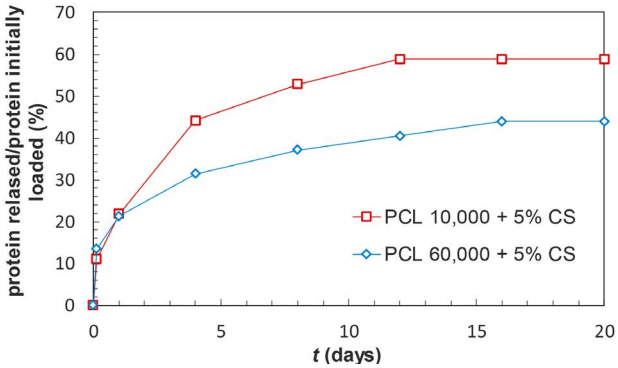

Figure 6. Total protein release normalized to the initial protein entrapped in the scaffold (for PCL 10,000 + 5% CS and PCL 60,000 + 5% CS) vs. time of release.

can be attributed to better porosity of the material. 58.8% of the protein was released from the composite with PCL (M_w = 10,000 g/mol) and 43.9% from composite with PCL (M_w = 60,000 g/mol) after 16 or 20 days of protein release testing.

4. Conclusion

Porous PCL-CS composite scaffolds with entrapped BSA were generated in $scCO_2$ as constructs for tissue engineering. Before the protein release studies, scaffolds were prepared for characterization of the composite material without incorporated BSA. DSC analysis confirmed the miscibility of the blend with a decrease in the melting points of the composites, compared to pure PCL. ESEM analysis showed that the resulting porous scaffolds have a closed cell structure that yields better isolating properties because of higher toughness and lower permeability.

When used as a model protein loaded into scaffolds, BSA showed two-stage release profiles. Larger concentrations of protein were released in the first few days in both investigated scaffolds. After 16 to 20 days of protein release testing, 58.8% of the protein was released from composite with PCL (M_w = 10,000 g/mol) and 43.9% from composite with PCL (M_w = 60,000 g/mol). The ability to simply incorporate and release thermolabile proteins at a controlled rate demonstrates the potential for using $scCO_2$ as a blowing agent for creating scaffolds and opens up the frontier for investigating encapsulation of healing agents and therapeutic enzymes for tissue engineering applications.

Table 3. Concentrations of protein, released from three equal parts of scaffolds (PCL 10,000 + 5% CS and PCL 60,000 + 5% CS).

Time (days)	Protein concentration in scaffold part 1 (mg/mL)	Protein concentration in scaffold part 2 (mg/mL)	Protein concentration in scaffold part 3 (mg/mL	Average concentration (mg/mL)	Total roteinp release (mg/mL)
PCL 10,000 + 5% CS					
0	0	0	0	0	0
0.125	0.249	0.204	0.205	0.219	0.219
1	0.169	0.162	0.320	0.217	0.436
4	0.113	0.680	0.550	0.448	0.883
8	0.106	0.291	0.121	0.173	1.056
12	0.122	0.144	0.096	0.121	1.177
16	0	0	0	0	1.177
20	0	0	0	0	1.177
PCL 60,000 + 5% CS					
0	0	0	0	0	0
0.125	0.385	0.118	0.302	0.268	0.268
1	0.090	0.103	0.281	0.158	0.426
4	0.123	0.398	0.152	0.225	0.651
8	0.108	0.115	0.121	0.115	0.765
12	0.018	0.079	0.080	0.113	0.878
16	0.060	0.068	0.083	0.070	0.949
20	0	0	0	0	0.949

5. Acknowledgement

The authors would like to acknowledge the Slovenian Research Agency (ARRS) for financing this research within the frame of program P2-0046 (Separation Processes and Production Design).

6. References

1. Y. Wan, H. Wu, X.Cao, S. Dalai, *Polym. Degrad. Stab.* **2008**, *93*, 1736–1741. **DOI:**10.1016/j.polymdegradstab.2008.08.001
2. H.-Y. Cheung, K-T. Lau, T.-P. Lu, D. Hui, *Composites, Part B.* **2007**, *38*, 291–300. **DOI:**10.1016/j.compositesb.2006.06.014
3. M. Leitgeb, K. Heržič, G. Hojnik Podrepšek, A. Hojski, A. Crnjac, Ž. Knez, *Acta Chim. Slov*. **2014**, *61*, 145–152.
4. S. Kovačič, N. B. Matsko, G. Ferk, C. Slugovc, *Acta Chim. Slov*. 2014, *61*, 208–214.
5. B. Dariš, P. Ferk, E. Markočič, Ž. Knez, *Acta Medi. Bio.* **2016**, *9*, 42–48.
6. R. M. Jin, N. Sultana, S. Baba, S. Hamdan, A. F. Ismail, *J. Nanomater*. **2015**, *2015*. **DOI:**10.1155/2015/357372
7. S. C. Neves, L. S. Teixeira Moreira, L. Moroni, R. L. Reis, C. A. Van Blitterswijk, N. M. Alves, M. Karperien, J. F. Mano, *Biomaterials*. **2011**, *32*, 1068–1079. **DOI:**10.1016/j.biomaterials.2010.09.073
8. M. Whitaker, R. Quirk, S. Howdle, K. Shakesheff, *J. Pharm. Pharmacol*. **2001**, *53*, 1427–1437. **DOI:**10.1211/0022357011777963
9. M. Škerget, Ž. Knez, *Acta Chim. Slov*. **2007**, *54*, 688–692.
10. E. Markočič, M. Škerget, Ž. Knez, *Ind. Eng. Chem. Res*. **2013**, *52*, 15594–15601. **DOI:**10.1021/ie402256a
11. S. M. Howdle, M. S. Watson, M. J. Whitaker, V. K. Popov, M. C. Davies, F. S. Mandel, J. D. Wang, K. M. Shakesheff, *Chem. Commun*. **2001**, 109–110. **DOI:**10.1039/b008188o
12. A. Salerno, J. Saurina, C. Domingo, *Int. J. Pharm*. **2015**, *496*, 654–663. **DOI:**10.1016/j.ijpharm.2015.11.012
13. G. Kravanja, M. K. Hrnčič, M. Škerget, Ž. Knez, *J. Supercrit. Fluids*. **2016**, *108*, 45–55. **DOI:**10.1016/j.supflu.2015.10.013
14. J. Yang, G. Shi, J. Bei, S. Wang, Y. Cao, Q. Shang, G. Yang, W. Wang, *J. Biomed. Mater. Res*. **2002**, *62*, 438–446. **DOI:**10.1002/jbm.10318
15. A. R. C. Duarte, J. F. Mano, R. L. Reis, *Polym. Degrad. Stab*. **2010**, *95*, 2110–2117. **DOI:**10.1016/j.polymdegradstab.2010.06.020
16. E. de Paz, A. n. Martín, S. Rodríguez-Rojo, J.Herreras, M. a. J.Cocero, *J. Chem. Eng. Data*. **2010**, *55*, 2781–2785. **DOI:**10.1021/je900997t
17. Kruger, N. J. in The protein protocols handbook, Springer, 2009, pp. 17–24. **DOI:**10.1007/978-1-59745-198-7_4
18. H. She, X. Xiao, R.Liu, *J. Mater. Sci*. **2007**, *42*, 8113–8119. **DOI:**10.1007/s10853-007-1706-7
19. H. Wu, Y. Wan, X. Cao, S. Dalai, S. Wang, S. Zhang, *Matter. Lett*. **2008**, 62, 2733–2736. **DOI:**10.1016/j.matlet.2008.01.029
20. V. N. Malheiro, S. G. Caridade, N. M. Alves, J. F. Mano, *Acta Biomater*. **2010**, *6*, 418–428. **DOI:**10.1016/j.actbio.2009.07.012
21. L. J. M. Jacobs, M. F. Kemmere, J. T. F. Keurentjes, *Green Chem*. **2008,** 10.7, 731–738. **DOI:**10.1039/b801895b
22. L. J. White, V. Hutter, H. Tai, S. M. Howdle, K. M. Shakesheff, *Acta Biomater*. **2012**, 8.1, 61–71. **DOI:**10.1016/j.actbio.2011.07.032
23. A. Salerno, S. Zeppetelli, E. Di Maio, S. Iannace, P. A. Netti, *Macromol. Rapid Commun*. **2011**, *32*(15), 1150–1156. **DOI:**10.1002/marc.201100119
24. M. A. Fanovich, J. Ivanovic, D. Misic, M. V. Alvarez, P. Jaeger, I. Zizovic, R. Eggers, *The J. Supercrit. Fluids.* **2013,** 78, 42–53. **DOI:**10.1016/j.supflu.2013.03.017
25. L. D. Gomez, A. Concheiro. C. A. Lorenzo, C. A. G. González, *Carbohydr. Polym*. **2016,** 142, 282–292. **DOI:**10.1016/j.ijpharm.2017.05.038
26. K. Zhang, Y. Wang, J. Jiang, X. Wang, J. Hou, S. Sun, Q. Li. *J. Mater. Sci*. **2019,** 54, pp 5112–5126. **DOI**: 1https://doi.org/10.1007/s10853-018-3166-7
27. H. Nie, S. T. Khew, L. Y. Lee, K. L. Poh, Y. W. Tong, C.-H. Wang, *J. Controlled Release*. **2009**, 138, 64–70. **DOI:**10.1016/j.jconrel.2009.04.027
28. D. D. Hile, M. L. Amirpour, A. Akgerman, M. V. Pishko, *J. Controlled Release*. **2000**, 66, 177–185. **DOI:**10.1016/S0168-3659(99)00268-0
29. S. B. Lee, Y. H. Kim, M. S. Chong, S. H. Hong, Y. M.Lee, *Biomaterials*. **2005**, 26, 1961–1968. **DOI:**10.1016/j.biomaterials.2004.06.032

Povzetek

Z namenom študija sproščanja proteina BSA iz kompozitnega materiala, smo pripravili s superkritičnim CO_2 porozne pene iz polikaprolaktona in hitozana, ki bi bile potencialno uporabne v tkivnem inženirstvu. Emulzijo, ki sestoji iz polimera, topila in puferne raztopine s proteinom smo nasitili s superkritičnim CO_2 pri 12 MPa in 37 °C in nato z odprtjem izhodnega ventila hitro zmanjšali tlak, ki je povzročil nukleacijo in nastanek poroznega kompozitnega materiala. Kontrolirano sproščanje proteina iz biorazgradljivih pen polikaprolaktona in 5 % hitozana (w/w) smo merili z Bradfordovo metodo za določevanje proteinov. Po 16 do 20 dneh sproščanja se je skupno izločilo iz kompozita s PCL (M_w=10,000 g/mol) 58.8 % proteina in iz kompozita s PCL (M_w = 60,000 g/mol) 43 %. Preliminarno smo izvedli študije za karakterizacijo pripravljenih kompozitnih biomaterialov z uporabo FTIR spektrov, ESEM foto analize in DSC analize.

DOI: 10.17344/acsi.2018.4841 *Acta Chim. Slov.* **2019,** *66,* 344–350

Scientific paper

Synthesis and Biological Evaluation of Some Novel S-β-D-Glucosides of 4-Amino-5-alkyl-1,2,4-triazole-3-thiones Derivatives

Anila Rahimi Aghkand,[1] Karim Akbari Dilmaghani,[1,*] Zahra Dono Ghezelbash[1] and Behvar Asghari[2]

[1] *Department of Organic Chemistry, Faculty of Chemistry, Urmia University, Urmia, 57159, Iran*

[2] *Department of Horticultural Sciences Engineering, Faculty of Agriculture and Natural Resources, Imam Khomeini International University, Qazvin, Iran*

* *Corresponding author: E-mail: k.adilmaghani@urmia.ac.ir*
Tel: (+98)914-443-1392. Fax: (+98)44-357153-165

Received: 11-10-2018

Abstract

A novel series of 3-S-β-D-glucosides-4-arylideneamino-5-alkyl-1,2,4-triazoles were designed and synthesized by reaction of 4-amino-5-alkyl-4H-1,2,4triazole-3-thiol Schiff bases and 2,3,4,6-tetra-O-acetyl-α-D-glucopyranosyl bromide. The structures of the target compounds have been characterized by ^{1}H NMR, ^{13}C NMR, FT-IR, and Microanalyses. All the newly synthesized compounds have been screened for their *in vitro* antibacterial and antifungal activities against two Gram-positive bacteria [*Bacillus cereus* (PTCC 1015) and *Staphylococcus aureus* (ATCC 25923)], two Gram-negative bacteria [*Pseudomonas aeruginosa* (ATCC 27853) and *Escherichia coli* (PTCC 1399) and two fungi [*Aspergillus niger* (PTCC 5012) and *Candida albicans* (PTCC 5027)].

Keywords: 4-amino-5-alkyl-4H-1,2,4-triazole-3-thiol; acetobromoglucose; thiocarbohydrazide; antimicrobial activity; antifungal activity; schiff base

1. Introduction

Antibiotics are drugs used for treating infection caused by microorganism such as bacteria or fungi and antibiotic resistance is the ability of microorganism to stand the effect of antibiotic. The resistance of infective bacteria to present antibiotics remains a clinical obstacle in the chemotrapy of many cancers to overcome the rapid development of drug resistance, new agents should preferably have chemical characteristics that clearly differ from those of existing agents. Thus led to the design and synthesize the new antimicrobial agents. 1,2,4-Triazole and its derivatives are an important class of compounds which possess diverse biological activities including anti-microbial,[1,2] antibacterial,[3,4] antifungal,[5,6] anti-inflammatory,[7] insecticidal,[8] anticonvulsant,[9,10] antitumor activity,[11] anti HIV activity,[12,13] hypoglycemic[14] and anticonvulsant.[15,16] Triadimefon and fluconazole which exhibits excellent fungicidal activities possessing 1,2,4-triazole nucleus.[17,18]

Compounds containing an azomethine group known as Schiff bases and are formed by the condensation of a primary amine with a carbonyl compound. Schiff bases attract much interest due to their synthetic availability along with antibacterial[19–22] and antitumor[23] properties.

The synthesis and investigation of biological activity of 1,2,4-triazole glycosides have been stimulated by the finding that Ribavirin, β-D-ribofuranosyl-1,2,4-triazole-3-carboxamide, as potent drug against DNA and RNA viruses.[24]

Moreover, sulfur-containing heterocycles represent an important group of sulfur compounds that are promising for use in practical applications. Therefore, it is interesting to report the synthesis of a new series of compounds in which the glycosyl moieties have been used as carriers for the heterocycles having the oxadiazole or triazole ring. It has been reported that the attachment of carbohydrate moieties to the 1,2,4-triazole nucleus through a thioglycosidic linkage enhances its antimicrobial activity.[25]

Some novel S-β-D-glucosides of 5-aryl-1,2,4-triazole-3-thiones derivatives exhibited antibacterial and an-

tifungal activities.[26] In our previous work,[27,28] we reported the synthesis and antibacterial properties of new series of thioglycoside derivatives of 1,2,4-triazole moieties.

The above facts and our interest on design of potent antibacterial agents with 1,3,4-oxadiazoles and 1,2,4-triazole moieties, promoted us to synthesis novel substituted thioglycosides by reaction of α-D acetobromoglucose **(6)** with 4-amino-5-alkyl-4H-1,2,4-triazole-3-thiol Schiff bases **5(a–g)**. The newly synthesized multicompounds **7(a–g)** are useful in probing biological activity such as antibacterial and antifungal effects.

1. 1. Antimicrobial Activity

1. 1. 1. Bacterial and Fungal Strains

Two Gram-positive bacteria *Bacillus cereus* (PTCC 1015) and *Staphylococcus aureus* (ATCC 25923)], two Gram-negative bacteria [*Pseudomonas aeruginosa* (ATCC 27853) and *Escherichia coli* (PTCC 1399) and two fungi *Aspergillus niger* (PTCC 5012) and *Candida albicans* (PTCC 5027)] were used in antimicrobial assays. Microbial strains were obtained from the Pasteur Institute of Iran.

1. 2. Determination of Inhibition Zone

The agar disc diffusion method was used for antimicrobial activity determination of the compounds using a previously described standard method.[29] 100 µl of the tested microorganisms suspensions, adjusted to 106–108 CFU/mL were spread on the solid media plates. The compounds were dissolved in dimethyl sulphoxide and filtered by 0.45 µm Millipore filters for sterilization. The paper discs (6 mm in diameter) werm saturated with 10 µl of sample solution and placed on the inoculated agar. DMSO was used as the untreated control. These plates were incubated for 24 h at 37 °C for bacterial strains and 48 h at 30 °C for the yeasts. The diameter of inhibition zone (IZ) was measured in mm (including 6 mm diameter of paper disc). Gentamicin (10 µg/disc) and nystatin (50 IU) were used as positive control in antibacterial and antifungal assays, respectively. Analyses were performed in triplicate and expressed as average values ± SEM.

1. 3. Determination of Minimum Inhibitory Concentrations (MICs)

The MIC values of the compounds were determined using the method of micro-well dilution assay.[30–31] Briefly, the inoculants of the microbial strains were prepared from freshly cultured microorganisms that were adjusted to 0.5 McFarland standard turbidity. Serial dilutions of the compounds and standard samples were made in a concentration range from 5 to 1000 µg/mL in 96-well plates, containing Mueller-Hinton broth for bacterial strains and Sabouraud dextrose broth for yeast. Gentamicin and nystatin were used as standard drugs in identical conditions to test materials. The plates were covered with sterile plate sealers and then incubated at 37 °C under normal atmospheric condition for 24 h for bacterial strains and at 30 °C for 48 h for yeasts. The MIC values were considered as the minimum concentration of the sample which could inhibit the growth of microorganisms.

2. Result and Discussion

4-amino-5-alkyl-4H-1,2,4-triazole-3-thioles **3(a-c)** were prepared by the condensation of aliphatic carboxylic acids **2(a–c)** with thiocarbohydrazide. The reaction is improved by using carboxylic acids at thiocarbohydrazide melting point. This reaction is the selective method for the preparation of 4-amino-5-aryl/alkyl-4H-1,2,4-triazole-3-thioles[32] (Scheme 1).

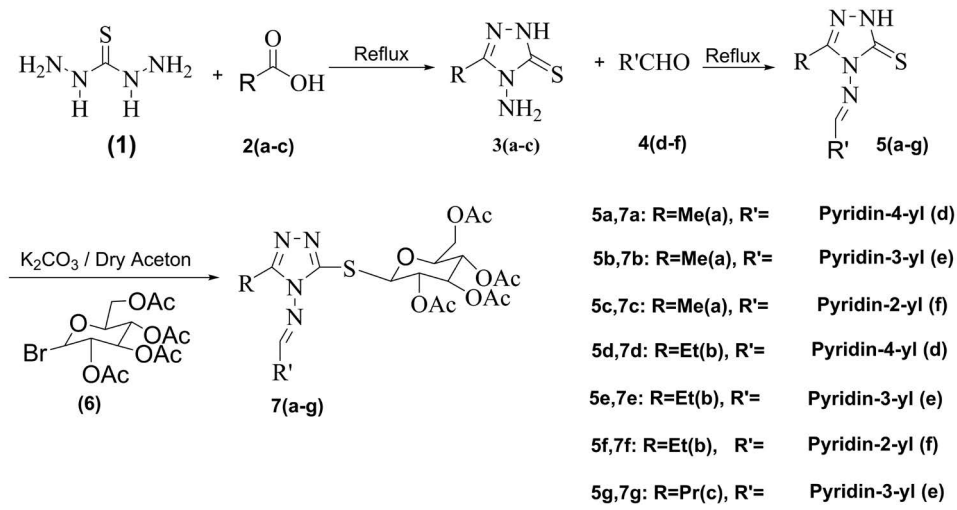

Scheme1. Synthesis of 3-S-β-D-glucosides-4-arylideneamino-5-alkyl-1,2,4-triazoles.

Table1. Diameter of inhibition zone (IZ) values of the compounds against 2 gram (+) bacteria, 2 gram (–) bacteria and 2 fungi (μg/mL)

	5a	7a	5b	7b	5c	7c	5d	7d	5e	7e	5f	7f	5g	7g	Gentamicin	Nystatin
Escherichia coli ***gram(–)***	–	6.7	–	6.3	–	6.7	–	–	–	6.1	–	–	–	7.2	23.4	–
Pseudomonas aeruginosa ***gram(–)***	–	6.6	–	–	–	6.5	–	6.5	–	–	–	–	–	6.7	27.3	–
Staphylococcus aureus ***gram(+)***	6.7	12.4	6.3	14.3	6.4	11.4	–	13.1	6.5	9.1	–	8.4	–	9.3	28.5	–
Bacillus cereus ***gram(+)***	6.4	14.7	7.1	15.6	6.5	9.8	6.2	13.9	6.6	8.2	–	10.7	–	9.5	31.6	–
Aspergillus niger ***fungi***	7.1	15.7	8.7	13.4	7.5	11.2	6.4	10.2	8.2	12.1	7.3	10.1	6.8	9.7	–	22.6
Candida albicans ***fungi***	6.3	17.5	7.9	14.1	7.3	10.1	6.3	14.2	8.7	12.4	6.6	12.7	6.4	11.3	–	26.8

Schiff bases **5(a–g)** have been synthesized by a reaction of 3-alkyl-4-amino-1,2,4-triazole-5-thione **3(a–c)** with pyridine aldehydes **4(d–f)** in absolute ethanol as solvent in presence of glacial acetic acid as a catalyst. The IR spectra of the compounds **3(a–c)** showed the absorptions at 3100, 1330 cm^{-1} which were attributed to N-H and C=S stretching vibration and a strong absorption at 1580 cm^{-1} which was assigned to the C=N stretching vibration. The ^1H NMR spectra showed a singlet signal at about 10 ppm due to (CH=N) and the absence of the chemical shift of 4-NH_2 in the spectra of **3(a–c)** proving that the title Schiff bases **5(a–g)** were formed.

In our attempt to obtain *α*-acetobromoglucose **(6)** at the first step D-glucose were treated with acetic anhydride in pyridine at room temperature gave 1,2,3,4,6-penta-*O*-acetyl-*β*-glucose and the anomeric bromination of this compound with hydrogen bromide in acetic acid gave 2,3,4,6-tetra-*O*-acetyl-*α*-glucopyranosyl bromide **(6)**.

The existence of thiol-thione tautomerism is known for the compounds **3(a–c)** and generally one forms is predominant.[34–37]

3-S-β-D-glucosides-4-arylideneamino-5-alkyl-1,2,4 -triazoles **7(a–g)** were synthesized by the reaction of 3-alkyl-4-amino-1,2,4-triazole-5-thione Schiff bases **5(a–g)** and the peracetylated *β*-pyranosyl bromide **(6)** in the presence of potassium carbonate as a weak base in dry acetone. (Scheme 1).

Anomeric β-configurations of the *S*-linked glycosides **7(a–g)** were supported by their ^1H NMR data. The chemical shifts of the anomeric proton signals of thioglycosides revealed around δ (6.20) with a large coupling constant $J_{1,2}$ values of (9.3) Hz which consistent with the reported data for S-β-D glycosides.

The result of the antibacterial and antifungal activity shows that all the compounds have lesser activity than corresponding standard compounds and the target compounds exhibited better antifungal activity than anti-bacterial activity. However the anti-bacterial results showed that against *Staphylococcus aureus* compounds **(7b)** and **(7d)**; against *Bacillus cereus* compounds **(7b)**, **(7a)** and **(7d)**; have comparable activity with *Gentamicin* as Standard. The antifungal study results revealed that against *Aspergillus niger* compounds **(7a)**

(7b) and **(7e)**; against *Candida albicans* **(7a)**, **(7b)** and **(7d)** have comparable activity with *Nystatin* as standard. Though compound **(7b)** was found to have the highest activity against *Bacillus cereus* and compound **(7a)** was found to have the highest activity against *Candida albicans* among all the tested compounds.

3. Experimental

3. 1. General

The melting points of all compounds were recorded on a Philip Harris C4954718 apparatus without calibration.IR and ^1H- and ^{13}C-NMR spectra were recorded on Thermo Nicolet Nexus 670 FT-IR and Bruker Avance 300 MHz spectrometers, respectively. Thin layer chromatography (TLC) analyses were carried out on silica gel plates. All chemicals were purchased from Merck (Tehran, Iran) and used as received by standard procedures. All of the instruments, chemicals and solvents were dried according to standard methods. Freshly distilled solvents were used throughout, and anhydrous solvents were dried according to the method reported by Perrin and Armarego.[38] Microanalyses were performed on a Leco Analyzer 932.

3. 2. General Procedure of Synthesis of 4-amino-5-alkyl-4H-1,2,4-triazole-3-thiol 3(a–c):

A mixture of thiocarbohydrazide (0.01 mol) and carboxylic acid (0.01 mol) was heated until it melted. The mixture was consistently refluxed for 40 min. The product obtained on cooling was treated with a sodium bicarbonate solution to neutralize the unreacted acid if any. The product was then washed with water and collected by filtration. The solid product was recrystallized from a distilled water.[32]

General Procedure for Synthesis of Schiff bases of (E) -5-alkyl-4-((pyridin-3-ylmethylene) amino)-2,4-dihydro-3H-1,2,4-triazole-3-thione 5(a-g):

To a suspension of substituted pyridine carboxaldehyde **4(d–f)** (0.2 mol) in ethanol (1 mL), an equimolar amount of corresponding 4-amino-5-alkyl-4H-1,2,4-triazole-3-thiol (0.1mol) **3(a–c)** was added. The suspension was heated until a clear solution was obtained. Then few drops of concentrated sulfuric acid were added, and the solution was heated for 6 hrs on a water bath, the precipitate solid was filtered off and recrystallized from in ethanol.[33]

General Procedure for Synthesis of 2,3,4,6-tetra-O-acetyl-α-D-glucopyranosyl bromide (6):

It was also prepared according to the literature procedure.[39]

General Procedure for Synthesis of 3-S-β-D-glucosides-4-arylideneamino-5-alkyl-1,2,4-triazoles (7a–g):

A mixture of compound **5(a–g)** (1 mmol) and potassium carbonate (1 mmol, 0.138 g) in dry acetone (25 mL) and 2 drops of Dimethylformamide were stirred for 1 hrs, then glycosyl bromide **(6)** (1.2 mmol, 0.410 g) was added. Stirring was continued overnight, and then the reaction mixture was heated under reflux for 2–4 hrs. After cooling, the mixture was filtered, then the precipitate of the compound was submitted to column chromatography (SiO_2, EtOAc/hexane, 3:8).[27]

(E)-5-methyl-4-((pyridin-4-ylmethylene) amino)-2,4-dihydro-3H-1,2,4-triazole-3-thione (5a):

(Yellow crystals), (Yield% = 74) (0.32 g) m.p: 267–269 °C, FT-IR (KBr, υ cm^{-1}): 3042 (C-H, Ar), 2839 (CH_3), 1592 (C=N), 1278 (C=S) cm^{-1}, ^{1}H NMR (300 MHz, DMSO): δ (ppm), 2.36 (s, 3H, CH_3), 7.82 (d, *J*=5.1 Hz, 2H Pyridin) 8.75 (d, *J*=5.1Hz, 2H Pyridin) 10.32 (s, 1H, HC=N) 13.75 (s, 1H, NH). ^{13}C-NMR (75 MHz, $CDCl_3$): δ (ppm), 11.15, 122.32, 139.97, 149.27, 151.38, 161.78, 162.33

(E)-5-methyl-4-((pyridine-3-ylmethylene) amino)-2,4-dihydro-3H-1,2,4-triazole-3-thione (5b):

(Light Yellow crystals) (Yield% = 76) (0.83 gr), m.p: 239–241°C, FT-IR (KBr, υ cm^{-1}: 3061 (C-H Ar), 2852 (CH_3), 1590 (C=N), 1274 (C=S) cm^{-1}, ^{1}H NMR (300 MHz, DMSO): δ (ppm), 2.35 (s, 3H, CH_3), 7.53–7.57 (m, 1H, pyridine), 8.29 (d, *J*=7.8 Hz, 1H pyridine) 8.73 (d, *J*=4.5 Hz, 1H pyridine) 9 (s, 1H, pyridine) 10.19 (s, 1H, HC=N) 13.79 (s, 1H, NH). ^{13}C-NMR (75 MHz, $CDCl_3$): δ (ppm), 11.17, 124.71, 128.75, 135.34, 135.40, 149.05, 150.38, 153.36, 161.63.

(E)-5-methyl-4-((pyridin-2-ylmethylene) amino)-2,4-dihydro-3H-1,2,4-triazole-3-thione) (5c):

(Pale green crystals), m.p :194–196 °C (Yield% = 82) (0.18 g) FT-IR (KBr, υ cm^{-1}): 3104 (NH), 3066 (C-H Ar) 2934 (CH_3), 1586 (C=N), 1287 (C=S) cm^{-1}, ^{1}H NMR (300 MHz, DMSO): δ (ppm), 2.37 (s, 3H,CH_3) 7.56 (t, *J*=3.9, 1H, pyridine) 7.83 (t, *J*=7.5, 1H, pyridine) 8.14 (d, *J*=5.4 1H, Pyridine) 8.25 (d, *J*=4.8, 1H, Pyridin) 10.35 (s, 1H, HC=N) 13.79 (s, 1H, NH). ^{13}C-NMR (75 MHz, $CDCl_3$): δ (ppm), 10.87, 120.66, 127.64, 136.54, 138.66, 149.20, 151.44, 160.23, 161.74.

(E)-5-ethyl-4-((pyridin-4-ylmethylene) amino)-2,4-dihydro-3H-1,2,4-triazole-3-thione) (5d):

(Yellow crystals), (Yield% = 73) (0.17 g) m.p: 246–248 °C, FT-IR (KBr, υ cm^{-1}): 3041 (C-H Ar), 2973 (Et), 1591 (C=N), 1268 (C=S) cm^{-1}. ^{1}H NMR (300 MHz, DMSO): δ (ppm), 1.22(t, *J*=7.2, 3H, CH_3), 2.73–2.81(m, 2H, CH_2) 7.82 (d, *J*= 4.5 Hz, 2H pyridine) 8.76 (d, *J*=4.5 Hz, 2H pyridine) 10.34 (s, 1H, HC=N) 13.85 (s, 1H, NH).^{13}C-NMR (75 MHz, $CDCl_3$): δ (ppm), 11.34, 18.65, 121.23, 140.03, 150.21, 153.14, 160.71, 161.93.

(5e): ((E)-5-ethyl-4-((pyridin-3-ylmethylene) amino)-2,4-dihydro-3H-1,2,4-triazole-3-thione

(Yellow crystals), m.p:188–190 °C, (Yield% = 72) (0.08 g), FT-IR (KBr, υ cm^{-1}): 3097 (NH), 3048 (CH-Ar), 2975 (Et), 1583 (C=N), 1278 (C=S) cm^{-1}. ^{1}H NMR (300 MHz, DMSO): δ (ppm), 1.22(t, *J*=7.2, 3H, CH_3), 2.72–2.80 (m, 2H, CH_2) 7.56–7.60 (m, 1H, pyridine), 8.31 (d, *J*=6.6 Hz, 1H Pyridine) 8.76 (d, *J*=4.5 Hz, 1H pyridine) 9.02 (s, 1H, pyridine) 10.19 (s, 1H, HC=N) 14.81(s, 1H, NH). ^{13}C-NMR (75 MHz, $CDCl_3$): δ (ppm), 9.73, 18.66, 125.79, 128.78, 134.38, 136.47, 151.58, 152.01, 159.53, 161.82.

(E)-5-ethyl-4-((pyridin-2-ylmethylene) amino)-2,4-dihydro-3H-1,2,4-triazole-3-thione (5f):

(Brown crystals**),** m.p:168–170 °C, (Yield% = 86) (0.2 g**),** FT-IR (KBr, υ cm^{-1}): 3119 (NH), 3068 (C-H Ar), 2918 (Et), 1579 (C=N), 1285 (C=S) cm^{-1}. ^{1}H NMR (300 MHz, DMSO): δ (ppm), 1.23 (t, *J*=7.5, 3H, CH_3) 2.74–2.81 (m, 2H, CH_2) 7.56 (t, *J*=6.6, 1H, pyridine) 7.97 (t, *J*=6.9, 1H, pyridine) 8.13 (d, *J*=8.1, 1H, Pyridin) 8.73 (d, *J*=4.2, 1H, Pyridin) 10.35 (s, 1H, HC=N) 13.83 (s, 1H, NH). ^{13}C-NMR (75 MHz, $CDCl_3$): δ (ppm), 11.33, 18.71, 120.71, 122.88, 127.77, 136.74, 138.88, 149.57, 159.87, 162.02.

(E)-5-propyl-4-((pyridin-3-ylmethylene) amino)-2,4-dihydro-3H-1,2,4-triazole-3-thione (5g):

(Yellow crystals), (Yield% = 77) (0.38 gr) m.p:166–168°C, FT-IR (KBr, υ cm^{-1}): 3057 (CH-Ar), 1586 (C=N),

1278 (C=S) cm^{-1}. ^1H NMR (300 MHz, DMSO): δ (ppm), 0.94 (t, *J*=7.5, 3H, CH_3), 1.63–1.72 (m, 2H, CH_2) 2.73 (t, *J*=7.5, 2H, CH_2) 7.56–7.60 (m, 1H, pyridine), 8.31 (d, *J*=6.3 Hz, 1H pyridine) 8.76 (d, *J*=4.8 Hz, 1H pyridine) 9.02 (s, 1H, pyridine) 10.19 (s, 1H, HC=N) 13.81 (s, 1H, NH). ^{13}C-NMR (75 MHz, $CDCl_3$): δ (ppm), 13.87, 19.34, 26.75, 124.79, 128.78, 135.40, 151.72, 153.44, 159.66, 161.85, 162.33.

Synthesis of 1,2,3,4,6-penta-O-acetyl-α-D-glucopyranose: It was also prepared according to the literature procedure.[36] (Yield% = 68) (7.5 gr)(White precipitate)**,** FT-IR (KBr, υ cm^{-1}):1748, 1374, 1227, ^1H NMR (300 MHz, $CDCl_3$), δ: 2.01 (s, 3H, OAc), 2.03 (s, 3H, OAc), 2.08 (s, 3H, OAc), 2.11 (s, 3H, OAc), 2.18 (s, 3H, OAc), 3.82–3.85 (m, 1H, H-5), 4.08–4.12 (m, 1H, H-6a), 4.26–4.32 (m, 1H, H-6b), 5.09–5.28 (m, 3H, H-2, H-4, H-3), 5.71 (d, 1H, $J_{1,2}$ = 8.4, H-1). ^{13}C NMR (75 MHz, $CDCl_3$), δ: 20.55 (3C), 20.69, 20.80 (5 × $OCOCH_3$), 61.41 (C-6), 67.70 (C-4), 70.18 (C-2), 72.69 (C-3), 72.75 (C-5), 91.66 (C-1), 168.94, 169.23, 169.37, 170.08, 170.59 (5 × O<u>C</u>OCH_3).

Synthesis of 2,3,4,6-tetra-O-acetyl-α-D-glucopyranosyl bromide (6): It was also prepared according to the literature procedure.[39] White precipitate; 57% (1.2 g); FT-IR (KBr, υ cm^{-1}): 1745, 1377, 1236, 607. ^1H NMR (300 MHz, $CDCl_3$), δ: 2.03 (s, 3H, OAc), 2.05 (s, 3H, OAc), 2.10 (s, 6H, OAc), 4.12 (d, 1H, H-6a), 4.28–4.36 (m, 2H, H-6b, H-5), 4.81–4.86 (dd, 1H, $J_{1,2}$ = 3.9, $J_{2,3}$ = 9.9, H-2), 5.16 (t, 1H, H-4), 5.56 (t, 1H, H-3), 6.61 (d, 1H, $J_{1,2}$ = 3.9, H-1). ^{13}C NMR (75 MHz, $CDCl_3$), δ: 20.53, 20.60 (2C), 20.63 (4 × OCO<u>C</u>H_3), 60.93 (C-6), 67.15 (C-4), 70.14 (C-2), 70.58 (C-3), 72.12 (C-5), 86.54 (C-1), 169.44, 169.77, 169.82, 170.48 (4 × O<u>C</u>OCH_3).

Synthesis of 4-(pyridine-4-yl methylene-amino) -5-methyl-2-yl-3- (2,3,4,6-tetra-O- acetyl-β-D-glucopyranosyl Sulfonyl) -1,2,4-triazole (7a): yellow crystals 76% (1.24 g), m.p :74–76 °C; FT-IR (KBr, υ cm^{-1}): 2947 (C-H), 1753 (C=O), 1601 (HC=N), 1371 (CH_3), 1047, 1230 (C-O), ^1H NMR (300 MHz, $CDCl_3$): δ 1.94 (s, 3H, OAc), 2.04 (s, 3H, OAc), 2.07 (s, 3H, OAc), 2.09 (s, 3H, OAc), 2.49 (s, 3H, CH_3), 3.97–4 (m, 1H, H-6a), 4.15 (d, *J*=12.3 Hz, 1H, H-6b), 4.28–4.34 (m, 1H, H-5), 5.25 (t, *J*=9.9Hz, 1H, H-4), 5.42 (t, *J*=9.3 Hz, 1H, H-2), 5.74 (t, *J*=9.3 Hz, 1H, H-3), 6.21 (d, *J*=9.3 Hz, 1H, H-1), 7.70 (d, *J*= 4.8 Hz, 2H pyridine) 8.78 (d, *J*=4.5 Hz, 2H pyridine) 10.83 (s, 1H, HC=N). ^{13}C-NMR (75 MHz, $CDCl_3$): δ(PPM), 11.22, 20.57, 61.67, 67.73, 69.14, 73.61, 74.59, 81.28, 121.85, 139.95, 149.30, 150.65, 162.33, 164.04, 168.89, 169.35, 170.15, 170.61. Calcd: C, 50.27; H, 4.95; N, 12.74; S, 5.83%; Found: C, 50.37; H, 4.85; N, 12.94; S, 5.92%.

Synthesis of 4-(pyridine-3-yl methylene-amino) -5-methyl-2-yl-3- (2,3,4,6-tetra-O-acetyl-β-D-gluco pyranosyl Sulfonyl) -1,2,4-triazole (7b):

White crystals 73% (0.8 g), m.p: 68–70 °C; FT-IR (KBr, υ cm^{-1}): 2958 (C-H), 1752 (C=O), 1599 (HC=N), 1370 (CH_3), 1046, 1231 (C-O).^1H NMR (300 MHz, $CDCl_3$): δ 1.93 (s, 3H, OAc), 2.02 (s, 3H, OAc), 2.05 (s, 3H, OAc), 2.07 (s, 3H, OAc), 2.46 (s, 3H, CH_3), 3.96–4 (m, 1H, H-6a), 4.06–4.16 (m, 1H, H-6b), 4.27–4.32 (m, 1H, H-5), 5.24 (t, *J*=9.9 Hz, 1H, H-4), 5.40 (t, *J*=9.6 Hz, 1H, H-2), 5.72 (t, *J*=9.3 Hz, 1H, H-3), 6.20 (d, *J*=9.3 Hz, 1H, H-1), 7.40–7.44 (m, 1H, pyridine), 8.19 (d, *J*=7.8 Hz, 1H pyridine) 8.74 (d, *J*=3.9 Hz, 1H pyridine) 8.99 (s, 1H, pyridine) 10.68 (s, 1H, HC=N). ^{13}C-NMR (75 MHz, $CDCl_3$): δ (PPM), 11.27, 20.60, 61.64, 67.66, 69.10, 73.58, 74.50, 81.29, 123.92, 128.63, 134.80, 149.22, 152.94, 157.59, 163.90, 168.94, 169.38, 170.17, 170.65. Calcd: C, 50.27; H, 4.95; N, 12.74; S, 5.83 %; Found: C, 50.17; H, 4.82; N, 12.86; S, 5.98%.

(Synthesis of 4-(pyridine-2-yl methylene-amino) -5-methyl-2-yl-3- (2,3,4,6-tetra-O-acetyl-β-D-gluco pyranosyl Sulfonyl) -1,2,4-triazole (7c):

White crystals 76% (1.24 g), m.p: 105–107 °C; FT-IR (KBr, υ cm^{-1}): 2948 (C-HAr), 1752 (C=O), 1590 (HC=N), 1373 (CH_3), 1045, 1234 (C-O), (C-^1H NMR (300 MHz, $CDCl_3$): δ 1.94 (s, 3H, OAc), 2.03 (s, 3H, OAc), 2.06 (s, 3H, OAc), 2.09 (s, 3H, OAc), 2.48 (s, 3H, CH_3) 3.96–4.01 (m, 1H, H-6a), 4.12 (d, *J*=7.2 Hz, 1H, H-6b), 4.28–4.34 (m, 1H, H-5), 5.25 (t, *J*=9.9 Hz, 1H, H-4), 5.41 (t, *J*=9.3 Hz, 1H, H-2), 5.73 (t, *J*=9.3 Hz, 1H, H-3), 6.23 (d, *J*=9.3 Hz, 1H, H-1), 7.40–7.44 (m,1H, Pyridin) 7.83 (t, *J*=7.5 Hz, 1H, Pyridin) 8.09 (d, *J*=7.8 Hz, 1H, Pyridin) 8.75 (d, *J*=4.8 Hz, 1H, Pyridin), 10.63 (s, 1H, CH=N). ^{13}C-NMR (75 MHz, $CDCl_3$): δ(PPM), 11.26, 20.58, 61.70, 67.75, 69.20, 73.59, 74.52, 81.37, 121.96, 125.91, 136.74, 149.13, 150.15, 151.92, 162.33, 164.12, 168.97, 169.39, 170.13, 170.65. Calcd: C, 50.27; H, 4.95; N, 12.74; S, 5.83%; Found: C, 50.17; H, 4.82; N, 12.86; S, 5.98%.

Synthesis of 4-(pyridine-4-yl methylene-amino) -5-ethyl-2-yl-3- (2,3,4,6-tetra-O-acetyl-β-D-gluco pyranosyl Sulfonyl) -1,2,4-triazole (7d):

Orange crystals 77% (0.085 g), m.p: 59–61 °C; FT-IR (KBr, υ cm^{-1}): 2934 (C-H), 1754 (C=O), 1594 (HC=N), 1372 (CH_3), 1042, 1228 (C-O)**,** ^1H NMR (300 MHz, $CDCl_3$): δ 1.92 (s, 3H, OAc), 2.03 (s, 3H, OAc), 2.06 (s, 3H, OAc), 2.08 (s, 3H, OAc), 1.35 (t, *J*=7.2Hz, 3H, CH_3), 2.83–2.87 (m, 2H, CH_2) 3.97–3.99 (m, 1H, H-6a), 4.16 (d, *J*=12 Hz, 1H, H-6b), 4.28–4.33 (m, 1H, H-5), 5.26 (t, *J*=9.6 Hz, 1H, H-4), 5.41 (t, *J*=9.6 Hz, 1H, H-2), 5.79 (t, *J*=9 Hz, 1H, H-3), 6.17 (d, *J*=9.3 Hz, 1H, H-1),7.69 (d, *J*=4.5 Hz, 2H pyridine), 8.77 (d, *J*= 3.9 Hz, 2H pyridine) 10.81 (s, 1H, HC=N), ^{13}C-NMR (75 MHz, $CDCl_3$): δ(PPM), 10.11, 18.92, 20.60, 61.64, 67.71, 68.98, 73.65, 74.50, 81.37, 121.86, 140.03, 150.64, 153.15, 155.90, 164.11, 168.76, 169.40, 170.20, 170.66. Calcd: C, 51.15; H, 5.19; N, 12.43; S, 5.69%; Found: C, 51.01; H, 5.21; N, 12.53; S, 5.73%.

Synthesis of 4-(pyridine-3-yl methylene-amino)-5-ethyl-2-yl-3-(2,3,4,6-tetra-O-acetyl-β-D-gluco pyranosyl Sulfonyl) -1,2,4-triazole (7e):

White crystals, 78% (0.43 g), m.p: 105–107 °C, FT-IR (KBr, υ cm^{-1}): 2947 (C-H), 1753 (C=O), 1591 (HC=N), 1371 (CH_3), 1042, 1229 (C-O) ,^{1}H NMR (300 MHz, $CDCl_3$): δ 1.92 (s, 3H, OAc), 2.03 (s, 3H, OAc), 2.06 (s, 3H, OAc), 2.08 (s, 3H, OAc), 1.34 (t, *J*=7.2Hz, 3H, CH_3), 2.79–2.88 (m, 2H, CH_2), 3.97–4.01 (m, 1H, H-6a), 4.17(d, *J*=12.6, 1H, H-6b), 4.28–4.33 (m, 1H, H-5), 5.26 (t, *J*=9.9 Hz, 1H, H-4), 5.41 (t, *J*=9.3 Hz, 1H, H-2), 5.79 (t, *J*=9.3 Hz, 1H, H-3), 6.18 (d, *J*=9.3 Hz, 1H, H-1),7.41–7.45 (m, 1H, pyridine), 8.18 (d, *J*=7.8 Hz, 1H pyridine) 8.75 (d, *J*=4.5 Hz, 1H pyridine) 9.01 (s, 1H, pyridine) 10.69 (s, 1H, HC=N). ^{13}C-NMR (75 MHz, $CDCl_3$): δ (PPM), 10.11, 18.93, 20.60, 61.65, 67.71, 68.99, 73.66, 74.46, 81.44, 123.92, 128.70, 134.79, 149.81, 153.05, 158.26, 164.02, 168.76, 169.40, 170.18, 170.66. Calcd: C, 51.15; H, 5.19; N, 12.43; S, 5.69%; Found: C, 51.07; H, 5.21; N, 12.60; S, 5.61%.

Synthesis of 4-(pyridine-2-yl methylene-amino) -5-ethyl-2-yl-3- (2,3,4,6-tetraO-acetyl-β-D-gluco pyranosyl Sulfonyl) -1,2,4-triazole (7f):

yellow crystals 79% (0.87 g), m.p :55–57 °C; FT-IR (KBr, υ cm^{-1}): 2974 (C-H), 1753 (C=O), 1586 (HC=N), 1372 (CH_3), 1044, 1229 (C-O). ^{1}H NMR (300 MHz, $CDCl_3$): δ 1.92 (s, 3H, OAc), 2.02 (s, 3H, OAc), 2.06 (s, 3H, OAc), 2.08 (s, 3H, OAc), 1.33 (t, *J*=7.2 Hz, 3H, CH_3), 2.77–2.89 (m, 2H, CH_2), 3.96–4 (m, 1H, H-6a), 4.16(d, *J*=11.4 Hz, 1H, H-6b), 4.27–4.33 (m, 1H, H-5), 5.25 (t, *J*=9.6 Hz, 1H, H-4), 5.40 (t, *J*=9.3 Hz, 1H, H-2), 5.77 (t, *J*=9.3 Hz, 1H, H-3), 6.19 (d, *J*=9.3 Hz, 1H, H-1), 7.39–7.43 (m,1H, pyridine) 7.81 (t, *J*=7.5 Hz, 1H, pyridine) 8.07 (d, *J*=7.8 Hz, 1H, pyridine) 8.73 (d, *J*=3.9 Hz, 1H, Pyridin), 10.61 (s, 1H, CH=N). ^{13}C-NMR (75 MHz, $CDCl_3$): δ(PPM), 10.10, 18.92, 20.56, 61.70, 67.82, 69.09, 73.68, 74.48, 81.52, 121.79, 125.84, 136.70, 150.18, 152.05, 152.95, 162.33, 164.27, 168.76, 169.38, 170.11, 170.63. Calcd: C, 51.15; H, 5.19; N, 12.43; S, 5.69%; Found: C, 51.25; H, 5.28; N, 12.33; S, 5.72%.

Synthesis of 4-(pyridine-3-yl methylene-amino) -5-propyl-2-yl-3- (2,3,4,6-tetra-O-acetyl-β-D-gluco pyranosyl Sulfonyl) -1,2,4-triazole (7g):

White crystals; 81% (0.93 g), m.p: 63–65 °C; FT-IR (KBr, υ cm^{-1}): 2962 (C-H), 1754 (C=O), 1590 (HC=N), 1369 (CH_3), 1048, 1229 (C-O). ^{1}H NMR (300 MHz, $CDCl_3$): δ 1.92 (s, 3H, OAc), 2.03 (s, 3H, OAc), 2.06 (s, 3H, OAc), 2.08 (s, 3H, OAc), 1.01 (t, *J*=7.5Hz, 3H, CH_3), 1.74–1.86 (m, 2H, CH_2) 2.73–2.86 (m, 2H, CH_2) 3.97–3.99 (m, 1H, H-6a), 4.13–4.19 (m, 1H, H-6b), 4.27–4.32 (m, 1H, H-5), 5.25 (t, *J*=9.6 Hz, 1H, H-4), 5.41 (t, *J*=9.3 Hz, 1H, H-2), 5.79 (t, *J*=9.3 Hz, 1H, H-3), 6.18 (d, *J*=9.6 Hz, 1H, H-1), 7.49–7.53 (m, 1H, pyridine), 8.25 (d, *J*=7.8 Hz, 1H pyridine) 8.77 (d, *J*=3.6 Hz, 1H pyridine) 9.04 (s, 1H, pyridine) 10.78 (s, 1H, HC=N): ^{13}C-NMR (75 MHz, $CDCl_3$): δ(PPM), 13.49, 19.22, 20.73, 26.93, 61.66, 67.78, 69, 73.69, 74.51, 81.45, 124.35, 129.37, 135.99, 151.91, 155.24, 157.16, 162.33, 163.99, 168.69, 169.35, 170.14, 170.60. Calcd: C, 51.99; H, 5.41; N, 12.12; S, 5.55%; Found: C, 51.89; H, 5.50; N, 12.23; S, 5.42%.

4. Conclusions

In summary, a series of 3-S-β-D-glucosides-4-arylideneamino-5-alkyl-1,2,4-triazoles **7(a–e)** was prepared by reaction of 4-amino-5-alkyl-4H-1,2,4-triazole-3-thiol Schiff bases **5(a-f)** and 2,3, 4,6-tetra-O-acetyl-α-D-glucopyranosyl bromide **(6)** in presence of potassium carbonate at room temperature for 24h and then 3h reflux. The structures of the target compounds have been characterized by ^{1}H NMR, ^{13}C NMR, and FTIR. All the newly synthesized compounds have been evaluated for their antimicrobial activities in vitro against two gram (+) bacteria, two gram (–) bacteria and two fungi**.** These compounds exhibited better antifungal activity than antibacterial activity. Though compound **(7b)** was found to have the highest activity against *Bacillus cereus* and compound **(7a)** was found to have the highest activity against *Candida albicans* among all the tested compounds.

5. Acknowledgments

The authors are grateful to Urmia University for providing a fellowship for the present work.

6. References

1. H. A. Burch, W. O. Smith, *J. Med. Chem*. **1966**, *9*, 405–408. **DOI:**10.1021/jm00321a033
2. A. Foroumadi, S. Mansouri, Z. Kiani, A. Rahmani, *Eur. J. Med. Chem*. **2003**, *38*, 851–854. **DOI:**10.1016/S0223-5234(03)00148-X
3. L. P. Guan, Z. S. Quan, *Mini Rev. Med. Chem*. **2016**, *16*, 323–342. **DOI:**10.2174/1389557515666150101100909
4. M. Ziaie, K. A. Dilmaghani, A. Tukmechi, *Acta Chimica Slovenica*. **2017**, *64*, 895–901. **DOI:**10.17344/acsi.2017.3506
5. A. Srinivas, M. Sunitha, P. Karthik, K. V. Reddy, *Acta Chimica Slovenica*. **2017**, *64*, 1030–1041. **DOI:**10.17344/acsi.2017.3805
6. X. Collin, A. Sauleau, J. Coulon, *Bioorg. Med. Chem. Lett.* **2003**, *1ff3*, 2601–2605.
7. Z. Rezaeia, S. Khabnadideha, K. Pakshirb, Z. Hossainia, F. Amiria, E. Assadpour, *European Journal of Medicinal Chemistry*. **2009**, *44*, 3064–3067. **DOI:**10.1016/j.ejmech.2008.07.012
8. G. Tanaka, *Japan Kokai.* **1974**, *973*, 7495. *Chem. Abstr.* **1975**, *82*, 156320h.

9. M. Kalhor, M. Shabani, I. Nikokar, SR. Banisaeed, *Iran. J. Pharm. Res.* **2015**, *14*, 67–75.
10. M. Amir, K. Shikha, *Eur. J. Med. Chem.* **2004**, *39*, 535–545. **DOI:**10.1016/j.ejmech.2004.02.008
11. S. Botros, O. M. Khalil, M. M. Kamel, Y. S. El-Dash, *Acta Chimica Slovenica*. **2017**, *64*, 102–116. **DOI:**10.17344/acsi.2016.2901
12. S. A. Abdel-Aziz, H. A. Allimony, H. M. El-Shaaer, *Phosphorus Sulfur Silicon Rel. Elem.* **1996**, *67*, 113.
13. T. K. Venkatachalam, E. A. Sudbeck, C. Mao, M. F. Uckun, *Med. Chem. Lett,* **2001**, *11*, 523–528. **DOI:**10.1016/S0960-894X(01)00011-7
14. M. Y. Mhasalkar, M. H. Shah, S. T. Nikam, K. G. Anantanarayanan, C. V. Deliwala, *Journal of Medicinal Chemistry.* **1970***, 13,* 672–674. **DOI:**10.1021/jm00298a021
15. S. Rollas, N. Kalyoncuoglu, D. Sur-Altiner, Y. Yegenoglu, *Pharmazie.* **1993***,* 48*,* 308–309.
16. S. Giri, H. Singh, L.D.S. Yadav, R. K. Kahre, *J. Indian Chem. Soc.* **1978***, 55*, 168–171.
17. D. J. Sheehan, C. A. Hitchcock, C. M. Sibley, *Clin. Microbiol. Rev*.**1999**, *12*, 40–79. **DOI:**10.1128/CMR.12.1.40
18. K. M. Crofton, V.M. Boncek, L.W. Reiter,–*Fundam Appl Toxicol.* **1988**, *10*, 459–465. **DOI:**10.1016/0272-0590(88)90292-8
19. K. Akbari Dilmaghani, N. H. Jazani, F. Nasuhi Pur, N. Shokoufeh F. Ghadiri, M. Fakhraee. *Chemistry of Heterocyclic Compounds.* **2012**, *48*, 362–367.
20. Deepa Gupta, D. K. Jain, *J. Adv. Pharm. Technol. Res.* **2015**, *6*, 145–146.
21. SUN. Xiao-Hong, TAO. Yan, LIU. Yuan-Fam, CHEN. Bang, JIA. Ying-Qi, YANG. Jian-Wu, *Chinese Journal of Chemistry*. **2008**, *26*, 1133–1136.
22. K. Akbari Dilmaghani, F. Nasuhi Pur, M. Hatami Nezhad, *Iran J Pharm Res.* **2015**, *14*, 693–699.
23. M. G. Dhapalapur, S.S. Sabnis. C.V. Deliwala, *J. Med. Chem.* **1968**, *11*, 1014–1019. **DOI:**10.1021/jm00311a022
24. S. A. M. K. Nasser, *Carbohydr. Res.* **2006**, *341*, 2187–2199. **DOI:**10.1016/j.carres.2006.06.007
25. Weal A. El-Sayed, Randa E. Abdel Megeid, Hebat-Allah S. Abbas, *Arch Pharm Res.* **2011**, *34*, 1085–1096. **DOI:**10.1007/s12272-011-0706-y
26. D. Ji, J. Lu, B. Lu, C. Xin, J. Mu, J. Li, C. Peng, X. Bao, *Bioorganic & Medicinal Chemistry Letters*. **2013**, *23*, 1997–2000. **DOI:**10.1016/j.bmcl.2013.02.038
27. K. Akbari Dilmaghani, F. Nasuhi Pur, N. H. Jazani, A. Alavi, Z. Niknam, F. Mirfakhraee, *Phosphorus Sulfur Silicon*. **2014**, *189*, 81–87. **DOI:**10.1080/10426507.2013.789877
28. K. Akbari Dilmaghani, F. Nasuhi Pur, M. Mahammad pour, J. Mahammad nejad, *Iranian Journal of Pharmaceutical Research.* 2016, *15*, 777–782.
29. NCCLS (National Committee for Clinical Laboratory Standards) Performance standards for antimicrobial disk susceptibility test (6th ed.). Wayne, PA: Approved Standard. M2-A6. **1997**, 35.
30. M. B. Bahadori, H. Valizadeh, B. Asghari, L. Dinparast, M. Moridi Farimani, S. Bahadori, *Journal of Functional Foods*. **2015**, *18*, 727–736. **DOI:**10.1016/j.jff.2015.09.011
31. M. B. Bahadori, B. Asghari, L. Dinparast, G. Zengin, C. Sarikurkcu, M. A. Mohammadi, Sh. Bahadori, LWT - Food Science and Technology. **2017**, *75*, 42–45. **DOI:**10.1016/j.lwt.2016.08.048
32. H. Beyer, C.F. Kroger, *Liebigs Ann. Chem***. 1960**, *637*, 135. **DOI:**10.1002/jlac.19606370111
33. K. S. Ashok, R.N. Singh, R. N. Handa, S. N. Dubey, P. J. Squattrito, *J. Mol. Struct.* **1998**, *470*, 61–69. **DOI:**10.1016/S0022-2860(98)00470-0
34. C. Guimon, G. Pfister-Guillouzo, *Tetrahedron.* **1974**, *30*, 3831–3838. **DOI:**10.1016/S0040-4020(01)97072-3
35. F. Malbec, R. Milcent, G. Barbier, *J. Heterocycl. Chem*. **1984**, *21*, 1689–1698. **DOI:**10.1002/jhet.5570210624
36. V. I. Kelarev, G. A. Shvekhgeimer, A. F. Lunin, *Khim. Geterotsikl. Soedin*. **1984**, 1271–1276.
37. S. Gopinathan, S. A. Pardhy, A. P. Budhkar, *C. Gopinathan Synth. React. Inorg. Metal. Org. Chem*. **1988,** *18*, 823–836. **DOI:**10.1080/00945718808060824
38. D. D. Perrin, W. L. F. Armarego, Purification of Laboratory Chemicals, Pergamon Press, Oxford. **1988**.
39. Vogel, I. Arthur, *Vogel's Textbook of Practical Organic Chemistry*. **1989**, 5th ed.

Povzetek

Z reakcijami med 4-amino-5-alkil-4*H*-1,2,4-triazol-3-tiolnimi Schiffovimi bazami in 2,3,4,6-tetra-*O*-acetil-α-D-glukopiranozil bromidom smo sintetizirali novo serijo 3-*S*-β-D-glukozid-4-arilidenamino-5-alkil-1,2,4-triazolov. Strukture pripravljenih spojin smo določili z ^{1}H NMR, ^{13}C NMR, FT-IR in elementno mikroanalizo. Za vse novopripravljene spojine smo *in vitro* določili antibakterijsko in protiglivično delovanje na dve Gram pozitivni bakteriji (*Bacillus cereus* (PTCC 1015) in *Staphylococcus aureus* (ATCC 25923)), dve Gram negativni bakteriji (*Pseudomonas aeruginosa* (ATCC 27853) in *Escherichia coli* (PTCC 1399)) ter na dve glivi (*Aspergillus niger* (PTCC 5012) in *Candida albicans* (PTCC 5027)).

Scientific paper

Exploring Bikaverin as Metal Ion Biosensor: A Computational Approach

Zakir Hussain,[1] Haamid Rasool Bhat,[2] Tahira Naqvi,[3] Malay K. Rana[2] and Masood Ahmad Rizvi[1,*]

[1] *Department of Chemistry, University of Kashmir, Hazratbal, Srinagar J&K, India.*

[2] *Department of Chemical Sciences, IISER, Berhampur, Odisha, India.*

[3] *Department of Chemistry, Degree College for Women M.A. Road Srinagar J&K, India*

* *Corresponding author: E-mail: masoodku2@gmail.com*

Received: 11-12-2018

Abstract

A computational exploration of fungi produced pigment bikaverin as a biosensor towards bioavailable metal ions is presented. Systematic studies of the optimized ground and excited state geometries were attempted for exploring metal ion binding pocket, comparative binding propensity and optical properties of the bikaverin and its adducts with studied metal ions. The screening of thirteen (13) bioavailable metal ions, revealed a range of binding strength towards bikaverin receptor with Ca^{2+}, Mg^{2+} and Al^{3+}as the strongest binders. Besides, upon binding to bikaverin receptor an enhancement in its fluorescence intensity was observed in the order Ca^{2+}> Al^{3+}> Mg^{2+}. The computationally predicted selectivity of bikaverin receptor towards $Ca^{2+}$was experimentally corroborated through the preliminary fluorescence studies. The bikaverin probe showed an enhancement of fluorescence emission in presence of Ca^{2+} ions in buffered aqueous medium.

Keywords: Computational chemistry; Biosensors; Fluorescence Spectroscopy; Quantum chemical calculations; Electronic structure

1. Introduction

The well designed computational studies can be good to predict the starting point for targeted experiments in a time and cost effective manner.[1] Experimental chemists use theoretical calculations to supplement, support and guide their experiments particularly in the areas of conformational analysis,[2] reaction mechanism,[3] transition states,[4] charge distributions,[5] modeling larger molecules like DNA and proteins,[6] structure-activity relationships,[7] orbital interactions,[8] and excited state studies.[9] Metal ions are required for a plethora of functions in biosystems. However, the metal ions can be like double-edged swords; at their proper concentrations, these remain coordinated to their natural binding sites and perform the desired functions; but a change in their normal concentration can lead to their de-compartmentalization and consequently bring onset of deleterious functions.[10] Therefore, selective sensors for detection and quantification of metal ions for the real time analytical monitoring and medical diagnosis are of considerable importance.[11] Thus, it becomes imperative to investigate the natural bioactive compounds for their *in vivo* metal ion sensing applications in order to potentiate the diagnosis for better therapeutic action. In continuation of our computational chemistry interests[12–15] and towards investigating the bioactivities of natural products,[16–18] we attempted to survey the fungi derived fluorescent bioactive natural product bikaverin for metal ion sensing ability. Bikaverin is a reddish pigment produced by different fungal species of the genus Fusarium with the diverse biological activities.[19–21] With the increasing reports on its pharmacological role, bikaverin is becoming a metabolite of biotechnological interest.[22] Commercially bikaverin as pure compound is costly and synthesizing bikaverin through a total chemical process is less viable and environmentally unfavorable. However, obtaining bikaverin from microbial sources present an environment friendly, continuousand cheap source. Thus for obtaining bikaverin in a cost effective and an environment friendly manner, we extracted bikaverin from fungal extracts using the standardized procedure from literature reports.[23] In this study, we present the

computational exploration of bikaverin as biosensor towards thirteen (13) bioavailable metal ions. The computational prediction was experimentally confirmed through preliminary florescence studies of studied metal ions as bikaverin adducts.

2. Experimental

2. 1. Computational Procedures and Materials

All density functional theory (DFT) and time-dependent density functional theory (TD-DFT) calculations were performed using the Gaussian 09 program package.[24] The geometries of all the studied molecules (bikaverin and its metals adducts) were fully optimized at the singlet ground (S0) and first excited (S1) states in the acetonitrile solvent using CAM-B3LYP, Coulomb-attenuating method based on Becke's three parameter hybrid exchange and nonlocal correlation functional of Lee, Yang and Parr (65% exchange and 35% correlation weighting at long-range).[25,26] The standard 6-311G, split-valence atomic basis set function of DFT has been employed for all the atoms except for the transition metal ions; Nickel (Ni^{2+}), Mercury (Hg^{2+}), Cadmium (Cd^{2+}), Manganese(Mn^{2+}), Iron (Fe^{2+}), Zinc(Zn^{2+}), Copper(Cu^{2+}) and Lead (Pb^{2+}) atoms for which effective core potential (ECP) of Wadt and Hay pseudo-potential with a double-ζ valence basis set LANL2DZ was used.[27–29] It is because the LANL2DZ reduces the computational cost as it uses an effective core potential for the core electrons, thus the core electrons are not explicitly considered in the computation. For the structural calculations of receptor-transition metal complexes, the relativistic LANL2DZ pseudopotential is the typical basis set asit has been identified to give close agreement between calculated and experimentally observed geometries. Frequency calculations were carried out to verify that the optimized molecular structures correspond to the energy minima, thus only positive frequencies were expected. The TD-DFT studies of all the molecules were performed by utilizing the same functional and the basis sets as CAM-B3LYP has been shown to be good for the excited state property calculations.[30] The Conductor-like Polarizable Continuum Model (CPCM) was utilized for taking care of the effect of solvation in acetonitrile (dielectric constant, ε = 37.5) on all the calculations as implemented in Gaussian 09. Natural Bond Orbital (NBO) method was employed for the natural population analysis, using the NBO 3.1 version as implemented in Gaussian 09 program.[31] Free energy changes (ΔG) and binding energies (ΔE) were calculated for the receptor-analyte complexes to comprehend the thermodynamic binding propensity of the selected bioavailable cations with receptor (**1**).The Gibb's free energy change (ΔG) of the fragments (**1**), Na^{+}, K^{+}, Ni^{2+}, Al^{3+}, Hg^{2+}, Cd^{2+}, Mn^{2+}, Fe^{2+}, Zn^{2+}, Cu^{2+}, Mg^{2+}, Pb^{2+} and $Ca^{2+}$and their complexes were calculated from equation 1:

$$\Delta G = Gcomplex - (Greceptor + Gcation) \quad (1)$$

Where Gcomplexis the free energy of receptor-cation adduct, Greceptor and Gcation are free energies of isolated receptor and cation respectively.The binding energy changes were also calculated to check the binding selectivity of the studied cations towards bikaverin receptor using the equation 2:

$$\Delta E = (Ecomplex) - (Ereceptor + Ecation) \quad (2)$$

Where Ecomplex is the total energy of the receptor-cation adduct, Ereceptor and Ecation are total energies of isolated receptor and cation respectively.In order to reduce basis set superposition error (BSSE) in these energy calculations, the Boys-Bernardi scheme was applied to yield the counterpoise corrected energies.[32]

2. 2. Extraction of Bikaverin from Fungal Extracts

Fungal mycelium showed a growth up to 5–6 cm on a PDA (potato dextrose agar) plate after 7 days. The morphological features supported the genus *Fusarium* resulting in 99% homology with the *Fusarium proliferatum*. Dichloromethane solvent was used to extract the crude bikaverin using National Cancer Institute's protocol. The extract was concentrated under vacuum and subjected to purification over column chromatography on silica gel using hexane-ethyl acetate (7:3 V:V) mobile phase leading to the isolation of pure bikaverin.

2. 3. Absorption and Emission Studies

All reagents were purchased from Aldrich and used without further purification. UV-Vis and fluorescence spectra were recorded on a Shimadzu UV-2450 and Shimadzu 5301 PC spectrophotometer respectively, with a quartz cuvette (path length 1 cm). A 10^{-3} M stock solution of bikaverin (probe 1) was prepared by dissolving the required amount of bikaverin in 10 mL of DMSO; 30μL of this stock solution was further diluted with CH_3CN and HEPES buffer (0.05 M, pH = 7.4) to prepare 3 mL solution of probe (1) and this solution was used for each UV–Visible and fluorescence experiment. The aliquots of freshly prepared standard solutions (10^{-2}M) of metal chloride/metal perchlorates {M = Hg^{2+}, Fe^{2+}, Pb^{2+}, Cd^{2+}, Cu^{2+}, Zn^{2+}, Ni^{2+}, Al^{3+}, Co^{2+}, Mg^{2+}, Ca^{2+}, Na^{+}, and K^{+}}, in distilled water were added to 3 mL solution of probe **(1)** taken in quartz cuvette and spectra's were recorded.

3. Results and Discussions

Quantum-chemical calculations are impressive for their step to step analysis and prediction whereas experi-

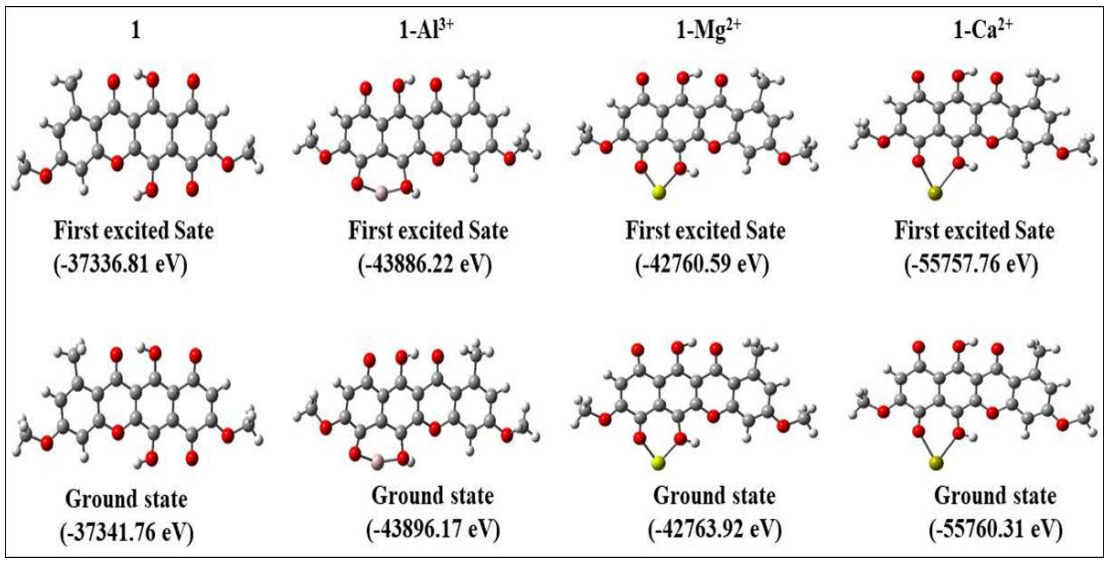

Figure 1. Optimized ground (S0) and the first excited state (S1) geometries of bikaverin receptor(1), 1-Al^{3+}, 1-Mg^{2+} and 1-Ca^{2+} and their corresponding energies [in electron volts (eV)].

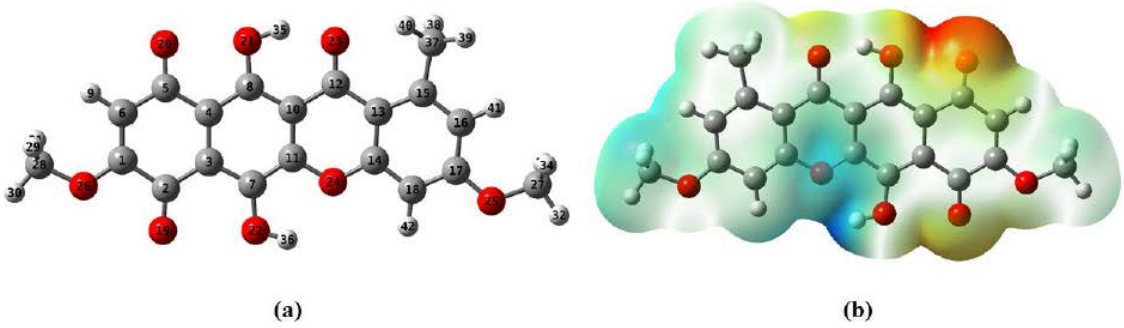

Figure 2. (a) Optimized geometry and (b) Electrostatic potential map of ground state (S_0) of bikaverin.

mental results are a net outcome of all the influencing factors in a blend.The optimized geometries and the corresponding energies of the ground and first excited state of bikaverin(**1**) and its receptor-analyte complexes with thirteen (13) studied bioavailable metal ions are shown in Figures 1, and S1 and S2 respectively (see Supplementary information).The natural charge distribution (Table 1) and electrostatic potential map of bikaverin (**1**) were calculated to identify its appropriate cation binding site. The charge distribution data in Table 1 and electrostatic potential map of bikaverin (1) indicate that the pocket for the electrophilic addition of cations is the carbonyl and the hydroxyl oxygen atoms Figure2 (see the ground state structure of bikaverin).

Table 1. The NPA Charge distribution on some crucial atoms of bikaverin **1** and **1-Ca^{2+}**in S0 calculated at CAM-B3LYP/6-311G level of theory.

Atom involved	NPA charge distribution	
	Bikaverin (1)	1-Ca^{2+}
O22	–0.685	–0.776
O19	–0.534	–0.678
O23	–0.645	–0.635
O21	–0.698	–0.685
O20	–0.588	–0.559
O24	–0.495	–0.495
O25	–0.532	–0.527
O26	–0.516	–0.513
H36	–0.523	–0.551
Ca43	….	1.964

The calculated free energy change (ΔG) and the binding energy (ΔE) values of receptor analyte complexes are presented in Table 2. The data in Table 2 reveals that the binding of all the studied bioavailablecations to bikaverin is thermodynamically feasible and these ions bind the bikaverin receptor (1) with a range of strength. The trend in the binding propensity of studied metal ions can be correlated to their charge densities and hard soft acid base strength. It is evident from the binding and free energy data of Table 2 that the electrophillic binding of Ca^{2+},

Table 2. Calculated free energy change (ΔG) and binding energy for receptor-analyte complexes using CAM-B3LYP/6-311Glevel of theory with basis set superposition error (BSSE) corrections.

S. No	Adduct	ΔG (Kcal/mol)	Binding energy (Kcal/mol)	S. No	Adduct	ΔG (Kcal/mol)	Binding energy (Kcal/mol)
01	**1-Na^{+}**	–22.44	–41.94	08	**1-Mn^{2+}**	–43.76	–31.81
02	**1-K^{+}**	–19.92	–39.31	09	**1-Fe^{2+}**	–55.39	–50.11
03	**1-Al^{3+}**	–53.09	–52.96	10	**1-Ni^{2+}**	–27.11	–29.72
04	**1-Pb^{2+}**	–51.31	–22.72	11	**1-Cu^{2+}**	–34.64	–39.94
05	**1-Hg^{2+}**	–15.29	–34.20	12	**1-Mg^{2+}**	–51.97	–58.63
06	**1-Cd^{2+}**	–22.64	–45.29	13	**1-Ca^{2+}**	–73.19	–69.21
07	**1-Zn^{2+}**	–31.66	–23.77				

Mg^{2+} andAl^{3+} with receptor (1) is stronger in comparison to the remaining cations. Among all the studied metal ions the binding of Ca^{2+} to bikaverin was found to be strongest which suggests a possible interaction between bikaverin and Ca^{2+} at lower concentrations. Thus a sensing application of bikaverin towards Ca^{2+} ions at its physiological concentrations can be possible

Motivated by the binding of metal ions to bikaverin receptor**(1)**, we attempted to explore the fluorescence behavior of the studied metal ions for predicted sensing applications. To get an insight into the origin of absorption and emission bands, the transitions of bikaverin(**1**) and its receptor-analyte complexes under consideration were simulated using preferred DFT/TD-DFT level of theory (Experimental section). The computationallypredicted spectra of studied metal ion bikaverin (**1**) adducts in the acetonitrile solvent depicted various peaks. However only the peaks of good intensity fluorescence were chosen for analysis. The major absorption and fluorescence intensity band of bikaverin (**1**) and its receptor-analyte adducts with studied metal ions are summarized in Table 3. The calculated absorption spectrumfor bikaverin (**1**) shows a major peak (λabs) at 491 nm (2.52 eV). The metal ion bikaverin adducts showed varied emission responses in which the fluorescence intensities in some cases were seen to be attenuated and in some cases enhanced. The calculated fluorescence intensities of 1-Ca^{2+}, 1-Mg^{2+} and 1-Al^{3+}adducts were found to be significantly higher than that of bikaverin (**1**) while as the absorption intensities of other receptor-analyte complexes don't show much deviation in comparison to pure bikaverin (1).

To have a further insight into the emission behavior of the bikaverin (**1**) metal ion adducts, the frontier molecular orbitals (FMOs) analysis was attempted. The FMOs of the bikaverin (1) and some representative receptor-analyte complexes are depicted in Fig. 3. The highest occupied molecular orbital (HOMO) and lowest unoccupied molecular orbitals (LUMO) energies of bikaverin (1) and all its metal ion adducts have been summarized in (Table S1, see supporting information).The interactions between the metal ions and the bikaverin (1) can be clearly observed from the frontier molecular orbital contour distribution.[33]

Table 3. Summary of absorption and fluorescence spectral data of bikaverin(1) and its analyte complexes

Molecule	Calculated λ_{abs}(nm)	Oscillator strength (f)	Calculated λ_{flu}(nm)	Oscillator strength (f)
1	491	0.2524	576	0.0102
1-Na+	412	0.1960	426	0.0081
1-K+	315	0.1910	370	0.0013
1-Ni2+	441	0.2103	494	0.0014
1-Al3+	342	0.1543	388	0.1976
1-Hg2+	377	0.1130	435	0.0045
1-Cd2+	389	0.1866	437	0.0043
1-Mn2+	422	0.2010	497	0.0036
1-Fe2+	360	0.2349	454	0.0045
1-Zn2+	390	0.1873	437	0.0033
1-Cu2+	391	0.1033	463	0.0002
1-Mg2+	372	0.1537	422	0.1278
1-Pb2+	418	0.1004	471	0.0037
1-Ca2+	525	0.1629	588	0.3722

In case of bikaverin (1), the HOMO and LUMO are spread evenly over the benzoquinone and hydroquinone rings of the molecule. The observed changes in the HOMO and LUMO contours of bikaverin (1) indicate a pi to pi* transition in absorption. However, HOMOs and LUMOs in the receptor-analyte adducts are budged on different regions of the adducts indicating intramoleculor charge transfer due to the binding of cationic species.

It can also be seen from the Fig. 3 that the orbital contour distribution of HOMO in case of bikaverin calcium ion adduct (1-Ca^{2+}) gets shifted towards the opposite end compared to free bikaverin (1) or 1-Al^{3+} and 1-Mg^{2+} adducts. The calculated fluorescence wavelength for bikaverin (1) was found to be 576 nm (2.15 eV) with oscillator strength of 0.0102, depicting low intensity fluorescence peak in bikaverin (1). While the calculated fluorescence spectrum of 1-Ca^{2+} shows an intense peak at 588 nm (2.19 eV) with oscillator strength of 0.3722.

Thus the observations of strong Ca^{2+} ion binding coupled with the enhancement in the fluorescence intensity of bikaverin (1) on Ca^{2+} ion binding predict the bikaverin

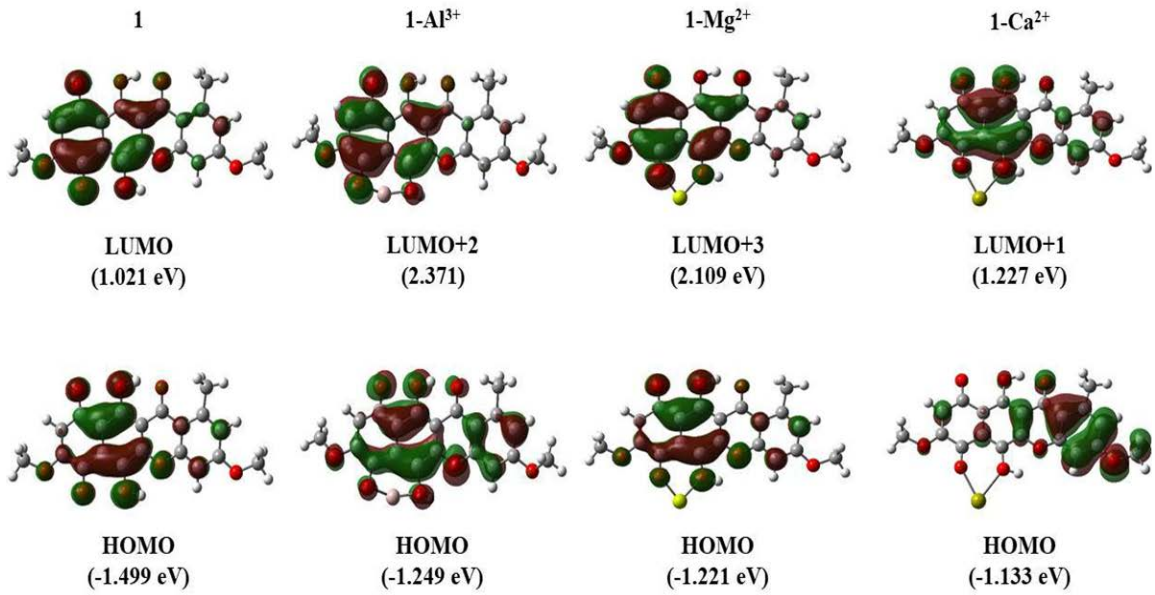

Fig. 3. Frontier molecular orbitals of bikaverin (1), 1-Al^{3+}, 1-$Mg^{2+}$and 1-Ca^{2+}.

(1) as the new possible fluorescent biosensor for Ca^{2+} ion. The fluorescence imaging of Ca^{2+} ions in the form of bikaverin (1) calcium adduct can serve as a method for analyzing signaling pathways involving calcium ions. Besides, the changes in the intracellular Ca^{2+} ion concentrations have been related to different physiological, pathological and immune responses, therefore bikaverin based calcium ion sensing can also be an important tool in diagnostics.

The calculated oscillator strengths of fluorescence intensities of studied bioactive metal ions with bikaverin

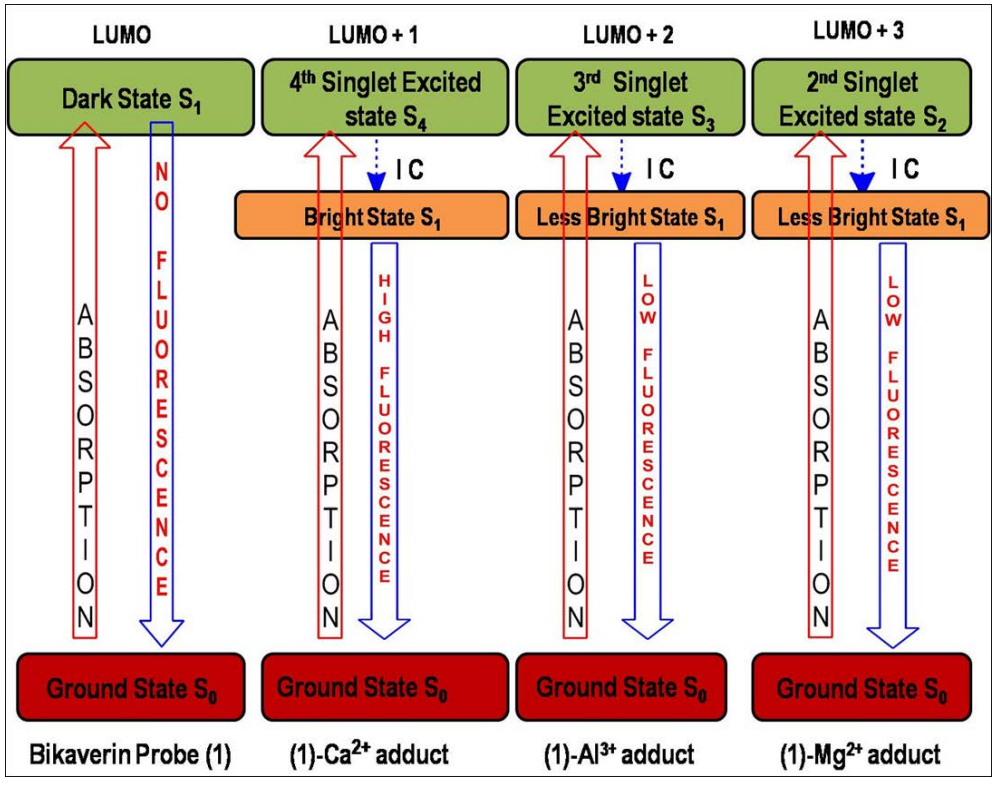

Fig. 4. Predicted electronic excitations and de excitations of bikaverin receptor (1) and its calcium adduct.

(1) also predict a mild to medium increase in the intensity in case of 1-Mg^{2+} and 1-Al^{3+} adducts. But the intensities of their fluorescence peaks are predicted to be smaller in comparison to Ca^{2+} as depicted by their oscillator strengths of 0.1976 and 0.1278, respectively. For the other cationic species, there is no significant effect on the fluorescence intensities once they bind with the bikaverin receptor (1) as can be seen from their oscillator strengths in Table 3. It is therefore predicted from the DFT/TD-DFT calculations that receptor (1) can strongly sense Ca^{2+} ions fluorometrically with the milder sensing ability towards Mg^{2+} and Al^{3+} among the studied bioactive metal ions. The probable reason for the fluorescence intensity enhancement in case of 1-Ca^{2+}, 1-Al^{3+}, and1-Mg^{2+} adducts is that their absorption transitions involve electron shifting to higher singlet excited states like fourth singlet excited state (S4),third singlet excited state(S3) and second singlet excited state(S2) in case of 1-Ca^{2+}, 1-Al^{3+}, and 1-Mg^{2+} respectively. As per Kasha's rule,[34] the fluorescence phenomenon occurs from the firstsinglet excited state (S1). In order for fluorescence to occur, the higher excited states have to relax to the first singlet excited state. For this relaxation process, internal conversions and the vibrational relaxations occur which lead to the loss of energy during the de-excitation. Due to this energy loss there is significant Stoke's shift (change between absorption and emission energies) While as in the other cations and in receptor (1), the transitions involve the lowest singlet excited state S1. So there is no internal conversion and hence no energy loss and eventually no Stoke's shift. Hence, in such cases, there is either no fluorescence or the intensity of the fluorescence is very weak.

TD-DFT calculated results show that the main transitions for bikaverin(1), 1-Al^{3+}, 1-$Mg^{2+}$and 1-Ca^{2+} are from HOMO → LUMO, HOMO → LUMO+2, HOMO → LUMO+3 and HOMO → LUMO+1 respectively see Fig 4. In all other receptor-analyte complexes, the main transitions involve HOMO→LUMO.

The experimental and theoretical fluorescence study of bikaverin (**1**) reveala major fluorescence peak corresponding to HOMO to LUMO transition with λ_{em} 576 nm in the theoretical spectra and λ_{em} 425 nm in experimental spectra. However on binding of Ca^{2+} the theoretical fluorescence peak gets shifted to a value λ_{em} 588 nm which closely corroborateswith the observed experimentalpeak of Bikaverin Ca^{2+}adduct around λ_{em} of 620 nm.Thus, the theoretically predicted red shift in fluorescence of bikaverin(1) on calcium ion binding was also experimentally observed and therefore can be rationalized with theoretical prediction of HOMO→LUMO+1 absorption in case bikaverin calcium ion adduct.

3. 1. Characterization of Bikaverin from Fungal Extract

The developments in synthetic biology has allowed tuning of microbial systems for generating industrially viable strains as the green and sustainable sources of value-added compounds.[35]The composition and amounts of metabolites(bikaverin) are specific to the species of genus Fusarium. The morphological features of our crude fungal extract matched to the species *Fusarium proliferatum*. The chemical structure of purified bikaverin was confirmed through comparative analysis of NMR, mass, λmax and TLC of isolated compound with bikaverin standard and further to the literature reported values.[36] ^{1}H-NMR (CDCl3, 400MHZ):δ 2.87 (3H, s, 1-Me), 3.93

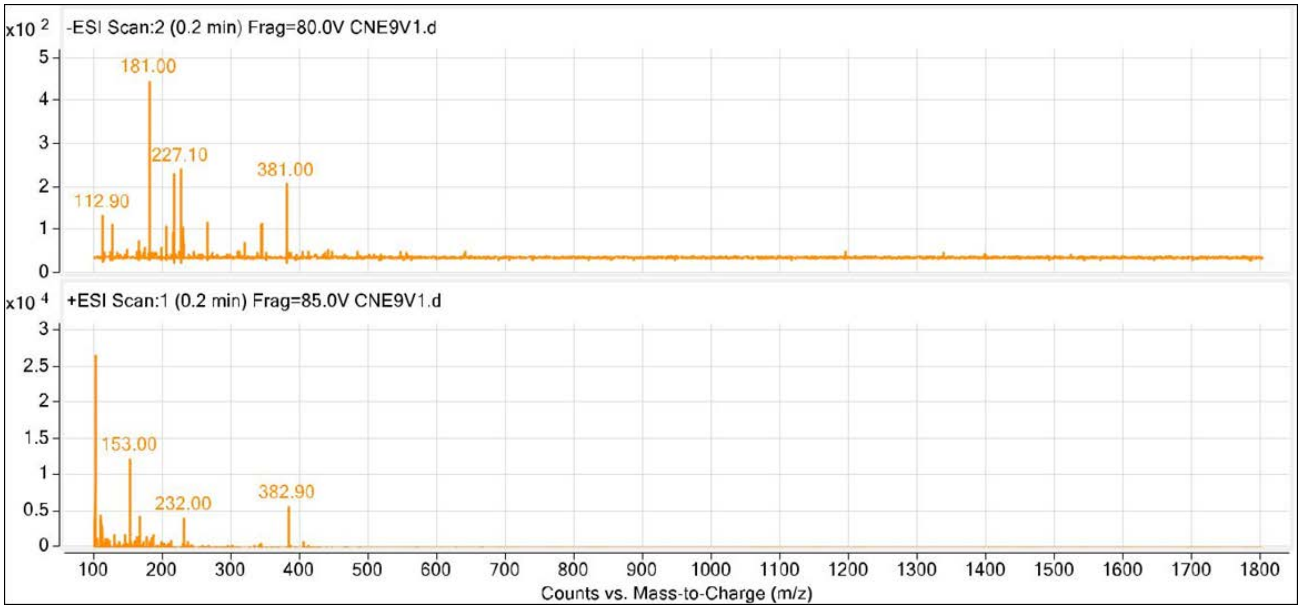

Fig. 5. Mass spectra of isolated product Bikaverin

(3H, s, 8-OMe), 3.96 (3H, s, 3-OMe), 6.35 (1H, s, H-9), 6.81 (1H, s, H-2), 6.93 (1H, s, H-4).HRMS (ESI$^+$) calculated for C20H14O8 [M+H]$^+$: 381.0761, found: 382.90 Fig.5.

3. 2. Metal Ion Sensing Applications

The preliminary metal ion sensing behavior of bikaverin (1) was studied towards selected bioactive metal ions as their chloride/perchlorate salts in CH_3CN/H_2O (6:4, v/v; buffered with PBS, pH 7.4) using fluorescence spectroscopy Fig 6. The fluorescence spectrum of receptor (1) (10.0 μM) exhibits a weak emission band at 620 nm corresponding to bikaverin moiety when excited at 596 nm in CH_3CN/H_2O (6:4, v/v; buffered with PBS, pH = 7.4). The weak fluorescence emission behavior of bikaverin is due to intramolecular charge transfer process as seen from HOMO- LUMO orbital contours.

It is evident from Figure 7 that on binding of calcium ions to bikaverin (1) its fluorescence profile gets modified. The free bikaverin shows very little to no fluorescence when excited at 596 nm while as the calcium bound bika-

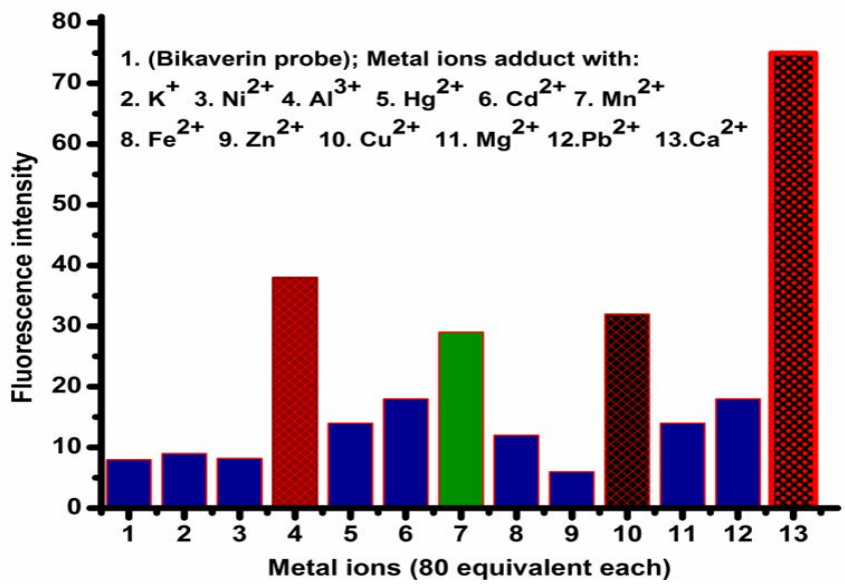

Fig. 6. Fluorescence response of bikaverin (1) towards various metal ions: Bars represent fluorescence selectivity (I/Io) of bikaverin (1) (10.0 μM) towards various metal ions (80 equiv each) in CH3CN:H2O (6:4, v/v) buffered with 0.05 M HEPES, pH = 7.4; λex = 596 nm. The experimental fluorescence spectra of bikaverin(1) and its calcium adduct under different excitation wavelengths are shown in Fig.7 (A,B) respectively.

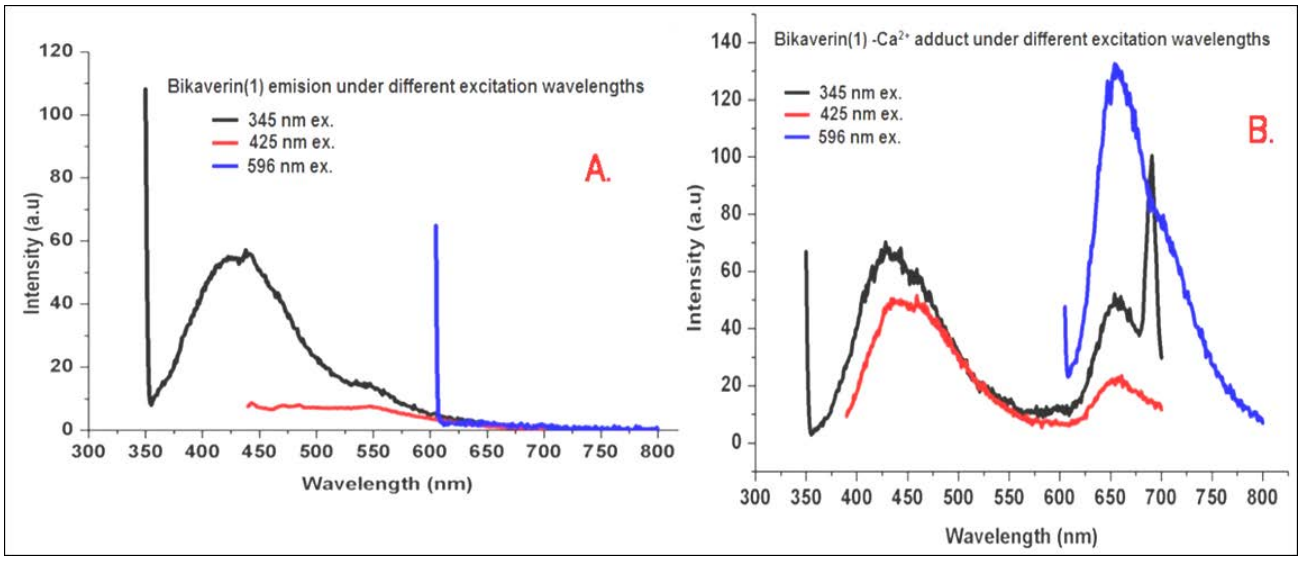

Fig. 7. Fluorescence response under different excitation wavelengths for A: bikaverin(1) B: Bikaverin Ca^{2+} adduct.

verin shows a major fluorescence when excited at the 596 nm wavelength. Among the fluorescence peaks obtained under the excitation wavelengths of 425 and 345 nm, the former gets an enhancement in the emission intensity while as the latter peak remains largely unchanged on calcium ion binding to bikaverin.

4. Conclusions

In summary, the present work describes a thorough computational investigation of metal ion sensing ability of natural pigment bikaverin as a fluorescent probe. An exploration of comparative metal ion binding affinities and optical properties of the bikaverin adducts through systematic studies using the appropriate level of theory are presented. The Ca^{2+}, $Mg^{2+}$and Al^{3+} metal ions are shown to bind the bikaverin receptor more strongly and with an enhancement in its florescence intensity. The strongest binding affinity with the most intense fluorescence emission in case of Ca^{2+} predicts bikaverin pigment as a possible Ca^{2+} biosensor. The concept of isolation of bikaverin receptor (1) from the natural source as an economical and sustainable method is also presented. The computationally predicted metal ion fluorescence behavior of bikaverin receptor (1) towards the studied metal ions was experimentally corroborated through the preliminary fluorescence studies. Among the studied metal ions, the bikaverin receptor (1) was seen to strongly detect Ca^{2+}ions with an enhancement of fluorescence emission in its μM concentration range in the buffered aqueous medium due to charge transfer phenomena. The inclusive experimental studies of the bikaverin receptor (1) towards the selective calcium ion sensing under physiological conditions, the complete analytical profile of bikaverin as biosensor, the real time imaging of Ca^{2+} ions in cells through confocal microscopy and other related studies for the buildup of bikaverin as Ca^{2+} ion biosensor are underway in our laboratory.

5. Acknowledgement

MAR thankfully acknowledges Dr Hemant J Purohit, Chief Scientist & Head Environmental Genomics Division, National Environmental Engineering Research Institute (NEERI), CSIR, Nagpur India for providing the Bikaverin crude extract for bikaverin extraction and University of Kashmir for assistance under UGC 12th innovative research activity. HRB and MKR are highly thankful to Indian Institute of Technology Kanpur, India for providing some computational facilities.

Conflict of Interest

All the authors declare no conflict of interest what so ever.

6. References

1. H. Nikoofard, M. Sargolzaei, F. Faridbod *Acta Chim. Slov.* **2017**, *64*, 842–848. **DOI:**10.17344/acsi.2017.3357
2. S. Krishnamurty, M. Stefanov, T. Mineva, S. Bégu, J. M. Devoisselle, A. Goursot, R. Zhu, D. R. Salahub, *J. Phys. Chem. B.* **2008,** *112*, 13433–13442. **DOI:**10.1021/jp804934d
3. G. J. Cheng, X. Zhang, L. W. Chung, L. Xu, Y. D. Wu, *J. Am. Chem. Soc.* **2015**, *137*, 1706–1725. **DOI:**10.1021/ja5112749
4. F. Odame, *Acta Chim. Slov.* **2018**, *65*, 328–332 **DOI:**10.17344/acsi.2017.4001
5. A. T. Castro, J. D. Figuero-Villar, *Int. J. Quantum Chem*. **2002,** *89*, 135–146. **DOI:**10.1002/qua.10302
6. M. Lintuluoto, J. M. Lintuluoto, *Biochemistry*. **2016,** *55*, 4697–4707. **DOI:**10.1021/acs.biochem.6b00423
7. S. Arulmozhiraja, M. Morita, *Chem. Res. Toxicol.* **2004,** *17*, 348–356. **DOI:**10.1021/tx0300380
8. N. Yasarawan, K. Thipyapong, V. Ruangpornvisuti, *J. Mol. Graphics Model.* **2014,** *51*,13-26. **DOI:**10.1016/j.jmgm.2014.04.009
9. F. Senn, M. Krykunov, *J. Phys. Chem. A*. **2015,** *119*, 10575–10581. **DOI:**10.1021/acs.jpca.5b07075
10. M. H. Bridge, E. Williams, M. E. G. Lyons, K. F. Tipton, W. Linert. *Biochim. Biophys. Acta*. **2004,** *1690*, 77–84. **DOI:**10.1016/j.bbadis.2004.05.007
11. Y. Wu, B. Midinov, R.J. White, *ACS Sens.,* **2019**, *4*, 498–503. **DOI:**10.1021/acssensors.8b01573
12. M. A. Rizvi, M. Mane, M. A. Khuroo, G. M. Peerzada, *Monatsh Chem.* **2017**, *148*, 655–668. **DOI:**10.1007/s00706-016-1813-8
13. Y. Dangat, M. A. Rizvi, P. Pandey, K. Vanka, *J Organomet Chem*. **2016,** *801*, 30-41. **DOI:**10.1016/j.jorganchem.2015.10.015
14. M.V. Mane, M. A. Rizvi, K. Vanka, *J. Org. Chem.* **2015,** *80*, 2081–2091. **DOI:**10.1021/jo5023052
15. M. Kumar, A. Kumar, M. Rizvi, M. Mane, K. Vanka, S. C. Taneja, B. A. Shah, *Eur. J. Org. Chem.* **2014,** *2014*, 5247–5255. **DOI:**10.1002/ejoc.201402551
16. A. Pandey, M. Rizvi, B. A. Shah, S, Bani, Cytokine, **2016,** *79*, 103-113. **DOI:**10.1016/j.cyto.2016.01.004
17. A. Goswami, B. A. Shah, A. Kumar, M. A. Rizvi, S. Kumar, S. Bhushan, F. A. Malik, N. Batra, A. Joshi, J. Singh,Chem.-Biol. Interact., **2014**, *222*, 60–67. **DOI:**10.1016/j.cbi.2014.08.011
18. R Chib, M. Kumar, M. Rizvi, S. Sharma, A. Pandey, S. Bani, S. S Andotra, S. C. Taneja, B. A Shah, RSC Advances, **2014**, *4*, 8632–8637. **DOI:**10.1039/c3ra46412a
19. J. Balan, J. Fuska, I. Kuhr, V. Kuhrova, *Folia Microbiol (Praha).* **1970,** *15*, 479–484. **DOI:**10.1007/BF02880192
20. J. F. Henderson, M. L. Battell, G. Zombor, J. Fuska, P. Nemec, *Biochem Pharmacol.* **1977** *26*, 1973–1977. **DOI:**10.1016/0006-2952(77)90004-1
21. D. Kjaer, A. Kjaer, C. Pedersen, J. D. Bulock, J. R. Smith, *J Chem Soc Perkin 1*. **1971**, *16,* 2792–2797. **DOI:**10.1039/J39710002792
22. M. C. Limon, R. Rodríguez, J. Avalos, *Appl Microbiol Biotechnol.* **2010**, *87*, 21–29. **DOI:**10.1007/s00253-010-2551-1

23. D. Arora, N. Sharma, V. Singamaneni, V. Sharma, M. Kushwaha, V. Abrol, S. Guru, S. Sharma, A. P. Gupta, S. Bhushan, S. Jaglan, P. Gupta, *Phytomedicine.* **2016,** *23*, 1312–1320. **DOI:**10.1016/j.phymed.2016.07.004
24. Frisch, M. J.; Trucks, G. W.; Schlegel, H. B.; Scuseria, G. E.; Robb, M. A.; Cheeseman, J. R.; Scalmani, G.; Barone, V.; Mennucci, B.; Petersson, G. A.; et al. Gaussian 09; Gaussian Inc: Wallingford, CT, 2009.
25. T. Yanai, D. P. Tew, N. C. Handy, Chemical Physics Letters, 2004, *393,* 51–57. **DOI:**10.1016/j.cplett.2004.06.011
26. Jacquemin, D.; Planchat, A.; Adamo, C.; Mennucci, B. J. Chem. Theory Comput. 2012, *8,* 2359−2372. **DOI:**10.1021/ct300326f
27. H. R. Bhat, P. C. Jha, *Chem. Phys. Lett.* **2017,** *669*, 9–16. **DOI:**10.1016/j.cplett.2016.12.025
28. H. R. Bhat, P. C. Jha, *Phys. Chem. Chem. Phys.* **2017,** *19*, 14811–14820. **DOI:**10.1039/C7CP02287E
29. H. R. Bhat, P. C. Jha, *J. Phys. Chem. A.* **2017,** *121*, 3757–3767. **DOI:**10.1021/acs.jpca.7b00502
30. S. F. Boys, F. Bernardi, *Mol. Phys.***1970,** *19*, 553–566. **DOI:**10.1080/00268977000101561
31. Reed, A. E.; Curtiss, L.; Weinhold, F. *Chem. Rev.* 1988, *88*, 899−926. **DOI:**10.1021/cr00088a005
32. J. W. Cornforth, G. Ryback, P. M. Robinson, D. Park, *J Chem Soc Perkin* **1971,** *1.16*, 2786-2788. **DOI:**10.1039/j39710002786
33. R. M. Jagtap, M. A. Rizvi, Y. B. Dangat, Satish K. Pardeshi, *J. Sulfur Chem.* **2016,** *37*, 401–425. **DOI:**10.1080/17415993.2016.1156116
34. M. Kasha, *Discuss. Faraday Soc.* **1950,** *9*, 14–19. **DOI:**10.1039/df9500900014
35. J. Du, Z. Shao, H. Zhao, *J Ind Microbiol Biotechnol.* **2011,** *38*, 873–890. **DOI:**10.1007/s10295-011-0970-3
36. D. Kjaer, A. Kjaer, C. Pedersen, J. D. BuLock, J. R. Smith, J. Chem. Soc. C **1971,** *0*, 2792–ww2797. **DOI:**10.1039/J39710002792

Povzetek

Članek predstavlja računalniško raziskovanje gliv, ki proizvajajo pigment bikaverin kot biosensor za biološko razpoložljive kovinske ione. Narejene so bile sistematične študije geometrije optimiziranega osnovnega in vzbujenega stanja za raziskovanje vezavnega žepa za kovinske ione, primerjalna vezavna nagnjenost in optične lastnosti bikaverina in njegovih aduktov s preiskovanimi kovinskimi ioni. Pregled trinajstih (13) biodostopnih kovinskih ionov je pokazal, da jakost vezanja na bikaverinski receptor ustreza zaporedju Ca^{2+}, Mg^{2+} in Al^{3+}. Po vezavi na bikaverinski receptor je bila opažena ojačitev fluorescence v vrstnem redu $Ca^{2+} > Al^{3+} > Mg^{2+}$. Računsko napovedana selektivnost bikaverinskega receptorja za Ca^{2+} je bila eksperimentalno podprta s predhodnimi fluorescenčnimi študijami. Bikaverinska sonda je pokazala povečanje fluorescenčne emisije v prisotnosti Ca^{2+} ionov v zapufranem vodnem mediju.

DOI: 10.17344/acsi.2018.4862 *Acta Chim. Slov.* **2019,** *66,* 360–366

Scientific paper

Ion-Associated Complex of the Anionic Chelate of Germanium(IV) with Nitro Derivative of the Catechol and the Cation of Monotetrazolium Salt

Kirila Stojnova and Vanya Lekova*

Department of General and Inorganic Chemistry with Methodology of Chemistry Education, Faculty of Chemistry, Plovdiv University "Paisii Hilendarski", 24 Tsar Assen Street, Plovdiv 4000, Bulgaria

** Corresponding author: E-mail: vanlek@uni-plovdiv.bg*
Tel.: +35932261420

Received: 11-21-2018

Abstract

The formation of an ion-associated complex between of the anionic chelate of germanium(IV) with 4-nitrocatechol (4-NC) and the cation of 3-(2-naphtyl)-2,5-diphenyl-2*H*-tetrazolium chloride (TV) was investigated by spectrophotometry. The optimum conditions for the chelate formation and the extraction of the complex in the liquid-liquid extraction system Ge(IV)–4-NC–TV–H_2O–$CHCl_3$ were established. The validity of Beer's law was checked and some analytical characteristics were calculated. The association process in the aqueous phase and the extraction equilibria were studied and quantitatively characterized by the following key constants: association constant, distribution constant, extraction constant and recovery factor. The molar ratios of the components in the ion-associated complex were determined by independent methods. Based on this, a reaction scheme, a general formula and a structure of the ion-associated complex were suggested.

Keywords: Ge(IV); ion-associated complex; chelate formation; extraction equilibriums

1. Introduction

The germanium is a forth-period post-transition metal which forms complexes with various natural organic ligands, containing O, N and S donor atoms, such as polyphenols and their functional derivatives, polyhydroxycarboxylic acids, aminopolyhydroxycarboxylic acids, thiopolycarboxylic acids, 8-hydroxyquinoline and its derivatives, aromatic derivates of hydroxyaldehydes and hydroxyketones, hydroxyazodyes.[1–9] The colored anionic chelates of Ge(IV) form ion-associated complexes with bulky organic cations, like tetradecyl(trihexyl)phosphonium, methyltrioctylammonium, cetylpyridinium, cetyltrimethylammonium, tetraphenylammonium, tetraphenylarsonium.[10–16]

The structure and the properties of the tetrazolium salts determine their ability to form ion-associated complexes.[17,18] The bulky hydrophobic organic substituents in the molecules of the tetrazolium salts increase the extractability of the ion-associated complexes. The presence of a quaternary nitrogen atom in the molecules of the tetrazolium salts determines the ability to form ionic associates with chelates of metals in aqueous phase without protonation, as opposed to the amines. The preparation and the application of ion-associated complexes of anionic chelates of metals with various natural organic and inorganic ligands containing N- or O-donor atoms and with the participation of mono- and ditetrazolium cations is a special scientific research field of chemistry of the coordination compounds. Tetrazolium salts are used as reagents for the preparation of various ion-associated complexes of metals, e.g. Mo(VI), Ga(III), Co(II).[19–26] The liquid-liquid extraction, as a part of the chemistry of the solutions and the coordination compounds, is applied to study the processes of complex formation and the extraction equilibria. The extraction spectrophotometry is a relatively simple, convenient, sensitive, selective, rapid to perform and inexpensive method for preparation and characterization of new complex compounds as well as for their application in the chemical analysis.[27–32]

The aim of this research was to study spectrophotometrically the formation of the ion-associated complex between the anionic chelate of germanium(IV) with 4-nitrocatechol (4-NC) and the cation of of 3-(2-naph-

tyl)-2,5-diphenyl-2*H*-tetrazolium chloride (TV) in the liquid-liquid system Ge(IV)–4-NC–TV–H_2O–$CHCl_3$ as well as to evaluate the possible applications of the system for determination of traces of germanium(IV) in alloys, biological, medical and pharmaceutical samples.

2. Experimental

2. 1. Reagents and Apparatus

GeO_2 (Sigma-Aldrich, Munich, Germany, p.a.): A 2.0×10^{-3} mol L^{-1} aqueous solution of Ge(IV) was prepared by dissolving GeO_2 in water upon moderate heating.

4-Nitrocatechol (4-NC) (Sigma-Aldrich, p.a.): 4-NC was dissolved in distilled water to give a 1.0×10^{-2} mol L^{-1} solution.

3-(2-Naphthyl)-2,5-diphenyl-2*H*-tetrazolium chloride (TV) (Fluka, p.a.): A chloroform 3.0×10^{-3} mol L^{-1} solution was prepared.

The acidity of the aqueous medium was set using a buffer solution prepared by mixing 2.0 mol L^{-1} aqueous solutions of CH_3COOH and NH_4OH.

The organic solvent $CHCl_3$ was additionally distilled.

The pH was checked by HI 83140 pH meter (Romania). A Camspec M508 spectrophotometer (United Kingdom), equipped with 10 mm path length cells, was employed for measurement of the absorbance.

2. 2. Procedure for Establishment of the Optimum Extraction-Spectrophotometric Conditions

Aliquots of Ge(IV), 4-NC, TV and buffer (pH = 3.5–4.5) solutions were filled into separatory funnels. The resulting solutions were diluted with distilled water to a total volume of 10 mL. Then 10 mL of chloroform was added and the funnels were shaken. A portion of the organic extract was filtered through a filter paper into a cell and the absorbance was measured against a blank sample.[20,23]

2. 3. Procedure for Determination of the Distribution Constant

In order to determine the distribution constant K_D, it is necessary to measure the light absorbances A_1 and A_3, which are the light absorbance after a single extraction in chloroform under the optimum conditions for complex formation (Table 1, column 1) and after a triple extraction performed under the same conditions, respectively. The distribution constant K_D can be calculated according to the ratio $K_D = A_1/(A_3 - A_1)$. *Single extraction*: the single extraction is conducted with 10 mL of chloroform. After the separation of the two phases, the organic extract is transferred into a 25 mL calibrated flask which is brought to volume with chloroform. The measurement of the light absorbance A_1 is performed against a blank sample, prepared under the same conditions. *Triple extraction*: the first stage of the triple extraction is performed with 10 mL of chloroform and the extract is transferred into a 25 mL calibrated flask. During the second stage of the extraction, 8 mL of chloroform are added to the aqueous phase remaining after the first stage. The organic layer is added to that from the first stage. For the third stage of extraction, 7 mL of chloroform are added to the aqueous phase remaining after the second stage and an extraction is performed for the third time. The organic layer is transferred to the previous two. The calibrated flask is brought to volume with chloroform. The measurement of A_3 is performed against a blank sample prepared in the same way.[22]

3. Results and Discussion

3. 1. Optimum Extraction-Spectrophotometric Conditions

3. 1. 1. Absorption Spectra

The colored anionic chelate of germanium(IV)–4-NC can be efficiently extracted in chloroform in the presence of the bulky hydrophobic organic cations of monotetrazolium salt (TV). The absorption spectrum of the extract of the ion-associated complex, formed between the anionic chelate of Ge(IV) with 4-NC and the cation of monotetrazolium salt in $CHCl_3$, is characterized by an absorption maximum in the visible range (λ_{max} = 420 nm) (Figure 1).

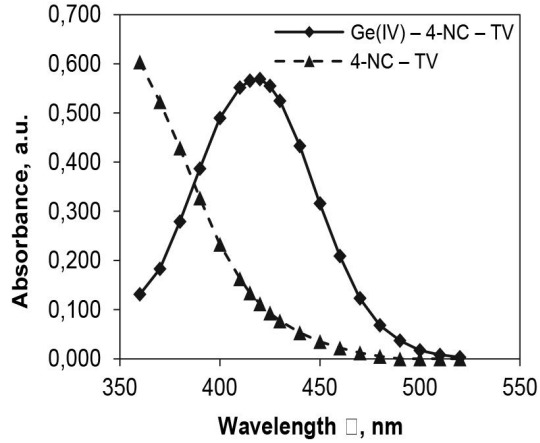

Figure 1. Absorption spectra of the complex Ge(IV)–4-NC–TV and of the blank sample 4-NC–TV in $CHCl_3$; $C_{Ge(IV)} = 2.0 \times 10^{-5}$ mol L^{-1}; $C_{4\text{-NC}} = 5.0 \times 10^{-4}$ mol L^{-1}; $C_{TV} = 1.5 \times 10^{-4}$ mol L^{-1}; pH = 4.0; λ = 420 nm; τ = 2 min

3. 1. 2. Effect the Acidity of the Aqueous Phase and the Shaking Time

The acidity of the aqueous phase has a substantial effect on the extraction of the anionic chelate Ge(IV)–4-NC into the organic phase. The maximum and constant extraction of the ion-associated complex is achieved in

the pH range from 3.5 to 4.5 (Figure 2). Acetate buffer solution with pH = 4.0 was used in all further experiments. The carried-out experiments, showed that the extraction equilibrium is achieved for shaking time of not less than 60 s. The longer shaking time did not affect the absorbance. The further experiments were performed with shaking time 2 min.

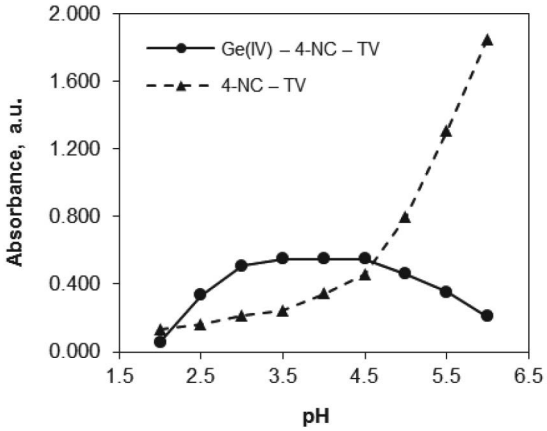

Figure 2. Absorbance of Ge(IV)–4-NC–TV extract against 4-NC-TV extract and of 4-NC–TV against $CHCl_3$ vs. pH of the aqueous phase; $C_{Ge(IV)} = 2.0 \times 10^{-5}$ mol L^{-1}; $C_{4\text{-NC}} = 5.0 \times 10^{-4}$ mol L^{-1}; $C_{TV} = 1.5 \times 10^{-4}$ mol L^{-1}; $\lambda = 420$ nm; $\tau = 2$ min

3. 1. 3. Effect of Reagents' Concentrations

The concentrations of the reagents are the most important factor, influencing the extraction equilibrium. The chelate formation of Ge(IV)-4-NC requires a 15.0–fold excess of 4-NC ($\geq 3.0 \times 10^{-4}$ mol L^{-1}). For a maximum association and extraction the amount of TV should not be lower than a 4.5–fold excess ($\geq 9.0 \times 10^{-5}$ mol L^{-1}).

3. 2. Beer's Law, Apparent Molar Absorptivity and other Analytical Characteristics

The range of obedience to the Beer's law, i.e. the linear relationship between the germanium(IV) concentration in the aqueous phase ($C_{Ge(IV)}$, μg mL^{-1}) and the absorbance of the ion-association complex in the organic phase after extraction was studied using regression analysis under the optimum conditions for complex formation. The equation of a straight line was found to be Y = 0.3933 X + 0.0020 with a correlation coefficient squared 0.9995. Under the optimum conditions for complex formation, the linearity is observed for concentrations up to 4.07 μg cm^{-3} Ge(IV). Further analytical characteristics, such as apparent molar absorptivity ε′, adherence to Beer's law, Sandell's sensitivity, limit of detection and limit of quantification, are shown in Table 1, column 2.

3. 3. Molar Ratios of the Ion-Associated Complex

The molar ratios of the ion-associated complex were determined by three independent methods: the mobile equilibrium method, the straight-line method of Asmus and the method of continuous variations.[33]

The mobile equilibrium method and the straight-line method of Asmus were applied to prove the molar ratios Ge(IV):4-NC and Ge(IV):TV. The values of the correlation coefficient squared R^2, determined by the straight-line method of Asmus are presented in Table 2.

Table 2. Values of the correlation coefficient squared (R^2), corresponding to various molar ratios of Ge(IV):4-NC and Ge(IV):TV (n and m, respectively)

Values of correlation coefficient squared (R^2), corresponding to molar ratios 1, 2 and 3, respectively	
Ge(IV):4-NC	Ge(IV):TV
(n = 1) $R^2 = 0.9303$	(m = 1) $R^2 = 0.9841$
(n = 2) $R^2 = 0.9814$	(m = 2) $R^2 = 0.9959$
(n = 3) $R^2 = 0.9988$	(m = 3) $R^2 = 0.9653$

The results from the application of the straight-line method of Asmus and the mobile equilibrium method are shown in Figure 3 and Figure 4, respectively.

Table 1. Optimum extraction-spectrophotometric conditions and analytical characteristics of the system Ge(IV)–4-NC–TV–H_2O–$CHCl_3$

Optimum Conditions	Analytical Characteristic
Absorption maximum (λ_{max}) 420 nm	Apparent molar absorptivity (ε′) $(2.87 \pm 0.05) \times 10^4$ L mol^{-1} cm^{-1}
Volume of the aqueous phase 10 cm^3	True molar absorptivity (ε) $(2.95 \pm 0.01) \times 10^4$ L mol^{-1} cm^{-1}
Volume of the organic phase 10 cm^3	Sandell's sensitivity (SS) 2.53 ng cm^{-2}
pH of the aqueous phase 3.5÷4.5	Adherence to Beer's law up to 4.07 μg cm^{-3}
Shaking time (τ) 2 min	Relative standard deviation (RSD) 1.98%
Concentration of 4-NC $\geq 3.0 \times 10^{-4}$ mol L^{-1}	Limit of detection (LOD) 0.10 μg cm^{-3}
Concentration of TV $\geq 9.0 \times 10^{-5}$ mol L^{-1}	Limit of quantification (LOQ) 0.33 μg cm^{-3}

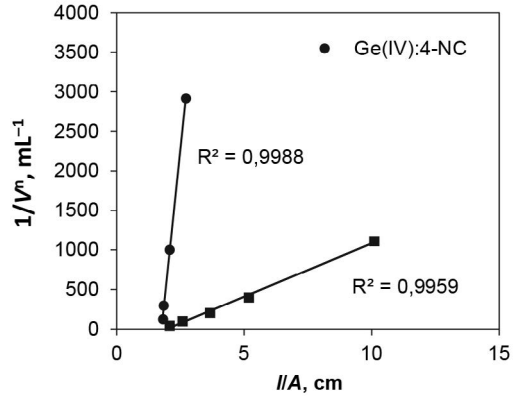

Figure 3. Determination of the molar ratios by the straight-line method of Asmus; $C_{Ge(IV)} = 2.0 \times 10^{-5}$ mol L^{-1}; pH = 4.0; λ = 420 nm; τ = 2 min; • Ge(IV):4-NC, $C_{TV} = 3.0 \times 10^{-4}$ mol L^{-1}, ▪ Ge(IV):TV, $C_{4\text{-NC}} = 5.0 \times 10^{-4}$ mol L^{-1}

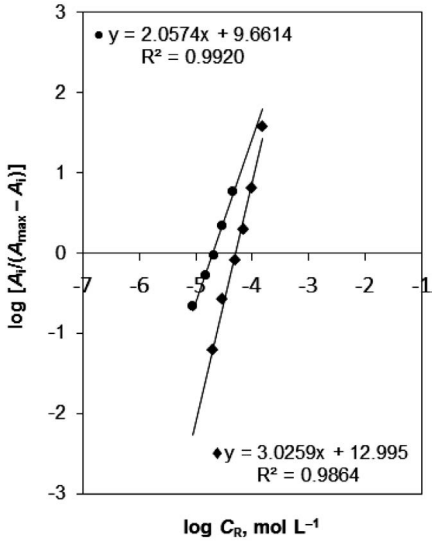

Figure 4. Straight lines by the mobile equilibrium method for determination of the molar ratios Ge(IV):4-NC and Ge(IV):TV; $C_{Ge(IV)} = 2.0 \times 10^{-5}$ mol L^{-1}; pH = 4.0; λ = 420 nm; τ = 2 min; ◆ Ge(IV):4-NC, $C_{TV} = 3.0 \times 10^{-4}$ mol L^{-1}; • Ge(IV):TV, $C_{4\text{-NC}} = 5.0 \times 10^{-4}$ mol L^{-1}

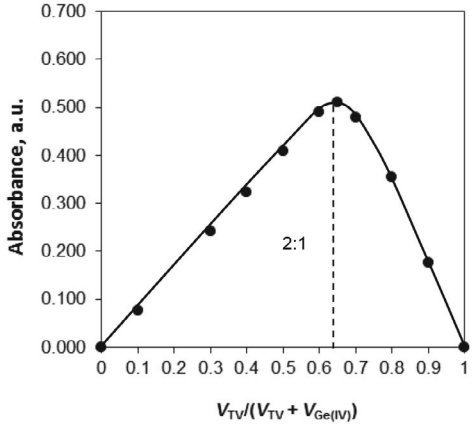

Figure 5. Determination of the molar ratio (n) Ge(IV):TV by the method of continuous variations; $C_{Ge(IV)} + C_{TV} = 6.0 \times 10^{-5}$ mol L^{-1}; $C_{4\text{-NC}} = 5.0 \times 10^{-4}$ mol L^{-1}; pH = 4.0; λ = 420 nm; τ = 2 min

On the basis of the results it can be concluded that Ge(IV), 4-NC and TV interact in molar ratio 1:3:2. The application of the method of continuous variations confirmed the molar ratio Ge(IV):TV = 1:2 (Figure 5).[33]

3. 4. Reaction Scheme and Suggested General Formula

Ions containing germanate $[Ge(OH)_6]^{2-}$ are already described in the literature although in dilute aqueous solutions the major determined ions appear to be $[GeO(OH)_3]^-$, $[GeO_2(OH)_2]^{2-}$ and $\{[Ge(OH)_4]_8(OH)_3\}^{3-}$.[1] The performed experiments showed that the complex formation and the extraction of the ion-associated complex have occurred in the dilute solutions and the molar ratio established by the independent methods mentioned above was Ge(IV):4-NC:TV = 1:3:2. Therefore, the complex formation of anionic chelate Ge(IV)–4-NC can be given by equation (1):

$$[GeO_2(OH)_2]^{2-}{}_{aq} + 3\ (HO)_2C_6H_3(NO_2)_{aq} \rightarrow \rightarrow \{Ge[O_2C_6H_3(NO_2)]_3\}^{2-}{}_{aq} + 4\ H_2O \quad (1)$$

Having in mind the molar ratio indicated above and the reaction of chelate formation of Ge(IV)–4-NC, it can be suggested that the formation of the ion-associated complex in the aqueous phase, its distribution between the aqueous and the organic phases and its extraction in chloroform can be given by the following equations (2–4).

$$2\ (TV)^+_{(aq)} + \{Ge[O_2C_6H_3(NO_2)]_3\}^{2-}{}_{(aq)} \rightleftharpoons \rightleftharpoons (TV)_2\{Ge[O_2C_6H_3(NO_2)]_3\}_{(aq)} \quad (2)$$

$$(TV)_2\{Ge[O_2C_6H_3(NO_2)]_3\}_{(aq)} \rightleftharpoons \rightleftharpoons (TV)_2\{Ge[O_2C_6H_3(NO_2)]_3\}_{(org)} \quad (3)$$

$$2\ (TV)^+_{(aq)} + \{Ge[O_2C_6H_3(NO_2)]_3\}^{2-}{}_{(aq)} \rightleftharpoons \rightleftharpoons (TV)_2\{Ge[O_2C_6H_3(NO_2)]_3\}_{(org)} \quad (4)$$

Therefore, the ion-associated anionic chelate of Ge(IV)–4-NC with the cation of monotetrazolium salt can be represented by the general formula $(TV)_2\{Ge[O_2C_6H_3(NO_2)]_3\}$.

3. 5. Equilibrium Constants, True Molar Absorptivity, Recovery Factor and Structure of the Ion-Associated Complex

The association process in aqueous phase and the extraction equilibria were investigated and quantitatively characterized with respect to the following key constants: distribution constant K_D, association constant β, extraction constant K_{ex} and recovery factor R%.

The distribution constant K_D was determined by equation (5), where A_1 and A_3 are the absorbances (measured against blanks) obtained after a single and triple extraction, respectively.

$$K_D = \{(TV)_2\{Ge[O_2C_6H_3(NO_2)]_3\}\}_{(org)} / / \{(TV)_2\{Ge[O_2C_6H_3(NO_2)]_3\}\}_{(aq)} = = A_1 / (A_3 - A_1) \quad (5)$$

The recovery factor was determined from the equation (6):

$$R\% = 100\ K_D / (K_D + 1) \quad (6)$$

The extraction constant K_{ex} was calculated by two independent methods:

(i) from the equation $\log K_{ex} = \log K_D + \log \beta$
(ii) by the method of Likussar-Boltz. [34] (7)

(i) The association constant β was determined by two independent methods: Komar–Tolmachev method and Holme–Langmyhr method and their values are given in Table 3, column 2.[33,34] The association constant β was calculated by the method of Komar-Tolmachev from equation (8).[33]

$$\beta = (l/n)^n / [\varepsilon\ (tg\ \alpha)^{n+1}] \quad (8)$$

where l is the cuvette thickness (l = 1 cm); n -the molar ratio between the components independently determined (e.g. by the mobile equilibrium method, the straight-line method of Asmus or the method of continuous variations) (n = 2), ε – the true molar absorptivity.

The true molar absorptivity ε was determined by the method of Komar-Tolmachev (Figure 6) from the equation of a straight line Y = 0.4182 X + 3.3895 ($\varepsilon = 1 / (b \times 10^{-5})$) and its value is given in Table 1, column 2.[33]

(ii) The method of Likussar-Boltz uses the data from the method of continuous variations (Figure 5). The extraction constant K_{ex} was calculated by the equation of Likussar-Boltz for molar ratio 1:2 (equation 9):[35]

$$\log K_{ex} = 0{,}3522 - 2 \log K + + \log Y_{max} - 3 \log (1 - Y_{max}) \quad (9)$$

where K is the total concentration of the reagents (K = $C_{Ge(IV)} + C_{TV} = 6.0 \times 10^{-5}$ mol L^{-1}); Y_{max} and $(1-Y_{max})$ are determined from the additionally plotted normalized absorption curve (Y_{max} = 0.900; $(1 - Y_{max})$ = 0.100).

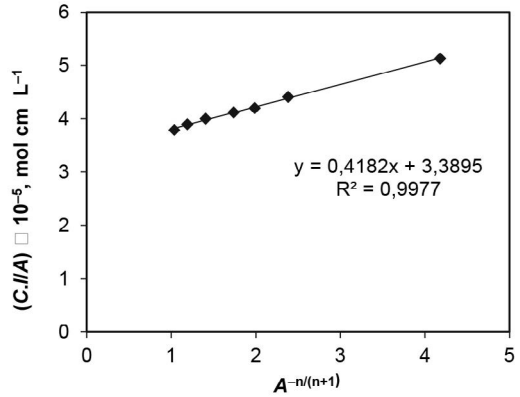

Figure 6. Dependency of $(C.l/A)$ on $A^{-n/(n+1)}$ (method of Komar–Tolmachev) ; $C = C_{Ge(IV)}$ mol L^{-1}; $C_{TV} = 2\ C_{Ge(IV)}$ mol L^{-1}; $C_{4\text{-NC}} = 5.0 \times 10^{-4}$ mol L^{-1}; pH = 4.0; λ = 420 nm; τ = 2 min; A – absorbance; l – cell thickness, l = 1 cm; n = 2

The values of the equilibrium constants and the recovery factor, describing quantitatively the equilibrium in the aqueous phase and the extraction of the ion- associated complex in the organic phase are presented in Table 3.

The results obtained by the independent methods are statistically similar and confirm the proposed scheme of the process of formation of the ion-associated complex in the aqueous phase, its distribution between the aqueous and the organic phases and its extraction in chloroform. Based on this, the proposed structure of the ion-associated complex is represented in Figure 7.

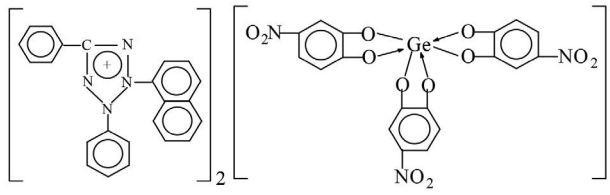

Figure 7. Structure of the ion-associated complex Ge(IV)–4-NC–TV

Table 3. Values of the Equilibrium Constants and the Recovery Factor

Equilibrium Constant and Recovery Factor	Value
Equilibrium (equation 2) – Association constant β	$\log \beta = (11.06 \pm 1.34)^a$
$\beta = (TV)_2\{Ge[O_2C_6H_3(NO_2)]_3\}_{(aq)} / \{[(TV)^+]^2_{(aq)} \times \{\{Ge[O_2C_6H_3(NO_2)]_3\}^{2-}\}_{(aq)}\}$	$\log \beta = (10.25 \pm 1.01)^b$
Equilibrium (equation 3) – Distribution constant K_D $K_D = \{(TV)_2\{Ge[O_2C_6H_3(NO_2)]_3\}\}_{(org)} / \{(TV)_2\{Ge[O_2C_6H_3(NO_2)]_3\}\}_{(aq)}$	$\log K_D = (1.20 \pm 0.01)^c$
Equilibrium (equation 4) – Extraction constant K_{ex}	$\log K_{ex} = (12.26 \pm 1.35)^d$
$K_{ex} = \{(TV)_2\{Ge[O_2C_6H_3(NO_2)]_3\}\}_{(org)} / \{\{[TV]^+\}^2_{(aq)} \times \{\{Ge[O_2C_6H_3(NO_2)]_3\}^{2-}\}_{(aq)}\}$	$\log K_{ex} = (11.76 \pm 0.01)^e$
Recovery factor R%	$R = (94.02 \pm 0.41)\%^f$

[a] Calculated by Komar-Tolmachev method (equation.(8)); [b] Calculated by Holme-Langmyhr method;[34] [c] Calculated by equation (5); [d] Calculated by equation (7), where β is determined by the Komar-Tolmachev method; [e] Calculated by Likussar-Boltz method (equation (9)); [f] Calculated by equation (6).

and 4-nitrocatechol (4-NC) with the cation of of 3-(2-naphtyl)-2,5-diphenyl-2*H*-tetrazolium chloride (TV) was studied by spectrophotometry. The yellow-colored anionic chelate of Ge(IV)-4-NC interacted with the organic cation of the monotetazolium salt (TV) leading to the formation of an ion-associated complex well soluble in chloroform. The bulky organic molecule of TV determined the extractability of the ion-associated complex in organic phase. The optimum conditions for the association in the aqueous phase and for the extraction of the ion-associated complex Ge(IV)-4-NC-TV were established. The equilibrium constants and analytical characteristics needed for the quantitative assessment of the extraction equilibrium were calculated, i.e. the association constant (β), the distribution constant (K_D), the extraction constant (K_{ex}), the recovery factor (R), the apparent molar absorptivity (ε'), the true molar absorptivity (ε), the limit of detection (*LOD*), the limit of quantification (*LOQ*) and the Sandell's sensitivity (*SS*). From the analytical characteristics of the extraction system Ge(IV)-4-NC-TV-H_2O-$CHCl_3$, it can be concluded that the ion-associated complex formed between the anionic chelate of Ge(IV)-4-NC and the monotetrazolium cation could allow determinations of Ge(IV) in various samples with a high sensitivity. The molar ratio of the components, determined by independent methods, showed that the ion-associated complex could be represented with the general formula $(TV)_2\{Ge[O_2C_6H_3(NO_2)]_3\}$. A corresponding reaction scheme of the complex formation and a structure of the ion-associated complex were also suggested.

5. Acknowledgements

The authors would like to thank the Research Fund of the University of Plovdiv for the financial support of the current research.

6. References

1. F. A. Cotton, G. Wilkinson, C. A. Murillo, M. Bochmann: *Advanced Inorganic Chemistry, Wiley Publishers*, New Jersey, **1999,** pp. 392–394.
2. V. V. Skopenko, A. Y. Tsivadze, L. I. Sabranskiy, A. D. Garnovskiy: *Coordination Chemistry, Akademkniga,* Moscow, Russia, *2007,* pp. 78–81.
3. V. S. Sergienko, L. K. Minacheva, A. V. Churakov, *Rus. J. Inorg. Chem.* **2010,** *55,* 2001-2030. **DOI:**10.1134/S0036023610130012
4. W. Levason, G. Reid, W. Zhang, *Coord. Chem. Rev.* **2011,** *255,* 1319-1341. **DOI:**10.1016/j.ccr.2010.11.019
5. M. F. Davis, W. Levason, G. Reid, M. Webster, *Dalton Trans. 2008, 17,* 2261–2269. **DOI:**10.1039/b716765b
6. I. I. Seifullina, N. V. Shmatkova, E. E. Martsinko, *Russ. J. Coord. Chem. 2010, 30,* 214–220. **DOI:**10.1023/B:RUCO.0000022120.49644.5c
7. F. Cheng, M. F. Davis, A. L. Hector, W. Levason, G. Reid, M. Webster, W. Zhang, *Eur. J. Inorg. Chem.* **2007,** 2007, 2488–2495. **DOI:**10.1002/ejic.200700233
8. G. S. Pokrovski, F. Martin, J. L. Hazemann, J. Schott, *Chem. Geol.* **2000,** *163,* 151–165. **DOI:**10.1016/S0009-2541(99)00102-3
9. D. Biller, C. Burschka, M. Penka, R. Tacke, *Inorg. Chem.* **2002,** *41,* 3901-3908. **DOI:**10.1021/ic0255757
10. V. A. Nazarenko: *Analytical Chemistry of Germanuim,* Nauka, Moscow, Russia, 1973, pp. 29–54.
11. I. I. Seifullina, A. G. Pesaroglo, L. Kh. Minacheva, E. E. Martsinko, V. S. Sergienko, *Russ. J. Inorg. Chem.* **2006,** *51,* 1892–1899. **DOI:**10.1134/S0036023606120096
12. L. Zaijun, P. Jiaomai, T. Jan, *Anal. Chim. Acta* **2001,** *445,* 153–159. **DOI:**10.1016/S0003-2670(01)01259-4
13. F. N. Shi, L. C. Silva, M. J. Hardie, T. Trindade, F. A. Paz, J. Rocha, *Inorg. Chem.* **2007,** *46,* 6502–6515. **DOI:**10.1021/ic700507j
14. F. A. Torralvo, C. Fernandez-Pereira, M. C. Campanario, *Ind. Eng. Chem. Res.* **2010,** *49,* 4817–4823. **DOI:**10.1021/ie901020f
15. S. Jagatap, S. Kolekar, S. Han, M. Anuse, *Inter. J. Anal. Bioanal. Chem.* **2012,** *2,* 235–240. http://www.urpjournals.com
16. K. T. Mahmudov, R. A. Aliyeva, S. Z. Hamidov, F. M. Chyragov, S. R. Mardanova, M. N. Kopylovich, A. J. L. Pombeiro, *Am. J. Anal. Chem.* **2012,** *3,* 790–799. **DOI:**10.4236/ajac.2012.312105
17. A. W. Nineham, *Chem. Rev.* **1955,** *55,* 355–483 **DOI:**10.1021/cr50002a004
18. H. Şenöz, Hacettepe *J. Biol. Chem.* **2012,** *40,* 293–301.
19. K. B. Gavazov, V. D. Lekova, G. I. Patrovov, *Acta Chim. Slov.* **2006,** *53,* 506–511.
20. V. Divarova, V. Lekova, P. Racheva, K. Stojnova, A. Dimitrov, *Acta Chim. Slov.* **2014,** *61,* 813–818.
21. K. Stojnova, V. Divarova, P. Racheva, G. Daskalov, V. Lekova, *Monatsh. Chem.* **2015,** *146,* 867–873. **DOI:**10.1007/s00706-014-1402-7
22. V. Divarova, K. Stojnova, P. Racheva, V. Lekova, *Acta Chim. Slov.* **2016**, *63,* 97–103. DOI:10.17344/acsi.2015.1987
23. K. Stojnova, P. Racheva, V. Divarova, K. Bozhinova, V. Lekova, *Acta Chim. Slov.* **2016,** *63,* 654-660. **DOI:**10.17344/acsi.2016.2513
24. K. Stojnova, P. Racheva, V. Divarova, K. Bozhinova, V. Lekova, Russ. J. Inorg. Chem. 2017, 62, 249–256. **DOI:**10.1134/S0036023617020188
25. P. Racheva, K. Stojnova, V. Divarova, V. Lekova, *Acta Chim. Slov.* **2017,** *64,* 365–372. **DOI:**10.17344/acsi.2017.3214
26. K. Stojnova, V. Divarova, P. Racheva, K. Bozhinova, V. Lekova, *Acta Chim. Slov.* **2018,** *65,* 213-220. **DOI:**10.17344/acsi.2017.3860
27. A. K. Babko, A. T. Pilipenko: *Photometric Analysis, Khimiya,* Moscow, Russia, **1968,** pp. 159-164.
28. V. A. Mikhaylov: *Extraction Chemistry, Nauka,* Novosibirsk, Russia, **1984,** pp. 194–249.
29. G. Kristian: *Analytical Chemistry, BINOM,* Moscow, Russia, **2009,** pp. 414–426.

30. Yu. A. Zolotov, V. A. Bodnya, A. N. Zagrusina, H. Freiser, *Anal. Chem.* **1982,** *14,* 93–174. **DOI:**10.1080/10408348208085525
31. V. V. Divarova, K. T. Stojnova P. V. Racheva, V. D. Lekova, J. *Appl. Spectrosc.* **2017,** *84,* 231–236. **DOI:**10.1007/s10812-017-0456-9
32. V. Divarova, K. Stojnova, P. Racheva, V. Lekova, *Russ. J. Inorg. Chem.* **2018,** *63,* 974–977. **DOI:**10.1134/S0036023618070057
33. M. I. Bulatov, I. P. Kalinkin: *Practical Handbook on Photometric Methods of Analysis, Khimiya,* Leningrad, Russia, 1986, pp. 174–264.
34. A. Holme, F. J. Langmyhr, *Anal. Chim. Acta* **1966,** *36,* 383–391. **DOI:**10.1016/0003-2670(66)80066-1
35. W. Likussar, D. F. Boltz, *Anal. Chem* **1971,** *43,* 1265–1272. **DOI:**10.1016/0003-2670(66)80066-1

Povzetek

S spektrofotometričnimi metodami smo raziskali tvorbo ionsko asociiranega kompleksa med anionskim kelatom germanija(IV) s 4-nitrokateholom (4-NC) in kationom iz 3-(2-naftil)-2,5-difenil-2*H*-tetrazolijevega klorida (TV). Določili smo optimalne pogoje za tvorbo kelata in za ekstrakcijo kompleksa v tekočina-tekočina ekstrakcijskem sistemu Ge(IV)-4-NC-TV-H_2O-$CHCl_3$. Preverili smo veljavnost Beerovega zakona ter izračunali nekatere analizne karakteristike. Asociacijski proces v vodni fazi in ekstrakcijsko ravnotežje smo proučili in kvantitativno karakterizirali sledeče ključne konstante: konstanto asociacije, porazdelitveno in ekstrakcijsko konstanto ter izkoristek ekstrakcije. Molsko razmerje komponent v ionsko asociiranem kompleksu smo določili na podlagi neodvisnih metod. Na podlagi dobljenih podatkov je predlagana reakcijska shema, splošna formula in struktura kompleksa.

Scientific paper

Effect of Microwave-Assisted Extraction on Polyphenols Recovery from Tomato Peel Waste

Marina Tranfić Bakić, Sandra Pedisić, Zoran Zorić, Verica Dragović-Uzelac and Antonela Ninčević Grassino*

Faculty of Food Technology and Biotechnology, University of Zagreb, Pierottijeva 6, 10000 Zagreb, Croatia

** Corresponding author: E-mail: aninc@pbf.hr*
Phone: +385 1 4605 062 Fax: +385 1 4836 083

Received: 11-22-2018

Abstract

This study describes the application of microwave-assisted extraction (MAE) as an innovative technique for isolation of polyphenols from tomato peel waste. Effects of solvents, temperatures (25, 55 and 90 °C) and times (5 and 10 min) were evaluated with regard to total phenols (TP), total flavonoids (TF) and phenolic compound contents. Tomato peel extracts contain high amounts of kaemferol-3-*O*-rutinoside (8.5 to 142.5 mg kg^{-1}), *p*-coumaric acid (3 to 111.5 mg kg^{-1}) and chlorogenic acid derivative (10.5 to 109 mg kg^{-1}). Results revealed that extraction time has no significant ($p > 0.05$) influence on TP, TF and phenolic compounds recovery (exception is *cis*-*p*-coumaric acid hexoside). On the other hand, the influence of temperature and chosen solvent on polyphenols yield is significant.

Considering interest of consumers to intake natural compounds exhibiting antioxidant properties, this work suggests that tomato peel waste can be used as one of sustainable resources for polyphenols production by MAE.

Keywords: Tomato peel waste; microwaves-assisted extraction; polyphenols; HPLC-DAD

1. Introduction

Tomato edible fruit of *Solanum lycopersicum*, which belongs to the *Solanaceae* family, is the second most produced and consumed vegetable in the world, either fresh or processed in the form of canned tomatoes, sauce, juice, ketchup and soup. Industrial processing of tomato generates significant amounts of waste, consisting mainly of tomato peels and seeds, but also leaves and stems. The management of tomato by-products is considered an important problem faced by tomato processing companies, due to its disposal to the environment. Usually, they are partially reused by composting or drying for animal feeding. However, modern eco-compatible technologies offer more efficient strategies to recycle these by-products and reuse them as a sustainable source of different nutrients and highly biologically active compounds, such as amino acids, fatty acids, minerals and carotenoids.[1–3] Apart from carotenoids, i.e. lycopene and β-carotene found in major amounts, tomato by-products are also rich in phenolic compounds.[2,4–6]

Variations in chemistry of phenolic compounds in fruits, vegetables and agri-industrial wastes are related to different proportions of simple and complex phenols, such as benzoic and cinnamic acids, coumarins, tannins, lignins, lignans and flavonoids.[7] These diverse forms of phenolic compounds show variable responses to different extraction conditions. Furthermore, the optimum recovery of phenolics differs from one substrate to the other and depends on the type of fruit, vegetable and their by-products.

In order to maximize the recovery of polyphenols from tomato waste, different conventional[8–15] and non-conventional (sonication or ultrasonic bath)[16,17] extraction techniques, as well as operation conditions (time, temperature, polarity of solvent and addition of hydrochloric acid or sodium hydroxide to organic solvents) were employed. Several researches[4,5,18,19] have reported that conventional methods, such as Soxhlet extraction and refluxing, had significant disadvantages like long extraction times, evaporation of the huge amounts of solvents, and thermal decomposition of thermo-labile compounds. To overcome these limitations, new and promising extraction methods, such as ultrasound-assisted extraction, enzyme-assisted extraction, and pressurized liquid extraction, were recently introduced for polyphenols isolation.[4,5,18,19] Another one of the innovative and advanced techniques is microwave-assisted extraction (MAE), which provides greater extraction efficiency in shorter time, at lower temperature and with smaller amount of

solvent.[20,21] In this method, the separation of solutes from sample matrix is based on the conversion of microwave energy to heat, by ionic conduction and dipole rotation.[22]

The structure and polarity of target compound, environmental safety, human toxicity, and financial feasibility are main factors in the choice of solvent. Water, methanol, ethanol, acetone, hexane and their combinations, are commonly used for polyphenols extractions from tomato waste.[8–10,12–17,23] The addition of hydrochloric acid or sodium hydroxide to water or water/organic solvent mixtures was also reported to enhance the extraction of phenolic compounds.[10,17]

Considering health benefits of phenolic compounds and growing interest of consumers to intake natural compounds exhibiting antioxidant properties, this work presents re-utilization of tomato peel waste from canning factory as an additional, low-cost, sustainable resources for the production of polyphenols.

Apart from direct addition of dried tomato waste to various food products, such as meat, bread and cookies,[24–26] the carotenoids, mostly lycopene, isolated from tomato by-products could be also utilized as a food colorants and functional ingredients.[6] In that context and from the agro-industrial point of view, the phenolic compounds extracted in this work could be further used for enrichment of different foodstuffs.

The fact that only a few papers[16,17,27] reported extraction of polyphenols from tomato wastes using non-conventional extraction method inspired us to focus our attention on utilization of MAE as a novel, not yet explored method for polyphenols isolation from tomato peel. Hence, this paper describes the effect of solvent type, acidity, temperature, and time on extraction of polyphenols using MAE as simple, quick and environmentally friendly technique, and defines the optimal parameters for MAE that yield the highest possible amounts of polyphenols with minimum expenditure of extraction resources.

2. Materials and Methods

2. 1. Materials

All the reagents, standards and solvents were of analytical grade. Folin-Ciocolateu reagent and all standards (gallic acid, rutin, caffeic acid, chlorogenic acid, *p*-coumaric acid, quercetin and kaempferol) were purchased from Sigma Aldrich (Steinheim, Germany). Ethanol, methanol, hydrochloric acid, sodium carbonate, sodium nitrite and aluminium chloride hexahydrate were obtained from Kefo (Zagreb, Croatia). Formic acid and acetonitrile (HPLC grade) was purchased from Prolabo (Lutterworth, UK). Deionised water used for the preparation of reagents, standards and solvents was obtained with Millipore-MilliQ apparatus.

Tomato peel waste was purchased from the manufacturing unit (after processing of fresh tomato) of Benin-

Table 1. Microwave-assisted extraction (MAE) of polyphenols from tomato peel waste using water, 1% HCl, 50 and 70% methanol (MeOH) with and without addition of 1% HCl, and 50 and 70% ethanol (EtOH), at temperature of 25, 55 and 90 °C, and time of 5 and 10 min

Run	Sample	Temperature/°C	Solvent	HCl	Time/min
1	**1A**	25			
2	**1A**	55			5
3	**1A**	90			
4	**1B**	25	H_2O	/	
5	**1B**	55			10
6	**1B**	90			
7	**2A**	25			
8	**2A**	55			5
9	**2A**	90			
10	**2B**	25	H_2O	1% (*v*/*v*)	
11	**2B**	55			10
12	**2B**	90			
13	**3A**	25			
14	**3A**	55			5
15	**3A**	90			
16	**3B**	25	50% (*v*/*v*) MeOH	1%(v/v)	
17	**3B**	55			10
18	**3B**	90			
19	**4A**	25			5
20	**4A**	55			
21	**4A**	90			
22	**4B**	25	70% (*v*/*v*) MeOH	1% (*v*/*v*)	
23	**4B**	55			10
24	**4B**	90			
25	**5A**	25			
26	**5A**	55			5
27	**5A**	90			
28	**5B**	25	50% (*v*/*v*) MeOH	/	
29	**5B**	55			10
30	**5B**	90			
31	**6A**	25			
32	**6A**	55			5
33	**6A**	90			
34	**6B**	25	70% (*v*/*v*) MeOH	/	
35	**6B**	55			10
36	**6B**	90			
37	**7A**	25			
38	**7A**	55			5
39	**7A**	90			
40	**7B**	25	50% (*v*/*v*) EtOH	/	
41	**7B**	55			10
42	**7B**	90			
43	**8A**	25			
44	**8A**	55			5
45	**8A**	90			
46	**8B**	25	70% (*v*/*v*) EtOH	/	
47	**8B**	55			10
48	**8B**	90			

casa S.r.l., canning industry located in the Agro Nocerina area of Campania (Angri, Italy). The tomato peel was dried, grounded and packed in polyethylene bags until analysis.

2. 2. Microwave-Assisted Extraction Procedure

Microwave-assisted extractions (MAEs) were carried out in a Milestone START S Microwave Labstation for Synthesis (Bergamo, Italy), using water and water solution of HCl (1%, *v*/*v*), methanol (50 and 70%, *v*/*v*), with or without addition of 1% HCl and ethanol (50 and 70% *v*/*v*) (Table 1). The MAE parameters were times of 5 and 10 min, and temperatures of 25, 55 and 90 °C (Table 1).

Tomato peel sample (1.00 g) was mixed with 50 mL of solvent in a round flask, placed in the MAE apparatus equipped with a condenser and subjected to microwave irradiation, at atmospheric pressure. The power of irradiation was varied from 0 to 500 W to maintain the set extraction temperature. After extraction, the mixture was left to cool down at room temperature and then filtered. The extracts were collected and stored at –8 °C until further analyses.

2. 3. Total Phenols Content

Total phenols (TP) content was determined using the Folin-Ciocalteu method, according to the procedure obtained by Spanos and Worlstad.[28] The detailed procedure is given in the Supporting Information (SI). TP content is expressed as g of gallic acid equivalent (GAE) per kg of tomato peel sample. All the experiments were performed in triplicate and the presented results are the mean values.

2. 4. Total Flavonoids Content

Total flavonoids (TF) content was determined using the aluminum chloride colorimetric assay developed by Zhishen, Mengcheng and Jianming.[29] The detailed procedure is given in the SI. TF content is expressed as g of rutin equivalent (RE) per kg of tomato peel sample. All the experiments were performed in triplicate and the results are reported as mean values.

2. 5. Phenolic Compounds Content

HPLC analysis of individual phenolic compounds in the tomato peel extracts was performed by a liquid chromatograph (Agilent Technologies 1260 series) with a quaternary pump, equipped with a diode array detector (DAD). The HPLC system was controlled by OpenLAB ChemStation Software. Phenolic compounds were separated on a 250 × 4.6 mm, 5 μm film thickness Nucleosil 100-5C18 column (Sigma Aldrich). The column temperature was 35 °C. The gradient elution conditions were previously described by Barros et al.[30] Identification of phenolic compounds was carried out by comparing the retention time and spectral data with those of standards, i.e. caffeic acid, chlorogenic acid, *p*-coumaric acid, quercetin and kaempferol (Sigma Aldrich). The results are expressed in mg of phenolic compounds per kg of tomato peel.

2. 6. Experimental Procedure and Statistical Analysis

The evaluation of under-utilized tomato peel waste as a potential source of polyphenols and MAE as an advanced technique for their extraction was performed in three steps. Firstly, TP and TF were quantified spectrophotometrically, screening the extraction parameters, i.e. solvent, time, temperature and addition of hydrochloric acid (Table 1), to determine which combination assures the highest amounts. Afterwards, selected phenolic compounds were identified and quantified by HPLC-DAD, and influence of extraction parameters on their yields was studied.

Finally, multivariate analyses of variance (MANOVA) were performed using Statistica 12 package (StatSoft) to compare the mean mass fraction values ($N = 3$) of TP, TF and individual phenolic compounds, depending on the used solvents, addition of hydrochloric acid, extraction time and temperature. Post-hoc Tukey HSD test provided additional insight by identifying the means that are significantly different from the other ($p < 0.05$).

3. Results and Discussion

3. 1. Influence of Experimental Conditions on Total Phenols and Flavonoids Recovery

Content of total phenols (TP) and total flavonoids (TF) in tomato peel samples, acquired by MAE are presented in Table 2.

Generally, all samples contained high amounts of TP with variations due to different extraction time, temperature, and solvent. The average TP content was 53.12 g kg^{-1}, and the lowest value was obtained for samples extracted at 25 °C, while higher values were found in samples extracted at 55 and 90 °C. Evidently, the temperature (Figure 1 and Figure S1, SI) had a significant influence on the extractions of phenols (p = 0.000125 for 25 °C vs 90 °C and p = 0.000770 for 55 °C vs 90 °C).

Regarding the TF content, the average amount was 50.36 g kg^{-1}. Again, higher extraction temperatures yielded higher average contents of TF. Like for phenols, the increase of temperature also improved the solubility of flavonoids (Figure 1 and Figure S1, SI). A rise from 25 to 55 and 90 °C significantly (p = 0.000126 and p = 0.000223) en-

Table 2. Content of total phenols (TP) and total flavonoids (TF) obtained from tomato peel waste, extracted by MAE, at temperature of 25, 55 and 90 °C for 5 min (**1–8A**) and 10 min (**1–8B**), using water (**1A–B**), 1% HCl (**2A–B**), 50 and 70% methanol with (**3A–B** and **4A–B**) and without (**5A–B** and **6A–B**) addition of 1% HCl, and 50 and 70% ethanol (**7A–B** and **8A–B**)

Sample	w(TP)/(g kg^{-1}) ± SD*			w(TF)/(g kg^{-1}) ± SD*		
	T (extraction)/°C					
	25	55	90	25	55	90
			t = 5 min			
1A	54.01 ± 0.06	55.03 ± 0.04	54.50 ± 0.12	39.84 ± 0.19	57.05 ± 0.17	36.57 ± 0.07
2A	57.18 ± 0.11	48.63 ± 0.01	59.86 ± 0.09	39.30 ± 0.11	36.08 ± 0.08	46.30 ± 0.09
3A	57.98 ± 0.06	50.91 ± 0.13	57.81 ± 0.03	39.28 ± 0.19	34.46 ± 0.15	43.95 ± 0.08
4A	35.08 ± 0.17	55.29 ± 0.70	63.57 ± 0.19	45.56 ± 0.24	36.92 ± 0.13	55.98 ± 0.09
5A	40.82 ± 0.12	52.25 ± 0.03	61.65 ± 0.06	50.14 ± 0.29	46.77 ± 0.16	61.76 ± 0.15
6A	32.55 ± 0.16	44.81 ± 0.19	62.69 ± 0.09	29.92 ± 0.18	49.60 ± 0.08	62.88 ± 0.22
7A	44.32 ± 0.05	54.81 ± 0.13	63.36 ± 0.02	38.73 ± 0.24	51.45 ± 0.33	71.37 ± 0.47
8A	37.15 ± 0.15	46.66 ± 0.29	59.45 ± 0.05	46.87 ± 0.25	57.77 ± 0.07	107.47 ± 0.05
			t = 10 min			
1B	57.67 ± 0.03	51.07 ± 0.12	57.21 ± 0.07	41.20 ± 0.15	33.05 ± 0.04	47.30 ± 0.04
2B	58.40 ± 0.21	55.32 ± 0.56	60.06 ± 0.22	39.97 ± 0.30	35.47 ± 0.09	43.28 ± 0.09
3B	57.38 ± 0.17	53.39 ± 0.73	59.29 ± 0.07	42.30 ± 0.10	37.08 ± 0.15	54.18 ± 0.04
4B	39.03 ± 0.33	59.36 ± 0.17	67.33 ± 0.05	51.80 ± 0.32	38.86 ± 0.18	60.32 ± 0.32
5B	36.49 ± 0.06	55.44 ± 0.07	78.06 ± 0.05	35.58 ± 0.12	49.63 ± 0.13	65.85 ± 0.18
6B	29.44 ± 0.07	44.79 ± 0.36	70.12 ± 0.10	32.62 ± 0.07	54.56 ± 0.10	72.14 ± 0.45
7B	43.37 ± 0.03	60.12 ± 0.16	71.85 ± 0.08	42.83 ± 0.05	56.87 ± 0.17	76.16 ± 0.11
8B	36.16 ± 0.20	45.13 ± 0.11	52.90 ± 0.02	49.73 ± 0.77	66.41 ± 0.50	104.36 ± 0.09
mean	44.81 ± 10.50	52.06 ± 4.94	62.48 ± 6.59	41.60 ± 6.15	46.38 ± 10.48	63.11 ± 20.22
grand mean				53.12 ± 10.52	50.36 ± 16.26	

*SD = standard deviation

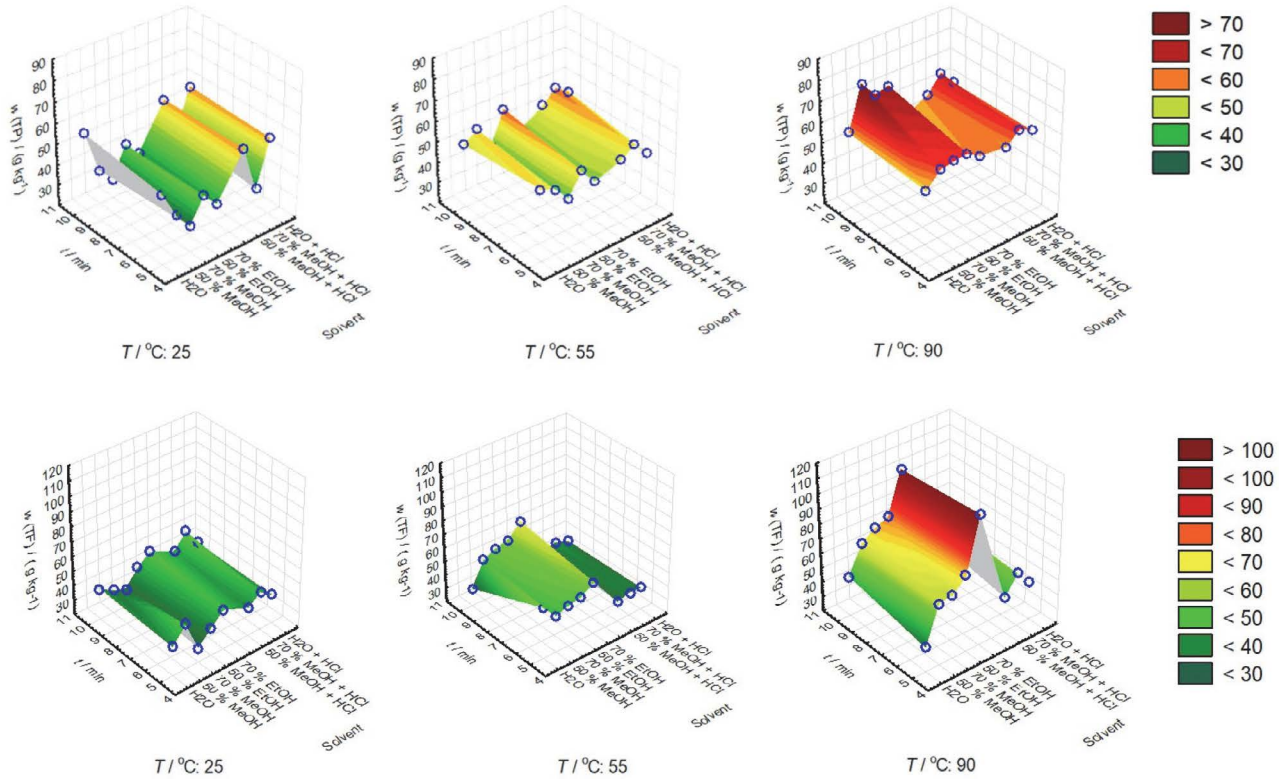

Figure 1. 3D categorized plots of temperature (25, 55 and 90 °C), time (5 and 10 min), and solvent interactions on contents of total phenols (TP) and total flavonoids (TF), extracted from tomato peel waste by MAE.

hanced TF content, due to acceleration of solvent diffusion into the sample matrix. However, some values obtained for TF were greater than the corresponding (same temperature, time and solvent) TP values, particularly that obtained after extraction at 90 °C, using water/organic solvent mixtures. This can be accounted by consideration that some of the phenolic compounds (isoflavone, antocyanin, cinnamic acid, flavanone, flavones, chalcone, flavonol and aurone),[31] as well as other organic compounds presented in tomato cuticle[32] were involved in complexation with $AlCl_3$. Due to the fact that $AlCl_3$ is unspecific reagent in its chelating power, we could suppose that in total sum of flavonoids were additionally included reactions with all of other mentioned compounds.

In contrast to effects of temperature, increase of extraction time from 5 to 10 min had no significant influence on TP ($p = 0.333826$) and TF ($p = 0.519694$) contents (Figure 1 and Figure S2, SI). Therefore, extraction time of 5 min is sufficient for a successful microwave-assisted extraction of phenols from tomato peel waste, and could be considered as optimal for further MAE extraction.

Considering solvents used for extractions, the data (Table 2 and Figure 1) revealed that higher proportion of water added to organic solvents provided better diffusion of phenols through tomato peel cuticle and consequently yielded higher amounts of TP. In that context, 50% methanol (**5A–B**) and ethanol (**7A–B**) provided better extraction of TP, compared to 70% methanol (**6A–B**) and ethanol (**8A–B**), with some exception (90 °C, 5 min, 5A and 6A). Although, slightly higher values were obtained using 50% ethanol than 50% methanol with somewhat lower values obtained at 90 °C (**5B–7B**), both solvents can be considered an adequate choice for further MAE, depending on applied temperatures.

Several researches[33,34] already suggested that a binary solvent system, with lower volume fractions of organic solvents were efficient for extractions of phenols. Moreover, pure water, particularly at lower temperatures of extraction (25 and 55 °C) acted as excellent solvent compared to organic solvent/water mixtures (Table 1 and Figure 1), depending on extraction time (5 min). Due to the fact that water has higher dielectric constant and can thus absorb more microwave energy (by ionic conduction and dipole rotation mechanisms) compared to less polar solvents, the result is higher extraction of phenols.

Pure water was used by El-Mahan et al.[27] for extraction of polyphenols from Egyptian tomato waste by MAE. They reported values of 355.5, 375.0 and 377.5 mg/100 g (TP) and 43.33, 46.66 and 49.89 mg/100 g (TF), for 30, 60 and 90 seconds of extraction, respectively.

Except water, 1% aqueous solution of HCl as polar solvent at lower extraction temperature (25 °C) also gave the high amounts of TP, regardless of the extraction time. However, addition of HCl to other solvents, i.e. 50 and 70% methanol, did not significantly ($p > 0.05$) influence on TP and TF amounts (Figure 1 and Figure S3, SI). Compared to 1% aqueous HCl, organic solvents/water mixture, particularly at temperatures of 55 and 90 °C assured better extractions of flavonoids (Table 2 and Figure 1). Considering common un-polar structure of flavonoids, it was expected that organic solvents/water mixtures will be more appropriate solvents than 50 and 70% methanol with addition of 1% hydrochloric acids.

In summary, tomato peel waste obtained from the canning industry possessed remarkable amounts of TP and TF, compared to values reported by other authors.[8,12–14,23,35] In reference to other extraction parameters, temperature had the greatest effect on extraction yields of phenols and flavonoids. However, their recovery was also associated with the appropriate choice of solvent and its combination with temperature of extraction. In that context, the temperature of 90 °C and 50% methanol with addition of 1% HCl, as well as temperature of 90 °C and 70% ethanol could be considered as optimal extraction conditions for phenols and flavonoids recovery from tomato peel waste, at time of 5 min.

3. 2. Influence of Experimental Conditions on Individual Phenolic Compounds Recovery

The quantification of individual phenolic compounds, namely phenolic acids and their derivatives: *p*-coumaric acid (***p*-CA**), cis-*p*-coumaric acid derivative (**cis-*p*-CA-der**), *p*-coumaric acids hexoside (**cis-*p*-CA hexoside**), chlorogenic acid (**ChA**), chlorogenic acid derivative (**ChA-der**), caffeic acid hexoside I (**CA hexoside I**), and caffeic acid hexoside II (**CA hexoside II**), and flavonols quercetin-pentosylrutinoside (**Q pentosylrutinoside**), quercetin-3-*O*-rutinoside (**Q-3-*O*-rutinoside**), kaempferol-pentosylrutinoside (**K pentosylrutinoside**), and kaempferol-3-*O*-rutinoside (**K-3-*O*-rutinoside**), in tomato peel extracts obtained after MAE was performed by HPLC-DAD analysis and are presented in Figure 2.

The studied compounds were identified in the majority of the extracts. Among them, CA hexoside I, CA hexoside II and ChA were not found in samples extracted by water, 1% HCl, and 50 and 70% ethanol, respectively. Furthermore, flavonols were not identified in samples extracted by water and 1% HCl. In addition, Q and K pentosylrutinoside, and Q-3-*O*-rutinoside was not found in 70% ethanol, and 50% methanol extracts, respectively.

Among phenolic acids and its derivatives (Figure 2), *p*-CA (3 to 111.5 mg kg^{-1}) and ChA der (10.5 to 109 mg kg^{-1}) was predominant, compared to ChA (6 to 62 mg kg^{-1}) and cis-*p*-CA-der (1 to 47.5 mg kg^{-1}). Regarding other derivatives, cis-*p*-CA hexoside, CA hexoside I and CA hexoside II were found in lower amounts, i.e. 0.5 to 29 mg kg^{-1}, 1.5 to 31 mg kg^{-1} and 9 to 25 mg kg^{-1}, respectively.

Several papers [8,10,15–17] reported the presence of phenolic acids (caffeic, chlorogenic, *p*-coumaric, ferulic, phloretic, sinapic, vannilic, syringic, gallic, and rosmarin-

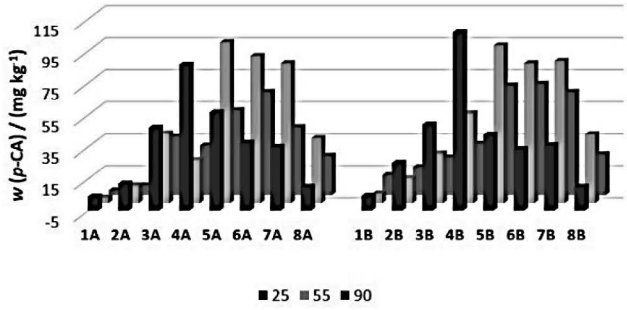
w (p-CA) / (mg kg-1)
115
95
75
55
35
15
-5
1A 2A 3A 4A 5A 6A 7A 8A
1B 2B 3B 4B 5B 6B 7B 8B
25 55 90

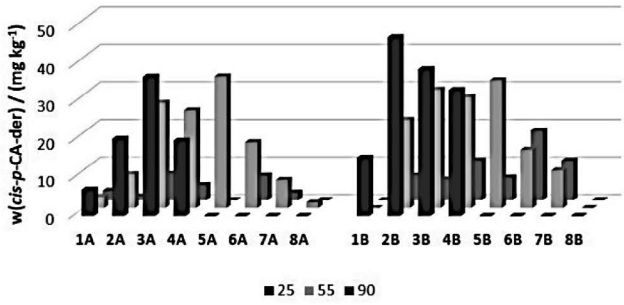
w(cis-p-CA-der) / (mg kg-1)
50
40
30
20
10
0
1A 2A 3A 4A 5A 6A 7A 8A
1B 2B 3B 4B 5B 6B 7B 8B
25 55 90

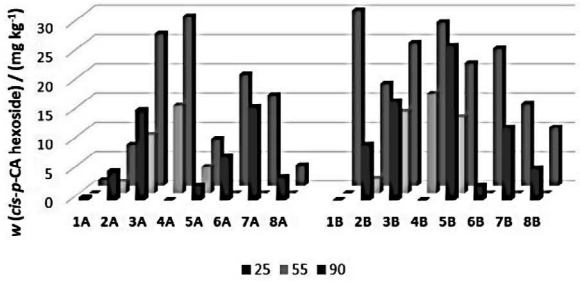
w (cis-p-CA hexoside) / (mg kg-1)
30
25
20
15
10
5
0
1A 2A 3A 4A 5A 6A 7A 8A
1B 2B 3B 4B 5B 6B 7B 8B
25 55 90

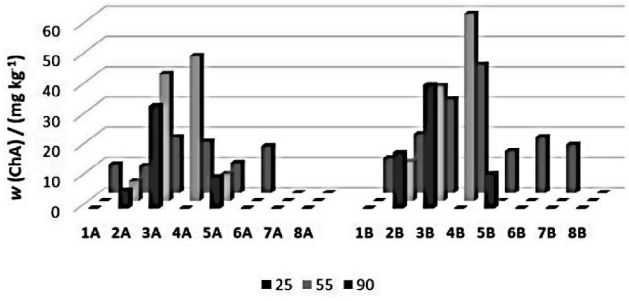
w (ChA) / (mg kg-1)
60
50
40
30
20
10
0
1A 2A 3A 4A 5A 6A 7A 8A
1B 2B 3B 4B 5B 6B 7B 8B
25 55 90

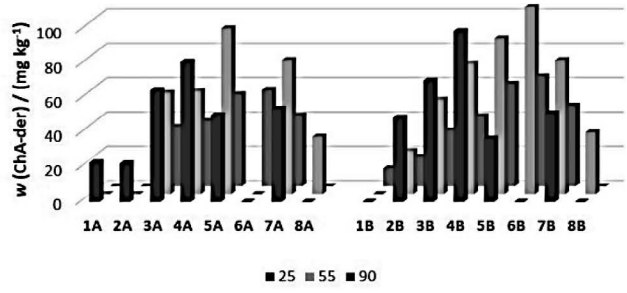
w (ChA-der) / (mg kg-1)
100
80
60
40
20
0
1A 2A 3A 4A 5A 6A 7A 8A
1B 2B 3B 4B 5B 6B 7B 8B
25 55 90

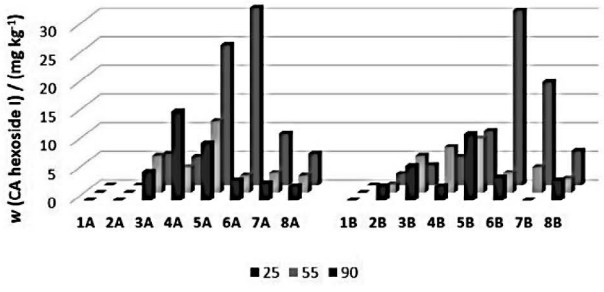
w (CA hexoside I) / (mg kg-1)
30
25
20
15
10
5
0
1A 2A 3A 4A 5A 6A 7A 8A
1B 2B 3B 4B 5B 6B 7B 8B
25 55 90

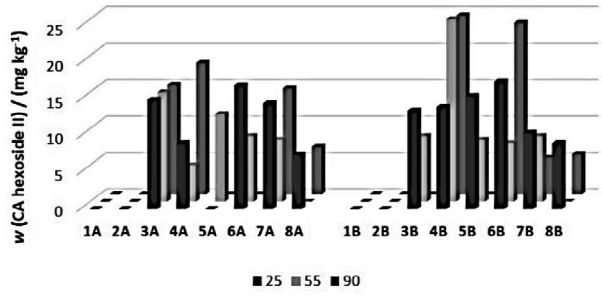
w (CA hexoside II) / (mg kg-1)
25
20
15
10
5
0
1A 2A 3A 4A 5A 6A 7A 8A
1B 2B 3B 4B 5B 6B 7B 8B
25 55 90

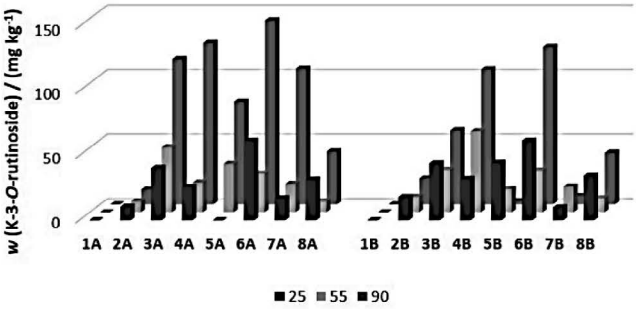
w (K-3-O-rutinoside) / (mg kg-1)
150
100
50
0
1A 2A 3A 4A 5A 6A 7A 8A
1B 2B 3B 4B 5B 6B 7B 8B
25 55 90

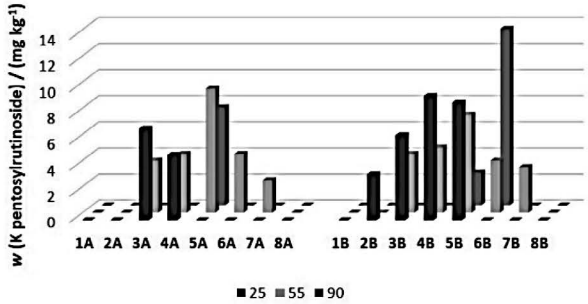
w (K pentosylrutinoside) / (mg kg-1)
14
12
10
8
6
4
2
0
1A 2A 3A 4A 5A 6A 7A 8A
1B 2B 3B 4B 5B 6B 7B 8B
25 55 90

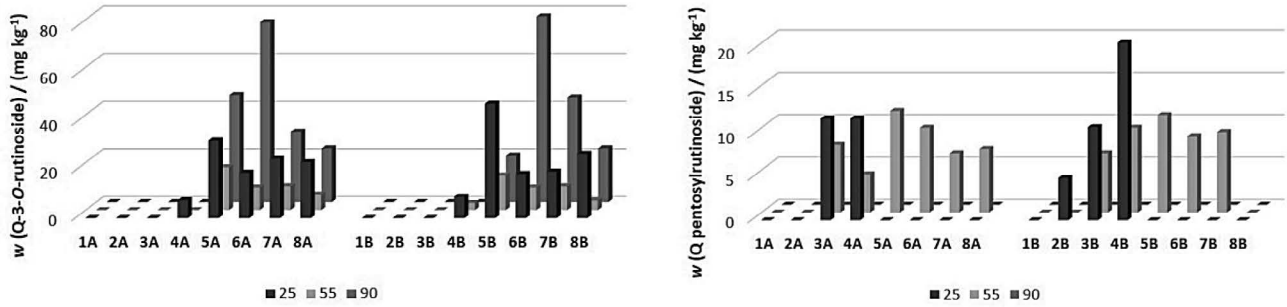

Figure 2. Content of individual phenolic compounds extracted from tomato peel waste by MAE, at temperature of 25, 55 and 90 °C, time of 5 min (**1A–8A**) and 10 min (**1B–8B**), using water, 1% HCl, 50 and 70% methanol with and without addition of 1% HCl, and 50 and 70% ethanol.

ic) and their derivatives (chlorogenic, *p*-coumaric, ferulic-*O*-hexoside, and caffeic-*O*-hexoside), flavonoids (quercetin, rutin, chrysin, epicatechin, catechin, kaempferol, luteonin, and naringenin) and their derivatives, extracted from different tomato wastes. For instance, Kalogeropoulos et al.[12] reported quantities of *p*-CA (10.7 mg kg^{-1}, dw) and ChA (51.7 mg kg^{-1}, dw) lower than ours. Navarro-González et al.[10] found *p*-CA and *p*-CA der in the range from 7.38 to 26.58 mg kg^{-1} (dw) and 33.00 to 141.10 mg kg^{-1}, respectively, depending on used extraction method (enzymatic treatment, maceration and sonication). ChA was also found in the works published by Lavelli and Torresani[9] in quantities of 97 and 121 mg kg^{-1} (dw) for raw and heat-treated tomato by-products, and Aires et al.[17] in the range from 17.3 to 43.7 mg kg^{-1} (dw), depending on the used extraction method and solvents.

Among flavonols (Figure 2) K-3-*O*-rutinoside was found in the highest amounts, 8.5 to 142.5 mg kg^{-1}, depending on used solvent, temperature, and time. Q-3-*O*-rutinoside was also found in considerable amounts (3 to 78 mg kg^{-1}), compared to Q pentosylrutinoside (4.5 to 21 mg kg^{-1}) and K pentosylrutinoside (2.5 to 13 mg kg^{-1}).

For comparison, the work of Kalogeropoulos et al.[12] showed quantities of K-3-*O*-rutinoside of 5.5 mg kg^{-1} (dw) in tomato processing by-products. Aires et al.[17] found 57.8 to 259.3 mg kg^{-1} (dw) of K-3-*O*-rutinoside and 15.0 to 45.1 mg kg^{-1} (dw) of Q-3-*O*-rutinoside, depending on the used extraction method and solvents.

With the purpose to estimate the significance of MAE experimental parameters and interactions between them that provide the highest contents of individual phenolic compounds, the results of statistical analyses are described below.

The increase of extraction times from 5 to 10 min (Figure S4, SI) significantly influenced (p = 0.044719) the content of cis-*p*-CA hexoside. However, raise of time did not significantly affect the recovery of other isolated phenolic compounds. Therefore, the extraction time of 5 min is appropriate for their extraction, according to main advantage of MAE, i.e. applying shorter extraction time.

Regarding applied temperatures of extraction, the increases from 25 vs 55 to 90 °C did not significantly influence the *p*-CA, ChA, ChA der, K pentosylrutinoside, and CA hexoside II contents (Figure 3).

However, the raise of temperature significantly influenced the recovery of cis-*p*-CA der (55 vs 90 °C, p = 0.005986) and Q pentosylrutinoside (25 vs 90 °C, p = 0.034721 and 55 vs 90 °C, p = 0.000742). In the case of these two compounds, the temperature of 90 °C should be avoided due to degradation effects. On the other hand, the temperature of 90 °C had a significant influence on the highest recovery of cis-*p*-CA hexoside (p = 0.000955 for 25 vs 90 °C and p = 0.000143 for 55 vs 90 °C), CA hexoside I (p = 0.029699 for 25 vs 90 °C and p = 0.028620 for 55 vs 90 °C), and K-3-*O*-rutinoside (p = 0.001415 for 25 vs 90 °C and p = 0.000466 for 55 vs 90 °C) from tomato peel extracts.

Regarding solvents used for *p*-CA extraction from tomato peel (Figure 3), 50 and 70% methanol with and without addition of 1% HCl, as well as 50% ethanol showed significant ($p < 0.05$) influence on *p*-CA recovery, compared to water or 1% HCl solution. Furthermore, significantly higher ($p < 0.05$) values were also obtained using 50 and 70% methanol compared to 50 and 70% ethanol.

In the case of cis-*p*-CA der, several solvents, such as 1% HCl, 50 and 70% methanol with and without addition of HCl can be considered as a good choice for cis-*p*-CA-der extraction by MAE. Due to the fact that temperature of 90 °C had a significant effect on degradation of cis-*p*-CA der, the temperature of 25 °C in combinations with 1% HCl and 50 and 70% methanol with addition of 1% HCl could be recommended for its extraction, particularly for 10 min. In addition, high contents of cis-*p*-CA-der, i.e. 35 and 34 mg kg^{-1} for 5 and 10 min of extraction, using 50% methanol, at 55 °C revealed that this combination could be also applied for further successful extraction of this compound by MAE.

High contents of cis-*p*-CA hexoside (Figures 2 and 3) were obtained at 90 °C, using 50 and 70% methanol with addition of 1% HCl, which confirmed these solvents efficiency not only for *p*-CA and cis-*p*-CA der extractions, but also for cis-*p*-CA hexoside. Mentioned solvents can be also recommended for extractions of ChA and its derivatives, due to significant ($p < 0.05$) influence on their quantities.

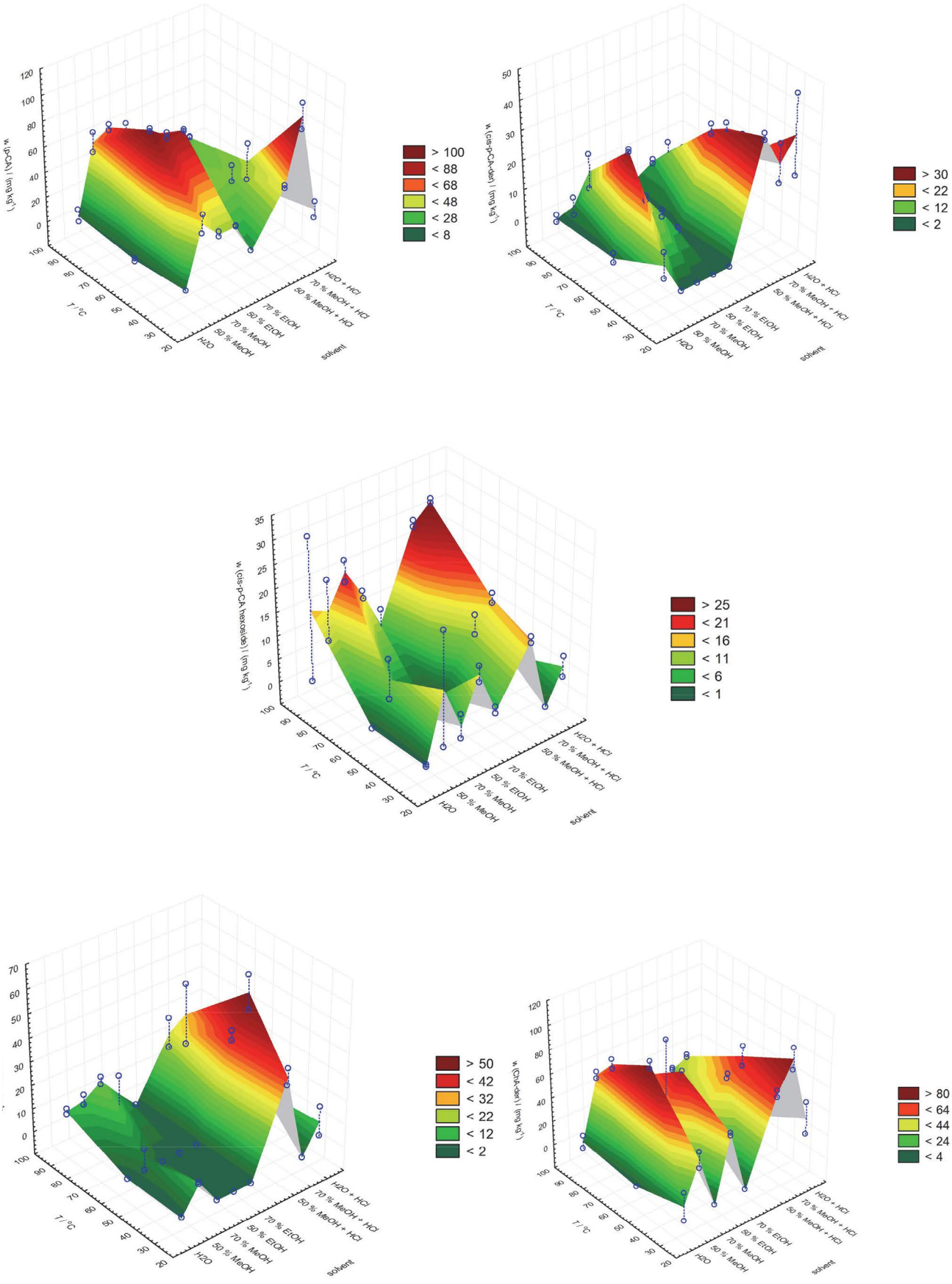
w (p-CA) / (mg kg⁻¹)
> 100
< 88
< 68
< 48
< 28
< 8
w (cis-p-CA-oxn) / (mg kg⁻¹)
> 30
< 22
< 12
< 2
w (cis-p-CA hexoside) / (mg kg⁻¹)
> 25
< 21
< 16
< 11
< 6
< 1
w (ChA-oxn) / (mg kg⁻¹)
> 50
< 42
< 32
< 22
< 12
< 2
> 80
< 64
< 44
< 24
< 4
T / °C
solvent
H2O
50 % MeOH
70 % MeOH
50 % EtOH
70 % EtOH
50 % MeOH + HCl
H2O + HCl

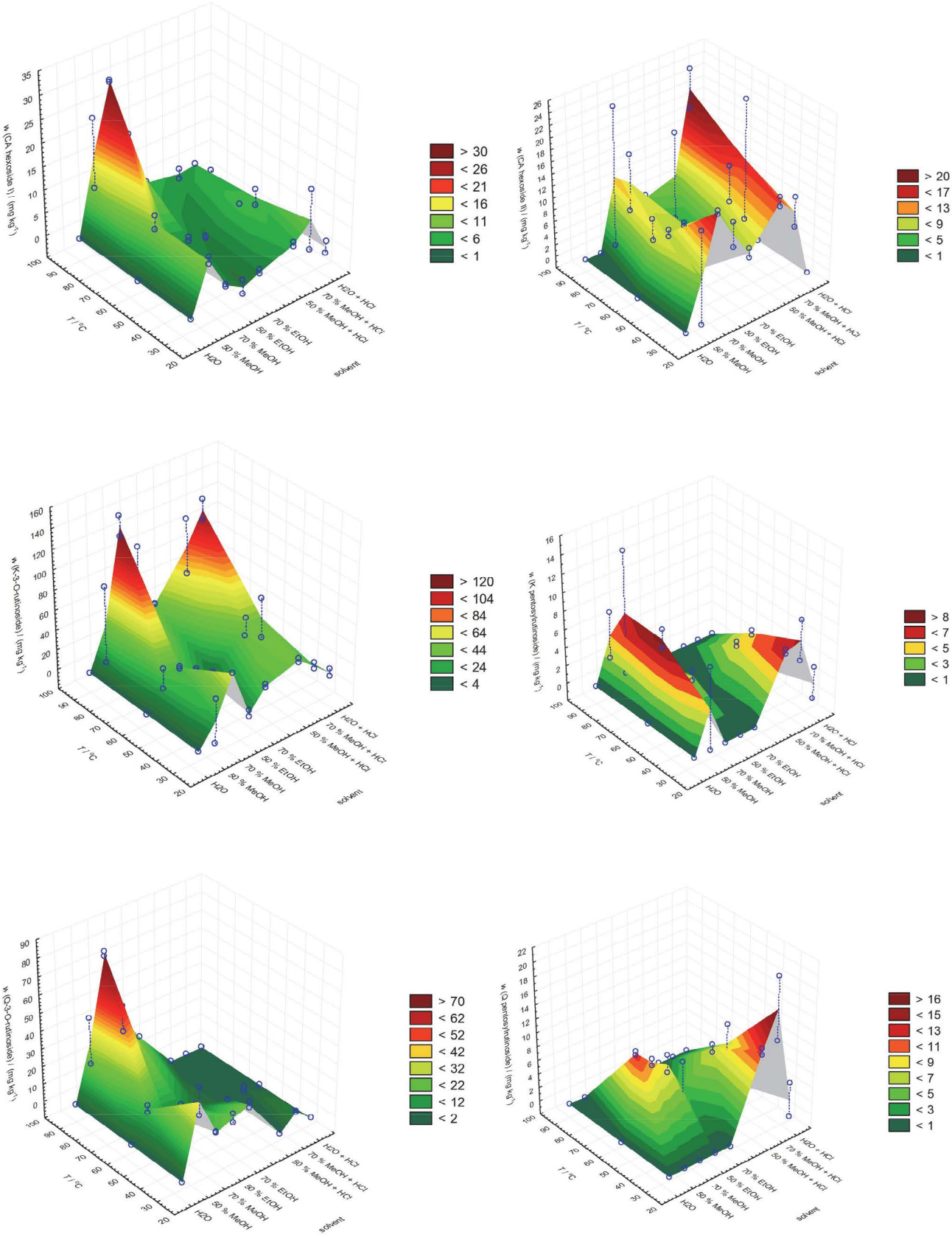

Figure 3. Influence of temperature (25, 55 and 90 °C) and solvent on contents of individual phenolic compounds extracted from tomato peel waste by MAE

For instance, using 50% methanol with addition of 1% HCl (**3A–B**) significant differences of ChA were observed vs water (p = 0.000486), 1% HCl (p = 0.020184), 50% methanol (p = 0.005655), 70% methanol (p = 0.001195), 50% ethanol (p = 0.000364) and 70% ethanol (p = 0.020184). By 70% ethanol with addition of 1% HCl (**4A–B**), the obtained p-values were also significant vs: water (p = 0.006096), 70% methanol (p = 0.015760), 50% ethanol (p = 0.004196) and 70% ethanol (p = 0.001284). Furthermore, 50 and 70% methanol or ethanol without addition of 1% HCl can also be used for ChA extraction, depending on temperature and extraction time.

In the case of CA hexoside I and II, 50 and 70% methanol with and without addition of 1% HCl showed significant influence on their contents, compared to water or 1% HCl.

Regarding flavonols, the extraction of Q-3-O-rutinoside was significantly influenced by 50% (p = 0.004893) and 70% methanol (p = 0.000641). The highest amounts were obtained by 70% methanol, i.e. 75.5 and 78 mg kg^{-1}, for 5 and 10 min of extraction.

The recovery of K-3-O-rutinoside was significantly influenced by 70% methanol (p = 0.000283), 50 and 70% methanol with addition of HCl (p = 0.007673 and p = 0.002455), compared to other used solvents. High extraction yield of this compound was obtained at temperature of 90 °C for 5 min, using 70% methanol (142.5 mg kg^{-1}), followed by 70% and 50% methanol with addition of 1% HCl, which gave values of 125 and 112.5 mg kg^{-1}, respectively.

Although found in minor amounts (Figures 2 and 3), extractions of Q pentosylrutinoside and K pentosylrutinoside were affected by application of organic solvents, regardless of addition of 1% HCl.

To summarize, the HPLC-DAD analyses revealed that tomato peel waste presents an important source for exploitation of phenolic compounds. However, their contents depend on extraction conditions, with emphasis on interaction between the chosen temperature and solvent. The addition of 1% HCl to 50 or 70% methanol assured good recovery of majority of phenolic acids and their derivatives. However, 50% and particularly 70% methanol provided better recovery of some flavonols, such as K-3-*O*-rutinoside. In addition, particular care should be taken regarding the temperature applied during MAE, since an increase in temperature can have a profound influence on degradation of cis-*p*-CA-der and Q pentosylrutinoside, as well as enhancement of amounts of cis-*p*-CA hexoside, CA hexoside I and K-3-*O*-rutinoside.

Therefore, taking into account that extraction time had no significant influence on extraction of majority of phenolic compounds, we propose the extraction time of 5 min in combination with the follow solvent and temperature as optimal, i.e. that which exhibited the highest recovery of phenolic compound: *i*) 50% methanol with addition of 1% HCl and 25 °C for cis-*p*-CA der, *ii*) 70% methanol with addition of 1% HCl and 55 °C for ChA, and 90 °C for cis-*p*-CA hexoside and CA hexoside II, respectively, *iii*) 50% methanol and 90 °C for *p*-CA, and 55 °C for ChA der, Q pentosylrutinoside and K pentosylrutinoside, respectively and *iv*) 70% methanol and 90 °C for CA hexoside I, Q-3-O-rutinoside and K-3-O-rutinoside.

4. Conclusion

The present study showed that tomato peel waste from the canning industry could be utilized as a sustainable, low cost source for polyphenols production.

Results revealed that polyphenols were isolated in remarkable amounts with minimal expenditure of time (5 min), applying MAE as an innovative and eco-friendly technique. Among evaluated extraction parameter, temperatures and solvents have a considerable influence on total phenols, total flavonoids, and individual phenolic compounds yields. Various combinations of these parameters result with isolation of different amounts of individual phenolic compounds.

Therefore, additional MAE extractions of tomato peel waste should be performed combining temperature and solvent type adequate for isolation of one or more target compounds with similar structures and properties.

5. Acknowledgements

This work was supported by the Croatian Ministry of Science, Education, and Sports, No. 058-0580000-3071. The authors are grateful to Giovanni Paolo Buoninconti from Benincasa S.r.l., Angri (SA) canning industry for providing the tomato peel waste.

6. Reference

1. A. Zuorro, R. Lavecchia, F. Medici and L. Piga, *Chem. Eng. Trans*. **2014**, *38*, 355–360.
2. K. Valta, P. Damala, V. Panaretou, E. Orli, K. Moustakas and M. Loizidou, *Waste Biomass Valor.* **2017**, *8,* 1629–1648. **DOI:**10.1007/s12649-016-9672-4
3. V. Nour, T. D. Panaite, M. Ropota, R. Turcu, I. Trandafir and A. R. Corbu. *Cyta - J. Food*. **2018**, *16,* 222–229. **DOI:**10.1080/19476337.2017.1383514
4. N. Balasundram, K. Sundram and S. Samman, *Food Chem*. **2006**, *99,* 191–203. **DOI:**10.1016/j.foodchem.2005.07.042
5. I. Ignat, I. Volf and V. I. A Popa, *Food Chem*. **2011**, *126,* 1821–1835. **DOI:**10.1016/j.foodchem.2010.12.026
6. C. Fritsch, A. Staebler, A. Happel, M. A. Cubero Márquez, I. Aguiló-Aguayo, M. Abadias, M. Gallur, I. Maria Cigognini, A. Montanari, M. J. López, F. Suárez-Estrella, N. Brunton, E. Luengo, L. Sisti, M. Ferri and G. Belotti, *Sustainability* **2017**, *9,* 1–46. **DOI:**10.3390/su9081492

7. N. Ahmad, Y. Zuo, X. Lu, F. Anwar and S. Hameed, *Food Chem.* **2016**, *190,* 80–89. **DOI:**10.1016/j.foodchem.2015.05.077
8. W. Peschel, F. Sánchez-Rabaneda, W. Diekmann, A. Plescher, I. Gartzía, D. Jiménez, R. Lamuela-Raventós, S. Buxaderas and C. Codina, *Food Chem*. **2006**, *97,* 137–150. **DOI:**10.1016/j.foodchem.2005.03.033
9. V. Lavelli and M. C. Torresani, *Food Chem*. **2011**, *125,* 529–535. **DOI:**10.1016/j.foodchem.2010.09.044
10. I. Navarro-González, V. García-Valverde, J. García-Alonso and M. J. Periago, *Food Res. Int.* **2011**, *44,* 1528–1535. **DOI:**10.1016/j.foodres.2011.04.005
11. V. Lavelli and A. Scarafoni, *J. Food Eng.* **2012**, *110,* 225–231. **DOI:**10.1016/j.jfoodeng.2011.05.025
12. N. Kalogeropoulos, A. Chiou, V. Pyriochou, A. Peristeraki and V. T. Karathanos, *LWT - Food Sci. Technol.* **2012,** *49,* 213–216.
13. A. Vallverdú-Queralt, A. Medina-Remón, I. Casals-Ribes, C. Andres-Lacueva, A. L. Waterhouse and R. M. Lamuela-Raventos, *LWT - Food Sci. Technol.* **2012**, *47,* 154–160.
14. A. Sarkar and P. Kaul, *J. Food Process Eng.* **2014**, *37,* 299–307. **DOI:**10.1111/jfpe.12086
15. E. Elbadrawy and A. Sello, *Arab. J. Chem.* **2016,** *9,* S1010-S1018. **DOI:**10.1016/j.arabjc.2011.11.011
16. S. Savatović, G. Ćetković, J. Čanadanović-Brunet and S. Djilas, *Acta Period. Technol.* **2010**, *41,* 187–194. **DOI:**10.2298/APT1041187S
17. A. Aires, R. Carvalho and M. J. Saavedra, *Int. J. Food Sci. Technol.* **2017**, *52*, 98–107. **DOI:**10.1111/ijfs.13256
18. C. D. Stalikas, *J. Sep. Sci.* **2007**, *30,* 3268–3295. **DOI:**10.1002/jssc.200700261
19. H. Wijngaard, M. B. Hossain, D. K. Rai and N. Brunton, *Food Res. Int*. **2012**, *46,* 505–513. **DOI:**10.1016/j.foodres.2011.09.027
20. P. Garcia-Salas, A. Morales-Soto, A. Segura-Carretero and A. Fernández-Gutiérrez, *Molecules.* **2010**, *15*, 8813–8826. **DOI:**10.3390/molecules15128813
21. A. Khoddami, M. Wilkes and T. Roberts, *Molecules*. **2013**, *18,* 2328–2375. **DOI:**10.3390/molecules18022328
22. I. S. M. Azmir, M. M. Zaidul, K. M. Rahman, A. Sharif, F. Mohamed, M. H. A. Sahena, Jahurul, K. Ghafoor, N. A. N. Norulaini and A. K. M. Omar, *J. Food Eng.* **2013**, *117,* 426–436. **DOI:**10.1016/j.jfoodeng.2013.01.014
23. J. R. K. Toor and G. P. Savage, *Food Res. Int.* **2005**, *38,* 487–494. **DOI:**10.1016/j.foodres.2004.10.016
24. M. Viuda-Martos, E. Sanchez-Zapata, E. Sayas-Barberá, E. Sendra, J. A. Pérez-Álvarez and J. Fernández-López. *J. Crit. Rev. Food Sci. Nutr.* **2014**, *54,* 1032–1049. **DOI:**10.1080/10408398.2011.623799
25. V. Nour, M. E. Ionica and I. Trandafir, *J. Food Sci. Technol.* **2015**, *52,* 8260–8267. **DOI:**10.1007/s13197-015-1934-9
26. U. Ahmad, Z. Mushtaq, R. S. Ahmad and N. Asghar, *The J. Anim. Plant Sci.* **2017**, *27,* 2045–2055.
27. M. H. El-Malah, M. M. M. Hassanein, M. H. Areif and E. F. Al-Amrousi, *Am. J. Food Technol.* **2015,** *10,* 14–25. **DOI:**10.3923/ajft.2015.14.25
28. G. A. Spanos and R. E. Wrolstad, *J. Agric. Food Chem.* **1990**, *38,* 1565–1571. **DOI:**10.1021/jf00097a030
29. J. Zhishen, T. Mengcheng and W. Jianming, *Food Chem.* **1999**, *64,* 555–559. **DOI:**10.1016/S0308-8146(98)00102-2
30. L. Barros, M. Dueñas, A. M. Carvalho, I. C. F. R. Ferreira and C. Santos-Buelga, *Food Chem. Toxicol.* **2012**, *50,* 1576–1582. **DOI:**10.1016/j.fct.2012.02.004
31. J. B. Harborne, in J. B. Pridhan (Ed.): Methods in Polyphenol Chemistry, Elsevier, Oxford, England, **1964,** pp. 13–36. **DOI:**10.1016/B978-0-08-010887-2.50006-2
32. K. H. Caffall and D. Mohnen, *Carbohydr. Res.* **2009**, *344,* 1879–1900. **DOI:**10.1016/j.carres.2009.05.021
33. M. Dent, V. Dragović-Uzelac, M. Penić, M. Brnčić, T. Bosiljkov and B. Levaj, *Food Technol. Biotechnol.* **2013**, *51*, 84–91.
34. P. Putnik, D. B. Kovačević, M. Penić, M. Fegeš and V. Dragović-Uzelac, *Food Anal. Methods*. **2016**, *9,* 2385–2394. **DOI:**10.1007/s12161-016-0428-3
35. S. Gharbi, G. Renda, L. La Barbera, M. Amri, C. M. Messina and A. Santulli, *Nat. Prod. Res.* **2017**, *31,* 626–631. **DOI:**10.1080/14786419.2016.1209671

Povzetek

V delu je preučena uporaba ekstrakcije z mikrovalovi (ang. MAE) kot inovativna tehnika za izolacijo polifenolov iz odpadnih olupkov paradižnika. Ovrednotili smo vpliv topila, temperature (25, 55 in 90 °C) in časa (5 in 10 min) glede vsebnosti celotnih fenolov (TP), celotnih flavonoidov (TF) in fenolnih spojin. Odpadni olupki paradižnikov vsebujejo visoke količine kaemferol-3-*O*-rutinozida (8.5 do 142.5 mg kg^{-1}), *p*-kumarinske kisline (3 do 111.5 mg kg^{-1}) in derivate klorogene kisline (10.5 do 109 mg kg^{-1}). Izkazalo se je, da čas ekstrakcije nima znatnega vpliva ($p > 0.05$) na izkoristek TP, TF in fenolnih spojin (z izjemo heksazida *cis-p*-kumarinske kisline). Po drugi strani pa se je izkazalo, da je izkoristek polifenolov odvisen od temperature in izbranega topila. Upoštevaje znatno zanimanje uporabnikov za uživanje naravnih snovi z antioksidativnimi lastnostmi, predstavljena raziskava kaže, da lahko ostanke paradižnikovih lupin uporabimo kot trajnostni vir polifenolov z uporabe MAE.

DOI:10.17344/acsi.2018.4876 *Acta Chim. Slov.* **2019,** *66,* 378–384

Scientific paper

Cyclometalated Iridium(III) Complexes Containing 2-Phenylbenzo[d]oxazole Ligand: Synthesis, X-ray Crystal Structures, Properties and DFT Calculations

Xiao-Han Yang,[1] Qian Zhang,[1] Hui Peng,[1] Zi-Cen Zuo,[1] Ding Yuan,[1] Yan Chen,[1] Qin Chen,[1] Guang-Ying Chen,[2] Zhi-Gang Niu[1,2] and Gao-Nan Li[1,*]

[1] *Key Laboratory of Electrochemical Energy Storage and Energy Conversion of Hainan Province, College of Chemistry and Chemical Engineering, Hainan Normal University, Haikou 571158, PR China*

[2] *Key Laboratory of Tropical Medicinal Plant Chemistry of Ministry of Education, Hainan Normal University, Haikou 571158, PR China*

* *Corresponding author: E-mail: ligaonan2008@163.com*

Received: 11-25-2018

Abstract

Two new iridium(III) complexes were synthesized and fully characterized, [$(bo)_2$Ir(pzpy)] (**2a**) and [$(bo)_2$Ir(pzpyz)] (**2b**) (where bo = 2-phenylbenzo[d]oxazole, pzpy = 2-(1H-pyrazol-3-yl)pyridine, pzpyz = 2-(1H-pyrazol-3-yl)pyrazine). The single crystal structures of **2a**-**2b** have been determined. Considering the relationship between their structures and photophysical properties, DFT calculations have been used to further support this inference. These Ir(III) complexes emit from the excited state of ^{3}MLCT/^{3}LLCT in the green and yellow region, and the quantum yields in the degassed CH_2Cl_2 solution at room temperature are 35.2% and 46.1%. Theoretical and experimental results show that iridium(III) complexes **2a**-**2b** are promising phosphorescent material.

Keywords: Iridium(III) complex; Crystal structure; 2-phenylbenzo[d]oxazole; Photoluminescence; DFT calculation

1. Introduction

Neutral mononuclear cyclometalated iridium complexes have been found to be suitable for use in organic light emitting diodes (OLEDs).[1–3] The privileged use is due to their interesting luminescence properties,[4–5] such as high quantum yields, long excited-state lifetimes, and tunable emission color over the entire visible spectrum.[6–7] Most often, the variation of their emission color was largely governed by the cyclometalated and/or ancillary ligands structures.

2-phenylbenzo[d]oxazole (bo) is one typical ligand framework for constructing Ir(III) complexes, and can be used to fine-tune the emission color of complexes by judicious modification.[8–10] For example, in 2015, we reported Ir$(bo)_2$(acac) derivatives with substituents on the benzoxazole ring and their emissions covered a narrow range from 560 to 566 nm.[11] The color adjusting by the change of cyclometalated ligands structures were not very satisfactory, although the quantum yield was up to 53.5%. Afterward, we designed a series of bo-based iridium(III) complexes with different N^O ancillary ligands. They exhibited a wide range of emission wavelengths (λ_{max} = 531–598 nm) with high quantum yields (19%–94%).[12] The research findings showed that the structures of ancillary ligands have obvious effect on tuning the emission color of bo-based iridium(III) complexes. Therefore, we wanted to further investigate other types of ancillary ligands. In this paper, we design two N^N ancillary ligands (**a** and **b**) and synthesize two bo-based iridium(III) complexes (**2a** and **2b**) (Scheme 1). The photophysical and electrochemical properties of these complexes were investigated, and the lowest energy electronic transitions were analyzed based on density functional theory (DFT) and time-dependent DFT (TDDFT).

2. Experimental

2. 1. Materials and Instrumentations

2-aminophenol and benzaldehyde were obtained from Hebei Guanlang Biotechnology Co., Ltd.. 2-(prop-1-

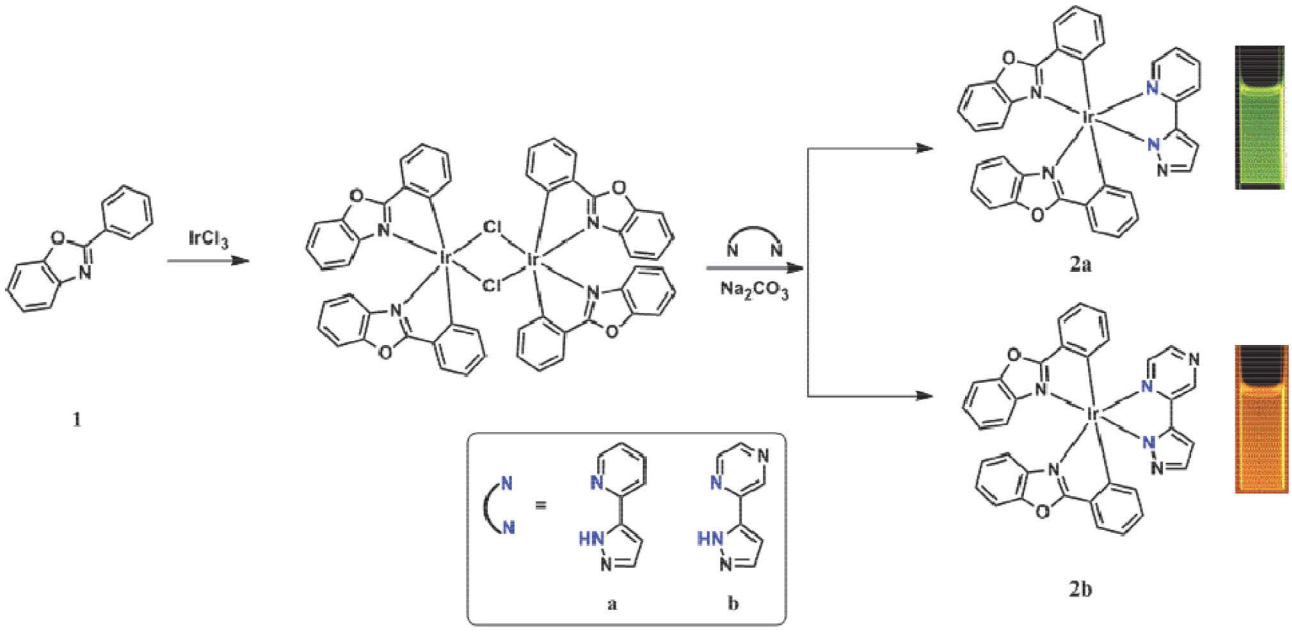

Scheme 1. Synthetic routes of Ir(III) complexes **2a**–**2b**.

en-2-yl)pyridine, 2-(prop-1-en-2-yl)pyrazine and 1,1-dimethoxy-N,N-dimethylmethanamine were obtained from Dayang Chemicals Co., Ltd., SAGECHEM LIMITED and Sigma-Aldrich, respectively. $IrCl_3 \cdot 3H_2O$ was industrial products. The target ligands 2-phenylbenzo[d]oxazole (**1**), 2-(1H-pyrazol-3-yl)pyridine (**a**) and 2-(1H-pyrazol-3-yl) pyrazine (**b**) were prepared according to the literature method.[13–15] All commercial chemicals were used without further purification unless otherwise stated. Solvents were dried and degassed following standard procedures. ^{1}H NMR spectra were recorded on a Bruker AM 400 MHz instrument. Chemical shifts were reported in ppm relative to Me_4Si as internal standard. UV-Vis spectra were recorded on a Hitachi U3900/3900H spectrophotometer. Fluorescence spectra were carried out on a Hitachi F-7000 spectrophotometer. The FTIR spectra were taken on a Nicolet 6700 FTIR spectrometer (400-4000 cm^{-1}) with KBr pellets.

2. 2. Synthesis of $(bo)_2Ir(pzpy)$ (2a)

A mixture of $IrCl_3 \cdot 3H_2O$ (306 mg) and 2-phenylbenzo[d]oxazole (500 mg) in 15 mL of 2-ethoxyethanol and H_2O (v: v = 2:1) was heated at 120 °C for 12 hours under N_2. After cooling to room temperature, the yellow precipitate was collected by filtration and washed with cooled ether and MeOH. After drying, the crude product of chlorine bridged dimer complex $[(bo)_2Ir(\mu\text{-}Cl)]_2$ can be used in the next step without further purification. This was followed by crude chlorine bridged dimer (207 mg), 2-(1H-pyrazol-3-yl)pyridine (54 mg, 2.2 eq) and Na_2CO_3 (88 mg, 5.0 eq). In 2-ethoxyethanol (10 ml), the mixture was heated at 120 °C under N_2 for 12 hours. After removing the solvent, the mixture was poured into water, extracted three times with CH_2Cl_2, and then evaporated. The residue was purified by flash column chromatography (DCM: MeOH = 50: 1) to obtain iridium complex **2a** as a yellow solid (76 mg, yield: 64.6%). ^{1}H NMR (400 MHz, $CDCl_3$) δ 7.93 (s, 1H), 7.80–7.67 (m, 4H), 7.56 (dd, *J* = 17.5, 9.0 Hz, 2H), 7.31 (d, *J* = 6.9 Hz, 2H), 7.14 (s, 2H), 6.96 (dd, *J* = 44.3, 7.6 Hz, 6H), 6.71 (s, 2H), 6.65 (s, 1H), 5.97 (dd, *J* = 16.8, 7.8 Hz, 2H). MS (ESI): m/z = 726.0 [M^+]. IR (KBr, cm^{-1}): 2856(w), 1649(w), 1592(vs), 1520(m), 1448(vs), 1387(s), 1252(w), 1188(w), 1130(s), 1084(s) 1045(w), 816(w), 742(m), 474(m). Calcd for $C_{33}H_{21}IrN_5O_2$ (%): C 56.34, H 3.06, N 9.66; Found: C 55.67, H 3.22, N 9.37.

2. 3. Synthesis of $(bo)_2Ir(pzpyz)$ (2b)

The complex **2b** (70 mg, yield: 59.4%) was obtained using 2-(1H-pyrazol-3-yl)pyrazine instead of 2-(1H-pyrazol-3-yl)pyridine by a method similar to that of preparing **2a**. ^{1}H NMR (400 MHz, $CDCl_3$) δ 9.04 (s, 1H), 8.22 (d, *J* = 2.3 Hz, 1H), 7.92 (s, 1H), 7.82 (dd, *J* = 16.8, 9.6 Hz, 3H), 7.69–7.56 (m, 2H), 7.42–7.33 (m, 2H), 7.19 (t, *J* = 7.8 Hz, 1H), 7.14–6.91 (m, 5H), 6.88 (s, 1H), 6.74 (d, *J* = 7.5 Hz, 1H), 6.65 (d, *J* = 7.6 Hz, 1H), 6.01 (dd, *J* = 26.9, 8.0 Hz, 2H). MS (ESI): m/z = 727.0 [M^+]. IR (KBr, cm^{-1}): 2962(m), 2920(m), 2854(w), 1595(m), 1520(m), 1452(m), 1387(m), 1335(w), 1259(s), 1092(vs), 1030(vs), 804(vs), 742(m), 476(w). Calcd for $C_{33}H_{21}IrN_6O_2$ (%): C 54.61, H 2.92, N 11.58; Found: C 54.95, H 3.08, N 11.04.

2. 4. Crystallographic Studies

X-ray diffraction data were collected with an Agilent Technologies Gemini A Ultra diffractometer equipped

with graphite-monochromated Mo Kα radiation (λ = 0.71073 Å) at room temperature. Data collection and reduction were processed with CrysAlisPro software.[16] The structure was solved and refined using Full-matrix least-squares based on F^2 with program SHELXS-97 and SHELXL-97[17] within Olex2.[18] All non-hydrogen atoms were found in alternating difference Fourier syntheses and least-squares refinement cycles and, during the final cycles, refined anisotropically. Hydrogen atoms were placed in calculated positions and refined as riding atoms with a uniform value of *U*iso.

2. 5. Computational Method

The geometry of complexes **2a**–**2b** was optimized starting from the X-ray data by the DFT (density functional theory) method with B3LYP (Becke three-parameter Lee-Yang-Parr) hybrid density functional theory and the 6-31G* basis set. All calculations were carried out with Gaussian 09 software package.[19]

3. Results and Discussion

3. 1. Description of Crystal Structure

The single crystal structures of **2a**–**2b** were obtained by X-ray diffraction studies, and ORTEP diagrams are shown in Fig. 1. The crystallographic data and structural details are given in Table 1. The selected bond lengths and bond angles are collected in Table S1.

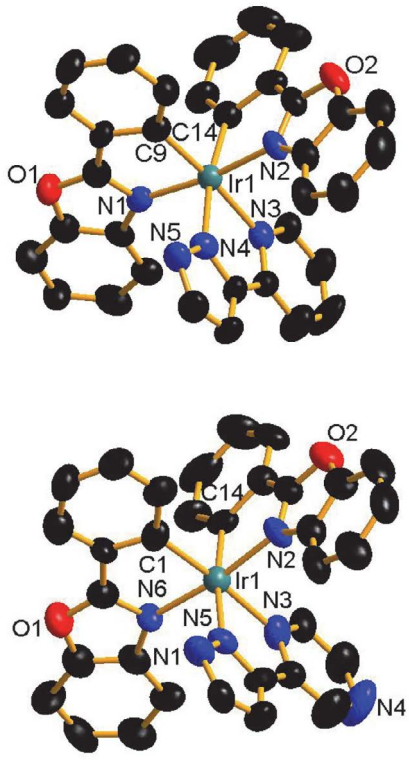

Fig. 1. ORTEP view of **2a** (up) and **2b** (down) with the thermal ellipsoids drawn at the 50% probability level. Hydrogen atoms and solvent molecules are omitted for clarity.

For the structures of these complexes, the Ir(III) centre adopts a twisted octahedral geometry, and the C^N ligands are in *cis*-C,C' and *trans*-N,N' configurations. The Ir–N average bond lengths of **2a** (2.077Å) and **2b** (2.100Å) are longer than the Ir–C average bond lengths of **2a** (2.019Å) and **2b** (2.041Å), which are reported in other iridium complexes.[20] Furthermore, the Ir–N bonds between the iridium and N^N ligands (2.081–2.152 Å) are longer than those between the iridium and C^N ligands (2.037–2.073Å), consistent with strong *trans* influence of the C^N ligands. The octahedral para-orbital angles range from 171.0(5)° to 174.6(5)° for **2a** and from 171.9(4)° to 174.9(4)° for **2b**, which is close to a straight line. The metric parameters of the two iridium complexes are similar owing to the same cyclometalated ligands and analogous ancillary ligands.

Table 1. Crystallographic data for complexes **2a**–**2b**.

	2a	**2b**
Empirical formula	$C_{34}H_{22}IrN_5O_2$	$C_{33}H_{21}IrN_6O_2{\cdot}H_2O$
M_r	724.76	743.77
Crystal system	Monoclinic	Monoclinic
Space group	$P2_1/c$	$P2_1/c$
Wavelength / Å	0.7107	0.7107
X-radiation (graphitemonochromator)	Mo-Kα	Mo-Kα
T / K	293(2)	293(2)
a (Å)	11.9035(5)	11.951(3)
b (Å)	17.9960(9)	18.130(6)
c (Å)	13.7103(7)	13.742(4)
α (°)	90	90
δ (°)	96.654(4)	98.00(2)
γ (°)	90	90
V (Å^3)	2917.2(2)	2948.4(15)
Z	4	4
D_{calcd} (Mg/m^3)	1.650	1.676
F(000)	1416	1456
Absorption coefficient (mm^{-1})	4.616	4.573
Index ranges	$-14 \le h \le 11$	$-14 \le h \le 14$
	$-21 \le k \le 22$	$-22 \le k \le 21$
	$-15 \le l \le 17$	$-17 \le l \le 17$
R_{int}	0.0484	0.1096
GOF (F^2)	1.037	1.028
$R_1{}^a$, $wR_2{}^b$ ($I>2\sigma(I)$)	0.0634, 0.1601	0.0694, 0.1674
$R_1{}^a$, $wR_2{}^b$ (all data)	0.1146, 0.2001	0.1262, 0.2336

$^aR_1 = \Sigma||F_o|-|F_c||/\Sigma|F_o|$. $^bwR_2 = [\Sigma w(F_o^2-F_c^2)^2/\Sigma w(F_o^2)]^{1/2}$

3. 2. Electronic Absorption Spectra

The UV-Vis absorption spectra of **2a**–**2b** were recorded at room temperature in CH_2Cl_2 solutions, as shown in Fig. 2, and the data are summarized in Table 2. All of the

complexes exhibit intense absorption bands in the ultraviolet region at wavelengths below 310 nm, which are assigned to the spin-allowed π–π* transitions on the C^N main ligands and the N^N ancillary ligands. The weaker absorption bands in the range 350–450 nm are likely attributed to metal-to-ligand charge-transfer transitions (^{1}MLCT and ^{3}MLCT).[21–22] Compared with complex **2a**, complex **2b** has a red-shifted, which may be caused by the ancillary ligand. This speculation will be confirmed by electrochemical analysis and DTF calculations.

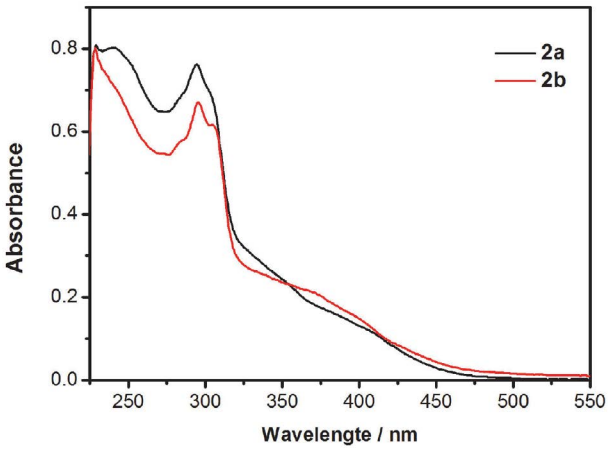

Fig. 2. UV-Vis absorption spectra of **2a–2b**, recorded in CH_2Cl_2 at room temperature.

3. 3. Emission Properties

The photoluminescence emission spectra of iridium complexes **2a–2b** in degassed CH_2Cl_2 solution at room temperature and corresponding data are described in Fig. 3 and Table 2, respectively. Complex **2a** exhibits green phosphorescence with the broad emission maxima peak at 518 nm and a shoulder peak at 547 nm, whereas **2b** is yellow emissive with the broad emission maxima peak at 529–552 nm. For their emission, the excited state of **2a** is attributed to the mixing of ^{3}MLCT and ^{3}LC,[23] while that of **2b** is mainly attributed to ^{3}MLCT.[24] As expected, the emission band of **2b** has red-shifted with respect to **2a** due to different ancillary ligands, which is consistent with absorption analysis. In addition, the quantum yields of **2a** and **2b** in solution at room temperature were measured to

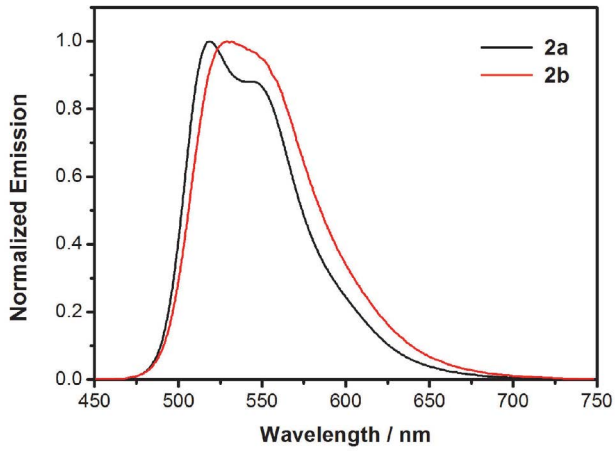

Fig. 3. The emission spectra of **2a–2b** in CH_2Cl_2 at room temperature.

be 35.2% and 46.1% with reference to *fac*-Ir(ppy)$_3$ (Φ = 0.40).[25]

3. 4. Theoretical Calculations

Density functional theory (DFT) and time-dependent DFT (TD DFT) calculations have been performed on the complexes **2a–2b** to obtain an insight into the lowest energy electron transition. The most representative molecular front orbital diagram of these complexes is shown in Fig. 4. The calculated spin-allowed electron transitions are provided in Table 3 and compared with the experimental absorption spectra data. The electron density distribution data are summarized in Table S2.

As shown in Fig. 4, the HOMOs of these complexes are mainly located on the metal center and C^N ligands. Meanwhile, the LUMO of **2a** is mostly dominated on C^N ligands, while LUMO of **2b** is mainly located on the whole ancillary ligands. In addition, the LUMO+1s of these complexes are primarily centered on the C^N main ligands, while HOMO-1s are delocalized over the metal center, C^N ligands and ancillary ligands. The theoretical calculation of DFT shows that the lowest energy spin-allowed transitions of **2a–2b** come from HOMO→LUMO/LUMO+1 and HOMO→LUMO+1/HOMO–1→LUMO transitions (Table 3), and therefore attributed to metal-to-ligand charge transfer transition and ligand-to-ligand π–π* transition. These calculations support the photophysical properties discussed above.

Table 2. Photophysical and electrochemical data of complexes **2a–2b**.

Complex	Absorption[a] λ_{abs} (nm)	Emission[a] λ_{em} (nm)	Φ_{em}[b] (%)	E_{ox}[a] (V)	HOMO[c] (eV)	HOMO[d] (eV)
2a	229, 240, 295	518, 547(sh)	35.2	1.57	–6.37	–5.44
2b	228, 295, 308(sh)	529, 552	46.1	1.62	–6.42	–5.54

[a]Data were collected from degassed CH_2Cl_2 solutions at room temperature. [b]*fac*-Ir(ppy)$_3$ as referenced standard (0.4).[25] [c]HOMO energies are deduced from the equation HOMO = – (E_{ox}+ 4.8 eV). [d]Obtained from theoretical calculations.

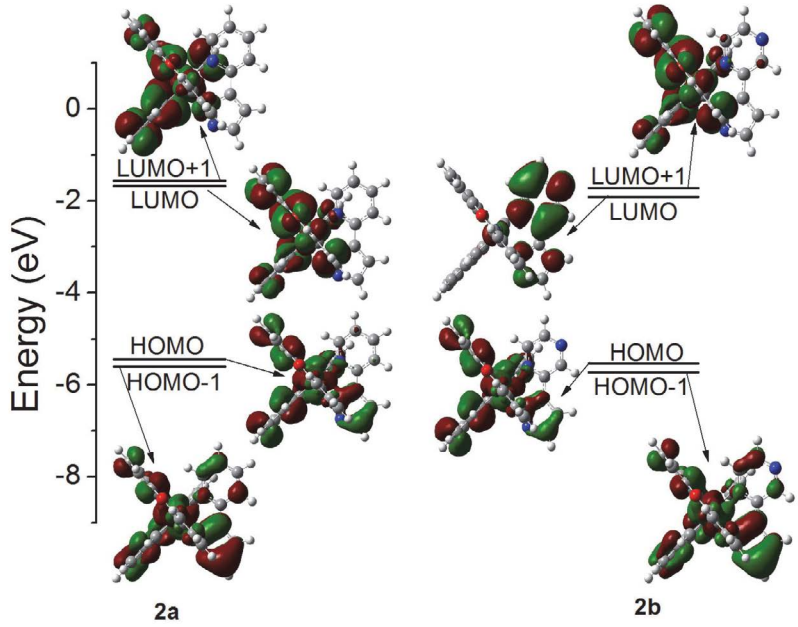

Fig. 4. The frontier molecular orbital energy-level diagrams of **2a–2b** from DFT calculations.

Table 3. Main experimental and calculated optical transitions for **2a–2b**.

Complex	Orbital Excitations	Transition	Character	Oscillation Strength	Calcd (nm)	Exptl (nm)
2a	HOMO → LUMO	MLCT/LLCT	$d\pi_{Ir}/\pi_{bo} \rightarrow \pi^*_{bo}$	0.0802	408	407
	HOMO → LUMO+1	MLCT/LLCT	$d\pi_{Ir}/\pi_{bo} \rightarrow \pi^*_{bo}$	0.0401	393	
2b	HOMO→LUMO+1	MLCT/LLCT	$d\pi_{Ir}/\pi_{bo} \rightarrow \pi^*_{bo}$	0.0242	403	372
	HOMO–1→LUMO	MLCT/LLCT	$d\pi_{Ir}/\pi_{bo}/\pi_{pzpyz} \rightarrow \pi^*_{pzpyz}$	0.0225	397	

3. 5. Electrochemical Properties

The electrochemical properties of **2a–2b** were studied by cyclic voltammetry and shown in Fig. 5. The corresponding electrochemical data and estimated HOMO energy levels are summarized in Table 2. The complexes **2a–2b** exhibit quasi-reversible oxidation peaks at 1.57 V and 1.62 V, respectively. From DFT calculations (Table S2), HOMO is mainly located on Ir ions (47.77% for **2a** and 46.90% for **2b**) and C^N ligands (40.97% for **2a** and 44.91% for **2b**). Thus, their oxidation processes are assigned to Ir (III) to Ir (IV) and some contributions of the C^N ligands.[26] Based on the oxidation potential, the HOMO energy is derived from the equation $E_{HOMO} = -(E_{ox} + 4.8\ eV)$, and the trend is consistent with the theoretical calculations (Table 2). From these results, it can be seen that because of the different number of nitrogen atoms in the ancillary ligands, the HOMO level of **2b** is more stable than that of the analogue **2a**, and the oxidation process of **2b** is more difficult than that of **2a**.

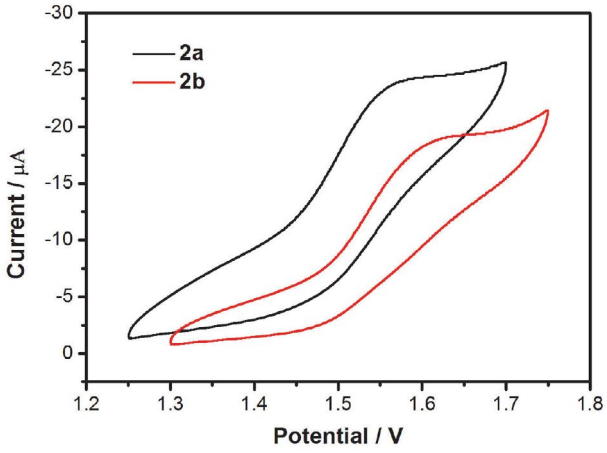

Fig. 5. Cyclic voltammograms for **2a–2b** in CH_2Cl_2 solution containing n-Bu_4NClO_4 (0.1 M) at a sweep rate of 100 mV/s.

4. Conclusions

In summary, the syntheses, characterization, as well as electrochemical, spectroscopic and photophysical prop-

erties of two new bo-based iridium(III) complexes are reported. The room-temperature phosphorescence of these complexes is tunable from green to yellow depending on the different ancillary ligands. It was also found that as the number of nitrogen atoms increased on the ancillary ligands, the quantum yields became larger and emission became brighter. The DFT calculated results are in good agreement with the actual absorption spectra, indicating that the lowest absorption is assigned to the MLCT/LLCT transition. These results will facilitate the design of new bo-based iridium(III) complexes for highly efficient OLEDs.

5. Acknowledgments

This work was supported by the Natural Science Foundation of Hainan Province (218QN236) and Program for Innovative Research Team in University (IRT-16R19).

6. Supplementary Material

The selected bonds and angles of complexes **2a–2b**, the frontier orbital energy and electron density distributions of complexes **2a–2b**, as well as the FTIR spectra of complexes **2a–2b**. Crystallographic data for the structural analyses have been deposited in the Cambridge Crystallographic Data Centre, CCDC reference number 1881007 (**2a**) and 1881008 (**2b**). Copies of this information may be obtained free of charge from The Director, CCDC, 12 Union Road, Cambridge CB2 1EZ, UK (fax: +44 1223 336033; e-mail: deposit@ccdc.cam. ac.uk).

7. References

1. M. C. Gather, A. Köhnen, K. Meerholz, *Adv. Mater.* **2011**, *23*, 233–248. **DOI:**10.1002/adma.201002636
2. C. Fan, C. Yang, *Chem. Soc. Rev.* **2014**, *43*, 6439–6469. **DOI:**10.1039/C4CS00110A
3. G. M. Farinola, R. Ragni, *Chem. Soc. Rev.* **2011**, *40*, 3467–3482. **DOI:**10.1039/c0cs00204f
4. L. Flamigni, A. Barbieri, C. Sabatini, B. Ventura, F. Barigelletti, *Top. Curr. Chem.* **2007**, *281*, 143–203. **DOI:**10.1007/128_2007_143
5. E. Baranoff, E. Orselli, L. Allouche, D. DiCenso, R. Scopelliti, M. Gr€atzel, M. K. Nazeeruddin, *Chem. Commun*. **2011**, *47*, 2799–2801. **DOI:**10.1039/c0cc05029f
6. M. A. Baldo, M. E. Thompson, S. R. Forrest, *Nature*. **2000**, *403*, 750–753. **DOI:**10.1038/35001541
7. E. Matteucci, A. Baschieri, A. Mazzanti, L. Sambri, J. Avila, A. Pertegas, H. J. Bolink, F. Monti, E. Leoni, N. Armaroli, *Inorg. Chem*. **2017**, *56*, 10584–10595. **DOI:**10.1021/acs.inorgchem.7b01544
8. X. Li, X. T. Yu, H. J. Chi, Y. Dong, G. Y. Xiao, P. Lei, D. Y. Zhang, Z. Cui, *Spectrochim. Acta, Part A*. **2013**, *116*, 473–477. **DOI:**10.1016/j.saa.2013.07.075
9. X. Li, H. J. Chi, Y. Dong, G. Y. Xiao, P. Lei, D. Y. Zhang, Z. Cui, *Opt. Mater.* **2013**, *36*, 265–270. **DOI:**10.1016/j.optmat.2013.09.006
10. H. W. Hong, T. M. Chen, *Mater. Chem. Phys.* **2007**, *101*, 170–176. **DOI:**10.1016/j.matchemphys.2006.03.011
11. Z.-G. Niu, T. Zheng, Y.-H. Su, P.-J. Wang, X.-Y. Li, F. Cui, J. Liang, G.-N. Li, *New. J. Chem.*, **2015**, *39(8)*, 6025–6033. **DOI:**10.1039/C5NJ00975H
12. G.-N. Li, C.-W. Gao, H.-H. Chen, T.-T. Chen, H. Xie, S. Lin, W. Sun, G.-Y. Chen, Z.-G. Niu, *Inorg. Chim. Acta*, **2016**, *445*, 22–27. **DOI:**10.1016/j.ica.2016.02.009
13. T. L. H. Doan, L. H. T. Nguyen, T. T. Nguyen, H. L. Nguyen, P. H. Tran, *Catalysis Science & Technology,* **2017**, *7(19),* 4346–4350. **DOI:**10.1039/C7CY01668A
14. X. Y. Yu, L. Deng, B. Zheng, B. R Zeng, P. Yi, X. Xu, *Dalton Trans,* **2013**, *43(4)*, 1524–1533. **DOI:**10.1039/C3DT51986D
15. C.-H. Cheng, *U.S. Pat. Appl. Publ.* 20080217606, 11 Sep **2008**.
16. CrysAlisPro Version 1.171.36.21; Agilent Technologies Inc., Santa Clara, CA, USA, 2012.
17. G. M. Sheldrick, *Acta Cryst*. **2008,** *A64* 112–122. **DOI:**10.1107/S0108767307043930
18. O. V. Dolomanov, L. J. Bourhis, R. J. Gildea, J. A. K. Howard, H. J. Puschmann, *Appl. Crystallogr.* **2009**, *42*, 339–341. **DOI:**10.1107/S0021889808042726
19. M. J. Frisch, G. W. Trucks, H. B. Schlegel, Gaussian 09, Revision A.01, Gaussian, Wallingford, Con, USA, **2009**.
20. C. D. Sunesh, K. Shanmugasundaram, M. S. Subeesh, R. K. Chitumalla, J. Jang, Y. Choe, *ACS Applied Materials & Interfaces,* **2015**, *7(14)*, 7741–7751. **DOI:**10.1021/acsami.5b00875
21. G. J. Zhou, Q. Wang, C. L. Ho, W. Y. Wong, D. G. Ma, L. X. Wang, Z. Y. Lin, *Chem. Asian. J.* **2008**, *3*, 1830–1841. **DOI:**10.1002/asia.200800074
22. N. M. Shavaleev, F. Monti, R. Scopelliti, A. Baschieri, L. Sambri, N. Armaroli, *Organometallics,* **2013**, *32(2)*, 460–467. **DOI:**10.1021/om300894m
23. M. Y. Wong, G. Xie, C. Tourbillon, M. Sandroni, D. B. Cordes, A. M. Z. Slawin, I. D. W. Samuelb, E. Zysman-Colman, *Dalton Trans.* **2015**, *44*, 8419–8432. **DOI:**10.1039/C4DT03127J
24. V. Chandrasekhar, B. Mahanti, P. Bandipalli, K. Bhanuprakash, *Inorg. Chem.* **2012**, *51*, 10536−10547. **DOI:**10.1021/ic300694m
25. K. A. King, P. J. Spellane, R. J. Watts, *J. Am. Chem. Soc*. **1985**, *107*, 1431–1432. **DOI:**10.1021/ja00291a064
26. G.-N. Li, S.-B. Dou, T. Zheng, X.-Q. Chen, X.-H. Yang, S. Wang, W. Sun, G.-Y. Chen, Z.-R. Mo, Z.-G. Niu, *Organometallics*, **2018**, *37*, 78–86. **DOI:**10.1021/acs.organomet.7b00740

Povzetek

Sintetizirali in karakterizirali smo dve novi kompleksni spojini Ir(III): $[(bo)_2Ir(pzpy)]$ (**2a**) in $[(bo)_2Ir(pzpyz)]$ (**2b**) (bo = 2-fenilbenzo[d]oksazol, pzpy = 2-(1H-pyrazol-3-yl)piridin, pzpyz = 2-(1H-pirazol-3-yl)pirazine). Spojinama smo z rentgensko strukturno analizo monokristalov določili kristalni strukturi. DFT izračune smo uporabili za interpretacijo lastnosti spojin v povezavi z njunima strukturama. Kompleksa Ir(III) imata prehod iz vzbujenega stanja ^{3}MLCT/^{3}LLCT v zelenem in rumenem območju s kvantnima izkoristkoma v raztopini CH_2Cl_2 pri sobni temperaturi 35,2% in 46,1%. Rezultati teoretičnih izračunov in eksperimentalni podatki kažejo, da sta kompleksa Ir(III) (2a in 2b) obetajoča fosforescenčna materiala.

Scientific paper

A Vortex-Assisted Deep Eutectic Solvent-Based Liquid-Liquid Microextraction for the Analysis of Alkyl Gallates in Vegetable Oils

Hasan Çabuk,* Yasemin Yılmaz and Elif Yıldız

Zonguldak Bülent Ecevit University, Faculty of Arts and Sciences, Department of Chemistry, 67100, Zonguldak, Turkey

** Corresponding author: E-mail: cabukhasan@hotmail.com*
Tel.: 00 90 372 291 1920; Fax: 00 90 372 257 41 81

Received: 11-27-2018

Abstract

This study investigates the feasibility of using hydrophilic deep eutectic solvent (DES) as green and effective extractant for the extraction and preconcentration of alkyl gallates from vegetable oils. In a typical experiment, 120 µL of choline chloride:ethylene glycol DES was added to 1.0 g of oil sample which was previously diluted with 1 mL of *n*-hexane. The extraction was accelerated by vortex stirring of the two phases. At this stage, hydrogen bonding interactions between the phenyl hydroxyls of alkyl gallates and chloride anion of choline salt were likely the main forces driving the extraction. After extraction, the analytes in the DES phase were separated and determined by high-performance liquid chromatography with ultraviolet detection. The method detection limits for propyl gallate and octyl gallate were 2.1 and 4.6 µg kg^{-1}, respectively. The precision of the method varied between 4.6–6.4% (intra-day) and 5.4–7.5% (inter-day). The recoveries (accuracies) obtained from spiked vegetable oil samples were in the range of 78–106%.

Keywords: Deep eutectic solvent, alkyl gallates, vegetable oils, high-performance liquid chromatography

1. Introduction

Synthetic antioxidants (SAs) are a class of compounds which are capable of preventing or slowing down the oxidation reactions of substrates in food, pharmaceuticals, and other consumer products.[1] Common SAs used as food additives in many countries include butylated hydroxyanisole, butylated hydroxytoluene, *tert*-butylhydroquinone, propyl gallate, octyl gallate and dodecyl gallate, due to their chemical stabilities, low costs and availabilities.[2] Among SAs, alkyl gallates have been widely used as food additives to slow down or prevent lipid oxidation in lipid-rich food.[3] Contrary to their versatile and beneficial properties, the addition of excess gallates to food might cause different degrees of adverse and toxic effects on human health. They can induce DNA damage and mutagenicity, and their antioxidant potential can turn pro-oxidant under certain conditions.[2,4] Therefore, the use of gallates as well as other SAs is strictly controlled in many countries worldwide. Generally, the allowed amounts of SAs in food range from 100 to 200 mg kg^{-1} in European Union, either singly or in combination.[5]

The determination of alkyl gallates in foodstuffs has been accomplished using specific electrochemical sensors[6–8] and different separation techniques such as high-performance liquid chromatography (HPLC),[5,9–12] micellar electrokinetic capillary chromatography[13,14] and capillary electrophoresis.[15,16] Electrochemical methods may offer relatively low operational costs and faster analysis. However, in the case of multiple analytes they require chemometric interpretation of the overlapping electrochemical signals for the estimation of individual analyte concentrations.[17] Among the separation techniques, HPLC with ultraviolet (UV) detection has become the most widely used technique for the determination of alkyl gallates following the extraction by liquid–liquid extraction (LLE) of the sample. Acetonitrile, previously saturated with *n*-hexane, is the most preferred solvent for extracting alkyl gallates from oil samples.[9,12] To a lesser extent, methods based on the direct injection of a diluted oil sample into the HPLC system have also been used.[18,19] However, a pretreatment step for sample enrichment and cleanup is always desirable prior to any chromatographic analysis due to the complexity of the sample matrix. Recently, some novel microextraction procedures, such as cloud-point extraction (CPE)[10] and dispersive liquid-liquid microextraction (DLLME)[5,20] have also been devel-

oped to detect alkyl gallates in oil samples as greener alternatives to classical LLE. In the last few years, the majority of the innovative studies on microextraction procedures are concerned with replacing toxic organic solvents with environmentally friendly ones, including supramolecular solvents, ionic liquids and deep eutectic solvents (DESs).

DESs are regarded as new generation green solvents because of their attractive properties such as easy synthesis, low cost, low volatility, high biodegradability, and feasibility of structural design.[21] A DES is typically prepared by mixing an appropriate amount of a hydrogen bond acceptor (HBA) and a hydrogen bond donor (HBD). The resulting mixture has a lower melting point than that of each individual component, which makes it liquid at room temperature. The formation of hydrogen bonding between the DES components is responsible for the decrease in the melting point.[22] The most common DESs are based on choline chloride (ChCl) paired with various HBDs, the most popular ones being urea, ethylene glycol, and glycerol, but other alcohols, amino acids, carboxylic acids, and sugars have also been used.[23] Due to their unique physicochemical characteristics, DESs have the potential to replace conventional organic solvents in separation and extraction processes. However, due to the hydrogen bonding ability of DESs, they are generally hydrophilic which restricts their application as extraction solvents in aqueous samples.[24] Therefore, the major applications have focused on the extraction of naturally occurring compounds from organic liquid samples (mainly vegetable oils) and solids (plants and foods). Phenolic compounds,[25,26] flavonoids[27,28] and terpenoids[29] are the most commonly determined bioactive compounds, with extraction procedures based on the use of hydrophilic DESs. Very recently, hydrophobic DESs combining quaternary ammonium salts, thymol or menthol with alkyl carboxylic acids have also been prepared and used for the extraction of pesticides,[30] polycyclic aromatic hydrocarbons[31] and benzophenone-type UV filters[32] from water samples. DESs possess tunable solvent properties that make them highly efficient in extracting compounds from different chemical classes. With respect to SAs, *tert*-butylhydroquinone is the only analyte that has been determined in vegetable oils with the extraction procedures based on the use of ChCl:ascorbic acid,[33] ChCl:sesamol[34] and ChCl:ethylene glycol[35] compositions. However, as far as we know, there is no DES-based extraction method reported in the literature for alkyl gallates. Therefore, the aim of this study was to investigate the feasibility of using a hydrophilic ChCl-based DES as an extraction solvent for the extraction and preconcentration of alkyl gallates including propyl gallate and octyl gallate (see their structures and some relevant data in Table 1) from vegetable oils. The dispersion of DES phase into the vegetable oil was achieved using vortex stirring, and then the resulting methodology was termed vortex-assisted DES-based liquid–liquid microextraction (VA-DES-LLME). Following the microextraction process, alkyl gallates in DES phase were separated and determined by HPLC-UV.

2. Experimental

2. 1. Reagents and Samples

All of the reagents used in the experiments were of analytical grade (≥98%). Ethylene glycol, glycerol, urea, choline chloride (ChCl), propyl gallate, octyl gallate and acetonitrile (ACN) were obtained from Sigma-Aldrich (Steinheim, Germany). Triflouroacetic acid (TFA) and *n*-hexane were purchased from Merck (Darmstadt, Germany). Isopropyl alcohol was provided from Kimetsan (Ankara, Turkey). Water was used after purification with a Milli-Q system (Millipore, Bedford, MA, USA).

Stock standard solutions were prepared in acetonitrile at a concentration of 100 μg mL^{-1} and stored at 4 °C for one month. The working solutions at different concentrations were freshly prepared in isopropyl alcohol and used for the spiking of the oil samples. Spiked samples were mixed well for the complete dissolution of the antiox-

Table 1. Chemical structure and properties of the selected alkyl gallates.

Analyte	Structure	pK_a [36]	LogK_{ow} [37]
Propyl gallate	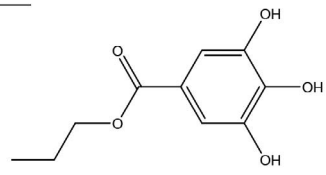	7.9	2.6
Octyl gallate	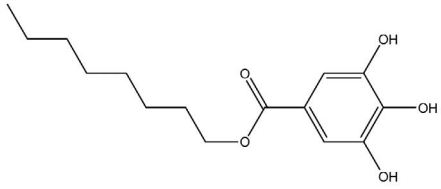	7.9	5.2

idants in the oil matrix before being extracted. The vegetable oil samples including sunflower oil, corn oil and hazelnut oil were collected from local supermarkets in Zonguldak, Turkey. The collected oil samples were packed in screw–cap glass tubes and stored at room temperature until analyzed.

2. 2. Instrumentation and Chromatographic Conditions

The HPLC system (Thermo Finnigan, San Jose, USA) consisted of a P1000 pump, a AS3000 automatic injector system, and a UV1000 UV detector. The system was controlled by a Spectra System Controller SN 4000 and a software package ChromQuest 4.0. A Phenomenex C_{12} Max-RP column (250 × 4.6 mm i.d., 4.0 μm) was used for separations. The mobile phase consisted of ACN and water with 0.1% TFA. The optimized elution program was set at 1.0 mL min^{-1}, starting with 40% acetonitrile and then a linear gradient elution from 40 to 90% acetonitrile at 20 min. Next, 10 min was necessary for returning to the initial conditions. Before another injection, the system was permitted to stabilize for 5 min under the initial conditions. The UV monitoring wavelength for quantification was set to 280 nm. The injection volume was 20 μL. A Perkin Elmer Frontier Fourier transform infrared (FT-IR) spectrometer with a diamond attenuated total reflectance (ATR) attachment was used to determine the functional groups of DESs. A magnetic stirrer (RSM-01H, Phoenix, Garbsen, Germany), a vortex mixer (SA8, BioCote, UK), a centrifuge (NF 200, Nuve, Ankara, Turkey) were used in the sample preparation step. A Kern ABJ 220–4 M model analytical balance (Kern & Sohn, Germany) was used for weighing the samples and standard materials.

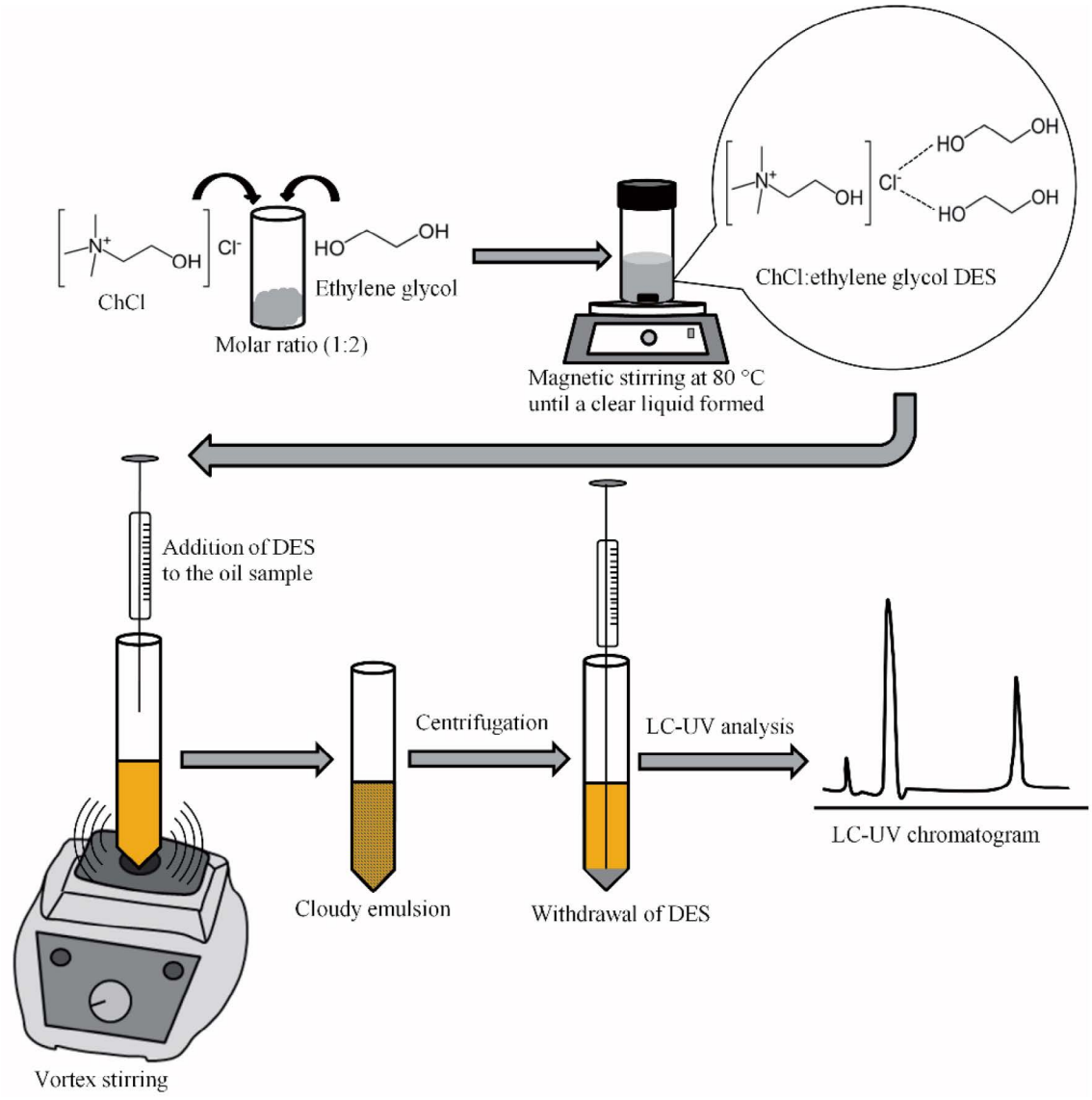

Figure 1. Schematic diagram of the preparation of ChCl:ethylene glycol DES and VA-DES- LLME method.

2. 3. Preparation of DESs

DESs were prepared by mixing ChCl with HBD (ethylene glycol, glycerol, or urea) at a constant molar ratio of 1:2 in screw-capped bottles. The mixture was stirred at a temperature of 80 °C until a clear liquid was formed. Figure 1 shows, as an example, the schematic of the preparation of ChCl:ethylene glycol DES. All DESs were used in the experiments without any further purification.

2. 4. VA-DES-LLME Procedure

Figure 1 shows the schematic of the VA-DES-LLME procedure. Oil sample (1.0 g) was accurately weighed into a 12 mL glass test tube with conical bottom and diluted with 1.0 mL of *n*-hexane, to which 120 μL of DES as extracting solvent was added. Afterwards, the mixture was vortex-stirred at 2500 rpm for 5 min and then centrifuged at 4000 rpm for 5 min. Finally, the DES extract was collected with a microsyringe and transferred to a glass vial for the HPLC-UV analysis.

3. Results and Discussion

Optimization of VA-DES-LLME was carried out using 1.0 g of sunflower oil sample, spiked with propyl gallate and octyl gallate at a concentration of 1.25 μg g^{-1} each. The type of DES, volume of diluent solvent, volume of DES and vortex stirring time were the variables investigated. The optimal conditions were selected based on the extraction recoveries (ERs) of the alkyl gallates. The ER was calculated based on the ratio of the amount of the analyte determined in the collected DES phase to the initial amount of analyte added in the sample. All the experiments were carried out in triplicate.

3. 1. Effect of the Types of DESs

The composition of DESs determines their physicochemical properties such as density, viscosity, and surface tension and consequently influences extraction efficiency of the target analytes. With the aim to select the most suitable DES for extraction of alkyl gallates from vegetable oils, three different ChCl-based DES, which contained ethylene glycol, glycerol, and urea as the HBDs at a constant molar ratio of 1:2 were tested. In all cases, aliquots of 1.0 g of sunflower oil sample were extracted with 100 μL of DES under vortex stirring for 5 min. When ChCl:urea DES was used, it was not effectively dispersed into the oil sample with vortex stirring. In addition, it could not be withdrawn into the micro-injector prior to chromatographic analysis. On the contrary, these difficulties were not observed when ethylene glycol and glycerol-based DESs were tested. The results observed here could be attributed to the difference in their viscosities and other physical properties. The ChCl:urea DES has much higher viscosity (750 cP) than those of the ChCl:ethylene glycol DES (37 cP) and ChCl:glycerol DES (259 cP) at 25 °C.[38] Most DESs have higher viscosities (>100 cP) than other molecular solvents due to the presence of extensive hydrogen-bonding interactions between the components, which slows down the mass transfer of the analytes to the extraction media.[23] Addition of water, in general, reduces the viscosity of these solvents, and therefore allows better mass transfer rates. However, at the same time the presence of water may reduce the extraction yields due to the weakening of the hydrogen bond interactions between the solvent and the target compounds.[39] Due to the opposite effects of water on the extraction efficiency, it was not investigated in the present experiment. As shown in Figure 2, the extraction efficiencies of ethylene glycol and glycerol-based DESs were close to each other, meaning that each of DESs could be used as a solvent for the extraction of alkyl gallates. However, ChCl:ethylene glycol DES provided some advantages in the solvent transfer and injection stages due to its lower viscosity; thus, it was selected as extraction solvent in the subsequent experiments.

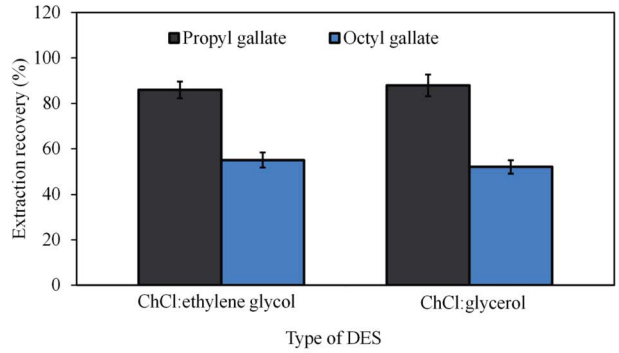

Figure 2. Effect of the type of DES. DES volume, 100 μL; vortex time, 5 min.

3. 2. Characterization of ChCl:ethylene Glycol DES

The formation of hydrogen bonding between the chloride anion of ChCl and ethylene glycol is the main force for the formation of DES. As shown in Figure 3, FT-IR spectra of ChCl, ethylene glycol, and ChCl:ethylene glycol DES were investigated. According to the FT-IR spectra, the broad band at 3294 cm^{-1} related to the stretching vibration of the O–H group in ethylene glycol shifted to 3303 cm^{-1} in ChCl:ethylene glycol DES. This shift towards higher wavenumber with the incorporation of ChCl and ethylene glycol was due to the decrease in the extent of intermolecular hydrogen bonding between ethylene glycol molecules.[40] The spectrum of DES was dominated by ethylene glycol, however, an additional characteristic band at 953 cm^{-1} originating from ChCl was observed. This new band was attributed to the C–N^+ stretching. In addition, DES presented vibrational bands at 2938 cm^{-1} and 2875

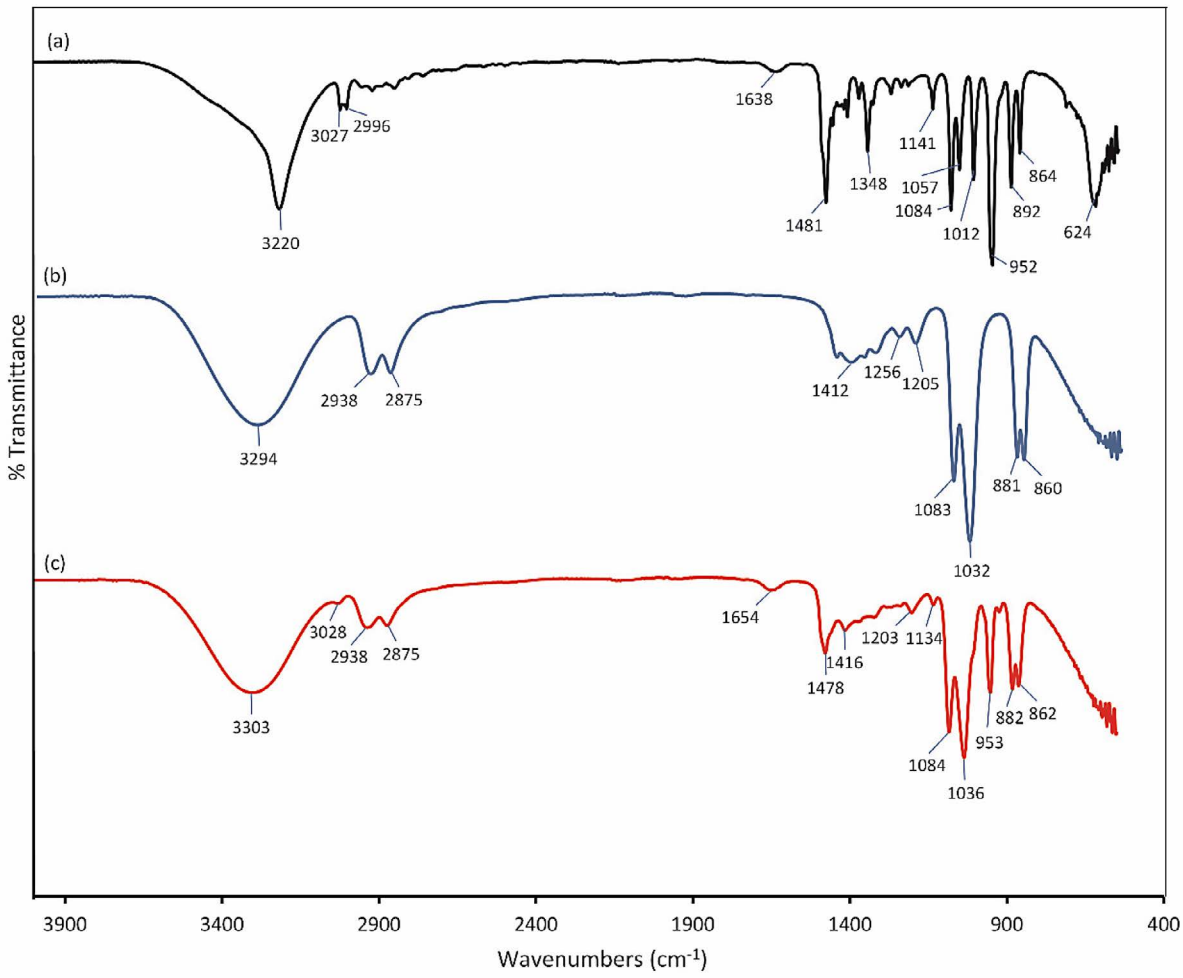

Figure 3. FT-IR spectra of (a) ChCl, (b) ethylene glycol, (c) ChCl:ethylene glycol DES.

cm^{-1} referring to C–H stretching, 1478 cm^{-1} to the CH_2 bending of an alkyl group, and 1084 cm^{-1}, 1036 cm^{-1}, and 882 cm^{-1} to functional groups, namely C–O stretching, C–C–O asymmetric stretching, and C–C–O symmetric stretching.[41] These results indicated the successful synthesis of ChCl:ethylene glycol DES.

3. 3. Effect of the Volume of Diluent Solvent

The dilution of oil sample with an appropriate solvent has a significant effect on the extraction efficiency since it reduces the viscosity of oil and facilitates the formation of the cloudy emulsion. In addition, the fat and other impurities are easily dissolved in the diluent solvent which may be beneficial for the removal of impurities.[42] Hexane is the most preferred solvent owing to its low toxicity, low cost and high miscibility with the oil.[43] In this work, *n*-hexane was selected as diluent solvent and the effect of its volume was studied in the range of 0–2 mL. Aliquots of 1.0 g of sunflower oil sample were diluted with hexane and subjected to vortex stirring for 5 min with 100 μL of ChCl:ethylene glycol DES as extraction solvent. As shown in Figure 4, the extraction efficiency of alkyl gallates increased slightly as the hexane volume was increased from 0 to 1 mL and remained nearly constant over this volume. The reason could be that the viscosity of oil sample reduced with the increase of the volume of hexane, which facilitated the mass transfer of the analytes from oil

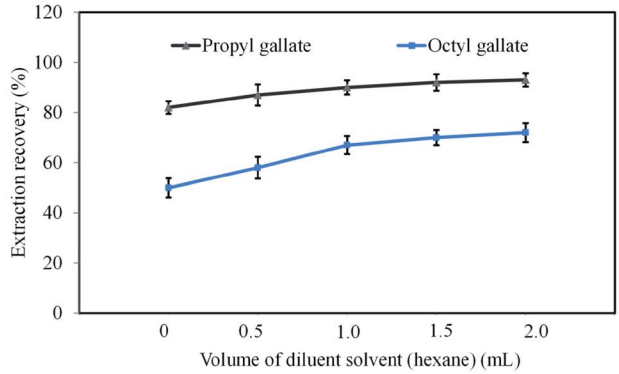

Figure 4. Effect of the volume of diluent solvent. DES, ChCl:ethylene glycol; diluent solvent, *n*-hexane; DES volume, 100 μL; vortex time, 5 min.

to the DES phase. Therefore, the diluent solvent (*n*-hexane) volume was selected as 1 mL for all further experiments.

3. 4. Effect of the Volume of DES

Selection of the optimum volume for the extraction solvent is another important step in the majority of microextraction methods. By the increase of extraction solvent volume, the final solvent volume collected after centrifugation is increased, resulting in a decrease in sensitivity towards the analytes. In order to increase the sensitivity, it is essential to keep the volume of extraction solvent as low as possible. However, it is not always possible to reduce the solvent volume as desired, because a sufficient volume of solvent needs to be collected after centrifugation for the analysis. To examine the effect of the extraction solvent volume on the extraction efficiency, different volumes of ChCl:ethylene glycol DES from 60 to 140 μL were investigated while the other experimental parameters, diluent solvent volume of 1 mL and vortex time of 5 min, were kept constant. The volumes less than 60 μL were not examined because of the difficulty in getting a separated DES phase. The obtained results (Figure 5) showed that the extraction efficiency increased with the increase of DES volume up to 120 μL and remained unchanged after that. Typically, a higher volume of solvent requires a longer mixing time to be broken up into fine droplets; here above 120 μL, the extraction recovery did not further increase maybe due to the incomplete formation of fine droplets within a fixed vortex time. Therefore, 120 μL was selected as the most suitable DES volume for subsequent experiments.

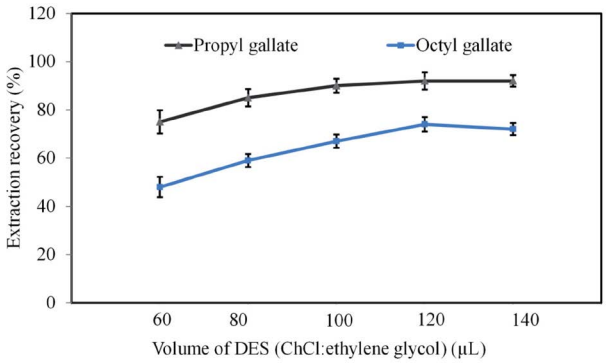

Figure 5. Effect of the volume of DES. DES, ChCl:ethylene glycol; diluent solvent, *n*-hexane; diluent solvent volume, 1 mL; vortex time, 5 min.

3. 5. Effect of Vortex Stirring Time

The vortex stirring process facilitates the dispersion of the extraction solvent into the sample solution resulting in enhancement of extraction efficiency. The time required to reach extraction equilibrium under vortex stirring is an important parameter to be optimized. In this work, the vortex rotational speed was kept at maximum (2500 rpm) and different vortex times were investigated, from 1 to 15 min. The experimental conditions were fixed and included the use of 1 mL of diluent solvent (*n*-hexane) and 120 μL of ChCl:ethylene glycol DES. The results (Figure 6) showed that the extraction efficiency increased with the increasing vortex time from 1 to 3 min, and then from 3 to 5 min, there was either a slight increase or no change, depending on the analyte. No significant change was observed at vortex times longer than 5 min. Therefore, 5 min was chosen as the optimum vortex time.

According to these results, the optimal conditions of this method for the determination of alkyl gallates were as follows: the type of DES was ChCl:ethylene glycol with a molar ratio of 1:2; the volume of diluent solvent (hexane) was 1 mL; the volume of ChCl:ethylene glycol DES was 120 μL; and the vortex stirring time was 5 min. Because the DES was not soluble in oil matrix, it could be collected after extraction without a significant loss in its volume.

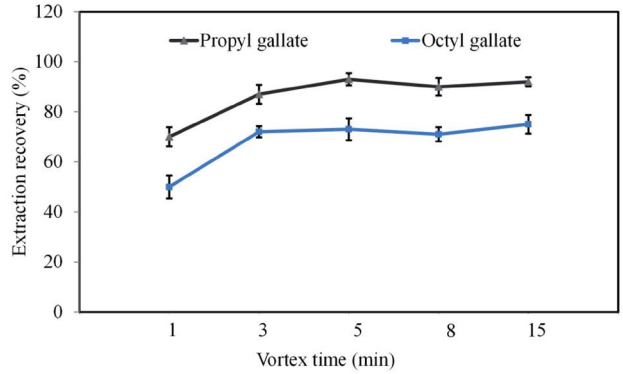

Figure 6. Effect of the vortex time. DES, ChCl:ethylene glycol; diluent solvent, *n*-hexane; diluent solvent volume, 1 mL; DES volume, 120 μL.

Under the optimized conditions, the mean extraction recoveries for propyl gallate and octyl gallate were 93 and 73%, respectively. The enrichment factors were also calculated based on the ratio of the analyte concentration in the DES phase to the initial analyte concentration in the oil phase. Under the optimized conditions, the mean enrichment factors for propyl gallate and octyl gallate were 8.5 and 6.7, respectively. Both propyl gallate and octyl gallate have the same pK_a value of about 7.9,[36] meaning that their hydrogen bonding potentials are similar. The difference in the extraction efficiencies of alkyl gallates was then likely the result of their different hydrophobic characteristics. The octanol-water partition coefficients (logK_{ow}) for propyl gallate and octyl gallate are 2.6 and 5.2, respectively.[37] The hydrophobicity of alkyl gallates increases with the increasing alkyl chain length (see the structures in Table 1), making the hydrophobic interaction between octyl gallate and oil stronger, and thus decreasing the hydrogen bonding strength between the phenyl hydroxyls of octyl gallate and chloride anion of choline salt.

3. 6. Analytical Performance

Linearity, limit of detection (LOD), limit of quantification (LOQ), and precision were investigated to verify the reliability of the method used in this study. The results are summarized in Table 2. Linearity was observed in the range of 0.01–5 μg g^{-1}, with the square of correlation coefficients (R^2) higher than 0.9995. LODs, based on a signal-to-noise ratio (S/N) of 3, ranged from 2.1 to 4.6 μg kg^{-1}. The precision of the method was determined by analyzing the spiked samples at concentration level of 0.5 μg g^{-1} on the same day and on three different days. The relative standard deviations (RSDs) were in the ranges of 4.6–6.4% and 5.4–7.5% for intra-day (n=5) and inter-day (n=3) precision, respectively, which indicates that the method is repeatable.

3. 7. Real Samples Analysis

The applicability of the proposed method was evaluated with three kinds of vegetable oil samples including sunflower oil, corn oil and hazelnut oil. The results indicated that the samples were free of alkyl gallates. To examine the applicability and accuracy of the method, all the samples were spiked at two concentration levels of 0.25 and 2.5 μg g^{-1}, and analyzed. The results are given in Table 3. The recoveries of alkyl gallates from oil samples spiked at low and high concentration levels were 78–93% and 87–106%, respectively. RSDs for these two levels were in the ranges 3.2–5.7% and 2.0–5.2%. These results demonstrated that the matrix had a negligible effect on the extraction. Figure 7 shows, as an example, the HPLC–UV chromatograms of the alkyl gallates extracted from a sunflower oil sample be-

Table 2. Quantitative features of VA-DES-LLME method combined with LC-UV.

Analyte	Linear range (μg g^{-1})	R^2	LOD (μg kg^{-1})	LOQ (μg kg^{-1})	Intra-day RSD (%, n=5)	Inter-day RSD (%, n=3)
Propyl gallate	0.01–5	0.9995	2.1	7.0	4.6	5.4
Octyl gallate	0.01–5	0.9996	4.6	15.3	6.4	7.5

Table 3. Spiked recoveries (accuracies of determination) of alkyl gallates in vegetable oil samples.

Oil sample	Added (μg g^{-1})	Propyl gallate		Octyl gallate	
		RR (%)	RSD (%, n=3)	RR (%)	RSD (%, n=3)
Sunflower-1	0.25	83	4.8	84	5.7
	2.50	96	2.4	98	3.2
Sunflower-2	0.25	78	3.8	93	4.2
	2.50	98	2.7	100	2.2
Sunflower-3	0.25	90	4.3	87	4.6
	2.50	99	4.0	106	5.2
Corn	0.25	86	5.4	79	5.5
	2.50	90	2.5	87	2.0
Hazelnut	0.25	92	3.2	86	4.7
	2.50	104	3.4	98	4.4

RR: Relative recovery

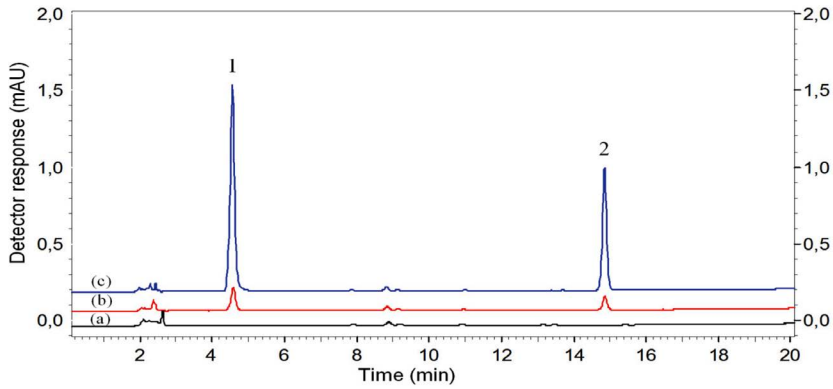

Figure 7. HPLC–UV chromatograms, corresponding to (a) sunflower oil sample, and the same sample after spiking of the alkyl gallates at the (b) 0.25 μg g^{-1} and (c) 2.5 μg g^{-1} levels. 1: Propyl gallate, 2: Octyl gallate.

Table 4. Comparison of the proposed method with other methods used in determination of alkyl gallates in vegetable oil samples.

Method	Analytes	Sample amount (g)	Extraction solvent	Solvent volume (mL)	Extraction time (min)	RSD (%)	LOD	Recovery (%)	Reference
CPE-HPLC-DAD	Propyl gallate	2	Triton X-114	5	30	<2.2	1.9 μg L^{-1}	86–88	10
UAE-HPLC-UV	Propyl gallate	10	Methanol + acetonitrile	45	15	<4.0	300 μg L^{-1}	103–108	11
LLE-LC-TOF-MS	Propyl gallate Octyl gallate	0.25	Acetonitrile + hexane	3	5	<6.3	20 μg kg^{-1} 20 μg kg^{-1}	82–96	12
DLLME-HPLC-DAD	Propyl gallate Octyl gallate	0.025	Hexane + acetonitrile	1	2	<2.7	10 μg L^{-1} 15 μg L^{-1}	94–105	5
DLLME-MSPE-HPLC-UV	Propyl gallate	2	Heptanol	0.16	~3	<6.7	1.2 μg L^{-1}	90–92	20
VA-DES-LLME-HPLC-UV	Propyl gallate Octyl gallate	1	ChCl:ethylene glycol DES	0.12	5	<7.5	2.1 μg kg^{-1} 4.6 μg kg^{-1}	78–106	This study

DAD: diode array detection; MSPE: magnetic solid-phase extraction; TOF-MS: time-of-flight-mass spectrometry; UAE: ultrasonic-assisted extraction

fore and after spiking. No interfering peaks from the sample matrix or DES solvent were observed at the retention times of compounds of interest, which demonstrated the good applicability of the proposed method.

Extraction and determination of alkyl gallates in vegetable oils by the proposed method was compared with those of other methods considering the performance parameters such as sample amount, type and volume of extraction solvent, extraction time, RSD, LOD, and relative recovery. The details of the comparison are summarized in Table 4. As shown, the proposed method offers lower consumption of sample amount and solvent volume, faster analyses, and lower detection limits than most of the existing methods while being comparable with respect to the precision and accuracy. More importantly, by using DES instead of conventional solvents, the main merits of the proposed method such as simplicity, low cost, and environmental benignity were enhanced.

4. Conclusions

A green and efficient analytical methodology (VA-DES-LLME-HPLC-UV) was developed for the extraction and analysis of alkyl gallates (propyl gallate and octyl gallate) in vegetable oil samples. The ChCl:ethylene glycol DES proved to be an excellent solvent for alkyl gallates of low and medium polarity thanks to the hydrogen bonding interaction between the phenyl hydroxyl groups and anion of choline salt. Vortex stirring was employed to promote the dispersion of the DES solvent into the oil sample, which resulted in high extraction efficiency with the obtained extraction recoveries ranging from 73 to 93%. The optimized procedure displayed a good precision with RSDs <7.5% and reliable analytical results with spiked recoveries (accuracies) in the range of 78–106%. LODs were in the range of 2.1–4.6 μg kg^{-1}, which is better than or comparable with other reported approaches applied to the determination of alkyl gallates in vegetable oils.

5. Acknowledgements

The authors would like to thank to Zonguldak Bülent Ecevit University for the opportunity and financial support.

6. References

1. D. W. Sin, Y. C. Wong, C. Y. Mak, S. T. Sze, W. Y. Yao, *J. Food Compos. Anal.* **2006**, *19*, 784–791. **DOI:**10.1016/j.jfca.2005.12.005
2. F. Shahidi, P. Ambigaipalan, *J. Funct. Foods* **2015**, *18*, 820–897. **DOI:**10.1016/j.jff.2015.06.018
3. Y. Hou, Z. Xie, H. Cui, Y. Lu, T. Zheng, S. Sang, L. Lv, *Food Chem.* **2018**, *269*, 396–403. **DOI:**10.1016/j.foodchem.2018.07.030
4. I. C. Silva, C. R. Polaquini, L. O. Regasini, H. Ferreira, F. R. Pavan, *Food Chem. Toxicol.* **2017**, *105*, 300–307. **DOI:**10.1016/j.fct.2017.04.033

5. S. Xu, L. Liu, Y. Wang, D. Zhou, M. Kuang, D. Fang, W. Yang, S. Wei, A. Xiao, L. Ma, *J. Sep. Sci.* **2016**, *39*, 3205–3211. **DOI:** 1https://doi.org/10.1002/jssc.201600434
6. U. Sivasankaran, A. E. Vikraman, D. Thomas, K. G. Kumar, *Food Anal. Methods* **2016**, *9*, 2115–2123. **DOI:**10.1007/s12161-015-0356-7
7. M. Cui, J. Huang, Y. Wang, Y. Wu, X. Luo, *Biosens. Bioelectron.* **2015**, *68*, 563–569. **DOI:**10.1016/j.bios.2015.01.029
8. G. Xu, Y. Chi, L. Li, S. Liu, X. Kan, *Food Chem.* **2015**, *177*, 37–42. **DOI:**10.1016/j.foodchem.2014.12.097
9. J.-M. Kim, S.-H. Choi, G.-H. Shin, J.-H. Lee, S.-R. Kang, K.-Y. Lee, H.-S. Lim, T. S. Kang, O.-H. Lee, *Food Chem.* **2016**, *213*, 19–25. **DOI:**10.1016/j.foodchem.2016.06.053
10. M. Chen, Q. Xia, M. Liu, Y. Yang, *J. Food Sci.* **2011**, *76*, C98–C103. **DOI:**10.1111/j.1750-3841.2010.01914.x
11. B. Saad, Y. Y. Sing, M. A. Nawi, N. Hashim, A. S. M. Ali, M. I. Saleh, S. F. Sulaiman, K. M. Talib, K. Ahmad, *Food Chem.* **2007**, *105*, 389–394. **DOI:** https://doi.org/10.1016/j.foodchem.2006.12.025
12. L. Xiu-Qin, J. Chao, S. Yan-Yan, Y. Min-Li, C. Xiao-Gang, *Food Chem.* **2009**, *113*, 692–700. **DOI:**10.1016/j.foodchem.2008.07.072
13. Y. Guan, Q. Chu, L. Fu, T. Wu, J. Ye, *Food Chem.* **2006**, *94*, 157–162. **DOI:**10.1016/j.foodchem.2005.01.015
14. M. M. Delgado-Zamarreno, A. Sanchez-Perez, I. G. Maza, J. Hernandez-Mendez, *J. Chromatogr. A* **2000**, *871*, 403–414. **DOI:**10.1016/S0021-9673(99)01020-1
15. Q. Xiang, Y. Gao, Y. Xu, E. Wang, *Anal. Sci.* **2007**, *23*, 713–717. **DOI:**10.2116/analsci.23.713
16. H.-Y. Huang, Y.-J. Cheng, C.-L. Lin, *Talanta* **2010**, *82*, 1426–1433. **DOI:**10.1016/j.talanta.2010.07.014
17. G. K. Ziyatdinova, A. A. Saveliev, G. A. Evtugyn, H. C. Budnikov, *Electrochim. Acta* **2014**, *137*, 114–120. **DOI:**10.1016/j.electacta.2014.06.009
18. J.-Y. Wang, H.-L. Wu, Y.-M. Sun, H.-W. Gu, Z. Liu, Y.-J. Liu, R.-Q. Yu, *J. Chromatogr. B* **2014**, *947*, 32–40. **DOI:**10.1016/j.jchromb.2013.12.009
19. J.-Y. Wang, H.-L. Wu, Y. Chen, Y.-M. Sun, Y.-J. Yu, X.-H. Zhang, R.-Q. Yu, *J. Chromatogr. A* **2012**, *1264*, 63–71. **DOI:**10.1016/j.chroma.2012.09.070
20. X. Li, D. Meng, L. Zhang, J. Zhao, Y. Yang, *Sep. Sci. Technol.* **2018**, *53*, 2224–2231. **DOI:**10.1080/01496395.2018.1446983
21. Z.-L. Huang, B.-P. Wu, Q. Wen, T.-X. Yang, Z. Yang, *J. Chem. Technol. Biotechnol.* **2014**, *89*, 1975–1981. **DOI:**10.1002/jctb.4285
22. T. Khezeli, A. Daneshfar, R. Sahraei, *Talanta* **2016**, *150*, 577–585. **DOI:**10.1016/j.talanta.2015.12.077
23. M. Ruesgas-Ramón, M. C. Figueroa-Espinoza, E. Durand, *J. Agric. Food Chem.* **2017**, *65*, 3591–3601. **DOI:**10.1021/acs.jafc.7b01054
24. H. Wang, L. Hu, X. Liu, S. Yin, R. Lu, S. Zhang, W. Zhou, H. Gao, *J. Chromatogr. A* **2017**, *1516*, 1–8. **DOI:**10.1016/j.chroma.2017.07.073
25. A. García, E. Rodríguez-Juan, G. Rodríguez-Gutiérrez, J. J. Rios, J. Fernández-Bolaños, *Food Chem.* **2016**, *197*, 554–561. **DOI:**10.1016/j.foodchem.2015.10.131
26. M. C. Bubalo, N. Ćurko, M. Tomašević, K. K. Ganić, I. R. Redovniković, *Food Chem.* **2016**, *200*, 159–166. **DOI:**10.1016/j.foodchem.2016.01.040
27. W. Bi, M. Tian, K. H. Row, *J. Chromatogr. A* **2013**, *1285*, 22–30. **DOI:**10.1016/j.chroma.2013.02.041
28. Q. Cui, J.-Z. Liu, L.-T. Wang, Y.-F. Kang, Y. Meng, J. Jiao, Y.-J. Fu, *J. Cleaner Prod.* **2018**, *184*, 826–835. **DOI:**10.1016/j.jclepro.2018.02.295
29. B. Tang, W. Bi, H. Zhang, K. H. Row, *Chromatographia* **2014**, *77*, 373–377. **DOI:**10.1007/s10337-013-2607-3
30. C. Florindo, L. C. Branco, I. M. Marrucho, *Fluid Phase Equilib.* **2017**, *448*, 135–142. **DOI:**10.1016/j.fluid.2017.04.002
31. P. Makoś, A. Przyjazny, G. Boczkaj, *J. Chromatogr. A* **2018**, *1570*, 28–37. **DOI:**10.1016/j.chroma.2018.07.070
32. D. Ge, Y. Zhang, Y. Dai, S. Yang, *J. Sep. Sci.* **2018**, *41*, 1635–1643. **DOI:**10.1002/jssc.201701282
33. W. Liu, K. Zhang, J. Chen, J. Yu, *J. Mol. Liq.* **2018**, *260*, 173–179. **DOI:**10.1016/j.molliq.2018.03.092
34. W. Liu, B. Zong, J. Yu, Y. Bi, *Food Anal. Methods* **2018**, *11*, 1797–1803. **DOI:**10.1007/s12161-018-1174-5
35. W. Liu, K. Zhang, J. Yu, Y. Bi, *Food Anal. Methods* **2017**, *10*, 3209–3215. **DOI:**10.1007/s12161-017-0891-5
36. A. Makahleh, B. Saad, M. F. Bari, in: F. Shahidi (Ed.): Handbook of antioxidants for food preservation, Woodhead Publishing, Cambridge, **2015**, pp. 51–78. **DOI:**10.1016/B978-1-78242-089-7.00003-8
37. C. André, I. Castanheira, J. M. Cruz, P. Paseiro, A. Sanches-Silva, *Trends Food Sci. Technol.* **2010**, *21*, 229–246. **DOI:**10.1016/j.tifs.2009.12.003
38. Q. Zhang, K. D. O. Vigier, S. Royer, F. Jerome, *Chem. Soc. Rev.* **2012**, *41*, 7108–7146. **DOI:**10.1039/c2cs35178a
39. M. H. Zainal-Abidin, M. Hayyan, A. Hayyan, N. S. Jayakumar, *Anal. Chim. Acta* **2017**, *979*, 1–23. **DOI:**10.1016/j.aca.2017.05.012
40. L. Vieira, R. Schennach, B. Gollas, *Phys. Chem. Chem. Phys.* **2015**, *17*, 12870–12880. **DOI:**10.1039/C5CP00070J
41. M. Hayyan, A. Abo-Hamad, M. A. AlSaadi, M. A. Hashim, *Nanoscale Res. Lett.* **2015**, *10*, 1–26. **DOI:**10.1186/s11671-015-1004-2
42. N. Li, L. Zhang, L. Nian, B. Cao, Z. Wang, L. Lei, X. Yang, J. Sui, H. Zhang, A. Yu, *J. Agric. Food Chem.* **2015**, *63*, 2154–2161. **DOI:**10.1021/jf505760y
43. P. Reboredo-Rodríguez, L. Rey-Salgueiro, J. Regueiro, C. González-Barreiro, B. Cancho-Grande, J. Simal-Gándara, *Food Chem.* **2014**, *150*, 128–136. **DOI:**10.1016/j.foodchem.2013.10.157

Povzetek

V tej študiji raziskujemo možnost uporabe hidrofilnih močnih evtektičnih topil (DES) kot zelenih in učinkovitih ekstraktantov za ekstrakcijo in predkoncentracijo alkil galatov iz rastlinskih olj. V tipičnem poskusu smo dodali 120 μL DES-a holin klorid:etilen glikol k 1,0 g vzorca olja, ki smo ga predhodno razredčili z 1 mL *n*-heksana. Ekstrakcijo smo pospešili z vrtinčastim mešanjem obeh faz. V tem koraku je bil verjetno glavni razlog za ekstrakcijo nastanek vodikovih vezi med fenil-hidroksilno skupino alkil galatov in kloridom iz holin klorida. Po ekstrakciji smo analite iz DES-faze ločili in določili z visokoločljivostno tekočinsko kromatografijo z ultravijolično detekcijo. Meje zaznave so bile 2,1 μg kg^{-1} za propil galat in 4,6 μg kg^{-1} za oktil galat. Natančnost metode je bila 4,6–6,4% (znotraj dneva) in 5,4–7,5% (med dnevi). Izkoristki (pravilnost) za vzorce rastlinskega olja z dodanimi analiti so bili v območju 78–106%.

Scientific paper

Molecular Dynamics Simulations of p97 Including Covalent, Allosteric and ATP-Competitive Inhibitors

Stefano Rendine,[1,†] Christian Orrenius,[2,*] Federico Dapiaggi,[1,3] Stefano Pieraccini,[1,3] Ilaria Motto,[2] Roberto D'Alessio,[2] Paola Magnaghi,[2] Antonella Isacchi,[2] Eduard Felder[2] and Maurizio Sironi[1,3,*]

[1] Dipartimento di Chimica, Università degli Studi di Milano, Via Golgi 19, Milano, Italy

[2] Business Unit Oncology, Nerviano Medical Sciences, 20014 Nerviano, Italy

[3] Consorzio Interuniversitario Nazionale per la Scienza e Tecnologia dei Materiali (INSTM), UdR Milano

[†] *Syngenta Crop Protection AG, Crop Protection Research, Schaffhauserstrasse, CH-4332 Stein, Switzerland*

** Corresponding author: E-mail: christian.orrenius@nervianoms.com, maurizio.sironi@unimi.it*

Received: 11-28-2018

Abstract

Binary (nucleotide-protein dimer and hexamer complexes) and ternary (nucleotide-protein-inhibitor complexes) p97 complexes were subjected to molecular dynamics simulations in an attempt to further our understanding of the p97 protein oligomer domain stability and, more importantly, of the recently reported diverse molecular mechanisms of inhibition including allosteric, ATP-competitive and covalent inhibitors. Analysis of stable states following equilibration phases indicated a higher intrinsic stability of the homohexamer as opposed to the dimer, and of N-D1 domains as opposed to the D2 domain. The molecular dynamics of the proposed allosteric binding model reproduced important molecular interactions identified experimentally with high frequency throughout the trajectory. Observed conformational changes occurring in the D2 nucleotide binding site provided a novel *bind-rearrange-react* hypothesis of stepwise molecular events involved in the specific covalent inhibitor mode of action.

Keywords: Drug design; protein-protein interaction; mm-pbsa; molecular dynamics

1. Introduction

The AAA+ (ATPases Associated with diverse cellular Activities) protein family carries out multiple functions, including chromatin decondensation, homotypic membrane fusion and ubiquitin dependent protein degradation by the proteasome. In particular, p97, or Valosine-containing Protein (VCP), is a 97 kDa protein belonging to the AAA+ protein family. p97 includes two copies of a nucleotide-binding domain, called D1 and D2 which are interconnected by a 20 amino-acids long loop (the D1-D2 linker) and preceded by a non-nucleotide binding domain, the N-domain, which is oriented outward to permit interaction with adapter proteins.[1]

p97 regulates a number of processes involving ubiquitin, due to its ability to segregate ubiquitinated substrates from unmodified partners. In particular, p97 plays an essential role in the ubiquitin-dependent proteasomal degradation, including endoplasmic reticulum-associated degradation (ERAD),[2,3] degradation of some cytosolic proteins by the ubiquitin-fusion domain (UFD) pathway[4] and rapid degradation of nascent peptides during heat shock.[5]

Crystallographic studies of p97[6] testify that it functions as a homo-hexameric ring, formed by the D1 and D2 domains with the N-terminal domain oriented outward to permit interaction with adapter proteins. The formation of this complex molecular machinery is driven by protein-protein interactions (PPIs).

In recent works,[7–9] small molecules able to inhibit p97 were identified (Figure 1a). Different mechanisms of inhibition were proposed for these molecules. NMS-873 seems to act as an allosteric inhibitor of p97, binding in

close proximity to the N-terminal of the D1-D2 linker. NMS-322 is a ATP competitor and binds in the nucleotide binding site in D2. Finally, NMS-859 is a covalent inhibitor that binds to Cys522. However, there is a lack of structural models rationalizing these postulated binding modes. In this work we employ computational techniques to investigate the binding mode of these inhibitors both from the conformational and energetical point of view. Molecular dynamics simulations were carried out on these systems and a subsequent computational alanine scanning allowed us to identify the fundamental residues for the binding of these compounds. The aforementioned technique has been extensively used to map, from the energetic point of view, the interaction pattern of protein in complex with small ligands both of peptidic[10] and non-peptidic[11] nature. In the case of the allosteric inhibitor (NMS-873) the need of a good starting structure for molecular dynamics simulations prompted us to employ molecular docking. It is well proven in literature, indeed, that molecular docking studies on biological systems can successfully predict the structures of intermolecular complexes formed by ligands and their receptors (ranging from proteins[12] to DNA[13]).

2. Materials and Methods

The reference p97 structure was obtained from the Protein Data Bank (PDB ID code: **3CF1**).The VCP hexamer, the relevant biological assembly according to the authors of the original paper[1] (as well as an analysis performed with the software PISA[14]), was derived from standard symmetry operations in PyMOL.[15] The missing residues in the D2 domain were rebuilt using the software Modeller 9v7.[16] Molecular dynamics simulations were carried out with Gromacs 4.5.3[17] using the Amber ff99SB[18] force field for the protein and the Generalized Amber Force Field (GAFF)[19] for the inhibitors and nucleotides. The complexes were solvated with TIP3P[20] waters and neutralized with sodium ions.

The molecular systems studied were first subjected to a steepest descent minimization run (10000 steps) with alpha carbons constrained by a force constant of 1000 kJ mol^{-1} nm^{-2}. Subsequently, an equilibration of 200 ps was performed under NVT conditions at 310 K using the v-rescale thermostat[21] with a time constant of 0.1 ps. Electrostatic interactions were treated with the Particle Mesh Ewald (PME)[22] algorithm using a 10 Å cutoff. All bonds were constrained using the LINCS[23] algorithm, allowing a 2 fs timestep. A further 200 ps equilibration run was performed under NPT conditions at 310 K and 1 atm using the Berendsen barostat method[24] with a 0.5 ps correlation time. Alpha carbons were kept constrained as above. A 20 ns production run followed at constant temperature and pressure (1 atm, 310 K), releasing the constraints on the alpha carbons.

In order to clarify relative importance of amino acid residues and their interactions, computational alanine scanning and free energy calculations were performed using the Molecular Mechanics Generalized Born Surface Area (MM-GBSA) approach[25] on snapshots extracted at 20 ps intervals from the last 10 ns of the trajectories (500 snapshots in total) once the systems reached equilibrium. A 0.15 M NaCl solution was simulated as the solvent. The entropic contribution to the free energy data was neglected in the free energy calculations used in this study mainly due to the lack of reliability of results for the molecular systems considered here. An extended discussion on this topic can be found in literature.[26–30]

The starting structures of the complexes containing the inhibitor molecules NMS-873, NMS-322 and NMS-859 (non covalently bound, see discussion) were generated by molecular docking with QXP v0705 program[31] setting the following parameters to the *mcdock* tool: *in house* modified QXP MacroModel forcefield, 1500 Monte Carlo steps saving 20 poses for visual inspection. The rather large number of poses saved enabled a procedure identifying orientations compatible with photo-affinity labeling experimental evidence reported by Magnaghi *et al*., 2013.[7] Candidate binding sites were studied in order to identify pockets suitable for hosting inhibitor substituents. According to standard modeling procedures, binding site side chains were scrutinized in order to address protonation and 180° rotations of crystallographically equivalent groups and correct eventual atomic overlap. Subsequently, all structures were subject to the pre-simulation and simulation phases described above.

The Cys522/NMS-859 covalently bound structure was prepared as follows. As the p97 crystal structure shows the side chain of Cys522 (covalent bond site) completely buried, the dynamical behaviour of the Walker A loop was evaluated with a 20 ns long MD simulation of the apo hexamer protein to verify if a suitable conformation of Cys522 side chain exists for the reaction with NMS-859. The change in the surface accessible area of Cys522 was monitored and, interestingly, Cys522 was found to protrude into the ATP binding site in a solvent accessible conformation during the simulation. The protomer showing the highest solvent accessible area for Cys522 was extracted with its adjacent protomer and a relevant structural model of NMS-859 covalently bound to the Cys522 side chain was obtained building the Cys522/NMS-859 bond.

A more energetically meaningful structure was sought for by subjecting this new model to 100 simulated annealing runs, raising the temperature to 600 K and then cooling down to 0 K. Even at high temperatures, NMS-859 did not undergo any major rearrangements within the binding site. A reference structure was obtained by performing a cluster analysis on the 100 final structures of the simulated annealing and choosing the central element of the most populated cluster. The structure resulting from the cluster analysis was used to generate the hexamer with a NMS-859 molecule bound in each of the D2 ATP binding sites. The hexamer was subsequently submitted to a 20 ns MD simulation.

3. Results and Discussion

A series of molecular dynamics simulations was performed on a p97 hexamer model in complex with NMS-873, NMS-322 and NMS-859 (Figure 1). Before doing so, we compared results from simulations performed on dimeric *vs* hexameric forms of p97 without inhibitors. The use of a dimeric in the place of the hexameric model constituted a significant advantage in terms of CPU-time required for these calculations. However, results from the test simulations excluded this possibility due to severe molecular instability observed with the dimer. Specifically, unlike the hexameric system, the p97 dimer suffered a gradual but complete detachment of the D2 domain from the D1 domain within the same protomer in the early stages of the production run. Such a dramatic rearrangement would interfere with the simulation of our set of ligands, which bind regions at the intra- and inter-protomer interfaces.

The allosteric binding site and NMS-873. NMS-873 was originally docked into a putative binding site that was subsequently confirmed by photo-affinity labeling experiments. Depending on the position of reactive groups on NMS-873 analogues, Lys615 and Asn616 were specifically targeted as previously reported.[11] The model was further refined according to the procedure in the material and methods section. The selected pose involved, among other pockets, the lateral tunnel leading to the central pore of the hexamer between the D1 and D2 domains of two adjacent protomers. On the basis of observed kinetics, a stoichiometry of 1:2 was applied with one molecule bound to the A–B, C–D and E–F interfaces, respectively.

ΔG and alanine scanning. The three NMS-873 molecules showed a consistent behaviour throughout the molecular dynamics run, with a ΔG of binding of –69.2 ± 3.1 kcal/mol (A–B interface), –67.8 ± 2.7 kcal/mol (C–D interface) and –71.5 ± 2.9 kcal/mol (E–F interface). The coherent results for the three molecules are likely to be due to the tight packing and good fit of the molecule among residues and cavities at the D1 and D2 interface of the two adjacent protomers. In this case, the use of a hexameric model system turned out to be particularly important, since the simulation of the dimer would have led to a slacker binding site and a progressive weakening of the network of interactions due to protomer separation.

Computational alanine scanning highlighted the most relevant protein residues involved in the binding of this inhibitor. Lys615 showed the highest ΔΔG values on average (4.4 kcal/mol) with its contribution consisting of both hydrophobic interactions with the biphenyl moiety of NMS-873 and the hydrogen bond between the ε-amino group and the pyridine moiety of the inhibitor. This particular hydrogen bond occurred in 20%, 34%, 71% of the snapshots in the A–B, C–D, E–F binding sites, respectively. The difference was due to the possible torsion of the pyridine moiety with respect to the triazole plane, allowing

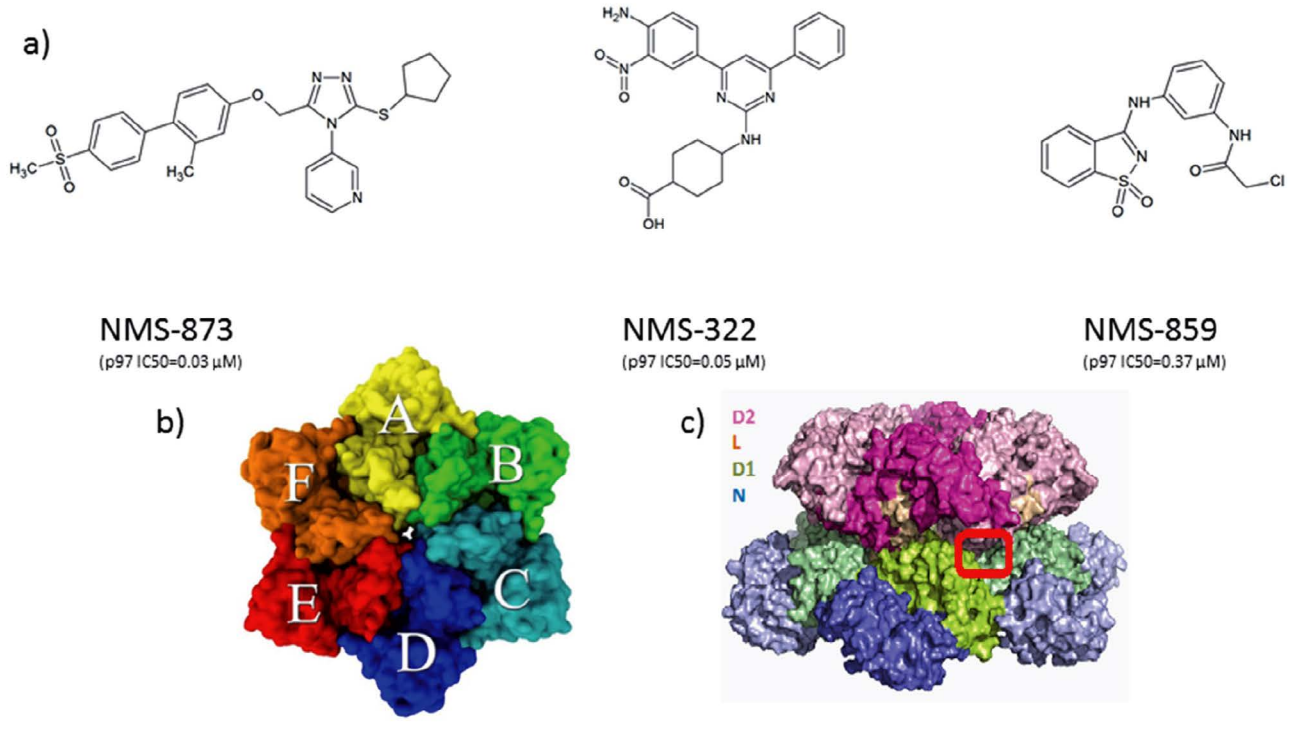

Figure 1.a) Structures of NMS-873, NMS-322 and NMS-859. b) Top view of the p97 hexamer: the single protomers are labelled with letters from A to F. c) Lateral view of the p97 hexamer coloured by domains and highlighting the NMS-873 binding site (red rectangle).

considerable variability in the making and breaking of this interaction. The aromatic pyridine ring was also found to effectively interact with Gln568 (1.3 kcal/mol) through van der Waals contacts.

Gln215 (2.9 kcal/mol), Gln212 (1.0 kcal/mol) and Leu456 (1.6 kcal/mol) further stabilized the binding at the opposite ends of the molecule through hydrophobic contacts with the cyclopentyl and the methylsulphonyl group. Most relevant interactions are shown in Figure 2a.

Other less frequent examples of amino acids that favourably took part in the binding with NMS-873, showing higher ΔΔG values only in specific couples of protomers were Arg453 (1.3 kcal/mol, A–B interface) and His406 (2.0 kcal/mol, B–C interface). Both formed hydrogen bonds with the terminal *p*-methylsulphonyl moiety. Gln458 (1.2 kcal/mol) and Asn460 (1.7 kcal/mol) participated in stabilizing the biphenyl part of the molecule in the C–D couple. Further hydrophobic interactions involved Arg365 (2.0 kcal/mol, A–B couple) and Lys211 (2.0 kcal/mol, E–F couple), which make favourable contact with the pyridine and the cyclopentyl moieties, respectively.

ATP-competitive inhibitors. NMS-322 belongs to the class of compounds sensitive to the ATP concentration.[13] Due to the complex and cooperative enzymatic mechanism of p97, it is impossible to distinguish between direct ATP competition and a mixed inhibitory mechanism where the binding of the compound affects the binding affinity of ATP in a different pocket of the hexamer. However, also in this case, there is experimental evidence of direct interactions within the nucleotide binding site in D2, namely the binding of Asp478 with a reactive azido analog of NMS-322 ("compound 35").[13]

ΔG and alanine scanning. Computational alanine scanning was performed to highlight the residues providing the principal interactions in NMS-322 binding. The results identified Thr525, Leu526 and Thr688 as the most important residues in all six protomers (Figure 2b). Leu526 showed the highest average ΔΔG value (2.5 kcal/mol) establishing hydrophobic interactions with the nitroaniline and the cyclohexane moieties of NMS-322. Thr688 (average ΔΔG of 1.1 kcal/mol) provided further hydrophobic interactions, whereas Thr525 (average ΔΔG = 1.3 kcal/mol) engaged hydrogen bonds with the carboxyl group of NMS-322, both through the backbone (44%) and the side-chain (52%).

Other aminoacids displayed varying ΔΔG values depending on the specific protomer, indicating some freedom of translation within this relatively large binding site. In particular, a group of residues in common for protomers A, B, D and E with cross-protomer interactions was identified. Only for these protomers, Arg635 showed average ΔΔG values of 1.7 kcal/mol, providing interactions with the hydrophobic part of NMS-322 and hydrogen bonds with the carboxylic moiety. Hydrogen bonding was relatively often observed in protomers A (25% frequency) and E (15%). For the same group of NMS-322 molecules, the carboxylic substituent frequently made interactions with Lys524. The molecules bound to protomer C and F exhibited a slightly different behaviour, extending towards the bottom of the ATP pocket, rather than towards the adjacent protomer, resulting in null ΔΔG values for Arg635, whereas Ile656 and Asn660 had higher ΔΔG values in relation to the above mentioned protomers. Being Thr525, Leu526 and Thr688 constantly involved in the interaction with the molecule in all protomers, it can be pointed out that the shifting between the two poses occurred around Thr525, acting as a hinge, with NMS-322 sliding between Thr525 and Leu526, allowing a deeper interaction inside the pocket or with the residues from the adjacent protomer.

In order to evaluate the NMS-322 displacement in the different protomers, the average RMSD on the molecule was calculated, after aligning the D2 domain backbone, with respect to the starting structure. The molecules bound to protomers A, B, D and E show an average RMSD over time of 3.82 Å, 2.92 Å, 3.45 Å and 3.30 Å, respectively, whereas the average RMSD rose to 5.93 Å and 4.71 Å for the molecules bound to protomers C and F, respectively. Despite the higher displacement for the molecule bound to protomer C, its ΔG of binding (–47.4 ± 3.8 kcal/mol) was consistent with the ΔG calculated for the molecules bound to protomers A (–44.4 ± 3.3 kcal/mol), B (–51.8 ± 3.2 kcal/mol), D (–46.2 ± 3.0 kcal/mol) and E (–53.3 ± 2.7 kcal/mol). In this case, NMS-322, as already highlighted by the alanine scanning results, could replace the original interactions with alternative ones, balancing the loss ΔG contributions. On the other hand, NMS-322 in protomer F was not found to efficiently rearrange to establish new binding interactions. Calculated ΔG of binding within protomer F and NMS-322 increased to –38.3 kcal/mol.

Covalent and specific class of inhibitors. NMS-859 is an irreversible protein modifier that was found by mass spectroscopy to covalently and specifically bind VCP at an active site cysteine. The Cys522 residue belongs to the Walker A motif, which is the ATP phosphate binding loop of the D2 domain nucleotide binding site. This covalent modification has been experimentally shown to totally impair the ATPase activity of the enzyme.

A possible mechanism of action would involve the binding of NMS-859 within the ATP binding site on the D2 domain, followed by the formation of a covalent bond with Cys522. In order to study the first step of the proposed binding process and evaluate the non-covalent fitting with the putative binding site, NMS-859 was docked in the D2 domain ATP pocket in the hexameric model (stoichiometry 1:1) and simulated for 20 ns. NMS-859 showed several similarities with NMS-322, primarily a significant contribution to the binding by hydrophobic contacts within the ATP site residues and the adjacent protomer. Computational alanine scanning performed on the last 10 ns of the trajectory highlighted Leu526, with an average ΔΔG of 1.6 kcal/mol and Thr688 (ΔΔG = 1.6 kcal/mol) as hot-spots in all six protomers (Figure 2c). The two

residues made up a hydrophobic cluster with the benzothiazole and phenyl moieties of NMS-859. Ile656, which was identified as a possible partner of interaction for NMS-322, was also found to contribute to the binding with NMS-859 in all the protomers with an average ΔΔG of 2.1 kcal/mol. The interaction with residues from the adjacent protomer also played a key role in the binding, in particular through Arg635, with an average ΔΔG of 1.1 kcal/mol. NMS-859 adopted slightly different poses in the six protomers, resulting in ΔG values ranging from –34.4 ± 2.7 kcal/mol (protomer E) to –44.9 ± 2.0 kcal/mol (protomer A), as observed for NMS-322. NMS-859 enters the space between Leu526 and Thr688 allowing the molecule to interact more favourably with the hydrophobic residues located at the bottom of the ATP pocket or with Arg635 of the adjacent protomer (as observed for NMS-322). Overall, the ligand showed a good affinity for the ATP pocket with the chlorine atom preferentially oriented towards the Walker A loop, possibly representing a favourable molecular arrangement for the reaction with Cys522.

The structural model of NMS-859 covalently bound to the Cys522 sidechain was obtained as described in the material and methods section.

A qualitative analysis of the trajectory highlighted a binding pose comparable to non-covalently bound NMS-859. Obviously, an evaluation of the free energy of binding was excluded, given the covalent bonding with the protein. The analysis of residues in proximity of NMS-859 highlighted some of the same amino acids seen for the unbound molecule as possible partners of hydrophobic interactions. In particular, Leu526, Asn660 and Thr688 remained in close contact with the benzothiazole and phenyl moieties of the molecule throughout the entire length of simulations in all six protomers (Figure 2d). Ile656 and Ile479 also contributed in stabilizing the binding with the benzothiazole part of NMS-859.

In a way similar to NMS-322, the Walker A motif provided a series of hydrogen bonds, in particular Lys524 and Thr525 backbone (41% and 48% of the snapshots, respectively) interacts with the amide group and the sulphur of NMS-859. A translation within the pocket, such as observed for the unbound molecule and for NMS-322, is also observed in the covalently bound NMS-859, in this case occurring by the pivoting of the ligand around Cys522. The molecules bound to protomers A and B preserved a pose close to the starting conformation, interact-

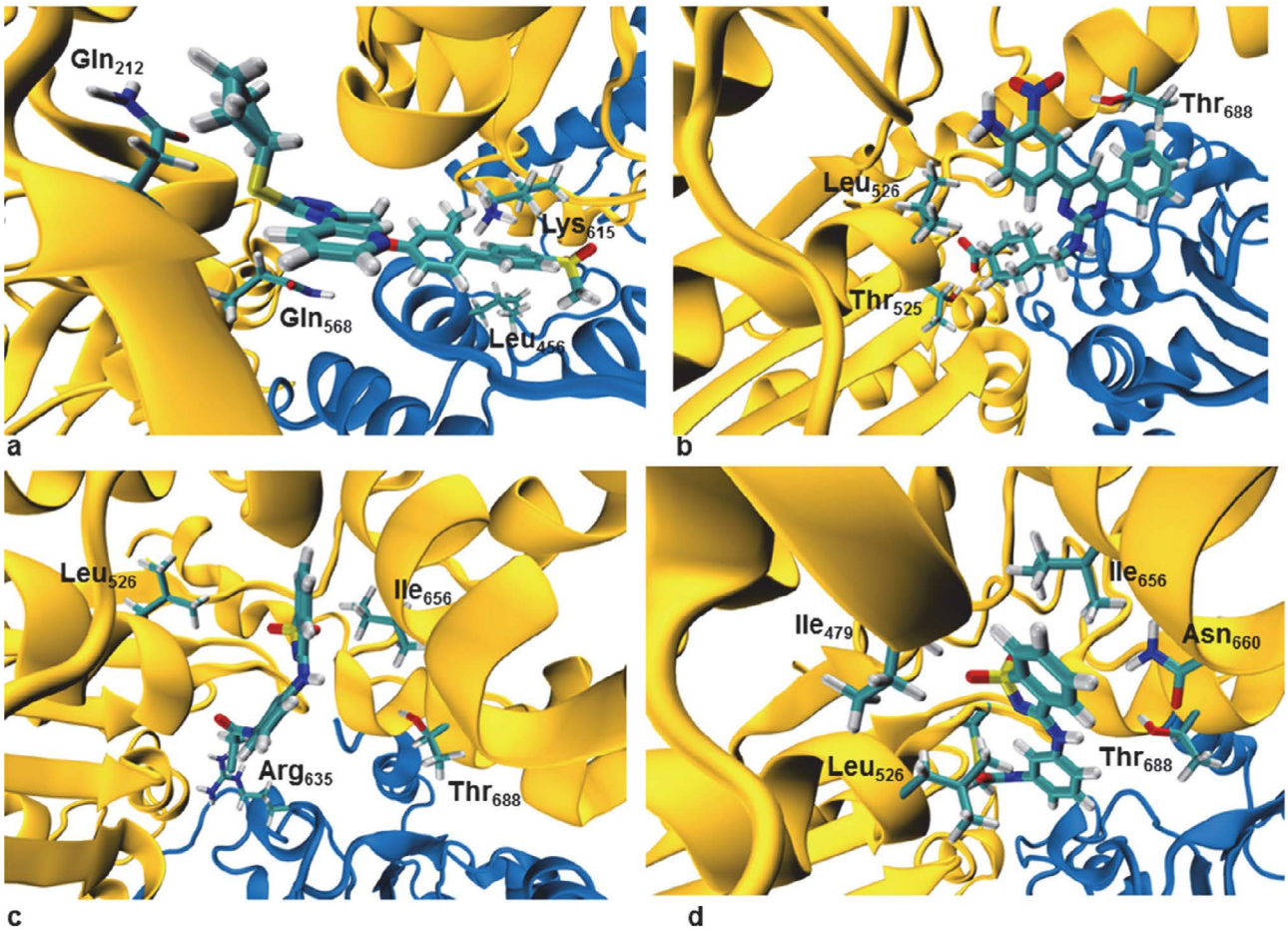

Figure 2a) NMS-873 in complex with p97. b) NMS-322 in complex with p97. c) NMS-859 in complex with p97. d) NMS-859 covalently bound to residue Cys522 of p97. Interaction diagrams of these compounds can be found in Supporting information.

ing preferentially with residues belonging to the ATP pocket. The average RMSD (calculated on the molecule after the alignment of the D2 domain) resulted to be 1.04 Å and 0.83 Å, respectively. In these two cases, Thr688 was also favourably oriented to establish a hydrogen bond with the amine hydrogen of NMS-859, detected in 33% of the snapshots for the molecule bound to protomer A and in 35% of the snapshots for the molecule bound to protomer B.

For the NMS-859 molecules bound to the protomers C to F, a preferential orientation towards Arg635 and Pro636 of the adjacent protomer was observed. Here the average RMSD with respect to the starting structure were 2.51 Å in protomer C, 4.21 Å in protomer D, 2.45 Å in protomer E and 2.57 Å in protomer F. In these cases, the loss of interactions with the inner residues of the ATP pocket was presumably balanced by a gain in hydrophobic interactions between Arg635 and Pro636 with the phenyl and thiomethylene moieties of NMS-859, as highlighted for NMS-322.

4. Conclusions

The simulations reported in the study reproduce experimental observations made for what concerns both general aspects of molecular stability of the p97 protein and specific molecular interactions with inhibitors. The biologically relevant hexameric assembly was more stable than the dimer and the most unstable part of the single protomer was represented by the D2 domain as observed in crystallographic structures and in trypsin protein digestion experiments. Simulations performed on the different protein-inhibitor complexes showed good stability and reproducibility all around the hexamer. In particular, the postulated allosteric binding site and the binding mode of NMS-873 were surprisingly well conserved throughout the MD trajectory and consistently reproduce some of the most important interactions observed experimentally. Even though the ability to design more potent inhibitors remains to be proven, the approach adopted is certainly useful in providing a dynamic structural model able to rationalize a number of experimental observations regarding the mechanism of action of the different classes of p97 inhibitors reported to date.

5. References

1. B. DeLaBarre, A. T. Brunger, *Nat. Struct. Mol. Biol.*, **2003**, *10*, 856–863. **DOI:**10.1038/nsb972
2. D. Nowis, E. McConnell, C. Wojcik, *Exp. Cell. Res.*, **2006**, *312*, 2921–32. **DOI:**10.1016/j.yexcr.2006.05.013
3. P. Ballar, S. Fang, *Biochem. Soc. Trans.*, **2008**, *36*, 818–822. **DOI:**10.1042/BST0360818
4. C. Wojcik, M. Rowicka, A. Kudlicki, D. Nowis, E. McConnell, M. Kujawa, N. De Martino, *Mol. Biol. Cell.*, **2006**, *17*, 4606–4618. **DOI:**10.1091/mbc.e06-05-0432
5. B. Medicherla, A. L. Goldberg, *J. Cell. Biol.*, **2008**, *182*, 663–73. **DOI:**10.1083/jcb.200803022
6. X. Zhang, A. Shaw, P. A. Bates, R. H. Newman, B. Gowen, E. Orlova, M. A. Gorman, H. Kondo, P. Dokurno, J. Lally, G. Leonard, H. Meyer, M. Heel, P. S. Freemont, *Molecular cell*, **2000**, *6*, 1473–1484. **DOI:**10.1016/S1097-2765(00)00143-X
7. P. Magnaghi, R. D'alessio, B. Valsasina, N. Avanzi, S. Rizzi, D. Asa, F. Gasparri, L. Cozzi, U. Cucchi, C. Orrenius, P. Polucci, D. Ballinari, C. Perrera, A. Leone, G. Cervi, E. Casale, Y. Xiao, C. Wong, D. J. Anderson, A. Galvani, D. Donati, T. O'Brien, P. K. Jackson, A. Isacchi, *Nat. Chem. Biol.*, **2013**, *9*, 548–556. **DOI:**10.1038/nchembio.1313
8. P. Polucci, P. Magnaghi, M. Angiolini, D. Asa, N. Avanzi, A. Badari, J. Bertrand, E. Casale, S. Cauteruccio, A. Cirla, L. Cozzi, A. Galvani, P. K. Jackson, Y. Liu, S. Magnuson, B. Malgesini, S. Nuvoloni, C. Orrenius, F. R. Sirtori, L. Riceputi, S. Rizzi, B. Trucchi, T. O'Brien, A. Isacchi, D. Donati, R. D'Alessio, *J. Med. Chem.*, **2013**, *56*, 437–450. **DOI:**10.1021/jm3013213
9. G. Cervi, P. Magnaghi, D. Asa, N. Avanzi, A. Badari, D. Borghi, M. Caruso, A. Cirla, L. Cozzi, E. Felder, A. Galvani, F. Gasparri, A. Lomolino, S. Magnuson, B. Malgesini, I. Motto, M. Pasi, S. Rizzi, B. Salom, G. Sorrentino, S. Troiani, B. Valsasina, T. O'Brien, A. Isacchi, D. Donati, R. D'Alessio, *J. Med. Chem.*, **2014**, *57*, 10443–10454. **DOI:**10.1021/jm501313x
10. F. Dapiaggi, S. Pieraccini, D. Potenza, F. Vasile, H. Macut, S. Pellegrino, A. Aliverti, M. Sironi, *New J. Chem.*, **2017**, *41*, 4308–4315. **DOI:**10.1039/C6NJ04014D
11. F. Dapiaggi, S. Pieraccini, M. Sironi, *Mol. BioSyst.*, **2015**, *11*, 2152–2157. **DOI:**10.1039/C5MB00348B
12. C. Marucci, M. S. Christodoulou, S. Pieraccini, M. Sironi, F. Dapiaggi, D. Cartelli, A. M. Calogero, G. Cappelletti, C. Vilanova, S. Gazzola, G. Broggini, D. Passarella, *Eur. J. Org. Chem.*, **2016**, *11*, 2029–2036. **DOI:**10.1002/ejoc.201600130
13. M. S. Christodoulou, F. Zunino, V. Zuco, S. Borrelli, D. Comi, G. Fontana, M. Martinelli, J. B. Lorens, L. Evensen, M. Sironi, S. Pieraccini, L. Dalla Via, O. M. Gia, D. Passarella, *ChemMedChem*, **2012**, *7*, 2134–2143. **DOI:**10.1002/cmdc.201200322
14. E. Krissinel, K. Henrick, *J. Mol. Biol.*, **2007**, *372*, 774–797. **DOI:**10.1016/j.jmb.2007.05.022
15. The PyMOL Molecular Graphics System, Version 2.0 Schrödinger, LLC.
16. A. Sali, T. L. Blundell, *J. Mol. Biol.*, **1993**, *234*, 779–815. **DOI:**10.1006/jmbi.1993.1626
17. B. Hess, C. Kutzner, D. V. D. Spoel, E. Lindahl, *J. Chem. Theory Comput.*, **2008**, *4*, 435–447. **DOI:**10.1021/ct700301q
18. K. Lindorff-Larsen, S. Piana, K. Palmo, P. Maragakis, J. L. Klepeis, R. O. Dror, D. E. Shaw, *Proteins: Struct., Funct., Bioinf.*, **2010**, *78*, 1950–1958.
19. J. Wang, R. M. Wolf, J. W. Caldwell, P. A. Kollman, D. A. Case, *J. Comput. Chem.*, **2004**, *25*, 1157–1174. **DOI:**10.1002/jcc.20035

20. W. L. Jorgensen, J. Chandrasekhar, J. D. Madura, R. W. Impey, M. L. Klein, *J. Chem. Phys.*, **1983**, *79*, 926–935. **DOI:**10.1063/1.445869
21. G. Bussi, D. Donadio, M. Parrinello, *J. Chem. Phys.*, **2007**, *126*, 141011–141017. **DOI:**10.1063/1.2408420
22. T. Darden, D. York, L. Pedersen, *J. Chem. Phys.*, **1993**, *98*, 10089–10092. **DOI:**10.1063/1.464397
23. B. Hess, H. Bekker, H. J. Berendsen, J. G. Fraaije, *J. Comput. Chem.*, **1997**, *18*, 1463–1472. **DOI:**10.1002/(SICI)1096-987X(199709)18:12<1463::AID-JCC4>3.0.CO;2-H
24. H. J. Berendsen, J. P. M. van Postma, W. F. van Gunsteren, A. R. H. J. DiNola, J. R. Haak, *J. Chem. Phys.*, **1984**, *81*, 3684–3690. **DOI:**10.1063/1.448118
25. I. Massova, P. A. Kollman, Perspect. *Drug Discovery Des.*, **2000**, *18*, 113–135. **DOI:**10.1023/A:1008763014207
26. D. Spiliotopoulos, A. Spitaleri, G. Musco, *PloS one*, **2012**, *7*, e46902. **DOI:**10.1371/journal.pone.0046902
27. R. T. Bradshaw, B. H. Patel, E. W. Tate, R. J. Leatherbarrow, I. R. Gould, *Protein Eng., Des. Sel.,* **2010**, *24*, 197–207. **DOI:**10.1093/protein/gzq047
28. S. P. Brown, S. W. Muchmore, *J. Med. Chem.*, **2009**, *52*, 3159–3165. **DOI:**10.1021/jm801444x
29. G. Saladino, S. Pieraccini, S. Rendine, T. Recca P. Francescato, G. Speranza, M. Sironi, *JACS*, **2011**, *133*, 2897–2903. **DOI:**10.1021/ja105030m
30. M. E. Crisan, P. Bourosh, M. E. Maffei, A. Forni, S. Pieraccini, M. Sironi, Y. M. Chumakov, *PLoS ONE*, **2014**, *9*, e101892. **DOI:**10.1371/journal.pone.0101892
31. C. McMartin, R. S. Bohacek, *J. Comput.-Aided Mol. Des.*, **1997**, *11*, 333–344. **DOI:**10.1023/A:1007907728892

Povzetek

Izvedli smo simulacije molekulske dinamike za binarne (kompleks nukleotid-dimer in heksamer proteina) in ternarne (kompleks nukleotid-inhibitor proteina) komplekse proteina p97, da bi razumeli stabilnost domene oligomera p97 in, kar je še bolj pomembno, molekularne mehanizme v inhibiciji, vključno z različnimi alosteričnimi, ATP-kompetitivnimi in kovalentnimi inhibitorji, o katerih so poročali kratkim. Analiza stabilnih stanj, ki sledijo uravnoteževalnim fazam, je pokazala, da je homoheksamer bolj stabilen v primerjavi z dimerom, in hkrati so domene N-D1 bolj stabilne v pirmerjavi z domeno D2. Molekulska dinamika predlaganega alosteričnega vezavnega modela reproducira pomembne molekulske interakcije, ki so bile ugotovljene eksperimentalno z visoko frekvenco vzdolž trajektorije. Opažene konformacijske spremembe, ki se pojavljajo v D2-vezavnem mestu nukleotidov, ponujajo novo hipotezo, imenovano *bind-rearrange-react*, o postopnih molekularnih dogodkih, ki so udeleženi pri specifičnem kovalentnem načinu delovanja inhibitorjev.

DOI: 10.17344/acsi.2018.4881 *Acta Chim. Slov.* **2019,** *66,* 402–413

Scientific paper

Sandpaper Wastes as Adsorbent for the Removal of Brilliant Green and Malachite Green Dye

Yasemin İşlek Coşkun,* Nur Aksuner and Jale Yanik

Department of Chemistry, Faculty of Science, Ege University, 35100 Bornova, Izmir, Turkey

** Corresponding author: E-mail: yasemin.islek@ege.edu.tr*
Telephone number: +90(232)3115447 Fax: +90(232)3888294

Received: 11-29-2018

Abstract

Sandpaper wastes were used as adsorbent after pyrolysis at 500 °C and calcination at 800 °C for the removal of brilliant green and malachite green cationic dye from an aqueous solution. The effects of the pH, the adsorbent dose, the contact time, and the initial dye concentration on the removal efficiencies were investigated. The isotherm studies were conducted by using the Langmuir, Freundlich, and Dubinin-Radushkevich models, and thermodynamic studies were also performed. The adsorption of the Brilliant green and malachite green were found to comply with the Langmuir isotherm model and the Freundlich isotherm model, respectively. The thermodynamic studies showed that the adsorption of dyes were endothermic. The E values obtained from the Dubinin-Radushkevich isotherm showed that the adsorption mechanism was chemical in nature. Furthermore, the three kinetic models (pseudo first-order, pseudo second-order, and intraparticle diffusion) were investigated. It was found that the pseudo second-order kinetic model fitted well for adsorption of dyes.

Keywords: Adsorption; brilliant green; malachite green; dye removal; sandpaper.

1. Introduction

Brilliant green and malachite green are cationic (basic) dyes. Many industries such as paper, textile, furniture, and food industries use dyes for coloring purposes.[1,2] Furthermore, in fish farming, brilliant green is used to protect fish from fungi, from parasites and from infections. However, the consumption of fish produced in this way is not recommended.[2–5] Cationic dyes have toxic, carcinogenic and mutagenic properties.[6] Significant risks arise after exposing these dyes to people. Therefore, the removal of the dyes prior to their discharge into the environment is crucial and essential.

Physical, chemical and biological methods are widely used for the removal of dyes from water. Among these methods, adsorption, the physical method has advantages such as simplicity, low cost, and ease of application. Natural materials (raw or activated forms of clay minerals), synthesized materials, nanomaterial based adsorbents, agricultural wastes and by-products (raw or modified leaf based materials, coffee wastes, peels) and industrial wastes and by-products (fly ash, aluminum oxides), and activated carbon are the most used adsorbents for dye removal.[1,7–11] Cost is an important parameter for choosing the adsorbent. Low-cost adsorbents include natural, agricultural and industrial by product wastes[12]. Furthermore, the waste materials have little or no economic value and usually present a disposal problem.[7] The use of these waste materials for the purpose of wastewater treatment can play a significant role in solving the disposal problems. Numerous inexpensive and abundant biosorbents especially agro waste materials, as well as industrial and municipal wastes, have been proposed by several researchers for the removal of malachite green and brilliant green dyes from aqueous solution.[13] The usage of waste as an adsorbent helps to reduce environmental pollution by recycling. In the literature some of the low-cost adsorbents used for dye removal were NaOH treated saw dust,[14] waste rubber tire,[15] white rice husk ash,[16] Neem leaf powder,[17] kaolin,[2] peach stone,[18] and medical cotton waste[19] etc.

Sandpaper is an abrasive used in the sanding process to correct the rough surfaces. It consists of sheets of paper or cloth with abrasive material glued with resin to one face. Formerly, sand and glass were used as abrasive surfaces, but nowadays materials such as aluminum oxide, zirconium oxide, and silicon carbide etc. are used.[20] The storage and disposal of the sandpaper waste is a problem in terms of time, space, and cost. With this work, a useful area for sandpaper waste has been created, which will be beneficial for the environment and waste water remediation.

The aim of the study is the removal of brilliant green and malachite green dyes from water by using sandpaper waste. Two adsorbents were prepared by applying pyrolysis and calcination process. To the best of our knowledge, it is the first study on brilliant green and malachite green removal using sandpaper waste based adsorbent. The important point of the study is that the pollution is reduced both by recycling of sandpaper waste, which is an industrial waste material and by removing the dyes from water. The effects of the experimental parameters such as the pH, the adsorbent dose, the contact time and the initial dye concentration were examined. The isothermal models (Langmuir, Freundlich and Dubinin-Radushkevich), thermodynamic and kinetic parameters (pseudo first order, pseudo second order and intraparticle model) were also evaluated.

2. Experimental

2. 1. Materials and Apparatus

All the reactive used was of an analytical grade. Distilled water was used throughout the study. Cationic dye Brilliant Green (BG) (CI 42040, MW: 462.65), malachite green oxalate (MG) (CI 42000, MW: 927.01) hydrochloric acid, sodium hydroxide, acetic acid, and sodium acetate were obtained from Merck. The chemical structure of brilliant green and malachite green are presented in Figure 1. The working dye solution was prepared daily by diluting 1000 mg/L stock dye solution. The spectrophotometric measurements were carried out by TG 80+ model double beam UV/Vis spectrophotometer with PG Instruments. The pH was measured using a Mettler Toledo Five Go FG-2 pH meter. A Biosan OS-10 orbital shaker at 350 rpm and Nuve ST-402 vibration water bath were used for the adsorption studies. The FTIR analyses of the adsorbents were carried out by using the Perkin Elmer 100 spectrum FT-IR spectrometer in the range of 4000–400 cm^{-1}. The pore and surface morphology images were captured by using the Thermo Scientific Apreo S LoVac model scanning electron microscope (SEM). The chemical compositions of SW500 and SW800 were analyzed by X-ray Fluorescence spectrometer (Spectro Xepos, Ametec). BET analysis were executed by Quantachrome ASiQwin. The sandpaper was supplied by a fibre disk pad production company in Izmir, Turkey, as sheets.

2. 2. Preparation of Adsorbent from Sandpaper Wastes

Two kind of adsorbent were obtained after pyrolysis and calcination processes. Pyrolysis and calcination processes were separately applied to the sandpaper sheets. The sandpaper sheets were cut into small pieces (≤ 2 cm) before the experiments. For pyrolysis, firstly, a quantity of 50 g of sandpaper was loaded into the reactor, and then the reactor was heated with a temperature rate of 7 °C per minute up to 500 °C and held at this temperature for 1 h. The reactor was continually purged with nitrogen at a flow rate of 25 mL/min. The nitrogen gas swept the volatile products from the reactor into the ice-cooled traps. The condensable volatiles, which were collected in the traps, were released. After pyrolysis, the furnace was cooled to room temperature in a nitrogen gas stream and the reactor content (carbonized residue) was withdrawn from the reactor.[18] The obtained adsorbent was named SW500. Then, another part of the sandpaper sheets was calcined at 800 °C in a furnace up to 16 h and then stored in desiccators. The obtained adsorbent was named SW800.

2. 3. Adsorption Studies

All of the adsorption studies were examined in batch mode. In order to find out the optimum experimental conditions, 25 mL of dye solutions were used. The initial concentration used was 20 mg/L. The contact time was 24 h unless otherwise stated. In the pH study, the adsorbent amounts were 10 mg for both adsorbents. The optimal sorbent doses were found to be 1.2 g/L of SW500 and 0.4 g/L of SW800 for the BG removal, while 2.4 g/L for SW500 and 0.6 g/L for SW800 for the MG removal after optimization study. The pH effect for the removal efficiencies was studied in the pH range between 3 and 10. The initial pH of the solutions was adjusted to the desired value using NaOH or HCl. The optimization studies, such as adsorbent dose (0.2, 0.4, 0.6, 1.2, 1.8 and 2.4 g/L), contact time (1, 5, 10, 15, 20, 40, 60, 120, 180, 240, and 1440 min), ini-

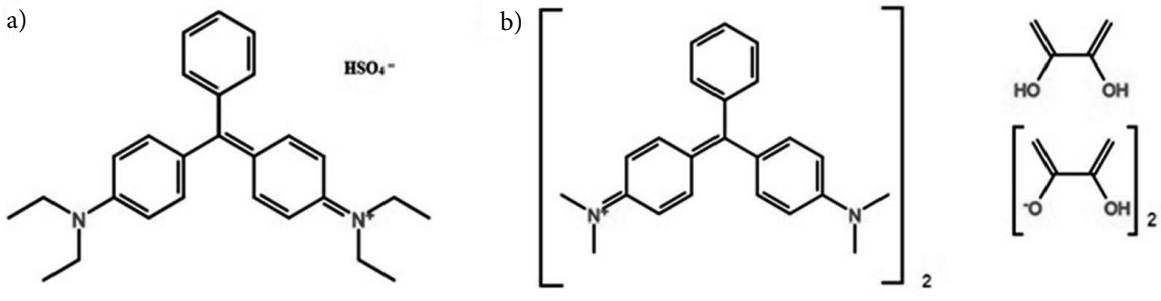

Figure 1. The chemical structure of brilliant green (a) and malachite green (b)

tial dye concentrations (5, 10, 25, 50, 100, 200, and 400 mg/L), and temperature (298 K, 303 K, 313 K, and 323 K) were performed. The adsorption isotherms were evaluated in the range of 5–500 mg/L of dyes. Kinetic studies were investigated between 1–1440 min. The remaining BG and MG dye concentrations after sorption were measured at 624 nm and 617 nm by using UV-Vis spectrophotometer, respectively. All the experiments were conducted in triplicate. Before the spectrophotometric measurements, the pH of the dye solutions and standard solutions for the calibration were adjusted to 5.5 by using an acetic acid/acetate buffer. The removal efficiencies (R, %) and adsorbed dye amounts (q, mg/g) were calculated, respectively;

$$R(\%) = \frac{(Ci-Ce)}{Ci} \times 100 \quad (1)$$

$$q = \frac{(Ci-Ce)}{W} \times V \quad (2)$$

Here, Ci and Ce are dye concentrations at an initial and equilibrium (mg/L), w is the amount of the adsorbent (g), and V is the volume of the dye solutions (L).

3. Results and Discussion

3. 1. Characterization of the Sandpaper Waste Adsorbent

The morphology of the bare SW500 and SW800 are depicted in Figure 2a and 2b, respectively. The morphology of the SW500 surface was irregular and porous. In Figure 2b, it was seen that the particles of SW800 were spherical and aggregate. The higher number of pores increased the adsorption of the dyes.

The FTIR spectra of the adsorbents before and after dye adsorption are shown in Figure 3a and 3b. In the spectrum of SW800, the peak at 3454.78 cm^{-1} could indicate –OH stretching of the phenolic structure and crystal water. The intense peak at 1439.07 cm^{-1} was attributed to the aliphatic C–H stretching band. The peaks belonging to the crystal water and aliphatic C–H stretching band could also be seen in the other spectra. The two bands at 873.67 and 577.56 cm^{-1} could be Al–O vibration bands in Al_2O_3. After the adsorption for both the adsorbents, the C = C bands belonging to the aromatic ring of BG and MG appeared in the range of 1600–1700 cm^{-1}. After BG adsorption on SW500, a peak assigning N–C band at 2969 cm^{-1} appeared. Besides, several adsorption peaks that emerged in the range of 1550–1380 cm^{-1} might be ascribed to the N–C groups after BG adsorption on SW500.[13,14,21–26]

The chemical compositions of SW500 and SW800 were determined by X-ray fluorimeter. It was found that SW500 contained 1.43% Al_2O_3, 0.31% SiO_2, 0.72% P_2O_5, 0.16% SO_3, 12.47% CaO, 0.68% TiO_2, 0.74% Fe_2O_3, 0.03% CuO, 0.24% ZnO, 0.03% SrO and 0.05% ZrO_2, while SW800 contained 3.6% Al_2O_3, 0.97% SiO_2, 0.67% P_2O_5, 0.16% SO_3, 44.06% CaO, 1.27% TiO_2, 1.99% Fe_2O_3, 0.01% CuO, 0.03% ZnO, 0.08% SrO and 0.09% ZrO_2. The amount of CaO in SW800, which was prepared by calcination, was found higher than that of SW500. Furthermore, higher dye removal efficiencies were obtained for SW800 in the adsorption studies. Therefore, that result could be a conclusion of existence of higher amount of CaO in SW800. Metal oxides containing calcium oxides are well known adsorbents for removal of various effluent gas streams. Because they have high adsorption capacity, high surface reactivity, low cost, and abundant.[27] Calcium mineral is also efficiently used for the dye removal in the literature. Calcium rich biochar from crab shell showed highly efficient removal for Malachite Green and Congo Red although it showed low specific surface area and total pore volume.[28] Jung et al. have synthesized an adsorbent using spent coffee grounds (SCG) calcium alginate beads for the removal of acid orange 7 and methylene blue. It was expressed that it was difficult to remove powdered SCG-based activated

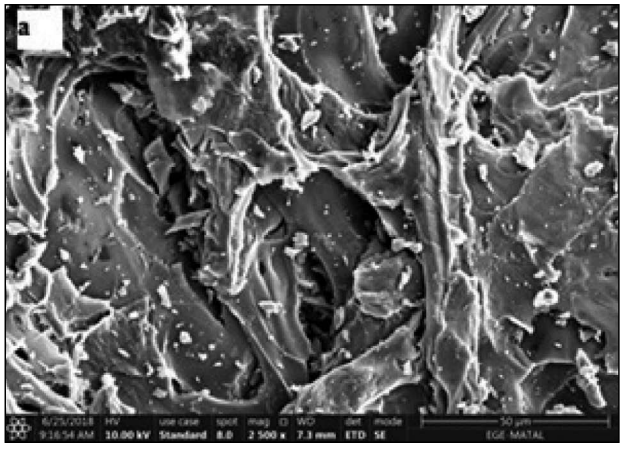

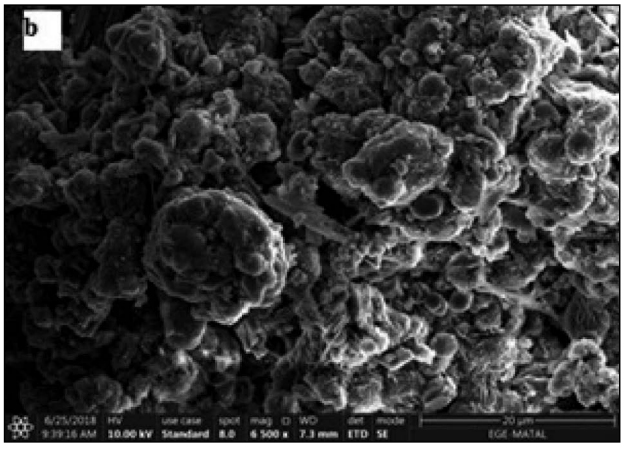

Figure 2. SEM images of bare adsorbents a) SW500 and b) SW800

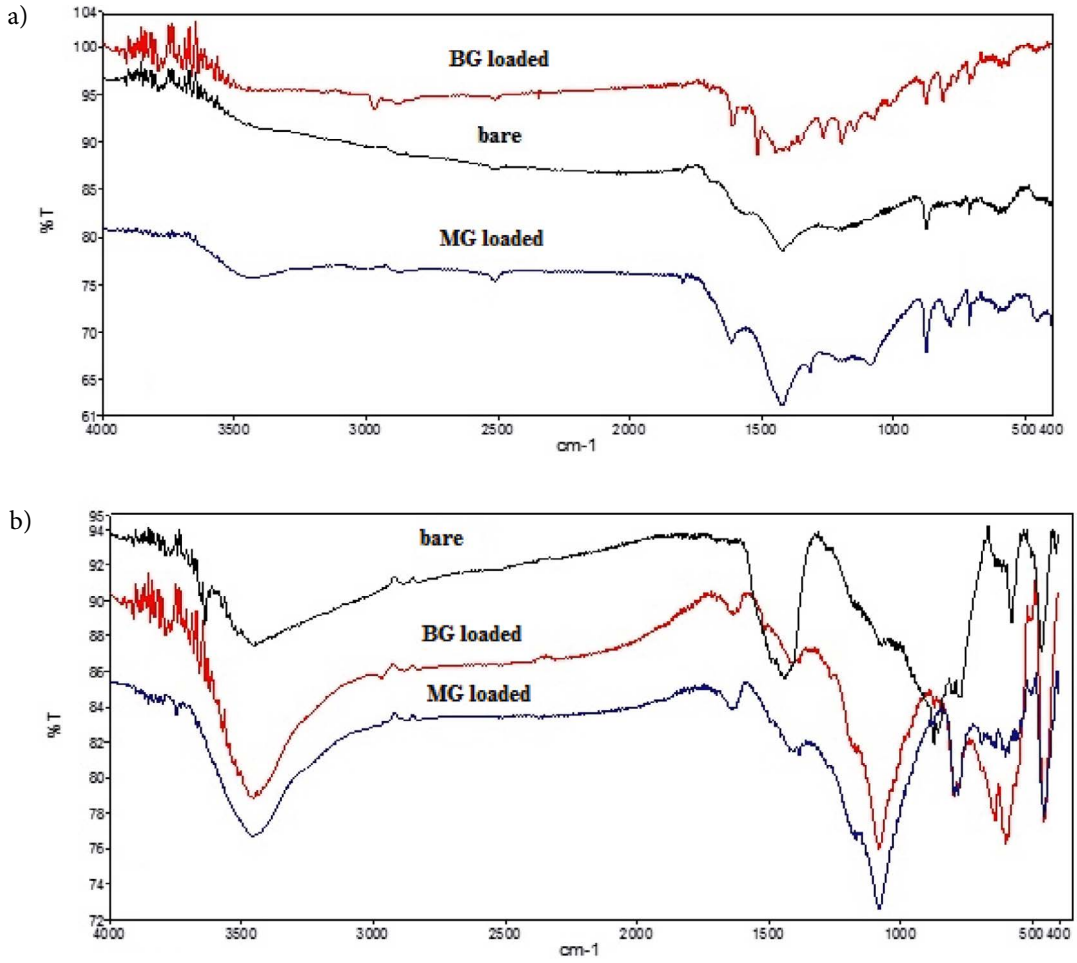

Figure 3. FTIR spectra of adsorbents before and after dye adsorption a) SW500 and b) SW800

carbon from aqueous solution after adsorption. Therefore, to form porous hydrogels beads powdered SCG based activated carbon was entrapped in calcium-alginate beads. It was reported that such heterogeneous surface might be take part in removal of dyes.[29] Basic Green 4 was successfully removed by using sea shell powder. It was reported the shell contained protein, calcite and calcium carbonate crystals, and the adsorbent had heterogeneous pores and cavities that gave large surface area for dye removal.[30] In study of Xia et al., it was expressed that the various metal oxides for the adsorption capacities of Congo red dye were increased in the following order: NiO< MnO_2<Cr_2O_3< Fe_2O_3<MgO<CaO.[27] Aguayo-Villarreal et al. clearly mentioned that the adsorption of acid blue 74, acid blue 25 and reactive blue 4 was governed by the calcium compounds existing in pecan shells. The electrostatic interactions between calcium ion and the sulphonyl groups of the dyes molecules were thought to be responsible for adsorption of dyes on pecan shells.[31]

The BET surface area, total pore volume and pore size were determined as 3.070 m^2/g, 0.004354 mL/g, 28.37 A° for SW500, and 1.103 m^2/g, 0.001933 mL/g, 35.04 A° for SW800, respectively.

3. 2. Adsorption Studies for BG and MG Removal

3. 2. 1. Effect of pH on BG and MG Removal

In order to define the optimum adsorption pH, the pHs of the solutions were set in the range of 3–10 by 0.01 mol/L HCl and NaOH. The removal efficiencies are shown in Figure 4. The optimum pH range of BG was found to be between 3 and 10, and the optimum pH of MG was in the range of 4–10 for SW800. The removal efficiencies of BG were reached to 96% at pH 5, while the removal efficiencies of MG reached 91.4% at pH 7 for SW 500. The point of zero charge (pH_{pzc}) was determined according to the following procedure.[32] 25 mL of 0.1 mol/L of KNO_3 solution was adjusted to different pH values using HCl or NaOH and was added to the adsorbents. Thereafter, the suspension was shaken for 24 h to obtain the equilibrium pH. The change of the pH during the equilibrium was calculated by subtracting the initial pH values from the final pH values. The ΔpH values were then plotted against the initial pH values. The initial pH at which the ΔpH was zero was taken to be the pH_{pzc}. The pH_{pzc} values were 7.30 for SW500 and 10.1 for SW800. At

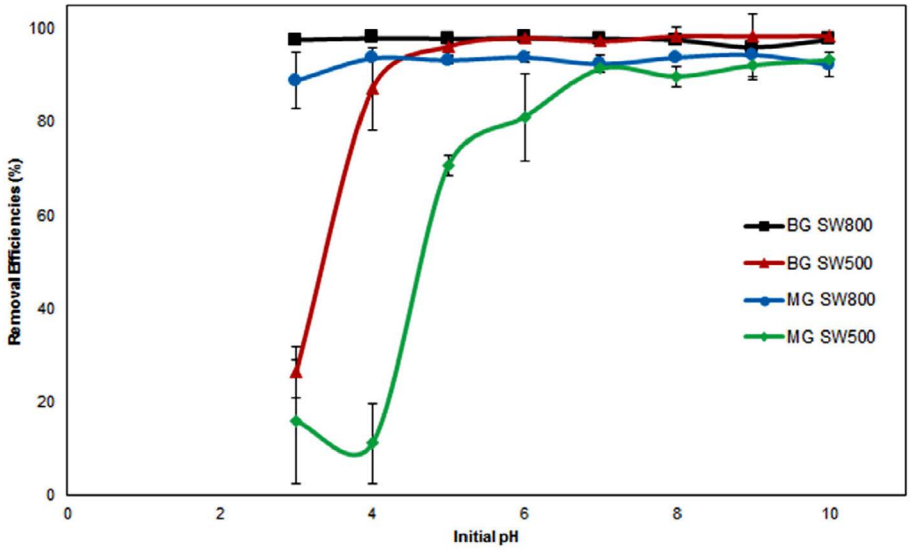

Figure 4. Effect of initial pH on the removal of BG and MG (adsorbent amount 10 mg, initial dye concentration 20 mg/L, volume 25 mL, contact time 24 h, pH range 3–10, n = 3)

the pH values higher than pHpzc, the surface charge was negative and attracted positively charged dye while at lower pH values, the surface charge was positive and attracted negatively charged dye.[32,33] It was found that the final pH of the solutions at the end of the adsorption was found to be 7.5 after the initial pH of 5 for SW500, and about 10.8 for SW800 in all the studied initial pHs., Before the pH_{pzc}, the adsorption efficiencies of BG and MG for SW500 were as low as expected because of electrostatic repulsion. As seen in Figure 4, the adsorption efficiencies of BG were above 98% for SW500 after the initial pH of 5 (final solution pH 7.5 for SW500). In addition, the low adsorption observed for SW500 at pH below 5 may be due to the competition between H^+ ions and dye cations for the adsorbent's active sites.[34] Furthermore, the same trend was observed for MG removal. Therefore, it was thought that electrostatic forces were effective for BG and MG removal. SW800 provided a wider working range than that of SW500 for BG and MG removal.

3. 2. 2. Effect of Adsorbent Dose on BG and MG Removal

The effect of the sorbent dose was investigated in the range of 0.2–2.4 g/L. The results are presented in Figure 5. As seen in the Figure, for SW800, the removal efficiencies of BG in the studied range did not change significantly; therefore, the optimum dose was selected as 0.4 g/L. For SW500, the removal efficiencies of BG and MG increased slightly and then reaching a constant value of 1.2 g/L and 2.4 g/L, respectively. The optimum sorbent dose was found to be 0.6 g/L for MG removal for SW800. That situation

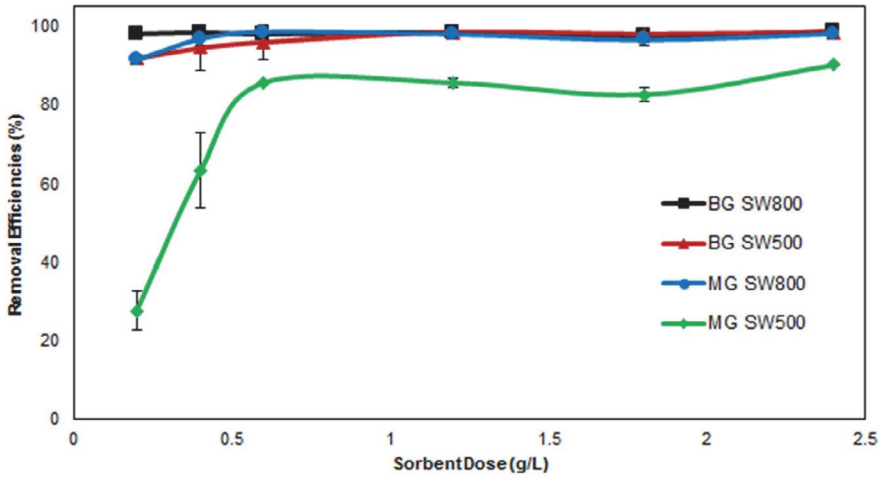

Figure 5. Effect of adsorbent dose on the removal of BG and MG (adsorbent dose range 0.2–2.4 g/L, initial dye concentration 20 mg/L, volume 25 ml, contact time 24 h, n = 3)

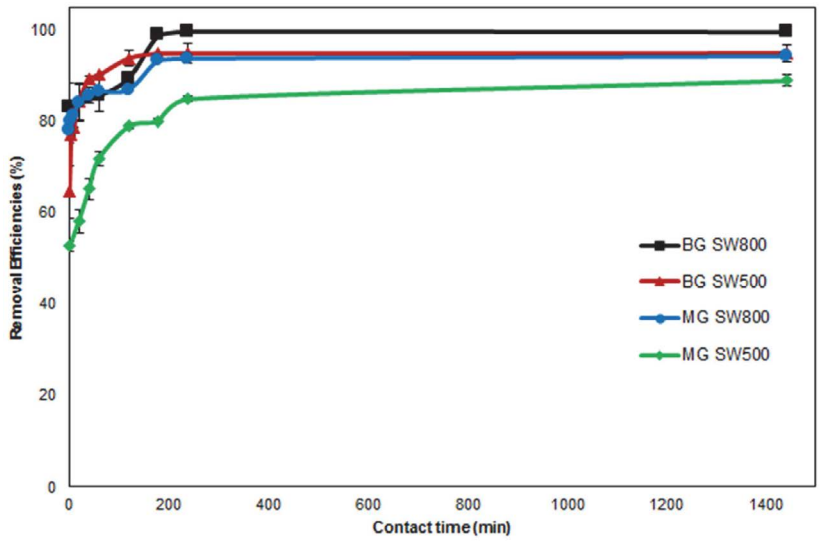

Figure 6. Effect of contact time on the removal of BG and MG (adsorbent dose of BG and MG: 0.4 and 0.6 g/L for SW800 and, 1.2 and 2.4 g/L for SW500, initial dye concentration 20 mg/L, volume 25 mL, contact time 1–1440 min, n = 3)

may be attributed to an increase in the number of active sites with the increase in the adsorbent dose[2].

3. 2. 3. Effect of Contact Time on BG and MG Removal

Figure 6 shows the effect of the contact time on the removal of BG and MG by SW500 and SW800 adsorbents in the range of 1–1440 min. It was observed that the adsorption equilibrium is reached faster for SW500 than for SW800 for BG removal. Within the first 40 minutes, 89% of BG dye was adsorbed by SW500 and reached 94% of the removal efficiency at 120 min. Meanwhile, 90% of BG dye adsorption took place within 120 min and equilibrium was reached at 180 min with 98.8% of the removal efficiency for SW800. The optimum contact times of BG dye were selected to be 120 min and 180 min for SW500 and SW800, respectively. The optimum contact times of MG removal were found to be 180 min and 240 min for SW500 and SW800, respectively. Taking into account the adsorbent doses used in the study, SW800 was superior to SW500. At the initial contact time, the rapid increase in adsorption was explained by the excess of vacant areas on the adsorbent surface, and as the sorption continues, the adsorption rate decreases with the decrease of the active areas on the sorbent surface.[3,14]

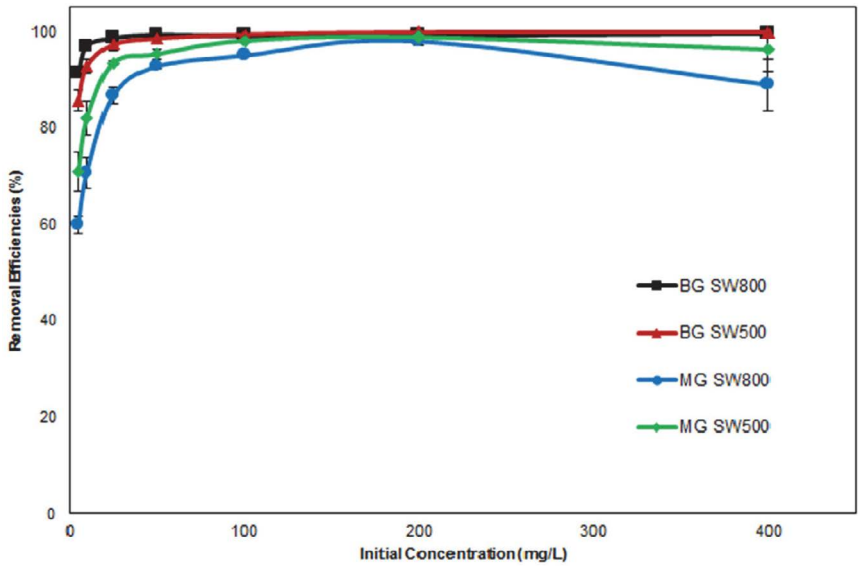

Figure 7. Effect of initial concentration on the removal of BG and MG (adsorbent dose of BG and MG: 0.4 and 0.6 g/L for SW800 and, 1.2 and 2.4 g/L for SW500, initial dye concentration range 5–400 mg/L, volume 25 mL, contact time 24 h, n = 3)

3. 2. 4. Effect of Initial Concentration on BG and MG Removal

The variations in removal efficiencies were investigated with initial dye concentrations ranging from 5 to 400 mg/L. The results are depicted in Figure 7. Sudden sharp increases were observed at the lower concentrations of BG and MG for both the adsorbents. The removal efficiencies became constant and then decreased at higher concentrations. It is thought that there is fixed number of available sites per unit mass of the adsorbent on the adsorbent surface. The number of available sites is higher for low initial dye concentration as against to the high initial concentration. Consequently, the most of the dye molecules are adsorbed by adsorbents at low initial dye concentrations and the removal efficiencies increases. On the other hand, when the certain initial dye concentrations is exceed, active sites of the adsorbent are completely retained, some of the dye molecules cannot be adsorbed, and the removal efficiencies become to decrease.[2,35] The removal efficiencies of BG reached equilibrium by 100 mg/L with 99.4% and 50 mg/L with 99.3% for SW500 and SW800, respectively. The removal efficiencies of MG reached equilibrium by 100 mg/L with 98.1% and 100 mg/L with 95.5% for SW500 and SW800, respectively.

3. 2. 5. Thermodynamic Studies

The effect of the temperature on BG and MG removal was investigated at 298, 303, 313 and 323 K. In order to calculate the thermodynamic parameters associated with the adsorption process, a change in Gibb's free energy (ΔG°), enthalpy (ΔH°) and entropy changes (ΔS°), used the equations below. The parameters exhibit spontaneity, randomness, and endothermicity/exothermicity of the adsorption processes.

$$\ln K_L = -\frac{\Delta H^o}{RT} + \frac{\Delta S^o}{R} \quad (3)$$

$$\Delta G^0 = -RT\ln K_L \quad (4)$$

$$\Delta G^o = \Delta H^o - T\Delta S^o \quad (5)$$

ΔG° is the free energy change (kJ/mol), R is the gas constant (8.314 J/mol K), K_L is the Langmuir equilibrium constant (L/mol),[36] and T is the temperature (K). K_L values were found from the ratio of the adsorbed dye concentration (mg) and equilibrium dye concentration in the solution (mg/L). The parameters of ΔH and ΔS were obtained from the slope and the intercept of the Van't Hoff graph between $\ln K_L$ and 1/T, respectively.[14]

The negative value of ΔG^o indicates the adsorption is spontaneous and favorable. ΔH^o values are positive whether the adsorption is endothermic, or vice versa. The positive ΔS^o reveals that randomness increased at the solid-liquid interface. The positive ΔS° also indicates the affinity of the adsorbent for BG and MG.[37,38] The calculated thermodynamic parameters are depicted in Table 1. As seen in Table 1, the adsorptions of BG and MG by both adsorbents were endothermic, favorable, and spontaneous. It was understood that the degree of randomness increased during the adsorption (ΔS° > 0). The value of ΔH^o presents an idea about different physical forces being involved in the adsorption process such as van der Waals forces (4–10 kJ/mol), hydrophobic bond forces (5 kJ/mol), hydrogen bond forces (2–40 kJ/mol), coordination exchange (40 kJ/mol), dipole bond forces (2–29 kJ/mol), and for chemical forces (>60 kJ/mol).[39] Our results indicated that the forces affecting the adsorption of BG could be hydrogen bond forces and dipole bond forces because of ΔH° values belonging to BG being calculated in our study as 2.65 and 28.50 kJ/mol for SW800 and SW500, respectively. However, ΔH° values of MG were calculated to be 28.38 and 47.79 kJ/mol for SW800 and SW500, respectively. Hence, it was thought that the adsorption of MG could be affected by hydrogen bond forces.

Table 1. Thermodynamic parameters for adsorption of BG and MG onto SW500 and SW800 (n = 3).

	T (K)	ΔH° (kJ/mol)	ΔS° (J/mol.K)	ΔG° (kJ/mol)
Brilliant Green				
SW800	298	2.650	103.9	–13.10
	303			–13.36
	313			–13.90
	323			–14.42
SW500	298	28.50	176.1	–8.972
	303			–9.372
	313			–10.17
	323			–10.97
Malachite Green				
SW800	298	28.38	174.3	–8.361
	303			–8.977
	313			–10.21
	323			–11.44
SW500w	298	47.79	219.9	–17.74
	303			–18.84
	313			–21.04
	323			–23.24

3. 2. 6. Isotherm Studies

The isotherm studies display the way of interactions between the dye molecules and the adsorbent, and also provide information about the nature of interactions. Experimental data was applied to the Langmuir,[40] Freundlich and Dubinin Radushkevic (D-R) isotherm models.[41] The Langmuir isotherm is based on the acceptance that the adsorption occurred at specific homogenous sites within the adsorbent while the Freundlich isotherm mentions the acceptance of a heterogeneous surface with a non-uniform distribution of heat of adsorption over the surface.[38] D-R

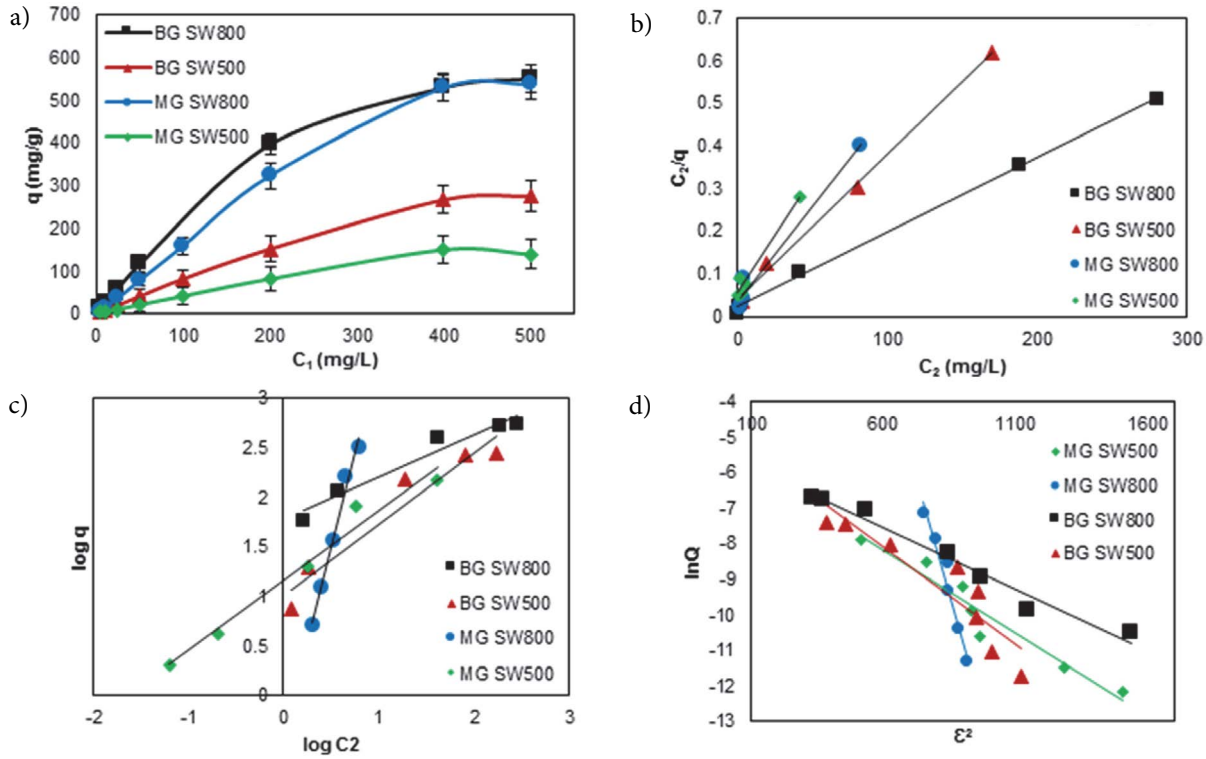

Figure 8. Adsorbed amount of dye as a function of initial concentration (a), Langmuir isotherms (b), Freundlich isotherms (c) and DR isotherms (d) for adsorption BG and MG, (initial dye concentration range 5–500 mg/L, volume 25 mL, adsorbent dose of BG and MG: 0.6 and 0.4 g/L for SW800 and, 1.2 and 2.4 g/L for SW500, contact time 24 h, n = 3)

Table 2. The isotherm parameters of Langmuir, Freundlich, and DR isotherms for BG and MG adsorption using SW500 and SW800 (n = 3).

		Brilliant Green		Malachite Green	
		SW800	SW500	SW800	SW500
Langmuir Isotherm					
$\frac{C_2}{q} = \left(\frac{1}{Q_{max}}\right) C_2 + \frac{1}{bQ_{max}}$	Q_{max}(mg/g)	555.6	294.1	222.2	185.19
	b (L/mg)	0.0833	0.0854	0.1372	0.1013
	R^2	0.9981	0.9963	0.9739	0.9732
	Separation factor	0.02–0.71	0.02–0.07	0.014–0.59	0.019–0.66
Freundlich Isotherm					
$\log q = \log K + \frac{1}{n} \log C_2$	1/n	0.4271	0.7233	3.7805	0.7041
	K (mg/g)(L/mg)$^{1/n}$	59.01	10.15	0.3975	14.3
	R^2	0.9541	0.9289	0.9882	0.9746
D-R Isotherm					
$\ln Q = \ln Q_m - k\varepsilon^2$	E (kJ/mol)	11.95	9.535	10.43	4.360
	Q_m (mol/g)	0.0041	0.0079	0.0044	4.251×10^6
$E = (2k)^{-0.5}$	k (mol^2/kJ^2)	0.0035	0.0055	0.0046	0.0263
	R^2	0.9741	0.8421	0.9351	0.95

C_2 is the equilibrium concentration of the solution (mg/L), q is the amount of adsorbed dye/amount of adsorbent (mg/g), b is the Langmuir constant (L/mg), Q_{max} is the monolayer adsorption capacity (mg/g), K is the Freundlich constant ((mg/g)(L/mg)$^{1/n}$), and 1/n is a dimensionless Freundlich constant for the intensity of the adsorbent, ε **(Polanyi potential) is (RTln(1 + 1/C_2))**, Q is the amount of dye adsorbed per unit weight of adsorbent (mol/g), Q_m is the adsorption capacity (mol/g), k is a constant related to adsorption energy (mol^2/kJ^2), R is the gas constant (kJ/mol K), and T is the absolute temperature (K).

isotherm expresses the mechanism of adsorption onto a heterogeneous surface.[42] In order to evaluate the adsorption isotherm, the used parameters were 25 mL of volume, an adsorbent dose of BG and MG 0.4 and 0.6 g/L for SW800 and 1.2 and 2.4 g/L for SW500, respectively and 24 h of contact time. Initial concentrations were in the range of 5–500 mg/L. Results and related equations were presented in Table 2 and Figure 8.

The correlation coefficients were evaluated to find the best fit isotherm model for the system. As seen in Table

2, the highest correlation coefficient (R^2) of BG was obtained for the Langmuir isotherm model while the highest R^2 of MG was for Freundlich isotherm model. Thus, the adsorption of BG by SW500 and SW800 were monolayer on homogeneous sites. However, the adsorption of MG was a multilayer adsorption on a heterogeneous site. The maximum monolayer adsorption capacities of BG and MG were calculated to be 294.1 mg/g and 185.19 mg/g for SW500 and 555.6 mg/g and 222.3 mg/g for SW800. 1/n values indicate the adsorption intensity. The higher 1/n values mean the higher affinity between the dye molecules and adsorbent.[38] The separation factor (R_L) shows whether the adsorption is favorable ($0 < R_L < 1$), unfavorable ($R_L > 1$), linear ($R_L = 1$) or irreversible ($R_L = 0$).[43] The separation factor is calculated by the equations given:

$$R_L = \left(\frac{1}{1+bC_1}\right) \quad (6)$$

where C_1 is the initial concentration and b is the Langmuir isotherm constant. Seeing that the R_L values were in the range of 0–1, adsorption was favorable for both the adsorbents.

The mechanism of adsorption can be determined by assessing E value (kJ/mol). The mean free energy of adsorption (E), which is defined as the free energy change when one mole of ion is transferred to the surface of a solid from the infinite space in the solution. Physical adsorption is valid if the value is below 8 kJ/mol. When the E value is between 8 kJ/mol and 16 kJ/mol, chemisorption or ion exchange occurs.[44] Since the values of BG (11.95; 9.54 kJ/mol for SW800; SW500) and MG (10.43; 4.36 kJ/mol for SW800; SW500) were between 8 and 16 kJ/mol, the presence of chemisorption or ion exchange could be mentioned.

3. 2. 7. Adsorption Kinetic Studies

In this study, to understand the adsorption mechanism, three simplified kinetic models were elucidated: Lagergren pseudo first order, pseudo second order and intraparticle diffusion model.[41] These models define the stages of the adsorption to be external film diffusion, adsorption, and intraparticle diffusion.[45] Figure 9 presents the time effects on the adsorption, pseudo first-order kinetic model, pseudo second-order kinetic model, and intraparticle diffusion kinetic model for the adsorption of BG and MG onto SW500 and SW800 adsorbents. The calculated parameters belonging to the kinetic models are depicted in Table 3. As can be seen from Table 3, the closest R^2 values to unity were obtained for the pseudo second order kinetic model for the studied dyes. The calculated ($q_{e,\,cal}$) and experimental ($q_{e,exp}$) values of adsorption capacities of BG and MG were very close to each other for the pseudo second order kinetic model. These findings indicated the adsorption fitted well with pseudo second order kinetic model and adsorption was chemisorption controlled.[46] In the

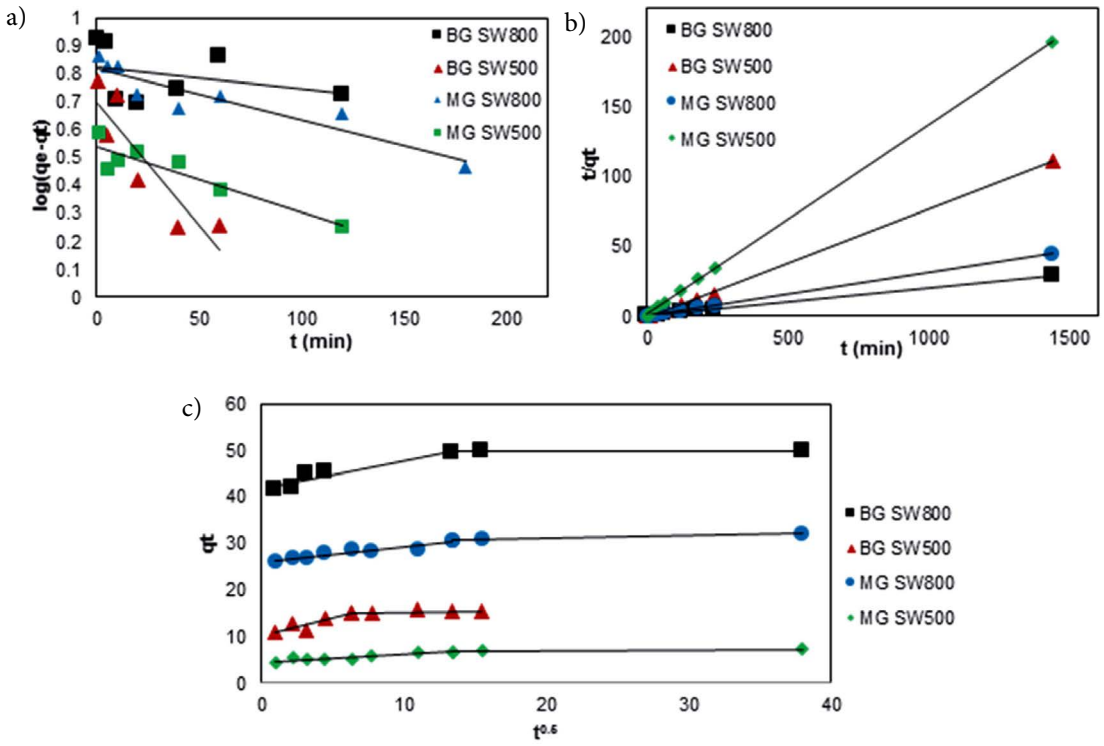

Figure 9. Kinetic studies for BG and MG adsorption a) pseudo first-order kinetic model, b) pseudo second-order kinetic model, c) intraparticle diffusion kinetic model (initial dye concentration 20 mg/L, volume 25 mL, adsorbent dose of BG and MG: 0.4 and 0.6 g/L for SW800 and, 1.2 and 2.4 g/L for SW500, contact time 24 h, temperature 25 °C, n = 3)

Table 3. The constants of the pseudo first-order, pseudo second-order kinetic models, and intraparticle kinetic model for BG and MG removal (n = 3).

Kinetic Models	Adsorbent SW800				SW500			
	$q_{e,exp}$ (mg/g)	$q_{e,cal}$ (mg/g)	k_1 (1/min)	R^2	$q_{e,exp}$ (mg/g)	$q_{e,cal}$ (mg/g)	k_2 (g/mgmin)	R^2
Pseudo first order								
$\log(q_e - q_t) = \log q_e - \frac{k_1 t}{2.303}$								
BG	49.67	6.668	0.00184	0.1121	14.84	5.041	0.0205	0.7996
MG	33.33	6.637	0.00438	0.8687	8.33	3.472	0.0053	0.8469
Pseudo second order								
$\frac{t}{q_t} = \frac{1}{k_2 q_e^2} + \frac{t}{q_e}$								
BG	49.67	50	0.005076	0.9999	14.84	12.89	–0.00735	0.9990
MG	33.33	32.26	0.005128	0.9999	8.33	7.369	0.01363	0.998
Intraparticle diffusion model								
$q_t = k_{int} t^{0.5} + I$		I (mg/g)	k (mg/gmin$^{0.5}$)	R^2		I (mg/g)	k (mg/gmin$^{0.5}$)	R^2
BG		Step 1	41.63	0.6047	0.8893	10.19	0.7498	0.7789
		Step 2	49.483	0.0082	0.2363	14.522	0.0647	0.5396
MG		Step 1	25.967	0.3118	0.8969	4.5719	0.1621	0.8509
		Step 2	29.652	0.0654	0.9851	6.5568	0.0207	0.7878

q*e* and qt indicate the adsorption capacity at equilibrium (mg/g) and at time t; k1 and k2 are the pseudo first-order (1/min) and pseudo second-order rate constants (g/mg min); t is the contact time (min) and kint (mg/g min$^{0.5}$) and I (mg/g) are the intraparticle diffusion constants.

intraparticle diffusion model, the plot q_t versus $t^{0.5}$ gives k and I as slope and intercept, respectively. The intercept indicates the effect of the boundary layer thickness. The higher the intercept length, the more the adsorption is boundary layer controlled.[46] Also, if the line passes through the origin (I = 0), the rate limiting mechanism is solely controlled by the intraparticle diffusion. Thus, it was concluded that the intraparticle diffusion was not the only rate limiting step. Since two separate regions were obtained for both the adsorbents, the adsorption process was affected by two or more steps. The initial region is ascribed to the bulk diffusion while the second to the intraparticle diffusion.[38]

4. Conclusion

The adsorbents used in this study were obtained from the sandpaper wastes. Hazardous and toxic reagents were not used during the preparation of the adsorbents. Thus, environmentally friendly adsorbents were obtained. Furthermore, the removal of brilliant green from aqueous solutions was successfully carried out using both the adsorbents. Optimization studies (pH, adsorbent dose, contact time, and initial concentration etc.) were carried out to investigate the removal performance of both adsorbents. According to the pH study, SW800 provided a wider pH range than that of SW500 for both dyes. The optimum adsorbent doses of BG and MG were selected as 0.4 and 0.6 g/L for SW800 while 1.2 and 2.4 g/L for SW500, respectively. The removal efficiencies of BG and MG reached a plateau after 120 min and 180 min for SW500 and 180 min and 240 min for SW800, respectively. The adsorption kinetics of the dyes fitted well with the pseudo second-order kinetic model. The adsorption of the BG showed good agreement with the Langmuir isotherm model and indicated monolayer adsorption on homogeneous sites. However, it was found that the adsorption of the MG obeyed the Freundlich isotherm model. The values of E indicated the adsorption mechanism of dyes could be chemical or through ion exchange. The adsorption of BG and MG were found to be favorable for both SW500 and SW800. The thermodynamic studies indicated that the process was endothermic, spontaneous, and feasible. The comparison of the maximum BG and MG adsorption capacities with the reported adsorbents in the literature can be found in Table 4. By comparing the maximum adsorption capacities in Table 4, the highest capacity values belonged to the sandpaper waste. As a result, environmentally friendly adsorbents were developed that facilitate fast and efficient removal.

Acknowledgments

Authors would like to thank to Münevver Özalp and Elif Cansu Tanrıverdi for their help on laboratory study.

Funding

This research did not receive any specific grant from funding agencies in the public, commercial, or not-for-profit sectors.

Table 4 Comparison of the maximum adsorption capacities of BG and MG with the reported adsorbents in the literature.

BG					MG				
Adsorbent	**Capacity (mg/g)**	**Isotherm**	**Kinetic model**	**Ref.**	**Adsorbent**	**Capacity (mg/g)**	**Isotherm**	**Kinetic model**	**Ref.**
Tannin gel (TG)	8.55	Langmuir	Pseudo second order	6	AMP clay	130.64	Langmuir	Pseudo first order	1
Amine modified TG	2.41	Langmuir	Pseudo second order	6	Coconot coir activated carbon	27.44	Langmuir Freundlich	Pseudo second order	7
Acorn	2.01	Langmuir	Pseudo second order	46	Rattan sawdust	62.71	Langmuir	Pseudo first order	12
Peganum harmala-L seeds	35.97	Langmuir	Pseudo second order	3	EM based compost	159.22	Sips	Pseudo second order	13
Saklıkent mud	1.18	Langmuir	Pseudo second order	45	Potato peel	35.61	Redlich-Peterson	Pseudo-nth order	50
White rice husk ash	85.56	–	Pseudo second order	16	GO–Fe_3O_4	160.7	Langmuir Freundlich	Pseudo second order	51
Red clay	125	Redlich-Peterson	Pseudo second order	35	Citrus limetta peel	8.733	D-R	Pseudo second order	22
Kaolin	65.42	Langmuir	Pseudo second order	2	Zea mays cob	16.72	D-R	Pseudo second order	22
NaOH treated saw dust	58.48	Redlich-Peterson and Temkin	Pseudo second order	14	Organically modified hydroxyapatite	188.18	Langmuir	–	21
Ni/Ni_xB nanoparticle-coated resin	147.1	Langmuir	Pseudo second order	49	SW800	222.2		Pseudo second order	This study
SW800	555.6	Langmuir	Pseudo second order	This study	SW500	185.19		Pseudo second order	This study
SW500	294.1	Langmuir	Pseudo second order	This study					

5. References

1. Y.-C. Lee, E. J. Kim, J.-W. Yang and H.-J. Shin, *J. Hazard. Mater.* **2011**, *192*, 62–70.
2. B. K. Nandi, A. Goswami and M. K. Purkait, *J. Hazard. Mater.* **2009**, *161*, 387–395. **DOI:**10.1016/j.jhazmat.2008.03.110
3. S. Agarwal, V. K. Gupta, M. Ghasemi and J. Azimi-Amin, *J. Mol. Liq.* **2017**, *231*, 296–305. **DOI:**10.1016/j.molliq.2017.01.097
4. L. Kong, F. Qiu, Z. Zhao, X. Zhang, T. Zhang, J. Pan and D. Yang, *J. Clean. Prod.* **2016**, *137*, 51–59. **DOI:**10.1016/j.jclepro.2016.07.067
5. M. Oplatowska, R. F. Donnelly, R. J. Majithiya, D. Glenn Kennedy and C. T. Elliott, *Food Chem. Toxicol.* **2011**, *49*, 1870–1876. **DOI:**10.1016/j.fct.2011.05.005
6. N. Akter, A. Hossain, M. J. Hassan, M. K. Amin, M. Elias, M. M. Rahman, A. M. Asiri, I. A. Siddiquey and M. A. Hasnat, *J. Environ. Chem. Eng.* **2016**, *4*, 1231–1241. **DOI:**10.1016/j.jece.2016.01.013
7. Uma, S. Banerjee and Y. C. Sharma, *J. Ind. Eng. Chem.* **2013**, *19*, 1099–1105. **DOI:**10.1016/j.jiec.2012.11.030
8. A. A. Adeyemo, I. O. Adeoye and O. S. Bello, *Appl. Water Sci.* **2017**, *7*, 543–568. **DOI:**10.1007/s13201-015-0322-y
9. L. Bulgariu, L. B. Escudero, O. S. Bello, M. Iqbal, J. Nisar, K. A. Adegoke, F. Alakhras, M. Kornaros and I. Anastopoulos, *J. Mol. Liq.* **2019**, *276*, 728–747. **DOI:**10.1016/j.molliq.2018.12.001
10. A. Kausar, M. Iqbal, A. Javed, K. Aftab, Z.-H. Nazli, H. N. Bhatti and S. Nouren, *J. Mol. Liq.* **2018**, *256*, 395–407. **DOI:**10.1016/j.molliq.2018.02.034
11. V. Katheresan, J. Kansedo and S. Y. Lau, *J. Environ. Chem. Eng.* **2018**, *6*, 4676–4697. **DOI:**10.1016/j.jece.2018.06.060
12. B. H. Hameed and M. I. El-Khaiary, *J. Hazard. Mater.* **2008**, *159*, 574–579. **DOI:**10.1016/j.jhazmat.2008.02.054
13. T. Bhagavathi Pushpa, J. Vijayaraghavan, S. J. Sardhar Basha, V. Sekaran, K. Vijayaraghavan and J. Jegan, *Ecotoxicol. Environ. Saf.* **2015**, *118*, 177–182. **DOI:**10.1016/j.ecoenv.2015.04.033
14. V. S. Mane and P. V. V. Babu, *Desalination* **2011**, *273*, 321–329. **DOI:**10.1016/j.desal.2011.01.049
15. V. K. Gupta, B. Gupta, A. Rastogi, S. Agarwal and A. Nayak, *J. Hazard. Mater.* **2011**, *186*, 891–901. **DOI:**10.1016/j.jhazmat.2010.11.091
16. M. P. Tavlieva, S. D. Genieva, V. G. Georgieva and L. T. Vlaev, *J. Colloid Interface Sci.* **2013**, *409*, 112–122. **DOI:**10.1016/j.jcis.2013.07.052

17. K. G. Bhattacharyya and A. Sarma, *Dye. Pigment.* **2003**, *57*, 211–222. **DOI:**10.1016/S0143-7208(03)00009-3
18. T. Uysal, G. Duman, Y. Onal, I. Yasa and J. Yanik, *J. Anal. Appl. Pyrolysis* **2014**, *108*, 47–55. **DOI:**10.1016/j.jaap.2014.05.017
19. M. Baghdadi, B. A. Soltani and M. Nourani, *J. Ind. Eng. Chem.* **2017**, *55*, 128–139. **DOI:**10.1016/j.jiec.2017.06.037
20. Sandpaper, https://en.wikipedia.org/wiki/Sandpaper, (accessed 1 November **2018**).
21. A. A. El-Zahhar and N. S. Awwad, *J. Environ. Chem. Eng.* **2016**, *4*, 633–638. **DOI:**10.1016/j.jece.2015.12.014
22. H. Singh, G. Chauhan, A. K. Jain and S. K. Sharma, *J. Environ. Chem. Eng.* **2017**, *5*, 122–135. **DOI:**10.1016/j.jece.2016.11.030
23. S. Milicevic, T. Boljanac, S. Martinovic, M. Vlahovic, V. Milosevic and B. Babic, *Fuel Process. Technol.* **2012**, *95*, 1–7. **DOI:**10.1016/j.fuproc.2011.11.005
24. M. J. Rwiza, S. Y. Oh, K. W. Kim and S. D. Kim, *Chemosphere* **2018**, *195*, 135–145. **DOI:**10.1016/j.chemosphere.2017.12.043
25. N. Kataria and V. K. Garg, *J. Environ. Chem. Eng.* **2017**, *5*, 5420–5428. **DOI:**10.1016/j.jece.2017.10.035
26. C. L. Lu, J. G. Lv, L. Xu, X. F. Guo, W. H. Hou, Y. Hu and H. Huang, *Nanotechnology* **2009**, *20*, 215604–215612. **DOI:**10.1088/0957-4484/20/21/215604
27. H. Xia, L. Chen and Y. Fang, *Sep. Sci. Technol.* **2013**, *48*, 2681–2687. **DOI:**10.1080/01496395.2013.805340
28. L. Dai, W. Zhu, L. He, F. Tan, N. Zhu, Q. Zhou, M. He and G. Hu, *Bioresour. Technol.* **2018**, *267*, 510–516. **DOI:**10.1016/j.biortech.2018.07.090
29. K.-W. Jung, B. H. Choi, M.-J. Hwang, T.-U. Jeong and K.-H. Ahn, *Bioresour. Technol.* **2016**, *219*, 185–195. **DOI:**10.1016/j.biortech.2016.07.098
30. S. Chowdhury and P. Saha, *Chem. Eng. J.* **2010**, *164*, 168–177. **DOI:**10.1016/j.cej.2010.08.050
31. I. A. Aguayo-Villarreal, L. A. Ramírez-Montoya, V. Hernández-Montoya, A. Bonilla-Petriciolet, M. A. Montes-Morán and E. M. Ramírez-López, *Ind. Crops Prod.* **2013**, *48*, 89–97. **DOI:**10.1016/j.indcrop.2013.04.009
32. N. Fiol and I. Villaescusa, *Environ. Chem. Lett.* **2009**, *7*, 79–84. **DOI:**10.1007/s10311-008-0139-0
33. F. de Castro Silva, M. M. F. da Silva, L. C. B. Lima, J. A. Osajima and E. C. da Silva Filho, *Int. J. Biol. Macromol.* **2018**, *114*, 470–478. **DOI:**10.1016/j.ijbiomac.2018.03.089
34. A. B. Karim, B. Mounir, M. Hachkar, M. Bakasse and A. Yaacoubi, *J. Hazard. Mater.* **2009**, *168*, 304–309. **DOI:**10.1016/j.jhazmat.2009.02.028
35. M. Saif, U. Rehman, M. Munir, M. Ashfaq, M. F. Nazar, M. Danish and J. Han, *Chem. Eng. J.* **2013**, *228*, 54–62. **DOI:**10.1016/j.cej.2013.04.094
36. E. C. Lima, A. Hosseini-Bandegharaei, J. C. Moreno-Piraján and I. Anastopoulos, *J. Mol. Liq.* **2019**, *273*, 425–434. **DOI:**10.1016/j.molliq.2018.10.048
37. Y. Bulut and H. Aydin, *Desalination* **2006**, *194*, 259–267. **DOI:**10.1016/j.desal.2005.10.032
38. V. S. Mane, I. D. Mall and V. C. Srivastava, *J. Environ. Manag.* **2007**, *84*, 390–400. **DOI:**10.1016/j.jenvman.2006.06.024
39. S. K. Srivastava, V. K. Gupta, M. K. Dwivedi and S. Jain, *Anal. Proc. Incl. Anal. Commun.* **1995**, *32*, 21–23. **DOI:**10.1039/AI9953200021
40. I. Langmuir, *J. Am. Chem. Soc.* **1918**, 40, 1361–1403. **DOI:**10.1021/ja02242a004
41. T. D. Çiftçi, *Cogent Chem.* **2017**, *3*, 1–15. **DOI:**10.1080/23312009.2017.1284296
42. M. Ghasemi, M. Naushad, N. Ghasemi and Y. Khosravi-fard, *J. Ind. Eng. Chem.* **2014**, *20*, 2193–2199. **DOI:**10.1016/j.jiec.2013.09.050
43. A. K. Meena, K. Kadirvelu, G. K. Mishraa, C. Rajagopal and P. N. Nagar, *J. Hazard. Mater.* **2008**, *150*, 619–625. **DOI:**10.1016/j.jhazmat.2007.05.011
44. N. K. Amin, *J. Hazard. Mater.* **2009**, *165*, 52–62. **DOI:**10.1016/j.jhazmat.2008.09.067
45. Y. Kismir and A. Z. Aroguz, *Chem. Eng. J.* **2011**, *172*, 199–206. **DOI:**10.1016/j.cej.2011.05.090
46. M. Ghaedi, H. Hossainian, M. Montazerozohori, A. Shokrollahi, F. Shojaipour, M. Soylak and M. K. Purkait, *Desalination* **2011**, *281*, 226–233. **DOI:**10.1016/j.desal.2011.07.068
47. N. Akter, M. A. Hossain, M. J. Hassan, M. K. Amin, M. Elias, M. M. Rahman, A. M. Asiri, I. A. Siddiquey and M. A. Hasnat, *J. Environ. Chem. Eng.* **2016**, *4*, 1231–1241. **DOI:**10.1016/j.jece.2016.01.013
48. M. S. Raghu, K. Y. Kumar, M. K. Prashanth, B. P. Prasanna, R. Vinuth and C. B. Pradeep Kumar, *J. Water Process Eng.* **2017**, *17*, 22–31. **DOI:**10.1016/j.jwpe.2017.03.001
49. M. Çınar, Y. İşlek Coşkun and T. Deniz Çiftçi, *Turkish J. Chem.* **2018**, *42*, 505–519.
50. E-K. Guechi and O. Hamdaoui, Arab. J. Chem. **2016**, *9*, 416–424. **DOI:**10.1016/j.arabjc.2011.05.011
51. M. S. Raghu, K.Y. Kumar, M.K. Prashanth et al., J. Water Process Eng. **2017**, *17*, 22–31. **DOI:**10.1016/j.jwpe.2017.03.001

Povzetek

Odpadke brusilnega papirja smo po pirolizi na 500 in kalcinaciji na 600 uporabili za odstranjevanje kationskih barvil briljantno zeleno in malahitno zeleno iz vodnih raztopin. Adsorpcijsko ravnotežje smo poskusili opisati z Langmuir-jevo, Freundlich-ovo, in Dubinin-Radushkevich-ovo izotermo ter izvedli termodinamske študije. Adsorbcijo na briljantno zeleno smo najbolje opisali z Langmuir-jevo izotermo, adsorpcijo na malahitno zeleno pa z Freundlich-ovo. Izkazalo se je, da je adsorpcija endotermna. E vrednost pridobljena iz Dubinin-Radushkevich-ove izoterme je pokazala, da gre za kemijsko adsorpcijo. Kinetiko adsorpcije smo preučili s tremi kinetični modeli (psevdo prvi-red, psevdo drugi-red reakcije in modelom znotraj-delčne difuzije) in pokazali, da model psevdo–drugega reda najbolje opiše adsorpcijo na obe barvili.

DOI: 10.17344/acsi.2018.4885 *Acta Chim. Slov.* **2019,** *66,* 414–420

Scientific paper

Preparation, Structure, Photoluminescent and Semiconductive Properties, and Theoretical Calculation of a Mononuclear Nickel Complex with 3-Hydroxy-2-Methylquinoline-4-Carboxylato Ligand

Xiao-Niu Fang,[1] Jia Li,[1,3] Xiu-Guang Yi,[1,2*] Qi Luo,[1] Jia-Yi Chen[1] and Yong-Xiu Li[2*]

[1] *Institute of Applied Chemistry, School of Chemistry and Chemical Engineering, Jinggangshan University, Ji'an, Jiangxi, 343009, China*

[2] *School of Materials Science and Engineering & Chemistry, Nanchang University, Nanchang, Jinagxi, 330031, China*

[3] *State Key Laboratory of Molecular Reaction Dynamics, Dalian Institute of Chemical Physics, Chinese Academy of Sciences, Dalian 116023, China*

* *Corresponding author: E-mail: jayxgggchem@163.com*
Tel: +86 (796)8100490; Fax: +86 (796)8100490

Received: 12-01-2018

Abstract

A novel nickel complex with mixed ligands $[Ni(L)_2(EtOH)_2(MeOH)_2]$ (HL = 3-hydroxy-2-methylquinoline-4-carboxylic acid) has been synthesized through solvothermal reaction and its crystal structure was determined by single-crystal X-ray diffraction technique. Single-crystal X-ray diffraction analyses reveals that the title compound crystallizes in the triclinic system of the *P*–1 space group, and exists as isolated mononuclear complex. The intermolecular hydrogen bonds lead to the formation of chains, and the layered supramolecular structure is formed by the strong π···π stacking interactions. Solid-state photoluminescent characterization reveals that the title compound has an emission in the green region. Time-dependent density functional theory (TDDFT) calculation shows that the nature of the photoluminescence of the title compound originates from the ligand-to-ligand charge transfer (LLCT; from the HOMO of the p-orbital of ligand HMCA to the LUMO of the oxygen atoms). A wide optical band gap of 2.25 eV is found by the solid-state UV/vis diffuse reflectance spectrum.

Keywords: Nickel; photoluminescence; semiconductor; TDDFT; LLCT

1. Introduction

In recent years, metallo-organic coordination polymers have attracted considerable interest due to their diverse structures and potential applications in fluorescence, magnetic materials, gas adsorption, catalysis and medicine and so forth.[1–6] The synthesis of coordination polymers with specific functions has gradually become a research hotspot in the field of material chemistry.[7] From the perspective of crystal engineering, the most useful and facile way to construct coordination complexes is to adopt a suitable ligand to connect metal centers. The ligand is better to possess as much donor atoms as possible that enable it to bridge metal centers together to yield extended architectures. The important feature of metallo-organic coordination polymers is the extension of low dimensional building blocks to high dimensional networks through weak intermolecular interactions, including weak van der Waals force, hydrogen bonding, π-π stacking, etc.[8–10]

Selecting a good ligand is very important in the design and preparation of complexes. Nitrogen heterocyclic compounds have attracted much attention due to their flexible coordination modes and easy coordination with metal ions. They are commonly used ligands for building complexes. A series of complexes based on these ligands have been reported.[11–14] But carboxyl groups not only have many coordination modes such as monodentate coordination, symmetrical chelation coordination, asymmetrical

chelation coordination, monooxy bridging coordination and so on, but also have strong coordination ability. They can coordinate with almost all metals to form complexes, and have a large number of unique structures and excellent properties. Various metal carboxylate complexes have been reported.[15–20] If carboxyl groups are introduced into heterocyclic compounds, a series of heterocyclic carboxylic acids with more abundant coordination sites and patterns can be obtained. For example, 4,5-imidazoledicarboxylic acid, 2-pyridine-4,5-imidazoledicarboxylic acid, and corresponding complexes. Up to now, there are few reports on the complexes of quinolinecarboxylates.[21,22]

Quinolinecarboxylate ligands, as ligands containing nitrogen atoms and carboxyl oxygen atoms, are easy to coordinate with metal ions. The coordination modes of carboxyl oxygen atoms are diverse, and the degree of deprotonation of carboxyl groups varies under different pH values, bringing more coordination modes. The coordination mode can exhibit various structures and unique properties. A new nickel coordination polymer (the title compound) was synthesized by hydrothermal method with 3-hydroxy-2-methyl-quinoline-4-carboxylic acid (HL) as ligand and nickel acetate. Its structure and properties were investigated with infrared spectrum, elemental analysis, single-crystal X-ray, solid-state diffuse reflectance spectrum, photoluminescent and theoretical calculations.

2. Experimental

2. 1. Materials and Instrumentation

All reagents and chemicals were of reagent grade, commercially available and directly applied for the reaction. ^{1}H NMR of the ligand were performed on Bruker Avance 400 MHz based on deuterium DMSO as solvent. Infrared spectra were obtained with a PE Spectrum-One FT-IR spectrometer using KBr discs. Elemental microanalyses of carbon, hydrogen and nitrogen were performed on an Elementar Vario EL elemental analyser. Solid-state UV/Vis diffuse reflectance spectroscopy was acted on a computer-controlled TU1901 UV/Vis spectrometer, Finely-ground powder sample was coated on barium sulfate for a 100% reflectance. Photoluminescence characterization was performed on a F97XP photoluminescence spectrometer. Time-dependent density functional theory (TDDFT) calculation were carried out by virtue of the Gaussian09 suite of program packages.

2. 2. Synthesis of 3-hydroxy-2-methylquinoline-4-carboxylic acid (HL)

Synthesis of isatin: indigo (262 g, 1.0 mol) and $K_2Cr_2O_7$ (147 g, 0.50 mol) were added into 500 mL of water and stirred. After cooling, $K_2Cr_2O_7$ (147 g, 0.50 mol), 300 mL of water and 500 mL of 10 % H_2SO_4 were added and kept stirring at 43 °C for 1.5 h. Then, the mixture was diluted with twice its volume of water, filtered off, dissolved in 10% KOH solution, filtered again, acidified with 10% HCl to pH = 7 and refiltered. Yield: 230 g (90%); m.p. 210 °C; HRMS *m/z* (ESI) calcd for $C_8H_5NO_2$ ($[M+H]^+$) 147.0320, found 147.0826.

Synthesis of HL: isatin (147 g, 1.0 mol) and KOH (56 g, 1.0 mol) were dissolved into a sufficient amount of water and filtered. The filtrate and KOH (56 g, 1.0 mol) were added into chloroacetone (184 g, 2.0 mol), and hydrochloric acid was added dropwise to adjust pH = 7, then filtered. Yield: 193 g (95%); m.p. 225 °C. IR peaks (KBr, cm^{-1}): 3433(vs), 3125(w), 3043(w), 2869(w), 2499 (m), 2040(m), 1621(m), 1553 (s), 1500 (m), 1462(m), 1410(m), 1242(vs), 1160(m), 1014(w), 906(m) and 686(s); HRMS *m/z* (ESI) calcd for $C_{11}H_9NO_3$ ($[M+H]^+$) 203.0582, found 203.0548; ^{1}H NMR (400MHz, DMSO) δ 9.15 (s, 1H), 7.93 (d, J = 8.0 Hz, 1H), 7.64 (t, J = 8.0 Hz, 1H), 7.60–7.52 (m, 1H), 2.70 (s, 3H).

2. 3. Synthesis of Complex 1

0.124 g $Ni(CH_3COO)_2{\cdot}4H_2O$ (0.50 mmol), 0.203 g HL (1.0 mmol), 5 mL methanol, 5 mL ethanol and 0.5 mL distilled water were added in turn into a 25 mL Teflon-lined stainless steel autoclave. The autoclave was heated to 100 °C in an oven and kept there for one week, then let to cool down to room temperature. Light yellow block crystals were obtained and used to collect the single-crystal X-ray data. Yield 0.434 g **1** (70% based on HL). IR (KBr, cm^{-1}): 3421(s), 1610(s), 1558 (s), 1416(m), 1348(m), 1228(vs), 826(s), 659(w) and 636(s); Anal. Calcd for $C_{28}H_{36}N_2NiO_{10}$: C, 54.30; H, 5.86; N, 4.52; found: C, 54.39; H,5.81; N, 4.66%.

2. 4. X-ray Structure Determination

The single-crystal data of the title complex were collected on the SuperNova CCD X-ray diffractometer equipped with a graphite monochromated Mo-Kα radiation source (0.71073 Å) at 293(2) K. The reduction and empirical absorption correction of the diffraction data were carried out with CrystalClear software. The crystal structure was successfully solved by using the direct methods and Siemens SHELXTLTM Version 5 software package and refined with a full-matrix least-squares refinement on F^2.[23] All of the non-hydrogen atoms were generated based on the subsequent Fourier difference maps and refined anisotropically. The hydrogen atoms were located theoretically and ride on their parent atoms. Due to the problem of crystal quality and the week high-angle diffraction points, lead to the low completeness 0.806. Crystallographic data and structural refinements for the title complex are summarized in Table 1. Selected bond lengths and bond angles for the crystal structure are displayed in Table 2. The hydrogen bonding interactions are presented in Table 3.

Table 1. Crystallographic data and structural analysis for the title compound

Empirical formula	$C_{28}H_{36}N_2NiO_{10}$
M_r	619.30
Color	yellow
Crystal system	Triclinic
Space group	*P*–1
a (Å)	7.8897(9)
b (Å)	8.8950(14)
c (Å)	10.4485(16)
α (°)	75.433(14)
β (°)	87.129(12)
γ (°)	70.233(12)
V (Å^3)	667.38(17)
Z	1
Reflections collected	5646
Independent, Observed reflections (R_{int})	1895, 1686 (0.0464)
$d_{calcd.}$(g/cm^3)	1.541
μ(mm^{-1})	0.791
F(000)	326
R_1, wR_2	0.0944, 0.2312
S	1.059
Largest and mean Δ/σ	0,0
Δ/σ(max, min)(e. Å^3)	1.147, –0.541

Table 2. Selected bond lengths (Å) and bond angles (°) for the title compound

Distance	**(Å)**	**Distance**	**(Å)**
Ni1–O1	2.044(5)	Ni1–O3	2.088(6)
Ni1–O4	2.052(5)	O1–C11	1.298(10)
O2–C11	1.248(10)	O3–C14	1.393(14)
O4–C13	1.412(10)	O5–C8	1.346(12)
N1–C9	1.307(10)	N1–C1	1.362(10)
Angle	**(°)**	**Angle**	**(°)**
O1–Ni1–O4	93.0(2)	N1–C1–C6	121.3(6)
O1–Ni1–O3	91.4(2)	N1–C9–C10	117.5(7)
O4–Ni1–O3	88.9(3)	N1–C9–C8	122.7(7)
C11–O1–Ni1	130.1(5)	O2–C11–O1	122.4(6)
C14–O3–Ni1	127.8(8)	O2–C11–C7	120.2(7)
C13–O4–Ni1	129.3(5)	O1–C11–C7	117.5(7)
C9–N1–C1	120.3(6)	O4–C13–C12	83.4(7)

Table 3. Hydrogen bonding interactions

D–**H**···*A*	*D*–H, Å	H···*A*, Å	*D*···*A*, Å	*D*–**H**···*A*, °
O4–H4B···N1^{i}	0.93	1.94	2.728(7)	141
O5–H5B···O1	0.82	1.89	2.605(10)	145
C5–H5A···O2	0.93	1.97	2.647(10)	128

Symmetric code: (i) *x*, *y*, 1 + *z*.

3. Results and Discussion

The 3-hydroxy-2-methylquinoline-4-carboxylic acid (HL) was prepared by the reaction of isatin with chloroacetone in alkali condition, and the isatin was obtained by the oxidation of indigo, as shown in Scheme 1. The experimental procedure was improved according to the basis of literature.[24,25]

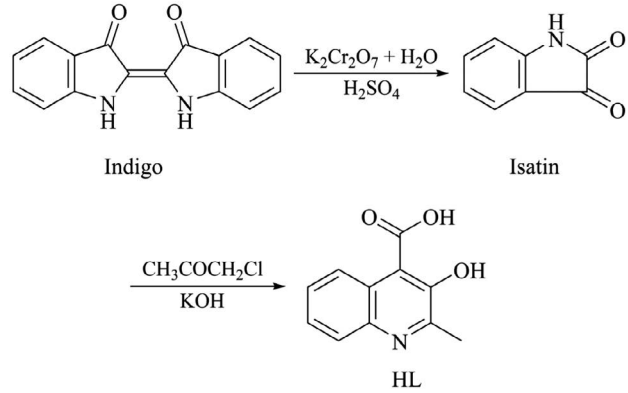

Scheme 1. Synthetic route of HL

In the first step, the amount of oxidant and temperature control is the key factors to the success of the oxidation. In the second progress, the amount of KOH and the feeding mode of chloroacetone make the important effects on reactions.

Single-crystal X-ray diffraction measurement revealed that the title compound crystallizes in the space group *P*–1 of the triclinic system. In the crystal structure of title compound **1**, the metal Ni atom is sitting at the inversion center. The nickel (II) ion is hexacoordinated octahedron by the doubly deprotonated HL, two methanol and two ethanol molecules, yielding an octahedral geometry, as presented in Fig. 1. The bond distance of Ni–O1 is 2.044(5) Å, for is Ni^{ii}–O3 2.088(6) Å, while that of Ni–O4 is 2.052(5) Å [ii = –*x*, –*y*, 1 – *z*]. These are comparable with that reported in the references.[26,27] Quinolinecarboxylate (L^-) acts as the monodentate ligand coordinated to the nickel metal center, and two such ligands occupy both axial positions. The four O atoms of methanol and ethanol are located in the equatorial plane with the good coplanarity. The intramolecular hydrogen bond can be found between the phenolic hydroxyl group and carboxylate group (O5–H5B···O1), and another week intramolecular hydrogen bond exist between the carbon atom and the carboxyl oxygen atom (C5–H5A···O2). The intermolecular hydrogen bond O4–H4B···N1^{i} can be found between ethanol oxygen and aromatic N atom of quinoline moiety, forming a one-dimensional supramolecular structure extending along the *c*-axis, as presented in Fig. 2. In the complex, there are strong offset face-to-face π···π stacking interactions between *Cg*1···*Cg*1^{iii} and *Cg*2···*Cg*1^{iv} [*Cg*1 and *Cg*2 are

N1/C1/C6–C9 and C1–C6 ring centroids; iii = –*x*, –*y*, –*z*; iv = 1 – *x*, –*y*, –*z*]. The centroid-centroid distance of *Cg*1···*Cg*1^{iii} is 3.6528(4) Å with the shift distance 1.3372(7) Å and the twist angle of 0.00(4)°. The centroid-centroid distance of *Cg*2···*Cg*1^{iv} is 3.5966(4) Å with the shift distance 1.0197(8) Å and the twist angle of 2.387(5)°. These π···π stacking interactions yield the two-dimensional supramolecular layers along the *ac*-axis plane, then *via* van der Waals attraction complete a crystal packing as presented in Fig. 3.

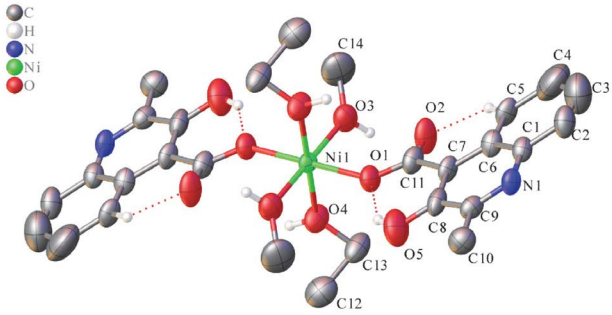

Figure 1. The molecular structure of the title compound. Hydrogen atoms not involved in the motif shown were removed for clarity.

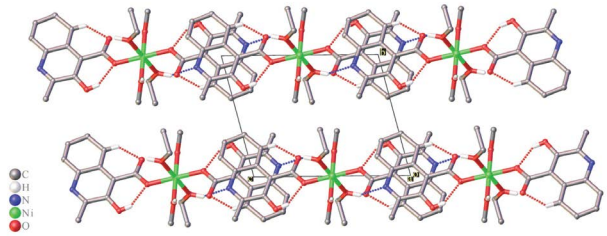

Figure 2. The 1-D chain structure of the title compound. Hydrogen atoms not involved in the motif shown were removed for clarity. The intramolecular hydrogen bond is shown as red stipple line, the intermolecular hydrogen bond is shown as blue stipple line.

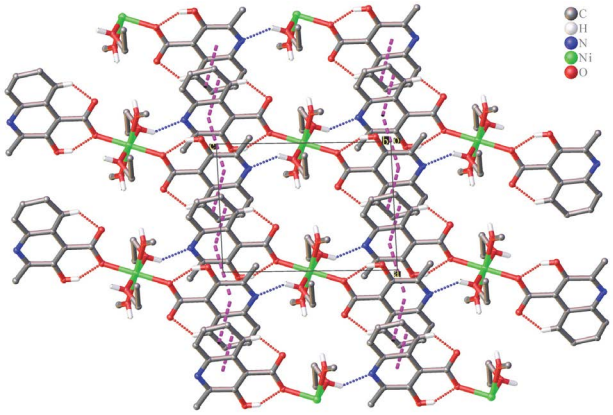

Figure 3. Packing diagram of the title compound viewed along the *b* axis. Hydrogen atoms not involved in the motif shown were removed for clarity. The intramolecular hydrogen bond is shown as red stipple line, the intermolecular hydrogen bond is shown as blue stipple line, and the magenta stipple line represent the π···π stacking interactions.

In recent years, the photoluminescence properties of coordination complexes have gained increasing interest. Generally, coordination complexes containing lanthanide and transition elements can exhibit photoluminescence behavior because they possess rich 4*f*-orbit and 3/4*d*-orbit electron configurations. Many studies about the photoluminescence performance of lanthanide and transition compounds have been conducted so for.[28–30] The title compounds contain Ni^{2+} ions; therefore, we deemed that nickel and HL complexes can possibly exhibit interesting photoluminescence performance. Based on the above considerations and in order to reveal its potential photoluminescent properties, we carried out the photoluminescence spectra with solid state samples at room temperature and the result is presented in Figs. 4. It is obvious that the photoluminesent spectrum of the title compound displays an effective energy absorption residing in the wavelength range of 350–450 nm. Upon the emission of 544 nm, the excitation spectrum shows a band at 408 nm. We further measured the corresponding photoluminescence emission spectrum of the title compound. Upon excitation at 408 nm, the emission spectrum is characterized by a sharp band at 544 nm in the blue region of the spectrum. The emission band of the title compound is located in the green light region with the CIE (Commission Internationale de l'Éclairage) Chromaticity coordinate (0.3551, 0.634) (Fig. 5). As a result, the title complex is a potential green photoluminescent material.

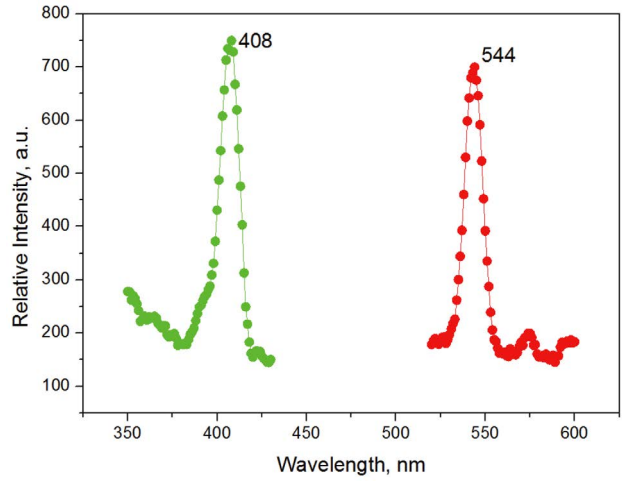

Figure 4. Solid-state photoluminescence spectra of the title compound measured at room temperature (green curve: excitation; red curve: emission).

In order to reveal the nature of the photoluminescence emission of the title compound, we truncated ground state geometry from its single-crystal X-ray diffraction data set (without optimization) and carried out its theoretical calculation in light of the time-dependent density functional theory (TDDFT) based on this ground state

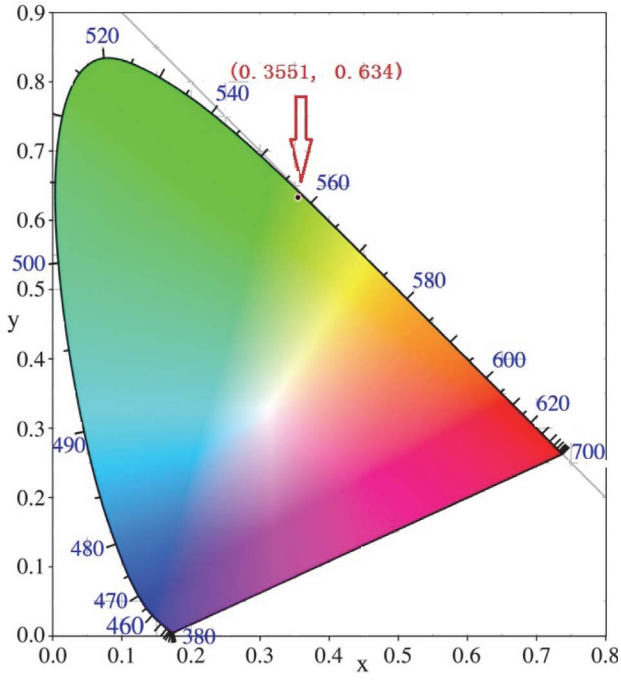

Figure 5. The CIE chromaticity diagram and chromaticity coordinates of the emission spectrum of the title compound.

geometry. The TDDFT calculations were performed using the B3LYP function[31,32] and carried out by means of the Gaussian09 suite of programs,[33] with SDD for Ni and 6-31G* basis for other atoms. The characteristics of HOMO (highest occupied molecular orbital) and LUMO (lowest unoccupied molecular orbital) of the title compound is shown in Fig. 6. It is easy to find out that the electron-density distribution of HOMO is totally resided at the coordinating the p-orbital of ligand HL with an energy being of –0.21787 Hartrees; however, the electron-density population of LUMO is mainly distributed on the oxygen atoms and the energy of the LUMO is calculated to be –0.19871 Hartrees. The energy difference between LUMO and HOMO is 0.01916 Hartrees that is small enough to allow the charge transfer from HOMO to LUMO. In light of this observation, it is proposed that the essence of the photoluminescence of the title compound could be assigned to the ligand-to-ligand charge transfer (LLCT; from the HOMO of the p-orbital of ligand HL to the LUMO of the oxygen atoms).

To investigate the semiconductive properties of the title complex, the solid-state UV/vis diffuse reflectance spectra was measured on a powder sample at room temperature, using barium sulfate as the reference for 100% reflectivity, its surface was coated with finely-ground powder samples for measurement. After measuring, the data were treated with the Kubelka-Munk function which is known as $\alpha/S = (1 - R)^2/2R$. With regard to this function, the parameter α means the absorption coefficient, S means the scattering coefficient, and the R means the reflectance, which is actually wavelength independent when the size of the particle is larger than 5 μm. From the α/S *vs.* energy gap diagram, we can obtain the value the optical band gap, which can be extrapolated from the linear portion of the absorption edges. In the way, the solid-state UV/vis diffuse reflectance spectrum reveals that the title compound has a wide optical energy band gap of 2.25 eV, as shown in Fig. 7. As a result, the title compound is a possible candidate for wide band gap semiconductors. The gentle slope of the optical absorption edge of title compound indicates that it must be an indirect transition.[34] The energy band gap of 2.25 eV is obviously larger than those of GaAs (1.4 eV), CdTe(1.5 eV) and $CuInS_2$

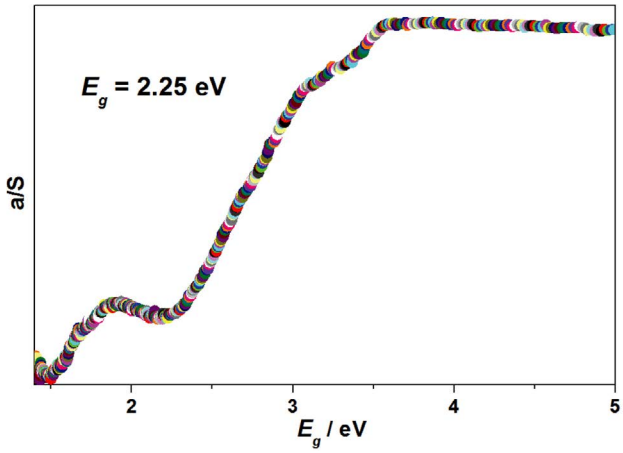

Figure 7. Solid-state UV/vis diffuse reflectance spectrum for the title compound.

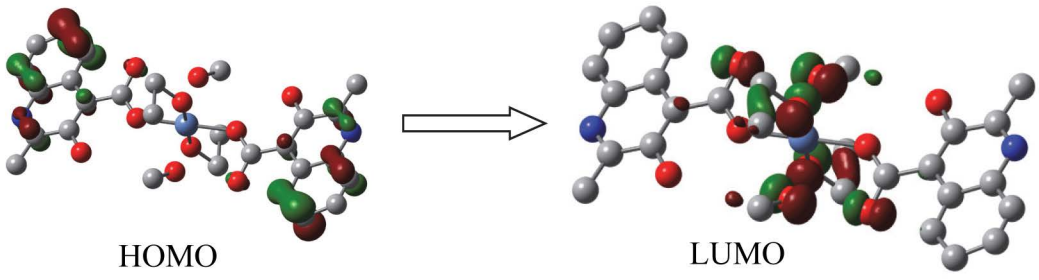

Figure 6. B3LPY predicted frontier molecular orbital of the title compound. The isovalue of 0.04 is used for plotting isosurfaces.

(1.55 ev),[35,36] all of them are well known as highly efficient band gap photovoltaic materials.

4. Conclusions

A novel nickel(II) complex $[Ni(L)_2(EtOH)_2(MeOH)_2]$ with the ligands of 3-hydroxy-2-methylquinoline-4-carboxylic acid (HL), MeOH and EtOH was synthesized by solvothermal synthesis, its structure and properties were investigated with infrared spectrum, elemental analysis, single-crystal X-ray, solid-state diffuse reflectance spectrum, photoluminescent and theoretical calculations. The title compound crystallizes in the triclinic system of the *P*–1 space group as isolated mononuclear complex. The intermolecular hydrogen bonds lead to the formation of chains, and the layered supramolecular structure is formed by the offset face-to-face π···π stacking interactions. Solid-state photoluminescence spectrum reveals that it shows an emission in the green region of the light spectrum. Time-dependent density functional theory (TDDFT) calculations reveal that this emission can be attributed to ligand-to-ligand charge transfer (LLCT). Solid-state diffuse reflectance data shows there is a narrow optical band gap of 2.25 eV.

5. Acknowledgements

We gratefully acknowledge the financial support of the NSF of China (51363009), Jiangxi Provincial Department of Education's Item of Science and Technology (GJJ160745, GJJ170652), Jinagxi Provincial Department of Education's Item of higher education and teaching reform (JXJG-17-9-14), the Science and Technology Plan project Fund of Jiangxi Provincial Health Planning Commission (20194083), and Natural Science Foundation Project of Jinggangshan University (JZ09029).

6. Supplementary Material

Crystallographic data for the structure reported in this paper have been deposited with the Cambridge Crystallographic Data Centre as supplementary publication no. CCDC 1876986. Copies of the data can be obtained free of charge on application to CCDC, 12 Union Road, Cambridge CB2 1EZ, UK (fax: +44 1223 336-033; e-mail: deposit@ccdc.cam.ac.uk).

7. References

1. X. Liu, C. Manzur, N. Novoa, S. Celedon, D. Carrillo, J. R. Hamon, *Coord. Chem. Rev.* **2018**, *357,* 144–172. **DOI:**10.1016/j.ccr.2017.11.030
2. T. Tominaqa, T. Mochida, *Chemistry* **2018**, *24,* 6239–6247. **DOI:**10.1002/chem.201800333
3. K. K. Li, D. Zhang, F. Raza, P. Puttapirat, Y. Liu, Y. Zhang, *J. Chem. Phys.* **2018**, *149,* 074310. **DOI:**10.1063/1.5034066
4. Y. M. So, W. H. Leung, *Coord. Chem. Rev.* **2017**, *340,* 172–197. **DOI:**10.1016/j.ccr.2016.12.009
5. X. G. Yi, W. T. Chen, J. G. Huang, D. W. Zhang, Y. F. Wang, *Acta Chim. Slov.* **2017**, *64,* 1042–1047. **DOI:**10.17344/acsi.2017.3838
6. C. C. Mokhtarzadeh, C. E. Moore, A. L. Rheingold, J. S. Figueroa, *Angew. Chem. Int. Ed.* **2017**, *56,* 10894–10899. **DOI:**10.1002/anie.201705877
7. J. W. Zhao, Y. Z. Li, L. J. Chen, G. Y. Yang, *Chem. Commun.* **2016**, *52,* 4418–4445. **DOI:**10.1002/chin.201619199
8. G. G. Wang, T. T. Chen, S. B. Li, H. J. Pang, H. Y. Ma, *Dalton Trans.* **2017**, *46,* 13897–13902. **DOI:**10.1039/C7DT02230A
9. X. S. Qu, H. Feng, C. Ma, Y. Y. Yang, X. Y. Xu, *Inorg. Chem. Commun.* **2017**, *81,* 22–26. **DOI:**10.1016/j.inoche.2017.04.023
10. M. A. Moussawi, N. L. Leclerc, S. Floquet, P. A. Abramov, M. N. Sokolov, S. Cordier, A. Ponchel, E. Monflier, H. Bricout, D. Landy, *J. Am. Chem. Soc.* **2017**, *139,* 12793–12803. **DOI:**10.1021/jacs.7b07317
11. X. F. Yang, M. Liu, H. B. Zhu, *Inorg. Chem. Commun.* **2017**, *83,* 40–43. **DOI:**10.1016/j.inoche.2017.06.007
12. X. G. Yi, Z. X. Zhang, W. T. Chen, L. Z. Lin, H. L. Chen, *J. Solid State Chem.* **2018**, *266,* 16–22. **DOI:**10.1016/j.jssc.2018.07.004
13. M. Zhu, M. T. Li, L. Zhao, K. Z. Shao, Z. M. Su, *Inorg. Chem. Commun.* **2017**, *79,* 69–73. **DOI:**10.1016/j.inoche.2017.03.020
14. W. T. Chen, J. G. Huang, X. G. Yi, *Acta Chim. Slov.* **2016**, *63,* 899–904. **DOI:**10.17344/acsi.2016.2897
15. B. Wang, H. Y. Zhao, D. P. Dong, H. Q. Wu, *Chem. Res.* **2018**, *29,* 245–252. **DOI:**10.14002/j.hxya.2018.03.004
16. Y. L. Liu, Q. Zhuo, Q. Wei, X. Ding, *Chem. Word* **2018**, *59,* 360–364. **DOI:**10.19500/j.cnki.0367-6358.20170609
17. J. L. Xie, H. N. Peng, Q. Hu, J. Zeng, *Chinese J. Anal. Lab.* **2018**, *37,* 954–958. **DOI:**10.13595/j.cnki.issn1000-0720.2018.0185
18. Y. Horikawa, T. Tokushima, O. Takahashi, A. Hiraya, A. Hiraya, S. Shin, *Phys. Chem. Chem. Phys.* **2018**, *20,* 23214–23221. **DOI**:10.1039/C7CP08305J
19. A. Tsaturyan, Y. Machida, T. Akitsu, I. Gozhikova, I Shcherbakov, *J. Mol. Struct.* **2018**, *1162,* 54–62. **DOI:**10.1016/j.molstruc.2018.02.082
20. X. Yang, Z. Liu, X. Chen, W. Wang, *J. Electroal. Chem.* **2016**, *782,* 202–206. **DOI:**10.1016/j.jelechem.2016.10.001
21. J. G. Małecki, R. Kruszyński, D. Tabak, J. Kusz. *Polyhedron* **2007**, *26,* 5120–5130. **DOI:**10.1016/j.poly.2007.07.023
22. X. G. Yi, Y. Z. Liu, X. N. Fang, X. Y. Zhou, Y. X. Li, *Chinese J. Struct. Chem.* **2019**, *38,* 325–330. **DOI:**10.14102/j.cnki.0254-5861.2011-2065
23. Siemens, SHELXTLTM Version 5 Reference Manual, Siemens Energy & Automation Inc., Madison, Wisconsin, USA, **1994**.
24. S. Y. Cho, J. H. Ahn, J. D. Ha, S. K. Kang, J. Y. Baek, S. S. Han,

E. Y. Shin, S. S. Kim, K. R. Kim, H. G. Cheon, J. K. Choi, *Bull. Korean Chem. Soc*. **2003**, *24(10),* 1455–1464. **DOI:**10.5012/bkcs.2003.24.10.1455

25. J. W. Yu, L. N. Song, *J. Taiyuan Normal University* (*Natural Science Edition*) **2016**, *15*, 77–80. **DOI:**10.1088/1475-7516/2016/04/019
26. Y. Hou, L. Xu, M. J. Cichon. S. Lense, K. I. Hardcastle, C. L. Hill, *Inorg. Chem.* **2010**, *49,* 4125–4132. **DOI:**10.1021/ic9024712
27. E. G Bajnoxzi, Z. Nemeth, G. Vanko, *Inorg. Chem.* **2017**, *56,* 14220–14226. **DOI:**10.1021/acs.inorgchem.7b02311
28. P. C. Ford, E. Cariati, J. Bourassa, *Chem. Rev*. **1999**, *99,* 3625–3648. **DOI:**10.1021/cr960109i
29. J. H. Zhang, J. L. Wang, L. Jia, Z. K Qu, Q. H. Kong, *Adv. Mater. Res.* **2011**, *284–286,* 2153–2156. **DOI:**10.4028/www.scientific.net/AMR.284-286.2153
30. F. Y. Liu, D. M. Zhou, Z. L. Zhao, J. F. Kou, *Acta Cryst.* **2017**, 73, 382–392. **DOI:**10.1107/S2053229617004697
31. A. D. Becke, *J. Chem. Phys.* **1993**, *98,* 5648–5652. **DOI:**10.1063/1.464913
32. C. Lee, W. Yang, R. G. Parr, *Phys. Rev. B.* **1988**, *37,* 785–789. **DOI:**10.1103/PhysRevB.37.785
33. M. J. Frisch *et al.,* Gaussian 09, Revision A.02; Gaussian, Inc.: Wallingford CT, **2009**.
34. F. Q. Huang, K. Mitchell, J. A. Ibers, *Inorg. Chem.* **2001**, *40,* 5123–5126. **DOI:**10.1021/ic0104353
35. W. Bensch, P. Dürichen, *Eur. J. Solid State Inorg. Chem.* **1996**, *129,* 1489–1492. **DOI:**10.1002/cber.19961291214
36. R. Tillinski, C. Rumpf, C. Näther, P. Duerichen, I. Jess, S. A. Schunk, W. Bensch, *Z. Anorg. Allg. Chem.* **1998**, *624*, 1285–1290. **DOI:**10.1002/(SICI)1521-3749(199808)624:8<1285::AID- ZAAC1285>3.0.CO;2-5

Povzetek

Sintetizirali smo nov nikljev kompleks s prisotnimi različnimi ligandi $[Ni(L)_2(EtOH)_2(MeOH)_2]$ (HL = 3-hidroksi-2-metilkinolin-4-karboksilna kislina) s solvotermalno tehniko in določili kristalno strukturo z monokristalno rentgensko difrakcijo. Monokristalna rentgenska analiza je razkrila, da spojina kristalizira v triklinskem sistemu v prostorski skupini *P*–1 kot izoliran enojedrni kompleks. Intermolekularne vodikove vezi sodelujejo pri tvorbi verig, plastovita supramolekularna struktura pa nastane zaradi močnih π···π interakcij. Fotoluminiscentne lastnosti v trdnem stanju kažejo, da ima spojina emisijo v zelenem območju. Izračuni na podlagi časovno odvisne teorije gostotnostnih funkcionalov (TDDFT) kažejo, da fotoluminiscenca spojine izvira v prenosu naboja ligand-ligand (LLCT; iz HOMO p-orbitale liganda L v LUMO kisikovega atoma). Široka razlika med optičnima pasovoma 2.25 eV je bila ugotovljena z UV/vis difuzno reflektanco v trdnem stanju.

Scientific paper

Synthesis and in vivo Anti-inflammatory Evaluation of Piperazine Derivatives Containing 1,4-Benzodioxan Moiety

Zhi-Ping Liu,[†,1] Chang-Da Gong,[†,2] Long-Yan Xie,[2] Xiu-Li Du,[2] Yang Li[2] and Jie Qin[*,2]

[1] *School of Medical, Pingdingshan University, Pingdingshan 467000, P. R. China*

[2] *School of Life Sciences, Shandong University of Technology, Zibo 255049, P. R. China*

** Corresponding author: E-mail: qinjietutu@163.com*
Tel.: 0086-533-2780271; Fax: 0086-533-2781329

† These authors contributed equally to this work.

Received: 12-01-2018

Abstract

Six piperazine derivatives **6a**–**f** containing 1,4-benzodioxan moiety have been synthesized and characterized by ^{1}H NMR, ESI-MS and elemental analysis. The structure of **6d** was further confirmed by single crystal X-ray diffraction. All these novel compounds were screened for their *in vivo* anti-inflammatory activity employing classical *para*-xylene-induced mice ear-swelling model. The results revealed that most of the target compounds showed significant anti-inflammatory activities, especially compound **6a** with *ortho*-substituted methoxy group on the phenylpiperazine ring exhibited the best activity among the designed compounds.

Keywords: Piperazine; 1,4-benzodioxan; crystal structure; anti-inflammatory activity

1. Introduction

Inflammation, a biological process response to harmful stimuli or infection, has threatened human health seriously.[1–3] Nonsteroidal anti-inflammatory drugs (NSAIDs) like diclofenac, indomethacin and naproxen are widely clinically used drugs for inflammatory disorders such as arthritis, peritendinitis and lupus erythematosus.[4–7] However, long-term use of NSAIDs has been associated with adverse side effects, including gastrointestinal ulceration, and even fatal internal bleeding.[8] The stomach damage from NSAIDs is generally attributed to their acidic character as most of them are weak acids with pK_a values ranging from 3 to 5.[8,9] Therefore, synthetic approaches based on design of non-acidic anti-inflammatory lead compounds have gained great interest nowadays.[1,10–13]

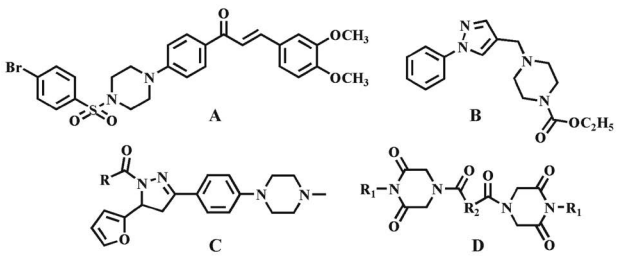

Figure 1. The structure of piperazine derivatives reported in previous literature sources.

Piperazine group, as a known pharmacophore, is part of many important alkaline heterocyclic compounds displaying a broad range of biological activities, *e.g.* antibacterial,[14] anti-tumor,[15] antidiabetic,[16] and anti-psychiatry.[17] Continuous efforts have also been made to prepare anti-inflammatory therapeutic agents containing piperazine scaffold. Li *et al*. reported a series of chalcone derivatives containing aryl-piperazine or aryl-sulfonyl-piperazine fragment and found compound **A** (Figure 1) as a potential anti-inflammatory agent.[18] Silva *et al.* evaluated the anti-inflammatory effect of 4-[(1-phenyl-1*H*-pyrazol-4-yl) methyl]-1-piperazinecarboxylic acid ethyl ester (**B**, Figure 1) and the involvement of the serotonergic pathway.[3] Mao

et al. synthesized a series of piperazine substituted 3-aryl-5-furanyldihydropyrazole amide derivatives (**C**, Figure 1), the *in vitro* anti-inflamatary activity evaluation indicated that theses compounds showed good inhibitory effect on the generation of inflammatory factor, NO.[19] A series of piperazine analogues bearing pyridine or thiophene moieties have been synthesized by Kumar *et al.* (**D**, Figure 1), they also showed favorable anti-inflammatory efficacy.[20]

Beyond that, it was reported that 1,4-benzodioxan afforded a new skeleton possessing anti-inflammatory activity.[10,21,22] Potent anti-inflammatory activity of analogues containing 1,4-benzodioxan ring may be ascribed to the strong hydrogen-bonding interactions with amino acids in the active domain.[10]

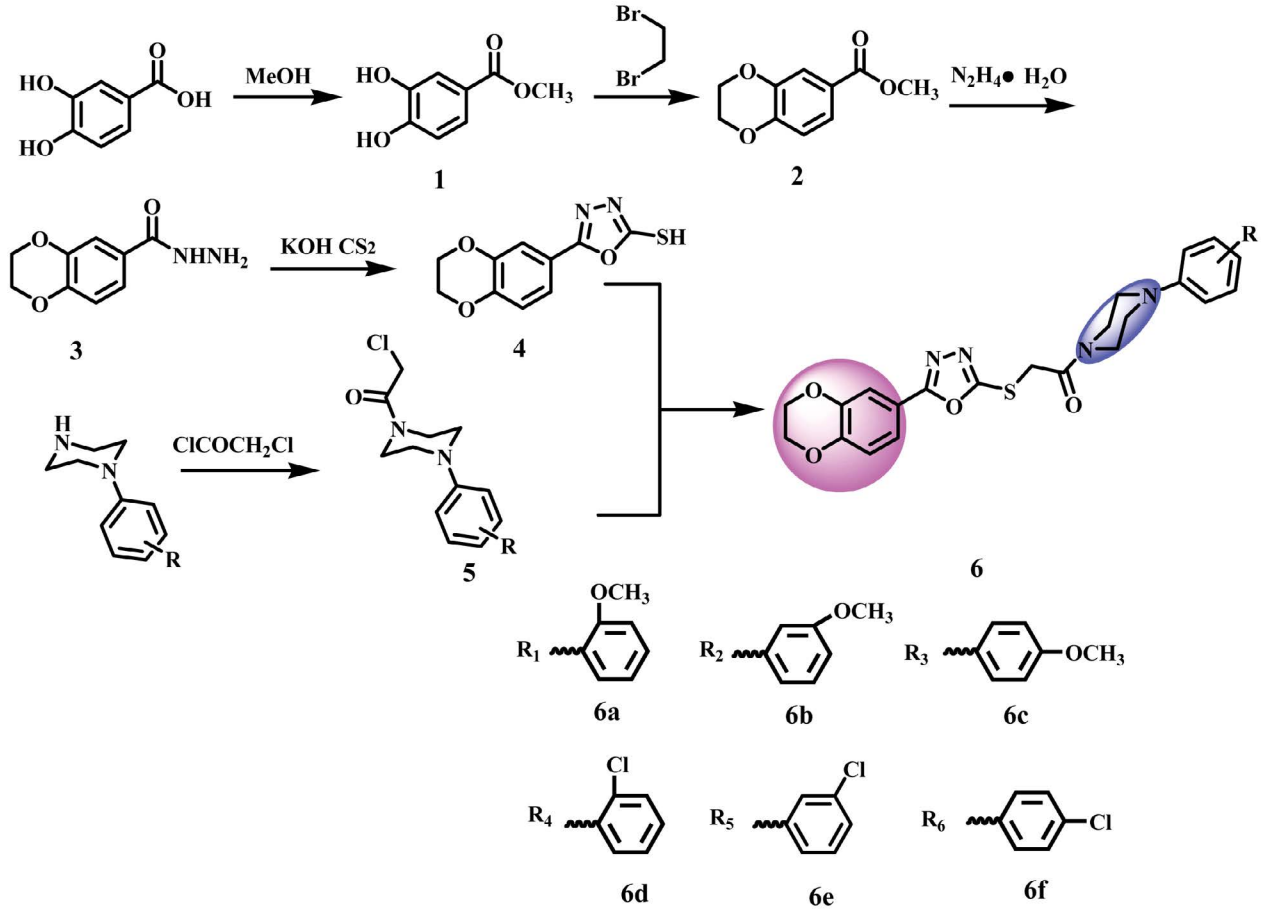

Scheme 1. Synthetic route to **6a–f**.

As mentioned above, it is a worthwhile goal to synthesize compounds containing piperazine and 1,4-benzodioxan rings utilizing molecular hybridization approach. The presence of the two bioactive skeltons in a single molecular frame may lead to potent derivatives possessing good anti-inflammatory activity.[10] With this in mind, we have synthesized six compounds (**6a–f**) possessing piperazine and 1,4-benzodioxan moieties (Scheme 1). Spectral analyses using ESI mass spectrometry and ^{1}H NMR spectroscopy have been applied in order to affirm the structure of the synthesized molecules. Furthermore, the synthesized molecules have been subjected to *in vivo* anti-inflammatory evaluation.

2. Experimental

2. 1. Physical Measurements and Materials

Reagents and solvents used in this study were analytical grade and purchased commercially from Aladdin Industrial Corporation (China). ^{1}H NMR spectra were measured on a Bruker AM 500 spectrometer. Mass spectra were determined with an Autoflex II TM instrument for ESI-MS. Elemental analyses were performed on a Perkin-Elmer model 2400 analyzer. The intermediate 5-(2,3-dihydrobenzo[*b*][1,4]dioxin-7-yl)-1,3,4-oxadiazole-2-thiol (**4**) was synthesized according to the literature method.[23,24]

2. 2. General Procedure for the Synthesis of Target Compounds 6a–f

To a solution of a substitued phenylpiperazines (6.0 mmol) in CH_2Cl_2 (30 mL) containing triethylamine (1

mL), chloroacetyl chloride (0.48 mL, 6.0 mmol) was added dropwise with stirring in ice water bath. Stirring was continued for 5 h and the reaction mixture was washed with 10% NaOH solution (2 × 5 mL). The organic layer was collected. After drying with anhydrous Na_2SO_4, the solvent was removed in vacuo to yield the intermediate **5a–f**.

Oxadiazole derivative **4** (0.24 g, 1.0 mmol) and KOH (0.056 g, 1.0 mmol) dissolved in CH_3OH (20 mL) was treated with chloro derivatives **5a–f** (1.0 mmol). The mixture was stirred at room temperature about 4 h until the solid was precipitated. The solids **6a–f** were filtered and purified by recrystallization from MeOH.

2-(5-(2,3-Dihydrobenzo[*b*][1,4]dioxin-7-yl)-1,3,4-oxadiazol-2-ylthio)-1-(4-(2-methoxyphenyl)piperazin-1-yl)ethanone (**6a**). White powder, 0.354 g, yield 75.5%, mp: 171.0–172.5 °C. ^{1}H NMR (400 MHz, $CDCl_3$) δ 3.08 (t, 2H, CH_2), 3.13 (t, 2H, CH_2), 3.78 (t, 2H, CH_2), 3.86 (t, 2H, CH_2), 3.89 (s, 2H, OCH_3), 4.29–4.33 (m, 4H, OCH_2CH_2O), 4.43 (s, 2H, SCH_2), 6.89–7.08 (m, 5H, ArH), 7.49–7.52 (m, 2H, ArH). ESI-MS: 959.33 ([2M+Na]$^+$). Anal. Calcd for $C_{23}H_{24}N_4O_5S$: C, 58.96; H, 5.16; N, 11.96. Found: C, 59.15; H, 5.13; N, 12.01%.

2-(5-(2,3-Dihydrobenzo[*b*][1,4]dioxin-7-yl)-1,3,4-oxadiazol-2-ylthio)-1-(4-(3-methoxyphenyl)piperazin-1-yl)ethanone (**6b**). White powder, 0.367 g, yield 78.3%, mp: 158.1–159.4 °C. ^{1}H NMR (400 MHz, $CDCl_3$) δ 3.16 (t, 2H, CH_2), 3.29 (t, 2H, CH_2), 3.81 (s, 5H, CH_2, OCH_3), 3.88 (t, 2H, CH_2), 4.29–4.34 (m, 4H, OCH_2CH_2O), 4.39 (s, 2H, SCH_2), 6.50–6.59 (m, 3H, ArH), 6.95 (d, 1H, ArH), 7.21 (t, 1H, ArH), 7.48–7.52 (m, 2H, ArH). ESI-MS: 491.33 ([M+Na]$^+$). Anal.Calcd for $C_{23}H_{24}N_4O_5S$: C, 58.96; H, 5.16; N, 11.96. Found: C, 58.78; H, 5.14; N, 11.98%.

2-(5-(2,3-Dihydrobenzo[*b*][1,4]dioxin-7-yl)-1,3,4-oxadiazol-2-ylthio)-1-(4-(4-methoxyphenyl)piperazin-1-yl)ethanone (**6c**). White powder, 0.358 g, yield 76.4%, mp: 194.2–196.3 °C. ^{1}H NMR (400MHz, $CDCl_3$) δ 3.07(t, 2H, CH_2), 3.12 (t, 2H, CH_2), 3.75 (t, 2H, CH_2), 3.78(s, 3H, OCH_3), 3.82 (t, 2H, CH_2), 4.29–4.34 (m, 4H, OCH_2CH_2O), 4.41 (s, 2H, SCH_2), 6.84–6.96 (m, 5H, ArH), 7.48–7.52 (m, 2H, ArH). ESI-MS: 491.25 ([M+Na]$^+$). Anal. Calcd for $C_{23}H_{24}N_4O_5S$: C, 58.96; H, 5.16; N, 11.96. Found: C, 59.20; H, 5.14; N, 11.99%.

2-(5-(2,3-Dihydrobenzo[*b*][1,4]dioxin-7-yl)-1,3,4-oxadiazol-2-ylthio)-1-(4-(2-chlorophenyl)piperazin-1-yl) ethanone (**6d**). Yellow crystals suitable for X-ray diffraction were obtained from evaporation of a solution of **6d** in dichloromethane/methanol solution. Brown powder, 0.308 g, yield 65.2%, mp: 173.1–174.6 °C. ^{1}H NMR (400 MHz, $CDCl_3$) δ 3.13 (t, 2H, CH_2), 3.15 (t, 2H, CH_2), 3.81 (t, Hz, 2H, CH_2), 3.84 (t, 2H, CH_2), 4.31–4.35 (m, 4H, OCH_2CH_2O), 4.44 (s, 2H, SCH_2), 6.97 (d, 2H, ArH), 7.04–7.06 (m, 2H, ArH), 7.41 (dd, 1H, ArH), 7.51–7.54 (m, 2H, ArH). ESI-MS: 495.17 ([M+Na]$^+$). Anal. Calcd for $C_{22}H_{21}ClN_4O_4S$: C, 55.87; H, 4.48; N, 11.85. Found: C, 56.09; H, 4.46; N, 11.90%.

2-(5-(2,3-Dihydrobenzo[*b*][1,4]dioxin-7-yl)-1,3,4-oxadiazol-2-ylthio)-1-(4-(3-chlorophenyl)piperazin-1-yl) ethanone (**6e**). White powder, 0.376 g, yield 79.5%, mp: 191.8–193.1 °C. ^{1}H NMR (400 MHz, $CDCl_3$) δ 3.22 (t, 2H, CH_2), 3.34 (s, 2H, CH_2), 3.89 (s, 2H, CH_2), 3.84 (s, 2H, CH_2), 4.32–4.36 (m, 4H, OCH_2CH_2O), 4.40 (s, 2H, SCH_2), 6.94–7.01 (m, 4H, ArH), 7.24 (t, 1H, ArH), 7.24 (m, 2H, ArH). ESI-MS: 495.25 ([M+Na]$^+$). Anal. Calcd for $C_{22}H_{21}ClN_4O_4S$: C, 55.87; H, 4.48; N, 11.85. Found: C, 56.03; H, 4.45; N, 11.91%.

2-(5-(2,3-Dihydrobenzo[*b*][1,4]dioxin-7-yl)-1,3,4-oxadiazol-2-ylthio)-1-(4-(4- chlorophenyl)piperazin-1-yl) ethanone (**6f**). White powder, 0.359 g, yield 76.1%, mp: 278.2–279.6 °C. ^{1}H NMR data for **6f** is unattainable because of its low solubility. ESI-MS: 495.25 ([2M+Na]$^+$). Anal. Calcd for $C_{22}H_{21}ClN_4O_4S$: C, 55.87; H, 4.48; N, 11.85. Found: C, 56.05; H, 4.46; N, 11.90%.

2. 3. Determination of Crystal Structure for 6d

Crystal diffraction data for compound **6d** were collected on a Bruker SMART APEX CCD-based diffractometer (Mo Kα radiation, λ = 0.71073 Å) at 298 K. Multi-scan absorption corrections were applied by SADABS.[25] The structures were solved by the directed method followed by

Table 1. Crystallographic data for **6d**.

	6d
Empirical formula	$C_{22}H_{21}ClN_4O_4S$
M_r	472.94
crystsyst	Monoclinic
Space group	$P2_1/c$
a (Å)	18.2038(19)
b (Å)	8.0092(8)
c (Å)	15.4024(16)
α (°)	90.00
β (°)	107.112(3)
γ (°)	90.00
V (Å^3)	2146.2(4)
Z	4
ρ_c (g cm^{-3})	1.464
F(000)	984
T / K	298(2)
μ(Mo-Kα)/ mm^{-1}	0.314
Data / param. / restr.	5257 /289 / 0
GOF (F^2)	1.037
R_1[a], [b]wR_2 ($I>2\sigma(I)$)	0.0634 / 0.1475
Large diff. peak / hole (e Å^{-3})	0.514 / –0.482

[a] $R_1 = \Sigma||C| - |F_c||/\Sigma F_o|$. [b] $wR_2 = [\Sigma w(F_o^2 - F_c^2)^2/\Sigma w(F_o^2)]^{1/2}$

Fourier syntheses. Structure refinement was performed by full-matrix least-squares procedures using SHELXL-97 program package.[26] Non-hydrogen atoms were refined using anisotropic thermal parameters. Hydrogen atoms were placed in their geometrically idealized positions and constrained to ride on their parent atoms. Details of crystallographic parameters, data collection, and refinements are summarized in Table 1. Relevant bond distances and bond angles are given in Table 2.

2. 4. *In vivo* Anti-Inflammatory Activities in Ear Edema

The animal studies were conducted according to the guideline issued by the State Food and Drug Administration (SFDA) of China. All experimental protocols were approved by the Animal Ethics Committee of Pingdingshan University. All efforts were made to minimize animal suffering. The anti-inflammatory activity was evaluated using *in vivo para*-xylene-induced mice ear-swelling model on Kunming mice,[18] 35–40 days old and weighing 18–22 g, supplied by Jinan Pengyue Experimental Animal Breeding Company. Kunming mice were divided into eight groups of eight each. Group I, the control, comprised of animals treated with vehicle (0.5% CMC, 10 mL/kg), and groups II–VIII were dosage groups. Group II was treated with standard reference drug diclofenac (20 mg/kg), groups III–VIII were treated with target compounds **6a**–**f** (30 mg/kg), respectively. One hour later, ear swelling was induced by smearing 50 μL *para*-xylene to each side of the right ears, the left ear served as a control. After 1 hour, the mice were sacrificed, and both ears at the same position were removed using a 6 mm diameter punch. Swelling degree and swelling inhibition were calculated according to the following formula:

Swelling degree (mg) = weight of right ear (mg) – weight of left ear (mg)

Swelling inhibition (%) = (average swelling degree of control group – average swelling degree of dosage group) / average swelling degree of control group × 100%

3. Results and Discussion

3. 1. Chemistry of Compounds 6a–f

Appropriate 2-chloro-1-(4-phenylpiperazin-1-yl) ethanone derivatives **5** were reacted with 5-(2,3-dihydrobenzo[*b*][1,4]dioxin-7-yl)-1,3,4-oxadiazole-2-thiol **4** in CH_3OH/KOH solution *via* nucleophilic substitution reaction to furnish the respective target compounds **6a**–**f** (Scheme 1). The structures of **6a**–**f** were established by elemental and ^{1}H NMR and electrospray ionization mass spectrometry. In the ^{1}H NMR spectra of **6a**–**e**, the protons of the piperazin ring resonated as four triplets appearing at δ 3.07–3.88 ppm. The multiplet corresponding to four protons characteristic of the –OCH_2CH_2– group was observed at δ 4.29–4.35 ppm. The –SCH_2– protons appeared as a sharp singlet around δ 4.39 ppm. The protons of the substituted phenyl ring resulted in the formation of the resonance signal at δ 6.94–7.54 ppm. The methoxy protons of **6a**–**c** appeared as a singlet at 3.78–3.89 ppm. The positive ion electrospray mass spectra of these compounds showed full abundance of the parent peak which corresponds to $[M+Na)]^+$ or $[2M+Na)]^+$.

3. 2. Crystal Structure

Table 2. Selected bond distances (Å) and angles (°) for **6d**.

C(1)–O(1)	1.439(3)	C(1)–C(2)	1.477(4)
C(2)–O(2)	1.431(3)	C(6)–C(9)	1.453(3)
C(9)–N(1)	1.280(3)	C(9)–O(3)	1.364(3)
N(1)–N(2)	1.417(3)	C(10)–N(2)	1.286(3)
C(10)–O(3)	1.353(3)	C(10)–S(1)	1.734(3)
C(11)–S(1)	1.805(3)	C(12)–N(3)	1.348(3)
O(1)–C(1)–C(2)	111.0(2)	O(2)–C(2)–C(1)	110.6(2)
C(3)–O(1)–C(1)	114.1(2)	C(8)–O(2)–C(2)	113.0(2)
N(1)–C(9)–C(6)	130.3(2)	N(2)–C(10)–S(1)	131.8(2)
C(10)–S(1)–C(11)	96.82(12)	N(3)–C(12)–C(11)	117.6(2)

Yellow crystals of **6d** suitable for X-ray structure analysis were obtained by slow evaporation of a mixture of dichloromethane and methanol. X-ray single-crystal diffraction reveals that compound **6d** crystallizes in monoclinic $P2_1/c$ space group. As shown in Figure 2, **6d** has a nonplanar chair-like conformation, the dihedral angle between 2-chlorobenzene ring and piperazine ring being 49.710(78)°; meanwhile the dihedral angle between 2-chlorobenzene ring and oxadiazole ring is 75.512(86)°. The piperazine ring in **6d** has a classical chair conformation.

3. 3. *In vivo* Anti-Inflammatory Activities

The anti-inflammatory activities of the synthesized piperazine derivatives **6a**–**f** were tested using *in vivo para*-xylene-induced mice ear-swelling model. All the target compounds were adminstered at a dose of 30 mg/kg and diclofenac (20 mg/kg) was used as the reference drugs. The results show that compounds **6a**, **6c**, **6d**, and **6f** exhibited significant anti-inflamatory activities ($p < 0.01$) (Table 3). In the present assay, compound **6a** bearing methoxy substituent at the *ortho* position of the phenyl piperazine showed the most effective anti-inflamatory activity; it was 1.3 times more active than diclofenac (inhibition values 68.02 *vs.* 52.03%). Preliminary structure–activity relationship analysis revealed that: (i) the substituent at different positions led to different activity, and the potency order was *ortho* > *para* > *meta*; (ii) in view of the comparison of

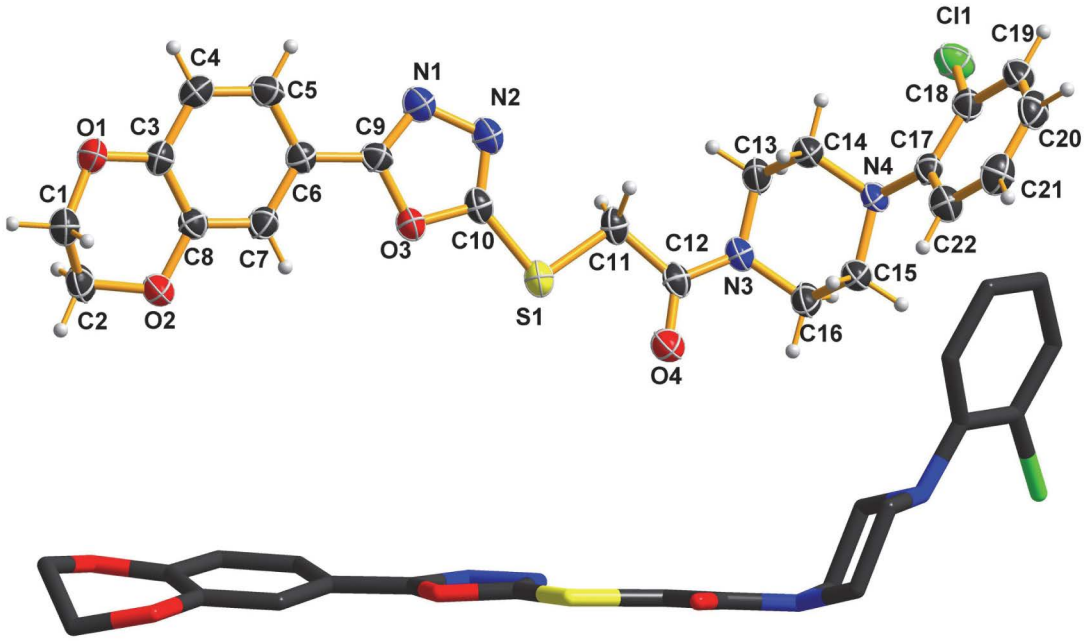

Figure 2. Molecular structure of **6d** (50% probability displacement ellipsoids), front and side views are presented.

the structures of compounds **6a** with **6d**, **6b** with **6e**, and **6c** with **6f**, the *in vivo* anti-inflammatory activities were **6a** > **6d**, **6b** > **6e**, and **6c** > **6f**. These results indicate that substitution at phenyl-piperazine with electron-donating methoxy group shows advantage over electron-withdrawing chlorine group at the same position, thus improving compound's anti-inflammatory activity. Meanwhile compared with the chalcone derivatives containing aryl-piperazine reported earlier, most of the compounds in the present assay were found to display enhanced *in vivo* anti-inflammatory activity.[18]

Table 3. Anti-inflammatory activities of the synthesized compounds **6a**–**f**.

Compound	Swelling degree (mg)	Inhibition (%)
6a	4.34 ± 0.24[a]	68.02
6b	6.81 ± 0.54[a]	49.82
6c	5.83 ± 0.74[a]	57.04
6d	6.36 ± 0.45[a]	59.15
6e	10.95 ± 0.31[a]	19.31
6f	7.12 ± 1.03[a]	52.47
Diclofenac	6.51 ± 0.95[a]	52.03
Control	13.57 ± 1.09	—

[a] Multiple comparison test $p < 0.01$ as compared to control

4. Conclusions

To sum up, a series of six piperazine derivatives **6a**–**f** containing 1,4-benzodioxan moiety were synthesized and screened primarily for *in vivo* anti-inflammatory activities potential in ear edema. The substituent at different positions led to different activity. Most of the synthetic compounds emerged as effective *in vivo* anti-inflammatory agents, demonstrating swelling inhibition even better than the reference control, diclofenac. Compound **6a** containing methoxy substituent at the *ortho* position of the phenyl piperazine displayed the most potent anti-inflammatory activity among the synthesized compounds. Our findings might provide information on developing potentially new and safe anti-inflammatory agents.

5. Supplementary Material

Crystallographic data (excluding structure factors) for the structural analysis have been deposited with the Cambridge Crystallographic Data Center as supplementary publication Nos. CCDC 1882249 (**6d**). Copies of the data can be obtained free of charge *via* www.ccdc.ac.uk/conts/retrieving.html (or from The Director, CCDC, 12 Union Road, Cambridge CB2 1EZ, UK, Fax: +44-1223-336-033. E-mail: deposit@ccdc.cam.ac.uk).

6. Acknowledgment

This work was supported by the National Natural Science Foundation of China (21301108).

7. References

1. L. Marín-Ocampo, L. A. Veloza, R. Abonia, J. C. Sepúlveda-Arias, *Eur. J. Med. Chem.* **2019**, *162*, 435–447.

DOI:10.1016/j.ejmech.2018.11.027
2. O. Kolomoets, O. Voskoboynik, O. Antypenko, G. Berest, I. Nosulenko, V. Palchikov, O. Karpenko, S. Kovalenko, *Acta Chim. Slov.* **2017**, *64*, 902–910.
3. D. P. B. Silva, I. F. Florentinoa, L. P. Oliveira, R. C. Lino, P. M. Galdino, R. Menegatti, E. A. Costa, *Pharmacol. Biochem. Be.* **2015**, *137*, 86–92. **DOI:**10.1016/j.pbb.2015.08.008
4. N. M. Davies, K. E. Anderson, *Clin. Pharmacokinet.* **1997**, *33*, 184–213. **DOI:**10.2165/00003088-199733030-00003
5. S. S. Fatahala, M. A. Khedr, M. S. Mohamed, *Acta Chim. Slov.* **2017**, *64*, 865–876. **DOI:**10.17344/acsi.2017.3481
6. F. A. Ragab, N. M. A. Gawad, H. H. Georgey, M. F. Said, *Eur. J. Med. Chem.* **2013**, *63*, 645–654. **DOI:**10.1016/j.ejmech.2013.03.005
7. M. T. El Sayed, M. A. M. Sh. El-Sharief, E. S. Zarie, N. M. Morsy, A. R. Elsheakh, A. Voronkov, V. Berishvili, G. S. Hassan, *Bioorg. Med. Chem. Lett.* **2018**, *28*, 952–957. **DOI:**10.1016/j.bmcl.2018.01.043
8. M. Gökçe, S. Utku, E. Küpeli, *Eur. J. Med. Chem.* **2009**, *44*, 3760–3764. **DOI:**10.1016/j.ejmech.2009.04.048
9. P. M. Brooks, R. O. Day, *N. Engl. J. Med.* **1988**, *324*, 1716–1725.
10. J. Sun, S. Wang, G. H. Sheng, Z. M. Lian, H. Y. Liu, H. L. Zhu, *Bioorg. Med. Chem.* **2016**, *24*, 5626–5632. **DOI:**10.1016/j.bmc.2016.09.023
11. S. S. Fatahala, M. A. Khedr, M. S. Mohamed, *Acta Chim. Slov.* **2017**, *64*, 865–876. **DOI:**10.17344/acsi.2017.3481
12. Y. Ali, M. S. Alam, H. Hamid, A. Husain, A. Dhulap, S. Bano, C. Kharbanda, *Bioorg. Med. Chem. Lett.* **2017**, *27*, 1017–1025. **DOI:**10.1016/j.bmcl.2016.12.069
13. S. Bansal, M. Bala, S. K. Suthar, S. Choudhary, S. Bhattacharya, V. Bhardwaj, S. Singla, A.Joseph, *Eur. J. Med. Chem.* **2014**, *80*, 167–174. **DOI:**10.1016/j.ejmech.2014.04.045
14. R. R. R. Taylor, H. C. Twin, W. W. Wen, R. J. Mallot, A. J. Lough, S. D. Gray-Owen, R. A. Batey, *Tetrahedron* **2010**, *66*, 3370–3377. **DOI:**10.1016/j.tet.2010.02.046
15. A. Kamal, R. Ramu, V. Tekumalla, G. B. R. Khanna, M. S. Barkume, A. S. Juvekar, S. M. Zingde, *Bioorg. Med. Chem.* **2008**, *16*, 7218–7224. **DOI:**10.1016/j.bmc.2008.06.034
16. M. Taha, M. Irshad, S. Imran, S. Chigurupati, M. Selvaraj, F. Rahim, N. H. Ismail, F. Nawaz, K. M. Khan, *Eur. J. Med. Chem.* **2017**, *141*, 530–537. **DOI:**10.1016/j.ejmech.2017.10.028
17. G. Maertensa, O. M. Saavedraa, V. Vecea, M. A. V. Reyesa, S. Hocinea, E. Öneya, B. Goumentb, O. Mirguetb, A. Le Tiranb, P. Gloanecb, S. Hanessiana, *Bioorg. Med. Chem. Lett.* **2018**, *28*, 2627–2630.
18. J. F. Li, D. Li, Y. M. Xu, Z. B. Guo, X. Liu, H. Yang, L. C. Wu, L. S. Wang, *Bioorg. Med. Chem. Lett.* **2017**, *27*, 602–606.
19. Z. W. Mao, B. Liu, P. Zhu, L. J. Zhang, J. H. Zhu, L. Z. Wu, C. P. Wan, *Chin. J. Org. Chem.* **2018**, *38*, 2167–2173. **DOI:**10.6023/cjoc201802010
20. S. Kumar, N. Kumar, P. Roy, S. M. Sondhi, *Med. Chem. Res.* **2014**, *23*, 3953–3969. **DOI:**10.1016/j.bmc.2007.04.050
21. Y. Harrak, G. Rosell, G. Daidone, S. Plescia, D. Schillaci, M. D. Pujol, *Bioorg. Med. Chem.* **2007**, *15*, 4876–4890.
22. W. Quaglia; A. Piergentili, F. Del Bello, Y. Farande, M. Giannella, M. Pigini, G. Rafaiani, A. Carrieri, C. Amantini, R. Lucciarini, G. Santoni, E. Poggesi, A. Leonardi, *J. Med. Chem.* **2008**, *51*, 6359–6370. **DOI:**10.1021/jm800461k
23. L. Ma, Y. Xiao, C. Li, Z. L. Xie, D. D. Li, Y. T. Wang, H. T. Ma, H. L. Zhu, M. H. Wang, Y. H. Ye, *Bioorg. Med. Chem.* **2013**, *21*, 6763–6770. **DOI:**10.1016/j.bmc.2013.08.002
24. X. M. Zhang, M. Qiu, J. Sun, Y. B. Zhang, Y. S. Yang, X. L. Wang, J. F. Tang, H. L. Zhu, *Bioorg. Med. Chem.* **2011**, *19*, 6518–6524. **DOI:**10.1016/j.bmc.2011.08.013
25. G. M. Sheldrick, SADABS. Program for Empirical Absorption Correction of Area Detector, University of Göttingen, Germany, **1996**.
26. G. M. Sheldrick, *Acta Crystallogr.* **2008**, *A64*, 112–122. **DOI:**10.1107/S0108767307043930

Povzetek

Sintetizirali smo šest piperazinskih derivatov **6a**–**f**, ki vsebujejo 1,4-benzodioksanski fragment, ter jih karakterizirali z ^{1}H NMR, ESI-MS in elementno analizo. Strukturo produkta **6d** smo dodatno potrdili z rentgensko difrakcijsko analizo monokristala. Za vse nove spojine smo s pomočjo klasičnega *para*-ksilenskega testa otekanja ušes miši *in vivo* določili protivnetno aktivnost. Rezultati kažejo, da večina preiskovanih spojin izkazuje opazno protivnetno aktivnost, še posebej spojina **6a**, ki vsebuje *orto*-metoksi skupino na fenilpiperazinskem obroču, saj kaže najboljšo aktivnost izmed vseh pripravljenih spojin.

Scientific paper

Growth of Silver Nanoparticles Using Polythiocyanatohydroquinone in Aqueous Solution

Valentina A. Litvin,[1,*] Boris F. Minaev,[1,2] Rostislav L. Galagan,[1] Glib V. Baryshnikov[1,2] and Hans Ågren[2]

[1] *Department of Chemistry, Bohdan Khmelnitsky National University, Cherkassy, 18031, Ukraine*

[2] *Division of Theoretical Chemistry and Biology, School of Biotechnology, KTH Royal Institute of Technology, Stockholm, 10691, Sweden.*

[*] *Corresponding author: E-mail: litvin_valentina@ukr.net*

Received: 12-01-2018

Abstract

Motivated by evidence that silver nanoparticles have found numerous technological applications we have explored in this work utilization of polythiocyanatohydroquinone as a new efficient reducing and stabilizing agent for the preparation of such nanoparticles. The formation of silver nanoparticles has been confirmed by the UV–Vis spectroscopy, X-ray powder diffraction and by transmission electron microscopy. The potentiometric and spectroscopy kinetic measurements during the nanoparticles growth are also presented. Thermodynamic activation parameters for the silver nanoparticle formation have been determined from the reaction kinetic studies at variable temperatures. On the ground of observations using these techniques, a mechanism for silver nanoparticle growth has been proposed. The narrow size (20–40 nm) and spherical shape distribution of the fabricated nanoparticles together with the high stability of colloids for sedimentation provide a firm basis for applications of the polythiocyanatohydroquinone polymer as a reducing and stabilizing material for the metal nanoparticles preparation and storage.

Keywords: Silver nanoparticles; polythiocyanatohydroquinone; potentiometric study; spectrophotometric study; kinetics

1. Introduction

Silver nanoparticles (AgNPs) are of special interest because of their unique physicochemical properties, including optical, magnetic and electronic characteristics, catalytic activity and biological impact,[1–3] which make these particles applicable in a variety of technological areas in medicine, agriculture, environment, and industry.[4,5] The AgNPs have also a high potential as commercial nanomaterials in cosmetics and as effective antimicrobial agents.[1,6]

There are several methods proposed for fabrication of AgNPs, including chemical and physical approaches.[7–9] Among them, the chemical reduction of silver ions in the presence of a protecting agent, is the most common and useful approach. Special attention is often devoted to the choice of reducing and capping agents since the physicochemical properties of the AgNPs are strongly dependent on the incorporated capping agent species.[10–12] Organic polymers are in this context of especial interest because they can perform a reduction function while simultaneously being adsorbed on the nanoparticles surfaces thereby stabilizing them.[13–16]

In this report we present the first attempt to synthesize AgNPs by using polythiocyanatohydroquinone (PTHQ)[17] as a reducing and stabilizing agent with the aim to form the small size and highly distributed AgNPs. We present here kinetic investigations in order to predict the mechanism of the Ag^+-ions reduction by PTHQ.

2. Experimental

2. 1. Materials

All reagents (analytical-grade) were used as received from Sigma-Aldrich. De-ionized water (18 MΩ/cm) from a Millipore Milli-Q water purification system was used to prepare all aqueous solutions. The synthesis of PTHQ has been described previously.[17] Briefly, the PTHQ was synthesized by the three-stage synthesis. The 1,4-benzoquinone crystal was dissolved in the glacial acetic acid (GAA) and treated with the NH_4SCN salt in the GGA medium.

The forming benzene-1,4-diol and thiocyanogen at the same conditions produce next the *ortho*-substituted 2-thiocyanatobenzene-1,4-diol which polymerizes rapidly into the target PTHQ compound. The orange-brown PTHQ polymer was precipitated by water, filtered, washed and dried upon 80 °C.

2. 1. Preparation of silver nanoparticles using PTHQ

In a typical experiment, a 19.6 mg of PTHQ was dissolved in 1.1 ml 1M solution of NaOH and the volume was adjusted to 60 mL with distilled water. The flask with resulting mixed solution was placed in a thermostat water bath at 30 °C. Next, 3.0 mL 0.2 M $AgNO_3$ was added under vigorous stirring. The final concentrations in the mixture were 1.67 mM PTHQ, 18.3 mM NaOH, and 10 mM $AgNO_3$.

Characterization. UV-Visible spectra were recorded as a function of reaction time on Lambda 35 Perkin Elmer UV-Visible spectrophotometer in the range of 320–520 nm. Aliquots of silver colloid (0.2 mL) were diluted to 25 ml for the UV-Visible experiments. The X-ray powder diffraction (XRD) analyses were performed on a DRON-2 X-ray diffractometer (LOMO, Russia) with Fe Kα radiation (λ = 1.9360 Å) at a scanning speed of 0.01°/s over the 2θ range of 20–120°. Transmission electron microscopy (TEM) was carried out by using a JEOL microscope (JEM-200A, Japan) with the accelerating voltage 200 kV. Samples for TEM investigations were prepared by evaporation of products on the surface of carbon films. The TEM images were registered with the CE video camera. The size of the particle can be calculated by using the scale provided in the micrograph. Potentiometric study the process of Ag-NPs formation was carried out on ionomer EV-74 with electrode system containing a glass electrode of type ESL-63–07 and a silver electrode of type EVL-1M3. As a reference electrode was used silver-oxide half-cell. The FT-IR spectra of the samples were recorded on Perkin-Elmer spectrometer (SpectrumGX) with a resolution of 2 cm^{-1} over a scan range 4000–500 cm^{-1} using KBr pellet method.

Computational details. The structure of PTHQ active site in different oxidized forms has been optimized as oligomer at the density functional theory (DFT) level using the B3LYP[18,19] hybrid functional and the 6–31G(d)[20] basis set. The edge vacancies within –(C=N)– chain of the PTHQ polymer have been terminated by methyl groups in the oligomer model. We have also calculated the IR spectra for the studied species. All vibration frequencies were found to be real, which indicates the global minimum finding on the potential energy hypersurface. For the correct estimation of ionization potential (IP) values the polarizable continuum model (PCM)[21] with water as a solvent has been used in the optimization procedure. The final IP values have been evaluated using Koopmans approach as the energy of the highest occupied molecular orbital (HOMO) with the opposite sign (IP = – ε(HOMO)). All the calculations have been carried out using the Gaussian- 16 program package.[22]

3. Results and Discussion

Stable aqueous colloids of AgNPs were prepared by chemical reduction of Ag^+ ions using the PTHQ in the presence of NaOH. Due to the presences of phenolic group in the PTHQ structure[17] the former reduces the Ag^+ ions to Ag^0 atoms and are then adsorbed on the surface of the growing AgNPs. In the alkaline medium the chemosorbed PTHQ species and their partially oxidized products possess a large negative charge due to ionization of the hydroxyl and carboxyl groups. The repulsive forces prevent the aggregation of nanoparticles and provide stability of the colloidal system. The final colloids are stable and can be stored more the one year without aggregation.

X-ray diffraction (XRD) results. The formation of the nanocrystalline AgNPs has been confirmed by the XRD analysis (Figure 1). Strong peaks observed at 48.6°, 56.8°, 84.5°, 104.1° and 110.9°, corresponding to the (111), (200), (220), (311) and (222) Bragg's reflections that determine the face-centered-cubic (fcc) crystal structure of Ag-NPs. The broadening of the Bragg's peaks indicates the formation of Ag NPs. The XRD pattern thus shows that the

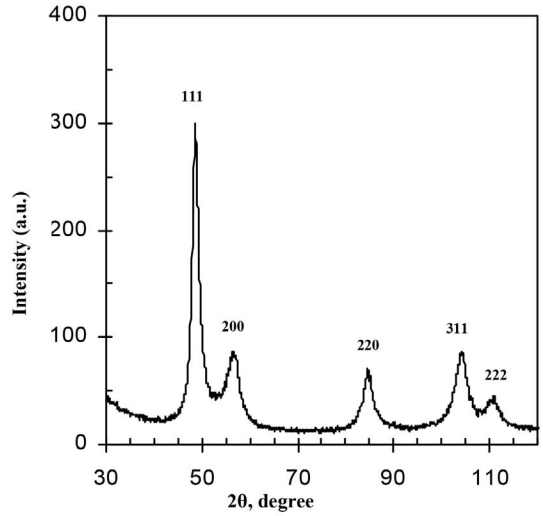

Fig. 1. XRD patterns of silver nanoparticles synthesized with PTHQ usage

Ag NPs formed by the reduction of Ag^+ ions by PTHQ polymer are of the crystalline nature. The average size of the Ag nanoparticles has been calculated from the XRD line width using the Debye-Scherrer equation[23] and was found to be equal 20.8 nm.

Transmission electron microscopy (TEM) study. TEM was used to determine the size and shape of the nanoparticles. The TEM images of the PTHQ, prepared

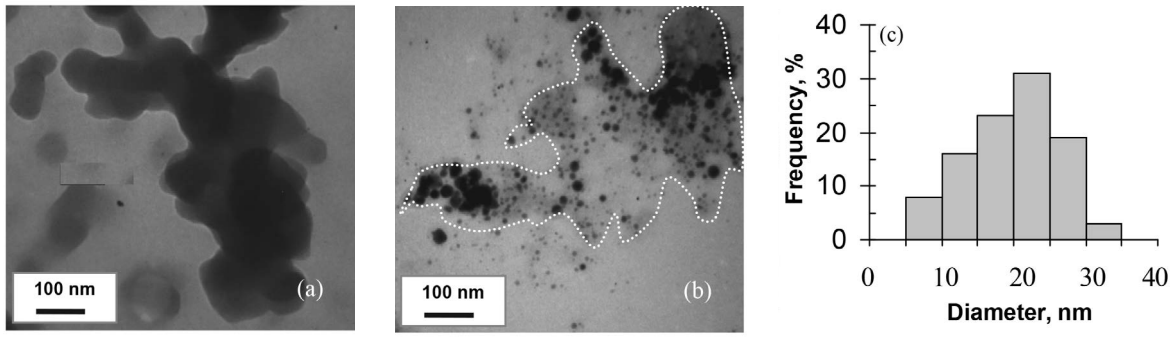

Fig. 2. The TEM images of PTHQ (a), AgNPs (b) and the corresponding size distribution histograms of AgNPs stabilized by PTHQ (c). The borders of the PTHQ globule are shown by the dotted line in part (b).

AgNPs are shown in the Fig. 2. TEM images show that they have spherical shape. A particle size distribution histogram determined from TEM is shown in Fig. 2c. The average AgNPs size is 19.8 nm. The particle sizes calculated from the XRD pattern have been found to vary within 5% of those obtained from TEM studies. The main difference of these hydrosols from similar nanosystems received with the use of other reducers, in particular the humic substances,[15] is that the metal nanoparticles are fixed on the globule of the polymer.

Study of the silver nanoparticles formation by UV–Vis spectroscopy. The most popular method applied for the measurements of the kinetics of nanocluster formation in solution is UV-Visible spectroscopy since the sharp surface plasmon resonance band with maximum at 400 nm is a distinctive feature of the silver colloids.[24,25] Evolution of the absorption spectrum of the silver colloidal solution during reduction of the Ag^+ ions by PTHQ at 30 °C is shown in Figure 3a. For the early stages of clusters formation, the broad absorption band near 480 nm appeared which indicates the formation of small Ag particles on the surface of the large Ag_2O particles. That position of this band absorption is the result in electronic interactions between the two types of materials because Ag_2O has semiconducting properties. Research by the authors[26] has explained this fact by electron density transfer from the pure metal to the metal oxide nanoparticles when the small silver particles are formed on the surface of the n-type Ag_2O semiconductor. At longer reaction times, the absorption band shifts continuously to shorter wavelengths. The increase of absorption maximum intensity over the time is connected with continuation of the Ag^+ ions reduction process and with the increase of the number of the colloidal particles. The final surface plasmon resonance band has been observed at 400 nm (Figure 3a).

To investigate the reaction kinetics of the AgNPs formation, the absorbance at 400 nm has been plotted against the reaction time (Figure 3b). The visible absorbance of the product can be observed immediately after the mixing of the reagents and rises rapidly at the beginning of the reaction. Then absorbance reaches a plateau, which indicates the reaction completion (Figure 3b).

Proposed mechanism of silver nanoparticles formation. Evidently, at the initial stage of the Ag^+ cations reaction with the OH^- anions in the presence of PTHQ the formation of an Ag_2O microphase occurs. However, the

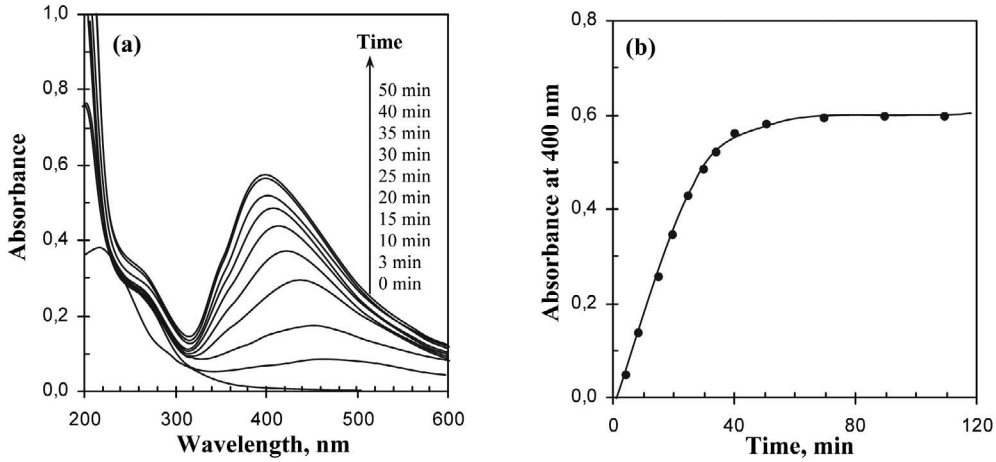

Fig. 3. The UV–Visible spectra of silver nanoparticles as a function of time (a); Absorbance at 400 nm *versus* time plot for the silver nanoparticles formation (b)

detection of Ag_2O microphase in similar systems by X-ray diffraction is extremely difficult, no mater how fast the separation of the precipitate from the solution is.[27] Huang et al.[26] have shown that it might be possible to capture some Ag_2O if the reaction was performed at a very low temperature (–45 °C).

The polymer chemisorbed on the Ag_2O particles in the alkaline environment has a negative charge due to ionization of the phenolic group, something that provides stabilization of nanoparticles. In the system "Ag_2O – organic reducer" few simultaneous processes can take place. The first of them is a dissolution of Ag_2O with the subsequent dissociation of AgOH:

$$Ag_2O + H_2O = 2AgOH \quad (1)$$

$$AgOH \Leftrightarrow Ag^+ + OH^- \quad (2)$$

The equilibrium within the Ag_2O – H_2O system can be considered as a metallo-buffer for the Ag^+ ions, and where the concentration of the latter shows a hyperbolic function of the OH^- ion concentration. Thus, in water suspension of the Ag_2O species under intense stirring condition, the Ag^+ ion concentration is expected to be constant and equal to $1.39 \cdot 10^{-4}$ M (the solubility of Ag_2O is $1.95 \cdot 10^{-8}$).

At the same time, the other important process of the NPs growth includes interaction of PTHQ with Ag^+ and OH^- ions, which results in the metal atom formation being aggregated into the nanoparticles. The major reducing groups in the structure of the PTHQ polymer are the phenolic groups, which are oxidized to the quinone structures. Thus, *in situ*-generated Ag_2O nanocrystallites act as heterogeneous nucleation centers. The reduction of Ag^+ ions proceeds according to the following scheme:

The reduction reaction will proceed in the system until the whole Ag_2O microphase is dissolved or the reductive possibilities of the organic reducer will be exhausted. However, during the synthesis the molar ratio "Ag^+: elementary link PTHQ" (r) did not exceed 6. If $r > 6$ a formation of a black deposit already in the course of the nanosystem synthesis was observed. Apparently, at excess of the ratio, the polymer will not have enough phenolic groups for delivery of a stabilizing charge to the complex particles $[Ag@PTOH]^{x-}$ according to Eq. 4 (Scheme 1).

From this equation, it is clear, that the reductive ability of the aromatic core was practically exhausted, and that there is no possibility of formation of a sufficient amount of ionized hydroxyl groups for the maintenance of a negative charge of the complex. However, from the scheme 1 the possibility of a stable nanosystem formation at $r = 8$ follows, but the real ratio r is much lower because of the presence of the ditiocianhydroquinone bridges in the PTHQ structure.

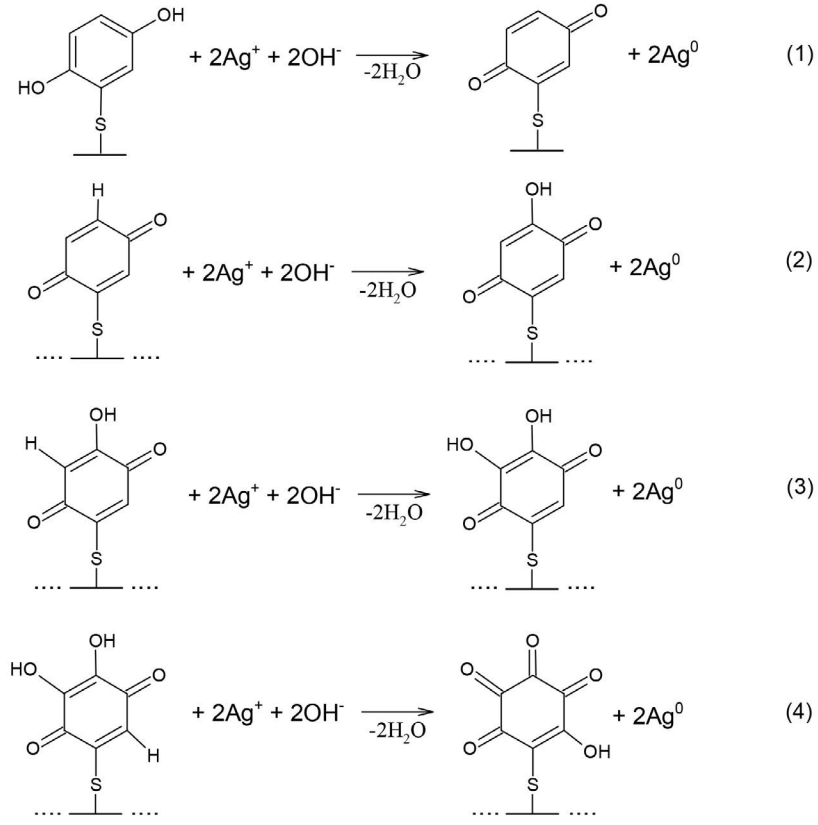

Scheme 1. Proposed mechanism for the reduction of Ag^+ ions by PTHQ in alkaline media

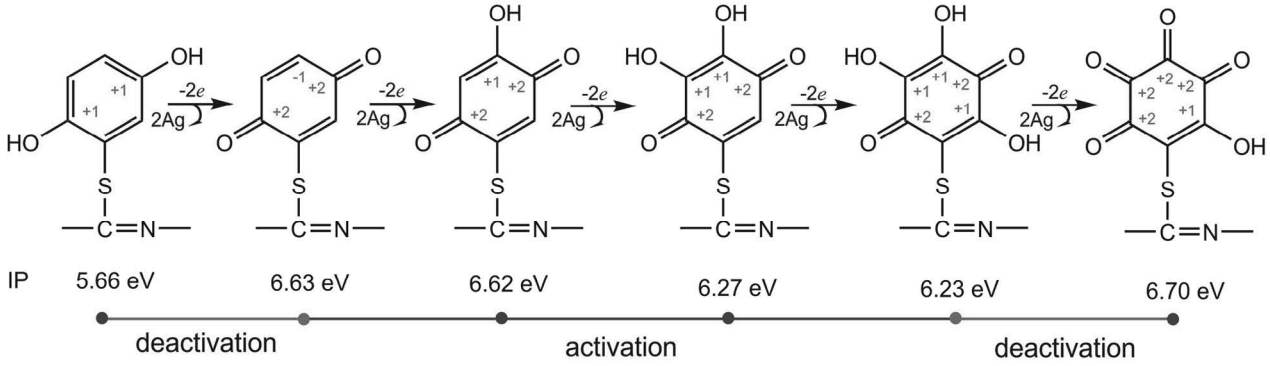

Scheme 2. The reductive ability of PTHQ active site upon the gradual rising of silver cluster

In order to explain how the reductive ability of PTHQ changes with the AgNPs growing we have performed the quantum-chemical estimations for ionization potentials of the PTHQ active site in different oxidation states. As can be seen from Scheme 2 the ionization potential of the PTHQ active site increases strongly (5.66 vs. 6.63 eV) right after the first stage when two hydroxyl groups transform into carbonyl groups. Actually, this stage provides the deactivation of PTHQ for the next reduction activity. However, assuming the possible next oxidation steps of the quinone ring in Scheme 1 we have found that the corresponding ionization potential (IP) decreases gradually with the appearance of OH groups (6.63 eV for quinone ring *vs.* 6.23 eV for trihydroxyquinone moiety), i.e. the reductive ability of PTHQ increases with the addition of new OH groups. We consider these stages as the activation of PTHQ for reductive activity. Finally, the oxidation of trihydroxyquinone ring into the tetra-carbonyl form provides a complete deactivation of PTHQ active site due to its final IP increase and the complete electronic exhaustion.

Concluding shortly, we should note that these computational findings additionally approve the proposed mechanism (scheme 1) for the reduction of Ag^+ ions by PTHQ in alkaline media. Moreover, the tendency for the IP changes upon PTHQ oxidation sequence is in a good agreement with the experimental kinetic measurements data for the silver cation reduction.

Potentiometric study of the kinetics and mechansim of the silver nanoparticles formation. For real-time control of the Ag^+ ion reduction process, we have used a potentiometric method, as ion-selective electrodes (ISE) responds continuously and instantaneously to the changes of the silver ion concentration.[28,29] The potentiometric method for studying the chemical reaction kinetic is based on measurements and interpretation of the time dependence of the redox potential for the indicator electrode reversible to the particles participating in the studied reaction. A use of this dependence in the kinetic studies is only possible if the rate of the establishment of the electrode equilibrium is higher than the rate of introduction of all others equilibriums in the system with the potential-determined particles. As the Ag^+/Ag system is one of the most prompt redox systems we can use the potentiometric method in our studies. Since the signal output of the ISE corresponds to the logarithm of the concentration of the solute ions, such a direct potentiometric control of the depleted metal ions provides additional information on the nanoparticle formation, which is not accessible by other techniques. In our work, we have used a simple silver electrode instead of ISE since the studied system does not contain any perturbing ions. The silver electrode is particularly useful for gaining information about the kinetic processes at later stages of the nanoparticle growth, in which case the solute ions become dilute and the concentration changes are much more easily discerned compared to other methods. The potentiometric curves of pAg as a function of time for the process of the AgNPs formation using PTHQ at different temperatures are shown in Fig. 4. The figure indicates a three-step growth process (*ab*; *bc* and *cd* site).

Let us consider the correspondence of different regions on the potentiometric curve (Fig. 4) to the kinetic stages of the process proposed in Scheme 1. The decrease of the pAg curve (***ab*** site*)* indicates the balance displace-

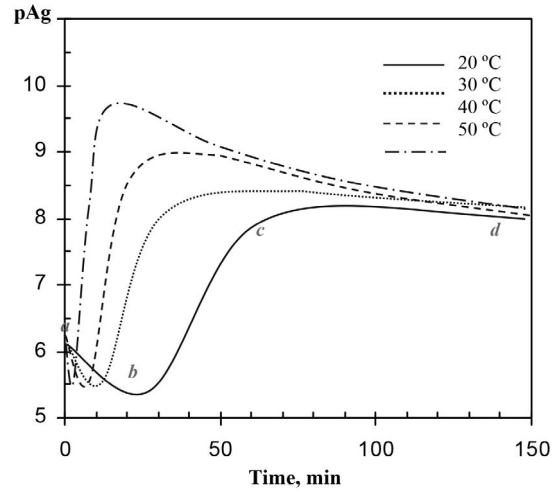

Fig. 4. The pAg potentiometric curves as a function of time for silver nanoparticles formation process at different temperatures

ment in Ag_2O dissociation as a result of a decrease in the concentration of the OH^- ions which are also the reagents of the given reaction.

As the reaction of silver ion reduction occurs on the surface of the Ag_2O particles (heterogeneous process), the rate of reaction does not depend on the Ag_2O concentration in solution. Thus, this stage is described by a zero-order kinetics in respect to Ag_2O and the rate constant (k_0) of the AgNPs formation at the initial stage can be found from the equation: $k_0 = dn(Ag_2O)/dt$, where $n(Ag_2O)$ – is an amount of the Ag_2O microphase (mole); t – time of the Ag_2O microphase existence in the system (s); k_0 – zero-order rate constant (mole · s^{-1}).

At the point ***b*** of the pAg curve the whole Ag_2O microphase is dissolved and begins the growth of pAg values according to the linear law that specifies the first order reaction with respect to Ag^+-ion. The rate constant at this stage can be found from the following equation: $k_1 = F/RT \cdot (\partial E/\partial t)_{T\ OH^-,\ [Ag_n^0]}$, where k_1 – is the first-order rate constant (s^{-1}), F – is the Faraday constant ($9.65 \cdot 10^4$ coulomb/mole); R – the universal gas constant (8.314 $JK^{-1}mol^{-1}$), T – temperature (K); $(\partial E/\partial t)_{T,\ OH^-,\ [Ag_n^0]}$ – the change of the equilibrium potential E of the Ag-electrode during the time t. The value of the derivative $(\partial E/\partial t)_{T,\ OH^-,\ [Ag_n^0]}$ was determined from the measurements of the slopes of the linear parts of the pAg plots versus time (***bc*** site, Fig. 5 A), taking into account that $E = 2.303 \cdot (RT/F) \cdot \Delta pAg$.

At a point ***c*** the pAg curve passes through a maximum. Some decrease of the pAg values (***cd*** site) corresponds to an increase in the concentration of the Ag^+ ions due to oxidation of the AgNPs by air oxygen[30,31] according to the equation:

$$4Ag^0 + O_2 + 4H^+ \rightarrow 4Ag^+ + 2H_2O. \quad (5)$$

The process described by Eq. (5) was controlled by N_2 barbotation through the reaction solvent. In this case the pAg potentiometric curve after the point ***c*** in Fig. 4 does not go down. This is because the AgNPs are quite small and very reactive (the surface/volume ratio is great) in comparison with the massive silver metal.

On the ground of potentiometric curves it is possible to make a conclusion that the formation mechanism of the AgNPs with the use of PTHQ is similar to those mechanisms which use the synthetic humic substances;[30] in particular: 1) a fast formation of the Ag_2O microphase in the system after mixing of reagents; 2) reduction of silver ions on the surface of the Ag_2O particles according to the zero-order kinetics; 3) growth of AgNPs due to reduction of silver ions from solution on a surface of already generated

Table 1. Dependence of the rate constants at various temperatures for different stages of silver nanoparticles formation using PTHQ

Initial stage zero-order rate constants $k_0 \cdot 10^3$ (mole · s^{-1})				Later stage first-order rate constants $k_1 \cdot 10^3$ (s^{-1})			
293 K	303 K	313 K	323 K	293 K	303 K	313 K	323 K
0.25	0.60	0.92	1.20	1.62	3.83	5.64	7.50

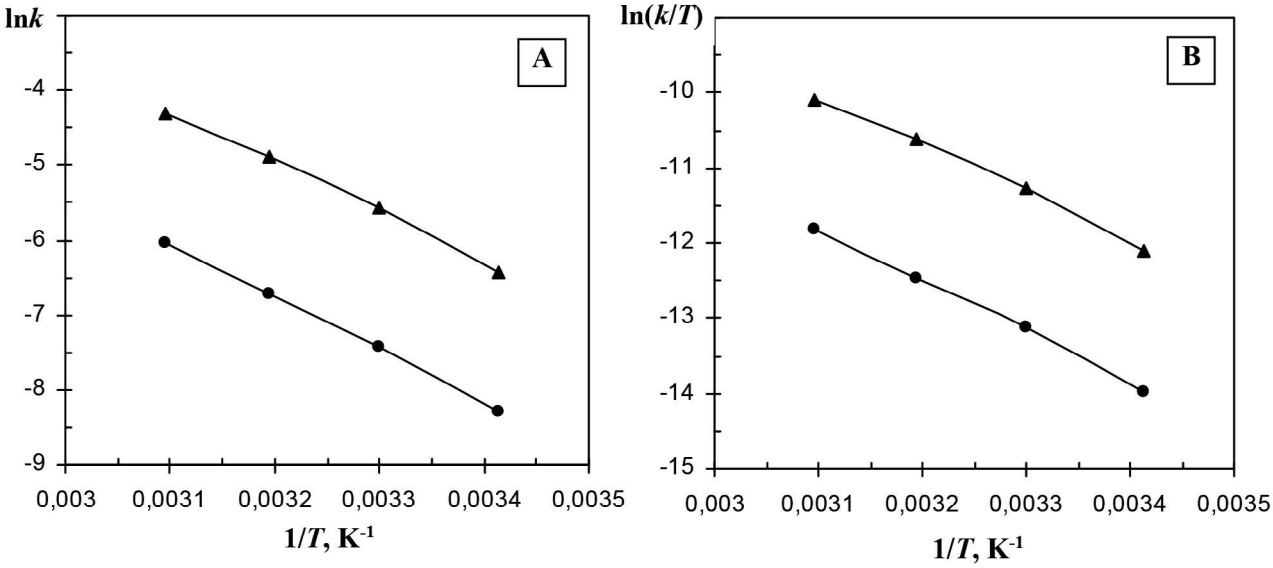

Fig. 5. The Arrhenius (A) and Eyring (B) plots of the silver nanoparticles formation for the initial (•) and later (▲) stages using the PTHQ reagent

nuclei of AgNPs according to the first order kinetics after the Ag_2O microphase dissolution.

The temperature influence on the reaction rate was also studied. Calculated values of the zero-order rate constant (k_0) for the initial stage of nanoparticles formation (before full dissolution of Ag_2O) and the first-order rate constants (k_1) at the later stages of the nanoparticle growth for different temperature are presented in Table 1. It is possible to observe that the reaction rate increases with temperature. No extra yield is obtained at higher temperature. The data suggest that the process can easily be promoted by the thermal activation mechanism.

Since the reduction of Ag^+ ions occurs at the surface of Ag^0 nuclei in the contact place of metal and silver oxide solid phases, the reaction rate does not depend on Ag_2O concentration in the solvent. Thus, the reaction rate constant of the Ag_2O depletion for the Ag NPs production at this initial stage is determined by the zero kinetic order according to equation $k_0 = dn(Ag_2O)/dt$

Finally, from the Arrhenius Equation ($k = Ae^{-Ea/RT}$) and the Eyring Equation plots (Fig. 5), the activation parameters, e.g. the activation energy (E_a), the enthalpy ($H^{\#}$) and entropy ($S^{\#}$) of activation, were calculated.

The estimated values of these parameters for different stage of silver nanoparticle formation with the use of PTHQ as reducing and stabilizing agent are presented in Table 2.

The Ag_2O suspension is the source of the Ag^+ ions at the initial stage. The rise of Ag^+ ion concentration in Fig. 4 (***ab*** site), being determined by the decrease in concentration of the OH^- ions working also as reagents in the reaction of Ag^+ with PTHQ polymer, is an important prerequisite for the upcoming activation process. The latter includes reduction of the ions with the simultaneous growth of nanoparticles. The organic polymer is a reservoir of electrons for the reduction processes, which is rather complicated; the Ag^+ ions at the first stage represent large rising concentration. The activation energy spent for electron transfer from PTHQ polymer (all averaged processes presented in Scheme 1) includes C-O and O-H bond cleavage with simultaneous ionization and subsequent electron attachment.

The similar processes occur at the later stage but in the limit of a decreased Ag^+ ion concentration; the reaction strongly depends on this concentration (first order reaction). That is why the activation energies are quite similar for both stages (Table 2). The small difference can be connected with the fact that electronic resources are exhausted at the late step of the process.

4. Conclusions

A facile approach for the synthesis of stable aqueous colloids of silver nanoparticles (AgNPs) is described in the present work using the polythiocyanatohydroquinone (PTHQ) polymer as a reducing and stabilizing reagent in water. The AgNPs were characterized by different techniques such as UV–vis spectroscopy, X-ray diffraction and transmission electron microscopy. The TEM experiments indicate that these nanoparticles are formed with spherical shapes. The X-ray diffraction pattern shows a high purity and face centered cubic structure of the AgNPs. On the basis of various observations a three-step mechanism is proposed for the reduction of the silver ions by PTHQ: 1) a fast formation of the Ag_2O microphase in the system after mixing of reagents; 2) a reduction of the silver ions on the surface of the Ag_2O particles according to the zero-order kinetics; 3) a growth of AgNPs due to reduction of silver ions from a solution on the surface of already generated nuclear of AgNPs according to the first order kinetics after the Ag_2O microphase dissolution. The kinetic constants at various temperatures and for different stages were calculated and thermodynamic activation parameters were determined by variable temperature kinetic studies.

5. Acknowledgements

The quantum-chemical calculations were performed with computational resources provided by the High Performance Computing Center North (HPC2N) which is a Swedish national center for Scientific and Parallel Computing through the project "Multiphysics Modeling of Molecular Materials" SNIC 2016-34-43. This work was supported by the Ministry of Education and Science of Ukraine (Project No. 0117U003908).

The authors declare that they have no conflict of interest.

6. References

1. Yu. Krutyakov, A. A. Kudrinskiy, A. Yu. Olenin, G. V. Lisichkin, *Russ. Chem. Rev.,* **2008**, *77*, 233–251. **DOI:**10.1070/RC2008v077n03ABEH003751
2. A. Polman, H. A. Atwater, *Mater. Today*, **2005,** *8*, 56. **DOI:**10.1016/S1369-7021(04)00685-6

Table 2. Activation parameters for different stages of silver nanoparticles formation using PTHQ.

Initial stage			Later stage		
Activation energy E_a, kJ	**$\Delta H^{\neq}$, kJ mol^{-1}**	**$\Delta S^{\neq}$, J K^{-1} mol^{-1}**	**Activation energy E_a, kJ**	**$\Delta H^{\neq}$, kJ mol^{-1}**	**$\Delta S^{\neq}$, J K^{-1} mol^{-1}**
58.90	56.34	–121.18	55.60	53.04	–116.74

3. K. Vasilev, V. R. Sah, R. V. Goreham, C. Ndi, R. D. Short, H. Griesser, *J. Nanotechnol.*, **2010**, *21*, 5102–5107.
4. S. Prabhu, E. Poulose, *Int. Nano Lett.*, **2012**, *2*, 1–10. **DOI:**10.1186/2228-5326-2-32
5. K. S. Lee, M. A. El-Sayed, *J. Phys. Chem. B.* **2006**, *110*, 19220–19225. **DOI:**10.1021/jp062536y
6. S. Kaviyaa, J. Santhanalakshmi, B. Viswanathan, J. Muthumary, K. Srinivasan, *Spectrochim. Acta A*, **2011**, *79*, 594–598. **DOI:**10.1016/j.saa.2011.03.040
7. R. F. Elsupikhe, K. Shameli, M. B. Ahmad, N. A. Ibrahim, N. Zainudin, *Nanoscale Res. Lett.*, **2015**, *10*, 302. **DOI:**10.1186/s11671-015-0916-1
8. J. Yang, H. Yin, J. Jia and Y. Wei, *Langmuir*, **2011**, *27*, 5047–5053. **DOI:**10.1021/la200013z
9. M. Harada, C. Kawasaki, K. Saijo, M. Demizu, Y. Kimura, *J. Colloid Interface Sci.*, **2010**, *343*, 537–545. **DOI:**10.1016/j.jcis.2009.11.066
10. M. Manoth, K. Manzoor, M.K. Patra, P. Pandey, S.R. Vadera, N. Kumar, *Mater. Res. Bull.*, **2009**, *44*, 714–717. **DOI:**10.1016/j.materresbull.2008.06.033
11. M. C. Rodriguez-Argüelles, C. Sieiro, R. Cao, L. Nasi, *J. Colloid Interface Sci.*, **2011**, *364,* 80–84. **DOI:**10.1016/j.jcis.2011.08.006
12. M. M. Kemp, A. Kumar, S. Mousa, T-J. Park, P. Ajayan, N. Kubotera, S. A. Mousa, R.J. Linhardt, *Biomacromolecules*, **2009**, *10*, 589–595. **DOI:**10.1021/bm801266t
13. V. A. Litvin, B. F. Minaev, G. V. Baryshnikov, *J. Mol. Struct.*, **2015**, *1086*, 25–33. **DOI:**10.1016/j.molstruc.2014.12.091
14. L. Quaroni, G. Chumanov, *J. Am. Chem. Soc.*, **1999**, *121*, 10642. **DOI:**10.1021/ja992088q
15. V. A. Litvin, B. F. Minaev, Mater. Chem. Phys., **2014**, *144*, 168–178. **DOI:**10.1016/j.matchemphys.2013.12.039
16. V. A. Litvin, R.L. Galagan, B. F. Minaev, *Russ. J. Appl. Chem.,* **2012**, *85*, 296–302. **DOI:**10.1134/S1070427212020243
17. G. V. Baryshnikov, R. L. Galagan, L. P. Shepetun, V. A. Litvin, B. F. Minaev, *J. Mol. Struct.*, **2015**, *1096*, 15–20. **DOI:**10.1016/j.molstruc.2015.04.040
18. D. Becke, *Phys. Rev. A*, **1988**, *38*, 3098–3100. **DOI:**10.1103/PhysRevA.38.3098
19. C. Lee, W. Yang, R.G. Parr, *Phys. Rev. B*, 1988, *37*, 785–789. **DOI:**10.1103/PhysRevB.37.785
20. M. M. Francl, W. J. Pietro, W. J. Hehre, J. S. Binkley, M. S. Gordon, D. J. DeFrees, J. A. Pople, *J. Chem. Phys.*, 1982, *77*, 3654–3665. **DOI:**10.1063/1.444267
21. S. Miertus, E. E. Scrocco, Tomasi, *J. Chem. Phys.,* **1981**, *55*, 117–129.
22. M. J. Frisch, G. W. Trucks, H. B. Schlegel, G. E. Scuseria, M. A. Robb, J. R. Cheeseman, G. Scalmani, V. Barone, G. A. Petersson, H. Nakatsuji, X. Li, M. Caricato, A. V. Marenich, J. Bloino, B. G. Janesko, R. Gomperts, B. Mennucci, H.P. Hratchian, J. V. Ortiz, A. F. Izmaylov, J. L. Sonnenberg, D. Williams-Young, F. Ding, F. Lipparini, F. Egidi, J. Goings, B. Peng, A. Petrone, T. Henderson, D. Ranasinghe, V. G. Zakrzewski, J. Gao, N. Rega, G. Zheng, W. Liang, M. Hada, M. Ehara, K. Toyota, R. Fukuda, J. Hasegawa, M. Ishida, T. Nakajima, Y. Honda, O. Kitao, H. Nakai, T. Vreven, K. Throssell, J. A. Montgomery, Jr., J. E. Peralta, F. Ogliaro, M. J. Bearpark, J. J. Heyd, E. N. Brothers, K. N. Kudin, V. N. Staroverov, T. A. Keith, R. Kobayashi, J. Normand, K. Raghavachari, A. P. Rendell, J. C. Burant, S. S. Iyengar, J. Tomasi, M. Cossi, J. M. Millam, M. Klene, C. Adamo, R. Cammi, J. W. Ochterski, R. L. Martin, K. Morokuma, O. Farkas, J. B. Foresman, D. J. Fox, Gaussian, Inc., Wallingford CT, 2016, Gaussian 16, Revision A.03.
23. C. Suryanarayana, M. Grantnorton X-Ray Diffraction: A Practical Approach, Plenum Publishing Corporation, New York, **1998**. **DOI:**10.1007/978-1-4899-0148-4
24. V. K. Vidhu, S. A. Aromal, D. Philip, *Spectrochim. Acta A*, **2011**, *83*, 392– 397. **DOI:**10.1016/j.saa.2011.08.051
25. V. A. Litvin, B. F., Minaev, *Spectrochim. Acta A,* **2013**, *108*, 115–122. **DOI:**10.1016/j.saa.2013.01.049
26. Z-Y. Huang, G. Mills, B. Hajek, *J. Phys. Chem.*, **1993**, *97*, 11542–11550. **DOI:**10.1021/j100146a031
27. K.-S. Chou, Yu-C. Lu, H.-H. Lee, *Mater. Chem. Phys.*, **2005**, *94*, 429–433. **DOI:**10.1016/j.matchemphys.2005.05.029
28. T. C. Prathna, N. Chandrasekaran, A. M. Raichur, A. Mukherjee, *Colloids Surf. A*, **2011**, *377*, 212–216. **DOI:**10.1016/j.colsurfa.2010.12.047
29. K. Y. Chumbimuni-Torres, E. Bakker, J. Wang, *Electroch. Commun.*, **2009**, *11*, 1964–1967. **DOI:**10.1016/j.elecom.2009.08.029
30. V. A. Litvin, R. L. Galagan, B. F. Minaev, *Colloids Surf. A*, **2012**, *414*, 234–243. **DOI:**10.1016/j.colsurfa.2012.08.036
31. J. Liu, R. H. Hurt, *Environ. Sci. Technol.*, **2010**, *44*, 2169–2175. **DOI:**10.1016/j.colsurfa.2012.08.036

Povzetek

Motivirani z dokazi, da imajo nanodelci srebra številne tehnološke aplikacije, smo v tem delu raziskali uporabo politiocianatohidrokinona kot novega učinkovitega redukcijskega in stabilizacijskega reagenta za pripravo takšnih nanodelcev. Nanodelce srebra smo karakterizirali z UV-Vis spektroskopijo, rentgensko praškovno difrakcijo in presevno elektronsko mikroskopijo (TEM). Predstavljene so tudi potenciometrične in spektrofotometrične kinetične meritve rasti nanodelcev srebra. Termodinamične aktivacijske parametre za tvorbo nanodelcev srebra smo določili iz reakcijskih kinetičnih študij pri različnih temperaturah. Predlagali smo mehanizem za nastanek nanodelcev srebra. Velikost (20–40 nm) in sferična porazdelitev nanodelcev skupaj z visoko stabilnostjo koloidov nam dajeta trdno osnovo za morebitno uporabo polimera kot redukcijskega in stabilizacijskega regenta za pripravo in shranjevanje kovinskih nanodelcev.

Scientific paper

On Topological Indices of *OT* [*m, n*] Octagonal Tillings and TiO_2 Nanotubes

Hafiz Usman Afzal[1] and Tahzeeb Fatima[2]

[1] *Department of Mathematics, GC University Lahore-54000, Pakistan*

[2] *Department of Biochemistry, University of Otago, New Zealand*

* *Corresponding author: E-mail: huafzal@gmail.com (coprresponding author), tahzeebfatima@gmail.com*

Received: 12-07-2018

Abstract

Some well defined connectivity topological indices are Randic index, atom-bond connectivity index, geometric-arithmetic index and Shigehalli & Kanabur indices, brought into light by M. Randic, Estrada *et al,* Vukicevic *et al* and V. S. Shigehalli, in their respective research articles. Topological indices preserve the symmetry of molecular structures and provide a mathematical formulation to predict their properties like boiling points, viscosity and the radius of gyrations,[1] mainly their study gets a cover under the category of physical chemistry. Due to its mathematical nature, this idea has caught the attention of many chemists. It has also been reported that these indices are useful in the study of anti- inflammatory activities of certain chemical instances. In this paper, we shall calculate these topological indices of an infinite class of octagonal tilling structures *OT [m, n]*, which is a molecular graph of a semiconductor allotrope consisting of octagons and rectangles, for all possible values of the parameters *m* and *n*. We shall also calculate Shigehalli & Kanabur indices of infinite structure of the titania TiO_2 nanotubes.

Keywords: Randic index; atom-bond connectivity index; octagonal tilling *OT [m, n]*; Shigehalli & Kanabur indices*;* TiO_2 nanotubes

1. Introduction

Mathematical chemistry is a branch of theoretical chemistry in which we discuss the chemical structures by using various mathematical techniques. Chemical graph theory is a branch of mathematical chemistry in which we apply techniques of graph theoretic ideas to form the chemical phenomenon mathematically. This theory plays an enigmatic part in different fields of chemical sciences. Primarily, a molecular graph is a simple graph in which vertices denote the atoms and edges denote the chemical bonding in the underlying chemical structure. Let *G* be a molecular graph with vertex set $V(G) = \{v_1, v_2, \ldots, v_n\}$ and edge set *E(G)*. The order and size of *G* are denoted by $p = |V(G)|$ and $q = |E(G)|$, respectively. Where, the order is defined to be number of vertices in *G* and size is defined to be number of edges in *G*. Also, an edge in *E(G)* with end vertices *u* and *v* is denoted by *uv*. A topological index is a molecular graph invariant which correlates the physic-chemical properties of a molecular graph with a number.[2] The first such topological index was introduced by a chemist, Harold Wiener, in 1947 to derive the boiling points of paraffins. This mathematical representation of a molecular graph has shown to be very useful quantity in quantitative structure- property relationship abbreviated as QSPR.[3] It has also many applications in communication, networking, coding theory and cryptography that are effectively modeled using a connected graph *G* under certain conditions.[4] This index was originally derived for tree alike structures to correlate specific physic- chemical properties of alkanes, alcohols, amines and their compounds.

H. Hosoya,[5] defined the notion of Wiener index for any graph *G* as;

$$W(G) = \sum_{\{u,v\}\subset V(G)} d(u,v).$$

A. Ashrafi *et al*,[6] calculated the PI, Szeged and edge Szeged indices of some nanostar dendrimers. Recently, authors also investigated *m*- order connectivity indices of nanostar dendrimers.[7] The atom-bond connectivity index

and geometric-arithmetic index of nanostar dendrimers and some polyomino- chains were studied by S. Hayat *et al.*[8] The atom-bond connectivity index and geometric-arithmetic index of some fullerenes were studied by M. Baca *et al.*[9] Rostami *et al.* studied the first kind of geometric- arithmetic index of some nanostar dendrimers.[10] Ghorbani *et al.* [11] did their study on the nullity of an infinite class of nanostar dendrimers.

The elemental two-dimensional *2D* materials such as graphene, silicene, germanene, and black phosphorus have pulled considerable attention due to their fascinating physic- chemical attributes. Structurally, they possess the honeycomb, distorted honeycomb and continuous honeycomb lattices, which are composed of six atom rings.

Recently,[12] P. Li and W. Luo have studied a new structure of *2D* allotropes of group *V* elements composed of eight-atom rings, which they termed as octagonal tilling structure, denoted generally by *OT*. These kinds of allotropes are comprehensively studied in materials sciences. Their findings indicated that these allotropes are dynamically stable and are also thermally stable at temperatures up to 600 *K*. They also showed, these allotropes are semiconductors with band gaps ranging from 0.3 to 2.0 *eV*, thus, they are potentially useful in near and mid- infrared devices. The molecular graph of these octagonal tilling structure, *OT[m, n]*, is presented in Figure 1, in which, *m* denotes the number of octagons in an alternate row and *n* denotes the number of octagons in an alternate column of *OT[m, n]*.

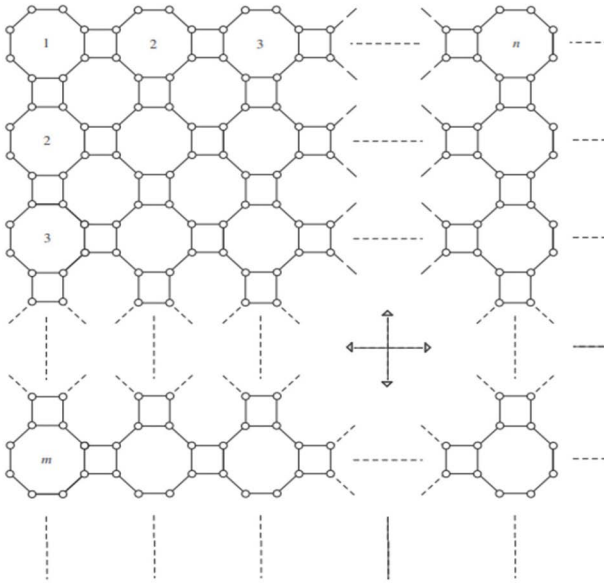

(a) Top View

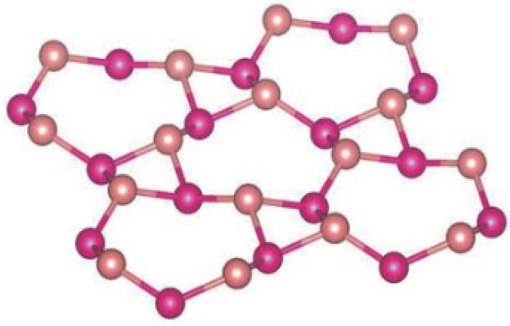

(b) Birds View (courtesy [12])

Figure 1. General formation of the molecular octagonal tilling structure *OT[m, n]*.

2. The Randić, ABC and GA Indices of Molecular Octagonal Tilling Structure *OT[m, n]*

Let H be a simple connected graph with vertex set $V(H)$ and edge set $E(H)$. The degree d_v of a vertex $v \in V(H)$ is the number of edges incident on v and $S_u = \sum_{v \in V(H)} d_v$ $N_H(u) = \{v \in V(H) \mid uv \in E(H)\}$.

M. Randic defined the Randic index as follows,[13]

$$\chi(H) = \sum_{uv \in E(H)} \frac{1}{\sqrt{d_u d_v}} \quad (1)$$

E. Estrada et al,[14] defined the atom-bond connectivity index, abbreviated as ABC-index, as:

$$ABC(H) = \sum_{uv \in E(H)} \sqrt{\frac{d_u + d_v - 2}{d_u d_v}} \quad (2)$$

Another well used connectivity topological descriptor for the molecular graphs is geometric-arithmetic index (GA-index), introduced by Vukicevic and Furtula and is defined by,[14]

$$GA(H) = \sum_{uv \in E(H)} \frac{2\sqrt{d_u d_v}}{d_u + d_v} \quad (3)$$

With each edge uv, we associate a pair (d_u, d_v). The edge partition of octagonal tilling *OT[m, n]* with respect to the degrees of the end-vertices of edges is presented in Table 1.

Table 1. The (d_u, d_v)- type edge partition of octagonal tilling *OT [m, n]*.

(d_u, d_v)-Partition	Edge Cardinality
(2, 2)	$2(m + n + 2)$
(2, 3)	$4(m + n - 2)$
(3, 3)	$4(3mn - 2m - 2n + 1)$

Theorem 1. For all *m* and *n*, the Randic index χ of the octagonal tilling structure *OT[m, n]* is

$$\chi(OT[m,n]) = 4mn + (\frac{2\sqrt{6}-5}{3})(m+n-2).$$

Proof. The (d_u, d_v)-type edge partition of the graph *OT[m, n]* is shown in Table 1. We prove the desired result by using partition of Table 1 and the formula of Randic index given by Equation 1 as follows.

$$\chi(OT[m,n]) = 2(m+n+2)\frac{1}{\sqrt{2\times 2}} + 4(m+n-2)\frac{1}{\sqrt{2\times 3}} + 4(3mn-2m-2n+1)\frac{1}{\sqrt{3\times 3}}$$

$$= (m+n+2) + (m+n-2)\frac{2\sqrt{2}}{\sqrt{3}} + (3mn-2m-2n+1)\frac{4}{3}$$

$$= m(1+\frac{2\sqrt{2}}{\sqrt{3}}-\frac{8}{3}) + n(1+\frac{2\sqrt{2}}{\sqrt{3}}-\frac{8}{3}) + 4mn + (2-\frac{4\sqrt{2}}{\sqrt{3}}+\frac{4}{3})$$

$$= m(\frac{2\sqrt{6}-5}{3}) + n(\frac{2\sqrt{6}-5}{3}) + 4mn + (\frac{10-4\sqrt{6}}{3})$$

$$= 4mn + (\frac{2\sqrt{6}-5}{3})(m+n-2)$$

$$\Rightarrow \chi(OT[m,n]) = 4mn + (\frac{2\sqrt{6}-5}{3})(m+n-2)$$

Example 1. *Consider a 2D structure of allotrope we are discussing called octagonal tilling OT [7, 8] consisting of 448 atoms and 642 chemical bonds, we obtain,*

$$\chi(OT[7,8]) = 223.5632.$$

Example 2. *The Randić index of 2D allotrope, octagonal tilling OT [m, n], for m = 1, 2, . . . , 5 and n = 1, 2, . . . , 10 are given as follows*

OT[m, n]	***X(OT[m, n])***
OT[1, 1]	4
OT[1, 2]	7.9664
OT[1, 3]	11.9328
OT[1, 4]	15.8992
OT[1, 5]	19.8656
OT[1, 6]	23.832
OT[1, 7]	27.7984
OT[1, 8]	31.7648
OT[1, 9]	35.7312
OT[1, 10]	39.6976
OT[2, 1]	7.9664
OT[2, 2]	15.9328
OT[2, 3]	23.8992
OT[2, 4]	31.8656
OT[2, 5]	39.832
OT[2, 6]	47.7984
OT[2, 7]	55.7648
OT[2, 8]	63.7312
OT[2, 9]	71.6976
OT[2, 10]	79.664
OT[3, 1]	11.9328
OT[3, 2]	23.8992
OT[3, 3]	35.8656
OT[3, 4]	47.832
OT[3, 5]	59.7984
OT[3, 6]	71.7648
OT[3, 7]	83.7312
OT[3, 8]	95.6976
OT[3, 9]	107.664
OT[3, 10]	119.6304
OT[4, 1]	15.8992
OT[4, 2]	31.8656
OT[4, 3]	47.832
OT[4, 4]	63.7984
OT[4, 5]	79.7648
OT[4, 6]	95.7312
OT[4, 7]	111.6976
OT[4, 8]	127.664
OT[4, 9]	143.6304
OT[4, 10]	159.5968
OT[5, 1]	19.8656
OT[5, 2]	39.832
OT[5, 3]	59.7984
OT[5, 4]	79.7648
OT[5, 5]	99.7312
OT[5, 6]	119.6976
OT[5, 7]	139.664
OT[5, 8]	159.6304
OT[5, 9]	179.5968
OT[5, 10]	199.5632

Theorem 2. For all *m* and *n*, the atom-bond connectivity index of the octagonal tilling structure *OT[m, n]* is

$$ABC(OT[m,n]) = 8mn + (\frac{9-8\sqrt{2}}{3\sqrt{2}})(2m+2n) + (\frac{8\sqrt{2}-12}{3\sqrt{2}}).$$

Proof. The (d_u, d_v)-type edge partition of the graph *OT[m, n]* is shown in Table 1. We prove the desired result by using partition of Table 1 and the formula of atom bond connectivity index given by Equation 2 as:

$$ABC(OT[m,n]) = 2(m+n+2)\sqrt{\frac{2+2-2}{2\times 2}} + 4(m+n-2)\sqrt{\frac{2+3-2}{2\times 3}} + 4(3mn-2m-2n+1)\sqrt{\frac{3+3-2}{3\times 3}}$$

$$= 2(m+n+2)\sqrt{\frac{2}{4}} + 4(m+n-2)\sqrt{\frac{3}{6}} + 4(3mn-2m-2n+1)\sqrt{\frac{4}{9}}$$

$$= 2(m+n+2)\frac{1}{\sqrt{2}} + 4(m+n-2)\frac{1}{\sqrt{2}} + (12mn-8m-8n+4)\sqrt{\frac{4}{9}}$$

$$= (2m+2n+4)\frac{1}{\sqrt{2}} + (4m+4n-8)\frac{1}{\sqrt{2}} + (12mn-8m-8n+4)\frac{2}{3}$$

$$= (2m+2n+4+4m+4n-8)\frac{1}{\sqrt{2}} + (12mn-8m-8n+4)\frac{2}{3}$$

$$= m(\frac{6}{\sqrt{2}}-\frac{16}{3}) + n(\frac{6}{\sqrt{2}}-\frac{16}{3}) + 8mn + (-\frac{4}{\sqrt{2}}+\frac{8}{3})$$

$$= m(\frac{18-16\sqrt{2}}{3\sqrt{2}}) + n(\frac{18-16\sqrt{2}}{3\sqrt{2}}) + 8mn + (\frac{8\sqrt{2}-12}{3\sqrt{2}})$$

$$\Rightarrow ABC(T[m,n]) = 8mn + (\frac{9-8\sqrt{2}}{3\sqrt{2}})(2m+2n) + (\frac{8\sqrt{2}-12}{3\sqrt{2}})$$

Example 3. *Consider a 2D structure of allotrope we are discussing called octagonal tilling OT [7, 9] consisting of 504 atoms and 724 chemical bonds. Then, its atom bond connectivity index is*

$$ABC(OT[7,9]) = 486.3887.$$

Example 4. *The atom bond connectivity index of 2D allotrope, octagonal tilling OT [m, n], for m = 1, 2, . . . , 5 and n = 1, 2, . . . , 10 are given as follows:*

OT[m, n]	***ABC(OT[m, n])***
OT[1, 1]	5.6571
OT[1, 2]	12.5665
OT[1, 3]	19.4759
OT[1, 4]	26.3853
OT[1, 5]	33.2947
OT[1, 6]	40.2041
OT[1, 7]	47.1135
OT[1, 8]	54.0229
OT[1, 9]	60.9323
OT[1, 10]	67.8417
OT[2, 1]	12.5665
OT[2, 2]	27.4759
OT[2, 3]	42.3853
OT[2, 4]	57.2947
OT[2, 5]	72.2041
OT[2, 6]	87.1135
OT[2, 7]	102.0229
OT[2, 8]	116.9323
OT[2, 9]	131.8417
OT[2, 10]	146.7511
OT[3, 1]	19.4759
OT[3, 2]	42.3853
OT[3, 3]	65.2947
OT[3, 4]	88.2041
OT[3, 5]	111.1135
OT[3, 6]	134.0229
OT[3, 7]	156.9323
OT[3, 8]	179.8417
OT[3, 9]	202.7511
OT[3, 10]	225.6605
OT[4, 1]	26.3853
OT[4, 2]	57.2947
OT[4, 3]	88.2041
OT[4, 4]	119.1135
OT[4, 5]	150.0229
OT[4, 6]	180.9323
OT[4, 7]	211.8417
OT[4, 8]	242.7511
OT[4, 9]	273.6605
OT[4, 10]	304.5699
OT[5, 1]	33.2947
OT[5, 2]	72.2041
OT[5, 3]	111.1135
OT[5, 4]	150.0229
OT[5, 5]	188.9323
OT[5, 6]	227.8417
OT[5, 7]	266.7511
OT[5, 8]	305.6605
OT[5, 9]	344.5699
OT[5, 10]	383.4793

Theorem 3. For all *m* and *n*, the geometric-arithmetic connectivity index of the octagonal tilling structure *OT[m, n]* is

$$GA(OT[m,n]) = 12mn + (\frac{4\sqrt{6}-15}{5})(2m+2n) + 8(\frac{5-2\sqrt{6}}{5}).$$

Proof. The (d_u, d_v)-type edge partition of the graph *OT[m, n]* is shown in Table 1. We prove the required result by using partition of Table 1 and the formula geometric-arithmetic connectivity index given by Equation 3 by following calculations:

$$GA(OT[m,n]) = 2(m+n+2)\frac{2\sqrt{2\times 2}}{2+2} + \quad (12)$$

$$4(m+n-2)\frac{2\sqrt{2\times 3}}{2+3} + 4(3mn-2m-2n+1)\frac{2\sqrt{3\times 3}}{3+3}$$

$$= 2(m+n+2)\frac{2\sqrt{4}}{4} + 4(m+n-2)\frac{2\sqrt{6}}{5} + 4(3mn-2m-2n+1)\frac{2\sqrt{9}}{6}$$

$$= 2(m+n+2)\frac{2.2}{4} + 4(m+n-2)\frac{2\sqrt{6}}{5} + 4(3mn-2m-2n+1)\frac{2.3}{6}$$

$$= 2(m+n+2) + (m+n-2)\frac{8\sqrt{6}}{5} + (12mn-8m-8n+4)$$

$$= 12mn + m(2+\frac{8\sqrt{6}}{5}-8) + n(2+\frac{8\sqrt{6}}{5}-8) + (4-\frac{16\sqrt{6}}{5}+4)$$

$$= 12mn + 2(\frac{4\sqrt{6}-15}{5})(m+n) + 8(\frac{5-2\sqrt{6}}{5})$$

$$= 12mn + (\frac{4\sqrt{6}-15}{5})(2m+2n) + 8(\frac{5-2\sqrt{6}}{5})$$

$$\Rightarrow GA(OT[m,n]) = 12mn + (\frac{4\sqrt{6}-15}{5})(2m+2n) + 8(\frac{5-2\sqrt{6}}{5}).$$

Example 5. *Consider a 2D structure of allotrope we are discussing called octagonal tilling OT [13, 14] consisting of 504 atoms and 724 chemical bonds. Then, its gepmetric arithmetic index is*

$$GA(OT[13,14]) = 2127.98. \quad (13)$$

Example 6. *The geometric-arithmetic index of 2D allotrope, octagonal tilling OT [m, n], for m = 1, 2, . . . , 5 and n = 1, 2, . . . , 10 are given as:*

OT[m, n]	*GA(OT[m, n])*
OT[1, 1]	8
OT[1, 2]	17.9192
OT[1, 3]	27.8384
OT[1, 4]	37.7576
OT[1, 5]	47.6768
OT[1, 6]	57.596
OT[1, 7]	67.5152
OT[1, 8]	77.4344
OT[1, 9]	87.3536
OT[1, 10]	97.2728
OT[2, 1]	17.9192
OT[2, 2]	39.8384
OT[2, 3]	61.7576
OT[2, 4]	83.6768
OT[2, 5]	105.596
OT[2, 6]	127.5152
OT[2, 7]	149.4344
OT[2, 8]	171.3536
OT[2, 9]	193.2728
OT[2, 10]	215.192
OT[3, 1]	27.8384
OT[3, 2]	61.7576
OT[3, 3]	95.6768
OT[3, 4]	129.596
OT[3, 5]	163.5152
OT[3, 6]	197.4344
OT[3, 7]	231.3536
OT[3, 8]	265.2728
OT[3, 9]	299.192
OT[3, 10]	333.1112
OT[4, 1]	37.7576
OT[4, 2]	83.6768
OT[4, 3]	129.596
OT[4, 4]	175.5152
OT[4, 5]	221.4344
OT[4, 6]	267.3536
OT[4, 7]	313.2728
OT[4, 8]	359.192
OT[4, 9]	405.1112
OT[4, 10]	451.0304
OT[5, 1]	47.6768
OT[5, 2]	105.596
OT[5, 3]	163.5152
OT[5, 4]	221.4344
OT[5, 5]	279.3536
OT[5, 6]	337.2728
OT[5, 7]	395.192
OT[5, 8]	453.1112
OT[5, 9]	511.0304
OT[5, 10]	568.9496

3. The Shigehalli & Kanabur Indices of the TiO_2 Nanotube

Another well known semiconductor, Titania is comprehensively discussed in materials sciences, which admits many aspects of various technological applications. Titania nanotubes were systematically synthesized in the course of last 10- 20 years using different methods in labs. The growth mechanism for TiO_2 nanotubes has been studied well.[16] Due to high applicability of the Titania nanotubes, their comprehensive theoretical studies are getting enhanced attention. Also, the TiO_2 sheets with a thickness of a few atomic layers were discovered to be remarkably stable.[17] In this section, We shall calculate three Shigehalli & Kanabur indices,[18] of the TiO_2 nanotubes. These expressions for these indices are given as follows:

$$SK(H) = \sum_{uv \in E(H)} \frac{d_u + d_v}{2} \quad (4)$$

$$SK_1(H) = \sum_{uv \in E(H)} \frac{d_u \times d_v}{2} \quad (5)$$

$$SK_2(H) = \sum_{uv \in E(II)} \left(\frac{d_u + d_v}{2}\right)^2 \quad (5)$$

Further, Figure 2 shows the graph of $TiO_2[m, n]$ nanotubes, where number of octagons represent m in rows and n in columns respectively.

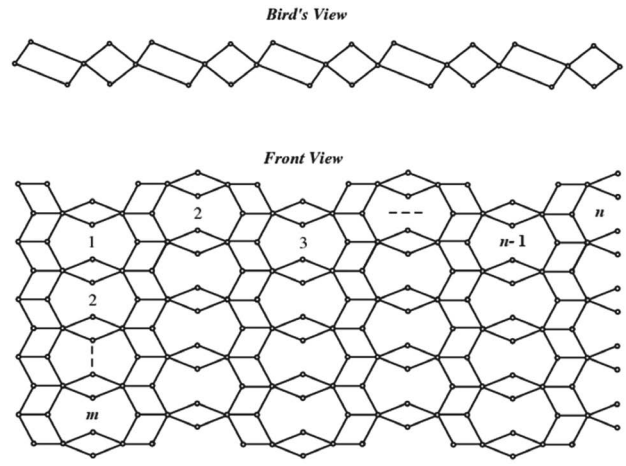

Figure 2. General formation of the molecular graph of titania $TiO_2[m, n]$ nanotubes.

Once again with each edge uv, we correspond a pair (d_u, d_v). The edge partition of TiO_2 $[m, n]$ nanotubes with respect to the degrees of the end-vertices of edges is presented in Table 2.[19]

Table 2. The (d_u, d_v)-type edge partition of titania $TiO_2[m, n]$ nanotubes.

(d_u, d_v)- Partition	Edge Cardinality
(2, 4)	$6n$
(2, 5)	$2n+ 4mn$
(3, 4)	$2n$
(3, 5)	$6mn- 2n$

Theorem 4. For all m and n, the 1st Shigehalli & Kanabur index, SK, of the titania $TiO_2[m, n]$ nanotubes is

$$SK(TiO_2[m,n]) = 24n + 38mn.$$

Proof. The (d_u, d_v)-type edge partition of the graph $TiO_2[m, n]$ are shown in Table 2. We prove the desired result by using partition of Table 2 and the formula of the 1st Shigehalli & Kanabur index given by Equation 4 as follows.

$$SK(TiO_2[m,n]) = (6n)\left(\frac{2+4}{2}\right) + (2n+4mn)\left(\frac{2+5}{2}\right) + (2n)\left(\frac{3+4}{2}\right) + [6mn-2n]\left(\frac{3+5}{2}\right)$$

$$= (6n)(3) + (2n+4mn)\left(\frac{7}{2}\right) + 7n + [6mn-2n]$$

$$= 18n + 2n\left(\frac{7}{2}\right) + 4mn\left(\frac{7}{2}\right) + 7n + 24mn - 8n$$

$$= 18n + 7n + 14mn + 7n + 24mn - 8n$$

$$\Longrightarrow SK(TiO_2[m,n]) = 24n + 38mn.$$

Example 7. *The* 1st Shigehalli & Kanabur of the *titania TiO_2 [8, 9] nanotube consisting of 784 chemical bonds is given as*

$$SK(TiO_2[8,9]) = 2928.$$

Theorem 5. For all m and n, the 2nd Shigehalli & Kanabur index, SK_1, of the titania $TiO_2[m, n]$ nanotubes is

$$SK_1(TiO_2[m,n]) = 31n + 65mn.$$

Proof. The (d_u, d_v)-type edge partition of the graph $TiO_2[m, n]$ are shown in Table 2. We obtain the required calculation by using partition of Table 2 and the formula of the 2nd Shigehalli & Kanabur index given by Equation 5 as follows.

$$SK_1(TiO_2[m,n]) = (6n)\left(\frac{2\times 4}{2}\right) + (2n+4mn)\left(\frac{2\times 5}{2}\right) + (2n)\left(\frac{3\times 4}{2}\right) + [6mn-2n]\left(\frac{3\times 5}{2}\right)$$

$$= (6n)(4) + (2n+4mn)(5) + (2n)(6) + [6mn-2n]\left(\frac{15}{2}\right)$$

$$= 24n + 10n + 20mn + 12n + [6mn-2n]\left(\frac{15}{2}\right)$$

$$= 24n + 10n + 20mn + 12n + 45mn - 15n$$

$$\Rightarrow SK_1(TiO_2[m,n]) = 31n + 65mn$$

Example 8. *The* 2nd Shigehalli & Kanabur index of the *titania TiO_2 [10, 12] nanotube consisting of 1280 chemical bonds is given as*

$$SK_1(TiO_2[10,12]) = 72440.$$

Theorem 6. For all m and n, the 3rd Shigehalli & Kanabur index, SK_2, of the titania $TiO_2[m, n]$ nanotubes is

$$SK_2(TiO_2[m,n]) = 71n + 145mn.$$

Proof. The (d_u, d_v)-type edge partition of the graph $TiO_2[m, n]$ are shown in Table 2. We obtain the required calculation by using partition of Table 2 and the formula of the 3rd Shigehalli & Kanabur index given by Equation 6 as follows.

$$SK_2(TiO_2[m,n]) = (6n)\left(\frac{2+4}{2}\right)^2 + (2n+4mn)\left(\frac{2+5}{2}\right)^2 + (2n)\left(\frac{3+4}{2}\right)^2 + [6mn-2n]\left(\frac{3+5}{2}\right)^2$$

$$= (6n)\left(\frac{6}{2}\right)^2 + (2n+4mn)\left(\frac{7}{2}\right)^2 + (2n)\left(\frac{7}{2}\right)^2 + [6mn-6n+4n]\left(\frac{8}{2}\right)^2$$

$$= (6n)(3)^2 + (2n+4mn)\left(\frac{49}{4}\right) + (2n)\left(\frac{49}{4}\right) + [6mn-2n](4)^2$$

$$= 54n + \frac{49}{2}n + 49mn + \frac{49}{2}n + 96mn - 32n$$

$$\Rightarrow SK_2(TiO_2[m,n]) = 71n + 145mn.$$

Example 9. *The* 3rd Shigehalli & Kanabur index of the *titania TiO_2 [20, 9] nanotube consisting of 1960 chemical bonds is given as*

$$SK_2(TiO_2[10,12]) = 29710.$$

4. Conclusion

In this article, we have calculated some degree based topological indices of an infinite class of molecular graph, termed as octagonal tilling structure $OT[m, n]$. Precisely, we have studied the Randic index, atom-bond connectivity index and geometric-arithmetic connectivity index of the $OT[m, n]$, defined by M. Randic,[13] Estrada *et al.*[14] and Vukicevic *et al.*,[15] respectively. Secondly, we

have studied the 1st, 2nd and 3rd Shigehalli & Kanabur indices of the *titania* TiO_2 *[m, n]* nanotube. These topological indices are mathematical predictors for various chemical properties of molecular structures as boiling point and viscosity,[1] they are also reported to be useful in anti-inflammatory properties of certain chemical instances. They have also been used as branching indices and have several applications in QSPR and QSAR studies.[2] We are confident that these indices will help the researchers and chemists in analyzing various chemical instances of the octagonal tilling *2D* allotrope structure $OT[m, n]$, discussed in this article and of the titania TiO_2 nanotubes. From these indices of OT $[m, n]$ and TiO_2 nanotubes, we can observe two strict chains which conclude our research. These chains are:

$$\chi(OT[m,n]) < ABC(OT[m,n]) < GA(OT[m,n]) \quad (1)$$

$$SK(TiO_2) < SK_1(TiO_2) < SK_2(TiO_2) \quad (2)$$

Graphically, these strict inequality MATLAB comparison is presented in Figures 3 and 4.

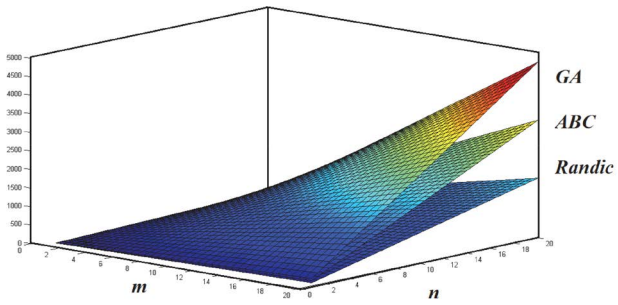

Figure 3. A comparison of *Randic*, *ABC* and *GA* indices of $OT[m, n]$; $m, n \in \{1, 20\}$.

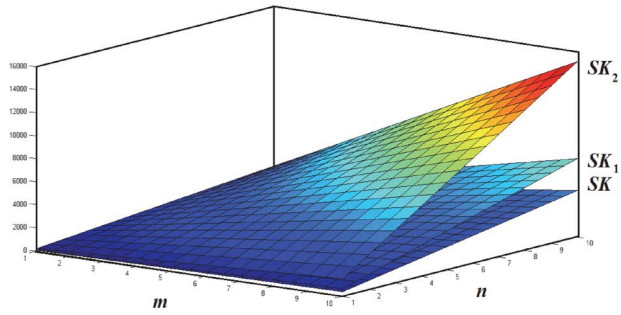

Figure 4. A comparison of *SK*, SK_1 and SK_2 indices of the titania TiO_2 $[m, n]$ nanotubes; where $m, n \in \{1, 10\}$.

5. Acknowledgement

We are cordially indebted to the anonymous referees for many valuable remarks which have improved the quality and precision of derived results in the final version of this article.

6. References

1. G. Rucker, C. Rucker, On topological indices, boiling points, and cycloalkanes, *J. Chem. Inf. Comput. Sci.,* **1999**, *39*, 788802. **DOI:**10.1021/ci9900175
2. C. Hansch and L. Leo, Exploring QSAR fundamentals and applicability in chemistry and biology, *Amer. Chem. Soc.,* Washington DC, **1996**.
3. J. Devillers and A. T. Balaban, *Topological Indices and Related Descriptors in QSAR and QSPR,* Gordon & Breach, Amsterdam, **1999**.
4. A. A. Dobrynin, R. Entringer and I. Gutman, Wiener Index of Trees: Theory and Applications, *Acta Applicandae Mathematicae,* **2001**, *66*, 211–249. **DOI:**10.1023/A:1010767517079
5. H. Hosoya, Topological index: A newly proposed quantity characterizing the topological nature of structural isomers of saturated hydrocarbons, *Bull. Chem. Soc. Jpn.,* **1971**, *4,* 2332–2339. **DOI:**10.1246/bcsj.44.2332
6. A. R. Ashrafi and M. Mirzargar, PI, Szeged, and edge Szeged indices of an infinite family of nanostar dendrimers, *Indian J. Chem.,* **2008**, *147*, 538–541.
7. A. R. Ashrafi and P. Nikzad, Connectivity index of the family of dendrimer nanostars, *Digest J. Nanomater. Biostruct.,* **2009**, *4*, 269–273.
8. S. Hayat, M. Imran and M. K. Shafiq, On topological indices of nanostar dendrimers and polyomino chains, Optoelectron. *Adv. Mater. Rapid Comm.,* **2014**, *9*, 8, 948–954.
9. M. Baca, J. Horvthov, M. Mokriov and A. Suhnyiov, On topological indices of fullerenes *App. Math. Comput.,* **2015**, *251*, 154–161.
10. M. Rostami, M. Shabanian and H. Moghanian, Some topological indices for theoretical study of two types of nanostar dendrimers, *Digest J. Nanomater. Biostruct.,* **2012**, *7*, 247–252.
11. M. Ghorbani, Some new results on the nullity of moecular graphs, *Studia Ubb Chem., LIX,* **2014**, *3,* 127–138.
12. P. Li, W. Luo, A new structure of two-dimensional allotropes of group V elements, *Sci. Rep. Article number:* 25423, **DOI:***10. 1038/srep25423* (**2016**), *6.*
13. M. Randic, On characterization of molecular branching, *J. Am. Chem. Soc.* **1975**, *97*, 6609–6615. **DOI:**10.1021/ja00856a001
14. E. Estrada, L. Torres, L. Rodrguez, I. Gutman, An atom-bond connectivity index: modelling the enthalpy of formation of alkanes, *Indian J. Chem.,* **1998**, *37*, 849–855.
15. D. Vukicevic and B. Furtula, Topological index based on the ratios of geometrical and arithmetical means of end-vertex degrees of edges, *J. Math. Chem.,* **2009**, *46*, 4, 1369–1376. **DOI:**10.1007/s10910-009-9520-x
16. D. Guan and Y. Wang, Synthesis and growth mechanism of multilayer TiO_2 nanotube arrays, *Nanoscale, 4,* **2012**, 9, 2968–2977.
17. R. A. Evarestov, Y. F. Zhukovskii, A. V. Bandura and S. Piskunov, Symmetry and models of single-walled TiO_2 nanotubes with rectangular morphology, *Cent. Eur. J. Phys.* **2011**, *9*, 2, 492–501.

18. V. S. Shigehalli, R. Kanabur, Computation of new degree-based topological indices of graphene., *Journal of Nanomaterials,* **2016**, 4341919.

19. Mehdi Rezaei, Wei Gao, Muhammad K Siddiqui, Mohammad R. Farahani, Computing Hyper Zagreb Index and M- Polynomials of Titania Nanotubes $TiO_2[m,n]$, *Sigma J. Eng. & Nat. Sci.* **2017**, *35 (4)*, 707–714.

Povzetek

Nekateri dobro definirani povezovalni topološki indeksi so Randićev indeks, povezovalni indeks atom-vez, geometrijsko-aritmetični indeks in Shigehalli & Kanabur indeksi, ki so jih v raziskovalnih člankih razjasnili M. Randic, Estrada *et al,* Vukicevic *et al* and V. S. Shigehalli. Topološki indeksi ohranjajo simetrijo molekulske strukture in zagotavljajo matematično formulacijo za napovedovanje lastnosti kot so vrelišča, viskoznost in radiji sukanja;[1] večinoma te študije sodijo v kategorijo fizikalne kemije. Zaradi svoje matematične narave je ta ideja pritegnila pozornost mnogih kemikov. Poročajo tudi, da so ti indeksi uporabni pri študiju protivnetnega delovanja določenih kemičnih primerov. V tem delu smo izračunali topološke indekse za neskončen razred osmerokotne predalčne strukture *OT [m, n]*, ki je molekularni graf polprevodniškega alotropa, sestavljenega iz osmerokotnikov in pravokotnikov, in sicer za vse možne vrednosti parametrov *m* in *n*. Uporabili smo Shigehalli & Kanabur indekse neskončne strukture nanocevk TiO_2.

Scientific paper

Adsorption Mechanism of Congo Red on Mg–Al-layered Double Hydroxide Nanocompound

Narges Safar Beyranvand, Babak Samiey* and Abbas Dadkhah Tehrani

Department of Chemistry, Faculty of Science, Lorestan University, Khoramabad 68137-17133, Lorestan, Iran

** Corresponding author: E-mail: babsamiey@yahoo.com , samiey.b@lu.ac.ir*

Received: 12-25-2018

Abstract

In this work, congo red (CR) was removed by applying carbonate intercalated Mg-Al-layered double hydroxide (Mg-Al-LDH) nanocompound as an adsorbent. Batch adsorption experiments performed under various temperatures, ionic strengths, initial CR concentrations, alkalinities and shaking rates. The maximum adsorption capacities of Mg-Al-LDH for CR were 100, 105 and 86.8 mg g^{-1} at 308, 318 and 328 K, respectively. Adsorption sites of Mg-Al-LDH for CR were –OH groups attached to Al atoms of adsorbent layers. Adsorption isotherms of the process were studied by the ARIAN model and analysis of obtained data showed that there were two kinds of adsorption sites on the surface of Mg-Al-LDH. Results of instrumental analysis showed that these adsorption sites were –OH groups located on the surface of mesopores and micropores of adsorbent and were named MP and 003 sites, respectively. The kinetic data were studied by the KASRA model and ISO and intraparticle diffusion (pore-diffusion) equations which showed that CR molecules were adsorbed at first on the MP sites. Also, during the adsorption of CR on MP sites the interaction of CR with adsorbent surface was rate-controlling step. Furthermore, during CR adsorption on 003 sites, adsorption kinetics was diffusion-controlled.

Keywords: Mg-Al-LDH; Congo red; Adsorption; ARIAN model; KASRA model; ISO equation

1. Introduction

Discharge of wastewater produced by industries is a main source of water pollution. These pollutants of the discharged wastewater are harmful to environment and human and animal health. Dye substances are one detrimental group of these pollutant compounds.[1] Large amounts of effluents containing dye compounds are generated by industries that produce paper,[2] textiles,[3] rubber,[4] food,[5] cosmetics[6] and leather.[7] Various chemical, physical and biological methods are used to remove pollutants from wastewaters. Some of these methods are biological degradation,[8] coagulation/flocculation,[9] membrane separation,[10] chemical oxidation,[11] ion exchange[12] and adsorption.[13] Among these methods, adsorption is a suitable candidate for dye removal due to its simplicity, high adsorption capacity and non-toxicity.

Congo red (CR), the sodium salt of 3,3′-([1,1′-biphenyl]-4,4′-diyl)bis(4-aminonaphthalene-1-sulfonic acid), is a benzidine-based diazo anionic dye.[14] CR is used as an acid-base indicator and for staining tissues in histology and microscopy.[15] It is mainly used for dyeing cotton, hemp, silk and paper products.[16] However, it is known to be carcinogenic.[17] Moreover, due to its complex structure, it is very stable to biological degradation and remains in the environment for a long period of time.[18]

For removing CR from effluents, different types of adsorbents like activated carbon,[19] shrimp shell powder,[20] mesoporous α-Fe_2O_3 nanorods,[21] nano-Fe_3O_4,[22] kaolin,[23] hydroxyapatite[24] and biogas waste slurry[25] have been used.

Layered double hydroxides (LDHs) or anionic clay or hydrotalcite-like compounds are natural or synthetic lamellar hydroxides. There are two types of metallic cations in their main layers and hydrated interlayer domains containing anionic species.[26,27] The general formula of LDHs is $[M^{2+}_{1-x},M^{3+}_{x}(OH)_2]^{x+}(A)^{n-}_{x/n}\cdot mH_2O$, where the M^{2+} and M^{3+} cations occupy the octahedral holes in a brucite-like layer surrounded by OH groups. The water and A^{n-} anions are in the interlayer spaces which A^{n-} anions balance the positive charge of M^{3+} cations in the layers.[28,29] LDHs are synthesized simply and have a high anion exchange capacity. The optical, thermal and mechanical properties of nanocomposites of LDH and polymers were improved compared to those of neat polymers.[30,31] Also, LDHs are used as ion-exchange mineral,[32] adsorbent,[33] catalysts[34,35] and coatings to protect metallic alloys.[36,37]

In this work, the synthesized Mg-Al-LDH nanocompound was characterized by different methods, like SEM,

BET, FTIR and XRD. The adsorption capacity of LDH for CR was measured under different experimental variables like CR concentration, pH, contact time, temperature, shaking rate and ionic strength. Adsorption mechanism of CR was studied by analysis of thermodynamics and kinetics of this adsorption process using the ARIAN and KASRA models respectively. These models made possible surveying adsorption isotherms and kinetic curves.

2. Experimental

2. 1. Chemicals

Aluminum nitrate ($Al(NO_3)_3{\cdot}9H_2O$), magnesium nitrate ($Mg(NO_3)_2{\cdot}6H_2O$), sodium hydroxide, sodium carbonate, hydrochloric acid, sodium chloride and congo red were purchased from Merck. All chemicals were used without further purification.

2. 2. Synthesis of Mg-Al-LDH

Mg-Al-LDH was synthesized based on the published procedure.[38] 5.32 g of aluminum nitrate and 11.534 g of magnesium nitrate (Mg/Al molar ratio is 2/1) were dissolved in 60 ml of distilled water (Solution A). Similarly, 4.8 g sodium hydroxide and 1.05 g sodium carbonate were dissolved by adding 60 ml of distilled water (Solution B). Then, the Solution B was added dropwise to Solution A while stirring at 300 rpm. The pH of mixture was monitored by a pH meter. After adding Solution B to the Solution A the final pH of mixture was 10. Afterwards, the resulting slurry was kept stirring at 300 rpm and the mouth of container was sealed by a single layer of Parafilm®. The container was subsequently heated at 60 °C in an oil bath for 24 h. Then distilled water was added to precipitate Mg-Al-LDH. The LDH solid was separated from its supernatant by a centrifuge at 6000 rpm. This washing process was repeated 5 times and finally the participate was dried at room temperature.

2. 3. Characterization of Mg-Al-LDH

The crystal structure of synthesized carbonate intercalated Mg-Al-LDH was characterized by a Rigaku D-max C III, X-ray diffractometer (XRD) using Ni-filtered Cu-Kα radiation (λ = 1.5406 Å). As shown in Fig. 1(a), XRD pattern of Mg-Al-DH showed a typical layered structure of Mg-Al-LDH ($Mg_6Al_2(OH)_{16}CO_3{\cdot}4H_2O$) with peaks at 11.6° and 23.1° corresponding to (003) and (006) planes of the Mg-Al-LDH phase. The interlayer distances d_{003} and d_{006} were 0.76 and 0.38 nm respectively which were consistent with published papers.[36]

This information showed that the Mg-Al-LDH nanocompound with carbonate anions in the interlayer had been synthesized successfully.[39] The average size of Mg-Al-LDH particles, estimated by Debye–Scherrer formula,[36] was about 65 nm. Also, XRD spectra of CR-adsorbed Mg-Al-LDH and Mg-Al-LDH modified with alkaline solutions, Figs. 1(b)-1(d), were similar to the XRD spectrum of pristine Mg-Al-LDH.[39]

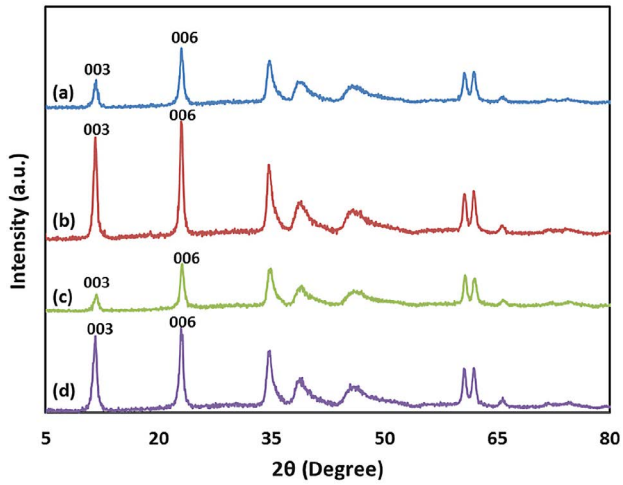

Figure 1. XRD spectra of (a) Mg-Al-LDH, (b) CR-adsorbed Mg-Al-LDH, (c) Mg-Al-LDH modified with NaOH solution at pH = 10 and (d) Mg-Al-LDH modified with NaOH solution at pH = 13.

IR spectra of Mg-Al-LDH were taken by a Nicolet IR 100 (Thermo Scientific) FTIR spectrophotometer using KBr pellet technique, Fig. 2(a). The bands at 3532.9 and 1643.1 cm^{-1} in the IR spectrum of pristine Mg-Al-LDH were assigned to the stretching vibration of interlayer –OH groups of Mg-Al-LDH nanocompound and water mole-

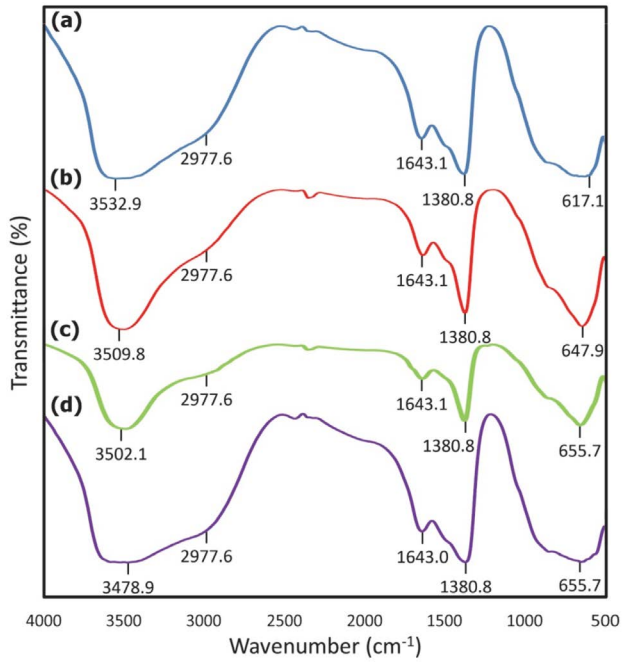

Figure 2. IR spectra of (a) Mg-Al-LDH, (b) CR-adsorbed Mg-Al-LDH, (c) Mg-Al-LDH modified with NaOH solution at pH = 10 and (d) Mg-Al-LDH modified with NaOH solution at pH = 13.

cules adsorbed on Mg-Al-LDH surface, respectively.[39–41] The peaks at 1380.8 and 617.1 cm^{-1} and the shoulder at 2977.6 cm^{-1} were attributed correspondingly to the C–O stretching mode of carbonate group, Al–O stretching mode and stretching vibration of carbonate–H_2O in the interlayer.[36,42,43]

Scanning electron micrographs of Mg-Al-LDH were taken using a MIRA3 TESCAN instrument at 15 keV. SEM photos indicated that the surface morphology of Mg-Al-LDH nanocompound and its samples modified with NaOH solutions at pHs of 10, 13 and 14 were aggregation of Mg-Al-LDH particles with a sand rose morphology, Figs. 3(a)–3(d). It seemed that after neutralization reaction of –OH groups of Mg-Al-LDH nanocompound with NaOH at alkaline solutions, Figs. 3(b)–3(d), repulsion interaction between resulted $–O^-$ groups of these particles made changes in the morphology of adsorbent.

EDS (Energy Dispersive X-Ray Spectroscopy) spectrum of the synthesized Mg-Al-LDH nanocompound was prepared by a MIRA3 TESCAN instrument. The results showed that atomic percentages of magnesium and aluminum on its surface were 18.88 and 6.62% respectively which validated the Mg-Al-LDH formation, Fig. 4.

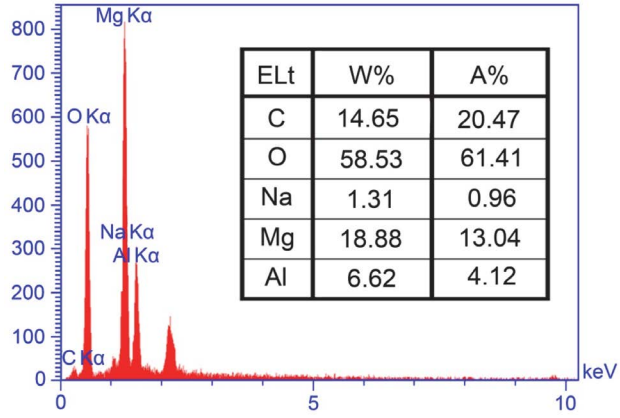

ELt	W%	A%
C	14.65	20.47
O	58.53	61.41
Na	1.31	0.96
Mg	18.88	13.04
Al	6.62	4.12

Figure 4. EDS spectrum of Mg-Al-LDH nanocompound.

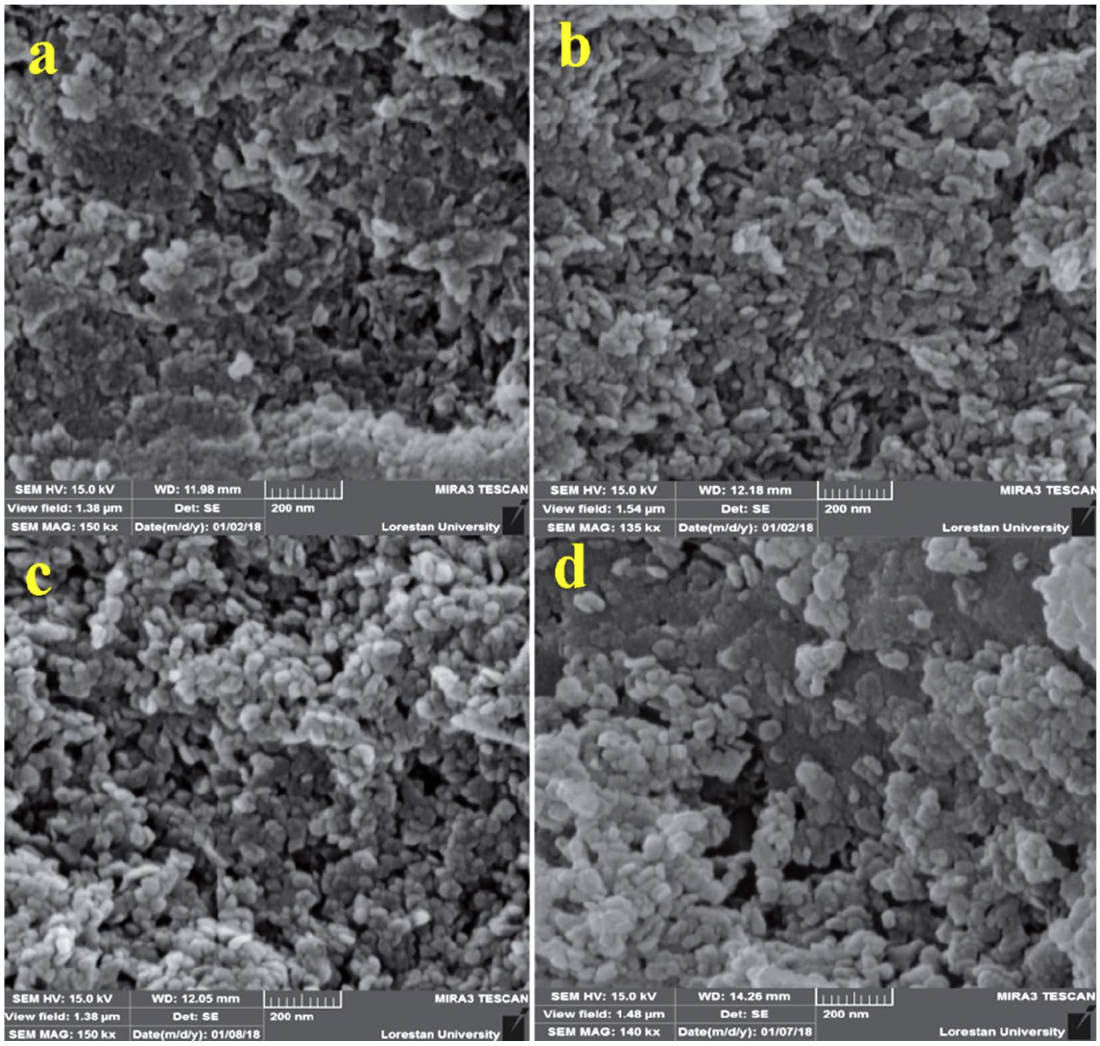

Figure 3. SEM images of (a) Mg-Al-LDH and Mg-Al-LDH modified with NaOH solutions at pHs of (b) 10, (c) 13 and (d) 14.

Also, EDS spectra of the CR-adsorbed Mg-Al-LDH sample and Mg-Al-LDH modified with NaOH solutions at pHs of 10, 12 and 13 showed small differences with pure Mg-Al-LDH nanocompound, Figs. 4 and S1(a)-(c).

The nitrogen-based BET specific surface areas of Mg-Al-LDH and Mg-Al-LDH modified with a NaOH solution of pH = 13 for 3 hours and after adsorption of CR in a neutral solution were measured by a Pore Size Micrometrics-tristar 3020 equipment, Figs. S2(a)-(c). These isotherms were Type IV and were implied that Mg-Al-LDHs are porous materials. Nitrogen molecules were condensed in the tiny adsorbent capillary mesopores and micropores. The BET surface area, adsorption average pore diameter (by BET), pore volume and micropore volume were 112.83 $m^2 g^{-1}$, 22.6 nm, 0.64 $cm^3 g^{-1}$ and 0.012 $cm^3 g^{-1}$ for Mg-Al-LDH, 89.45 $m^2 g^{-1}$, 24.1 nm, 0.54 $cm^3 g^{-1}$ and 0.009 $cm^3 g^{-1}$ for Mg-Al-LDH at pH = 13 and 101.75 $m^2 g^{-1}$, 22.4 nm, 0.57 $cm^3 g^{-1}$ and 0.015 $cm^3 g^{-1}$ for CR-adsorbed Mg-Al-LDH sample, respectively. Results showed that the most of pores were mesopore (with an average diameter of 23 nm) and a small part of them were micropore and also verified that CR molecules were adsorbed on the mesopore and interlayer micropore sites and also the neutralization of interlayer –OH groups decreased adsorbent surface area. The hysteresis loop of these three BET isotherms were H1 which was ascribed to agglomerates or spherical particles in a cylindrical pore geometry, indicating relatively high pore size uniformity and facile pore connectivity.[45]

2. 4. Adsorption Studies

2. 4. 1. Adsorption Experiments

The adsorption experiments were carried out in a series of 10-ml glass bottles. 0.0025 g of adsorbent (Mg-Al-LDH) was added to each bottle and then charged with 10 ml of CR solution with a certain initial concentration. The bottles were shaken at 100 rpm in a temperature controlled shaking water bath (Fater electronic Co., Persian Gulf model) at 308, 318 and 328 K within ±0.1 K for 6 h to reach equilibrium. The initial concentration ranges of CR were 3 × 10^{-6}–10^{-4} M. After adsorption, the CR concentration in each bottle was determined by photometry (UV mini 1240V, Shimadzu) at their λ_{max} values in these solutions. The λ_{max} value of CR in water was 489 nm. The CR adsorption capacity on the adsorbent, q_e (mg g^{-1}), was calculated as follows

$$q_e = \frac{(c_0 - c_e)Mv}{1000\,w} \quad (1)$$

where c_0 and c_e are the initial and equilibrium concentrations of adsorbate in each solution (M) respectively, v is the volume of solution (ml), w is the weight of the used adsorbent (g) and M is the molecular weight of adsorbate (mg $mole^{-1}$).

In adsorption kinetic experiments, 0.0025 g samples of Mg-Al-LDH were added to a series of bottles including 10 ml of CR solutions with initial concentrations (10^{-5}, 6 × 10^{-5} or 9 × 10^{-5} M). The solutions were shaken at 30, 70 and 100 rpm and at 308, 318 and 328 K. At determined contact times, the concentrations of CR in the solutions were measured by photometry at their λ_{max} values. In this type of experiments, q_e and c_e in Eq. (1) were replaced by q_t (adsorption capacity at time t) and c_t (concentration of adsorbate at time t), respectively.

2. 4. 2. Adsorption Thermodynamic Isotherms and Models

The adsorption isotherms were studied by "*adsorption isotherm regional analysis model*" or abbreviated as the ARIAN model.[46,47] It is good to say that ARIAN is a Persian word meaning Iranian. This model has been introduced for studying adsorption isotherms up to four regions. In the ARIAN model, it is assumed that region I obeys the Henry's law:

$$q_e = Kc_e \quad (2)$$

where K is the binding constant of adsorbate on the surface and adsorption increases linearly with concentration. Region II starts from the *starting second region concentration* (abbreviated as *ssc*) point. In this region only monolayer adsorption occurs and can be studied by an appropriate isotherm such as the Langmuir and Temkin equations and etc. The linearized form of the Langmuir equation[48] is represented as

$$\frac{c_e}{q_e} = \frac{1}{q_{max}K} + \frac{c_e}{q_{max}} \quad (3)$$

where q_{max} is the monolayer capacity of adsorbent and K is the Langmuir adsorption equilibrium constant. The Temkin equation[49] is given by

$$q_e = c_1 \ln(c_2 c_e) \quad (4)$$

where c_1 is a constant and c_2 is adsorption equilibrium constant.

In region III, new surface aggregates of molecules (or admicelles) and new surface clusters (in the case of surfactants) form. The *starting third region concentration* (abbreviated as *stc*) point defines the beginning of this region. The bilayer isotherm, Eq. (5), and those derived from it, Eqs. (6) and (7) are used for analysis of data of this region.[46] In region III, by assuming adsorption occurs mostly in the first and second layers, we have

$$\frac{c_e}{q_e} = \frac{1 + c_e K_{sa} + x c_e^2 K_{sa}}{q_{mon} K_{sa} + 2 q_{mon} x c_e K_{sa}} \quad (5)$$

where q_{mon} and q_e are the monolayer and equilibrium adsorption capacity, respectively. K_{sa} and x are the adsorption equilibrium constants of adsorbate molecules in the first layer surface aggregates and that of adsorbate mole-

cules in all layers excluding the first layer, respectively. If adsorbate molecules are adsorbed mostly on the first layer,[46] Eq. (5) can be written as

$$\frac{c_e}{q_e} = \frac{1}{q_{mon}K_{sa}} + \frac{c_e}{q_{mon}} + \frac{xc_e^2}{q_{mon}} \quad (6)$$

which is used for surface low bilayer coverage (abbreviated as LBC isotherm) and if the adsorption process results in the formation of a monolayer,[46] Eq. (5) is reduced to

$$\frac{c_e}{q_e} = \frac{1}{q_{mon}K_{sa}} + \frac{c_e}{q_{mon}} \quad (7)$$

where Eq. (7) is a Langmuir-type equation. The region IV starts where the adsorption capacity reaches the maximum, showing a plateau on the isotherm, or where the isotherm begins to go down. The second situation in region IV is called the reverse desorption and obeys from the reverse desorption equation.[46] Depending upon the adsorbate and adsorption sites characteristics, two or more sub-regions in each of regions II or III or IV may be observed in an adsorption isotherm. Each of these sub-regions are called a section and to discriminate between them, they are denoted using English capital letters and written as IIA, IIB etc.

Also, in some cases, due to some factors like repulsion interaction between adsorbate-adsorbed surface and free adsorbate molecules, adsorption process is stopped in a certain adsorbate concentration range.[50] This adsorbate concentration range is called CRAC. CRAC is an abbreviation for "*concentration range of leveling off between two successive adsorption isotherm curves*". Schematic adsorption isotherm of CR on Mg-Al-LDH according to the ARIAN model was shown in Fig. 5.

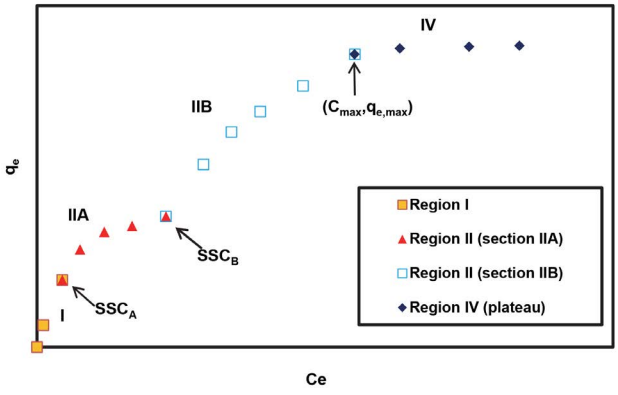

Figure 5. Typical adsorption isotherms of CR on Mg-Al-LDH nanocompound. Different regions according to the ARIAN model are shown in the diagram.

2. 4. 3. Adsorption Kinetic Equations and Models

The kinetic data were analyzed by several equations. The intraparticle diffusion equation[51] is shown as:

$$q_t = k_{dif}t^{0.5} + I \quad (8)$$

Where k_{dif} is the rate constant for intraparticle diffusion and I is proportional to the boundary layer thickness.

Also, the KASRA model and KASRA equation[47,52,53] were used to analyze the adsorption kinetics. KASRA is an abbreviation for "*kinetics of adsorption study in the regions with constant adsorption acceleration*" and is a synonym of "king" in Persian. The KASRA model is based on the following assumptions: (1) each time range that adsorption acceleration in it is constant, is named a *"region"*, (2) there are two regions before reaching the plateau region, and (3) the boundaries between the first and second regions and the second and third (plateau) regions are named *starting second region* (abbreviated as *ssr*) point and *kinetics of adsorption termination* (abbreviated as *kat*) point, respectively. Both *ssr* and *kat* points are determined by the KASRA equation[52] given as follows:

$$q_t = \frac{1}{2}a_i t^2 + (v_{0i} - a_i t_{0i})t + q_{0i} - \frac{1}{2}a_i t_{0i}^2 - (v_{0i} - a_i t_{0i})t_{0i} \quad (9)$$

Where q_{0i}, v_{0i} and t_{0i} are q_t, velocity and time at the beginning of the *ith* region, respectively, a_i is the acceleration of adsorption kinetics in the *ith* region whereas $i = 1–3$. Each a_i is a negative value because of the decrease in the adsorbate concentration during adsorption process. In the first region, t_{01} and q_{01} are equal to zero. The second region starts from *ssr* point which is assigned with the coordinates t_{02} and q_{02}. Finally, plateau (third) region begins at the equilibrium time, t_e and equilibrium adsorption capacity, q_e which are coordinates of *kat* point. In this region, $v_{03} = a_3 = 0$, $t_{03} = t_e$ and $q_{03} = q_e$ and Eq. (9) is simplified to $q_t = q_e$. Due to different features of the first and second regions, parameters obtained for these two regions such as rate constants are different from each other and the related equations for these regions come different pathways from the point $q_t = 0$ at $t = 0$.

In this work, to avoid confusion in relation to the regions in isotherms and kinetic curves, kinetic regions are shown using numbers like region 1 and etc. A schematic adsorption kinetic curve of CR on Mg-Al-LDH according to the KASRA model was shown in Fig. 6.

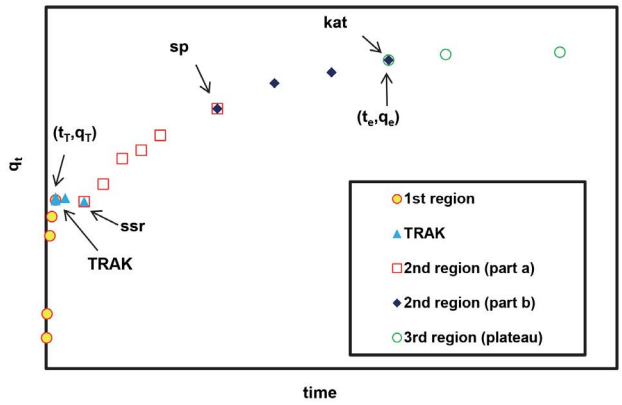

Figure 6. Typical bi-curve adsorption kinetic diagram of CR adsorption on Mg-Al-LDH. Different regions according to the KASRA model are shown in the diagram.

The *ideal-second-order* (or abbreviated as ISO) equation[47,54] is shown as

$$\ln\left(\frac{q_e - q_t}{ac_t}\right) = -\frac{k_I c_e}{q_e}t + A' \quad (10)$$

where $k_I = k_I^2 q_e$ [53] and k_I^2 are the first- and second-order adsorption rate constants of the ISO equation in each region and are in M^{-1} mg g^{-1} min^{-1} and M^{-1} min^{-1}, respectively and $A' = \ln\left(\frac{q_e}{ac_0}\right)$. $a = \frac{Mv}{1000w}$, where v is the volume of solution (ml), w is the weight of the used adsorbent (g) and M is the molecular weight of adsorbate (mg $mole^{-1}$). Some adsorbents have m different adsorption sites and adsorption occurs in sequence on their first, then second, . . . , (m–1)*th* and *mth* sites respectively. In these cases, there are m kinetic curves and in Eq. (10) q_e and c_e are used for *mth* site and for m – 1 other sites these symbols are replaced with $q^i_{t,\max}$ and $c_{t,\max}$, where i = 1, ... m – 1. $q^i_{t,\max}$ and $c^i_{t,\max}$ are the maximum adsorption capacity of adsorbent and adsorbate concentration after absorption completion on the *ith* adsorption site, respectively. Thus, the ISO equation is used m times to analyze these m kinetic curves. [50,54]

As referred before, based on the KASRA model, there are two regions in adsorption kinetic curves before reaching the plateau which result from non-ideality in adsorption. In the first one, completely ideal adsorption occurs on the bare surface of adsorbent. The progressively changes occurred on the surface of adsorbent in region 1 finally result in emerging another ideal region (region 2) in which adsorption carries out on a partly adsorbate-covered surface. Using the ISO equation shows that region 2 is composed of two another ideal parts that are named 2a and 2b. The first part of the second region, 2a, starts after *ssr* point and the second one, 2b, starts after *starting second part* (or abbreviated as *sp*) point and ends at the *kat* point.[50,54]

The ISO first-order rate constant of region 1 is shown with k_{I1} and those of the second region are shown with k_{I2a} and k_{I2b}. Also, the ISO second-order rate constant of region 1 is shown with k^2_{I1} and those of the second region are shown with k^2_{I2a} and k^2_{I2b}. As referred, in some adsorbents, there are two or more different adsorption sites which result in observing two or more successive adsorption kinetic curves in adsorption kinetic diagram. In these cases, region 1, (completely ideal) is only observed in the first adsorption kinetic curve, Fig. 6.[54]

Sometimes, due to braking effect[50] an interval is observed between two successive adsorption kinetic curves or between regions 1 and 2 of the first adsorption curve. The "*time range of interval between two successive adsorption kinetic curves*" (abbreviated as TRAK) is used to compare this effect in different cases.[50] On the other hand, the initial concentration of adsorbate has an important role in appearing the TRAK in an adsorption kinetic curve. Thus, for comparing kinetic curves including TRAK(s) with together and other kinetic curves, their first-order rate constants obtained from the ISO equation are used. Also in some cases, due to some factors like repulsion interaction between adsorbent surface and adsorbate, it takes time for adsorption process to occur and then region 1 starts with time delay. In this work, this time period is named *TD* which is an abbreviation for "*Time Delay*". If adsorption results in a TRAK, $q_{t,\max}$ and $c_{t,\max}$ are replaced by q^n_T and c^n_T, respectively. q^n_T and c^n_T are adsorption capacity of adsorbent and adsorbate concentration at the beginning of the TRAK between *nth* and (n + 1)*th* kinetic curves, respectively. In these cases, $k_I = k^2_I q^n_T$ and subscript T is an abbreviation for TRAK.[53]

3. Results and Discussion

3. 1. Thermodynamics of Adsorption of CR on Mg-Al-LDH in Neutral Aqueous Solutions

Using adsorption experimental isotherms and models is a very important tool to elucidate the mechanism of an adsorption process. In this study, Mg-Al-LDH nanocompound was used as the adsorbent for CR molecules. Analysis of results by the ARIAN model showed that isotherms of this process composed of regions I and II and finally reached to region IV (plateau), Figs. 5 and 7 and Tables 1–3. Here, region II was formed from two sections that based on the nomenclature used in the ARIAN model were shown as sections IIA and IIB.

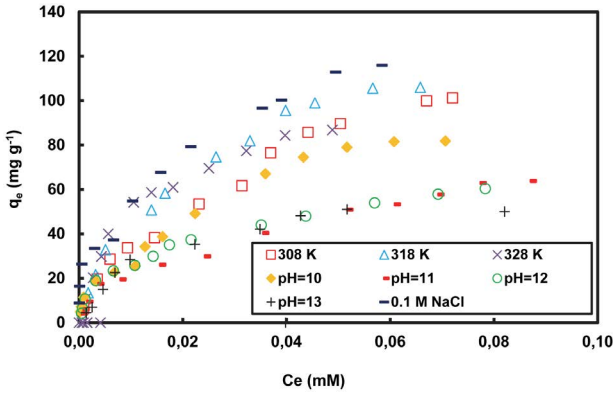

Figure 7. q_e *vs.* c_e for adsorption of CR on Mg-Al-LDH nanocompound from neutral aqueous solutions at 308–328 K and from alkaline and 0.1 M NaCl solutions at 318 K.

As shown in Fig. 8, hydrogen atoms of –OH groups attached to Al atoms of LDH layers were the adsorption sites for negatively charged oxygen atoms of sulfonate groups and delocalized electrons of CR molecules.

As seen in Fig. 1(a), XRD spectra of Mg-Al-LDH, peak at 11.6° corresponding to the basal spacing distances

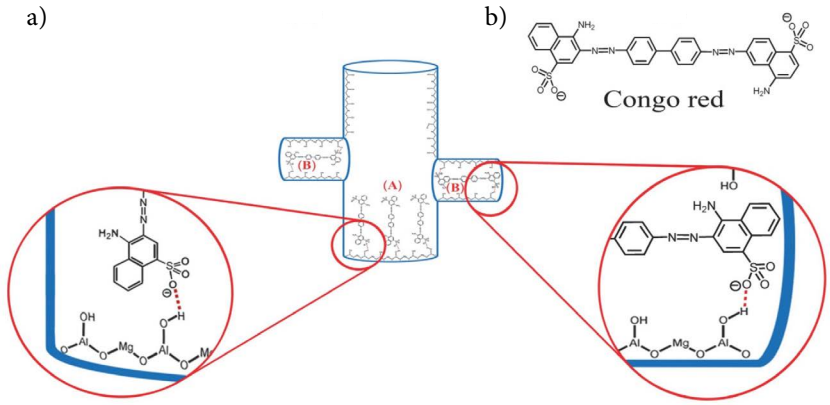

Figure 8. (a) Schematic representation of (A) MP and (B) 003 adsorption sites of Mg-Al-LDH and (b) CR molecule structure.

d_{003} was equal to 0.76 nm and classified as micropore. Furthermore, comparison of data of nitrogen-based BET specific surface area tests for average pore diameter for Mg-Al-LDH and CR-adsorbed Mg-Al-LDH showed that CR molecules adsorbed on the mesopores didn't occupy the pore apertures. On the other hand, the width and length of CR molecule were 0.7 and 2.5 nm, respectively and thus were less than interlayer distance of (003) indexed brucite-like planes. Therefore, the two kinds of adsorption sites involved in the adsorption process were –OH groups placed in the micropores between (003) planes with 0.76 nm interlayer distance and –OH groups located in the mesopores. The former adsorption site was denoted as 003 and the latter one defined as *mesopore* (abbreviated as MP) adsorption sites. Based on the size of pores, CR molecules at first interacted with MP sites and then by penetration into the interlayer galleries of 003 layers interacted with 003 sites.

Data obtained from analysis of adsorption isotherms at different temperatures were shown in Tables 1–3. To calculate the thermodynamic parameters of region I, section IIA and section IIB the binding constants obtained from the Henry, Temkin and Temkin isotherms were used, respectively.

As seen in Table 1, the adsorption binding constants of CR to the most active MP adsorption sites in region I at different temperatureswere comparable and the process was slightly endothermic and ΔH and ΔS values of the process in this region were 9.3 kJ mol^{-1} and –70.4 J mol^{-1} K^{-1}, respectively. But, the adsorption of CR on less active MP sites in section IIA was exothermic and ΔH and ΔS values of the process in this region were –32.4 kJ mol^{-1} and 14.2 J mol^{-1} K^{-1}, respectively, Table 2.

In region I, CR molecules were adsorbed on the bare surface of adsorbent. In section IIA, CR molecules were adsorbed on adsorption sites nearby adsorbed CR molecules and due to spatial hindrance and negative charge of formerly adsorbed CR molecules adsorption in section IIA was exothermic.

On the other hand, adsorption binding constants to 003 site in section IIB at different temperatures were smaller than those in section IIA and the process was endothermic and ΔH and ΔS values of the process in this region were 50.8 kJ mol^{-1} and 262.9 J mol^{-1} K^{-1}, respectively, Table 3.

Direction of adsorbed CR molecules in 003 sites depended on the distance between Mg-Al-LDH layers.[41] It

Table 1. Parameters obtained from the Henry's law an ssc_A and q_{sscA} values for adsorption of CR on Mg-Al-LDH nanocompound in water and 0.1 M NaCl solutions in region I (on MP site) at 308–328 K.

Solvent	T (K)	Henry's law A	Henry's law K	R^2	ssc_A (mM)	q_{sscA} (mg g^{-1})
Water	308	0.66	5.48×10^6	0.99	3.51×10^{-3}	19.7
	318	1.00	6.66×10^6	0.98	3.18×10^{-3}	21.6
	328	1.22	6.82×10^6	0.99	4.30×10^{-3}	29.8
0.1 M NaCl	318	0.19	1.65×10^8	0.99	9.99×10^{-5}	16.4
pH = 10	318	0.15	1.79×10^7	0.98	4.07×10^{-4}	7.2
pH = 11	318	0.09	6.99×10^6	0.98	8.61×10^{-4}	6.0
pH = 12	318	–0.09	9.89×10^6	0.99	6.47×10^{-4}	6.6
pH = 13	318	0.20	2.78×10^6	0.99	2.51×10^{-3}	6.9

Dimensions of A and K are in mg g^{-1} and mg g^{-1} M^{-1}, respectively. Henry's law for experimental data is as $q_e = Kc_e + A$

Table 2. Parameters obtained from the Temkin and Langmuir equations and ssc_B and q_{sscB} values for adsorption of CR on Mg-Al-LDH nanocompound in water, 0.1 M NaCl and alkaline solutions in section IIA (on MP site) at 308–328 K.

Solvent	T	Temkin				Langmuir			ssc_B	q_{sscB}
	(K)	c_1	c_2	R^2	q_{mon}	K	R^2		(mM)	(mg g^{-1})
Water	308	11.3	1.86×10^6	0.96	56.0	1.64×10^5	0.98		1.79×10^{-2}	38.3
	318	19.4	1.00×10^6	0.99	100.0	9.17×10^4	0.98		1.40×10^{-2}	50.8
	328	24.0	8.64×10^5	0.96	111.1	9.05×10^4	0.97		1.22×10^{-2}	60.9
0.1 M NaCl	318	4.9	3.27×10^8	0.98	34.6	8.92×10^6	0.99		2.50×10^{-3}	37.2
pH = 10	318	5.6	8.83×10^6	0.98	25.9	9.37×10^5	0.99		1.08×10^{-2}	25.5
pH = 11	318	7.0	2.64×10^6	0.99	32.8	2.58×10^5	0.99		2.43×10^{-2}	29.8
pH = 12	318	7.0	4.06×10^6	0.98	34.5	3.71×10^5	0.97		1.07×10^{-2}	25.8
pH = 13	318	13.4	7.19×10^5	0.99	450.5	6.55×10^3	0.97		2.23×10^{-2}	36.3

Dimension of q_{mon} and c_1 is in mg g^{-1}. Dimension of c_2 and K is in M^{-1}.

Table 3. Parameters obtained from the Temkin and Langmuir equations and c_{max} and $q_{e,max}$ values for adsorption of CR on Mg-Al-LDH nanocompound in section IIB (on 003 site) in water, 0.1 M NaCl and alkaline solutions at 308–328 K.

Solvent	T	Temkin				Langmuir			c_{max}	$q_{e,max}$
	(K)	c_1	c_2	R^2	q_{mon}	K	R^2		(mM)	(mg g^{-1})
Water	308	47.8	1.27×10^5	0.98	307.0	8.36×10^3	0.97		6.79×10^{-2}	100.0
	318	37.6	2.77×10^5	0.99	153.0	3.60×10^4	0.99		5.66×10^{-2}	105.0
	328	29.7	4.24×10^5	0.97	121.8	5.47×10^4	0.96		5.27×10^{-2}	86.8
0.1 M NaCl	318	36.3	4.18×10^5	0.99	158.0	4.76×10^4	0.99		5.84×10^{-2}	116.0
pH = 10	318	34.0	2.00×10^5	0.99	200.0	1.49×10^4	0.97		6.07×10^{-2}	81.6
pH = 11	318	27.3	1.23×10^5	0.99	120.5	1.37×10^4	0.99		8.71×10^{-2}	63.8
pH = 12	318	17.4	4.07×10^5	0.98	75.2	4.80×10^4	0.97		7.83×10^{-2}	60.4
pH = 13	318	19.2	2.67×10^5	0.97	76.9	3.76×10^4	0.98		5.17×10^{-2}	51.1

Dimension of q_{mon} and c_1 is in mg g^{-1}. Dimension of c_2 and K is in M^{-1}.

was clear that CR molecules orientation in section IIB was parallel to 003 layers, Fig. 8, and due to the negatively charged adsorbent surface, the adsorption interaction was weaker than that in section IIA. Also, it was seen from IR spectra in Figs. 2(a) and 2(b) that due to the interaction of CR molecule with adsorbent, peaks of –OH group and Al–O stretching mode of Mg-Al-LDH at 3532.9 and 617.1 cm^{-1} shifted to 3509.8 and 647.9 cm^{-1} at CR-adsorbed Mg-Al-LDH. Here, the interaction of CR molecule with –OH group of adsorbent decreased its wavenumber and by shifting electron density of O–H bond toward the oxygen atom increased wavenumber of Al–O stretching mode. Besides, as seen from Table S1, a large decrease in the relative magnitude of section IIB ($\frac{q_{e,\max} - ssc_B}{q_{e,\max}}$) resulted in a disorder change of experimental maximum adsorption capacity ($q_{e,\max}$) with an increase in temperature, Table 3.

3. 2. Effects of pH and Ionic Strength on the Adsorption of CR on Mg-Al-LDH

As shown in Tables 1–3, the increase in ionic strength in alkaline and 0.1 M NaCl solutions had different effects on the adsorption capacity of adsorbent and adsorption binding constants of adsorbate with MP (in region I and section IIA) and 003 (in section IIB) adsorption sites. The ionic atmosphere of Na^+ ions surrounded interlayer carbonate ions of Mg-Al-LDH[55] and CR molecules. The shielding effect of Na^+ ions decreased the repulsion interaction between CR molecules and Mg-Al-LDH surface and consequently increased the adsorption binding constant values in region I and section IIA compared to those values in water at 318 K. But, the increase in pH of solutions and neutralization of more –OH groups of adsorbent increased its negative charge and finally resulted in a decrease in adsorption binding constant of the process at pH = 13 compared to that of neutral water at 318 K. Also, adsorption of CR molecules on the Mg-Al-LDH surface increased negative charge of adsorbent surface and finally decreased adsorption binding constant of CR on Mg-Al-LDH from region I to section IIB, Tables 1–3.

On the other hand, the adsorption capacity of Mg-Al-LDH for CR molecules in region I, section IIA and section IIB and thus $q_{e,\max}$ decreased with increase in pH of solution compared to those in water, Tables 1–3.

As reported,[55] the point of zero charge (pzc) of Mg-Al-LDH, i.e. the pH at which the surface charge is neutral, was at pH = 10 and the zeta potential of Mg-Al-LDH decreases with increase in pHs. Due to interaction of OH^- ions

with a number of interlayer –OH groups of Mg-Al-LDH, Figs. 2(a), (c) and (d), –OH and the waveumbers of Al–O stretching modes of Mg-Al-LDH at 3532.9 and 617.1 cm^{-1} shifted to 3502.1 and 655.7 cm^{-1} in Mg-Al-LDH at pH = 10 solution and to 3478.9 and 655.7 cm^{-1} in Mg-Al-LDH at pH = 13 solution. It implied that in alkaline solution interaction of OH^- ions with hydrogen atom of –OH groups of adsorbent surface decreased –OH wavenumber and by shifting electron density of O–H bond to its O atom caused an increase in wavenumber of Al–O vibration stretching mode.

These evidence showed that an increase in pH value neutralized more –OH groups of adsorbent. In addition, there was a competition of OH^- ions with CR molecules for interaction with adsorption sites which increased the repulsion interaction between Mg-Al-LDH surface and CR molecules and resulted in a decrease in the adsorption capacity of adsorbent.

By comparison of results of measurement of the nitrogen-based BET specific surface areas of Mg-Al-LDH and its sample after being in a solution at pH = 13, it seems that the hydrogen bonding between –OH and $–O^-$ groups of adsorbent caused its structure shrinkage. As it is clear from Tables 1–3, a decrease in BET surface area and pore volume of Mg-Al-LDH in alkaline solutions could also result in a decrease in the adsorption capacity of adsorbent for CR molecules in alkaline solutions and also the random change in their adsorption binding constants, Tables 1–3. Because of dissolution of adsorbent and precipitation of congo red in acidic solutions, experiments didn't carry out in acidic pHs.

3. 3. Adsorption Kinetic Equations and Modeling

The adsorption kinetic experiments were carried out in CR initial concentrations of 0.01, 0.06 and 0.09 mM, shaking rates of 30, 70 and 100 rpm, 0.1 M NaCl and alkaline (pHs of 10, 12 and 13) solutions at 308, 318 and 328 K. The adsorption of 0.01 mM CR initial concentration was in region II (section IIA) of the ARIAN thermodynamic model and included just MP adsorption sites. However, the adsorption of 0.06 and 0.09 mM CR initial concentration were in the region II (section IIB) of this model and included both MP and 003 sites. The results were analyzed by the KASRA model and ISO and intraparticle diffusion

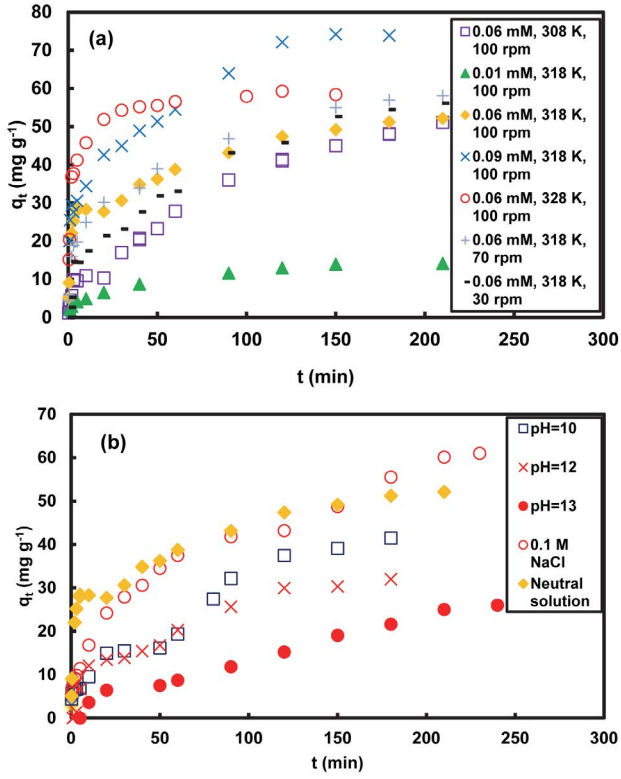

Figure 9. q_t *vs.* c_t for adsorption of CR on Mg-Al-LDH nanocompound (a) from CR solutions at different temperatures, shaking rates and initial concentrations and (b) from 0.06 mM CR in water, 0.1 M NaCl and alkaline solutions at 318 K and 100 rpm.

Table 4. TDs and TRAKs for adsorption of CR on Mg-Al-LDH nanocompound in water, 0.1 M NaCl and alkaline solutions at 308–328 K.

Solvent	*T* (K)	$[CR]_0$ (mM)	rpm	*TD* (min)	$TRAK_{C_1-C_2}$ (min)	$TRAK_{C_2-C_3}$ (min)	t_e (min)	q_e (mg g^{-1})
Water	318	0.01	100	–	–	–	150	13.9
	308	0.06	100	–	3–20	–	180	48.0
	318	0.06	100	–	3–20	–	150	49.2
	318	0.09	100	–	2–5	–	150	74.2
	318	0.06	70	–	3–5	–	180	57.0
	318	0.06	30	0–0.5	2–5	–	180	54.4
	328	0.06	100	–	2–3	–	30	54.3
0.1M NaCl	318	0.06	100	–	1–3	90–120	210	60.1
pH = 10	318	0.06	100	–	0.75–5	30–50	180	41.5
pH = 12	318	0.06	100	0–2	10–40	–	120	30.0
pH = 13	318	0.06	100	0–5	20–50	–	240	26.0

$TRAK_{C_1-C_2}$ and $TRAK_{C_2-C_3}$ are the observed TRAKs between the first and second kinetic curves and between the second and third kinetic curves, respectively. t_e and q_e are the time and adsorption capacity of starting plateau and reaching equilibrium.

equations, Figs. 9(a) and (b), Tables 4 and 5 and S2-S4. As shown in Table 4, there was a TD at the beginning of adsorption in 0.06 mM of CR at 30 rpm and 0.06 mM of CR at 100 rpm and pHs of 12 and 13. The observed TD at 30 rpm was due to the low rate of CR diffusion to the surface of adsorbent and the TDs at pHs of 12 and 13 were due to negatively-charged surface of adsorbent which was generated by the neutralization of a number of –OH groups of adsorbent.

In this study, $TRAK_{C_1-C_2}$ showed the time delay range between adsorption on MP and 003 sites and $TRAK_{C_2-C_3}$ identified the time delay range between two steps of adsorption on 003 sites. These TRAKs happened because of repulsion interaction between negatively charged CR-adsorbed Mg-Al-LDH with CR molecules in the solution.

The adsorption of 0.01 mM of CR initial concentration was in section IIA (based on the ARIAN thermodynamic model) and CR molecules were adsorbed on MP site. The analysis of kinetic data of 0.01 mM of CR initial concentration by the KASRA model showed that it was placed in regions 1 and 2 of its kinetic curves. But, the adsorptions using the initial concentrations of 0.06 and 0.09 mM CR were in section IIB (based on the ARIAN thermodynamic model) and CR molecules were adsorbed on MP (in region I and section IIA) and 003 sites (in section IIB). The kinetic study of both concentrations (0.06 and 0.09 mM) by the KASRA model showed that they were in region1 (adsorbed on MP sites) and region 2 (adsorbed on 003 sites), Tables 5 and S2. An increase in ionic strength in 0.1 M of NaCl and pH = 10 resulted in observing the third kinetic curves in these cases.

Also the analysis of adsorption results of CR on MP sites of Mg-Al-LDH by the KASRA model and intraparticle diffusion equation showed that adsorption acceleration, velocity and k_{dif} increased with the increase of experimental variables, such as initial concentration of CR, shaking rate, ionic strength and temperature. An opposite trend was observed to those kinetic parameters, when pH of solution was increased. This confirmed that adsorption kinetics on MP site was reaction-controlled, Tables 5 and S3. But, the adsorption acceleration and the velocity of adsorption of CR on 003 sites were approximately constant with increase in above-mentioned factors. The results verified that the adsorption kinetics was diffusion-controlled, Tables S2 and 5. As the CR concentration in the solution dropped during the course of adsorption, the adsorption acceleration, velocity and k_{dif} values decreased from region 1 to region 2, Tables S2, S3 and 5.

As seen in Table 5, in 0.1 M NaCl and pH of 10 solutions, adsorption was continued after the second TRAK and formed the third kinetic curves. This occurred because Na^+ ionic atmosphere surrounding adsorbent surface and CR molecules decreased the repulsion interaction between them. As shown in Table 5, k_{dif} values of these two processes were similar to k_{dif} values of other adsorption processes in the second kinetic curves. Thus, in the third kinetic curve, the adsorption kinetics of CR molecules towards 003 sites was diffusion-controlled.

On the other hand, a detailed study of kinetic data by the ISO equation showed that k_{I1} values for the adsorption of CR on MP sites (similar to trend of changes in the adsorption acceleration, velocity and k_{dif} parameters) in-

Table 5. Adsorption acceleration values, intraparticle diffusion constants and ISO rate constants for kinetics of CR adsorption on Mg-Al-LDH nanocompound at different temperatures and in various shaking rates and initial CR concentrations.

Solvent	T (K)	$[CR]_0$ (mM)	rpm	KASRA region 1 (1st curve)			KASRA region 2 (1st curve)						
				a_1	k_{dif}	k_{I1}	a_2	k_{dif}	k_{I2a}	k_{I2b}	a_3	k_{dif}	k_{I2b}
Corresponding to thermodynamic				**ARIAN region I (MP Site)**			**ARIAN section IIA (MP Site)**						
Water	318	0.01	100	–0.45	1.85	6.34×10^4	–0.001	1.0	3.05×10^4	6.81×10^4	–	–	–
Corresponding to thermodynamic				**KASRA region 1 (1st curve) ARIAN region I and section II A (MP Site)**			**KASRA region 2 (2nd curve) ARIAN section IIB (003 Site)**				**KASRA region 2 (3rd curve) ARIAN section IIB (003 Site)**		
Water	308	0.06	100	–3.54	4.36	1.75×10^5	–0.002	4.2	1.57×10^4	2.35×10^4	–	–	–
	318	0.06	100	–5.70	15.5	5.01×10^5	–0.002	2.8	2.00×10^4	4.76×10^4	–	–	–
	318	0.09	100	–20.40	21.7	1.22×10^6	–0.003	4.5	1.64×10^4	5.97×10^4	–	–	–
	318	0.06	70	–3.52	11.4	3.18×10^5	–0.002	3.3	1.64×10^4	3.72×10^4	–	–	–
	318*	0.06	30	–1.52	20.9	2.15×10^5	–0.002	3.8	1.13×10^4	3.69×10^4	–	–	–
	328	0.06	100	–14.66	25.9	7.37×10^5	–0.05	4.5	1.13×10^5	6.33×10^5	–	–	–
0.1M NaCl	318	0.06	100	–11.69	8.6	3.65×10^5	–0.008	4.3	2.72×10^4	–	-5.4×10^{-4}	4.9	2.93×10^4
pH = 10	318	0.06	100	–29.94	7.5	5.26×10^5	–0.034	2.8	5.33×10^4	–	–0.004	4.7	2.16×10^4
pH = 12*	318	0.06	100	–0.25	8.0	5.67×10^4	–0.002	3.2	4.90×10^3	1.59×10^4	–	–	–
pH = 13*	318	0.06	100	–0.06	2.8	1.77×10^4	-3.0×10^{-4}	2.3	5.22×10^3	2.51×10^4	–	–	–

Units of a_1, a_2 and a_3 are in mg g^{-1} min^{-2}. Unit of k_{dif} is in mg g^{-1} $min^{-0.5}$. Units of k_{I1} , k_{I2a} and k_{I2b} are in mg g^{-1} M^{-1} min^{-1}. Except for 0.01 mM of CR, there is a TRAK between each two successive kinetic curves (Table 4). *There is a TD (time delay) before the first curve (Table 4).

creased with increase in initial concentration of CR, shaking rate, ionic strength and temperature and decreased with the increase in solution's pH values, Tables S4 and 5. An increase in pH increased the negative charge of adsorbent surface and thus increased the repulsion interaction between CR molecules and adsorbent. This consequently decreased kinetic parameters values.

Results showed that kinetics of adsorption of CR on MP site was reaction-controlled[51] and its E_{act} by using k_{I1} values at 308-328 K was 60.7 kJ mol^{-1}.

For the adsorption of CR on 003 sites, k_{I2a} values (in part 2a), except at 328 K and pHs of 12 and 13, were similar to each other and k_{I2a} values in the range of 308–328 K did not obey the Arrhenius equation. This showed that in part 2a the diffusion of CR molecules towards adsorbent surface was rate-controlling step, Table 5, which was similar with the adsorption of CR on GO/PAMAM.[49] A decrease in k_{I2a} values with the increase in pH was due to an increase in the repulsion interaction between the adsorbent surface and adsorbed CR molecules. Also, k_{I2b} values did not obey from Arrhenius equation which showed that in part 2b (like part 2a) kinetics of CR adsorption was diffusion-controlled,[49] Table 5.

4. Conclusions

Adsorption of congo red (CR) on Mg-Al-LDH was carried out under different CR initial concentrations, alkaline pHs, temperatures, ionic strengths and shaking rates. Based on adsorbent structure and IR spectra it was clear that adsorption site of adsorbent were –OH groups attached to Al atoms of adsorbent layers. Analysis of adsorption isotherms by the ARIAN model showed that there were two types of adsorption sites on the adsorbent. These adsorption sites were –OH groups attached to Al atoms located in the surface of mesopores (named as MP sites) and micropores located in interlayer galleries between (003) layers (named as 003 sites) of adsorbent. Based on the ARIAN model, MP sites were in region I and section IIA and 003 sites were in section IIB. Adsorption in region I and sections IIA and IIB were endothermic, exothermic and endothermic, respectively. Kinetic data were analyzed by the KASRA model and ISO and intraparticle diffusion equations. It was verified that CR adsorption at first occurred on MP sites and its adsorption kinetics was reaction-controlled. Then, CR was adsorbed on 003 sites and the kinetics of adsorption on them was diffusion-controlled.

5. References

1. M. Ghaedi, H. Tavallali, M. Sharifi, S. N. Kokhdan and A. Asghari, *Spectrochimica Acta Part A*, **2012**, *86*, 107–114. **DOI:**10.1016/j.saa.2011.10.012
2. S. Maeda, S. Hongyou, K. Kunitou and K. Mishima, *TRJ*, **2002**, *72*, 240–244. **DOI:**10.1177/004051750207200310
3. I. A. Bhatti, S. Adeel, S. Siddique and M. Abbas, *J. Saudi. Chem. Soc.*, **2014**, *18*, 606–609. **DOI:**10.1016/j.jscs.2012.11.006
4. A. Hebeish, A. Waly and F. A. Abdel Mohdy, *Macromol. Mater. Eng.*, **1981**, *95*, 55–66. **DOI:**10.1002/apmc.1981.050950105
5. K. A. Amina, H. Abdel Hameid and A. H. Abd Elsttar, *Food Chem. Toxicol.*, **2010**, *48*, 2994–2999. **DOI:**10.1016/j.fct.2010.07.039
6. A. Guerra-Tapia and E. Gonzalez-Guerra, *Actas Dermosifiliogr.,* **2014**, *105*, 833–839. **DOI:**10.1016/j.ad.2014.02.004
7. J. O. B. Boahin, J. Adu-Agyem and Y. S. Peligah, *JST*, **2011**, *31*, 68–73. **DOI:**10.4314/just.v31i2.69395
8. H. Ali, *Water, Air and Soil Pollution*, **2010**, *213*, 251–273. **DOI:**10.1007/s11270-010-0382-4
9. A. Y. Zahrim and N. Hilal, *Water Resources and Industry*, **2013**, *3*, 23–34. **DOI:**10.1016/j.wri.2013.06.001
10. X. Ma, P. Chen, M. Zhou, Z. Zhong, F. Zhang and W. Xing, *Ind. Eng. Chem. Res.*, **2017**, *56*, 7070–7079. **DOI:**10.1021/acs.iecr.7b01440
11. İ. Arslana, I. A. Balcioğlua and D. W. Bahnemann, *Dyes and Pigments*, **2000**, *47*, 207–218. **DOI:**10.1016/S0143-7208(00)00082-6
12 S. Karcher, A. Kornmüller and M. Jekel, *Water Research*, **2002**, *36*, 4717–4724. **DOI:**10.1016/S0043-1354(02)00195-1
13. M. T. Yagub, T. K. Sen, S. Afroze and H. M. Ang, *Adv. Colloid Interface Sci.*, **2014**, *209*, 172–184. **DOI:**10.1016/j.cis.2014.04.002
14. K. Hunger, P. Mischke, W. Rieper, R. Raue, K. Kunde and Aloys Engel: "Azo Dyes" in Ullmann's Encyclopedia of Industrial Chemistry, Wiley-VCH, Weinheim, **2005**.
15. G. Klatskin, *Am. J. Pathol.*, **1969**, *56*, 1–13. **DOI:**10.1484/J.MSS.3.601
16. M. A. Mohammad Razi, M. N. A. Mohd Hishammudin and R. Hamdan, *MATEC Web of Conferences* **2017**, *103*, 06015. **DOI:**10.1051/matecconf/201710306015
17. A. Afkhami and R. Moosavi, *J. Hazard. Mater.*, **2010**, *174*, 398–403. **DOI:**10.1016/j.jhazmat.2009.09.066
18. A. C. Jalandoni-Buan, A. L. A. Decena-Soliven, E. P. Cao, V. L. Barraquio and W. L. Barraquio, *Philipp. J. Sci*., **2010**, *139*, 71–78.
19. E. Lorenc-Grabowska and G. Gryglewicz, *Dyes and Pigments*, **2007**, *74*, 34–40. **DOI:**10.1016/j.dyepig.2006.01.027
20. Y. Zhou, L. Ge, N. Fan and M. Xia, *Adsorpt. Sci. Technol.*, **2018**, *36*, 1310–1330. **DOI:**10.1177/0263617418768945
21. D. Maiti, S. Mukhopadhyay and P. S. Devi, *ACS Sustainable Chem. Eng.*, **2017**, *5*, 11255–11267. **DOI:**10.1021/acssuschemeng.7b01684
22. Z. X. Tang, Y. Chen, J. Xue and S. Yue, *Adv. Mater. Res.*, **2012**, *503–504*, 262–265. **DOI:**10.4028/www.scientific.net/AMR.503-504.262
23. V. Vimonse, S. Lei, B. Jin, C. W. K. Chow and C. Saint, *Appl. Clay Sci.*, **2009**, *4*, 465–472. **DOI:**10.1016/j.clay.2008.11.008
24. Y. H. Zhan and J. W. Lin, *Huan Jing ke Xue*, **2013**, *34*, 3143–3150.

25. C. Namasivayam and R. T. Yamuna, *JCTB*, **1992**, *53*, 153–157. **DOI:**10.1002/jctb.280530208
26. G. Mishra, B. Dash and S. Pandey, *Appl. Clay Sci.*, **2018**, *153*, 172–186. **DOI:**10.1016/j.clay.2017.12.021
27. D. G. Evans and R. C. T. Slade, *Struct. Bond.*, **2006**, *119*, 1–87.
28. B. Zümreoglu-Karan, *Chemical Papers*, **2012**, *66*, 1–10. **DOI:**10.2478/s11696-011-0100-8
29. Q. Wang and D. O'Hare, *Chem. Rev.*, **2012**, *112*, 4124–4155. **DOI:**10.1021/cr200434v
30. H. Acharya, S. K. Srivastava and A. K. Bhowmick, *Compos. Sci. Technol.*, **2007**, *67*, 2807–2816. **DOI:**10.1016/j.compscitech.2007.01.030
31. M. Herrero, P. Benito, F. M. Labajos, V. Rives, Y. D. Zhu, G. C. Allen and J. M. Adams, *J. Solid State Chem.*, **2010**, *183*, 1645–1651. **DOI:**10.1016/j.jssc.2010.05.014
32. A. Halajnia, S. Oustan, N. Najafi, A. R. Khataee and A. Lakzian, *Appl. Clay Sci.*, **2013**, *80–81*, 305–312. **DOI:**10.1016/j.clay.2013.05.002
33. Y. You, G. F. Vance and H. Zhao, *Appl. Clay Sci.*, **2001**, *20*, 13–25. **DOI:**10.1016/S0169-1317(00)00043-0
34. N. Baliarsingh, L. Mohapatra and K. Parida, *J. Mater. Chem. A*, **2013**, *1*, 4236–4243. **DOI:**10.1039/c2ta00933a
35. T. Li, H. N. Miras and Y. F. Song, *Catalysts*, **2017**, *7*, 260. **DOI:**10.3390/catal7090260
36. F. Zhang, Z. G. Liu, R. C. Zeng, S. Q. Li, H. Z. Cui, L. Song and E. H. Hanc, *Surf. Coat. Technol.*, **2014**, *258*, 1152–1158. **DOI:**10.1016/j.surfcoat.2014.07.017
37. J. Liu , Z. Zhan, M. Yu, Q. Wang, J. Zhang and M. Wang, *Surf. Interface Anal.*, **2012**, *44*, 863–869. **DOI:**10.1002/sia.4923
38. E. Ge´raud, V. Pre´vot and F. Leroux, *J. Phys. Chem. Solids*, **2006**, *67*, 903–908. **DOI:**10.1016/j.jpcs.2006.01.002
39. M. Ogawa and H. Kaiho, *Langmuir*, **2002**, *18*, 4240–4242. **DOI:**10.1021/la0117045
40. W. Z. Yin, Q. Tan, L. Liu and X. L. Li, *Adv. Mat. Res.*, **2012**, *454*, 101–104. **DOI:**10.4028/scientific5/AMR.454.101
41. T. Kameda, M. Saito and Y. Umetsu, *Mater. Trans.*, **2006**, *47*, 923–930. **DOI:**10.2320/matertrans.47.923
42. N. Ayawei, S. S. Angaye, D. Wankasi and E. D. Dikio, *Open Journal of Physical Chemistry*, **2015**, *5*, 56–70. **DOI:**10.4236/ojpc.2015.53007
43. E. Otgonjargal, G. Burmaa, B. Enkhmaa, M. Enkhtuul, L. Nyam-Ochir, S. Ryun and D. Khasbaatar, *Mong. J. Chem.*, **2014**, *15*, 36–39. **DOI:**10.5564/mjc.v15i0.319
44. Z. P. Xu, G. Stevenson, C. Q. Lu and G. Q. Lu, *J. Phys. Chem. B*, **2006**, *110*, 16923–16929. **DOI:**10.1021/jp062281o
45. K. S. W. Sing, D. H. Everett, R. A. W. Haul, L. Moscou, R. A. Pierotti, J. Rouquerol and T. Siemieniewska, *Pure Appl. Chem.*, **1985**, *57*, 603–619.
46. B. Samiey and S. Golestan, *Cent. Eur. J. Chem.*, **2010**, *8*, 361–369. **DOI:**10.2478/s11532-009-0135-7
47. B. Samiey and S. Abdollahi Jonaghani, *J. Pollut. Eff. Con.*, **2015**, *3*, 2.
48. I. Langmuir, *J. Am. Chem. Soc.*, **1918**, *40*, 1361–1403. **DOI:**10.1021/ja02242a004
49. M. Boudart and G. Djega-Mariadassou, Kinetics of Heterogeneous Catalytic Reactions, University Press, Princeton, NJ, **1984**. **DOI:**10.1515/9781400853335
50. M. Rafi, B. Samiey and C.-H. Cheng, *Materials*, **2018**, *11*, 496. **DOI:**10.3390/ma11040496
51. M. Ozacar, I.A. Şengil, *Colloids Surf. A,* **2004**, *242*, 105–113.
52. B. Samiey and S. Farhadi, *Acta Chim. Slov.*, **2013**, *60*, 763–773.
53. S. Nam, R. Slopek, B. D. Condon and P. Sawhney, *TRJ*, **2015**, *85*, 1221–1233. **DOI:**10.1177/0040517514561918
54. B. Samiey and A. Dadkhah Tehrani, *JCCS*, **2015**, *62*, 149–162. **DOI:**10.1002/jccs.201400093
55. Q. Wang, Y. Gao, J. Luo, Z. Zhong, A. Borgna, Z. Guo and D. O'Hare, *RSC Advances*, **2013**, *3*, 3414–3420. **DOI:**10.1039/c2ra22607c

Povzetek

V delu je opisana uporaba plastovitih Mg-Al- dvojnih hidroksidov (Mg-Al-LDH) z interkaliranim karbonatom kot adsorbentom za odstranjevanje kongo rdečega (CR). Šaržni adsorpcijski eksperimenti so bili izvedeni pri različnih temperaturah, ionski moči, začetnih koncentracijah CR, alkalnosti in stresanju. Maksimalne adsorpcijske kapacitete Mg-Al-LDH za CR so znašale 100 mg g^{-1} pri temperaturi 308 K, 105 pri 310 K in 86.6 pri 328 K. Adsorpcijska mesta na katere se je CR vezal so bile –OH skupine vezane na Al atome. Adsorpcijske izoterme so bile analizirane z modelom ARIAN. Izkazalo se je, da obstaja dva tipa adsorpcijskih mest na površini Mg-Al-LDH. Rezultati instrumentalne analize so pokazali, da gre v obeh primerih za –OH skupine, enkrat prisotne v mezoporah, poimenovane MP, in enkrat v mikroporah, poimenovane 003. Rezultati kinetičnih meritev so bili analizirani z modelom KASRA, ISO ter enačbami, ki opisujejo difuzijo v porah. Analiza je pokazala, da se CR molekule najprej vežejo na MP mesta, kjer predstavlja interakcija s površino limitni korak. Po drugi strani pa se je izkazalo, da je adsorpcija na 003 mesta difuzijsko omejena.

Scientific paper

Preparation of Magnetite by Thermally Induced Decomposition of Ferrous Oxalate Dihydrate in the Combined Atmosphere

Josef Kopp,[1] Petr Novak,[1,*] Josef Kaslik[2] and Jiri Pechousek[1]

[1] *Department of Experimental Physics, Faculty of Science, Palacký University, 17. listopadu 1192/12, 77 146 Olomouc, Czech Republic*

[2] *Regional Centre of Advanced Technologies and Materials, Palacký University, Šlechtitelů 27, 783 71 Olomouc, Czech Republic*

* *Corresponding author: E-mail: petr.novak@upol.cz*

Received: 01-04-2019

Abstract

This study presents an investigation of thermal decomposition of ferrous oxalate dihydrate in the combined atmosphere of inert and conversion gases to find an optimal route for a simple magnetite preparation. Homogenized precursor was isothermally treated inside the stainless-steel cells at 8 equidistant temperatures ranging from 300 to 650 °C for 1, 6, and 12 hours. The enclosure of samples inside the cells with the combined atmosphere eliminates the necessity of the inert gas to flow over the treated samples. Structural, magnetic, and morphological aspects of the prepared materials were examined by the combination of experimental techniques, such as Mössbauer spectroscopy, X-ray powder diffraction, and scanning electron microscopy.

Keywords: Mössbauer spectroscopy; XRD; maghemite/magnetite mixture.

1.Introduction

Magnetite is a form of an iron oxide, which finds numerous applications in the fields of materials science, information storage, medicine[1,2] or catalysis (e.g. hydrogenation of CO_2,[3] and water gas shift reaction[4]). Since the boom of nanotechnology, the synthesis of magnetite in the form of nanoparticles have been discussed in many studies.[5–11] Among the methods reported the thermally induced solid state synthesis represents a facile and cost effective method for preparation of iron oxides in the size of nanometres.[12,13]

Ferrous oxalate dihydrate is considered being a versatile precursor for iron oxides preparation. It is a metal organic mineral whose thermal decomposition leads to various forms of oxide, both pure or mixtures.[14] The individual transformation routes of $FeC_2O_4 \cdot 2H_2O$ are influenced by many experimental conditions, but the composition of reaction atmosphere, temperature and time of calcination process are among the most important ones. For example, Zhou et al.[15] reported the use of different reaction atmospheres to prepare rod-like particles composed of different forms of iron oxides.

The thermal decomposition of ferrous oxalate dihydrate in oxygen rich atmosphere (e.g., in air) has been reported in many studies.[16–24] If the $FeC_2O_4 \cdot 2H_2O$ is decomposed in air, the reaction is straight-forward and proceeds in two consecutive steps. It was shown that these two steps (endo + exothermal) partially overlap in differential thermal analysis (DTA) in the range up to 450 °C.[19] Firstly, approximately at 180 °C the water evaporates from the crystals; and then the anhydrous ferrous oxalate decomposes to iron oxides. At the temperature of 210 °C the amorphous ferric oxide is formed.[25,26] With increased temperature and prolonged calcination, the amorphous ferric oxide transforms to hematite, which is the final product of the reaction.[25] It is also possible to obtain hematite in mixture with maghemite by employing specific reaction conditions, for example, changing the thickness of the precursor layer and the annealing temperature, which allows to control the hematite/maghemite ratio.[19] Nanoparticles prepared in a such simple way were reported to have the superior catalytic activity in degradation of hydrogen peroxide.[16,27] In addition, Rao et al.[28] reported an occurrence of the maghemite in the composition of the final decomposition product if the

reaction atmosphere contained a significant amount of moisture.

Another decomposition process was reported to take place under the inert atmosphere (e.g., nitrogen or argon).[23,29–33] The differential thermal analysis (DTA) of this process generally show two major events in the range up to 450 °C, which are well separated and both of them are endothermic.[29] The first event corresponds to the evaporation of water molecules (180 °C), while the other one, a large asymmetric peak that starts at approximately 320–350 °C, is attributed to the decomposition of oxalate group and the formation of oxides. One of the generally accepted decomposition mechanisms assumes that the anhydrous ferrous oxalate decomposes to wüstite, which immediately transforms to magnetite and α-iron, due to its instability under 570 °C. [31] However, the experimental confirmation of this mechanism is still required, as the formation of wüstite phase has never been observed directly. This mechanism was indirectly supported by the findings in studies[31–33] which identified magnetite and α-iron as major and minor phases of the final product at the temperature up to 550 °C. Another accepted mechanism[34] assumes that the anhydrous oxalate decomposes directly to ultra-fine magnetite particles with no wüstite intermediate. The two Mössbauer spectroscopy investigations[35,36] of thermal decomposition of ferrous oxalate dihydrate in the inert atmosphere did not exhibit any formation of α-iron, although the experiments as well as Mössbauer measurements were performed inside the glass tube, which prevented the oxidation of small particles of α-iron.[36] Nevertheless, some authors[15,37] reported completely different composition of the decomposition product in the inert atmosphere. For example, hematite was determined as a major phase of the decomposition in nitrogen at 440 °C in the study of Mohamed et al.[37] In addition, Zhou et al.[15] reported that the maghemite was the only decomposition product after treating the sample at 400 °C for 2 h in nitrogen atmosphere.

A unique study of iron oxalate´s decomposition in the atmosphere of its conversion gases was reported by Hermanek et al.,[34] in which both Mössbauer spectroscopy and XRD were used to determine the composition of the samples. The magnetite was reported to be the main product of the thermal decomposition in the temperature range between 400–550 °C. In contrast to Hermanek et al.,[34] the pure magnetite was obtained in three other studies,[15,38,39] which reported the decomposition of ferrous oxalate dihydrate in the atmosphere of its conversion gases as a very facile method of magnetite preparation. In each of these studies the ferrous oxalate was reported to be sealed inside a container and then calcined for a certain period.

Being aware of the discrepancies concerning the possible contamination of magnetite by other iron phases, in this work we present a systematic study of thermal decomposition of ferrous oxalate in the combined atmosphere of inert and conversion gases to find an optimal synthetic route for magnetite preparation. The usage of conversion gases eliminates the necessity of the inert gas to flow through the furnace thus simplifying the magnetite synthesis process. All the samples were prepared inside the stainless-steel cells. To eliminate the possible effects of residual oxygen on the sample composition, the cells were sealed inside the box with nitrogen atmosphere. The composition and properties of the decomposition products were studied by Mössbauer spectroscopy and XRD.

2. Experimental Section

2. 1. Chemicals

Ferrous Oxalate Dihydrate (500 g) supplied by Sigma Aldrich was utilized for all the experiments.

2. 2. Synthesis

The ferrous oxalate dihydrate (Sigma Aldrich) was homogenized in the ceramic mortar for 5 minutes. This process was accompanied by a visible change in the material colour. Approximately 100 mg of homogenized material was enclosed inside each of the prepared sealable stainless-steel cells. The filling of the cells was conducted inside the box with a controlled atmosphere (nitrogen). Once filled and sealed, the cells were put inside the high-temperature laboratory furnace LAC LE/05 with HP40 controller. The decomposition of ferrous oxalate dihydrate and the subsequent formation of magnetite were observed at 8 equidistant temperature steps from 300 °C to 650 °C (one step each 50 °C). The temperature range was chosen in accordance with the previous thermogravimetric analysis (TGA) or DTA studies performed on the ferrous oxalate dihydrate.[23,28,31–34] In addition, the samples were calcinated during 3 different time intervals: 1, 6 and 12 hours, for each of the temperature steps, to study the influence of calcination time on properties of the prepared samples. Overall, twenty-four samples with the different temperature and time combinations were prepared. The temperature was measured by both in-built thermometer of the furnace and by an external thermocouple situated in the same place as the sample cell.

2. 3. Characterization

Transmission ^{57}Fe **Mössbauer spectra** of the studied samples were measured at room temperature using the MS2007 Mössbauer spectrometer based on virtual instrumentation technique.[40,41] Constant acceleration mode and ^{57}Co(Rh) source were employed. The Mössbauer spectra were processed by use of MossWinn software program.[42] The isomer shift values were referred to the value of an α-Fe foil sample at room temperature.

All the X-ray diffraction (**XRD**) patterns were measured by use of the X'PertPRO MPD diffractometer (Malvern Panalytical, Ltd) in the Bragg–Brentano geometry

equipped with a Co X-ray tube (iron filtered Co Kα radiation: λ = 0.178901 nm), programmable divergence and diffracted beam anti-scatter slits and a fast X'Celerator detector. The patterns were recorded in the 2θ range of 5–120° (2θ resolution of 0.017°) at room temperature. Line positions determination and instrumental line broadening evaluation were carried out using commercially available standards SRM640 (Si) and SRM660 (LaB_6) from the NIST (National Institute of Standard and Technologies). High Score Plus software in conjunction with the PDF-4+ and ICSD databases was employed for crystalline phase identification and Rietveld refinement.

The Scanning electron microscopy (**SEM)** images were recorded by employing the Scanning electron microscope VEGA3 LMU equipped with Everhart-Thornley type secondary electron detector (TESCAN, Brno, Czech Republic). The accelerating voltage was set to 30 kV. The pressure inside the chamber during the measurements was decreased to 10^{-2} Pa using an in-built rotary vacuum pump.

3. Results and Discussion

Before starting, the calcination of homogenized ferrous oxalate dihydrate precursor a portion of it was examined by room temperature Mössbauer spectroscopy. The acquired spectrum exhibited a symmetrical doublet with an isomer shift of δ = 1.19 mm/s and quadrupole splitting of ΔE_Q = 1.72 mm/s. Both the spectrum shape and the parameter values are typical for ferrous oxalate dihydrate.[23,34] The results obtained by XRD and Mössbauer spectroscopy of all 24 prepared samples are presented below. The individual samples are presented within the series, where each of them was prepared at different temperature (8 series, 3 samples each). All the samples were labelled T*x*H*y*, where *x* stands for temperature in °C and *y* stands for calcination time in hours. The complete list of obtained XRD and Mössbauer results is shown in Table 1. and Table 2., respectively.

3. 1. The T300 Series

The calcination of the first series of samples was conducted at 300 °C (i.e., T300 series). The Mössbauer spectrum of the first sample T300H1 showed an asymmetrical doublet composed of two components. The first one, forming most of the spectrum, was a doublet with hyperfine parameters of δ = 1.19 mm/s and ΔE_Q = 2.03 mm/s that could be assigned to anhydrous ferrous oxalate. In comparison with its hydrated counterpart, the quadrupole splitting was slightly higher, possibly because of the increased asymmetry of the electric field in the surroundings of the iron cations, which was caused by the missing water molecules. The ferrous oxalate doublet formed most of the MS spectrum. The other component was small, singlet resembling doublet with an isomer shift of δ = 0.33 mm/s and quadrupole splitting of ΔE_Q = 0.45 mm/s. It possibly originated from the presence of amorphous iron oxide or superparamagnetic magnetite. The similar doublet was also observed by Hermanek et al.,[34] who identified the doublet as a superparamagnetic magnetite based on low temperature Mössbauer spectroscopy measurements in magnetic field. Due to relative similarity of the observed components we could suggest that the doublet was a superparamagnetic magnetite (SP). The relative area of the smaller doublet component was around 7 %. The other two samples of the series were comparable in the sample composition to the first one. The gradual increase up to 13 % in the relative area corresponding to the smaller doublet was observed in the second sample T300H6. Then, in the third sample, it dropped to 8 %. However, another component or components, which have the magnetic field, could be observed in a form of small distortions in the background (see Figure 1.) taking roughly 10 % of the relative area. This component or components could be small particles of crystalline magnetite, but they were too small to specify their nature. As it was expected, the calcination of ferrous oxalate at 300 °C did not result in a complete decomposition of the precursor, but some minor part of it was transformed.

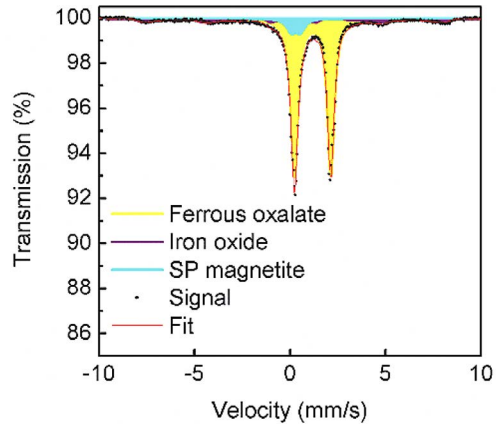

Figure 1. Mössbauer spectrum of T300H12.

3. 2. The T350 Series.

The temperature 350 °C used for calcination of the samples of the second series T350 fits well inside the range of the second DTA peak as it was reported in previous works, e.g.[31–33] The T350 series showed a gradual decomposition of anhydrous ferrous oxalate and formation of crystalline oxides. The Mössbauer spectra of all the three samples of the series exhibited the combination of a doublet and three sextets. The doublet could be again assigned to the remains of the precursor in the sample. Two new sextets were recognised to belong to two different cation sites (i.e., octahedral (O) and tetrahedral (T)) of a spinel structure of magnetite. The last sextet was ascribed to maghemite, whose presence in the spectra was probably the product of oxidation of nano-sized magnetite, which occurred after the sample cells were opened and the mate-

rial located inside was exposed to ambient atmosphere. The presence of maghemite in the spectra explains the ratio between the two left-most spectral lines. To distinguish the mixture of magnetite and maghemite from non-stoichiometric magnetite based on Mössbauer spectra is generally very difficult.[43] To fit all three sextet components, hyperfine parameters of magnetite sub-spectra were allowed to oscillate in a small interval around the fixed previously reported values.[44] Generally, the maghemite spectra compose of two very similar sextets.[44] To simplify the overall fit, maghemite was fitted by only one sextet whose hyperfine parameter values could belong only to an interval where the lower and upper limits were chosen to comply with the hyperfine parameters of both maghemite sub-spectra.[44] Moreover, the ratio between the O and T sites of magnetite was firmly fixed at 2:1. The described approach was also employed for all the remaining series. The obtained hyperfine parameters of the samples are shown in Table 2. Compared with T300 series no superparamagnetic magnetite was detected in any of the T350 samples. In contrast with our results, Hermanek et al.[34] reported that at 363 °C the doublet of superparamagnetic magnetite formed about 30 % of their Mössbauer spectrum area. Discrepancies could be explained by the absence of the prolonged calcination process in the study.[34] The evaluation of diffraction patterns of the samples of both T300 and T350 series could be done from qualitative point of view. Although quantitative analysis was also employed for evaluation of all other diffraction patterns, the lack of suitable available patterns with different grade of iron oxalate dihydrate decomposition disabled quantification in this case. Nevertheless, the diffraction patterns displayed relatively broad peaks that could be qualitatively ascribed to anhydrous ferrous oxalate and magnetite. It was observed that the weight ratio of magnetite to oxalate increased with longer calcination and was higher for all the samples in the T350 series compared to the samples of T300 series. By evaluation of both Mössbauer and XRD data of the T350 series, the temperature 350 °C seemed sufficient for decomposition of the majority of ferrous oxalate and subsequent formation of iron oxides. However, even after 12 h of calcination a part of the precursor remained undecomposed.

3. 3. The T400 Series

Regarding the third series, after heating up to 400 °C and treating the sample for 1 hour, i.e. sample T400H1, the product did not exhibit any traces of the precursor probably because the whole of the oxalate had been decomposed already. Employing the approach described above, Mössbauer spectrum of the sample T400H1 displayed three partially overlapping sextets that could be assigned to a contribution of Fe^{3+} and $Fe^{2,5+}$ cations in tetrahedral (T) and octahedral (O) sites of magnetite and maghemite. Based on the XRD analysis four additional sextets were fitted in Mössbauer spectrum and ascribed to iron carbides. Three sextets were assigned the three different sites of iron nuclei in the structure of Hagg´s carbide (Fe_5C_2) whereas the fourth sextet was assigned to cementite (Fe_3C). Fitting such small sub-spectra into an overall fit the hyperfine parameters values of sextets corresponding to carbides were strictly fixed to the values previously reported by Malina et al.[45] Although the inclusion of the carbides sub-spectra into the overall fit was based strictly on the XRD analysis, the carbide sub-spectra corresponded well with the distortions in the background of the spectra e.g. T400H1 spectrum (Figure 2.).

The obtained XRD pattern of T400H1 agreed with the acquired Mössbauer data. Apart from the diffraction peaks that could be assigned to the spinel-structured iron oxide, a small amount of cementite (2.4 wt.%) and Hagg´s carbide, (2.0 wt.%) were detected. Moreover, three additional small diffraction peaks could be observed at 17°, 28° and 31° 2θ for the sample T400H1. Although some authors[15] reported these peaks to be an unambiguous sign of maghemite, they might represent a reduction in crystal symmetry of cubic spinel structure driven by partial ordering of vacancies, which is also generated by magnetite non-stoichiometry.

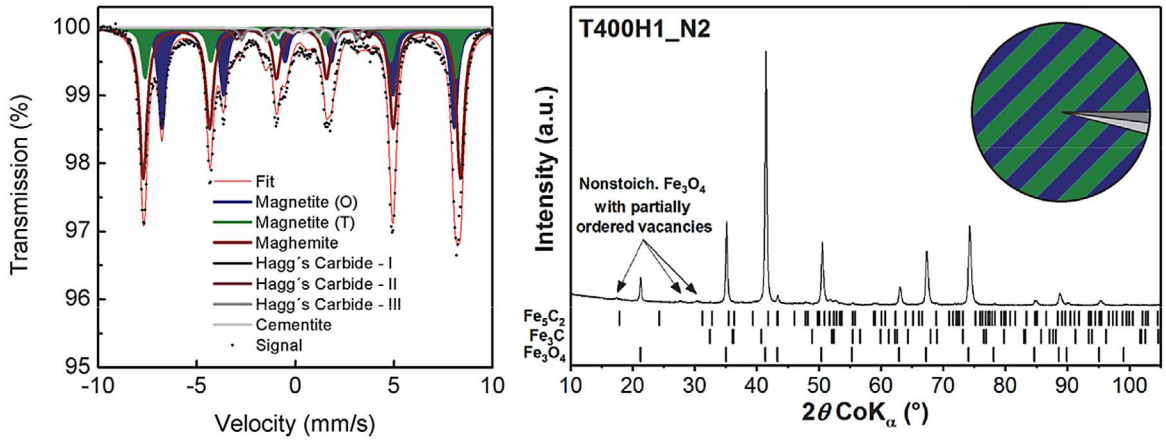

Figure 2. Mössbauer and XRD data of sample T400H1.

Table 1. XRD parameters of the measured samples.

Sample	Magnetite/Maghemite			α-iron		Cementite		Hagg's carbide		Wüstite	
	a [Å]	*w* [%]	MCL [nm]	*w* [%]	MCL [nm]	*w* [%]	MCL [nm]	*w* [%]	MCL [nm]	*w* [%]	MCL [nm]
T300H1											
T300H6											
T300H12											
T350H1					COULD NOT BE ACCURATELY QUANTIFIED*						
T350H6											
T350H12											
T400H1	8.390	95.6	41	–	–	2.0	60	2.4	26	–	–
T400H6	8.393	98.0	44	–	–	1.4	59	0.6**	15	–	–
T400H12	8.392	100.0	50	–	–	–	–	–	–	–	–
T450H1	8.396	100.0	51	–	–	–	–	–	–	–	–
T450H6	8.391	99.0	50	–	–	–	–	1	–	–	–
T450H12	8.395	97.9	55	–	–	1.0	58	1.1	26	–	–
T500H1	8.396	98.2	53	–	–	0.8**	85	1.0	73	–	–
T500H6	8.393	98.8	55	–	–	0.6**	–	0.6**	–	–	–
T500H12	8.394	98.0	56	–	–	2.0	85	–	–	–	–
T550H1	8.394	100.0	56	–	–	–	–	–	–	–	–
T550H6	8.394	100.0	65	–	–	–	–	–	–	–	–
T550H12	8.396	100.0	162	–	–	–	–	–	–	–	–
T600H1	8.396	80.1	80	6.6	89	–	–	–	–	13.3	25
T600H6	8.393	86.3	76	2.5	86	–	–	–	–	11.2	31
T600H12	8.392	86.3	57	1.9	84	–	–	–	–	11.7	30
T650H1	8.398	41.0	64	0.3**	–	–	–	–	–	58.8	32
T650H6	8.396	44.5	69	4.6	458	–	–	–	–	50.9	32
T650H12	8.388	40.5	25	1.1	109	–	–	–	–	58.4***	21(26)

a – lattice parameter, *w* – weight ratio, MCL – mean coherence length

* XRD patterns contain peaks belonging to anhydrous ferrous oxalate and magnetite. amount of magnetite gradually increases

** Quantification limit is 1 %

*** Two different structures of wüstite were observed in ratio of 15.5 % to 42.9 %.

This idea was supported by values of acquired cell parameters (see Table 1.), which reflected the presence of non-stoichiometric magnetite instead of the mixture of magnetite and maghemite. On the other hand, Mössbauer spectrum suggested the presence of maghemite in the sample, as its absence in the spectrum would lead to highly unprobeable reversed magnetite stoichiometry of 1:2 (O:T). Similar results were obtained for the other two remaining spectra of the series T400. The presence of maghemite in the samples due to gradual oxidation of nano-sized magnetite could explain the discrepancies in the results of these two techniques as both measurements were carried out at different time. The crystallite size of iron oxide particles was determined by Rietveld refinement and varied for all the samples in the T400 series between 40 and 50 nm.

3. 4. The T450/T500 Series

No major changes were observed in the results of the following two series, i.e. T450 and T500 series. The results

Table 2. Mössbauer parameters of the measured samples.

Sample	$\delta \pm 0.01$ (mm/s)	$\Delta E_Q \pm 0.01$ (mm/s)	$H \pm 0.3$ (T)	RA ± 2 (%)	Site assignment
T300H1	1.19	2.04	–	92	Ferrous oxalate
	0.33	0.45	–	8	SP magnetite
T300H6	1.17	2.21	–	87	Ferrous oxalate
	0.33	0.45	–	13	SP magnetite
T300H12	1.19	1.90	–	78	Ferrous oxalate
	0.30	0.48	–	8	SP magnetite
	0.18	–	43.3	14	Magnetite/Maghemite
T350H1	1.19	2.20	–	78	Ferrous oxalate
	0.25	–	48.9	5	Magnetite (site T)
	0.65	–	45.7	11	Magnetite (site O)
	0.23	0,03	49.7	5	Maghemite
T350H6	1.16	2.24	–	12	Ferrous oxalate
	0.26	–	48.9	12	Magnetite (site T)
	0.65	–	45.7	24	Magnetite (site O)
	0.33	0.02	49.7	52	Maghemite
T350H12	1.19	2.20	–	12	Ferrous oxalate
	0.25	–	48.9	17	Magnetite (site T)
	0.65	–	45.7	34	Magnetite (site O)
	0.29	0.03	49.7	37	Maghemite
T400H1	0.28	–	49.1	14	Magnetite (site T)
	0.65	–	46.1	28	Magnetite (site O)
	0.32	0.02	50.0	46	Maghemite
	0.24	0.09	21.5	2	Hagg´s Carbide – I
	0.17	0.06	18.2	3	Hagg´s Carbide – II
	0.22	0.13	10.9	3	Hagg´s Carbide – III
	0.20	0.03	19.9	4	Cementite
T400H6	0.28	–	49.1	21	Magnetite (site T)
	0.65	–	45.9	42	Magnetite (site O)
	0.31	0.02	49.7	24	Maghemite
	0.24	0.09	21.5	4	Hagg´s Carbide – I
	0.17	0.06	18.2	5	Hagg´s Carbide – II
	0.22	0.13	10.9	2	Hagg´s Carbide – III
	0.20	0.03	19.9	2	Cementite
T400H12	0.28	–	48.9	27	Magnetite (site T)
	0.68	–	45.7	54	Magnetite (site O)
	0.32	0.02	49.7	19	Maghemite
T450H1	0.27	–	48.9	12	Magnetite (site T)
	0.65	–	45.7	25	Magnetite (site O)
	0.34	0.02	49.7	63	Maghemite
T450H6	0.28	–	48.9	27	Magnetite (site T)
	0.67	–	45.7	54	Magnetite (site O)
	0.35	0.03	49.7	19	Maghemite
T450H12	0.28	–	48.9	24	Magnetite (site T)
	0.67	–	45.9	50	Magnetite (site O)
	0.31	0.03	49.7	12	Maghemite
	0.24	0.09	21.5	2	Hagg´s Carbide – I

Sample	$\delta \pm 0.01$ (mm/s)	$\Delta E_Q \pm 0.01$ (mm/s)	$H \pm 0.3$ (T)	RA ± 2 **(%)**	Site assignment
	0.17	0.06	18.2	2	Hagg´s Carbide – II
	0.22	0.13	10.9	2	Hagg´s Carbide – III
	0.20	0.03	19.9	6	Cementite
T500H1	0.26	–	48.9	24	Magnetite (site T)
	0.66	–	45.7	48	Magnetite (site O)
	0.33	0.02	49.7	18	Maghemite
	0.20	0.03	19.9	10	Cementite
T500H6	0.27	–	49.2	24	Magnetite (site T)
	0.66	–	46.1	48	Magnetite (site O)
	0.32	0.02	49.8	18	Maghemite
	0.24	0.09	21.5	3	Hagg´s Carbide – I
	0.17	0.06	18.2	3	Hagg´s Carbide – II
	0.22	0.13	10.9	2	Hagg´s Carbide – III
	0.20	0.03	19.9	2	Cementite
T500H12	0.28	–	48.9	28	Magnetite (site T)
	0.67	–	45.9	56	Magnetite (site O)
	0.28	0.02	49.7	7	Maghemite
	0.24	0.09	21.5	4	Hagg´s Carbide – I
	0.17	0.06	18.2	3	Hagg´s Carbide – II
	0.22	0.13	10.9	1	Hagg´s Carbide – III
	0.20	0.03	19.9	1	Cementite
T550H1	0.28	–	49.1	23	Magnetite (site T)
	0.67	–	46.1	46	Magnetite (site O)
	0.30	0.02	– 49.7	31	Maghemite
T550H6	0.28	–	48.9	22	Magnetite (site T)
	0.66	–	45.9	43	Magnetite (site O)
	0.32	0.02	49.7	35	Maghemite
T550H12	0.28	–	49.0	27	Magnetite (site T)
	0.67	–	45.9	54	Magnetite (site O)
	0.31	0.02	49.7	18	Maghemite
T600H1	0.28	–	48.9	20	Magnetite (site T)
	0.67	–	45.9	41	Magnetite (site O)
	0.26	0.02	49.7	5	Maghemite
	0.00	–	33.0	17	α–Iron
	1.04	0.05	–	16	Wüstite
T600H6	0.28	–	48.9	24	Magnetite (site T)
	0.67	–	46.0	48	Magnetite (site O)
	0.29	0.02	49.7	6	Maghemite
	0.00	0.24	32.8	7	α–Iron
	1.05	–	–	14	Wüstite
T600H12	0.28	–	48.9	22	Magnetite (site T)
	0.67	–	46.1	44	Magnetite (site O)
	0.33	0.03	49.7	15	Maghemite
	0.00	–	33.1	5	α–Iron
	1.03	0.25	–	14	Wüstite
T650H1	0.27	–	49.1	14	Magnetite (site T)
	0.65	–	46.0	29	Magnetite (site O)
	0.00	–	32.8	8	α–Iron
	1.06	0.12	–	49	Wüstite
T650H6	0.25	–	48.9	14	Magnetite (site T)
	0.65	–	45.7	28	Magnetite (site O)
	0.00	–	32.8	14	α–Iron
	1.05	0.19	–	44	Wüstite
T650H12	0.25	–	48.9	12	Magnetite (site T)
	0.65	–	47.0	24	Magnetite (site O)
	0.00	–	32.8	5	α–Iron
	1.04	0.27	–	40	Wüstite
	0.86	0.72	–	20	Wüstite

δ – isomer shift, ΔE_Q – quadrupole splitting, H – hyperfine magnetic field, RA – relative area. The f–factor was considered equal to 1 for all reported phases.

demonstrated similar composition of phases compared to the series T400 (see Table 1. and Table 2.). In both series, the crystallite size of iron oxide particles was slightly higher (50–56 nm) as excepted due to the increased calcination temperature. A slight rise in the crystallite size was also observed within individual series with prolonged calcination time. Mossbauer spectra displayed three overlapping sextets that could be ascribed to magnetite and maghemite. In some cases, according to XRD analysis, iron carbides were present in the samples and were fitted along in the Mössbauer spectra. However, there was no observed trend in the overall amount of iron carbides in individual samples and some samples of the series did not contain any carbides at all. The presence of carbides in the samples of T400, T450 and T500 series was probably caused by the reducing effect of CO molecule, which evolve during the decomposition of the oxalate anion. The molecules of CO then reacted with still undecomposed ferrous oxalate to form iron carbides (1).

$$8\,FeC_2O_4 + 6\,CO \rightarrow Fe_3C + Fe_5C_2 + 19\,CO_2. \qquad (1)$$

Here, this reaction mechanism, firstly introduced by Hermanek et al.,[34] is modified to accommodate the formation of Hagg´s carbide as well. Hong et al.[46] even used the thermal decomposition of ferrous oxalate in dynamic atmosphere of CO to prepare the microcubes of Hagg´s carbide for their subsequent application in Fischer-Tropsch synthesis.

Concerning the observed overall amounts of carbides, Hermanek[34] reported that up to 20 % of iron ions belonged to cementite in Mössbauer spectra, that is higher compared to our results, where only up to 12 % of iron ions was ascribed to iron carbides. In contrast, no carbides were registered in other studies,[15,38,39] where the conversion gases synthesis route was used for magnetite preparation. In addition, no carbides were also reported in the study by Angermann and Töpfer[47] who decomposed ferrous oxalate in a combined atmosphere of CO/CO_2. These discrepancies allowed us to conclude that the presence of iron carbides might depend on the partial pressure of CO inside the cells. The high amount of carbides in Hermanek´s study[34] could be explained by enclosing the sample into a relatively small container, which caused the high partial pressure of the formed CO. When the relatively larger containers were used[15,38,39] the samples did not contain any iron carbides or their amounts were simply undetectable by the employed instruments. Some of the evolved CO could also react with the remaining oxygen to form CO_2. On the basis of our experimental results, we could suggest that although the sealing of the sample cells prevented the intrusion of the oxygen into the cells, it was not sufficient to withstand the pressure evolved inside during decomposition of the ferrous oxalate. After reaching the critical level of pressure, a part of the gas leaked out and lowered the partial pressure of CO, which might explain the low amount of iron carbides or even their absence in the composition of the samples and the randomness in the carbide´s occurrence.

3. 5. The T550 Series

The next series was calcinated at 550 °C. All three samples of the T550 series were composed of spinel-structured iron oxides according to the data acquired from both Mössbauer spectroscopy and XRD (see Table 1., Table 2.). No signs of carbides or any other material were observed. Although the evaluation of the XRD patterns, especially the cell parameter, pointed to a non-stoichiometric magnetite, the relative areas of individual spectral lines in Mössbauer spectra suggest the presence of maghemite and magnetite mixture, see Figure 3. Compared with our results, Hermanek et al.[34] also reported a significant amount of α-iron (around 20 % in Mössbauer spectrum) in the temperature range of 500–570 °C. They suggested that the α-iron was a product of iron carbides decomposition. The missing α-iron in our samples might be explained by relatively lower amount of iron carbides. In addition, the eventual traces of α-iron might have been

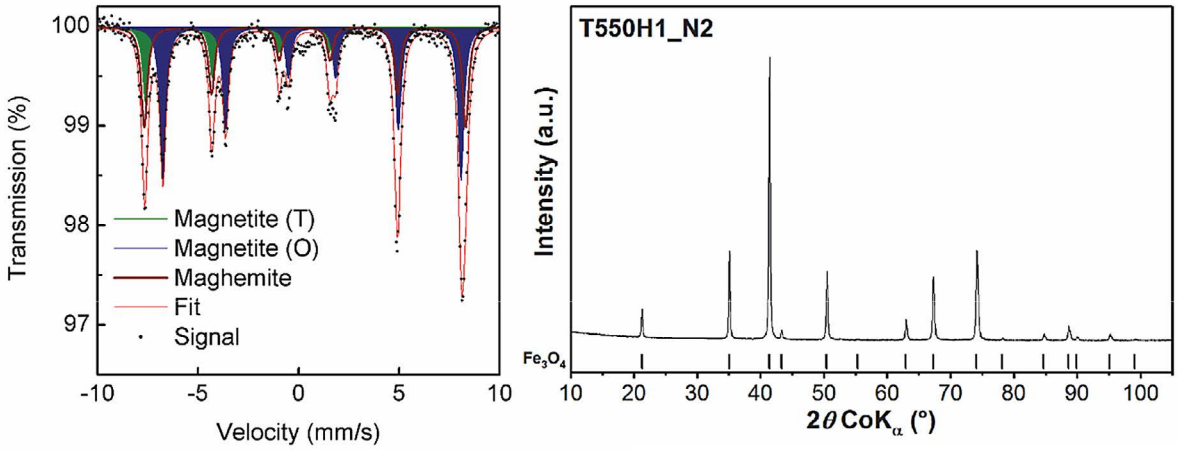

Figure 3. Mössbauer and XRD data of sample T550H1.

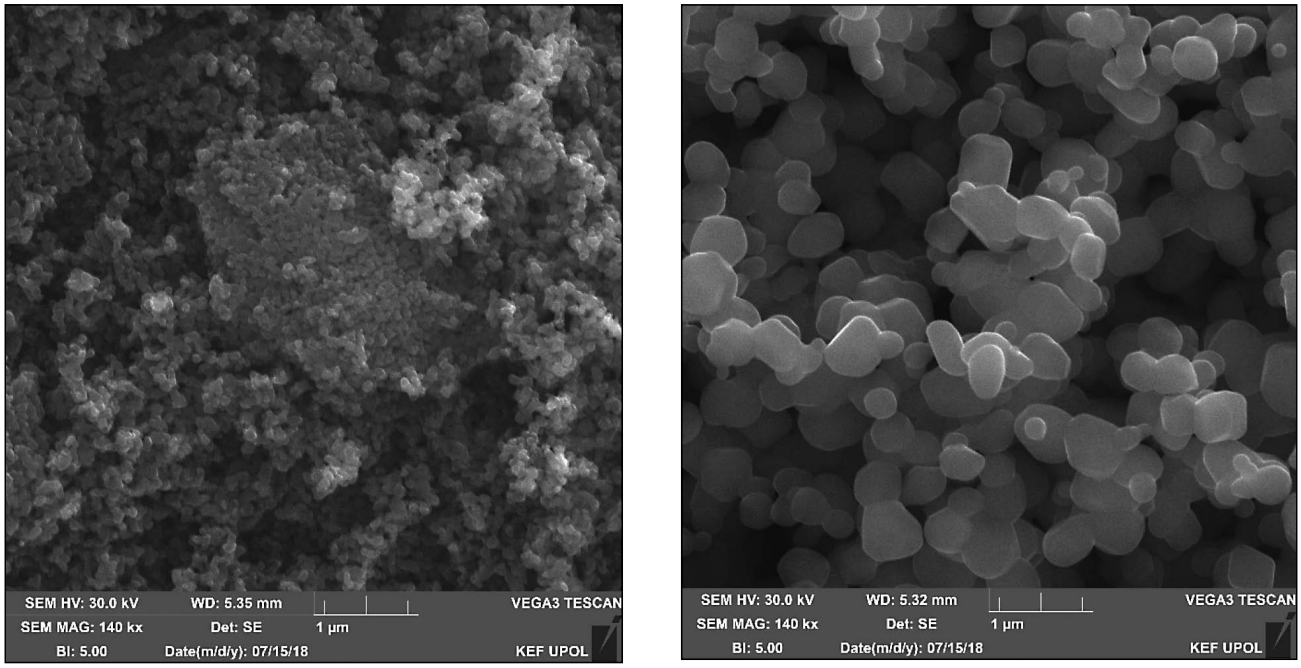

Figure 4. SEM images of samples T550H1 (left) and T550H12 (right).

re-oxidised upon its exposure to the ambient atmosphere after the cells were open. The relatively high temperature of 550 °C is probably the cause of gradually increasing crystallite size within the series; from 56 nm to 162 nm for samples T550H1 and T550H12, respectively. The dramatic increase in particle size was also observed in SEM images of samples T500H1 and T550H12 (Figure 4.).

3. 6. The T600 Series

After the samples of the seventh series had been calcinated at 600 °C, the significant change in Mössbauer spectra was observed. The two sextets which were ascribed to magnetite remained, but they were reduced in area and only a trace amount of maghemite was detected. Additionally, two new components appeared. Firstly, a relatively narrow sextet with hyperfine parameters δ = 0.0 mm/s, H = 33.0 T was identified as α-iron. Secondly, a doublet with a low quadrupole splitting, which was assigned to non-stochiometric wüstite. The exhibition of quadrupole splitting in Mössbauer spectra is a manifestation of the non-equivalent surroundings of iron cations and implies that the observed wüstite phase is non-stoichiometric. The non-stoichiometry of wüstite is generally caused by missing iron cations in its structure.[44] On the other hand, in some cases it is also possible to fit wüstite component with broad singlet, which suggests it being stochiometric.[44] The detailed hyperfine parameters obtained for individual samples of the T600 series are listed in Table 2. The results obtained by Mössbauer spectroscopy were in good agreement to those obtained by XRD (Table 1.). All diffraction peaks could be ascribed to magnetite, wüstite and α-iron. Such significant change in both Mössbauer spectra and XRD patterns was probably caused by the combination of increased temperature and reducing nature of conversion gases, which resulted in thermally induced reduction of magnetite to wüstite and α-iron, as it was suggested by Hermanek et al.[34] The increase in quadrupole splitting of wüstite phase, which was observed in samples T600H6 and T600H12, was probably caused by the prolonged exposure of wüstite to high temperature and it could be suggested that this rise was a result of wüstite increasing non-stoichiometry. Similar trend was also observed in the T650 series.

3. 7. The T650 Series

Evaluation of data acquired for samples of the last T650 series showed very similar composition in comparison to the samples of T600 series. Mössbauer spectra revealed the increased amount of wüstite and decreased amount of α-iron and magnetite. An increase in a quadrupole splitting of the wüstite was observed with prolonged calcination, similarly to the previous series. Moreover, the large middle component in the spectrum of the sample T650H12 could not be fitted by only one doublet. Two doublets with following hyperfine parameters were thus ascribed to wüstite in overall T650H12 spectrum fit, δ = 1.04 mm/s, ΔE_Q = 0.27 mm/s for the first one of the two doublets and δ = 0.86 mm/s, ΔE_Q = 0.72 mm/s for the other one. Concerning the XRD analysis of the sample T650H12, the acquired patterns were composed of two wüstite structures with different cell parameters thus pointing to the presence of two different forms of wüstite. The second wüstite structure was probably the result of the increased non-stoichiometry after the wüstite had been exposed to high temperatures for 12 h. In addition to

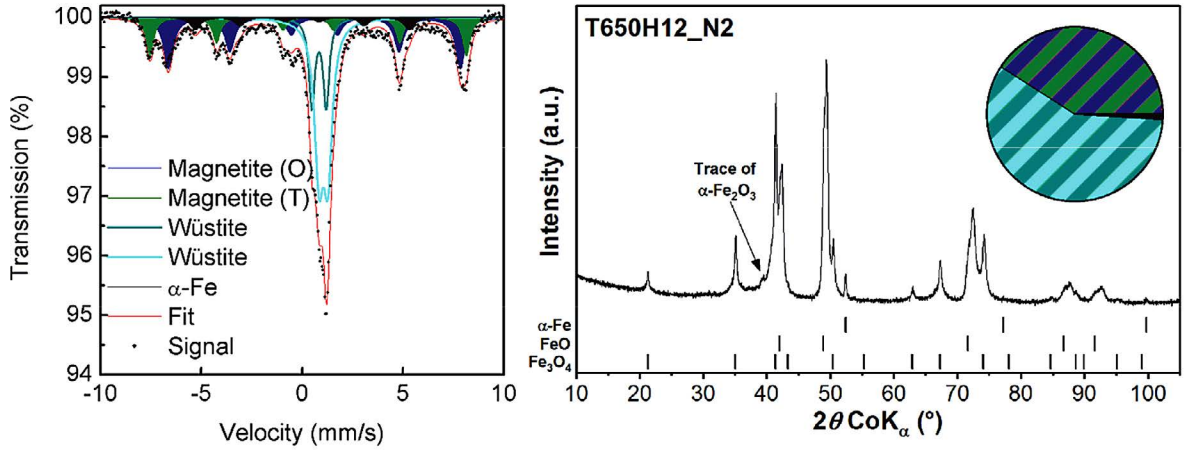

Figure 5. Mössbauer and XRD data of sample T650H12.

quantified phases, part of the α-Fe might have been re-oxidised back the most stable iron oxide, i.e., hematite, which was in a trace amount identified in the diffraction pattern of the sample T650H12 (Figure 5.).

4. Conclusion

Ferrous oxalate dihydrate was enclosed inside stainless-steel cells under the nitrogen atmosphere. Thermal decomposition of the precursor was systematically carried out at 24 different temperature/time combinations (300–650 °C; 1, 6 and 12 hours) to find the optimal route for magnetite preparation. The prepared materials were studied by Mössbauer spectroscopy and XRD. However, all decomposition routes resulted in obtaining the magnetite particles containing impurities. The remains of the precursor were observed in all the samples calcined below 400 °C, even after long calcination time (12 h). Almost spinel-structured iron oxide particles, magnetite and maghemite, (e.g. 90 %) were prepared in the temperature range of 400–500 °C. Maghemite was most probably formed by oxidation of small particles of magnetite, which is unstable in the air. Other phases consisted solely of iron carbides phases (i.e., Fe_3C and Fe_5C_2). Mixture of magnetite and maghemite, free of carbides, was obtained at 550 °C. Above that temperature the formation of wüstite and α-iron was observed. Both of them seemed to be products of thermally induced reduction of magnetite and maghemite by CO. The crystallite size of the obtained iron oxide particles was in the range of 41 to 162 nm, depending on the temperature and the calcination time of the preparation process.

5. Acknowledgment

The authors gratefully acknowledge the financial support from the internal IGA grants of Palacký University (IGA_PrF_2019_002 and IGA_PrF_2019_023) and from the Czech-China mobility project Nr. 8H17065 of Ministry of Education, Youth and Sports of the Czech Republic. Authors would also like to thank Mgr. Ivo Medřík for sharing his expertise and offering a practical advice, Mgr. Tomáš Ingr for SEM images and Helena Sedláčková for her help with the paper.

6. References

1. A. S. Teja, P. Y. Koh, *Prog. Cryst. Growth Charact. Mater.* **2009**, *55*, 22–45. **DOI:**10.1016/j.pcrysgrow.2008.08.003
2. A. Ito, M. Shinkai, H. Honda, T. Kobayashi, *J. Biosci. Bioeng.* **2005**, *100*, 1–11. **DOI:**10.1263/jbb.100.1
3. S. Saeidi, N. A. S. Amin, M. R. Rahimpour, *J. CO2 Util.* **2014**, *5*, 66–81.
4. M. Zhu, I. E. Wachs, *ACS Catal.* **2016**, *6*, 722–732. **DOI:**10.1021/acscatal.5b02594
5. J. M. Honig, *Proc. Indian Acad. Sci. (Chemical Sci.)* **1986**, *96*, 391–409. **DOI:**10.1007/BF02936294
6. X. Li, Z. Si, Y. Lei, J. Tang, S. Wang, S. Su, S. Song, L. Zhao, H. Zhang, *CrystEngComm* **2010**, *12*, 2060–2063. **DOI:**10.1039/b926780h
7. S. Komarneni, W. Hu, Y. D. Noh, A. Van Orden, S. Feng, C. Wei, H. Pang, F. Gao, Q. Lu, H. Katsuki, *Ceram. Int.* **2012**, *38*, 2563–2568. **DOI:**10.1016/j.ceramint.2011.11.027
8. S. H. Sun, H. Zeng, *J. Am. Chem. Soc.* **2002**, *124*, 8204–8205. **DOI:**10.1021/ja026501x
9. D. Amara, I. Felner, I. Nowik, S. Margel, *Colloids Surfaces A Physicochem. Eng. Asp.* **2009**, *339*, 106–110. **DOI:**10.1016/j.colsurfa.2009.02.003
10. J.-N. Park, P. Zhang, Y.-S. Hu, E. W. McFarland, *Nanotechnology* **2010**, *21*, 225708 (8).
11. D. Maity, S. G. Choo, J. Yi, J. Ding, J. M. Xue, *J. Magn. Magn. Mater.* **2009**, *321*, 1256–1259. **DOI:**10.1016/j.jmmm.2008.11.013
12. M. Stefanescu, O. Stefanescu, M. Stoia, C. Lazau, *J. Therm. Anal. Calorim.* **2007**, *88*, 27–32. **DOI:**10.1007/s10973-006-8003-6

13. R. Zboril, M. Mashlan, D. Petridis, *Chem. Mater.* **2002**, *14*, 969–982. **DOI:**10.1021/cm0111074
14. E. J. Baran, *Chemie der Erde - Geochemistry* **2016**, *76*, 449–460.
15. W. Zhou, K. Tang, S. Zeng, Y. Qi, *Nanotechnology* **2008**, *19*, 065602 (9).
16. C. Gregor, M. Hermanek, D. Jancik, J. Pechousek, J. Filip, J. Hrbac, R. Zboril, *Eur. J. Inorg. Chem.* **2010**, *2010*, 2343–2351.
17. R. Zboril, L. Machala, M. Mashlan, M. Hermanek, M. Miglierini, A. Fojtik, *Phys. Status Solidi C Conf.* **2004**, *1*, 3583–3588.
18. N. Koga, Y. Sato, *J. Phys. Chem. A* **2011**, *115*, 141–151. **DOI:**10.1021/jp110407n
19. M. Hermanek, R. Zboril, *Chem. Mater.* **2008**, *20*, 5284–5295. **DOI:**10.1021/cm8011827
20. Y. Feng, T. Hu, Z. Pu, M. Wu, J. Mi, *J. Therm. Anal. Calorim.* **2015**, *122*, 947–953. **DOI:**10.1007/s10973-015-4757-z
21. L. Yue, R. Liu, D. Jin, *Russ. J. eletrochemistry* **2015**, *51*, 299–304.
22. A. K. Ganguli, T. Ahmad, *J. Nanosci. Nanotechnol.* **2007**, *7*, 2029–2035. **DOI:**10.1166/jnn.2007.763
23. P. Hermankova, M. Hermanek, R. Zboril, *Eur. J. Inorg. Chem.* **2010**, *2010*, 1110–1118.
24. V. Borker, K. S. Rane, V. N. Kamat Dalal, *J. Mater. Sci.* **1993**, *4*, 241–248.
25. D. Smrčka, V. Procházka, P. Novák, J. Kašlík, V. Vrba, *AIP Conf. Proc.* **2016**, *1781*, 020012 (8).
26. L. Machala, R. Zboril, A. Gedanken, *J. Phys. Chem. B* **2007**, *111*, 4003–4018. **DOI:**10.1021/jp064992s
27. M. Hermanek, R. Zboril, I. Medrik, J. Pechousek, C. Gregor, *J. Am. Chem. Soc.* **2007**, *129*, 10929–10936. **DOI:**10.1021/ja072918x
28. V. Rao, A. L. Shashimohan, A. B. Biswas, *J. Mater. Sci.* **1974**, *9*, 430–433. **DOI:**10.1007/BF00737843
29. M. A. Mohamed, A. K. Galwey, *Thermochim. Acta* **1993**, *213*, 269–278. **DOI:**10.1016/0040-6031(93)80021-2
30. M. E. Mendoza, F. Donado, R. Silva, M. A. Peréz, J. L. Carrillo, *J. Phys. Chem. Solids* **2005**, *66*, 927–931. **DOI:**10.1016/j.jpcs.2004.06.019
31. E. D. Macklen, *J. inorg. nucl. Chem.* **1967**, *29*, 1229–1234. **DOI:**10.1016/0022-1902(67)80362-2
32. D. Broadbent, D. Dollimore, J. Dollimore, *J. Chem. Soc.* **1967**, *0*, 451–454. **DOI:**10.1039/j19670000451
33. R. A. Brown, S. C. Bevan, *J. inorg. nucl. Chem.* **1966**, *28*, 387–391. **DOI:**10.1016/0022-1902(66)80316-0
34. M. Hermanek, R. Zboril, M. Mashlan, L. Machala, O. Schneeweiss, *J. Mater. Chem.* **2006**, *16*, 1273–1280. **DOI:**10.1039/b514565a
35. M. J. Halsey, A. M. Pritchard, *J. Chem. Soc.* **1968**, 2878–2880. **DOI:**10.1039/J19680002878
36. M. Katada, T. Ogimoto, *J. Radioanal. Nucl. Chem.* **2000**, *246*, 7–14. **DOI:**10.1023/A:1006744006158
37. M. A. Mohamed, A. K. Galwey, S. A. Halawy, *Thermochim. Acta* **2005**, *429*, 57–72. **DOI:**10.1016/j.tca.2004.08.021
38. T. Plachy, M. Cvek, Z. Kozakova, M. Sedlacik, *Smart Mater. Struct.* **2017**, *26*, 025026 (8).
39. Z. Kozakova, I. Kuritka, P. Bazant, M. Pastorek, V. Babayan, *Mater. Lett.* **2015**, *138*, 116–119. **DOI:**10.1016/j.matlet.2014.09.125
40. J. Pechoušek, D. Jančík, J. Frydrych, J. Navařík, P. Novák, *AIP Conf. Proc.* **2012**, *1489*, 186–193. **DOI:**10.1063/1.4759489
41. J. Pechousek, R. Prochazka, D. Jancik, J. Frydrych, M. Mashlan, *J. Phys. Conf. Ser.* **2010**, *217*, 012006 (4).
42. Z. Klencsár, E. Kuzmann, A. Vértes, *J. Radioanal. Nucl. Chem.* **1996**, *210*, 105–118. **DOI:**10.1007/BF02055410
43. G. M. Da Costa, E. De Grave, P. M. A. De Bakker, R. E. Vandenberghe, *Clays Clay Miner.* **1995**, *43*, 656–668. **DOI:**10.1346/CCMN.1995.0430602
44. R. M. Cornell, U. Schwertmann, *The Iron Oxides*, **2003**.
45. O. Malina, P. Jakubec, J. Kašlík, J. Tuček, R. Zbořil, *Nanoscale* **2017**, *9*, 10440–10446. **DOI:**10.1039/C7NR02383A
46. S. Y. Hong, D. H. Chun, J.-I. Yang, H. Jung, H.-T. Lee, S. Hong, S. Jang, J. T. Lim, C. S. Kim, J. C. Park, *Nanoscale* **2015**, *7*, 16616–16620. **DOI:**10.1039/C5NR04546K
47. A. Angermann, J. Töpfer, *J. Mater. Sci.* **2008**, *43*, 5123–5130. **DOI:**10.1007/s10853-008-2738-3

Povzetek

V tej študiji predstavljamo raziskavo termičnega razkroja železovega oksalat dihidrata v kombinirani atmosferi inertnih in pretvorbenih plinov, z namenom iskanja optimalne poti za pripravo magnetita. Homogeniziran prekurzor je bil izotermično obdelan v celicah iz nerjavnega jekla pri različnih temperaturah v območju od 300 °C do 650 °C. Spreminjali smo tudi čas razkroja (1 uro, 6 ur in 12 ur). Vzorce smo zaprli v celice s kombinirano atmosfero in s tem odpravili potrebo po pretoku inertnega plina. Strukturne, magnetne in morfološke vidike pripravljenih materialov smo preučili s kombinacijo eksperimentalnih tehnik, kot so Mössbauerjeva spektroskopija, rentgenska praškovna difrakcija in vrstična elektronska mikroskopija (SEM).

DOI: 10.17344/acsi.2019.4988 *Acta Chim. Slov.* **2019,** *66,* 466–472

Scientific paper

Phase Equilibria in the $MnGa_2Te_4$-$MnIn_2Te_4$ System, Crystal Structure and Physical Properties of $MnGaInTe_4$

Faig Mamedagha Mammadov,[1] Imamaddin Rajabali Amiraslanov,[2] Yegana Rasul Aliyeva,[2] Sadiyar Sultan Ragimov,[2] Leyla Farkhad Mashadiyeva[1] and Mahammad Baba Babanly[1,*]

[1] *Institute of Catalysis and Inorganic Chemistry, Azerbaijan National Academy of Science, 113, H.Javid. ave., AZ-1143, Baku, Azerbaijan,*

[2] *Institute of Physics, Azerbaijan National Academy of Science, 131, H.Javid. ave., AZ-1143, Baku, Azerbaijan*

* *Corresponding author: E-mail: babanlymb@gmail.com*

Received: 03-01-2019

Abstract

The phase equilibria in the $MnGa_2Te_4$-$MnIn_2Te_4$ system were experimentally investigated by means of differential thermal analysis and powder X-ray diffraction technique. It was found that this system is quasi-binary and characterized by dystectic and eutectic equilibria and the formation of a wide area of solid solutions based on the starting compounds. The crystal structures of the $MnGaInTe_4$ and $MnIn_2Te_4$ were refined by the Rietveld method using powder X-ray diffraction data. It was established, that both phases crystallize in the tetragonal system (Space group *I-42m*). Electron paramagnetic resonance and Raman spectra, as well as the temperature dependences of the electrical conductivity and the Hall effect for the $MnGaInTe_4$ crystal, were studied.

Keywords: $MnGa_2Te_4$-$MnIn_2Te_4$ system; phase diagram; solid solutions; $MnGaInTe_4$ crystal structure; rietveld method; EPR spectroscopy; raman spectroscopy

1. Introduction

Complex metal chalcogenides are essential functional materials possessing optical, photoelectric, thermoelectric, magnetic and other properties.[1–7] Recent studies have shown that some of these phases are topological insulators and are considered promising for use in spintronics and quantum computing.[8–11] Among the chalcogenide materials, magnetic semiconductors of the type MB_2X_4 (where M – Mn, Fe, Co, Ni; B – Ga, In; X – S, Se, Te) and phases on their basis are very promising for use in the manufacture of lasers, light modulators, photodetectors and other electronic devices controlled by a magnetic field.[12–17]

Search and development of methods for the directed synthesis of new multicomponent phases and materials requires the study of phase equilibria in the relevant systems.[18,19] For this case, the systems including compounds which are structural or formula analogs are the greatest interest since the formation of broad areas of substitutional solid solutions can be expected in them.[20–24]

Herein, the phase equilibria in the $MnGa_2Te_4$-$MnIn_2Te_4$ system are studied, the crystal structures of the $MnGaInTe_4$ and $MnIn_2Te_4$ are refined, as well as the EPR and Raman spectra for the $MnGaInTe_4$ crystals are measured, and the temperature dependences of the electrical conductivity and the Hall Effect of the $MnGaInTe_4$ are investigated.

The starting compounds $MnGa_2Te_4$ and $MnIn_2Te_4$ were studied in detail. According to authors,[25] the $MnGa_2Te_4$ compound melts congruently at 1118 K (at 1093±10 K,[26]) and has a homogeneity region of 49.8–50.2 mol% MnTe over the MnTe-Ga_2Te_3 section. The $MnIn_2Te_4$ compound also melts congruently at 1013 K,[27] (at 1040 K according to reference,[28]).

The crystal structure of the $MnGa_2Te_4$ was studied in a number papers.[26, 29, 30] The authors,[29] showed that this compound has a pseudo-tetragonal monoclinic unit cell with parameters: $a = b = 0.847$ nm; $c = 4.83$ nm; $\alpha = \beta = \gamma \sim 90°$; $Z = 16$. Close parameters were obtained: $a = b = 0.8486$

nm; c = 4.840 nm; α = β = γ ~ 90°; Z = 16.[26] The crystal structure of $MnGa_2Te_4$ was studied by the Laue method.[30] It was shown that this compound crystallizes in the monoclinic structure (Sp. gr. *C2/c*) with parameters: a = 1.1999(3); b = 1.1999(3); c = 2.4922(6) nm; β = 104.01(2)°; Z = 16.

The $MnIn_2Te_4$ compound crystallizes in a tetragonal structure (Sp. Group $I\ \bar{4}2m$) with the parameters: a = 0.6191(2) nm; c = 1.2382(3) nm; Z = 2.[31]

Mn-00003

2. The Experimental Part

2. 1. Synthesis

For research ternary compounds $MnGa_2Te_4$ and $MnIn_2Te_4$ were synthesized. Simple substances from the company EVOCHEM ADVANCED MATERIALS GMBH (Germany) of high purity were used for the synthesis: gallium ingots (Ga-00009; 99.999%), indium in granules (In-00005; 99.999%), manganese pieces (Mn-00003; 99.98%), tellurium pieces (Te-00005; 99.9999%). The synthesis was carried out by melting of elemental components in stoichiometric ratios in evacuated to about 10^{-2} Pa quartz ampoules at temperatures ~50 K higher than their melting points followed by slow cooling in the furnace off mode to room temperature. In order to prevent the interaction of quartz with manganese, the synthesis of compounds and alloys of the studied system was carried out in graphitized ampoules.

The individuality of the synthesized compounds was controlled by differential-thermal analysis (DTA) and powder X-ray diffraction technique (PXRD). According to the DTA data, the $MnGa_2Te_4$ and $MnIn_2Te_4$ compounds melt congruently correspondingly at 1075 ± 3 K and 1021 ± 3 K, which is somewhat different from the literature data.[25–28] Analysis of the powder X-ray diffraction patterns confirmed the single-phase of both compounds.

The $MnGa_2Te_4$-$MnIn_2Te_4$ alloys were prepared from the starting ternary compounds also by vacuum alloying in graphitized quartz ampoules. All alloys were subjected to thermal annealing at 900 K for 500 hours in order to achieve complete homogenization and then slowly cooled in the furnace off.

2. 2. Methods

Phase equilibria in the $MnGa_2Te_4$-$MnIn_2Te_4$ system were investigated by means of DTA and PXRD methods.

DTA of the equilibrated alloys was carried out using a NETZSCH 404 F1 Pegasus system. The measurement was performed between room temperature and ~1300 K with a heating and cooling rate of 5 K · min^{-1} under the inert gas (Ar) flow. Temperatures of thermal effects were determined from the heating curves with an accuracy of ± 2 K. NETZSCH Proteus Software was used for measuring and evaluating data.

Scanning Electron Microscopy combined with Energy-Dispersive X-ray spectroscopy (SEM/EDXS) was used for elemental analysis of samples. SEM/EDXS was performed using a JEOL JSM 6610-LV Scanning Electron Microscope.

The PXRD analysis was performed using a "D2 Phaser" diffractometer with $CuK\alpha_1$ radiation (5°≤2-theta≤120°). The solution and refinement of the crystal structure were done by the Rietveld method using the TOPAS-4.2 Software (Bruker).

Electron Paramagnetic Resonance (EPR) spectroscopy of $MnGaInTe_4$ crystals was carried out with the ELEXSYS E 580 spectrometer (Bruker), and the Raman spectra were obtained using the "Nanofinder 30" 3D Laser Raman Microspectroscopy System (Tokyo Instruments).

The temperature dependences of the electrical conductivity and the Hall effect for the $MnGaInTe_4$ were studied in the temperature range 100–400 K on the "HL5500 PC-Hall effect measurement system" (Nanometric).

3. Results and Discussion

3. 1. Phase equilibria in the $MnGa_2Te_4$-$MnIn_2Te_4$ system

From the DTA data (Table 1) and PXRD studying of annealed $MnGa_2Te_4$-$MnIn_2Te_4$ alloys, it is established that this system is characterized by the dystectic (D) and eutectic (e) equilibria (Fig. 1a). The β-phase of the $MnGaInTe_4$ composition melts with an open maximum at 1028 K. The eutectic has a composition of 30 mol% $MnIn_2Te_4$ and crystallizes at 1012 K. Wide regions of solid substitutional solutions based on starting compounds are formed. At the

Table 1. Experimental DTA and PXRD data for the $MnGa_2Te_4$-$MnIn_2Te_4$ system

Composition, mol% $MnIn_2Te_4$	The thermal effect, K	Parameters of the tetragonal lattice, nm	
		a	c
0 ($MnGa_2Te_4$)	1083		
10	1030–1062		
15	1013–1050		
20	1012–1034	0.60816(3)	1.21308(8)
25	1012		
30	1011–1016	0.60812(3)	1.21310(8)
35	1013–1020		
40	1018–1024	0.60852(3)	1.21403(8)
45	1026		
50	1030	0.610293 (7)	1.21766(2)
60	1013–1023	0.61207(3)	1.22232(7)
70	1004–1011		
80	1000	0.61553(3)	1.23026(7)
90	1005–1012		
100 ($MnIn_2Te_4$)	1022	0.61949(5)	1.23956(2)

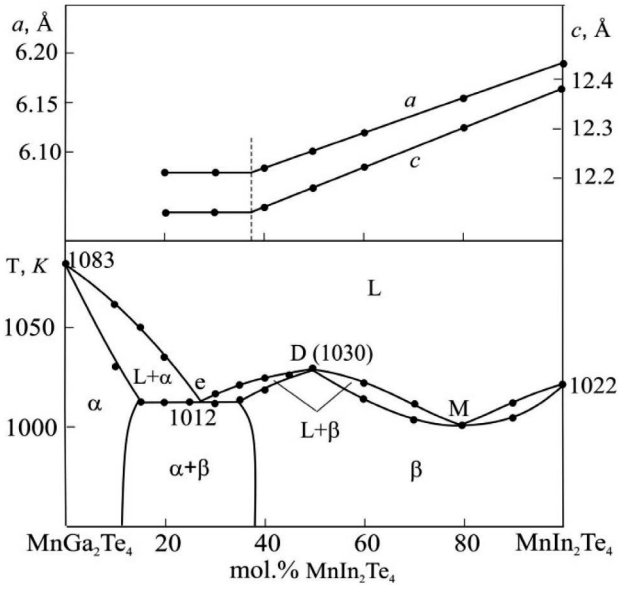

Fig. 1. The phase diagram of the $MnGa_2Te4$-$MnIn_2Te_4$ system and the concentration dependences of the crystal lattice parameters of the β-phase

eutectic temperature the solubility based on $MnGa_2Te_4$ (α-phase) is 15 mol%, and on the basis of $MnIn_2Te_4$ is 65 mol% (β-phase). On the liquidus and solidus curves of the β-phase there is a minimum point (M) at 1000 K. The congruent melting of both starting compounds, the presence of the invariant three-phase eutectic equilibrium L ↔ α + β and the extreme points D and M, as well as the absence of multiphase areas on the phase diagram, show the quasi-binary nature of this system.

PXRD results confirmed the formation of broad areas of solid solutions in the system. Figure 2 shows that powder diffraction images of the alloys from 40–100 mol% $MnIn_2Te_4$ composition area are qualitatively identical with the diffraction pattern for pure $MnIn_2Te_4$ and characterized by a certain shift of reflection lines with composition changing. The PXRD pattern of the alloy with composition 20 mol% $MnIn_2Te_4$ consists of reflection lines of both phases $MnGa_2Te_4$ (α-phase) and $MnIn_2Te_4$ (β-phase).

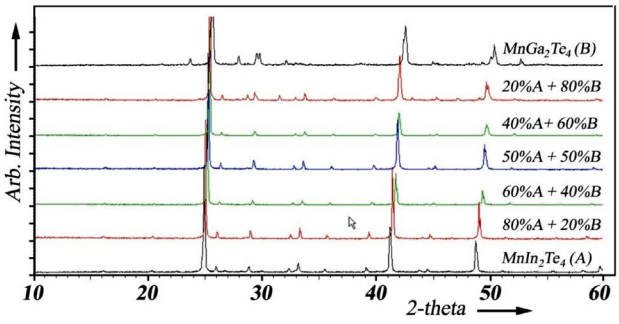

Fig. 2. PXRD patterns for some alloys of the $MnGa_2Te_4$-$MnIn_2Te_4$ system

The concentration dependence of the parameters of the crystal lattice (Table 1, Fig. 1b) of the β-phase has linear character and allows refining the region of its homogeneity at room temperature (38 mol% $MnIn_2Te_4$).

3. 2. Crystal structure of $MnIn_2Te_4$ and $MnGaInTe_4$

Based on the PXRD data, we determined the crystallographic characteristics of the $MnIn_2Te_4$ and $MnGaInTe_4$ samples (Table 2). PXRD patterns for $MnIn_2Te_4$ and $MnGaInTe_4$ and the intensities differences between the experimental and calculated by Rietveld method data are shown in Fig.3. The obtained results show good agreement of symmetry and cell parameters of these samples with the corresponding characteristics.[31] The indexing of the diffraction patterns based on obtained crystallographic parameters showed that the studied samples are single-phase. Comparison of the unit cell parameters of $MnIn_2Te_4$ and $MnGaInTe_4$ shows a noticeable difference in their values ($\Delta a \sim 0.0092$ nm; $\Delta c \sim 0.0219$ nm), which exceeds the value of errors many times. This clearly confirms the entry of Ga atoms into the structure. Despite solving the crystal structure of $MnIn_2Te_4$ on the basis of single crystals data,[31] we also used their results to refine the structure of this compound, but on the basis of powder data and the Rietveld method. The above results were also used to refine the structure of the compound $MnGaInTe_4$ by the Rietveld method. The Mn and In atoms in the structure are located in identical positions statistically, where the ratio of the number of Mn atoms to In is 1:2.[31] This structure belongs to the defective type of chalcopyrite and all metals are located in the tetrahedron of tellurium atoms. In order to refine the crystal structures of $MnIn_2Te_4$ and $MnGaInTe_4$, first, for both compounds, the Lebail and Pawley methods were used to approximate the profiles of the diffraction peaks and to refine the unit cell parameters. For both methods, the obtained results turned out to be almost identical. Later, on the basis of the obtained diffraction data, the crystal structures of the noted compounds were refined. The final results are presented in Tables 2-4. Figure 4 shows a three-dimensional presentation of the crystal structure of these phases.

Table 2. Refined structure parameters for $MnIn_2Te_4$ and $MnGaInTe_4$

Structure parameters	$MnIn_2Te_4$	$MnGaInTe_4$
Space group	*I*-42m	*I*-42m
Cell parameters: *a* (nm)	0.619490(5)	0.610293 (7)
c (nm)	1.23956(2)	1.21766(2)
The cell volume (nm^3)	0.47583(3)	0.453528(13)
Density (g/cm^3)	5.56 (2)	5.50 (2)
R-LeBail (%)	0.406	0.155
R-Pawley (%)	0.435	0.171
R-Bragg (%)	1.898	0.235

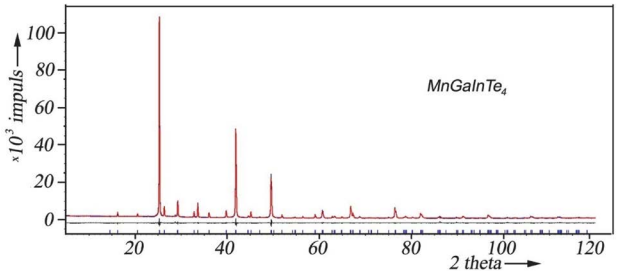

Fig. 3. PXRD patterns of $MnIn_2Te_4$ and $MnGaInTe_4$. The difference between the experimentally obtained and calculated by the Rietveld method intensities is given under the X-ray diffraction spectrum

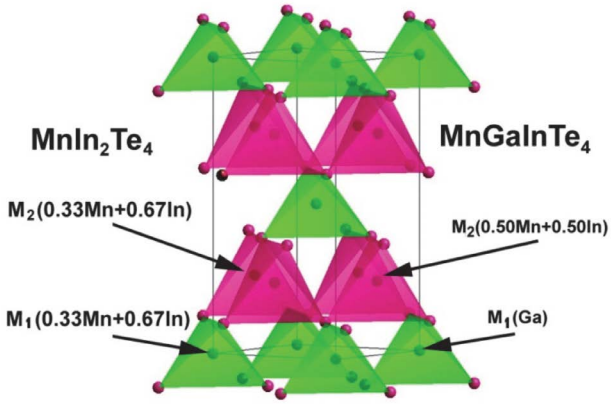

Fig. 4. Occupancy of metal positions in $MnIn_2Te_4$ and $MnGaInTe_4$ crystal structures

The results of the elemental analysis (Table 5) and X-ray fluorescence spectrum of $MnGaInTe_4$ crystals (Fig. 5) are in good agreement with the chemical formula.

Table 5. Elemental analysis results for $MnGaInTe_4$

Element	Weight %	Atomic %
Mn *K*	7.03	13.76
Ga *K*	9.26	14.27
In *L*	15.74	14.73
Te *L*	67.97	57.24
Total	**100.00**	**100.0**

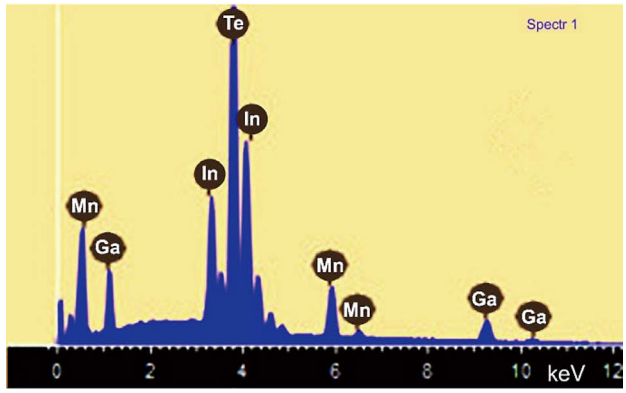

Fig. 5. The XRF spectrum for the $MnGaInTe_4$ crystal

Table 3. Atomic positional parameters in the $MnIn_2Te_4$ crystal

Atoms	Multiplicity and Wyckoff letter	x	y	z	Atom type and relative occupation	B_{eq}, (nm^2)
M_1(In+Mn)	2a	0	0	0	Mn^{+2} 0.33(1)	0.005 (1)
In^{+3} 0.67(1)						0.005 (1)
M_2(In+Mn)	4d	0	0.5	0.25	Mn^{+2} 0.33(1)	0.009 (1)
					In^{+3} 0.67(1)	0.009 (1)
Te	8i	0.2756(2)	0.2756(2)	0.1142(1)	Te 1	1.001(1)
Interatomic distances (nm)		$M_1(In_1, Mn_1)$ – Te = 0.2772(1)			$M_2(In_2,Mn_2)$ – Te = 0.2800(1)	

Table 4. Atomic positional parameters in the $MnGaInTe_4$ crystal

Atoms	Multiplicity and Wyckoff letter	x	y	z	Atom type and relative occupation	B_{eq}, (nm^2)
Ga	2a	0	0	0	Ga^{3+} 1.018(26)	0.006(3)
M(In+Mn)	4d	0	0.5	0.25	In^{3+} 0.495(22)	0.007(1)
					Mn^{2+} 0.505(22)	0.007(1)
Te	8i	0.2651(4)	0.2651(4)	0.1129(2)	Te 1	0.008(1)
Interatomic distances (nm)		Ga – Te =0.2669(3)			M(In, Mn) – Te = 0.2731(1)	

As can be seen from Tables 3 and 4, and also from Fig. 4, the crystal lattices of $MnIn_2Te_4$ and $MnGaInTe_4$ differ significantly in the occupancy of crystallographic positions. In the $MnIn_2Te_4$ structure, the *2a* and 4d positions are occupied in ratio 1:2 by the Mn and In atoms. In the structure, positions *2a* are completely occupied by gallium atoms, and the Mn and In atoms are statistically located in *4d* positions with a 1:1 ratio. The localization of Ga atoms in position *2a* in $MnGaInTe_4$ is apparently due to the fact that the ionic radius of Ga^{3+} is noticeably smaller (~ 0.018 nm) of the ionic radius of In^{3+}. Such occupancy of crystallographic positions in the $MnGaInTe_4$ phase allows us to characterize it as an ordered solid solution based on the $MnIn_2Te_4$ compound. This is in good agreement with the phase diagram (Fig. 1a), according to which the stoichiometric composition of $MnGaInTe_4$ corresponds to the dystectic point D.

3. 3. Physical Properties of the $MnGaInTe_4$

3. 3. 1. EPR Spectrum of $MnGaInTe_4$ Crystal

In fig. 6 showing the EPR spectrum of MnGaInTe4 crystals, where only one broad peak is observed. Based on the composition of this phase, it is clear that this peak refers to the resonant frequencies of manganese. If in the structure the smallest distances between Mn atoms are

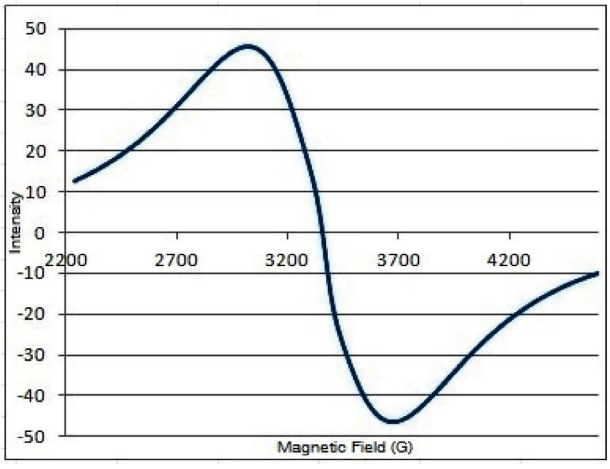

Fig. 6. EPR spectrum for the $MnGaInTe_4$ crystal

more than 1 *nm*, then their EPR spectra are characterized by a fine structure consisting of six nearby lines. However, the decrease in the distances between these paramagnetic ions leads to the merging of these fine lines to a single broad peak.[32] In our case, the distance between the Mn atoms is equal to the translational parameter of the cell ***a*** (***a*** = 0.610293 *nm*), which is significantly less than 1 *nm*. Consequently, the EPR spectrum should consist of one broad peak, which was confirmed experimentally.

3. 3. 2. Raman Spectrum of $MnGaInTe_4$ Crystal

The Raman spectrum for the $MnGaInTe_4$ crystal was represented in Fig.7. As can be seen three peaks at 96, 119 and 139 cm^{-1} are observed in the low-frequency region of the spectrum. Raman spectra of $CdIn_2Te_4$, $ZnIn_2Te_4$, and $MnIn_2Te_4$ were studied by authors of,.[33] All these compounds crystallize in the tetragonal system and their structures such as $MnGaInTe_4$ belong to the defective type of chalcopyrite.[34] This closeness is well reflected in their Raman spectra (Table 6). As is seen from Table 6 the overall characteristics of the spectra of $MnGaInTe_4$ are the same as its ternary analogs. Some distinction between the frequencies of the Raman-active modes of these materials is due to the difference in their chemical composition.

Table 6. Raman spectra data for $MnGaInTe_4$ and some of its structural analogs

Phase	Raman peaks, (cm^{-1})		
$MnGaInTe_4$	96	119	139
$MnIn_2Te_4$ [33]	97	123	153
$CdIn_2Te_4$ [33]	102	128	159
$ZnIn_2Te_4$ [33]	100	123	143; 155

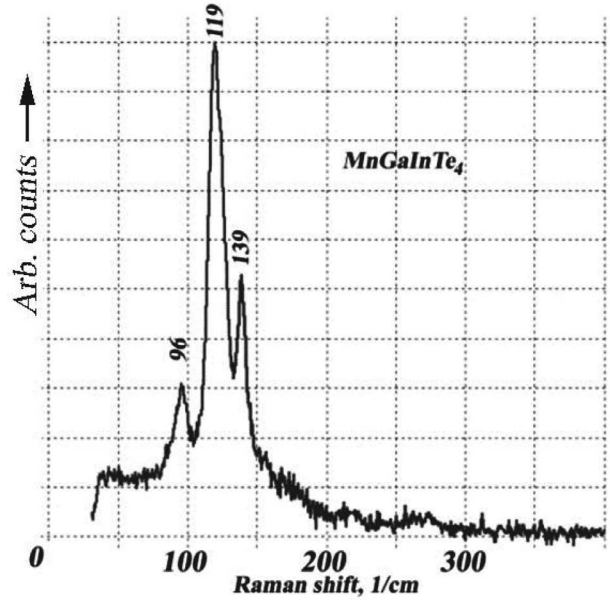

Fig. 7. Raman spectrum for the $MnGaInTe_4$ crystal

3. 3. 3. Conductivity and Hall Effect of the $MnGaInTe_4$ Crystal

The temperature dependences of the electrical conductivity (Fig. 8a) and the Hall effect (Fig. 8b) for the $MnGaInTe_4$ in the temperature range 100–400 K were studied. The value of electrical conductivity increases with increasing temperature. However, above 300 K, the electrical conductivity begins to increase more sharply. The sign of the

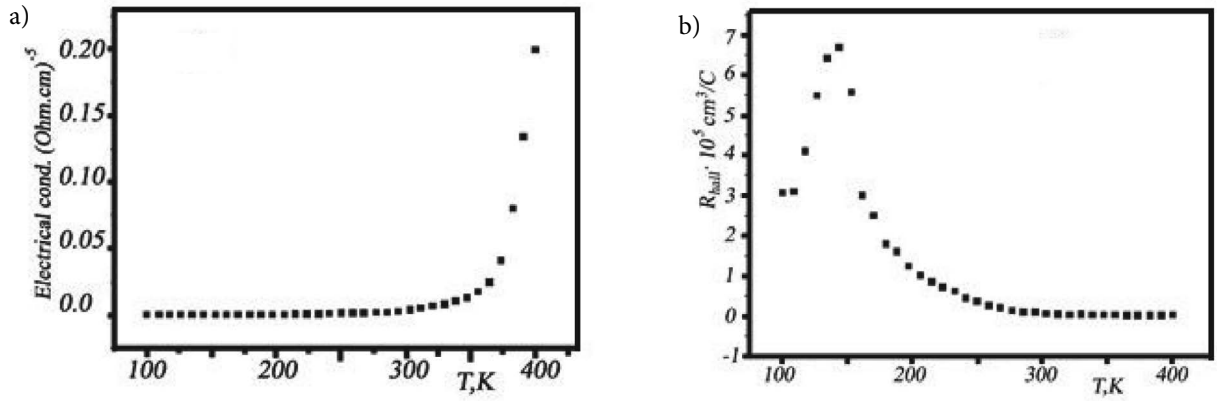

Fig. 8. The temperature dependences of the electrical conductivity (a) and the Hall Effect (b) for the $MnGaInTe_4$ crystal

Hall coefficient indicates the hole type of conductivity in the entire range of temperatures of 100-400 K. The hole concentration at room temperature calculated from measurements of the Hall coefficient is $p = 1.25 \cdot 10^{15}$ cm^{-3}. The dependence R_{Hall} (T) passes through a maximum at the 140 K and then decreases with increasing temperature (Fig. 8b).

In the literature, we did not find any information about the electrical conductivity and Hall Effect in $MnGa_2Te_4$ and $MnGaInTe_4$ compounds. Only,[35] reports the energy gap width of $MnGa_2Te_4$ E_g is 1.52 eV at 300K, which is determined from optical measurements. The determination of E_g for $MnGaInTe_4$ compounds from our measurements is impossible since its expected temperature region of intrinsic conductivity is much higher than 400 K. The presence of a maximum on the temperature dependence of the Hall coefficient for $MnGaInTe_4$ may be explained by the impurity band existence. At temperatures above T_{max}, charge transfer is performed by holes in the valence band. Below the maximum temperature, the transfer is carried primarily by thermally activated jumps between the acceptors.

The decrease in the value of the Hall coefficient above T_{max} with increasing temperature indicates an increase in the concentration of charge carriers. As a result, an increase in the value of electrical conductivity is observed (Fiq.8a). With increasing temperature, the activated electrons from the valence band are captured at these levels and become increasing of concentration of holes. The activation energy E_a has estimated from the temperature dependences of electrical conductivity was about 28 meV.

4. Conclusion

The $MnGa_2Te_4$-$MnIn_2Te_4$ quasi-binary system is characterized by a phase diagram with dystectic and eutectic equilibria and the formation of broad regions of solid solutions with a monoclinic structure (0-12 mol% $MnIn_2Te_4$) and a defect structure of chalcopyrite (38-100 mol% $MnIn_2Te_4$). Using powder X-ray diffraction data by means of the Rietveld method the crystal structures of the $MnGaInTe_4$ and $MnIn_2Te_4$ were refined. It was established, that both phases crystallize in the tetragonal system (Space group *I-42m*), but they differ significantly in the occupancy of the crystallographic positions. This allows characterizing $MnGaInTe_4$ as an individual chemical compound, which is in accordance with the phase diagram. Comparison of Raman peaks of $MnGaInTe_4$ with isostructural compounds MIn_2Te_4 (M = Zn, Mn, Cd) showed that the overall characteristics of the spectra are the same and differ only in values of the peaks frequencies. The observed EPR signal for $MnGaInTe_4$, consisting of one broad peak, indicates the presence of long-range ordering in the arrangement of Mn atoms, which is in accordance with the crystallographic data. The Hall effect study was used to determine the type of conductivity and the concentration of holes in $MnGaInTe_4$ crystals.

5. Acknowledgment

This work was supported by the Science Development Foundation under the President of the Republic of Azerbaijan – **Grant № EİF-BGM-4-RFTF-1/2017-21/11/4-M-12**

6. References

1. G. K. Ahluwalia (Ed.), Applications of Chalcogenides: S, Se, and Te, Springer, **2016**.
2. A. V. Kolobov, J. Tominaga, Two-Dimensional Transition-Metal Dichalcogenides, Springer International Publishing, **2016**.
3. I. Chung, M. G. Kanatzidis, Chem. Mater. **2014**, *26*, 849–869. **DOI:**10.1021/cm401737s
4. M.-R. Gao, Y.-F. Xu, J. Jiang, S.-H. Yu, Chem. Soc. Rev. **2013,** *42,* 2986–3017. **DOI:**10.1039/C2CS35310E.

5. B. Sa, Z. Sun Z, B. Wu, *Nanoscale*. **2016**, *8,* 1169–1178. **DOI:**10.1039/C5NR06871A
6. X. Congxin, L. Jingbo, *J. Semicond*. **2016,** *37*, 051001-1–051001-9. **DOI:**10.1088/1674-4926/37/5/051001
7. C. Gayner, K. K. Kar, *Prog. Mater. Sci.* **2016**, *83*, 330–382. **DOI:**10.1016/j.pmatsci.2016.07.002
8. S. V. Eremeev, G. Landolt, T. V. Menshchikova, V. Slomski, Y. M. Koroteev, Z. S. Aliev, M. B. Babanly, J. Henk, A. Ernst, L. Patthey, A. Khajetoorians, J. Wiebe, P. M. Echenique, S. S. Tsirkin, I. R. Amiraslanov, J. H. Dil, E. V. Chulkov, *Nat. Commun*. **2012**, *3*, 635–638. **DOI:**10.1038/ncomms1638
9. M. Papagno, S. Eremeev, J. Fujii, Z. S. Aliev, M. B. Babanly, S. Mahatha, I. Vobornik, N. Mamedov, D. Pacile, E. V. Chulkov, *ACS Nano.* **2016,** *10*, 3518–3524. **DOI:**10.1021/acsnano.5b07750
10. L. Viti, D. Coquillat, A. Politano, K. A. Kokh, Z. S. Aliev, M. B. Babanly, O. E. Tereshchenko, W. Knap, E. V. Chulkov, M. S. Vitiello, *Nano Lett*. **2016,** *16*, 80–87. **DOI:**10.1021/acs.nanolett.5b02901
11. I. A. Shvets, I. I. Klimovskikh, Z. S. Aliev, M. B. Babanly, J. Sánchez-Barriga, M. Krivenkov, A. M. Shikin, E. V. Chulkov, *Phys. Rev*. B. **2017,** *96*, 235124–7. **DOI:**10.1103/PhysRevB.96.235124
12. B. R. Myoung, J. T. Lim, C. S. Kim, *J. Magn. Magn. Mater*. **2017,** *438*, 121–125. **DOI:**10.1016/j.jmmm.2017.04.056.
13. Memo, W. Kwarteng-Acheampong, H. Heauseler, *Mater.Res. Bull*. **2003,** *38*, 1057–1061. **DOI:**10.1016/S0025-5408(03)00079-5
14. T. Torres, V. Sagredo, L. M. de Chalbaund, G. Attolini, F. Bolzoni, *Phys. B: Condensed Matter*, **2006,** *384,* 100–102. **DOI:**10.1016/j.physb.2006.05.162
15. N. A. Moroz, J. S. Lopez, H. Djieutedjeu, K. G. Ranmohotti, A. Olvera, P. Ren, *Chemistry of Materials*, **2016,** *28*, 8570–8579. **DOI:**10.1021/acs.chemmater.6b03293
16. R. Cadenasa, M. Quintero, E. Quintero, R. Tovar, M. Morocoima, J. Gonzalez, J. Ruiz, J. M. Broto, H. Rakoto, J. C. Woolley, G. Lamarche, *Physica B.* **2004,** *346–347*, 413–415. **DOI:**10.1016/j.physb.2004.01.117
17. F. López-Vergara, A. Galdámez , V. Manríquez, P. Barahona, and O. Peña, *Phys. Status Sol.B.* **2014,** *251*, 958–964. **DOI:**10.1002/pssb.201350038
18. P. Villars, A. Prince, H. Okamoto, Handbook of Ternary Alloy Phase Diagrams (10 volume set), American Technical Publishers, **1995**
19. M. B. Babanly, E. V. Chulkov, Z. S. Aliev, A. V. Shevel'kov, I. R. Amiraslanov, *Russ. J. Inorg. Chem*. **2017,** *62*, 1703–1729. **DOI:**10.1134/S0036023617130034
20. S. Z. Imamaliyeva, D. M. Babanly, D. B.Tagiev, M. B. Babanly, *Russ. J. Inorg.Chem.,* **2018**, *13*, 1703–1027. **DOI:**10.1134/S0036023618130041
21. I. J. Alverdiyev, Z. S. Aliev, S. M. Bagheri, L. F. Mashadiyeva, Y. A. Yusibov, M. B. Babanly, *J. Alloys Compd*. **2017,** *691*, 255–262. **DOI:**10.1016/j.jallcom.2016.08.251
22. Imamaliyeva S. Z., Gasanly T. M., Gasymov V. A., M. B. Babanlı, *Acta Chim. Slov.* **2017**, *64*, 221–226. **DOI:** 10.17344/acsi.2017.3207
23. Imamaliyeva S. Z., Alakbarzade G. I., Mahmudova M. A., Amiraslanov I. R., M. B. Babanly, *Acta Chim.Slov.* **2018**, *65,* 365–371. **DOI:**10.17344/acsi.2017.4053
24. F. M. Mammadov, S. Z. Imamaliyeva, I. R. Amiraslanov, M. B. Babanly, *Condensed matter and interphases*, **2018**, *20,* 604–610. **DOI:**10.17308/kcmf.2018.20/633
25. P. G. Rustamov, B. K. Babayeva, D. S. Ajdarova, *Azerb.Chem. Journ*. **1978,** *5*, 112–114 (in Russian).
26. L. Garbato, A. Geddo-Lehmann, F. Ledda, M. Cannas, O. Devoto, *Jpn. J. Appl. Phys*. **1993,** *32*, 389–390. **DOI:**10.7567/JJAPS.32S3.389
27. J. T. Kelliher, K. J. Bachmann, *MRS Proceedings.* **1990,** *216,* 479–482. doi:10.1557/proc-216-479
28. B. K. Babayeva, P. G. Rustamov, *Azerb.Chem.Journ*. **1983,** *2,* 124–127 (in Russian).
29. K.-J. Range, H.-J. Hubner, Z. *Naturforsch*. **1976,** *31b*, 886–887. **DOI:**10.1515/znb-1976-0632
30. M. Cannas, A. Garbato, L. Garbato, F. Ledda, G. Navarra, *Prog. Cryst. Growth Charact. Mater*. **1996,** *32*, 171–183. **DOI:**10.1016/0960-8974(95)00020-8 .
31. K.-J.Range, H.-J.Hubner, Z. *Naturforsch.* B. **1975,** *30*, 145–148. **DOI:**10.1515/znb-1975-3-401 .
32. S. Jain, M. Willander, R. Van Overstraeten, Compound Semiconductors Strained Layers and Devices, Springer Science, Business Media, LLC, **2000**.
33. J.-F. Lambert, P.V. Huong, J. Limtraku, J.-C. Launay, *J. Mol. Struct*. **1993,** *294*, 159–162. **DOI:**10.1016/0022-2860(93)80339-W
34. H. Hahn, G. Frank, A. D. Stoerger, W. Klingler, G. Stoerger, *Z. Anorg. Allg. Chem*. **1955,** *279*, 241–270. **DOI:**10.1002/zaac.19552790502
35. G. A. Medvedkin, Yu.V. Rud, M. A. Tairov, *Phys. stat. sol.* (a). **1988,** *110***,** 631–643. **DOI:**10.1002/pssa.2211100236

Povzetek

Fazno ravnotežje v sistemu $MnGa_2Te_4$-$MnIn_2Te_4$ smo eksperimentalno raziskali s pomočjo diferencialne termične analize in rentgenske praškovne difrakcije. Ugotovili smo, da je ta sistem kvazi-binaren in ima karakteristična distetična in evtektična ravnotežja ter široka območja trdnih raztopin na osnovi izhodnih spojin. Kristalni strukturi $MnGaInTe_4$ in $MnIn_2Te_4$ smo določili z Rietveldovo metodo z uporabo podatkov rentgenske praškovne difrakcije. Ugotovili smo, da obe fazi kristalizirata v tetragonalnem kristalnem sistemu (prostorska skupina *I-42m*). Kristale $MnGaInTe_4$ smo preučevali tudi z elektronsko paramagnetno resonanco (EPR), ramansko spektroskopijo in meritvami električne prevodnosti v odvisnosti od temperature.

Scientific paper

Subcritical Water for Recovery of Polyphenols from Comfrey Root and Biological Activities of Extracts

Jelena Vladic,[1] Natasa Nastic,[1] Tatjana Stanojkovic,[2] Zeljko Zizak,[2] Jelena Cakarevic,[1] Ljiljana Popovic[1] and Senka Vidovic[1,*]

[1] *Faculty of Technology, University of Novi Sad, Bulevar cara Lazara 1, 21000 Novi Sad, Serbia*

[2] *Institute of Oncology and Radiology of Serbia, Pasterova 14, 11000 Belgrade, Serbia*

* *Corresponding author: E-mail: senka.curcin@yahoo.com*

Received: 02-01-2019

Abstract

In the present study, subcritical water was used for extraction of bioactive compounds of *Symphytum officinale* root. Temperature (120–200 °C), extraction time (10–30 min) and HCl concentration in extraction solvent (0–1.5%) were investigated as independent variables in order to obtain the optimal conditions for extraction and to maximize the yield of total phenols, flavonoids and antioxidant activity of obtained extracts. The application of optimal conditions (200 °C, 25.6 min and 0.0075%) provided extracts rich in total phenols and flavonoids and high antioxidant activity. Results also demonstrated that subcritical water extraction showed significant advantages for recovery of comfrey root bioactive compounds comparing to maceration and ultrasound-assisted extraction techniques. In addition, subcritical water extracts of *S. officinale* root are the promising sources of compounds with antioxidant, ACE inhibition, and antiproliferative properties and could potentially be used for production of new pharmacologically-active formulations.

Keywords: *Symphytum officinale* root; Subcritical water extraction; Antioxidant activity; ACE inhibition activity; Antiproliferative activity

1. Introduction

Comfrey (*Symphytum officinale* L.), a member of the genus *Boraginacae*, is a well-known medicinal plant with large hairy leaves and small purple bell-shaped flowers, found predominantly in moist habitats especially beside river. Native in Europe and Asia, the plant has a striking record of medicinal use. The root and leaf have been used externally to treat a wide variety of ailments as well as internally as a decoction for oral and pharyngeal gargle or as a part of dietary supplements.[1] Comfrey root is used by both traditional and modern herbalists for closing up joint inflammations, musculoskeletal injuries, inflamed breasts and wounds.[2–4] Its pharmacological properties and clinical efficacy are ascribed mainly to allantoin, rosmarinic acid, mucopolysaccharides, triterpenoids and tannins.[5] Allantoin is responsible for the stimulation of cell proliferation. It protects tissues and accelerates the healing process, with abundant growth of healthy granulation tissue in slowly healing suppurative wounds. The root of comfrey is also a good source of bioactive compounds including antioxidant polyphenols, A, B and C vitamins, steroidal saponins, proteins, inulin, calcium, potassium, copper, sulfur and selenium.[6]

Extraction of bioactive compounds from comfrey root has been investigated in the last few years focusing mainly on conventional solid/liquid extraction.[7,8] Conventional extraction techniques, however, are quite laborious, time- and solvent-consuming.[9] They present low efficiency, insufficient selectivity, and use of toxic solvents which further requires additional purification and consequently increases costs. The rising interest in the bioactive compounds and products on basis of herbal materials has resulted in increased demand of the industry to implement contemporary extraction technologies. These technologies aim to provide high yield and standardized quality of products, in a short amount of time. Therefore, a great deal of effort is invested into development of modern extraction technologies, such as ultrasound-assisted extraction (UAE) and subcritical water extraction (SWE), in order to overcome aforementioned disadvantages of classical technologies. Application of innovative technologies and optimization of

production processes to produce natural products has been in the focus of numerous scientific studies.[10–14]

Ultrasound-assisted extraction has been demonstrated as an advisable tool to recover polyphenols from plant materials, due to its cheapness and maintenance cost.[15] Report by Wang et al. indicates that UAE reduces processing time, accelerates heat and mass transfer and requires a simple and easy to operate apparatus which helps in easy extraction of thermolabile compounds, without any degradation.[16] The enhancement of extraction process by ultrasounds is attributed to the cavitation phenomenon and its consequent thermal and mechanical effects which can result in disruption of the cell walls, reduction of the particle size and enhanced mass transfer across cell membrane caused by the collapse of the numerous tiny bubbles.

From the literature review, subcritical water extraction, as a potential alternative to conventional extraction techniques, has been successfully applied to extract target compounds from various matrices mainly due to its safety and compatibility with consecutive applications, environmental concerns and solvent recovery operations.[17–21] SWE is based on the use of water at temperatures ranging from boiling point to the critical temperature and pressures high enough to keep the water in a liquid state throughout the extraction process. The change of the dielectric constant of water with temperature results in the possibility of tuning its polarity, for high-selectivity extractions.[22]

The aim of this study was to optimize SWE of polyphenol antioxidants from *S. officinale* root. Response surface methodology and Box-Behnken experimental design were employed to investigate the effect of three process parameters (temperature, time and amount of added acidifier) on the extraction of targeted compounds. Their effect on total phenols and total flavonoids content, as well as on antioxidant activity, was evaluated. Investigated responses were compared in extracts obtained by conventional and novel extraction techniques (UAE, SWE). In addition, ACE inhibition and antiproliferative activities of extracts obtained by using contemporary SWE and UAE, and classical maceration extraction of *S. officinale* root were determined.

2. Materials and Methods

2. 1. Chemicals and Reagents

1,1-Diphenyl-2-picryl-hydrazyl-hydrate was purchased from Sigma-Aldrich (Sternheim, Germany; CAS Number 1898-66-4). Folin–Ciocalteu reagent and gallic acid (CAS Number 149-91-7) were purchased from Merck (Germany). All other reagents used were either analytical or HPLC grade.

2. 2. Plant Sample

All analysis was performed by using commercial dry *S. officinale* root supplied by a producer of medicinal plants (Chamomilla, Banatski Karlovac, Vojvodina, Serbia).

2. 3. Preparation of Extracts

2. 3. 1. Maceration

Conventional solid-liquid extraction was performed with two different extraction solvents: methanol and ethanol solution (50%, w/w). All the extractions were performed by macerating 5.0 g of dry sample with 50 mL of extraction solvent at room temperature (25 °C) for 48 h in a shaker with temperature control (KS 4000i, IKA, Germany) at 150 rpm. After extraction, obtained extracts were filtrated through filter paper. Extracts were collected into glass vials and stored at 4 °C prior analysis.

2. 3. 2. Ultrasound-Assisted Extraction

Ultrasound-assisted extraction was performed in sonication water bath (EUP540A, Euinstruments, France). The bath consisted of a rectangular container with frequency fixed at 40 kHz. The samples of dried powdered *S. officinale* root (5 g) were placed in a flask (250 mL) and mixed with 50 mL of selected solvent (methanol and 50% ethanol (w/w)). The sonication was performed at temperature of 30 °C and ultrasonic power of 60 W/L for 40 min. Flasks with condensers were always positioned in the same distance from the transducer in order to provide constant ultrasonic power. After extraction, extracts were filtered through filter paper under vacuum, collected into glass vials and stored in a dark place at 4 °C prior analysis.

2. 3. 3. Subcritical Water Extraction

Subcritical water extraction (SWE) was carried out in a batch-type high-pressure extractor (Parr Instrument Company, USA) using the same experimental process previously described by Zeković et al.[23] For each run, the extraction cell was filled with 5 g of dried ground *S. officinale* root and 50 mL of double-distilled water. All SFE extractions were performed at 30 bar with different combinations of temperature (120–200 °C), extraction time (10–30 min) and concentration of HCl (0–1.5%). Obtained extracts were filtrated through filter paper under vacuum, collected into glass vials and stored in a dark place at 4 °C prior analysis.

2. 4. Analyses of Extracts

2. 4. 1. Determination of Total Phenols Content and Flavonoids Content

The total phenolics (TP) content in obtained *S. officinale* extracts was determined spectrophotometrically using standard Folin–Ciocalteu procedure.[24] Absorbances of the samples were measured at 750 nm (6300 Spectrophotometer, Jenway, UK). The results are expressed as g of gallic acid equivalents (GAE) per 100 g dry weight (DW).

The total flavonoids (TF) content in *S. officinale* extracts was determined using aluminium chloride colorimetric assay, as reported by Markham.[25] The absorbance for all tested extracts was measured at 510 nm. The content of total flavonoids was expressed as g of catechin equivalents (CE) per 100 g DW.

2. 4 .2. Determination of Antioxidant Activity-DPPH Assay

Free radical scavenging activities of *S. officinale* subcritical water extracts were evaluated following the procedure previously reported by Espín et al.[26] Antioxidant activity were expressed as IC_{50} value, defined as the inhibition concentration of the sample required to inhibit 50% of radical scavenging capacity (mg/mL).

2. 4. 3. Analysis of Angiotensin-I-converting Enzyme Inhibition Activity

Angiotensin-I-converting enzyme (ACE) inhibitory activity was measured following the assay described by Yoshie-Stark et al.[27] The IC_{50} value of samples was defined as the inhibition concentration of the sample (in μg/mL) required to inhibit 50% of ACE activity.

2. 4. 4. Cell Lines – Treatment

Malignantly cell lines used in this assay (human cervix adenocarcinoma HeLa, breast carcinoma MDA-MB-453, human myelogenous leukemia K562 and human fetal lung fibroblasts MRC-5 cells) were obtained from the American Type Culture Collection (Manassas, VA, USA). All cancer cells were kept in the RPMI-1640 medium supplemented with 10% heat-inactivated (56 °C) fetal bovine serum (FBS), l-glutamine (3 mmol/L), streptomycin (100 mg/mL), penicillin (100 IU/mL) and 25 mM HEPES, and adjusted to pH 7.2 by bicarbonate solution. Upon reaching confluence, cells were cultured in an atmosphere of 5% CO_2 and 95% relative humidity at 37 °C. 200 mg/ml of Stock solutions of compounds were prepared in dimethylsulfoxide (DMSO), and afterwards diluted in RPMI-1640 medium. HeLa cells (2000 cells per well), MDA-MB-453 cells (3000 cells per well), and MRC-5 cells (5000 cells per well) were distributed in sterile 96-well microtiter plates, and were cultured for 20 h. Thereafter, the cells were treated with investigated extracts of various concentrations. The concentrations tested were in the range of 0.0625 to 2 mg/mL. In control wells, only nutrient medium was added to the cells. The investigated extracts were added to a suspension of K562 cells (5000 cells per well) 2 h after cell seeding, in the same final concentrations. The cultures were incubated for 72 h at 37 °C in a humidified incubator with 5% CO_2.

Determination of cell survival (MTT test)

The influence of *S. officinale* extracts on the viability of malignantly transformed cell lines was determined by MTT (microculture tetrazolium test) following the procedure described by Mosmann[28] with slight modification by Ohno and Abe,[29] 72 hours after the investigated extract was added. Briefly, 20 μL of MTT solution (5 mg/mL in phosphate buffered saline (PBS)) was added to each well and plates were incubated for a further 4 h at 37 °C in 5% CO_2 humidified atmosphere. After incubation, the MTT formazan crystals were dissolved by adding 100 μl of 10% SDS to each well. The number of viable cells was measured by detecting absorbance in an ELISA microplate reader at a wavelength of 570 nm 24 h later. The cell survival (%) was calculated as absorbance of treated cells divided with absorbance of control cells and multiplied with 100. Cell growth inhibitions were expressed as IC_{50} values, defined as the concentrations of sample required to inhibit 50% of cell survival. All experiments were done in triplicate.

2. 5. Design of Experiments and Statistical Analysis

Response surface methodology was employed to study the effect of independent variables temperature (X1, 120–200 °C), extraction time (X2, 10–30 min) and HCl concentration (X3, 0–1.5%) on the total phenols content, total flavonoids content and antioxidant activity parameters as responses. The Box-Behnken experimental design (BBD) was selected to propose the model for the investigated responses. The experimental design consisted of fifteen trials in random order, including three replicates at the central point. Table 1 shows the three independent variables encoded to three levels (–1, 0 and 1).

Table 1. Box-Behnken experimental design with natural and coded levels of SWE parameters

Independent variable	Factor levels		
	(–1)	**(0)**	**(1)**
Temperature (°C)	120	160	200
Extraction time (min)	10	20	30
Concentration HCl (%)	0	0.75	1.5

A second-order polynomial model (Eq. (3)) was fitted to results in order to correlate the relationship of each factor to the response:[30]

$$Y = \beta_0 + \Sigma \beta_i X_i + \Sigma b_{ii} X_{ii}^2 + \Sigma b_{ij} X_i X_j \quad (1)$$

where Y represents the response variable, Xi, Xii and XiXj represent the linear, quadratic, and interactive terms of the coded independent variables, respectively, and β0, βi, βii, and βij are the regression coefficients for intercept, linearity, quadratic, and interaction intercept terms, respectively. Analysis of variance (ANOVA) was carried out to identify the adequacy of the developed model with the significance levels of 0.05 (significant) and 0.10 (moderately significant). The coefficient of multiple determination (R^2), coefficient of variance (CV) and p-values for the model and lack of fit coefficient were obtained from analysis of variance. The statistical software Design-Expert v.7 Trial (Stat-Ease, Minneapolis, Minnesota, USA) was employed for the all computation and graphics in this study.

3. Results and Discussion

3. 1. Statistical Analysis and Model Fitting

In this study, a Box-Behnken design was carried out to optimize the procedure for the extraction of phenolic compounds using SWE. The investigated response values (TP and TF content, and antioxidant activity) for different combination of SWE parameters (extraction temperature, extraction time and HCl concentration) are presented in Table 2.

The experimental results of SWE were fitted to a second-order polynomial model (Eq. (3)). Multiple regression coefficients for linear, interaction and quadratic terms were achieved using method of least square (MLS) (Table 3).

Table 3. Estimated coefficients of second-order polynomial models for investigated responses

Regression coefficient	Response TP	TF	IC_{50}
Intercept			
β_0	+3.99696	+1.43103	+0.016078
Linear			
β_1	+2.02431*	+0.60021*	-9.04385×10^{-3}*
β_2	+0.44419	+0.12192	-4.92939×10^{-4}
β_3	−0.13947	−0.39902*	$+2.44993 \times 10^{-3}$*
Interaction			
β_{12}	+0.082186	+0.080163	$+4.22203 \times 10^{-4}$
β_{13}	−0.63150	−0.41380*	-9.44828×10^{-5}
β_{23}	−0.60841	−0.10725	$+5.20550 \times 10^{-4}$
Quadratic			
β_{11}	+0.21706	+0.14668	$+1.96614 \times 10^{-3}$
β_{22}	+0.22050	+0.27633*	$+3.11321 \times 10^{-3}$
β_{33}	−0.45832	+0.15653	-1.53053×10^{-3}
R^{2a}	0.9654	0.9738	0.9569

* Significant at 0.05 level
a Coefficient of multiple determination

Analysis of variance (ANOVA) was employed to check adequacy of the applied models and the results are summarized in Table 4. Statistical analysis suggested that the experimental values correlate well with the models. Good model fitness has been confirmed by highly significant p-values ($p < 0.05$) for all models.

Table 2. Natural values of independent variables for Box-Behnken design and experimentally observed responses (TP, TF, IC_{50}) in obtained extracts

Run order	Independent variables T (°C)	t (min)	c HCl (%)	Investigated responses TP (g GAE/100 g)	TF (g CE/100 g)	IC_{50} (mg/mL)
1	160	10	1.5	3.24	1.33	0.0191
2	120	20	0	1.11	0.97	0.0203
3	120	10	0.75	2.16	1.23	0.0329
4	160	20	0.75	3.90	1.39	0.0160
5	160	20	0.75	3.91	1.49	0.0175
6	200	10	0.75	6.34	2.23	0.0105
7	200	30	0.75	6.87	2.64	0.0103
8	160	20	0.75	4.19	1.41	0.0147
9	200	20	0	6.13	3.04	0.0059
10	200	20	1.5	5.14	1.67	0.0125
11	160	30	0	5.49	2.62	0.0152
12	160	10	0	2.87	2.17	0.0171
13	120	20	1.5	2.65	1.26	0.0273
14	160	30	1.5	3.44	1.34	0.0192
15	120	30	0.75	2.37	1.32	0.0310

For all three investigated responses, mathematical models proved to be statistically acceptable due to insignificant lack of fit ($p > 0.05$). Validity of the models has been also confirmed by significant regression ($p < 0.05$). Furthermore, considering particularly high determination coefficients ($R^2 > 0.90$) for the TP content, TF content, and IC_{50} values (0.965, 0.974 and 0.957, respectively), applied second-order polynomial model is well adjusted to the experimental results. Considering the obtained values, these data were used for creation of response surface 3D plots for each experimental model.

Table 4. Analysis of variance (ANOVA) of the fitted second-order polynomial model for TP content, TF content and IC_{50} value

	Sum of squares	DF	Mean Square	*F*-value	*p*-value
TP content					
Model	38.84	9	4.32	15.51	0.0038
T	32.78	1	32.78	117.84	0.0001
t	1.58	1	1.58	5.67	0.0630
c	0.16	1	0.16	0.56	0.4882
T x t	0.027	1	0.027	0.097	0.7679
T x c	1.60	1	1.60	5.73	0.0620
t x c	1.48	1	1.48	5.32	0.0692
T^2	0.17	1	0.17	0.63	0.4649
t^2	0.18	1	0.18	0.65	0.4583
c^2	0.78	1	0.78	2.79	0.1558
Residual	1.39	5	0.28		
Lack of Fit	1.34	3	0.45	16.28	0.0584
Pure Error	0.055	2	0.027		
Cor Total	40.23	14			
TF content					
Model	5.43	9	0.60	20.65	0.0019
T	2.88	1	2.88	98.63	0.002
t	0.12	1	0.12	4.07	0.0997
c	1.27	1	1.27	43.59	0.0012
T x t	0.026	1	0.026	0.88	0.3914
T x c	0.68	1	0.68	23.44	0.0047
t x c	0.046	1	0.046	1.57	0.2650
T^2	0.079	1	0.079	2.72	0.1601
t^2	0.28	1	0.28	9.65	0.0267
c^2	0.090	1	0.090	3.10	0.1388
Residual	0.15	5	0.029		
Lack of Fit	0.14	3	0.047	15.83	0.0600
Pure Error	5.905×10^{-3}	2	2.952×10^{-3}		
Cor Total	5.58	14			
IC_{50} value					
Model	7.664×10^{-4}	9	8.515×10^{-5}	12.30	0.0065
T	6.543×10^{-4}	1	6.543×10^{-4}	94.49	0.0002
t	1.944×10^{-6}	1	1.944×10^{-6}	0.28	0.6189
c	4.802×10^{-5}	1	4.802×10^{-5}	6.93	0.0463
T x t	7.130×10^{-7}	1	7.130×10^{-7}	0.10	0.7613
T x c	3.571×10^{-8}	1	3.571×10^{-8}	5.157×10^{-3}	0.9455
t x c	1.084×10^{-6}	1	1.084×10^{-6}	0.16	0.7087
T^2	1.427×10^{-5}	1	1.427×10^{-5}	2.06	0.2106
t^2	3.579×10^{-5}	1	3.579×10^{-5}	5.17	0.0721
c^2	8.649×10^{-6}	1	8.649×10^{-6}	1.25	0.3145
Residual	3.462×10^{-5}	5	6.925×10^{-6}		
Lack of Fit	3.053×10^{-5}	3	1.018×10^{-5}	4.97	0.1721
Pure Error	4.097×10^{-5}	2	2.049×10^{-6}		
Cor Total	8.010×10^{-4}	14			

3. 2. Influence of Independent Variables on the Investigated Dependent Variables

Total phenolic content observed in *S. officinale* root extracts obtained under different SWE conditions ranged from 1.11 to 6.87 g GAE/100 g DW. The highest TP content was observed at temperature of 200 °C, extraction time of 30 min and HCl concentration of 0.75%, while the lowest TP content was obtained at temperature of 120 °C and extraction time of 20 min without added acid modifier (Table 2). All SWE extracts obtained at 200 °C had significantly higher TP content comparing to extracts obtained at 120 and 160 °C. According to ANOVA analysis, the linear temperature terms had an important influence ($p < 0.05$), while other effects were not statistically important (Table 4). Based on the sum of squares, the importance of the independent variables on TP content was insignificant, as well as their interactions. Determination of regression coefficients using the least squares method provided the predictive model equation for TP extraction depicted in the Table 5.

ed highly significant influence on TF content, while linear influence of extraction time was insignificant. Extraction temperature expressed the most significant positive effect on TF meaning that TF will significantly increase with increasing the temperature, which is in accordance with experimental results obtained for TP content. Linear term of HCl concentration exhibited negative influence on TF content, which imply that comfrey root flavonoids were better extracted if reduced acidifier concentration in extraction solvent were applied. Also, the interaction term between temperature and HCl concentration interaction affected TP content negatively. This means that elevated temperature and increased HCl concentration caused reduction in TF content, probably due to thermal degradation of flavonoid compounds on these severe extraction conditions. Quadratic term of extraction time exhibited significant positive influence on TF content. This suggested that an increase of extraction time increased the TF content of *S. officinale* extract. The response surface plots describing influences of SWE parameters on TF content of *S. officinale* root ex-

Table 5. Model equations which are able to predict response values within investigated experimental domain

Response	Second-order polynomial equation
TP content	$TP = 3.9969 + 2.0243\ X_1$
TF content	$TF = 1.43103 + 0.60021\ X_1 - 0.39902\ X_3 - 0.41380\ X_1\ X_3 + 0.27633\ X_2^2$
IC_{50} value	$IC_{50} = 0.0161 - 9.04385 \times 10^{-3}\ X_1 + 2.44993 \times 10^{-3}\ X_3$

The combined effect of the extraction parameters on the TP content of *S. officinale* root extracts obtained by SWE is presented in Figure 1a. The TP content increased linearly with temperature, while the extraction time did not influence this investigated response. The HCl concentration effect on phenols extraction of obtained extracts was rather insignificant. Similar findings for SWE of phenolic compounds were previously reported for other plant species.[23,31] In subcritical water extraction, temperature is one of the most prominent operational parameter that affect the efficiency and selectivity of the process. Water at high temperatures breaks bonds between phenolics and cell wall releasing them more efficiently.[32] Elevated temperatures enhance also the diffusion rate and desorption kinetics, resulting in a decrease in its viscosity and surface tension.[22] A decrease in solvent surface tension allows better pore filling, thus permitting analytes to be better solubilised.

Concerning the total flavonoids content, predictive second-order polynomial model equation, which is able to describe influence of SWE parameters on investigated response, is presented on Table 5. The linear terms of temperature and HCl concentration exhibit-

tracts are shown in Figure 1b. TF content of extracts ranged from 0.97 to 3.04 g CE/100 g DW. The highest TF value was measured in the samples obtained at a temperature of 200 °C and extraction time of 20 min, but with the absence of HCl. Extracts obtained at 120 °C, for 20 min, without using acid modifier, exhibited the lowest TF content.

Experimentally obtained values of antioxidant activity observed in *S. officinale* root extracts obtained by SWE are presented in Tables 2 and 4. The antioxidant activity of comfrey root extracts is not affected by extraction time, while the temperature and HCl concentration had a significant influence on this property, as it was the case with TF content. Linear terms of temperature displayed highly significant negative influence on investigated response (IC_{50} value). On the other hand, HCl concentration exhibited significant positive influence on IC_{50} value, which means that pure, or slightly acidified water should be used as extraction solvent. The final equation which could predict the behaviour of the investigated response is shown in Table 5. Depending on the extraction parameters antioxidant activity of extracts varied from 0.0059 to 0.0329 mg/

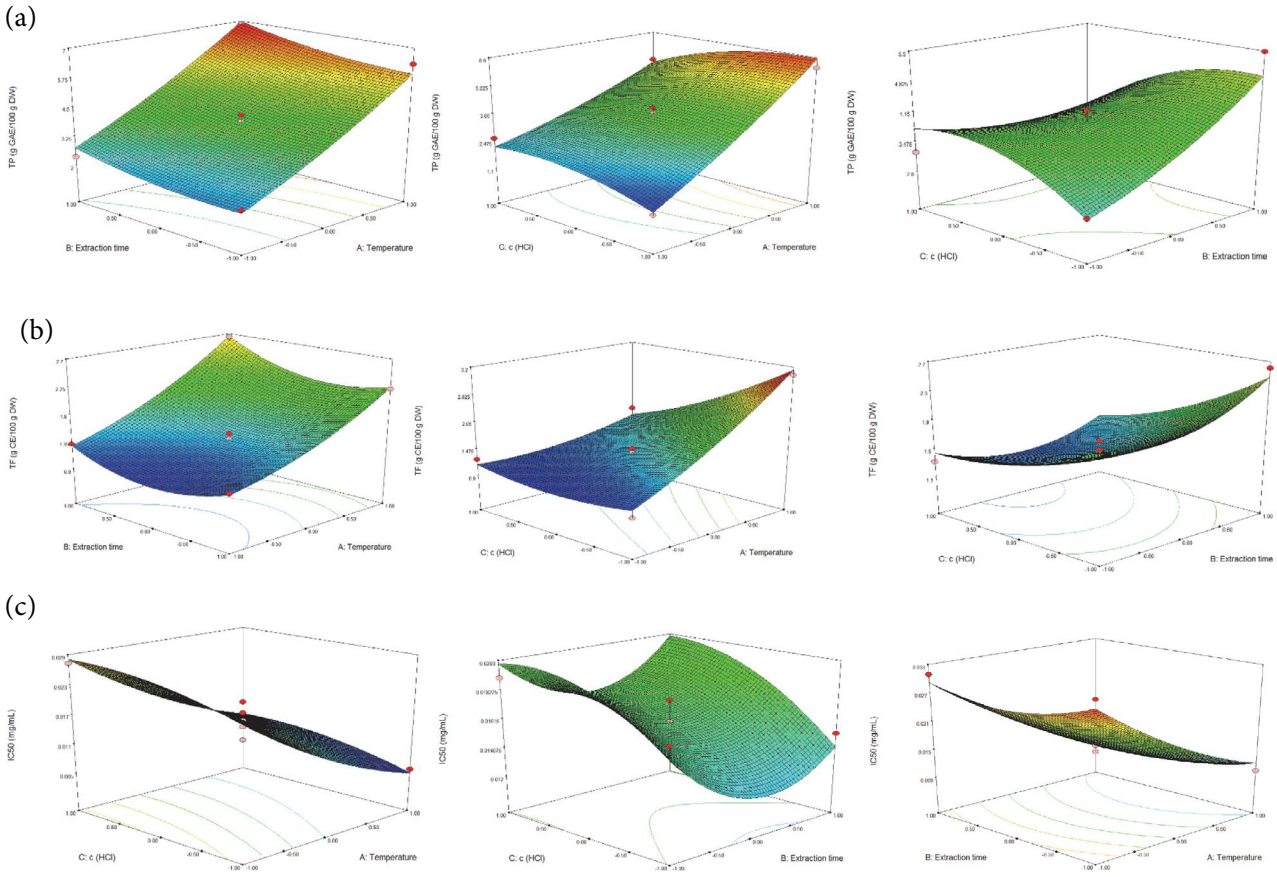

Figure 1. Response surface of TP content (a), TF content (b) and IC_{50} value (c) as simultaneous function of temperature, extraction time and HCl concentration

mL. The highest antioxidant activity was measured in the extracts obtained at a temperature of 200 °C and extraction time of 20 min without using HCl modifier. On the other hand, extracts obtained at 120 °C for 10 min using 0.75% HCl as extraction solvent, showed the lowest antioxidant activity. Antioxidant activity significantly increased with the increase in extraction temperatures from 120 to 200 °C being in accordance with the content of polyphenols and flavonoids. These findings were in agreement with previously published studies on using SWE for the isolation of natural antioxidants where antioxidant activity increased with temperature up to 200 °C in SWE of deodorized thyme.[33] He et al.[34] also examined the effects of temperature on the antioxidant activity of pomegranate seed residues extracts. The highest antioxidant activities were seen when extraction was performed at temperature between 180 and 240 °C. The high antioxidant activity of extracts acquired at such relatively high temperature may have been related to the formation of new bioactive compounds during the extraction process via Maillard reactions.[33] Visual representation of extraction parameters influence on antioxidant activity in comfrey root extracts is given in Figure 1c. Moreover, moderate correlation between $IC_{50,}$ TP and TF can be noticed, proving that polyphenols were the most important compounds responsible for antioxidant activity of *S. officinale* root.

Regarding all these aspects, the efficiency of extraction of phenolic compounds and antioxidative activity of SWE extracts depend on temperature directly. Extraction time had a negligible effect on all three investigated variables, while HCl concentration affected TF content and antioxidant activity. Other authors that dealt with subcritical water extraction came to similar conclusion.[17, 31. 35] However, in order to gain complete information about extraction parameters effect on investigated responses during SWE of *S. officinale* root, further studies including chemical characterization of the extracts and the identification of responsible bioactive compounds are required.

3. 3. Optimization of Process Parameters

Optimization of SWE process was the primary subject of this work, which allowed setting process parameters that maximized the value of all investigated

responses. Optimized extraction conditions for maximized yields of TP, TF, and minimized IC_{50} value, i.e. maximized antioxidant activity are presented in Table 6. By applying the response surface methodology and the multiple response optimization in the experimental domain investigated, the optimal process parameters of all three responses simultaneously of *S. officinale* root were determined to be as follows: temperature of 200 °C, extraction time of 25.6 min and 0.0075% HCl concentration in extraction solvent. Predicted values of investigated responses on these conditions were 7.26 g GAE/100 g DW, 3.40 g CE/100 g DW and 0.0058 μg/mL, for TP, TF and IC_{50}, respectively. Determination of optimal conditions and predicted values was based on desirability function, D = 1. The results showed that there was no significant difference observed between the predicted values and experimental ones, indicating that the model was adequate for reflecting the expected optimization. In addition, the extract obtained under optimal conditions was used for further analysis.

Table 6. Optimized extraction conditions for maximized yields of TP and TF and minimized IC_{50} value

		Investigated variable		
		TP	**TF**	**IC_{50}**
Optimal extraction condition	Temperature	200	197.60	200
	Extraction time	29.2	29.9	21.1
	c (HCl)	0.3375	0.075	0.0225
	Optimal value	7.50	3.52	0.00527

3. 4. Comparison of Extraction Techniques

Currently, literature data concerning *S. officinale* root extracts is very limited. In the present study, subcritical water extracts of *S. officinale* root obtained under optimal conditions (200 °C, 25.6 min, and 0.0075% HCl) were compared to those obtained by conventional extraction and ultrasound-assisted extraction, where ethanol (50%) and methanol were used as extraction solvents (Figure 2; Supplementary data, Table 1).

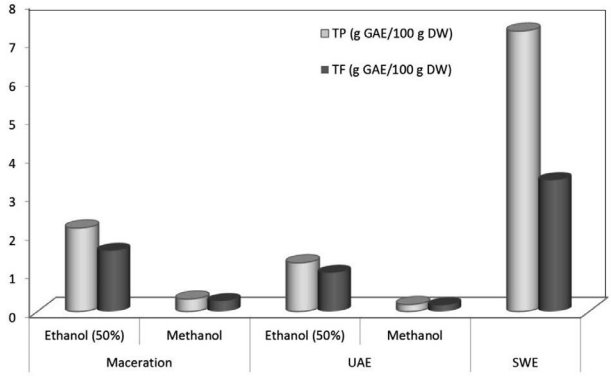

Figure 2. Total phenolic, total flavonoid contents of comfrey root extracts obtained by different extraction techniques

SWE was found to be much more efficient for extraction of TP and TF from *S. officinale* root in comparison to maceration and UAE. Lower TP and TF contents were observed by Alkan et al.[36] in methanolic and aqueous extracts of comfrey root obtained by Soxhlet extraction and decoction method. Furthermore, antioxidant activity obtained by SWE was significantly higher comparing to that obtained by maceration and UAE with ethanol and methanol. Moderately high antioxidant activity of *S. officinale* ethanolic extract (0.0397 mg/mL) was reported by Alkan et al.[36] According to the results from Figure 2, addition of methanol showed the lowest recovering capacity for bioactive compounds from comfrey root. Addition of ethanol to the water improved her capabilities to extract these bioactive compounds. But, by application of increased pressure and temperature, and transformation of water into the subcritical state, these capabilities were much more improved. These observations are related to dielectric constant of extraction solvent. In subcritical conditions, as the temperature of water is increased, the polarity of water decreases. That allows dissolving compounds of intermediate or low polarity. The dielectric constant of water decreases with the temperature (e.g., from ε = 80 at ambient temperature to ε = 27 at 250 °C) and becomes close to that of methanol (ε = 33.6 at 25 °C) and ethanol (ε = 24.5 at 25 °C).[37]

In addition, SWE process only needed 25.6 min to reach significantly higher values of investigated responses, while extraction time for maceration was 48 h and for UAE 40 min. This might be due to the dissolving properties of subcritical water, thus providing a much faster mass transfer. Given the advantages of used solvent, including its safety, selectivity and low cost, functionality, good yields of target compounds and reduced energy consumption, make this technique favorable for potential industrial applications.

3. 5. ACE Inhibition Activity

Angiotensin-I-converting enzyme (ACE) is a glycosylated zinc dipeptidyl-carboxypeptidase whose main function is to regulate arterial blood pressure by converting angiotensin I to angiotensin II, a potent vasoconstrictor.[38] Thus, inhibition of ACE has been considered as important in the chronic treatment of various cardiovascular diseases. A series of synthetic ACE inhibitors, which have been clinically used as antihypertensive drugs, cause some adverse side effects in humans.[39] Last years of the twentieth century were marked with increased worldwide interest in herbal medicine and the development of new drugs based on naturally occurring biologically active compounds.

Within this context, in the present study the extracts obtained by maceration, UAE, and SWE extract obtained under optimal conditions (temperature of 200 °C, extraction time of 25.6 min and HCl concentration of 0.0075%) were assayed for their ACE inhibitory activity. The results of the ACE inhibition activity of *S. officinale* extracts are depicted in Figure 3 (Supplementary data, Table 1).

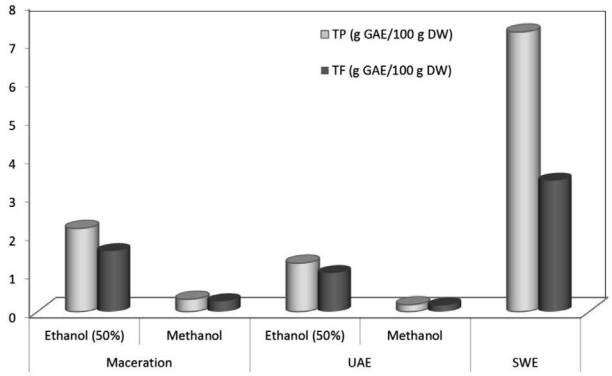

Figure 3. Antioxidant and ACE inhibition activity of comfrey root extracts obtained by different extraction techniques

All samples exhibited ACE inhibition. The subcritical water extract of comfrey root showed the highest ACE inhibitory with the IC_{50} being 0.18 μg/mL. The lowest inhibitory activity was recorded for methanol extracts obtained by maceration (5.24 μg/mL). Ethanol fractions showed higher ACE inhibition activities than did methanol fractions. This is the first report with ACE inhibition evaluation from this plant. Previous studies on the ACE inhibition of some other plant extracts obtained by different extraction techniques indicated their strong activity.[40,41] According to Wagner et al.,[42] the *in vitro* activity of some flavonoids was due to the formation of chelate complexes within the active centre of ACE. This chelate complex could be formed between a heterocyclic oxygen and a phenolic hydroxyl group in its vicinity. In studies reported by other authors, phenolic acids inhibited ACE via interaction with the zinc ion and this interaction was stabilized by other interactions with amino acids in the active site of ACE.[31] Early works with *S. officinale* root extract indicated presence of some phenolic compounds such as rosmarinic acid, chlorogenic acid, caffeic acid, rutin, kaempferol, apigenin, quercetin.[7, 8] Some of these compounds such as caffeic acid,[31] rutin,[43] quercetin,[44] apigenin and kaempferol,[45] were evaluated for their potency for ACE inhibition. The screening results of several plant methanolic extracts showed a low ACE inhibition activity of the isolated chlorogenic acid.[32] Thus, based on the reported previous and present studies, it is feasible to suppose that the ACE inhibition activity of *S. officinale* root extracts may be due to its rich content of phenolic compounds. However, further research is needed to provide structural information of the ACE-inhibitory compounds from *S. officinale* root.

In addition, the present findings indicated the efficiency and potential use of subcritical water extracts for the development of antihypertensive functional foods and nutraceuticals formulation that would be economical and a natural alternative therapy to commercial synthetic drugs.

3. 6. Antiproliferative Activity

Research for new anticancer drugs with improved pharmacological profiles is a very active domain. Natural products represent an important source of new drugs. A number of studies have demonstrated the anticancerogenic effects of bioactive compounds isolated from various plants.

In the current research, the influence of the extraction techniques on antiproliferative activity of comfrey root extracts was evaluated. MTT assay was used in the analysis of subcritical water extract obtained at optimal conditions and extracts obtained by maceration and UAE. Antiproliferative effects of extracts were determined for three human cancer cell lines: the human cervix carcinoma (HeLa), breast cancer cell line (MDA-MB-453) and chronic myelogenous leukemia cell line (K562), as well as toward normal human lung fibroblast (MRC-5). Calculated activities of the tested extracts are summarized in Table 7.

Table 7. Antiproliferative activity of comfrey root extracts

Extraction		IC_{50} (mg/mL)			
		HeLa	MDA-MB-453	K562	MRC-5
Maceration	Ethanol (50%)	>2	>2	>2	>2
	Methanol	>2	>2	>2	>2
UAE	Ethanol (50%)	0.719±0.028	>2	0.578±0.054	>2
	Methanol	>2	>2	>2	>2
SWE	0.337±0.005	0.319±0.028	0.209±0.027	0.483±0.005	

Values are expressed as average ± standard deviation

Regarding antiproliferative effects, subcritical water extract of *S. officinale* root was the most toxic of all extracts screened (Table 7). The viability of cell lines was minimally affected by the extract obtained by maceration. The extract prepared by the SWE was the most active against K562 cell line (IC_{50} = 0.209 mg/mL). Moderate IC_{50} values could be explained by the presence or synergistic activities of polyphenolic compounds in the extracts since the number of studies have suggested that anticarcinogenic activity is closely associated with this group of secondary metabolites.[46, 47] Qualitative phytochemical screening of *S. officinale* root have identified the presence of allantoin, rosmarinic acid, ellagic acid, caffeic acid, rutin, tannin, which are believed to contribute to the antiproliferative activity.[7,8,36] Antiproliferative activity of plant extracts is also closely related to the extraction technique and the operational parameters applied during the process. Namely, subcritical water has much better selectivity in comparison to methanol and ethanol, being able to simultaneously extract different chemical classes. Therefore, by selecting the appropriate extraction parameters of subcritical water extraction, it is possible to influence the antiproliferative activity of extracts.

4. Conclusions

The results of the present study demonstrate that subcritical water extracts of *S. officinale* root are the promising sources of compounds with antioxidant, ACE inhibition and antiproliferative properties. Applied second-order polynomial model provided adequate mathematical description of SWE of investigated responses: TP, TF and antioxidant activity. Optimization of extraction conditions, in order to provide maximum yields for the observed responses, was successfully performed. Numerical optimization determined the optimum extraction conditions to be temperature of 200 °C, extraction time of 26.5 min and HCl concentration of 0.0075%. Predicted values of investigated responses on these conditions were 7.26 g GAE/100 g DW, 3.40 g CE/100 g DW and 0.0058 μg/mL, for TP, TF and IC_{50}, respectively. Extraction temperature had notable influence on each investigated response, followed by effect of HCl concentration in extraction solvent. When compared to other extraction techniques, SWE indicated better bioactivity. According to the results, subcritical water extracts of *S. officinale* root can find application in the development and production of new safe, pharmacologically-active formulations. Taking into consideration the efficiency, functionality, and safety of the SWE process, present investigation also demonstrates the potency of subcritical water application in food and pharmaceutical technology.

5. References

1. F. Stickel, H. K. Seitz, *Public Health Nutr.* **2000**, *3,* 501–508.
2. M. Kucera, J. Kálal, Z. Polesna, *Adv. Ther.* **2000**, 17, 204–211. **DOI:**10.1007/BF02850297
3. J. A. Duke, Chemicals and their biological activities, in: *Symphytum officinale* L. (*Boraginaceae*)-Comfrey, Phytochemical Database, USDA–ARS-NGRL, Beltsville Agricultural Research Center, Beltsville, MD, USA, **2002**.
4. H. G. Predel, B. Giannetti, R. Koll, M. Bulitta, C. Staiger, *Phytomed.* **2005**, *12*, 707–714. **DOI:**10.1016/j.phymed.2005.06.001
5. R. Andres, R. Brenneisen, J. T. Clerc, *Planta Med.* **1989**, *55*, 643–644. **DOI:**10.1055/s-2006-962224
6. B. Grabias, L. Swiatek, *Pharm. Pharmacol. Lett.* **1998**, *8*, 81–84.
7. G. Paun, E. Neagu, S. C. Litescu, P. Rotinberg, G. L. Radu, *J. Serb. Chem. Soc.* **2012**, 77.
8. V. L. Savić, S. R. Savić, V. D. Nikolić, L. B. Nikolić, S.J. Najman, J. S. Lazarević, A. S. Đorđević, *Hem. Ind.* **2015**, *69*, 1–8. **DOI:**10.2298/HEMIND131202013S
9. I. Ignat, I. Volf, V. I. Popa, *Food Chem.* **2011**, *126*, 1821–1835. **DOI:**10.1016/j.foodchem.2010.12.026
10. J. Wang, B. Sun, Y. Cao, Y. Tian, X. Li, *Food Chem.* **2008,** *106*, 804–810. **DOI:**10.1016/j.foodchem.2007.06.062
11. W. Setyaningsih, I. E. Saputro, C. A. Carrera, M. Palma, *Food Chem*. **2019**, *288*, 221–227. **DOI:**10.1016/j.foodchem.2019.02.107
12. J. C. Martínez-Patiño, B. Gullón, I. Romero, E. Ruiz, M. Brnčić, J. S. Žlabur, E. Castro, *Ultrason. Sonochem.* **2019**, *51*, 487–495. **DOI:**10.1016/j.ultsonch.2018.05.031
13. G. Joana Gil-Chávez, J. A. Villa, J. Fernando Ayala-Zavala, J. Basilio Heredia, D. Sepulveda, E. M. Yahia, G. A. González-Aguilar, *Compr Rev Food Sci Food Saf.* **2013,** *12*, 5–23. **DOI:**10.1111/1541-4337.12005
14. R. G. Maroun, H. N. Rajha, N. El Darra, S. El Kantar, S. Chacar, E. Debs, E. Vorobie, N. Louka, **2018**. In Polyphenols: Properties, Recovery, and Applications (pp. 265–293).
15. H. F. Zhang, X. H. Yang, L. D. Zhao, Y. Wang, *Innov. Food Sci. & Emer. Technol.* **2009**, *10*, 54–60. **DOI:**10.1016/j.ifset.2008.09.007
16. J. Wang, Y. M. Zhao, Y. T. Tian, C. L. Yan, C. Y. Guo, *Scientific World Journal*, **2013**.
17. J. Vladić, O. Canli, B. Pavlić, Z. Zeković, S. Vidović, M. Kaplan, *J. Supercrit. Fluid.* **2017**, *120*, 86–94.
18. M. Munir, H. Kheirkhah, S. Baroutian, S. Y. Quek, B. R. Young, *J Clean Prod.* **2018**, *183*, 487–494. **DOI:**10.1016/j.jclepro.2018.02.166
19. S. Erşan, O. G. Üstündağ, R. Carle, R. M. Schweiggert, *Food Chem*, **2018**, *253*, 46–54. **DOI:**10.1016/j.foodchem.2018.01.116
20. J. H. Lee, M. J. Ko, M. S. Chung, *J. Supercrit. Fluid.* **2018,** *133*, 177–183.
21. K. S. Duba, A. A. Casazza, H. B. Mohamed, P. Perego, L. Fiori, *Food Bioprod. Process.* **2015***, 94*, 29–38. **DOI:**10.1016/j.fbp.2015.01.001

22. M. Herrero, A. Cifuentes, E. Ibañez, *Food Chem.* **2006**, *98*, 136–148. **DOI:**10.1016/j.foodchem.2005.05.058
23. Z. Zeković, S. Vidović, J. Vladić, R. Radosavljević, A. Cvejin, M. A. Elgndi, B. Pavlić, *J. Supercrit. Fluid.* **2014**, *95*, 560–566.
24. M. P. Kähkönen, A. I. Hopia, H. J. Vuorela, J. P. Rauha, K. Pihlaja, T. S. Kujala M. Heinonen, *J. Agric. Food Chem.* **1999**, *47,* 3954–3962. **DOI:**10.1021/jf990146l
25. K. R. Markham, in: Harborne, J. B., Dey, P.M. (Eds.), Methods in Plant Biochemistry, Academic Press, London, **1989**, pp. 193–237
26. J. C. Espín, C. Soler-Rivas, H. J. Wichers, *J. Agric. Food Chem.* **2000**, *48*, 648–656. **DOI:**10.1021/jf9908188
27. Y. Yoshie-Stark, Y. Wada, A. Wäsche, *Food Chem.* **2008**, *107*, 32–39. **DOI:**10.1016/j.foodchem.2007.07.061
28. T. Mosmann, *J. Immunol. Methods.* **1983**, *65*, 55–63. **DOI:**10.1016/0022-1759(83)90303-4
29. M. Ohno, T. Abe, *J. Immunol. Methods.* **1991**, *145,* 199–203. **DOI:**10.1016/0022-1759(91)90327-C
30. M. A. Bezerra, R. E. Santelli, E. P. Oliveira, L. S. Villar, L. A. Escaleira, *Talanta.* **2008**, *76*, 965–977. **DOI:**10.1016/j.talanta.2008.05.019
31. A. Tomšik, B. Pavlić, J. Vladić, M. Cindrić, P. Jovanov, M. Sakač, A. Mandić, S. Vidović, *J. Supercrit. Fluid.* **2017**, *128*, 79–88.
32. R. K. Toor, G.P. Savage, *Food Chem.* **2006**, *94*, 90–97. **DOI:**10.1016/j.foodchem.2004.10.054
33. J. R. Vergara-Salinas, J. Pérez-Jiménez, J. L. Torres, E. Agosin, J. R. Pérez-Correa, *J. Agric. Food Chem.* **2012**, *60*, 10920–10929.
34. L. He, X. Zhang, H. Xu, C. Xu, F. Yuan, Ž. Knez, Z. Novak, Y. Gao, *Food Bioprod. Process.* **2012**, *90*, 215–223. **DOI:**10.1016/j.fbp.2011.03.003
35. A. Naffati, J. Vladić, B. Pavlić, R. Radosavljević, A. Gavarić, S. Vidović, *J. Supercrit. Fluid.* **2017**, *121,* 1–9.
36. F. U. Alkan, C. Anlas, O. Ustuner, T. Bakırel, A. B. Sari, *Asian J. Plant Sci. Res.* **2014**, *4*, 62–68.
37. M. Uematsu, E. U. Frank, *J. Phys. Chem. Ref. Data.* **1980**, *9*, 1291–1306. **DOI:**10.1063/1.555632
38. G. H. Li, G. W. Le, Y. H. Shi, S. Shrestha, *Nutr. Res.* **2004**, *24*, 469–486. **DOI:**10.1016/S0271-5317(04)00058-2
39. L. Paiva, E. Lima, A. I. Neto, J. Baptista, *J. Funct. Foods.* **2016**, *26*, 65–76. **DOI:**10.1016/j.jff.2016.07.006
40. N. Al Shukor, J. Van Camp, G.B. Gonzales, D. Staljanssens, K. Struijs, M. J. Zotti, K. Raes, G. Smagghe, *J. Agric. Food Chem.* **2013**, *61*, 11832–11839. **DOI:**10.1021/jf404641v
41. M. A. Lacaille-Dubois, U. Franck, H. Wagner, *Phytomed.* **2001**, *8*, 47–52. **DOI:**10.1078/0944-7113-00003
42. H. Wagner, G. Elbl, H. Lotter, M. Guinea, *Pharm. Pharmacol. Lett.* **1991**, *1*, 15–18.
43. H. M. Shaw, J. L. Wu, M. S. Wang, *J. Funct. Foods.* **2017**, *35*, 68–73. **DOI:**10.1016/j.jff.2017.05.033
44. H. Wagner, ACS Symposium Series. **1998**, 691, 46–61.
45. L. Guerrero, J. Castillo, M. Quiñones, S. Garcia-Vallvé, L. Arola, G. Pujadas, B. Muguerza, *PLOS one.* **2012**, *7,* e49493. **DOI:**10.1371/journal.pone.0049493
46. S. Vuorela, K. Kreander, M. Karonen, R. Nieminen, M. Hämäläinen, A. Galkin, L. Laitinen, J.P. Salminen, E. Moilanen, K. Pihlaja, H. Vuorela, *J. Agric. Food Chem.* **2005**, *53*, 5922–5931. **DOI:**10.1021/jf050554r
47. K. A. Lee, K. T. Kim, P. S. Chang, H. D. Paik. *J. Ginseng Res.* **2014**, *38*, 289–292. **DOI:**10.1016/j.jgr.2014.05.009

Povzetek

Študija preučuje možnost uporabe vode v subkritičnih pogojih za ekstrakcijo bioaktivnih substanc iz korenine Symphytum officinale (navadni gabez). Preverili smo vpliv temperature (120–200 °C), časa ekstrakcije (10–30 min) in koncentracije HCl v ekstrakcijskem topilu (0–1.5 %), da bi določili optimalne pogoje ekstrakcije ter maksimirali izkoristek skupnih fenolov, flavonoidov ter antioksidativne aktivnosti ekstrakta. Z uporabo optimalnih pogojev (200 °C, 25.6 min in 0.0075 %) smo dobili ekstrakt bogat s skupnimi fenoli in flavonoidi ter visoko antioksidativno aktivnostjo. Rezultati kažejo izrazite prednosti uporabe subkritične vode za pridobivanje biokativnih substance iz korenin gabeza v primerjavi z maceracijo in ultrazvočno ekstrakcijo. Poleg tega pa ekstrakti korenine *S. officinale* pridobljeni z ekstrakcijo z vodo v subkritičnih pogojih predstavljajo obetaven vir snovi z antioksidativnimi, ACE inhibitornimi in antiproliferativnimi lastnostmi in bi lahko predstavljale potencialen vir za proizvodnjo novih farmakološko aktivnih formulacij.

DOI: 10.17344/acsi.2019.5019 *Acta Chim. Slov.* **2019,** *66,* 484–489

Scientific paper

Synthesis, Crystal Structure and Antimicrobial Activity of a Linear Trinuclear Nickel(II) Complex with Schiff Base Ligand

Cui-Lin Zhang,[1] Xiao-Yang Qiu,[1,2,*] Shu-Juan Liu[1]

[1] *College of Science & Technology, Ningbo University, Ningbo, 315212, P. R. China*

[2] *State Key Laboratory of Structural Chemistry, Fujian Institute of Research on the Structure of Matter, Chinese Academy of Sciences, Fuzhou, Fujian 350002, P. R. China*

** Corresponding author: E-mail: xiaoyang_qiu@126.com*

Received: 02-03-2019

Abstract

A new linear trinuclear Schiff base nickel(II) complex, $[Ni\{NiL(\mu_2\text{-}\eta^1{:}\eta^1\text{-}OAc)(OH_2)\}_2]\cdot H_2O$, where L is the dianionic form of *N,N'*-bis(5-chloro-2-hydroxybenzylidene)-1,3-propanediamine (H_2L), was synthesized and characterized by elemental analyses, IR spectroscopy, and X-ray single-crystal determination. There are three bridges across the Ni-Ni atom pairs, involving two phenolate O atoms of a Schiff base ligand, and an O–C–O moiety of a $\mu_2\text{-}\eta^1{:}\eta^1$-OAc group. The Ni atoms have octahedral coordination. The acetate bridges linking the central and terminal nickel atoms are mutually *trans*. The adjacent Ni···Ni distances are 3.047(1) Å. The complex was evaluated for its antibacterial (*Bacillus subtilis*, *Staphylococcus aureus*, *Escherichia coli*, and *Pseudomonas aeruginosa*) and antifungal (*Candida albicans* and *Aspergillus niger*) activities by MTT (3-(4,5-dimethylthiazol-2-yl)-2,5-diphenyltetrazolium bromide) method.

Keywords: Nickel(II) complex; Trinuclear complex; Schiff base; Crystal structure; Antibacterial activity

1. Introduction

Schiff bases are biological active compounds bearing the –N=CH– functional groups, which can be prepared by the condensation reactions of carbonyl-containing compounds with primary amines. The compounds have been attracted considerable attention for their wide range of biological activities, such as antibacterial,[1] antifungal,[2] antitumor,[3] anti-inflammatory,[4] and cytotoxic.[5] Metal-organic complexes containing Schiff bases and bridging ligands are of current interest because of their interesting molecular topologies as well as the fact that they may be designed with specific functionalities.[6] Among the bridging groups, acetate anion is highly flexible, and can coordinate to metal atoms in a variety of coordination modes such as monodentate, chelating, bidentate bridging, monoatomic bridging, and chelating bridging (Scheme 1).[7] Bis-Schiff bases

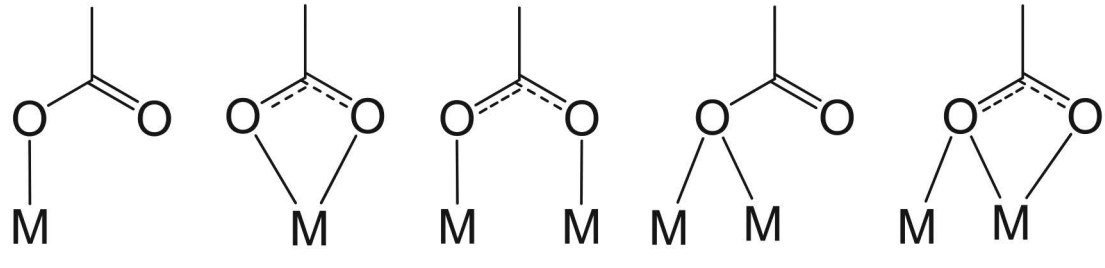

Scheme 1. Various coordination modes of acetate anion

derived from salicylaldehyde and its derivatives with various diamines usually coordinate to metal atoms through NNOO donor atoms,[8] thus, it is possible for the introduction of bridging groups. It was reported that Schiff bases bearing electron-withdrawing groups can improve their antimicrobial activities.[9] Rai and co-workers reported a series of fluoro, chloro, bromo, and iodo-substituted compounds, and found that they have significant antimicrobial activities.[10] A number of metal complexes have been reported with the bis-Schiff base *N,N'*-bis(5-chloro-2-hydroxybenzylidene)-1,3-propanediamine (H_2L; Scheme 2).[11] As a continuation of work on the exploration of new antimicrobial agents, in this paper, a new trinuclear nickel complex was obtained.

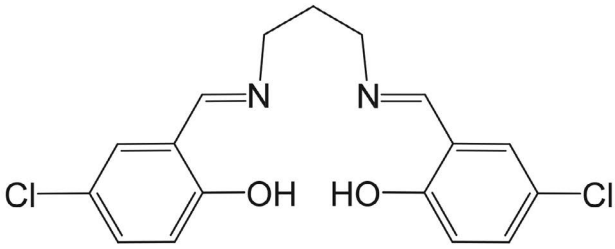

Scheme 2. H_2L

2. Experimental

2. 1. General Methods and Materials

5-Chlorosalicylaldehyde and 1,3-propanediamine with AR grade were purchased from Sigma-Aldrich. All other chemicals (reagent grade) used were commercially available. Elemental analyses for C, H and N were performed on a Perkin-Elmer 240C elemental analyzer. IR spectra were recorded on a Nicolet AVATAR 360 spectrometer as KBr pellets in the 4000–400 cm^{-1} region. ^1H NMR and ^{13}C NMR spectra were recorded on a Bruker Avance 300 spectrometer operating at 300 MHz for ^1H NMR and 75.5 MHz for ^{13}C NMR. Molar conductivity value was measured with a Shanghai DDS-11A conductometer.

2. 2. Synthesis of H_2L

5-Chlorosalicylaldehyde (2.0 mmol, 0.31 g) was dissolved in methanol (20 mL), to which a methanol solution (10 mL) of 1,3-propanediamine (1.0 mmol, 0.074 g) was added dropwise with stirring at room temperature. The mixture was stirred at room temperature for 30 min, and most of the solvent was removed by distillation. The yellow crystalline product was obtained by filtration. Yield: 93% (0.33 g). IR data (cm^{-1}, KBr): 3353w, 1645s, 1585s, 1487s, 1382w, 1329w, 1258s, 1213m, 1127w, 1033m, 985w, 865m, 831m, 772m. ^1H NMR (300 MHz, DMSO) δ 12.33 (s, 2H, O*H*), 8.54 (s, 2H, C*H*=N), 7.58 (s, 1H, Ar*H*), 7.37 (d, 1H, Ar*H*), 6.92 (d, 1H, Ar*H*), 3.73 (t, 4H, CH_2), 1.99 (m, 2H, CH_2). ^{13}C NMR (75 MHz, DMSO) δ 158.77, 156.32, 134.57, 131.26, 124.81, 121.05, 117.73, 61.78, 32.50. Elemental analysis found: C, 58.32; H, 4.67; N, 7.91%, $C_{17}H_{16}Cl_2N_2O_2$ calcd: C, 58.13; H, 4.59; N, 7.98%.

2. 3. Synthesis of the Complex

H_2L (0.2 mmol, 0.70 g) was dissolved in methanol (20 mL), to which a methanolic solution (20 mL) of nickel acetate tetrahydrate (0.3 mmol, 0.75 g) was added with stirring. The mixture was stirred at room temperature for 30 min to give a green solution, which was kept still to slow evaporate of the solvents. Green block-like single-crystals suitable for X-ray diffraction were formed. Yield: 45% (0.16 g). IR data (cm^{-1}, KBr): 3451, 2910, 2862, 1637, 1580, 1464, 1416, 1385, 1306, 1164, 1075, 948, 859, 712, 549, 517, 465. Elemental analysis found: C, 43.77; H, 3.98; N, 5.27%, $C_{38}H_{40}Cl_4N_4Ni_3O_{11}$ calcd: C, 43.61; H, 3.85; N, 5.35%.

2. 4. X-ray Crystallography

X-ray diffraction was carried out at a Bruker SMART 1000 CCD area diffractometer equipped with MoKα radiation (λ = 0.71073 Å). The collected data were collected with SMART and reduced with SAINT,[12] and multi-scan absorption correction was performed using SADABS.[13] The structure of the complex was solved by direct method, and refined against F^2 by full-matrix least-squares method using SHELXTL.[14] All of the non-hydrogen atoms were refined anisotropically. The H5A and H5B atoms attached to O5 was located in a difference Fourier map and refined

Table 1. Crystallographic information for the complex

Parameter	Value
Formula	$C_{38}H_{40}Cl_4N_4Ni_3O_{11}$
Fw	1046.67
T, K	298(2)
Crystal system	Monoclinic
Space group	$P2_1/c$
a, Å	11.049(2)
b, Å	13.148(2)
c, Å	14.988(2)
b, °	90.971(1)
V, Å ^{3}	2177.0(6)
Z	2
D_c, g cm^{-3}	1.597
F(000)	1072
Measured reflections	11692
Observed reflections [I ³ 2s(I)]	4052
Data/restraints/parameters	2008/3/284
Goodness-of-fit on F^2	1.049
R_1, wR_2 [I ³ 2s(I)][a]	0.0642, 0.1684
R_1, wR_2 (all data)[a]	0.1429, 0.2024

[a] R_1 = å||*Fo*| – |*Fc*||/å|*Fo*|, wR_2 = [åw(Fo^2 – Fc^2)^2/åw(Fo^2)^2]$^{1/2}$, w = [σ^2(Fo)^2 + (0.091(Fo^2 + 2Fc^2)/3)^2 + 0.5732(Fo^2 + 2Fc^2)/3]$^{-1}$.

isotropically, with O–H and H···H distances restrained to 0.85(1) and 1.37(2) Å, respectively. The remaining H atoms were placed in geometrically ideal positions and constrained to ride on their parent atoms. The O6 atom is disordered and its hydrogen atoms cannot be added reasonably. The crystallographic data for the complex are summarized in Table 1. Selected bond lengths and angles are given in Table 2.

Table 2. Selected bond lengths (Å) and angles (°) for the complexes with estimated standard deviations (e.s.d.s) in parentheses

Ni1–O1	1.985(5)	Ni1–O2	2.018(4)
Ni1–N1	2.009(5)	Ni1–N2	2.000(6)
Ni1–O3	2.051(6)	Ni1–O5	2.248(8)
Ni2–O2	2.092(5)	Ni2–O1	2.117(4)
Ni2–O4	2.121(7)		
O1–Ni1–N2	170.4(2)	O1–Ni1–N1	91.2(2)
N2–Ni1–N1	96.1(2)	O1–Ni1–O2	83.13(18)
N2–Ni1–O2	89.0(2)	N1–Ni1–O2	172.0(2)
O1–Ni1–O3	92.2(3)	N2–Ni1–O3	94.0(2)
N1–Ni1–O3	90.3(2)	O2–Ni1–O3	95.5(2)
O1–Ni1–O5	82.8(3)	N2–Ni1–O5	91.5(3)
N1–Ni1–O5	85.0(3)	O2–Ni1–O5	88.7(3)
O3–Ni1–O5	173.1(2)	O2–Ni2–O1A	101.73(18)
O2–Ni2–O1	78.27(17)	O2–Ni2–O4A	92.0(2)
O1–Ni2–O4A	90.4(2)	O2–Ni2–O4	88.0(2)
O1–Ni2–O4	89.6(2)		

Symmetry code for A: 1 – *x*, – *y*, – *z*.

2. 5. Antimicrobial Assay

The antibacterial activity of the compounds was tested against *Bacillus subtilis*, *Staphylococcus aureus*, *Escherichia coli*, and *Pseudomonas aeruginosa* using LB medium. The antifungal activities of the compounds were tested against *Candida albicans* and *Aspergillus niger* using RPMI-1640 medium. The IC_{50} (half inhibitory concentration) of the test compounds were determined by a colorimetric method using the dye MTT (3-(4,5-di-methylth-iazol-2-yl)-2,5-diphenyltetrazolium bromide). A stock solution of the synthesized compound (1000 μg mL^{-1}) in DMSO was prepared and graded quantities of the test compounds were incorporated in specified quantity of sterilized liquid LB medium. Suspension of the microorganism was prepared and applied to 96-well assay plate with serially diluted compounds to be tested. 10 μL of tested samples at pre-set concentrations were added to wells with penicillin G as a positive reference, the solvent control (5% DMSO) in medium and incubated at 37 °C for 24 h. After 24 h exposure, 10 μL of PBS (phosphate buffered saline 0.01 mol L^{-1}, pH = 7.4) containing 4 mg mL^{-1} of MTT was added to each well. After 4 h, the medium was replaced by 150 μL DMSO to dissolve the purple formazan crystals produced. The absorbance at 492 nm of each well was measured with an ELISA plate reader. The IC_{50} value was defined as the concentration at which 50% of the bacterial strain could survive.

3. Results and Discussion

The Schiff base ligand H_2L was readily prepared by the condensation reaction of 5-chlorosalicylaldehyde with 1,3-propanediamine in 2:1 molar ratio. Recently, two mononuclear nickel complexes were prepared in a 1:1 molar ratio of nickel acetate and H_2L under reflux in methanol.[15] And also an acetate and phenolate bridged trinuclear nickel complex was prepared by nickel acetate with H_2L under solvothermal condition.[16] Interestingly, the present complex was prepared by the reaction of the Schiff base ligand with nickel acetate in a 2:3 molar ratio under ambient condition. Crystals of the complex are stable in air at room temperature, soluble in DMF, DMSO, MeOH, EtOH and MeCN, insoluble in water. The elemental analyses of the complex agree well with the component determined by X-ray analysis. The molar conductivity of the complex measured in DMSO/water at concentration of 10^{-3} mol L^{-1} is 25 Ω^{-1} cm^2 mol^{-1}, indicating the non-electrolytic nature of the complex in solution.[17]

3. 1. Crystal Structure Description of the Complex

The molecular structure of the complex is shown in Fig. 1. The asymmetric unit of the compound contains half of a trinuclear complex. The molecule of the complex possesses crystallographic inversion center symmetry, with the inversion center located at the site of Ni2 atom. There are three bridges across the Ni···Ni atom pairs, involving two phenolate O atoms of a Schiff base ligand, and an O–C–O moiety of a μ_2-η^1:η^1-OAc group. The acetate bridges linking the central and terminal nickel atoms are mutually *trans*. The trinuclear nickel complex molecule consists of two NiL units connected to each other by a completely encapsulated third metal atom, Ni2. The adjacent Ni1···Ni2 distance is 3.047(1) Å.

The cage of Ni2 is formed by phenolate bridges, O1 and O2, from the Schiff base ligands, and by two O atoms from two μ_2-η^1:η^1-OAc ligands that furthermore connect the central metal with the two outer metal atoms resulting in an octahedral environment. The coordination around Ni2 atom displays only slight distortion. The bond distances Ni–O are relatively similar and range from 1.985(5) to 2.121(7) Å. The greatest deviation of the bond angles from those expected for an ideal octahedral geometry is found for O1–Ni2–O2 with 78.3(2)°, and O1–Ni2–O2A with 101.7(2)°. The remaining bond angles are close to the ideal values for the octahedral coordination.

The coordination around the inversion-related terminal Ni atoms is also octahedral, with two imino N and two phenolate O atoms from a Schiff base ligand defining

the equatorial plane, and with two O atoms respectively from a methanol and a μ_2-η^1:η^1-OAc ligands occupying the axial positions. The coordination around the terminal metal atoms also displays slight distortion. The greatest deviation of the bond angles from those expected for an ideal octahedral geometry is O1–Ni1–O2 (81.9(2)°), which is caused by the strain created by the four-membered chelate ring Ni1–O1–Ni2–O2.

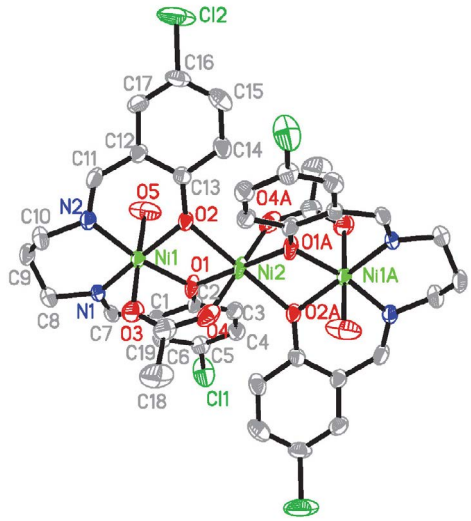

Fig. 1. Molecular structure of the complex. Displacement ellipsoids are drawn at the 30% probability level and H atoms are omitted for clarity. Atoms labeled with the suffix A or unlabeled are related to the symmetry position 1 – *x*, – *y*, – *z*.

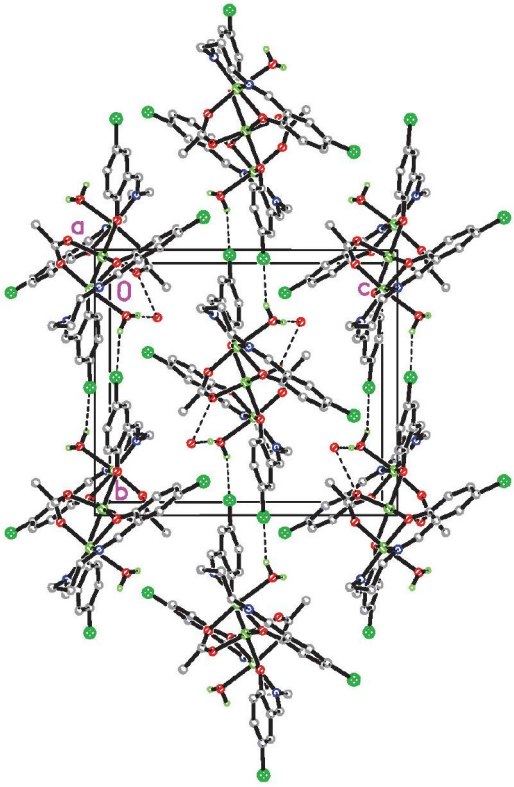

Fig. 2. Molecular packing diagram of the complex, viewed along the *a* axis. Hydrogen bonds are drawn as dashed lines.

The NiL units in the complex are butterfly-shaped, with the dihedral angles formed by the two benzene rings of the Schiff base ligands of 53.2(5)°. In the crystal structure of the complex, the water hydrate molecules are linked to the nickel complex molecules through O5–H5A···O6^{i}, O5–H5B···Cl2^{ii} and C18–H18B···O6^{iii} hydrogen bonds [O5–H5A = 0.86 Å, H5A···O6^{i} = 1.66 Å, O5···O6^{i} = 2.518(5) Å, O5–H5A···O6^{i} = 173°; O5–H5B = 0.85 Å, H5B···Cl2^{ii} = 2.48 Å, O5···Cl2^{ii} = 3.251(5) Å, O5–H5B···Cl2^{ii} = 151°; C18–H18B = 0.96 Å, H18B···O6^{iii} = 2.36 Å, C18···O6^{iii} = 3.207(5) Å, C18–H18B···O6^{iii} = 147°; symmetry codes: i: *x*, ½ – *y*, ½ + *z*; ii: 1 – *x*, –*y*, 1 – *z*; iii: 1 – *x*, ½ + *y*, ½ – *z*], forming chains along the *b* axis (Fig. 2).

3. 2. Infrared Spectra

The IR spectra of the free Schiff base ligand and the nickel complex provide information about the metal-ligand bonding. The assignments are based on the typical group frequencies. The broad absorptions centered at 3353 cm^{-1} for H_2L and 3451 cm^{-1} for the complex are generated by the ν(O–H) of the hydroxy groups or methanol molecules. The strong absorption band at 1645 cm^{-1} for H_2L is assigned to the azomethine groups, ν(C=N). The band is shifted to 1637 cm^{-1} in the spectrum of the complex, what can be attributed to the coordination of the nitrogen atoms of the azomethine groups to the metal atoms. The phenolic ν(Ar–O) for the free ligand exhibits medium band at 1213 cm^{-1}.[18] However, in the complex, the band appears at 1164 cm^{-1}. This may be assigned to the skeletal vibrations related to the phenolic oxygen of the Schiff base ligands, and the bands are known to shift to lower frequency when the phenolic oxygen coordinates to metal atoms.[19] There exhibit typical acetate vibrations ν_{asym}(OAc) at 1580 cm^{-1} and ν_{sym}(OAc) at 1464 cm^{-1}.[20]

3. 3. Antibacterial Activity

The complex and the free Schiff base were screened for antibacterial activity against two Gram (+) bacterial strains (*B. subtilis* and *S. aureus*) and two Gram (–) bacterial strains (*E. coli* and *P. aeruginosa*) by MTT method. The IC_{50} values of the compounds against four bacteria are listed in Table 3. Penicillin G was used as the standard drug. The Schiff base H_2L showed medium activity against the bacteria *B. subtilis*, *S. aureus*, and *E. coli*, while no activity against *P. aeruginosa*. The complex has strong activity against *B. subtilis*, medium activity against *S. aureus*, while no activity against the other two bacteria. From the results, it is difficult to give a definite conclusion about which one is good for the antibacterial activities of the free Schiff base and the complex. For example, the complex has stronger activities against *B. subtilis* and *S. aureus* than the Schiff base. However, as for *E. coli*, the Schiff base has stronger activity than the complex. The particular interest is that

Table 3. IC_{50} values (μg mL^{-1}) of the tested material

Tested material	*B. subtilis*	*S. aureus*	*E. coli*	*P. aeruginosa*	*C. albicans*	*A. niger*
H_2L	15.50	29.11	12.35	> 50	> 50	> 50
Complex	2.16	13.33	> 50	> 50	17.72	> 50
Penicillin G	2.38	0.71	18.23	16.31	> 50	> 50
Ketoconazole	> 50	> 50	> 50	> 50	2.45	9.97

the complex showed the most effective activity against *B. subtilis*, which is even more effective than penicillin G.

The antifungal activities of the complex and the free Schiff base were also evaluated against two fungal strains (*C. albicans* and *A. niger*) by MTT method. Ketoconazole was used as a reference drug. It is interesting that the complex has effective activity against *C. albicans*, with IC_{50} value of 17.72 μg mL^{-1}.

4. Conclusion

In summary, a new linear trinuclear Schiff base nickel(II) complex derived from *N,N'*-bis(5-chloro-2-hydroxybenzylidene)-1,3-propanediamine was presented. Structure of the complex was confirmed by single-crystal X-ray determination. The Ni atoms are in octahedral coordination. The complex has interesting antibacterial activities against *B. subtilis* and *S. aureus*, and antifungal activity against *C. albicans*.

5. Supplementary Material

CCDC-1507164 contain the crystallographic data for the complex. The data can be obtained at https://www.ccdc.cam.ac.uk or from the Cambridge Crystallographic Data Centre (CCDC), 12 Union Road, Cambridge CB2 1EZ, UK; fax: +44(0)1223-336033 or e-mail: deposit@ccdc.cam.ac.uk.

6. Acknowledgments

This work was financially supported by K.C. Wong Magna Fund in Ningbo University, Ningbo natural science fund (Project No. 201701HJ-B01019), State Key Laboratory Development Fund of Structural Chemistry and Ningbo Education Research Project (Project No. 2017YZD001).

7. References

1. (a) P. J. Low, *Coord. Chem. Rev.* **2013**, *257*, 1507–1532; **DOI:**10.1016/j.ccr.2012.08.008
(b) R. T. Acha, E. L. Gavey, J. Wang, J. M. Rawson, M. Pilkington, *Polyhedron* **2014**, *76*, 122–127; **DOI:**10.1016/j.poly.2014.04.001
(c) D.-L. Peng, N. Sun, *Acta Chim. Slov.* **2018**, *65*, 895–901; **DOI:**10.17344/acsi.2018.4543
(d) X. W. Zhu, *Russ. J. Coord. Chem.* **2018**, *44*, 335–339;
(e) H. Y. Qian, X. W. Zhu, *Russ. J. Coord. Chem.* **2018**, *44*, 32–38. **DOI:**10.3103/S1068367418040213
2. A. Bienka, R. Kruszynski, D. Bienko, *Polyhedron* **2014**, *75*, 1–8. **DOI:**10.1016/j.poly.2014.02.045
3. (a) U. Kumar, J. Thomas, N. Thirupathi, *Inorg. Chem.* **2010**, *49*, 62–72; **DOI:**10.1021/ic901100z
(b) R. Biswas, S. Mukherjee, P. Kar, A. Ghosh, *Inorg. Chem.* **2012**, *51*, 8150–8160. **DOI:**10.1021/ic300547w
4. (a) C. Biswas, M. G. B. Drew, E. Ruiz, M. Estrader, C. Diaz, A. Ghosh, *Dalton Trans.* **2010**, *39*, 7474–7484; **DOI:**10.1039/c0dt00331j
(b) B. Cristovao, J. Klak, B. Miroslaw, *Polyhedron* **2012**, *43*, 47–54. **DOI:**10.1016/j.poly.2012.05.045
5. (a) F. Cimpoesu, F. Dahan, S. Ladeira, M. Ferbinteanu, J.-P. Costes, *Inorg. Chem.* **2012**, *51*, 11279–11293; **DOI:**10.1021/ic3001784
(b) M. L. Mejia, K. Agapiou, X. P. Yang, B. J. Holliday, *J. Am. Chem. Soc.* **2009**, *131*, 18196–18199. **DOI:**10.1021/ja906773g
6. (a) H.-H. Li, Z.-L. You, C.-L. Zhang, M. Yang, L.-N. Gao, L. Wang, *Inorg. Chem. Commun.* **2013**, *29*, 118–122; **DOI:**10.1016/j.inoche.2012.12.023
(b) Z.-L. You, D.-M. Xian, M. Zhang, *CrystEngComm* **2012**, *14*, 7133–7137; **DOI:**10.1039/c2ce25662b
(c) X.-S. Zhou, X.-S. Cheng, Y.-H. Li, F.-Y. Tian, Z.-L. You, *Chinese J. Inorg. Chem.* **2013**, *29*, 397–402;
(d) H.-H. Li, X.-X. Zhou, Z.-L. You, *Chinese J. Inorg. Chem.* **2013**, *29*, 649–653;
(e) Y.-J. Ren, J.-L. Zhu, L.-X. Zhang, Y.-X. Xu, S.-S. Qian, *Acta Chim. Slov.* **2017**, *64*, 825–831.
7. (a) X.-S. Tai, W.-H. Zhao, F.-H. Li, *Chinese J. Inorg. Chem.* **2013**, *29*, 1328–1332;
(b) M. M. Kamel, H. I. Ali, M. M. Anwar, N. A. Mohamed, A. M. Soliman, *Eur. J. Med. Chem.* **2010**, *45*, 572–580; **DOI:**10.1016/j.ejmech.2009.10.044
(c) S. M. Sondhi, S. Arya, R. Rani, N. Kumar, P. Roy, *Med. Chem. Res.* **2012**, *21*, 3620–3628. **DOI:**10.1007/s00044-011-9899-3
8. (a) M. S. Alam, J.-H. Choi, D.-U. Lee, *Bioorg. Med. Chem.* **2012**, *20*, 4103–4108; **DOI:**10.1016/j.bmc.2012.04.058
(b) D. Sunil, A. M. Isloor, P. Shetty, B. Chandrakantha, K. Sat-

yamoorthy, *Med. Chem. Res.* **2011**, *20*, 1024–1032; **DOI:**10.1007/s00044-010-9433-z
(c) A. Iqbal, H. L. Siddiqui, C. M. Ashraf, M. H. Bukhari, C. M. Akram, *Chem. Pharm. Bull.* **2007**, *55*, 1070–1072; **DOI:**10.1248/cpb.55.1070
(d) M. B. Ferrari, S. Capacchi, G. Reffo, G. Pelosi, P. Tarasconi, R. Albertini, S. Pinelli, P. Lunghi, *J. Inorg. Biochem.* **2000**, *81*, 89–97. **DOI:**10.1016/S0162-0134(00)00087-8

9. (a) L. Shi, H.-M. Ge, S.-H. Tan, H.-Q. Li, Y.-C. Song, H.-L. Zhu, R.-X. Tan, *Eur. J. Med. Chem.* **2007**, *42*, 558–564; **DOI:**10.1016/j.ejmech.2006.11.010
(b) M. Zhang, D.-M. Xian, H.-H. Li, J.-C. Zhang, Z.-L. You, *Aust. J. Chem.* **2012**, *65*, 343–350. **DOI:**10.1071/CH11424
10. (a) N. P. Rai, V. K. Narayanaswamy, T. Govender, B. K. Manuprasad, S. Shashikanth, P. N. Arunachalam, *Eur. J. Med. Chem.* **2010**, *45*, 2677–2682; **DOI:**10.1016/j.ejmech.2010.02.021
(b) N. P. Rai, V. K. Narayanaswamy, S. Shashikanth, P. N. Arunachalam, *Eur. J. Med. Chem.* **2009**, *44*, 4522–4527;
(c) J. Meletiadis, J. F. G. M. Meis, J. W. Mouton, J. P. Donnelly, P. E. Verweij, *J. Clin. Microbiol.* **2000**, *38*, 2949–2954.
11. (a) L. W. Xue, Y. J. Han, G. Q. Zhao, Y. X . Feng, *Russ. J. Coord. Chem.* **2012**, *38*, 24–28; **DOI:**10.1134/S1070328411120104
(b) M. Maiti, D. Sadhukhan, S. Thakurta, S. Roy, G. Pilet, R. J. Butcher, A. Nonat, L. J. Charbonniere, S. Mitra, *Inorg. Chem.* **2012**, *51*, 12176–12187; **DOI:**10.1021/ic3012958
(c) F. Pan, Z.-M. Wang, S. Gao, *Inorg. Chem.* **2007**, *46*, 10221–10228; **DOI:**10.1021/ic701387z
(d) G. Bhargavi, M. V. Rajasekharan, J.-P. Costes, J.-P. Tuchagues, *Dalton Trans.* **2013**, *42*, 8113–8123; **DOI:**10.1039/c3dt31966k
(e) J. H. Yoon, D. W. Ryu, H. C. Kim, S. W. Yoon, B. J. Suh, C. S. Hong, *Chem. Eur. J.* **2009**, *15*, 3661–3665. **DOI:**10.1002/chem.200900250
12. *Bruker, SMART and SAINT.* Bruker AXS Inc, Madison, **2002**.
13. G. M. Sheldrick, *SADABS*. University of Göttingen, Germany, **1996**.
14. G. M. Sheldrick, *SHELXTL V5.1*, *Software Reference Manual*, Bruker AXS Inc, Madison, **1997**.
15. A. Elmali, C. T. Zeyrek, Y. Elerman, T. N. Durlu, *J. Chem. Crystallogr.* **2000**, *30*, 167–171. **DOI:**10.1023/A:1009526913565
16. Z.-L. You, M. Zhang, D.-M. Xian, *Dalton Trans.* **2012**, *41*, 2515–2524. **DOI:**10.1039/c1dt11566a
17. W. J. Geary, *Coord. Chem. Rev.* **1971**, *7*, 81–122. **DOI:**10.1016/S0010-8545(00)80009-0
18. G. C. Percy, D. A. Thornton, *J. Inorg. Nucl. Chem.* **1972**, *34*, 3357–3362. **DOI:**10.1016/0022-1902(72)80230-6
19. C. Fukuhara, E. Asato, T. Shimoji, K. Katsura, M. Mori, K. Matsumoto, S. Ooi, *J. Chem. Soc. Dalton Trans.* **1987**, 1305–1311.
20. B.-H. Ye, X.-Y. Li, I. D. Williams, X.-M. Chen, *Inorg. Chem.* **2002**, *41*, 6426–6431. **DOI:**10.1021/ic025806+

Povzetek

Sintetizirali smo nov linearni trijedrni nikljev(II) kompleks s Schiffovo bazo, $[Ni\{NiL(\mu_2\text{-}\eta^1\text{:}\eta^1\text{-}OAc)(OH_2)\}_2]\cdot H_2O$, kjer je L dianionska oblika *N,N'*-bis(5-kloro-2-hidroksibenziliden)-1,3-propandiamina (H_2L), in ga okarakterizirali z elementno analizo, IR spektroskopijo in rentgensko monokristalno analizo. Trije mostovi povezujejo Ni-Ni atomske pare, in sicer preko dveh fenolatnih O atomov Schiffove baze in O–C–O skupine $\mu_2\text{-}\eta^1\text{:}\eta^1$-OAc liganda. Nikljevi atomi imajo oktaedrično koordinacijo. Acetatna mostova, ki povezujeta sredinski in terminalna nikljeva atoma, sta v medsebojnem *trans* položaju. Ni···Ni razdalja je 3.047(1) Å. Kompleksu smo določili antibakterijske (*Bacillus subtilis*, *Staphylococcus aureus*, *Escherichia coli* in *Pseudomonas aeruginosa*) in antimikotične (*Candida albicans* in *Aspergillus niger*) lastnosti z uporabo MTT (3-(4,5-dimetiltiazol-2-il)-2,5-difeniltetrazolijev bromid) metode.

DOI: 10.17344/acsi.2019.5066 *Acta Chim. Slov.* **2019,** *66,* 490–500

Scientific paper

Synthesis, X-Ray Structure Determination and Related Physical Properties of Thiazolidinone Derivative by DFT Quantum Chemical Method

Youcef Megrouss,[1,*] Fayssal Triki Baara,[2] Nourdine Boukabcha,[1] Abdelkader Chouaih,[1] Antonis Hatzidimitriou,[3] Ayada Djafri,[2] Fodil Hamzaoui[4]

[1] *LTPS Laboratory, University Abdelhamid Ibn Badis - Mostaganem, 27000 Mostaganem, Algeria*

[2] *Laboratory of Applied Organic Synthesis (LSOA), Department of Chemistry, Faculty of Sciences, University of Oran-1 Ahmed Ben Bella, 31000 Oran, Algeria*

[3] *Department of General and Inorganic Chemistry, Faculty of Chemistry, Aristotle University of Thessaloniki, GR-54124 Thessaloniki, Greece*

[4] *LPFM Académie de Montpellier, France*

** Corresponding author: E-mail: youmeg@hotmail.fr*

Received: 02-20-2019

Abstract

In this paper we report the synthesis and characterization of the (*Z*)-3-*N*-(ethyl)-2-*N*'-((3-methoxyphenyl)imino)thiazolidine-4-one by means of FT-IR, ^{1}H and ^{13}C NMR and by single crystal X-ray diffraction. The experimental determination of the crystal structure of the compound has been achieved using X-ray diffraction data. The important characteristic of the structure is the existence of a dihedral angle formed by the benzene and thiazolidinone rings being equal to 86.0° indicating an absence of π–π stacking as well as that the structure is non planar. In the crystal, the molecules are linked by C–H···O and C–H···N hydrogen bonds, these bonds being responsible for the three-dimensional molecular structure packing. In order to compare the experimental results with those of the theoretical calculation, quantum chemical DFT calculations were carried out using B3LYP/6-311G(d,p) basis set. In this context, the molecular electrostatic potential around the molecule and HOMO–LUMO energy levels were also computed. The dipole moment orientations were determined in order to understand the nature of inter- and intramolecular charge transfer. Finally, the stability of the title compound was confirmed throughout the calculation of the chemical reactivity descriptors.

Keywords: X-ray diffraction; single crystal; DFT calculations; spectroscopy; FT-IR; ^{1}H and ^{13}C NMR.

1. Introduction

Heterocyclic compounds are the major family of organic compounds; in medicinal chemistry thiazole derivatives are of great importance for their chemical and pharmacological properties, consequently thiazole derivatives have an extended range of pharmacological applications. Over the years, interesting biological activities were combined with thiazole derivatives.[1–2] These materials are extremely necessary with wide range of synthetic, pharmaceutical and industrial applications and are famous for their biological activities.[3,4] Recently, in drug development the application of thiazoles was required for the treatment of allergies,[5] hypertension,[6] inflammation,[7] schizophrenia,[8] bacterial[9] and HIV infections,[10] as hypnotics[11] and more recently for pain treatment,[12] as fibrinogen receptor antagonists with antithrombotic activity.[13] In addition, thiazolidinones and thiazoles present a very powerful activity as anti mycobacterium in tuberculosis.[14] In this context, we have tried to realize the synthesis of the title compound, to characterize and perform its structural analysis as well as the theoretical density functional theory (DFT) calculations. In this work we present the synthesis, single crystal structure, IR and NMR spectroscopic characterizations as well as DFT calculations of this new thiazole derivative compound, namely the (*Z*)-3-*N*-(ethyl)-2-*N*'-((3-methoxyphenyl)imi-

no)thiazolidine-4-one. Furthermore, theoretical vibrational frequencies and ^{1}H and ^{13}C NMR chemical shifts were calculated and compared to the experimental values. Additional parameters as molecular orbitals and chemical reactivity descriptors are evaluated in order to confirm the stability of the title compound. Finally, the molecular electrostatic potential was computed to determine electrophilic and nucleophilic regions of the title molecule.

2. Experimental

2. 1. Synthesis and Crystallization

An equimolar solution of *N*-ethyl-3-*N*'-(3-methoxyphenyl)thiourea and ethyl bromoacetate in absolute ethanol in the presence of sodium acetate was refluxed for 6 h. The solvent was removed by vacuum distillation and the residue was isolated, washed with cold water, filtered, dried and crystallized from ethanol to yield (*Z*)-3-*N*-(ethyl)-2-*N*'-((3-methoxyphenyl)imino)thiazolidin-4-one as presented in the scheme 1.

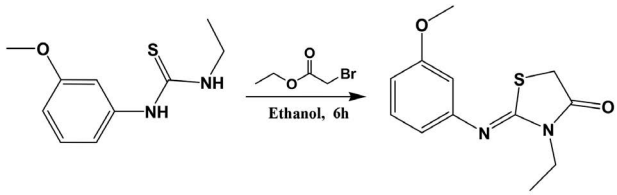

Scheme 1. Reaction sequence for the title compound synthesis.

2. 2. Spectral Data Measurements

Infrared (IR) spectrum of the molecule (*Z*)-3-*N*-(ethyl)-2-*N*'-((3-methoxyphenyl)imino)thiazolidine-4-one was recorded in the range 500–4000cm^{-1} on a Nicolet FT-IR 6700 spectrometer using sample prepared as KBr pellets. ^{1}H NMR (500 MHz) and ^{13}C NMR (125 MHz) spectra of the molecule using $CDCl_3$ as the solvent were recorded on Bruker AC250 spectrometer at 298 K.

2. 3. X-Ray Data Collection and Processing

A transparent-yellowish parallelepiped crystal was selected and separated from the mother liquor, immediately cooled to 130 K and mounted on a Bruker Kappa APEX 2 diffractometer, equipped with a Triumph monochromator using MoKa radiation. The crystal presented no decay during the data collection. The frames collected (running ϕ and ω scans) were integrated with the Bruker SAINT Software package,[15] using a narrow-frame algorithm. Data were corrected using the SADABS program.[16] The structure was solved by the SUPERFLIP package.[17] Crystals program package version 14.40[18] has been used for the refinement and all the rest subsequent calculations through full-matrix least-squares on F^2. All non-hydrogen atoms have been refined anisotropically. Hydrogen atoms were found at their expected positions and refined using proper riding constraints to the pivot atoms. Molecular illustrations were made through the MoPro-viewer crystallographic program.[19] Crystallographic and experimental details are summarized in Table 1.

Table 1. Crystallographic and experimental details.

Crystal data	
Chemical formula	$C_{12}H_{14}N_2O_2S$
M_r	250.32
Crystal system	Monoclinic
Space group	*C*2/*c*
a (Å)	23.7067 (19)
b (Å)	6.8884 (6)
c (Å)	15.7244 (12)
β (°)	111.6504 (17)
V (Å^3)	2386.66 (18)
Z	8
μ (mm^{-1})	0.26
Crystal size (mm)	0.31 × 0.28 × 0.19
Diffractometer	Bruker Kappa Apex2
Absorption correction	Numerical Analytical Absorption (De Meulenaer & Tompa, 1965)
T_{min}, T_{max}	0.93, 0.95
Radiation type, λ (Å)	Mo *K*α, 0.71073
Temperature (K)	130
Measured	17268
Independent	
Observed [$I > 2.0\sigma(I)$]	3006
2843	
R_{int}	0.015
$R[F^2 > 2\sigma(F^2)]$	0.029
$wR(F^2)$	0.066
S	1.00
No. of reflections	2843
No. of parameters	154
$\Delta\rho_{max}$, $\Delta\rho_{min}$ (e Å^{-3})	0.33, 0.21

3. DFT Calculations

In this theoretical study, the hybrid functional B3LYP with the 6-311G (d, p)[20] basis set were used in all calculations by using the Gaussian 09 program,[21] the X-ray structure was used as starting geometry to optimize a molecular structure of the investigation compound. Vibrational frequencies were calculated and the Gauss-view molecular visualization program[22] and VEDA software[23] were used for the assignment. Additionally, ^{1}H and ^{13}C NMR chemical shifts were calculated using the same level of theory. The theoretical calculation also allowed us to compute the energy values of the highest occupied molecular orbital (HOMO) and lowest unoccupied molecular orbital (LUMO). Furthermore, the molecular electrostatic

potential was calculated with B3LYP/6-311G(d, p) to highlight the electrophilic and nucleophulic attack sites.

4. Results and Discussion

4. 1. Structure Description

The molecular geometry of the title compound is defined by the presence of two fragments, methoxyphenyl and thiazolidine rings forming a dihedral angle of 86°. Detailed results containing atomic positions and thermal parameters are given in the CIF file. Selected bond lengths, bond and torsion angles for all atoms by X-ray diffraction and theoretical calculations are listed in Tables 2, 3 and 4, respectively. An ORTEPIII diagram[24] of the title compound showing the X-ray structure with thermal ellipsoids of the different atoms and the theoretical structure are given in Figure 1. In our study we employed full geometry optimization for the molecule without symmetry constraint. The results of our calculations showed that S1–C5, S1–C1, C1–N1, N1–C2, N1–C4, C6–N2 and O 2–C8 bonds exhibit single bond characteristics, while C4–O2 (1.23 Å) and N2–C1 (1.26 Å) bonds show typical double bond characteristics.[25] The amine N2 atom exhibits a geometry that is typical for an sp^2 rather than an sp^3 atom hybridisation. In addition, the difference in the thiazole ring bonds between theoretical calculation and experimental values does not exceed 0.13 Å. Bond angles C6–N2–C1, C2–N1–C4 and C1–N1–C4 are also near 120° (119.56°, 121.08° and 116.72°, respectively).[26]

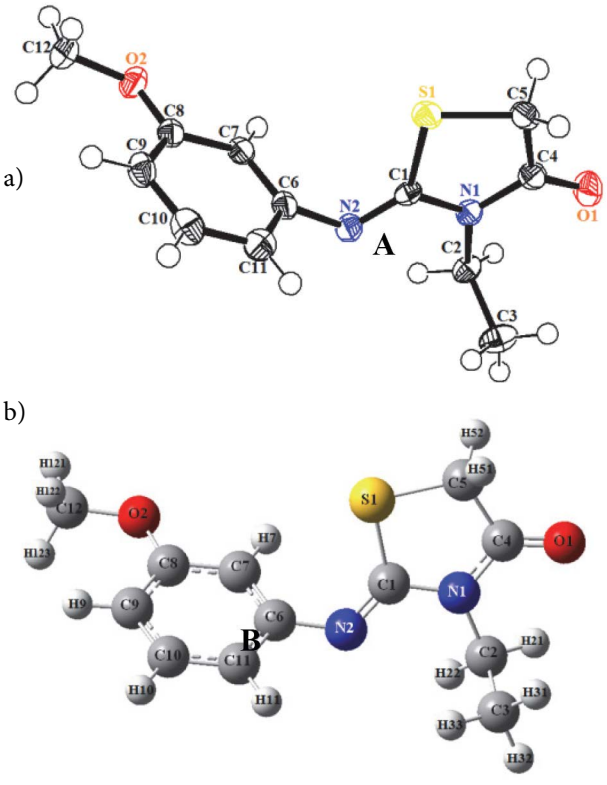

Figure 1. Experimental (a) and theoretical (b) structure of (*Z*)-3-*N*-(ethyl)-2-*N*'-((3-methoxyphenyl)imino)thiazolidine-4-one.

The bond angles centered on C1 are all between 109° and 129°. The C1 atom is of sp^2 hybridization type because the total adds up to 360° at B3LYP/6-311G(d,p) level. The corresponding theoretical values of this angle is 64° (C7–C6–N2–C1). The C8–O2–C12 angle is 116.98°, and the C2–N1–C4–O1 fragment is approximately planar (Table 4).

Generally, the observed difference between experimental and calculated geometrical parameters does not seem very large.

Table 2. Experimental and optimized bond lengths (Å).

Bond lengths	X-ray	B3LYP/6-311G(d,p)
S1–C5	1.811(1)	1.887
S1–C1	1.767(1)	1.893
O1–C4	1.216(1)	1.233
N1–C2	1.469(1)	1.485
N1–C1	1.399(1)	1.392
N1–C4	1.371(1)	1.388
N2–C6	1.425(1)	1.407
N2–C1	1.263(1)	1.264
O2–C8	1.367(1)	1.386
O2–C12	1.431(1)	1.459
C6–C7	1.389(1)	1.398
C6–C11	1.402(1)	1.408
C7–C8	1.398(1)	1.401
C5–C4	1.509(1)	1.527
C2–C3	1.518(1)	1.537
C10–C9	1.393(1)	1.399
C10–C11	1.386(1)	1.387
C8–C9	1.395(1)	1.397

Table 3. Experimental and optimized bond angles (°).

Bond angles	X-ray	B3LYP/6-311G(d,p)
C5–S1–C1	92.24	90.13
C2–N1–C1	122.15	120.13
C2–N1–C4	121.08	119.58
C1–N1–C4	116.72	29.83
C6–N2–C1	119.56	129.18
C8–O2–C12	116.98	117.97
N2–C6–C7	119.43	124.07
N2–C6–C11	119.94	116.82
C7–C6–C11	120.34	119.08
C6–C7–C8	119.87	120.72
S1–C5–C4	107.51	108.27
N1–C2–C3	112.36	111.42
S1–C1–N1	110.92	109.07
S1–C1–N2	127.32	129.12
N1–C1–N2	121.76	121.81
O1–C4–N1	123.71	123.73
O1–C4–C5	123.91	124.08
N1–C4–C5	112.37	112.18
C9–C10–C11	121.52	120.98
O2–C8–C7	115.23	115.22
O2–C8–C9	124.48	124.87
C7–C8–C9	120.27	119.91
C10–C9–C8	119.01	119.34
C6–C11–C10	118.98	119.96

Table 4. Experimental and optimized torsion angles (°).

Torsion angles	X-ray	B3LYP/6-311G(d,p)
C1–S1–C5–C4	3.6	2.4
C5–S1–C1–N1	–4.7	–2.4
C5–S1–C1–N2	174.5	176.7
C1–N1–C2–C3	–99.6	–86.2
C4–N1–C2–C3	77.9	92.2
C2–N1–C1–S1	–177.7	–179.7
C2–N1–C1–N2	3.1	1.1
C4–N1–C1–S1	4.7	1.8
C4–N1–C1–N2	–174.6	–177.3
C2–N1–C4–O1	–0.2	1.7
C2–N1–C4–C5	–179.5	–178.4
C1–N1–C4–O1	177.4	–179.9
C1–N1–C4–C5	–1.9	0.1
C1–N2–C6–C7	86.0	64.5
C1–N2–C6–C11	–100.2	–119.3
C6–N2–C1–S1	1.6	4.4
C6–N2–C1–N1	–179.2	–176.7
C12–O2–C8–C7	–170.8	179.8
C12–O2–C8–C9	10.9	–0.1
N2–C6–C7–C8	172.3	178.5
C11–C6–C7–C8	–1.5	0.6
N2–C6–C11–C10	–173.1	–179.4
C7–C6–C11–C10	0.6	–1.3
C6–C7–C8–O2	–177.2	–179.5
C6–C7–C8–C9	1.3	0.4
S1–C5–C4–O1	178.9	178.06
S1–C5–C4–N1	–1.8	–1.9
C11–C10–C9–C8	–0.8	–0.1
C9–C10–C11–C6	0.5	1.1
O2–C8–C9–C10	178.2	179.2
C7–C8–C9–C10	–0.1	–0.7

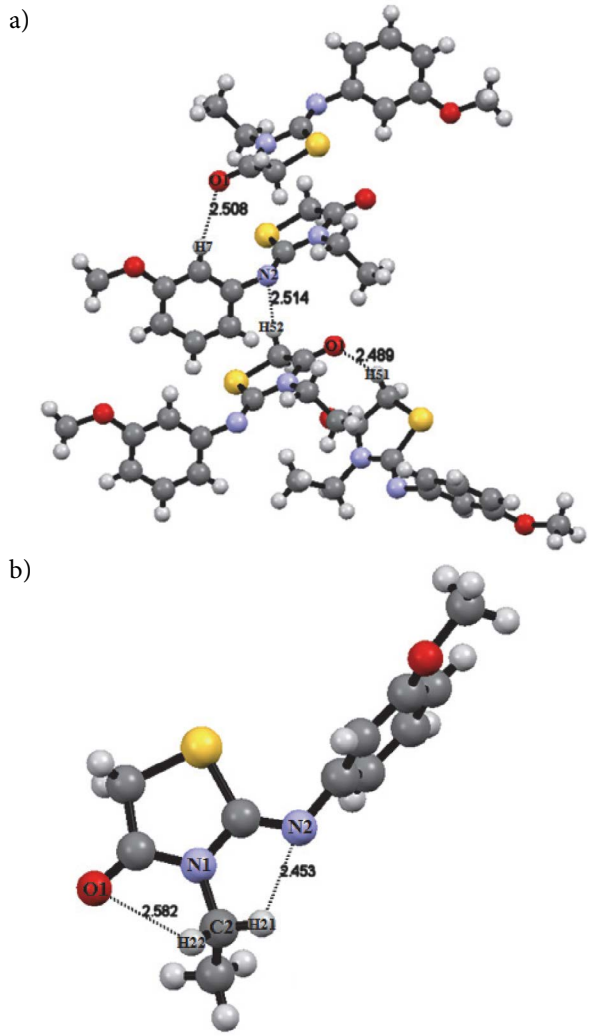

Figure 2. Hydrogen bonding view in the crystal showing: (A) intermolecular interactions, (B) C2–H21···N2 and C2–H22···O1 intramolecular interactions.

4. 2. Hydrogen Bonding

Hydrogen bonds join chains of molecules to stabilize the crystal structure of the title compound. Along the *b* axis in the unit cell, the translation of equivalent molecules allows the linking of the almost linear hydrogen bonding. C–H···O and C–H···N intra- and intermolecular interactions are present in the crystal structure. The molecular conformation is in part influenced by the formation of two weak intramolecular C2–H22···O1 and C2–H21···N1 hydrogen bonds that enclose S(5) rings (Figure 2 and Table 5).

These interactions are responsible for the stability of the molecular packing, as the C2, C3, C5, C12 and C7 carbon atoms act as donor groups and both oxygen and nitrogen atoms play the acceptor role. Hydrogen bond interactions are presented in Table 5. Figure 2 shows all interaction types in the crystal. The molecular stacking that has been provided by the different existing hydrogen bonds in the

Table 5. Geometry of the C–H···O and C–H···N hydrogen bonds in (*Z*)-3-*N*-(ethyl)-2-*N*'-((3-methoxyphenyl)imino)thiazolidine-4-one crystal by X-ray diffraction.

D–H···A	D–H (Å)	D–A (Å)	H···A (Å)	D–H···A (°)	Bond type
C2–H21···N2	0.981	2.852	2.453	103.88	Intramolecular
C2–H22···O1	0.962	2.817	2.582	93.97	Intramolecular
C5–H51···O1$^{(i)}$	0.987	3.380	2.489	149.92	Intermolecular
C7–H7···O1$^{(ii)}$	0.947	3.432	2.508	164.98	Intermolecular
C5–H52···N2$^{(iii)}$	0.955	3.370	2.514	149.26	Intermolecular

Symmetry codes: *(i)* –*x*, *y*, –*z* + 1/2; *(ii)* –*x*, –*y*, –*z*; *(iii)* *x*, –*y*, *z* + 1/2

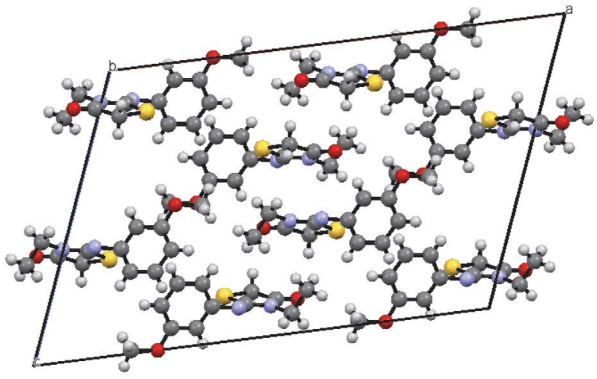

Figure 3. View of the crystal packing along the *b* axis of (*Z*)-3-*N*-(ethyl)-2-*N*'-((3-methoxyphenyl)imino)thiazolidine-4-one molecule.

crystal is shown in Figure 3. This figure shows the existence of eight molecules in the unit cell which is in good agreement with the multiplicity of the space group C2/c.

4. 3. Vibrational Frequencies Assignments

Using analytic second derivatives to validate the convergence to minima on the potential energy surface the fundamental frequencies of the studied molecule have been calculated to understand the nature of these modes of vibration IR absorption spectroscopy based on DFT calculation. A theoretical analysis has been realized using B3LYP/6-311G(d,p) level of theory in gas phase. The probable assignments were performed by means of VEDA 4 program.[23] The vibrational frequencies obtained from B3LYP functional calculations have been scaled by a factor of 0.967.[27] Table 6 shows the calculated (unscaled and scaled) and experimental frequencies of the title compound. Simulated and experimental IR spectra of (*Z*)-3-*N*-(ethyl)-2-*N*'-((3-methoxyphenyl)imino)thiazolidine-4-one are shown in Figure 4. As can be seen in Figure 4, the experimental fundamentals are in better agreement with the scaled fundamentals.

4. 3. 1. Carbon–Hydrogen Vibrations

In the aromatic compounds, multiple weak bands are exhibited in the region of 3100–3000 cm^{-1}.[28] They appear in this range of like multiple weak bands due to the stretching vibrations of C–H.[29] In the present work, the carbon–hydrogen of aromatic ring (C–H) stretching (νCH modes) were found in a range of 3000 and 3100 cm^{-1} using the B3LYP/6-311G(d,p) calculations. These modes involve exact contribution of >91% suggesting that they are pure stretching modes. The C–H stretching of aromatic ring showed symmetric modes at 3001, 3070 and 3080 cm^{-1} while asymmetric stretching mode was observed at 2989 cm^{-1}.

4. 3. 2. C=O and C=N Vibrations

Usually, the C=O stretching vibration mode can be easily observed as a strong band in the region 1850–1550 cm^{-1}.[30] The π–π bonding between carbon and oxygen is responsible for forming a double bond between the carbon and oxygen atoms. The electronic distribution in this link is not equal because these atoms have different electronegativities. The lone pair of electrons on oxygen is responsible for the polar nature of the carbonyl group. In the present study, the single C=O stretching vibration mode was observed as a high-intense peak in FT-IR at 1716 cm^{-1} while the calculated value shows at 1726 cm^{-1} with a PED (potential energy distribution) of 79%. The stretching frequency of the double bond C=N is perfectly observed at the high absorption 1640 cm^{-1}. DFT/B3LYP functional with 6-311G(d,p) basis set gives exactly the same value of 1640 cm^{-1} for the C=N vibration.

4. 3. 3. Thiazolidine Ring Vibrations

The C–S stretching vibration presents average bands in the region 1020–1010 cm^{-1}.[31] In this paper C–S vibrations were observed at 704, 647 and 526 cm^{-1}. The examination of the theoretical results gives us the following values with their PED contribution: 720 (21%), 642 (10%), 522 (12%) and 482 (23%) respectively, which shows a good agreement between theoretical and experimental ones as shown in the Table 6. C–N vibration is a difficult task to identify since the appearance of several bands is possible in the region, Gunasekaran *et al.*[32] have observed C–N stretching band at 1312 cm^{-1},[33] and C–N assigned stretching vibration in the region 1350–1000 cm^{-1} for amines. In thiazolidine, C–N stretching band is found to be present at 1382 and 1307 cm^{-1}. The C–N stretching vibrations are expected to occur in the region 1200–1130 cm^{-1}.[34] In our present work of the title molecule FTIR bands were observed at 896 cm^{-1} and 1234 cm^{-1}, the theoretically calculated bands at 940, 1405, 1357, 1301, 1257, 1131 are shifted

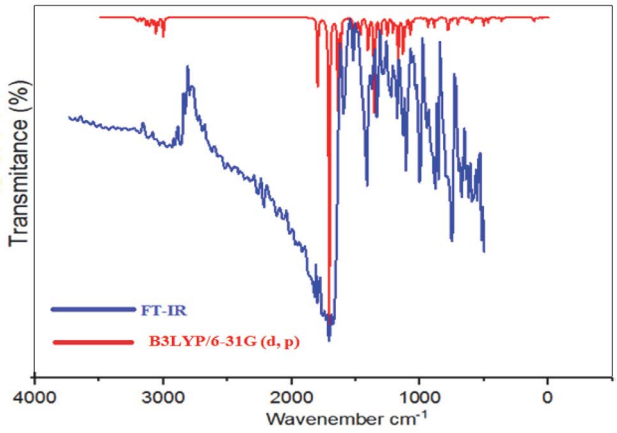

Figure 4. Comparison of FT-IR and calculated IR Spectra for (*Z*)-3-*N*-(ethyl)-2-*N*'-((3-methoxyphenyl)imino)thiazolidine-4-one.

Table 6. Comparison of the calculated harmonic frequencies using B3LYP method 6-311G(d,p) basis set and experimental (FT-IR) wavenumbers (cm^{-1}) for (*Z*)-3-*N*-(ethyl)-2-*N'*-((3-methoxyphenyl)imino)thiazolidine-4-one.

No	Experimental	B3LYP/6-311G(d,p) Unscaled	Scaled	I_{IR}	Assignments with PED>10%
87		3209	3080.64	8.75	ν CH (91%) Ar ring
86		3198	3070.08	0.77	ν CH (92%) Ar ring
85		3127	3001.92	9.61	ν CH (100%) Ar ring
83		3139	3013.44	9.25	ν CH (79%) + ν_{as} CH (11%)
81		3127	3001.92	0.33	ν CH (100%)
80	2971	3114	2989.44	13.61	ν_{as} CH (92%)
74		3001	2880.96	61.94	ν CH (92%)
73	1716	1798	1726.08	182.70	ν C=O (79%)
72	1640	1709	1640.64	943.72	ν N=C (73%)
71		1640	1574.4	329.64	ν CC_{asy} (63%) Ar ring +δ HCC (14%) Ar ring
70		1617	1552.32	93.33	ν CC (51%)$_{asy}$ Ar ring+ δ HCC (11%) Ar ring+ δ CCC (12%) Ar ring
69	1482	1518	1457.28	72.82	δ HCC_{asy} (44%) Ar ring+ δ CCC (19%) Ar ring
68		1508	1447.68	33.99	δ HCH (67%)+
67		1506	1445.76	3.59	δ HCH(71%)+ τ$HCCN_{asy}$ (22%) Th ring
66		1498	1438.08	8.56	δ HCH(71%)+ τ$HCCN_{asy}$ (24%) Th ring
65		1492	1432.32	7.71	δ HCH_{asy}(69%)+ τ$HCOC_{asy}$(24%) Ar ring
64		1482	1422.72	0.82	δ HCH(48%)
62		1465	1406.4	40.95	ν CC_{asy} (31%) Ar ring+ δ HCC (31%) Ar ring+ δ HCC_{asy} (16%)
61		1462	1403.52	8.14	δ HCH (88%)
60	1391	1420	1363.2	18.06	δ HCC (13%)+ δ HCH (15%)+ τHCNC (46%) Th ring
59		1405	1348.8	110.90	ν NC(13%) Th ring+ δ HCC (10%)+ δ HCH (39%)+ τ$HCNC_{asy}$ (10%) Th ring
58		1401	1344.96	12.94	δ HCC (56%)+ δ HCH (14%)
57		1357	1302.72	247.21	ν NC(46%) Th ring
56	1284	1350	1296	24.41	ν CC_{asy} (59%) Ar ring+ δ HCC (23%)
55		1312	1259.52	111.70	ν CO_{asy}(79%) Ar ring+ δ HCC (37%) Ar ring
54	1234	1301	1248.96	13.79	ν CC (10%) Ar ring+ ν NC_{th}(12%) Ar ring+ δ HCC (11%) Ar ring+ δ HCH_{asy} (14%)
53		1257	1206.72	43.11	ν NC_{asy} (16%)+ Th ring +ν CO(13%) Ar ring+ τHCCN (12%) Th $ring_{asy}$
52		1253	1202.88	25.58	τ$HCSC_{asy}$(84%) Th ring
51		1212	1163.52	40.44	δ HCH_{asy}(15%)+ τHCOC(44%) Ar ring
50	1148	1194	1146.24	22.35	ν CC (10%) Ar ring+ δ HCC (38%) Ar ring+ τ$HCOC_{asy}$(14%) Ar ring
49		1172	1125.12	45.03	δ HCH(21%)+ τHCOC(35%) Ar ring
48		1171	1124.16	101.55	δ HCC_{asy} (13%) Ar ring+ τ$HCOC_{asy}$(17%) Ar ring
47		1148	1102.08	3.08	δ HCS_{asy} (52%) Th ring+ τHCSC(28%) Th ring
46		1131	1085.76	146.72	ν NC_{asy} (15%) Th ring+ ν CC(11%) Th ring
45		1111	1066.56	17.22	δ HCH_{asy}(12%)+ δ CCN_{asy} (13%) Th ring+ τHCCN (36%) Th $ring_{asy}$
44		1109	1064.64	12.00	ν CC(14%) Ar ring+ δ HCC(33%) ar ring+
43	1046	1075	1032	63.45	ν OC(55%) Ar ring+ δ HCC(17%) Ar ring
41		1007	966.72	0.82	ν CC_{asy} (52%) Ar ring+ δ CCC_{asy}(39%) Ar ring
40		973	934.08	4.63	ν CC_{asy} (33%) Th ring
39	927	968	929.28	0.03	τHCCC (77%) Ar ring
38	896	940	902.4	27.82	ν NC(10%) Ar ring+ ν OC_{asy}(10%) Ar ring+ ν CC_{asy} (27%) Th ring
37		922	885.12	7.21	δ HCS(45%) Th ring+ τHCSC (21%) Th ring+ τ$CCNC_{asy}$(19%) Th ring+ γ $OCNC_{asy}$(15%)
36		891	855.36	29.40	ν CC_{asy} (12%) Th ring+ δ NCN_{asy} (10%)+ τHCCC (12%) Ar ring
35		872	837.12	7.58	τHCCC (68%) Ar ring
34		863	828.48	5.52	τHCCC (68%) Ar ring
33	775	791	759.36	5.21	δ NCN_{asy} (32%) Th ring+ τHCNC (33%) Th ring
32		782	750.72	30.71	τHCCC (17%) Ar ring+ τ$HCCC_{asy}$ (17%) Ar ring+τ$CCCC_{asy}$(29%) Ar ring
31	740	779	747.84	20.41	δ CNC (27%) Th ring
30	704	751	720.96	8.75	ν CC_{asy} (10%) Ar ring+ ν CC(10%) Th ring+ ν SC(21%) Th ring
29		705	676.8	22.45	τ$HCCC_{asy}$ (56%) Ar ring+ τ$CCCC_{asy}$(10%) Ar ring
28	647	669	642.24	0.28	ν SC(10%) Th ring+ τ$HCCC_{asy}$ (12%) Ar ring+ τCCCC(43%) ar ring
27	609	643	617.28	4.95	ν CC(28%) Th ring+ δ CCC_{asy}(11%) Ar ring

26		617	592.32	4.44	γSNNC $_{asy}$(54%) Ar ring
25	584	610	585.6	5.88	δ CNC$_{asy}$ (11%) Th ring
24		593	569.28	17.41	δ CCC$_{asy}$ (14%) Ar ring+ γOCNC(19%) Th ring
23		581	557.76	1.53	τHCSC$_{asy}$ (16%) Th ring+ γOCNC$_{asy}$ (30%) Th ring
22	526	544	522.24	3.20	ν SC(12%) Th ring+ δ CCC (25%) Ar ring+ τCCCC (12%) Ar ring
21		503	482.88	23.21	ν SC$_{asy}$ (23%) Th ring+ δ CCN$_{asy}$(14%) Ar ring
20		484	464.64	0.63	δ CNC$_{asy}$(10%) Ar ring+ δ CCO$_{asy}$(32%) Ar ring
19		471	452.16	16.37	δ CNC$_{asy}$(19%) Th ring+ δ CCN$_{asy}$(16%) Th ring+ δ CCO$_{asy}$(12%) Th ring
18		454	435.84	1.08	δ CCO$_{asy}$(11%) Ar ring+ τCCCC$_{asy}$ (36%) Ar ring
17		403	386.88	2.62	δ CCC(12%) Ar ring+ δ COC$_{asy}$ (21%) Ar ring

ν: stretching(elongation); sy: symmetric; asy: asymmetric; β: in plane bending; γ: out-of-plane bending, ω: wagging; τ: twisting; δ: bending; ρ: rocking; vibrational modes are based on potential energy distribution (PED) and only contributions over 10% are given; scaled frequencies are in unit of cm^{-1}; I_{IR} infrared intensities are in unit of km mol^{-1}.

down by scaling the previous values to 902 (10%), 1348 (13%), 1302 (46%), 1248 (12%), 1206 (16%), 1085 (15%), respectively with the percentage of the PED contribution indicated between brackets.

4. 4. ^{1}H and ^{13}C NMR Calculations

To calculate isotropic chemical shifts (δ) with respect to tetramethylsilane (TMS): $\delta^x_{iso} = \sigma^{TMS}_{iso} - \sigma^{x}_{iso}$,[34] isotropic shielding values 184.2796 and 32.2899 ppm of σ^{TMS}_{iso} were used for C and H NMR spectra, respectively. It is known that the range of ^{13}C NMR chemical shifts for analogous organic molecules usually are >100 ppm.[35,36] Methanol solvent has been used for chemical shift measurements. The atoms were labeled according to the numbering presented in Figure 1 (B). Calculated and experimental values for ^{1}H and ^{13}C NMR are collected in Table 7. In this research, aromatic carbons give signals in overlapped areas of the spectrum with chemical shift values from 106 to 170 ppm while experimental chemical shift values of aromatic carbon atoms are in the range 107 to 160 ppm as they would be expected (Table 7). Carbon atoms (C1, C4 and C6) attached to the N atom have larger chemical shifts due to the more electronegative property of the N atom which polarizes the electron distribution in its binding to the atom adjacent carbon and reduces the value of the chemical shifts. Usually, the chemical shifts obtained and calculated for the ^{1}H atoms of the methyl groups are quite weak. The maximum chemical shift value for all the hydrogen atoms is 7.24 ppm.

Table 7. Experimental and calculated ^{1}H and ^{13}C NMR data for (*Z*)-3-*N*-(ethyl)-2-*N*'-((3-methoxyphenyl)imino)thiazolidine-4-one.

Chemical shifts		
^{1}H	Experimental	B3LYP/6-311G(d)
H_{51}	3.78	4.03
H_{52}	3.78	3.94
H_{21}	3.90	4.49
H_{22}	3.90	4.25
H_{31}	1.29	1.02
H_{32}	1.29	1.92
H_{33}	1.29	1.19
H_9	6.52	6.26
H_7	6.67	6.71
H_{11}	6.56	6.64
H_{10}	7.24	7.42
H_{121}	3.79	4.32
H_{122}	3.79	3.74
H_{123}	3.79	3.73
^{13}C		
C1	154.23	158.27
C2	32.76	37.78
C3	12.52	15.06
C4	171.55	176.61
C5	38.26	37.57
C6	149.32	158.15
C7	110.39	113.89
C8	160.37	170.89
C9	107.22	106.29
C10	129.99	136.22
C11	113.20	120.10
C12	55.25	58.70

4. 5. Frontier Molecular Orbitals (FMOs)

The highest occupied molecular orbitals (HOMO) and the lowest unoccupied molecular orbitals (LUMO) are named as frontier molecular orbitals (FMO). The HOMO represents the ability to donate an electron, whereas LUMO as an electron acceptor represents the ability to obtain an electron.[37] The calculation of these parameters is very important because it allowed us to verify a lot of properties, such as the kinetic stability and chemical reactivity. Figure 5 shows the atomic orbital HOMO–LUMO plot of the frontier molecular orbitals computed at B3LYP/6-311G(d,p) level for the title compound. As shown in Figure 5, in HOMO density, electrons are mainly located on the methoxyphenyl group. However, when an electron transition occurs, the electron enters into the LUMO, and then the electron will mainly be localized on thiazole ring and carboxylic group. The positive phase is red and the negative one is green coloured. The HOMO–

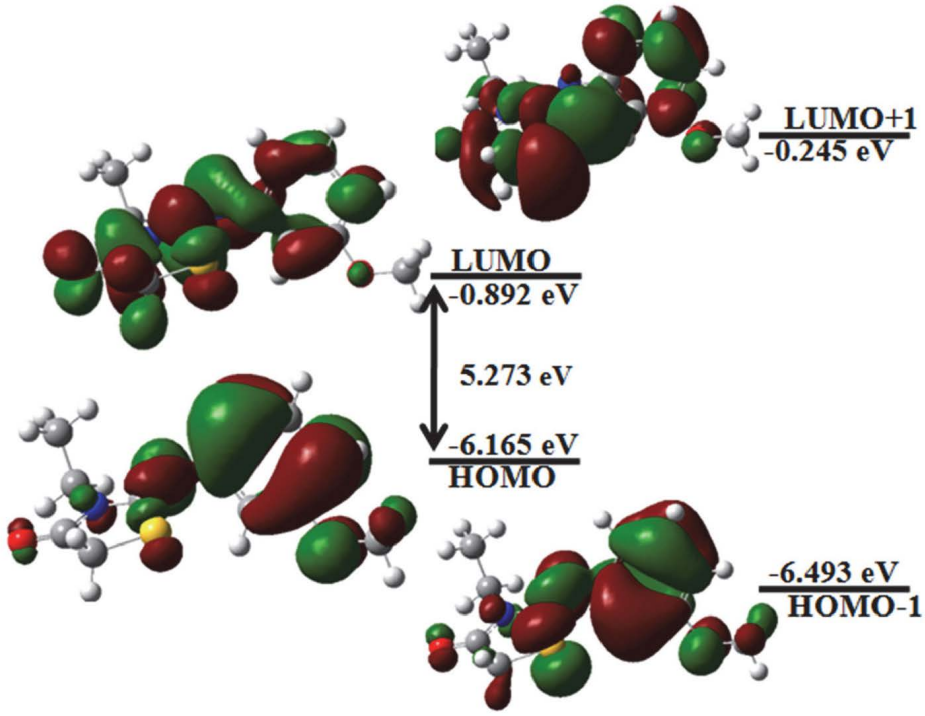

Figure 5. Electron distribution of the HOMO–1, HOMO, LUMO and LUMO+1 energy levels for the title molecule.

LUMO energy gap of our molecule was calculated at the B3LYP/6-311G (d,p) level with HOMO energy –6.165 eV, LUMO energy –0.892 eV and HOMO–LUMO energy gap 5.273 eV. The second highest occupied MO (HOMO–1) and the second lowest unoccupied MO (LUMO+1) were calculated using the same level of theory. 3D plots of the HOMO–1, HOMO, LUMO and LUMO+1 orbitals of the studied molecule are drawn in Figure 4.

4. 6. Chemical Reactivity

Global chemical reactivity descriptors (GCRD) parameters are a good indication to highlight the relationship between chemical reactivity and strength of structure. As are mentioned in literature, GCRD parameters can be obtained by using the following equations: $\eta = \frac{1}{2}(E_{LUMO}-E_{HOMO})$; $\mu = -\left(\frac{I+A}{2}\right)$; $S = \frac{1}{2\eta}$; $\chi = \left(\frac{I+A}{2}\right)$; $\omega = \frac{\mu^2}{2\eta}$. $A = -E_{LUMO}$ and $I = -E_{HOMO}$. The electron affinity (A) and ionization potential (I) can be evaluated as and . The calculated values of GCRD parameters for the title molecule are summarized in Table 8.

The chemical hardness (η) value is 2.636 eV indicating that the charge transfer occurs within the molecule. From Table 8, the electrophilic behaviour of the molecule is confirmed by the global electrophilicity index (ω) which has a greater value of 2.361 eV. On the other hand, the chemical stability of the title molecule is explained by the chemical potential (μ) value which is –3.528 eV.

Table 8. Calculated energy values of the title compound by B3LYP/6-311G(d,p) method.

Parameters	Calculated energies
E_{HOMO}	–6.165
E_{LUMO}	–0.892
Energy gap (ΔE)	5.273
Ionization potential (I)	6.165
Electron affinity (A)	0.892
Electronegativity (χ)	3.528
Chemical potential (μ)	–3.528
Chemical hardness (η)	2.636
Chemical softness (s)	0.189
Electrophilicity index (ω)	2.361

4. 7. Electrostatic Potential

In a crystal, the location of positive and negative charges allowed us to define very interesting physical properties such as the molecular electrostatic potential (MEP).[38] Nowadays, theoretical and experimental MEP surfaces are determined using quantum chemistry and X-ray diffraction.[39–42] The MEP around the title molecule was calculated from the total density (TD) for the title compound, the two maps (TD and MEP) are represented in the Figure 6. From the figure it can be seen that the negative MEP is related to the electronegativity and partial charges of oxygen atoms O1 and O2. The blue color in Figure 6B gives the maximum positive region as the preferred

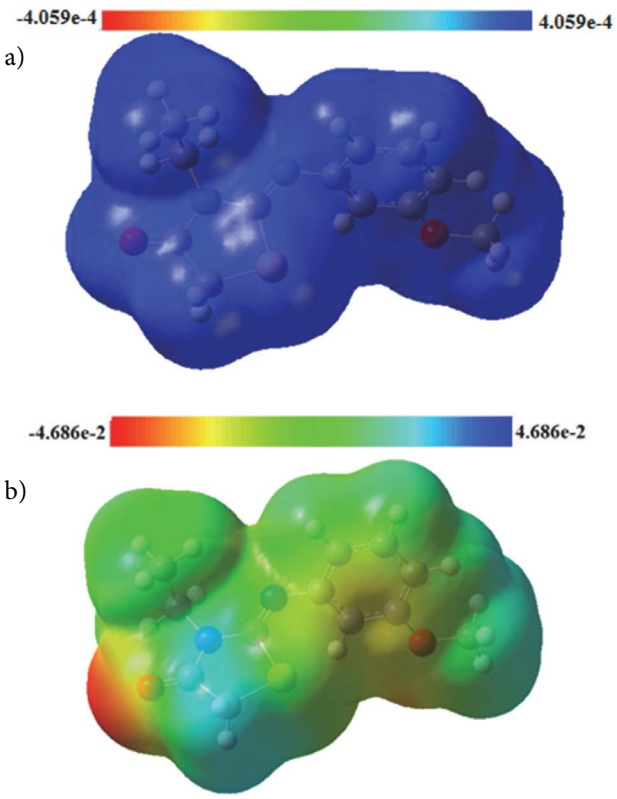

Figure 6. MEP plots for (*Z*)-3-*N*-(ethyl)-2-*N*'-((3-methoxyphenyl) imino)thiazolidine-4-one: (a) total electron density, (b) MEP surface.

site for nucleophilic attack. In terms of color, the MEP plot lies in the fact that it simultaneously displays molecular size, shape as well as positive, negative and neutral electrostatic potential regions (Figure 6). The MEP indicate well the relationship between the molecular structure and these physico-chemical properties.[43–47] Among them, the molecular dipole moment can be calculated. The orientation of the molecular dipole moment for the title compound is represented in Figure 7. This orientation confirms the electrostatic distribution previously defined. The calculated dipole moment value is 2.24 D.

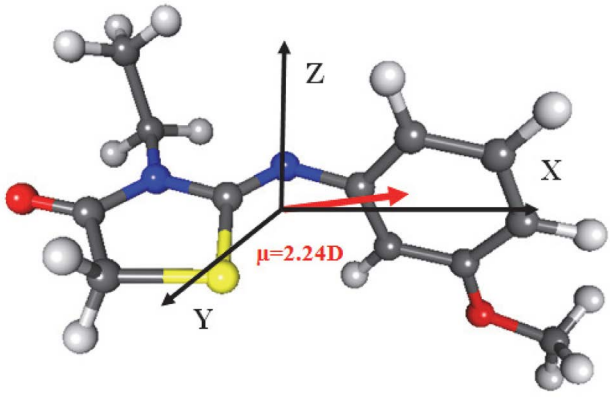

Figure 7. Orientation of the molecular dipole moment from DFT calculation.

5. Conclusion

In this study, (*Z*)-3-*N*-(ethyl)-2-*N*'-((3-methoxyphenyl)imino)thiazolidine-4-one was synthesized and characterized by IR, ^{1}H and ^{13}C NMR and X-ray single-crystal diffraction techniques. The crystal structure determination shows that the title compound crystallizes in monoclinic system with space group C2/c. Theoretical calculations of the molecular structures, wavenumbers and NMR spectra of the title compound have been carried out using DFT-B3LYP/6-311G(d,p). As result, the experimental and the optimized crystal structures of the title compound were slightly different. Most of the experimental bond lengths and bond angles are slightly larger than the optimized values. These differences are due to that the theoretical calculations are performed for isolated molecule in gaseous phase and the experimental results are for a molecule in the crystalline environment. The geometry of the solid-state structure is subject to intermolecular forces, such as Van der Waals interactions and crystal packing contacts. Comparison between the chemical shifts and the experimental data shows a very good agreement for both ^{1}H and ^{13}C NMR shift values. The HOMO–LUMO gap and chemical reactivity descriptors indicate that the compound is more stable. The general conclusion from the estimation of the dipolar moment (2.24 D) and the electrostatic potential of ((*Z*)-3-*N*-(ethyl)-2-*N*'-((3-methoxyphenyl)imino)thiazolidine-4-one molecule is that the region of the thiazolidinone group is electronegative and the methyl and hydrogen atoms connected to the benzene ring are electropositive.

6. Supplementary Material

Crystallographic data for the structure reported in this article have been deposited with Cambridge Crystallographic Data Center, CCDC 1871013. Copies of this information may be obtained free of charge from the Director, CCDC, 12 Union Road, Cambridge, CB2 1EZ, UK. Facsimile (44) 01223 336 033, E-mail: deposit@ccdc.cam.ac.uk or http//www.ccdc.com.ac.uk/deposit.

7. References

1. J. Quiroga, P. Hernandez, B. Insuasty, R. Abonia, J. Cobo, A. Sanchez, M. Nogueras, *J. Chem. Soc. Perkin Trans. 1* **2002**, *4*, 555–559. **DOI:**10.1039/b109676a
2. I. Hutchinson, S. A. Jennings, B. R. Vishnuvajjala, A. D. Westwell, M. F. G. Stevens, *J. Med. Chem.* **2002**, *45*, 744–747. **DOI:**10.1021/jm011025r

3. R. I. Bahoussi, A. Djafri, A. Chouaih, A. Djafri, F. Hamzaoui, *Acta Cryst*. **2017**, *E73*, 173–176. **DOI:**10.1107/S205698901700041X
4. A. Srinivas, M. Sunitha, P. Karthik, K. V. Reddy, *Acta Chim. Slov.* **2017**, *64*, 1030–1041. **DOI:**10.17344/acsi.2017.3805
5. K. D. Hargrave, F. K. Hess, J. T. Oliver, *J. Med. Chem*. **1983**, *26, 1158*–1163. **DOI:**10.1021/jm00362a014
6. W. C. Patt, H. W. Hamilton, M. D. Taylor, M. J. Ryan, J. R. Taylor, C. J. C. Connolly, *J. Med. Chem.* **1992**, *35*, 2562–2572. **DOI:**10.1021/jm00092a006
7. R. N. Sharma, F. P. Xavier, K. K. Vasu, S. C. Chaturvedi, S. S. Pancholi, *J. Enz. Inhib. Med. Chem.* **2009**, *24*, 890–897. **DOI:**10.1080/14756360802519558
8. J. C. Jaen, L. D. Wise, B. W. Caprathe, H. Tecle, S. Bergmeier, C. C. Humblet, T. G. Heffner, *J. Med. Chem.* **1990**, *33*, 311–317. **DOI:**10.1021/ jm00163a051
9. K. Tsuji, H. Ishikawa, *J. Med. Chem. Lett*. **1994**, *4*, 1601–1606. **DOI:**10.1016/S0960-894X(01)80574-6
10. F. W. Bell, A. S. Cantrell, M. Hogberg, S. R. Jaskunas, N. G. Johansson, C. L. Jordon, *J. Med. Chem*. **1995**, *38*, 4929–4936. **DOI:**10.1021/jm00025a010
11. N. Ergenc, G. Capan, N. S. Gunay, S. Ozkirimli, M. Gungor, S. Ozbey, E. Kendi, *Arch. Pharm*. **1999**, *332*, 343–347. **DOI:**10.1002/ (SICI)1521-4184(199910)332:10<343::AID -ARDP343>3.0.CO;2-0
12. J. S. Carter, S. Kramer, J. J. Talley, T. Penning, P. Collins, M. J. Graneto, K. Eibert, *Bioorg. Med. Chem. Lett*. **1999**, *9*, 1171–1174. **DOI:**10.1007/s00706-010-0392-3
13. A. Badorc, M. F. Bordes, P. De Cointet, P. Savi, A. Bernat, A. Lale, M. Petitou, *J. Med. Chem.* **1997**, *40*, 3393–3401. **DOI:**10.1021/jm970240y
14. G. Aridoss, S. Amirthaganesan, M. S. Kim, J. T. Kim, Y. T. Jeong, *Eur. J. Med. Chem*. **2009**, *44*, 4199–4210. **DOI:**10.1016/j.ejmech.2009.05.015
15. Bruker Analytical X-ray Systems, Inc, Apex2, Version 2 User Manual, M86–E01078, **2006**, 6, Madison, WI.
16. Siemens Industrial Automation, Inc. SADABS: Area-Detector Absorption Correction, **1996**, Madison, WI.
17. P. W. Betteridge, J. R. Carruthers, R. I. Cooper, K. Prout, D. J. Watkin, *J. Appl. Crystallogr*. **2003**, *36*,1487. **DOI**:10.1107/S0021889803021800
18. L. Palatinus, G. Chapuis, *J. Appl. Crystallogr*. **2007**, *40*, 782–785. **DOI**:10.1107/S002188980702420X
19. C. Jelsch, B. Guillot, A. Lagoutte, C. Lecomte, *J. Appl. Crystallogr*. **2005**, *38*, 38–54. **DOI:**10.1107/S0021889804025518
20. A. D. Becke, *J. Chem. Phys*. **1997**, *107*, 8554–8560. **DOI:**10.1063/1.475007
21. P. C. R. Kumar, V. Ravindrachary, K. Janardhana, B. Poojary, *J. Cryst. Growth* **2012**, *354*, 182–187. **DOI:**10.1016/j.jcrysgro.2012.06.006
22. A. Frish, A. B. Nielsen, A. J. Holder, Gaussview Users Manual, Gaussian Inc, Pittsburg, **2000**.
23. M. H. Jamróz, J. C. Z. Dobrowolski, *J. Mol. Struct*. **2001**, *565*, 475–480. **DOI:**10.1016/S0022-2860(00)00908-X
24. L. J. Farrugia, "ORTEP-3 for windows-a version of ORTEPI-II with a graphical user interface (GUI), *J. Appl. Crystallogr*. **1997**, *30*, 565–568. **DOI:**10.1107/S0021889897003117
25. S. Yahiaoui, A. Moliterni, N. Corriero, C. Cuocci, K. Toubal, A. Chouaih, A. Djafri, F. Hamzaoui, *J. Mol. Struct*. **2019**, *1177*, 186–192. **DOI:**10.1016/j.molstruc.2018.09.052
26. N. Khelloul, K. Toubal, N. Benhalima, R. Rahmani, A. Chouaih, A. Djafri, F. Hamzaoui, *Acta. Chim. Slov*. **2016**, *63*, 619–626. **DOI:**10.17344/acsi.2016.2362
27. S. P. V. Chamundeeswari, E. R. J. J. Samuel, N. Sundaraganesan, *Eur. J. Chem*. **2011**, *2*, 136–145. **DOI:**10.5155/eurjchem.2.2.136-145.169
28. A. Eşme, S. Güneşdoğdu Sağdınç, *Spectrochim. Acta A Mol. Biomol. Spectrosc*. **2018**, *188*, 443–455. **DOI:**10.1016/j.saa.2017.07.034
29. G. Muhammad, A. Muhammad, A. M. Khalid, *J. Mol. Struct*. **2018**, *1160*, 129–141. **DOI:**10.1016/j.molstruc.2018.01.100
30. P. K. Murthy, G. Krishnaswamy, S. Armaković, S. J. Armaković, P. A.Suchetan, N. R. Desai, V. Suneetha, R. Sreenivasa Rao, G. Bhargavi, D. B. Arunakumar, *J. Mol. Struct*. **2018**, *1162*, 81–95. **DOI:**10.1016/j.molstruc.2018.02.081
31. A. Teimouri, A. N. Chermahini, M. D. Emami, *Arkivoc* **2008**, *8*, 172–187.
32. H. Dammak, A. Yangui, S. Triki, Y. A. H. Feki, *J. Lumin.* **2015**, *161*, 214–220. **DOI:**10.1016/j.jlumin.2015.01.010
33. M. Silverstein, G. C. Basseleer, C. Moril, Spectrometric Identification of Organic Compounds, Wiley, New York, **1981**.
34. S. Muthu, J. U. Maheswari, T. Sundius, *Spectrochim. Acta A Mol. Biomol. Spectrosc*. **2013**, *108*, 307–318. **DOI:**10.1016/j.saa.2013.02.022
35. G. Socrates, Infrared Characteristic Group Frequencies, Wiley Inter Science Publication, 1980.
36. G. Varsanyi, Vibrational Spectra of Benzene Derivates, Academic Press, New York, 1969.
37. K. Toubal, N. Boukabcha, Ö. Tamer, N. Benhalima, S. Altürk, D. Avcı, A. Chouaih, Y. Atalay, A. Djafri, F. Hamzaoui, *J. Mol. Struct*. **2017**, *1147*, 569–581. **DOI:**10.1016/j.molstruc.2017.06.102
38. R. Rahmani, N. Boukabcha, A. Chouaih, F. Hamzaoui, S. Goumri, *J. Mol. Struct*. **2018**,*1155*, 484–495. **DOI:**10.1016/j.molstruc.2017.11.033
39. H. Benaissi, M. Drissi, S. Yahiaoui, Y. Megrouss, A. Chouaih, F. Hamzaoui, *J. Optoelectron. Biomed. M*. **2018**, *10*, 73–82
40. N. Boukabcha, A. Feddag, R. Rahmani, A. Chouaih, F. Hamzaoui, *J. Optoelectron. Adv. M.* **2018**, *20*, 140–148
41. N. Boubegra, Y. Megrouss, N. Boukabcha, A. Chouaih, F. Hamzaoui, *Rasayan. J. Chem*. **2016**, *9*, 751–761.
42. M. Drissi, N. Benhalima, Y. Megrouss, R. Rahmani, A. Chouaih, F. Hamzaoui, *Molecules* **2015**, *20*, 4042–4045. **DOI:**10.3390/molecules
43. J. S. Murray, K. Sen, Molecular Electrostatic Potentials, Concepts and 399 Applications, Elsevier, Amsterdam, 1996.
44. E. Scrocco, J. Tomasi, in: P. Lowdin (Ed) Advances in Quantum Chemistry, Academic Press, New York. 1978. 402.
45. F. J. Luque, M. Orozco, P. K. Bhadane, S. R. Gadre, *J. Phys.*

Chem. **1993**, *97*, 9380–9384. **DOI:**10.1021/j100139a021
46. J. Sponer, P. Hobza, *Int. J. Quant. Chem*. **1996**, *57*, 959–970. **DOI:**10.1002/(SICI)1097-461X(1996)57:5<959::AID-QUA16>3.0.CO;2-S
47. M. Govindarajan, M. Karabacak, *Spectrochim. Acta A Mol. Biomol. Spectrosc*. **2012**, *96*, 421–435. **DOI:**10.1016/j.saa.2012.05.067

Povzetek

V prispevku poročamo o sintezi in karakterizaciji (*Z*)-3-*N*-(etil)-2-*N*'-((3-metoksifenil)imino)tiazolidin-4-ona z FT-IR, ^{1}H in ^{13}C NMR ter z rentgensko difrakcijo monokristala. Eksperimentalna potrditev kristalne strukture temelji na pridobljenih rentgenskih difrakcijskih podatkih. Pomembna značilnost strukture je obstoj dihedralnega kota, ki ga tvorita ravnini benzenskega in tiazolidinonskega obroča, v vrednosti 86.0°, kar kaže na odsotnost π–π interakcij, hkrati pa nakazuje na neplanarno strukturo. V kristalu so molekule povezane s C–H···O in C–H···N vodikovimi vezmi, ki so odgovorne za trodimenzionalno molekulsko pakiranje v strukturi. Da bi lahko eksperimentalne rezultate primerjali s teoretično izračunanimi, smo izvedli kvantno kemijske DFT izračune s pomočjo B3LYP/6-311G(d,p) baznega seta. Ob tem smo izračunali še elektrostatski potencial okoli molekule ter HOMO in LUMO energijske nivoje. Ugotovili smo orientacije dipolnih momentov in s tem razkrili naravno inter- in intramolekularnih prenosov naboja. Nazadnje smo s pomočjo izračuna deskriptorjev kemijske reaktivnosti potrdili še stabilnost opisane spojine.

Scientific paper

Feedback Regulation of Cathepsin C by the Propeptide Dipeptides of Granzymes A and B

Janja Božič[1] and Iztok Dolenc[1,*]

[1] *Department of Biochemistry and Molecular and Structural Biology, Jozef Stefan Institute, Jamova 39, SI-1000 Ljubljana, Slovenia*

** Corresponding author: E-mail: iztok.dolenc@ijs.si*
Tel.: +386 1 477 3776 Fax: +386 1 477 3984

Received: 04-11-2019

Abstract

Granzymes A and B are activated by proteolytic removal of their N-terminal dipeptides by cathepsin C (dipeptidyl-peptidase I). However, the possible physiological role of the cleaved dipeptides Glu-Lys and Gly-Glu is not yet understood. In this study, adding either of the two dipeptides to NK-92 cells, resulted in enhanced cytotoxicity toward the targeted K562 cells and increased death rate of the target cells. Cathepsin C is known to generate cytotoxic polymers from various dipeptides, however, in the case of the dipeptides Glu-Lys and Gly-Glu, cathepsin C was unable to polymerize them. Unexpectedly the dipeptides were found to be inhibitors of the transferase activity of cathepsin C (IC50 < 20 mM), and weak competitive inhibitors of the peptidase activity with K_i values in the millimolar range. This suggests that the dipeptides can play role in a feedback loop that controls transferase and proteolytic activities of cathepsin C in various biological processes.

Keywords: Cathepsin C; granzyme; HPLC; dipeptides; transferase activity; product inhibition

1. Introduction

Natural killer cells (NK cells) are a subpopulation of lymphocytes, and as a part of the innate immune response mediate cytotoxic activity against cancer cells and virally infected cells.[1] A finely controlled mechanism is necessary to eliminate harmful cells from spreading in the body. Recognition of the infected and MHC class I-deficient cells triggers different cascades of the cytotoxic process.[2] One of the most important processes is the granzyme's route, including the movement of granules toward the immunological synapse.[2] Granzymes A and B are the most abundant granzymes and thought to play a leading role in granzyme-mediated cytotoxicity.[3] They are synthesized in the form of inactive zymogens, and during the activation of NK cells, cysteine cathepsin C (dipeptidyl-peptidase I) activates granzymes by removing the N-terminal dipeptide.[4] Following the removal of dipeptide, conformational rearrangements of the newly formed N-terminal occur.[5] The conserved N-terminal tail of the mature enzyme is further inserted in the interior of the protein, forming an active granzyme.[6] Afterward, these granzymes are vectorially released into the submicroscopic intercellular cleft between the NK cell and the target cell.[2] From this immunological synapse, granzymes, with the support of perforin, translocate into the cytoplasm of the target cells, where they cleave and activate multiple critical protein substrates, resulting in the death of the target cell.[7]

The activating protease, cathepsin C,[4] is a cysteine protease and member of the papain family,[8] inhibited by cystatins.[9] The enzyme is ubiquitously expressed in various tissues,[10,11] having several important functions.[12–14] The inherited mutation in the cathepsin C gene, generating an inactive enzyme, causes autosomal-recessive disease Papillon-Lefévre syndrome.[15] Opposite, deficiency of cathepsin C lighten severity of acute pancreatitis by reduction of neutrophil elastase activation and cleavage of E-cadherin.[16] Cathepsin C is synthesized as a single chain preproenzyme.[17] During activation, the tetrameric form of the mature enzyme is assembled.[18] From the crystal structure of the mature enzyme it is evident that the monomer consists of N-terminal fragment of 119 residues from Asp1 to Gly119, termed "exclusion domain", and 233 residues of the papain-like structure.[18] However, the enzyme is functionally active only as tetramer composed of four identical subunits,[19,20] with four active site clefts positioned at the tetrahedral corners of the molecule.[18] At the end of each active site cleft is positioned the N-terminus of the exclusi-

on domain, which determines dipeptidyl peptidase activity.[18] The carboxylic group of Asp1 side chain controls the entry into the S2 binding pocket by recognizing the N-terminal amino group of the substrate.[18] At the bottom of the pocket are chloride ions which provide additional negative charges and are required for cathepsin C activity.[18] The enzyme is optimally proteolytically active at slightly acidic pH[17] and is relatively unspecific. It cleaves dipeptides from proteins and peptidyl substrates until the N-terminus is no more available or a stop sequence of proline is reached.[21] Relatively unspecific cleavage patterns exclude cleavages of substrates with positively charged amino acids (Arg and Lys) on the N-terminal part of proteins (P2 position).[22] At neutral pH and above, the enzyme exhibits dipeptidyl transferase activity.[23] Its perhaps the best known example is the lysosomotropic detergent LeuLeuOMe, which accumulates in the lysosomes.[24] Once polymerized, it triggers the lysosomal pathway of cell death.[25,26]

In this study, we found that the dipeptides Glu-Lys and Gly-Glu, released during activation of granzymes A and B, promote cell death of target cells when incubated together with NK cells, but cannot be polymerized by cathepsin C. Instead, they act as weak competitive inhibitors of the enzyme, blocking both the proteolytic and transferase activities of the enzyme.

2. Experimental

2. 1. Materials

Acetonitrile (ACN) and pentafluoropropionic acid (PFPA) were supplied by Sigma (Germany). Ultrapure water was obtained from a Milli-Q system (Millipore, Bedford, MA, USA). Dipeptides Glu-Lys and Gly-Glu, their amides, and the fluorogenic substrate Gly-Phe-AMC were obtained from Bachem (Switzerland). The human NK cell line was derived from blood, mononuclear cells, NK-92, and human hematopoietic malignant cell line K562, were kindly provided by E. Vivier (Marseille, France). The growth medium was RPMI-1640 (Sigma-Aldrich).

2. 2. Cytotoxicity Assay

A fluorescence-activated cell sorter (FACS) was used to perform the NK cell cytotoxicity assay, as described previously.[27] The following day, the target K562 cell (10^5 cells) were added at the desired ratio, 10:1, and the mixture was incubated for 4 h at 37 °C and 5% CO_2 . 0.5 μM propidium iodide (Sigma-Aldrich) was used to evaluate cell viability. The analysis was performed using a FACSCalibur flow cytometer (Becton-Dickinson, USA), and the data acquisition was performed using Cellquest software. The cells were incubated overnight with a supplement of 1 mM dipeptides Glu-Lys or Gly-Glu. The obtained results are presented as mean values with standard deviations of at least three replicates.

2. 3. Cathepsin C expression, Activation, and Purification

Human recombinant procathepsin C was expressed, activated and purified, essentially as described earlier with some minor modifications.[28] Briefly, activation by cathepsin L was performed overnight at 4 °C in an activating buffer (250 mM sodium acetate pH 5.5, 150 mM NaCl, 10 mM DTT). Afterward, the protein mixture was loaded into a Sepharose 12 size-exclusion column, using fast protein liquid chromatography (AKTA system, GE Healthcare, Sweden), equilibrated with 50 mM of sodium acetate, 1mM EDTA, and 300 mM of NaCl, at a pH level of 5.5, and a flow rate of 0.5 ml/min. The protein peak at 200 kDa was collected, concentrated to concentration 1 mg/ml, and analyzed using SDS-PAGE.

2. 4. High-performance Liquid Chromatography (HPLC) Analysis of Dipeptide Polymerization

The dipeptides were dissolved in double distilled water to 1 M concentration and further used in the reaction with a final concentration of 40 mM. The final concentration of cathepsin C was 75 nM (an active concentration, determined as earlier described[18]) and the buffer in the reaction was PBS (10 mM NaH_2PO_4, 1.8 mM KH_2PO_4, 137 mM NaCl, 2.7 mM KCl, pH 7.4), with 5 mM DTT. Next, polymerization reaction was performed in 100 μl volume for four hours at 37 °C, and then an aliquot of 20 μl was applied on an Ascentis Express Peptide ES-C18 reversed phase column (150 mm × 2.1 mm, 2.7 μm) (Sigma, Germany). The analysis was completed on an HPLC system (Waters, Milford, MA, USA) using the Waters M600 solvent delivery module and the Waters M2489 detector system. The analysis of the reaction mixture was optimized for the separation of dipeptides, using 0.1% PFPA as anionic ion-pairing reagents for reversed-phase high-performance liquid chromatography (RP-HPLC).[29] A gradient elution from water/0.1% PFPA (phase A) to acetonitrile/water 60%/ 40% (v/v) with 0.1% PFPA (phase B) was used to separate the products.

2. 5. Determination of Inhibition Constants for Glu-Lys and Gly-Glu

The active site titration of cathepsin C, the determination of the inhibition type, and the inhibition constant (K_i) for the interaction of dipeptides with cathepsin C were carried out as described earlier.[18] Briefly, measurements were performed in 50 mM sodium acetate, 1 mM EDTA, and 300 mM NaCl, pH 5.5. Five hundred μl of the reaction mixture contained 0.02 nM cathepsin C and increased concentration of the dipeptides Glu-Lys or Gly-Glu. In addition, these experiments were performed at different concentrations of the substrate Gly-Phe-AMC to

identify the inhibition type. The release of the product at 25 °C was monitored with a Perkin-Elmer spectrofluorimeter.

2. 6. Molecular Docking

UCSF Chimera 1.13rc[30] has been used to prepare the structure of cathepsin C (PDB: 1K3B) for docking. Docking simulations of ligands were performed using the Autodock Vina Plugin[31] and the results were examined with UCSF Chimera. Dipeptides were docked with the enzyme's structure giving a Vina score, which is the predicted affinity of the molecule to bind to the PDB structure, calculated in kcal mol^{-1}.

2. 7. Molecular Modeling of Progranzyme B

The three-dimensional model of human granzyme B was generated with the online server program I-TASSER,[32] using the progranzyme K crystal structure (PDB entry 1MZA)[5] as the primary template. Structures were visualized with UCSF Chimera 1.13rc.[30]

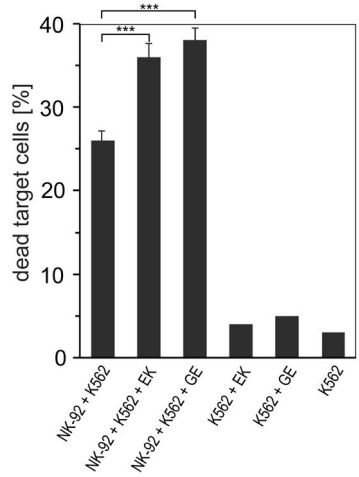

Figure 1. Dipeptides Glu-Lys (EK) or Gly-Glu (GE) enhanced the cytotoxic effect of NK-92 cells toward K562 target cells. NK-92 cells were incubated overnight with 1 mM dipeptide supplement, and a number of dead target cells was compared to the control samples. The impact of the dipeptides on the target cells is seen as their enhanced death. The data are expressed as mean ± standard deviations (SD) of at least three independent experiments performed in duplicate. A t-test is used to compare the mean of two given samples. P value (***) is below 0.001.

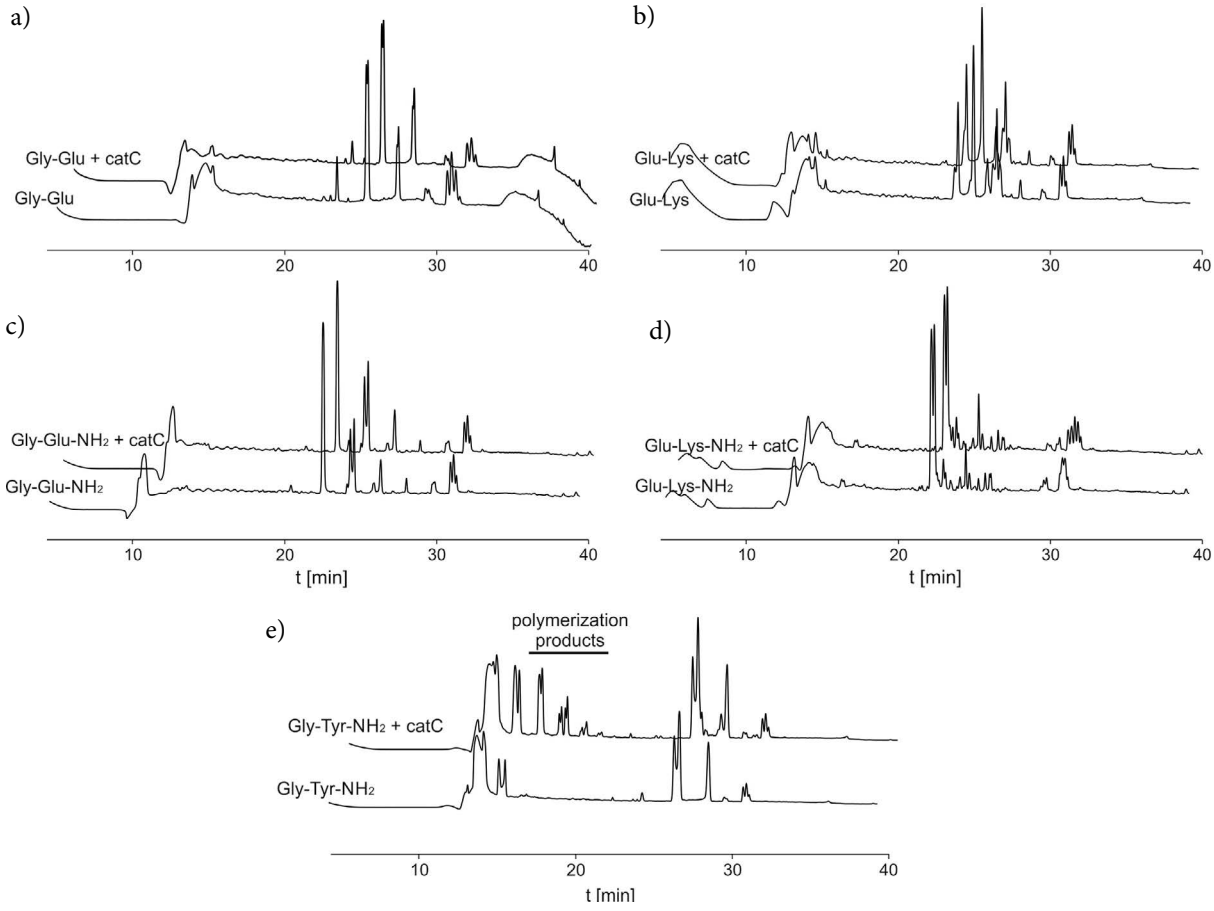

Figure 2. Dipeptides Gly-Glu, Glu-Lys or their amide forms are not polymerized by cathepsin C. Reverse phase HPLC using 0.1% pentafluoropropionic acid (PFPA) as anionic ion-pairing reagents for separation, following a four-hour reaction with cathepsin C, in comparison to the control samples (a) Gly-Glu, (b) Glu-Lys, (c) Gly-Glu-NH_2, (d) Glu-Lys-NH_2. (e) Polymerization of Gly-Tyr-NH_2 by cathepsin C as a control. For clarity purposes, the upper chromatograms are slightly shifted.

3. Results

3. 1. Dipeptides Glu-Lys and Gly-Glu Enhance the Cytotoxicity of NK-92 Cells

In order to test, whether the released granzyme propeptides Glu-Lys and Gly-Glu, have an additional role in NK cell-mediated cytotoxicity, we incubated the dipeptides overnight with the target K562 cells, prior to addition of NK-92 cells. The reaction resulted in a substantially enhanced cytotoxicity, which was almost 1.5-fold in case of Gly-Glu dipeptide (Figure 1).

3. 2. Cathepsin C is unable to Polymerize Dipeptides Gly-Glu and Glu-Lys, Nor their Amide Forms

As the increased cytotoxicity could have resulted from cathepsin C-mediated polymerization of the dipeptides, we next tested whether the enzyme was able to polymerize both dipeptides. Therefore, we incubated the reaction mixture containing the dipeptides Gly-Glu or Glu--Lys, for four hours with cathepsin C. However, no larger peptides were found after separation of the mixture on a reverse phase C18 column of the HPLC system (Figure 2A and Figure 2B). As cathepsin C is known to prefer dipeptide-amides, we next used the amide forms of the two dipeptides, Gly-Glu-NH_2 and Glu-Lys-NH_2. To our surprise, the amide dipeptides were not polymerized, similar to the free dipeptides (Figure 2C and Figure 2D). In contrast, cathepsin C polymerized the dipeptide-amide Gly-Tyr--NH_2, which was already reported to be a transferase substrate of cathepsin C[33] (Figure 3).

3. 3. Dipeptides Glu-Lys and Gly-Glu are Inhibitors of Cathepsin C

Finally, we investigated, whether the two dipeptides, Glu-Lys and Gly-Glu, have any effect on cathepsin C activities. Both dipeptides were found to inhibit the transferase activity of cathepsin C, monitored by the polymerization of the Gly-Tyr-NH_2 substrate. The separation of products on a reverse phase C18 column of HPLC system, obtained from the polymerization reaction of Gly-Tyr-NH_2 with cathepsin C is illustrated (Figure 3). The formation of the polymerization product was completely inhibited by both dipeptides at 40 mM concentration, indicating an inhibition of the cathepsin C transferase activity at neutral pH (pH 7.4; Fi-

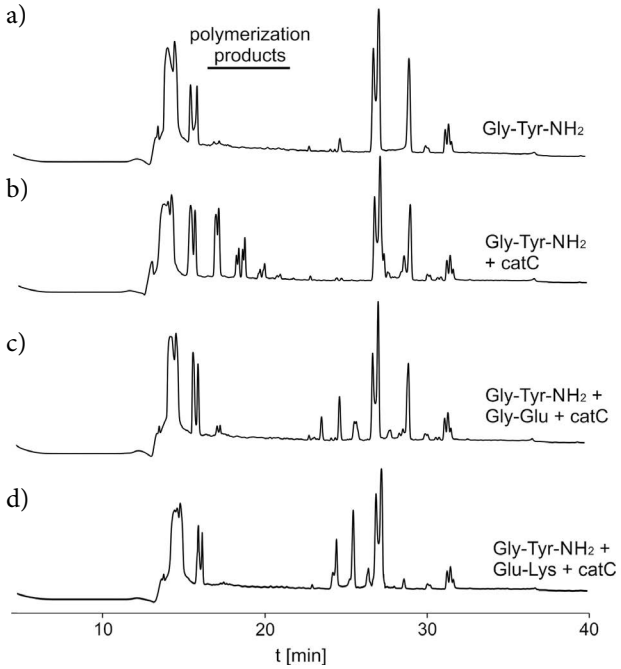

Figure 3. Gly-Glu, the prodipeptide from granzyme B, inhibits the transferase and the peptidase activity of cathepsin C. (a) The dipeptide Gly-Tyr-NH_2 as a control sample. (b) Polymerization of Gly-Tyr-NH_2 by cathepsin C (catC) using a reverse phase HPLC. The products of polymerization are eluted with a retention time 15–20 minutes. Dipeptides Gly-Glu (b) and Glu-Lys (c) inhibit polymerization reaction of Gly-Tyr-NH_2 by catC.

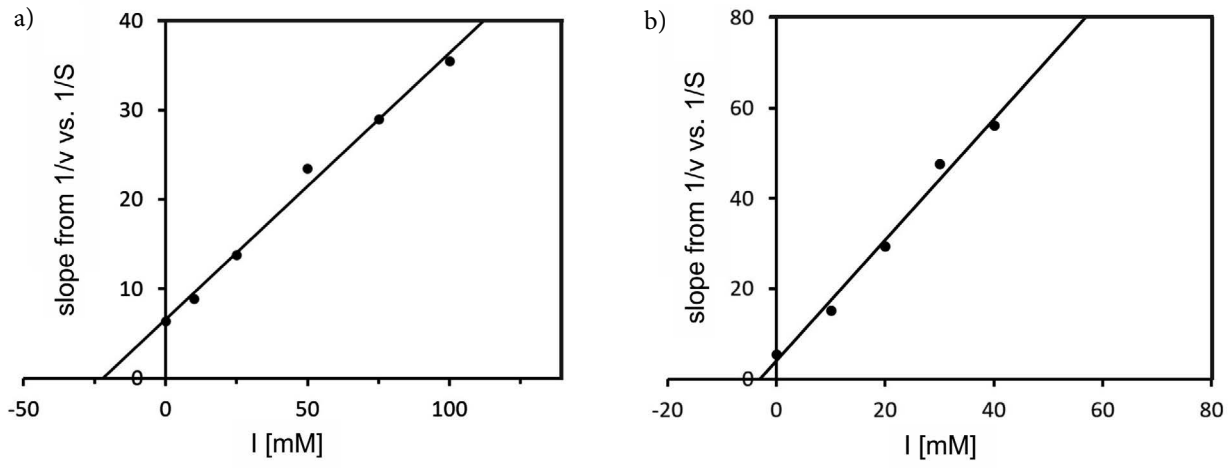

Figure 4. Proteolytic inhibition of cathepsin C by dipeptides Glu-Lys and Gly-Glu. K_i values for inhibition of cathepsin C by dipeptides (a) Glu-Lys (20 mM) and (b) Gly-Glu (2.5 mM) were determined by secondary plots.

gure 3). Moreover, both dipeptides inhibited also the peptidase activity of cathepsin C as monitored by the hydrolysis of fluorogenic substrate Gly-Phe-AMC at the more acidic pH 5.5 (Figure 4). The dipeptides Glu-Lys and Gly-Glu inhibited cathepsin C with K_i values of 20 mM and 2.5 mM, respectively. The results revealed that both dipeptides are weak competitive inhibitors of cathepsin C.

3. 4. Molecular Docking of Dipeptides

In order to understand the potential mechanism of dipeptide binding at the structural level, we modelled the dipeptides into the active site of human cathepsin C. The crystal structure of human cathepsin C (PDB: 1K3B)[18] was used to assess the fitness and orientation of the docked dipeptides. As Glu-Lys and Gly-Glu shown to be competitive inhibitors of cathepsin C, suggesting a binding into the active site of the enzyme, we limited our docking in the area of a substrate binding. Despite the similarities in docking sites, some differences were apparent (Figure 5). All representative docking predictions with a high score of probability fitted into the S1 position of the active cleft. The best fit was calculated for the Gly-Tyr-NH_2 dipeptide, the substrate which was successfully polymerized (Figure 5A), and can be compared with the position of the inhibitor Ser-Tyr-CN (Figure 5B). Docking of Gly-Tyr-NH_2 into the 3D structure of cathepsin C placed the dipeptide in the position stabilized by the amino acid residues Gly232 and Glu275 of the S1 binding site, and Asp1 at the entrance of the S2 pocket. The amide group was facing towards the S1' site, interacting with Asn380.

Docking studies for dipeptides Glu-Lys and Gly-Glu suggested representative positions with similar scores. Their top-ranked positions were placed in the active site cleft of cathepsin C, where both dipeptides were well stabilized. The dipeptide Glu-Lys interacts with Trp405, Asn380, Thr379, and Asp1, expanding the side chain towards S2 (Figure 5C). Opposite, Gly-Glu stretches between S1 and S1', and is stabilized with Val352, Asn380, Trp405, Gln228, Gly232, and Cys234 (Figure 5D). However, the predicted positions do not favor catalysis by the enzyme. Namely, the docking studies predicted their binding to the S1 and S1' positions, with peptide bond in a position that cannot be cleaved.

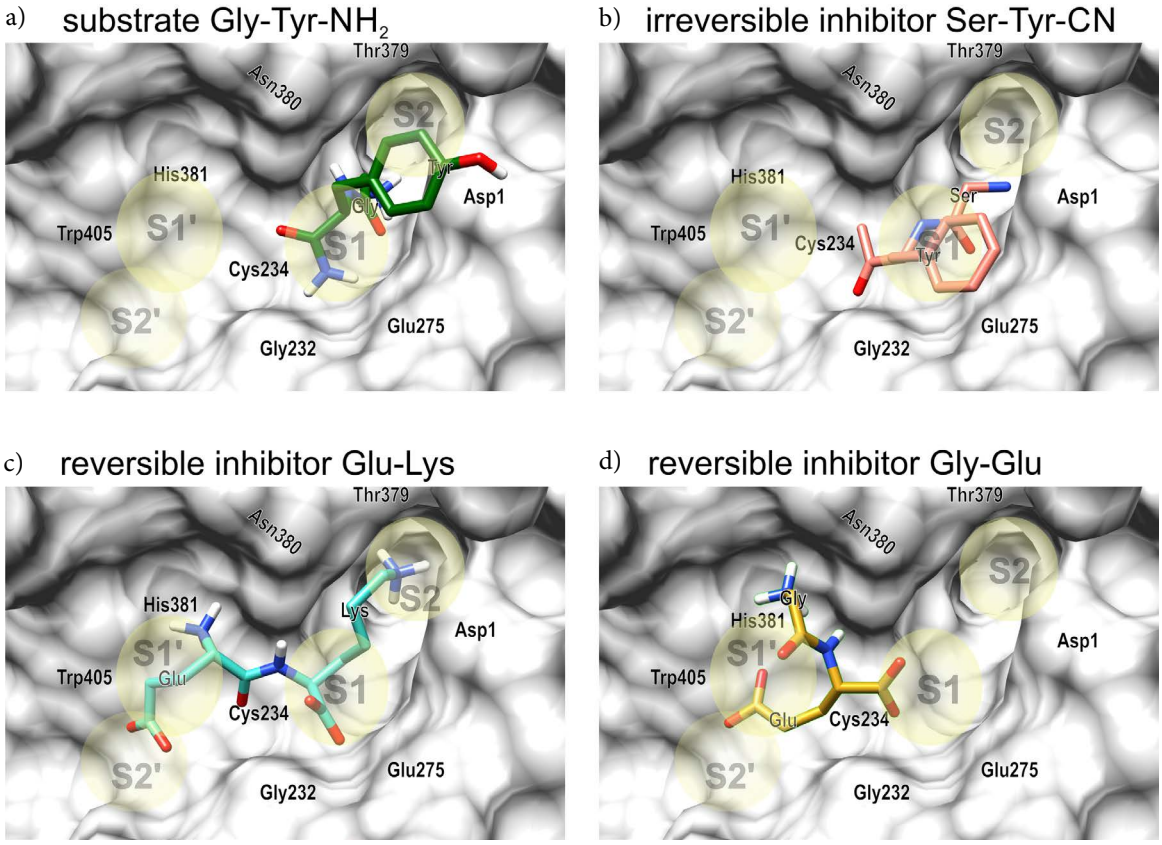

Figure 5. The active site of cathepsin C with selected predicted positions of dipeptides using docking predictions in comparison to the experimentally determined position of the inhibitor Ser-Tyr-CN in the crystal structure of cathepsin C.[22] Docking simulations of ligands were performed using the Autodock Vina Plugin[31] and the results were visualized with UCSF Chimera 1.13rc.[30] (a) The predicted accommodation of dipeptide-amide Gly-Tyr-NH_2, a substrate for polymerization by cathepsin C; (b) the covalently bound irreversible inhibitor Ser-Tyr-CN in the crystal structure of cathepsin C. (c) The best predicted binding of the inhibitory dipeptide Glu-Lys, the prodipeptide of granzyme A. (d) The best predicted position of the inhibitory dipeptide Gly-Glu, the prodipeptide of granzyme B.

3. 5. Comparison of the Putative Structure of Progranzyme B with Granzyme B

To further investigate the inhibitory role of N-terminal dipeptides from granzymes, we performed sequence alignment of the N-terminal parts of granzymes A and B in comparison to selected serine proteases with dipeptide proregions (Figure 6A). This similarity enabled the modeling of the structure of progranzyme B, using the crystal structure of progranzyme K as a template. The obtained result, with the C-score value of 1.52, signifies an accurate model with high confidence. Comparing both 3D structures, the model structure of progranzyme B, and the crystal structure of granzyme B, revealed exposure of the N-terminal prodipeptide (Figure 6B), which is removed by cathepsin C. The N-terminus of the mature granzyme B is buried inside the protein (Figure 6C).

4. Discussion

Activation of neutrophil serine proteases, granzymes, and cathepsin G is achieved by a rapid truncation of the N-terminal dipeptide by cathepsin C.[4] Possible involvement of these dipeptides in the cellular protection system is supported by the immunomodulatory effect of dipeptidyl derivatives, described earlier.[34] Therefore, the cytotoxic activity of the NK-92 cells towards the target K562 cells was evaluated in the presence of prodipeptides from granzyme A (Glu-Lys) or granzyme B (Gly-Glu). The presence of either dipeptide enhanced the cytotoxic response and cell death of the target cells (Figure 1). One possible explanation for this increased cytotoxicity would be polymerization of the released dipeptides by cathepsin C into membranolytic forms, as seen for Leu-Leu-OMe,[24] acting as substance with cytotoxic activity.[35] However, cathepsin C failed to polymerize any of the two N-terminal dipeptides of granzymes A and B (Figure 2).

Moreover, cathepsin C even failed to polymerize the amide forms of the two dipeptides, i.e. Glu-Lys-NH_2 and Gly-Glu-NH_2, although the enzyme preferentially polymerizes dipeptidyl esters or amides,[21,33] such as also seen for Gly-Tyr-NH_2 we used for the positive control.[33] Furthermore, the two granzymes-originating dipeptides Glu-Lys and Gly-Glu inhibited transferase and peptidase activities of cathepsin C in the millimolar range. Similarly, it has been shown that some dipeptides inhibit dipeptidyl peptidase IV in mM range and have potential influence on of the enzyme's function in diabetes.[36,37] Our observation is in agreement with previous findings, where some dipepti-

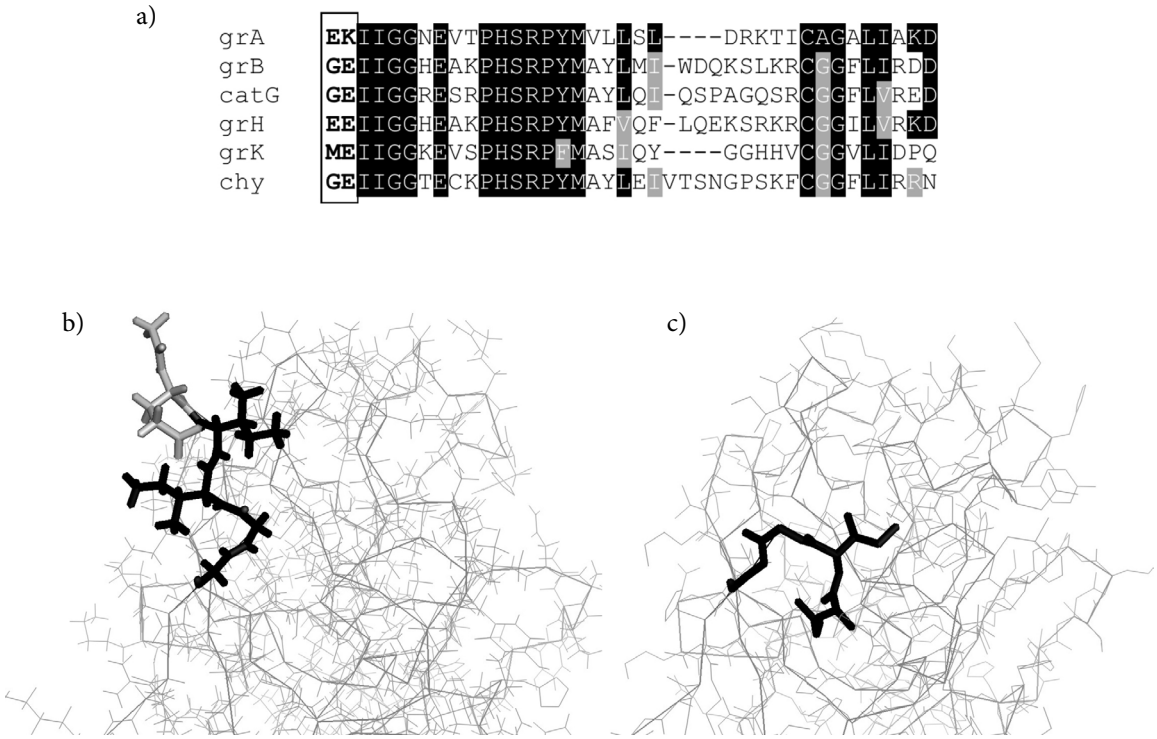

Figure 6. Prodipeptides of granzymes A and B, together with highly similar N-terminal parts are preventing the activity of the granzymes. Following the removal of prodipeptide, the truncated enzyme undergoes structural rearrangement yielding an active enzyme. (a) Sequence alignment of N-terminal of human granzymes A, B, H, and K (grA, grB, grH, grK, respectively), cathepsin G (catG), and chymase (chy). Prodipeptides are marked by the box. Identical amino acids have a black background, and similar amino acids have a grey background. The alignment was performed using Clustal Omega, and shading was done using the BoxShade online service. (b, c) A comparison of modeled progranzyme B (b) with the structure of mature granzyme B (c) (PDB entry 1IAU). N-terminal residues of both molecules are marked with thicker lines. The prodipeptide of granzyme B, pointed out and accessible to cathepsin C, is marked by light gray. The N-terminal part of the reposition of the mature granzyme is perceived.

des competitively inhibited cathepsin C with the K_i values in the same range.[21] However, it seems that the P1' position of the substrate is also important for hydrolysis by cathepsin C. Comparing the interaction of several dipeptide-amides[21] and dipeptidyl-fluorogenic or protein substrates[21] with cathepsin C, seems that a bulky group like β-naphthylamide in Gly-Phe-β-naphthylamide or AMC in Gly-Glu-AMC facilitate hydrolysis,[21,22] whereas an amide group or a free N-terminus such as in Gly-Phe-NH_2,[21] Gly--Glu and Gly-Glu-NH_2 in some cases facilitate inhibition of the enzyme.

To gain insight in the inhibitory nature of prodipeptides we performed molecular docking predictions. The calculated prediction for the dipeptide amide Gly-Tyr--NH_2, a substrate which is polymerized by cathepsin C, on S2 and S1 positions corresponds to the experimentally positioned inhibitor Ser-Tyr-CN, bound into cathepsin C cleft,[22] as well to the predicted position of the tetrapeptide Glu-Arg-Ile-Ile.[18] However, the inhibitory dipeptides bind differently. In contrast to Gly-Tyr-NH_2, docking predictions for dipeptides Glu-Lys and Gly-Glu show non-productive binding to the active site of cathepsin C. The inhibitory dipeptides bind to the enzyme on positions in the area of S1 and S1', and are stabilized by surrounding amino acids of cathepsin C. Thus, by binding to the active site of the enzyme, dipeptides interfere the interaction of cathepsin C with substrates. Knowing that the proregion dipeptides of granzyme A and B can not polymerize, but are weak inhibitors of cathepsin C, raises the question regarding the physiological importance of the prodipeptides. The model of progranzyme B structure revealed very different N-termini positions of progranzyme B and granzyme B.[38] Only the exposed N-terminus of progranzyme B is accessible to cathepsin C. As observed in granzyme C[39] and K,[5] the truncation of the polypeptide chain for two amino acids with cathepsin C results in a rapid allosteric reorientation, remodeling of the activation domains, and activation. We suggest that the released propeptide, together with the newly formed N-terminus Ile-Ile,[40] may at least partially block the activities of cathepsin C within the granules, especially at high local concentrations. The importance of native sequence of granzymes was revealed by mutation studies. Namely, introduction of any mutation in the region of the six N-terminal amino acid residues resulted in lower stability or in an incorrect activation process.[41,42] Expressing granzyme B without the N-terminal dipeptide yielded a low level of active enzyme which was unstable.[41] Moreover, a Glu residue at the P1 position of granzyme K was shown to be critical, as any mutations resulted in expression of inactive enzyme.[42]

Little is known about the regulation of cathepsin C activity. Basically, the enzyme activity is regulated by the endogenous protein inhibitors to prevent a granzyme maturation to the active form. Based on the size of granules,[43] we can estimate that mM concentration is reached by 2000 dipeptide molecules, when granules have diameter of 200 nm. The concentration of the released propeptide dipeptides may be too low to inhibit cathepsin C. However, granzymes and other serine proteases listed in the Figure 6A have similar structure of propeptides. Therefore, we suggest that all the released dipeptides from granule serine proteases may have effect on cathepsin C.

The development of cathepsin C inhibitors might serve as effective therapeutics for the treatment of diseases, such as inflammatory diseases including rheumatoid arthritis, cystic fibrosis and pulmonary disease. The current therapeutic strategy is based on inhibitors derived from the dipeptidyl substrates, which contain an electrophilic "warhead", such as diazoketones, vinyl sulfones, nitriles, and cyanamides, forming reversible or irreversible covalent bonds with the enzyme active site Cys234.[44] Their effective inhibition is at concentration of μM range. However, only few data show biological effects *in vivo*. Currently, a variety of cathepsin C inhibitors are used in preclinical and clinical studies.[12]

5. Conclusion

In the present study we suggest that the proregion dipeptides of granzymes A and B represent a feedback loop to control the transferase and peptidase activities of cathepsin C. This insight sheds light on the regulation of cathepsin C activity in biological processes and broadens the knowledge about the role of dipeptides in the mechanisms of cytotoxicity of NK cells. Moreover, the studied dipeptides show immunomodulatory effect. In conclusion, an increase in cytotoxicity is not the result of potentially toxic polymers produced by cathepsin C, but is rather due to modulation of NK cell activity as shown for Glu--Tyr.[45] This study might be important for possible design of immunosuppressive dipeptide-like drugs.

6. Acknowledgments

The authors wish to thank Dr. Vito Turk for critical comments on the manuscript, Dr. Boris Turk for discussion, advice and continuous support. I am grateful to Dr. Dušan Turk for his critical discussion about structural aspects, and to Andreja Sekirnik for expression of recombinant cathepsin C. This study was supported by grants from the Slovenian Research Agency research program P1-0140 lead by Dr. Boris Turk.

7. References

1. E. Vivier, E. Tomasello, M. Baratin, T. Walzer and S. Ugolini, *Nat. Immunol.* **2008**, *9*, 503–10. **DOI**:10.1038/ni1582
2. L. Martinet and M. J. Smyth, *Nat. Rev. Immunol.* **2015**, *15*, 243–54. **DOI**:10.1038/ni1582

3. I. Voskoboinik, J. C. Whisstock and J. A. Trapani, *Nat. Rev. Immunol.* **2015**, *15*, 388–400. **DOI**:10.1038/nri3839
4. C. T. Pham and T. J. Ley, *Proc. Natl. Acad. Sci. U. S. A.* **1999**, *96*, 8627–32.
5. C. Hink-Schauer, E. Estebanez-Perpina, E. Wilharm, P. Fuentes-Prior, W. Klinkert, W. Bode and D. E. Jenne, *J. Biol. Chem.* **2002**, *277*, 50923–33. **DOI**:10.1074/jbc.M207962200
6. J. Rotonda, M. Garcia-Calvo, H. G. Bull, W. M. Geissler, B. M. McKeever, C. A. Willoughby, N. A. Thornberry and J. W. Becker, *Chem. Biol.* **2001**, *8*, 357–68. **DOI**:10.1016/S1074-5521(01)00018-7
7. J. W. Heusel, R. L. Wesselschmidt, S. Shresta, J. H. Russell and T. J. Ley, *Cell.* **1994**, *76*, 977–87. **DOI**:10.1016/0092-8674(94)90376-X
8. V. Turk, V. Stoka, O. Vasiljeva, M. Renko, T. Sun, B. Turk and D. Turk, *Biochim. Biophys. Acta.* **2012**, *1824*, 68–88. **DOI**:10.1016/j.bbapap.2011.10.002
9. V. Turk, D. Turk, I. Dolenc and V. Stoka, *Acta Chim. Slov.* **2019**, *66*, 5–17. **DOI**:10.17344/acsi.2018.4639
10. N. V. Rao, G. V. Rao and J. R. Hoidal, *J. Biol. Chem.* **1997**, *272*, 10260–5. **DOI**:10.1074/jbc.272.15.10260
11. E. R. Unanue, V. Turk and J. Neefjes, *Annu. Rev. Immunol.* **2016**, *34*, 265–97. **DOI**:10.1146/annurev-immunol-041015-055420
12. B. Korkmaz, G. H. Caughey, I. Chapple, F. Gauthier, J. Hirschfeld, D. E. Jenne, R. Kettritz, G. Lalmanach, A. S. Lamort, C. Lauritzen, M. Legowska, A. Lesner, S. Marchand-Adam, S. J. McKaig, C. Moss, J. Pedersen, H. Roberts, A. Schreiber, S. Seren and N. S. Thakker, *Pharmacol. Ther.* **2018**, *190*, 202–236. **DOI**:10.1016/j.pharmthera.2018.05.011
13. B. Turk, D. Turk, I. Dolenc and V. Turk, in: G. Salvesen and N. D. Rawlings (Eds.): Handbook of Proteolytic Enzymes, Academic Press, Amsterdam, Netherlands, **2013**, pp. 1968–1974. **DOI**:10.1016/B978-0-12-382219-2.00447-6
14. V. Stoka, V. Turk and B. Turk, *Ageing Res Rev.* **2016**, *32*, 22-37. **DOI**:10.1016/j.arr.2016.04.010
15. C. Hewitt, D. McCormick, G. Linden, D. Turk, I. Stern, I. Wallace, L. Southern, L. Zhang, R. Howard, P. Bullon, M. Wong, R. Widmer, K. A. Gaffar, L. Awawdeh, J. Briggs, R. Yaghmai, E. W. Jabs, P. Hoeger, O. Bleck, S. G. Rudiger, G. Petersilka, M. Battino, P. Brett, F. Hattab, M. Al-Hamed, P. Sloan, C. Toomes, M. Dixon, J. James, A. P. Read and N. Thakker, *Hum. Mutat.* **2004**, *23*, 222–8. **DOI**:10.1002/humu.10314
16. D. S. John, J. Aschenbach, B. Kruger, M. Sendler, F. U. Weiss, J. Mayerle, M. M. Lerch and A. A. Aghdassi, *J. Biol. Chem.* **2019**, *294*, 697–707. **DOI**:10.1074/jbc.RA118.004376
17. A. Paris, B. Strukelj, J. Pungercar, M. Renko, I. Dolenc and V. Turk, *FEBS Lett.* **1995**, *369*, 326–30. **DOI**:10.1016/0014-5793(95)00777-7
18. D. Turk, V. Janjic, I. Stern, M. Podobnik, D. Lamba, S. W. Dahl, C. Lauritzen, J. Pedersen, V. Turk and B. Turk, *EMBO J.* **2001**, *20*, 6570–82. **DOI**:10.1093/emboj/20.23.6570
19. I. Dolenc, B. Turk, G. Pungercic, A. Ritonja and V. Turk, *J. Biol. Chem.* **1995**, *270*, 21626–31. **DOI**:10.1074/jbc.270.37.21626
20. I. Dolenc, B. Turk, J. Kos and V. Turk, *FEBS Lett.* **1996**, *392*, 277–80. **DOI**:10.1016/0014-5793(96)00828-9
21. J. K. McDonald, B. B. Zeitman, T. J. Reilly and S. Ellis, *J. Biol. Chem.* **1969**, *244*, 2693–709.
22. J. K. Rubach, G. Cui, J. L. Schneck, A. N. Taylor, B. Zhao, A. Smallwood, N. Nevins, D. Wisnoski, S. H. Thrall and T. D. Meek, *Biochemistry.* **2012**, *51*, 7551–68. **DOI**:10.1021/bi300719b
23. R. M. Metrione, A. G. Neves and J. S. Fruton, *Biochemistry.* **1966**, *5*, 1597–604. **DOI**:10.1021/bi00869a021
24. D. L. Thiele and P. E. Lipsky, *Proc. Natl. Acad. Sci. U. S. A.* **1990**, *87*, 83–7.
25. G. Droga-Mazovec, L. Bojic, A. Petelin, S. Ivanova, R. Romih, U. Repnik, G. S. Salvesen, V. Stoka, V. Turk and B. Turk, *J. Biol. Chem.* **2008**, *283*, 19140–50. **DOI**:10.1074/jbc.M802513200
26. U. Repnik, M. Hafner Cesen and B. Turk, *Mitochondrion.* **2014**, *19 Pt A*, 49–57. **DOI**:10.1016/j.mito.2014.06.006
27. J. Bozic, V. Stoka and I. Dolenc, *PLoS One.* **2018**, *13*, e0200757. **DOI**:10.1371/journal.pone.0200757
28. S. W. Dahl, T. Halkier, C. Lauritzen, I. Dolenc, J. Pedersen, V. Turk and B. Turk, *Biochemistry.* **2001**, *40*, 1671–1678. **DOI**:10.1021/bi001693z
29. M. Shibue, C. T. Mant and R. S. Hodges, *J. Chromatogr. A.* **2005**, *1080*, 58–67. **DOI**:10.1016/j.chroma.2005.02.047
30. E. F. Pettersen, T. D. Goddard, C. C. Huang, G. S. Couch, D. M. Greenblatt, E. C. Meng and T. E. Ferrin, *J. Comput. Chem.* **2004**, *25*, 1605–12. **DOI**:10.1002/jcc.20084
31. O. Trott and A. J. Olson, *J. Comput. Chem.* **2010**, *31*, 455–61. **DOI**:10.1002/jcc.21334
32. Y. Zhang, *BMC Bioinformatics.* **2008**, *9*, 40. **DOI**:10.1186/1471-2105-9-40
33. K. K. Nilsson and J. S. Fruton, *Biochemistry.* **1964**, *3*, 1220–4. **DOI**:10.1021/bi00897a006
34. S. D. Abbott, L. Gagnon, M. Lagraoui, S. Kadhim, G. Attardo, B. Zacharie and C. L. Penney, *J. Med. Chem.* **1998**, *41*, 1909–1926. **DOI**:10.1021/jm970734v
35. B. K. Tubic, S. S. Vladimirov, B. D. Markovic and T. J. Sabo, *Acta Chim. Slov.* **2018**, *65*, 59–64. **DOI**:10.17344/acsi.2017.3477
36. A. B. Nongonierma and R. J. FitzGerald, *Peptides.* **2013**, *39*, 157–63. **DOI**:10.1016/j.peptides.2012.11.016
37. Y. Zhang, R. Chen, X. Chen, Z. Zeng, H. Ma and S. Chen, *J. Agric. Food Chem.* **2016**, *64*, 831–9. **DOI**:10.1021/acs.jafc.5b05429
38. S. M. Waugh, J. L. Harris, R. Fletterick and C. S. Craik, *Nat. Struct. Biol.* **2000**, *7*, 762–5. **DOI**:10.1038/78992
39. D. Kaiserman, A. M. Buckle, P. Van Damme, J. A. Irving, R. H. Law, A. Y. Matthews, T. Bashtannyk-Puhalovich, C. Langendorf, P. Thompson, J. Vandekerckhove, K. Gevaert, J. C. Whisstock and P. I. Bird, *Proc. Natl. Acad. Sci. U. S. A.* **2009**, *106*, 5587–92. **DOI**:10.1073/pnas.0811968106
40. T. V. Tran, K. A. Ellis, C. M. Kam, D. Hudig and J. C. Powers, *Arch. Biochem. Biophys.* **2002**, *403*, 160–70. **DOI**:10.1016/S0003-9861(02)00217-5
41. M. J. Smyth, M. J. McGuire and K. Y. Thia, *J. Immunol.* **1995**, *154*, 6299–305.
42. E. Wilharm, M. A. Parry, R. Friebel, H. Tschesche, G. Matschiner, C. P. Sommerhoff and D. E. Jenne, *J. Biol. Chem.* **1999**, *274*, 27331–7. **DOI**:10.1074/jbc.274.38.27331

43. J. P. Goodridge, B. Jacobs, M. L. Saetersmoen, D. Clement, Q. Hammer, T. Clancy, E. Skarpen, A. Brech, J. Landskron and C. Grimm, *Nat. commun.* **2019**, 10, 514. **DOI**:10.1038/s41467-019-08384-x
44. D. I. Laine and J. Busch-Petersen, *Expert Opin. Ther. Pat.* **2010**, 20, 497–506. **DOI**:10.1517/13543771003657172
45. D. L. Smith, J. Cai, S. Zhu, W. Wei, J. Fukumoto, S. Sharma, R. Masood and P. S. Gill, *Int. J. Cancer.* **2003**, 106, 528–33. **DOI**:10.1002/ijc.11253

Povzetek

Katepsin C (dipeptidil peptidaza I) aktivira grancima A in B s proteolitično odstranitvijo N-terminalnih dipeptidov. Možna fiziološka vloga odcepljenih dipeptidov Glu-Lys in Gly-Glu ni znana. V naši študiji smo pokazali, da je dodatek omenjenih dipeptidov k celicam NK-92 povzročil njihovo povečano citotoksičnost in s tem hitrejšo smrt tarčnih celic K562. Katepsin C lahko tvori citotoksične polimere iz različnih dipeptidov, vendar dipeptidov Glu-Lys in Gly-Glu encim ni sposoben polimerizirati. Pri tem smo ugotovili, da sta dipeptida šibka inhibitorja transferazne aktivnosti katepsina C (IC50 <20 mM) in kompetitivna inhibitorja njegove proteolitične aktivnosti, z vrednostmi K_i v milimolarnem območju. Rezultati odkrivajo potencialno vlogo teh dveh dipeptidov, ki lahko s povratno regulacijo vplivajo na transferazno in proteolitično aktivnost katepsina C v različnih bioloških procesih.

DRUŠTVENE VESTI IN DRUGE AKTIVNOSTI
SOCIETY NEWS, ANNOUNCEMENTS, ACTIVITIES

Vsebina

Doktorska in magistrska dela, diplome v letu 2018 ..... S3
Koledar važnejših znanstvenih srečanj s področja kemije,
kemijske tehnologije in kemijskega inženirstva S37
Navodila za avtorje S40

Contents

Doctoral theses, master degree theses, and diplomas in 2018 ..... S3
Scientific meetings – chemistry, chemical technology and chemical engineering S37
Instructions for authors S40

UNIVERZA V LJUBLJANI
FAKULTETA ZA KEMIJO IN KEMIJSKO TEHNOLOGIJO
1. januar – 31. december 2018

DOKTORATI

DOKTORSKI ŠTUDIJSKI PROGRAM KEMIJSKE ZNANOSTI

KEMIJA

TANJA ZIDARIČ
RAZVOJ IN ŠTUDIJ UPORABE BIZMUTOVIH IN DRUGIH MODIFICIRANIH ELEKTROD V SODOBNI ELEKTROANALIZI
Mentor: znan. svet. dr. Samo Hočevar
Somentor: prof. dr. Marjan Veber
Datum zagovora: 12. 01. 2018

BARBARA VOLARIČ
KONVERZIJSKE PREVLEKE NA OSNOVI LANTANOIDNIH SOLI ZA ZAŠČITO ALUMINIJEVIH ZLITIN
Mentorica: znan. svet. dr. Ingrid Milošev
Somentor: prof. dr. Miran Gaberšček
Datum zagovora: 2. 02. 2018

EVA KRANJC
DOLOČANJE METABOLITOV NAVADNEGA VOLČJEGA JABOLKA (PHYSALIS ALKEKENGI L.) S KROMATOGRAFSKIMI IN SKLOPLJENIMI TEHNIKAMI
Mentorica: viš. znan. sod. dr. Irena Vovk
Somentorica: prof. dr. Helena Prosen
Datum zagovora: 30. 03. 2018

URŠA TOMAŽIN
PRIPRAVA, KARAKTERIZACIJA IN UPORABA ENAMINONSKIH LIGANDOV
Mentor: prof. dr. Jurij Svete
Datum zagovora: 13. 04. 2018

MATIJA URŠIČ
SINTEZA IN KARAKTERIZACIJA RUTENIJEVIH KOMPLEKSOV S FOSFINSKIMI LIGANDI
Mentor: prof. dr. Anton Meden
Somentor: prof. dr. Iztok Turel
Datum zagovora: 20. 04. 2018

ANDREJ EMANUEL COTMAN
ASIMETRIČNE REDUKCIJE KETONOV, KATALIZIRANE S KOVINSKIMI KOMPLEKSI
Mentorica: viš. znan. sod. dr. Barbara Mohar
Somentor: prof. dr. Boris Šket
Datum zagovora: 26. 04. 2018

TADEJA JANC
VPLIVI SOLI IN DRUGIH DODATKOV NA SAMOZDRUŽEVANJE GLOBULARNIH PROTEINOV V VODNIH RAZTOPINAH
Mentor: izr. prof. dr. Miha Lukšič
Datum zagovora: 8. 05. 2018

KATJA TRAVEN
NOVE RUTENIJEVE(II) KOORDINACIJSKE SPOJINE Z N,N-, N,O- IN N,N,N-DONORSKIMI LIGANDI
Mentor: prof. dr. Iztok Turel
Datum zagovora: 10. 05. 2018

PETRA KUZMAN
SINTEZA, KARAKTERIZACIJA IN VREDNOTENJE KINAZOLINSKIH RUTENACIKLIČNIH KOMPLEKSOV
Mentor: prof. dr. Anton Meden
Somentor: izr. prof. dr. Bogdan Štefane
Datum zagovora: 22. 06. 2018

KLARA RETKO
RAZVOJ NOVIH SUBSTRATOV ZA PREISKAVE BARVNIH SLOJEV NA UMETNIŠKIH DELIH S POVRŠINSKO OJAČENO RAMANSKO SPEKTROSKOPIJO
Mentor: izr. prof. dr. Romana Cerc Korošec
Somentorica: znan. sod. dr. Angelja Kjara Surca
Datum zagovora: 12. 10. 2018

MARTIN GLADOVIĆ
MOLEKULARNO MODELIRANJE ALKILACIJE DNA
Mentor: izr. prof. dr. Urban Bren
Somentor: prof. dr. Tomaž Urbič
Datum zagovora: 12. 10. 2018

BIOKEMIJA

JASNA BRČIĆ
STRUKTURNE ŠTUDIJE Z GVANINI IN CITOZINI BOGATIH OLIGONUKLEOTIDOV POVEZANIH Z NEVRODEGENERATIVNIMI OBOLENJI
Mentor: prof. dr. Janez Plavec
Datum zagovora: 13. 04. 2018

MATEVŽ KORENČ
MEHANIZMI INTERAKCIJ MED CISTEINSKO PEPTIDAZO KATEPSINOM K IN KOLAGENOM NA MOLEKULSKEM NIVOJU
Mentorica: prof. dr. Brigita Lenarčič
Datum zagovora: 24. 10. 2018

ALJAŽ GABER
OLIGOMERIZACIJA PROTEINA EPCAM IN NJEGOVA VLOGA PRI CELIČNI ADHEZIJI
Mentorica: prof. dr. Brigita Lenarčič
Datum zagovora: 9. 11. 2018

KEMIJSKO INŽENIRSTVO

NATAŠA MILOŽIČ
ENCIMSKO KATALIZIRANA TRANSAMINACIJA V MIKROREAKTORSKIH SISTEMIH
Mentor: prof. dr. Igor Plazl
Datum zagovora: 19. 04. 2018

ŽIGA ŠTIRN
NAČRTOVANJE IN UPORABA POLIMERNIH MATERIALOV S SPOSOBNOSTJO SAMOCELJENJA NA OSNOVI DIELS-ALDER REAKCIJE
Mentor: prof. dr. Matjaž Krajnc
Datum zagovora: 1. 06. 2018

SARA DRVARIČ TALIAN
ŠTUDIJ VPLIVA IZBRANIH PROCESOV IN PARAMETROV NA NOTRANJO UPORNOST LITIJ-ŽVEPLOVIH AKUMULATORJEV
Mentor: izr. prof. dr. Robert Dominko
Datum zagovora: 9. 10. 2018

MAJA PIVKO
DVOSTOPENJSKI POSTOPEK ZA PRIPRAVO LIMNPO4 KOT KATODNEGA MATERIALA V LITIJ IONSKIH AKUMULATORJIH
Mentor: prof. dr. Miran Gaberšček
Datum zagovora: 12. 10. 2018

ANA BJELIĆ
KATALITSKE PRETVORBE DERIVATOV LIGNINA IN NJIHOVA REAKCIJSKA KINETIKA
Mentor: doc. dr. Blaž Likozar
Datum zagovora: 8. 11. 2018

MAGISTRSKI ŠTUDIJ – 2. STOPNJA

KONDA, MOJCA
PREUČEVANJE VKLJUČEVANJA VSEBIN O ALTERNATIVNIH GORIVIH V POUK KEMIJE V SPLOŠNIH GIMNAZIJAH
Mentor: Vesna Ferk Savec
Datum zagovora: 16. 1. 2018

BANIČ, MOJCA
VALIDACIJA OBETAVNIH BIOOZNAČEVALCEV GLIOBLASTOMA IN OPREDELITEV UČINKA ZANJE SPECIFIČNIH NANO-TELES NA IZBRANIH CELIČNIH LINIJAH
Mentor: prof. dr. Radovan Komel
Datum zagovora: 22. 1. 2018

KUŠAR, KAJA
ANODNI MATERIALI NA OSNOVI KOMPLEKSNIH KOVINSKIH OKSIDOV ZA KERAMIČNE GORIVNE CELICE
Mentor: doc. dr. Klementina Zupan
Datum zagovora: 24. 1. 2018

ROZMARIČ, TOMAŽ
PRIMERJAVA METILACIJSKIH VZORCEV DNA PRI ČEZMERNO PREHRANJENIH OTROCIH Z IN BREZ INZULINSKE REZISTENCE
Mentor: doc. dr. Primož Kotnik
Somentor: prof. dr. Simon Horvat
Datum zagovora: 24. 1. 2018

MEŠKO, TOMAŽ
KARAKTERIZACIJA IN OCENA VISOKO–KONCENTRIRANIH ELEKTROLITOV
Mentor: prof. dr. Miran Gaberšček
Datum zagovora: 31. 1. 2018

JOŠIĆ, DANIJELA
PRIPRAVA IN KARAKTERIZACIJA LASTNOSTI KULTURE ASTROCITOV Z ZVEZDASTO OBLIKO TER IZRAŽANJE MOLEKULSKIH OZNAČEVALCEV PODTIPOV ASTROCITOV V PRIMARNI KULTURI PODGANE
Mentor: Matjaž Stenovec
Somentor: prof. dr. Robert Zorec
Datum zagovora: 1. 2. 2018

MOHAR, MAŠA
SINTEZA DERIVATOV KURKUMINA, MODIFICIRANIH S HIDROFILNIMI SKUPINAMI
Mentor: doc. dr. Martin Gazvoda
Datum zagovora: 12. 2. 2018

ŠKRJANC, MONIKA
IZRAŽANJE GENOV IN GENSKI POLIMORFIZMI POVEZANI Z ODPORNOSTJO NA MASTITIS PRI KOZAH
Mentor: prof. dr. Peter Dovč
Datum zagovora: 14. 2. 2018

KMETIČ, MIRJAM
UPORABA TEHNOLOGIJE ROGFP ZA DOLOČANJE CELIČNEGA REDOKS STANJA PRI KROMPIRJU
Mentor: prof. dr. Kristina Gruden
Somentor: izr. prof. dr. Marko Dolinar
Datum zagovora: 15. 2. 2018

ZAKOTNIK, SAMO
IZDELAVA PROMOTORSKE KNJIŽNICE Z MUTAGENEZO PROMOTORJA PTEF1 KVASOVKE SACCHAROMYCES CEREVISIAE
Mentor: izr. prof. dr. Uroš Petrovič
Datum zagovora: 16. 2. 2018

ŽAGAR, JAKA
PRIPRAVA BIOOGLJA IZ STABILIZIRANEGA AKTIVNEGA BLATA IN NJEGOVA UPORABA ZA ČIŠČENJE ODPADNIH VOD
Mentor: izr. prof. dr. Andreja Žgajnar Gotvajn
Datum zagovora: 14. 3. 2018

CEZAR, KLEMEN
HIDROLIZA ODPADNEGA BLATA IZ BIOLOŠKE ČISTILNE NAPRAVE PAPIRNIŠKE INDUSTRIJE
Mentor: izr. prof. dr. Andreja Žgajnar Gotvajn
Datum zagovora: 28. 3. 2018

PRAZNIK, MONIKA
ULTRASTRUKTURA APIKALNEGA IN BAZALNEGA LABIRINTA V ČREVESNIH CELICAH TER DIFERENCIACIJA MED RAZVOJEM EMBIJEV IN LIČINK PRI NEVRETENČARSKEM MODELNEM ORGANIZMU
Mentor: doc. dr. Nada Žnidaršič
Datum zagovora: 29. 3. 2018

KALAN, MARCEL
ŠIRJENJE OGLJIKOVEGA MONOKSIDA IN OPTIMALNA NAMESTITEV DETEKTORJA V PROSTORU
Mentor: doc. dr. Mitja Robert Kožuh
Datum zagovora: 19. 4. 2018

PREZELJ, PETER
MOLEKULARNI IN SEKRETORNI PROFIL MIŠIČNE IN NE-MIŠIČNE CELIČNE KULTURE
Mentor: prof. dr. Tomaž Marš
Datum zagovora: 19. 4. 2018

PUCELJ, KATARINA
IMOBILIZACIJA BIOKATALIZATORJA V MIKROREAKTORJU Z NANOVZMETMI
Mentor: prof. dr. Polona Žnidaršič Plazl
Datum zagovora: 19. 4. 2018

DUŠAK, BARBARA
VLOGA GENOV STRBOHA IN STRBOHD1 PRI ODZIVU KROMPIRJA NA VIRUS PVY
Mentor: prof. dr. Kristina Gruden
Somentor: izr. prof. dr. Marko Dolinar
Datum zagovora: 23. 4. 2018

ROJC, AJDA
AKTIVNOST KATEPSINOV C, L, B IN S V MODELU DIFERENCIRANIH ČREVESNIH EPITELIJSKIH CELIC CACO-2
Mentor: prof. dr. Boris Turk
Somentor: doc. dr. Tina Zavašnik Bergant
Datum zagovora: 17. 5. 2018

SAVANDIĆ, PETRA
VPLIV KALIBRACIJE NA DOLOČANJE MIKROKOMPONENT
Mentor: izr. prof. dr. Nataša Gros
Datum zagovora: 28. 5. 2018

MEGLEN, ANŽE
ALKALNO KARBONATNA REAKCIJA V BETONU
Mentor: izr. prof. dr. Marjan Marinšek
Datum zagovora: 30. 5. 2018

MLINARIČ, KATARINA
SINTEZA IN KARAKTERIZACIJA NEKATERIH IZBRANIH BIOPOLIMERNIH MATERIALOV
Mentor: izr. prof. dr. Romana Cerc Korošec
Datum zagovora: 7. 6. 2018

ŠIVEC, ROK
VPLIV NAČINA SEGREVANJA, DIMENZIJ CELICE IN UPORABLJENIH MATERIALOV NA NASTALE MEHANSKE NAPETOSTI V TROSLOJNEM SOFC SISTEMU
Mentor: izr. prof. dr. Marjan Marinšek
Datum zagovora: 12. 6. 2018

ANDREJČIČ, MIHA
PH-PREHODI IN DEBELINA ADSORPCIJE NA MONOLITNIH KROMATOGRAFSKIH NOSILCIH
Mentor: izr. prof. dr. Aleš Podgornik
Datum zagovora: 14. 6. 2018

BOŽIČ, DARJA
EVALVACIJA METOD DINAMIČNEGA IN STATIČNEGA SIPANJA SVETLOBE ZA KARAKTERIZACIJO ZUNAJCELIČNIH MEŠIČKOV V BIOLOŠKIH VZORCIH
Mentor: prof. dr. Ksenija Kogej
Datum zagovora: 15. 6. 2018

MAJC, BERNARDA
PRIPRAVA IN KARAKTERIZACIJA PROTEINA C9ORF72
Mentor: doc. dr. Vera Župunski
Datum zagovora: 19. 6. 2018

ŠUŠTERŠIČ, MOJCA
OCENA BIODOSTOPNOSTI POTENCIALNO STRUPENIH ELEMENTOV V HIŠNIH PRAHOVIH
Mentor: doc. dr. Marija Zupančič
Datum zagovora: 20. 6. 2018

HORVAT, MONIKA
SINTEZA TRIFLUOROMETILTIOLIRANIH AROMATOV IN NJIHOVA OKSIDACIJA Z VODIKOVIM PEROKSIDOM
Mentor: izr. prof. dr. Jernej Iskra
Datum zagovora: 20. 6. 2018

HORVAT, MARJETA
METILACIJA DNA IN SAMOMORILNO VEDENJE
Mentor: doc. dr. Alja Videtič Paska
Datum zagovora: 27. 6. 2018

KAPŠ, URŠA
SOODVISNOST MED IZRAŽANJEM UROPLAKINOV IN KERATINA 20 TER VEZAVO LEKTINOV PRI PAPILARNIH UROTELIJSKIH KARCINOMIH
Mentor: doc. dr. Daša Zupančič
Datum zagovora: 3. 7. 2018

BENCIK, TIM
PREUČEVANJE STABILNOSTI DERIVATIZIRANE CELULOZE Z VELIKOSTNO IZKLJUČITVENO KROMATOGRAFIJO
Mentor: izr. prof. dr. Irena Kralj Cigić
Datum zagovora: 4. 7. 2018

JUDEŽ, EVA
SINTEZA IN KARAKTERIZACIJA KOORDINACIJSKIH SPOJIN PREHODNIH KOVIN Z LIGANDI, KI VSEBUJEJO SALICILNO SKUPINO
Mentor: doc. dr. Nives Kitanovski
Datum zagovora: 5. 7. 2018

PERŠIČ, ŠPELA
ORGANORUTENIJEVI KOMPLEKSI Z ENOVEZNIM DUŠIKOVIM LIGANDOM LETROZOLOM
Mentor: prof. dr. Iztok Turel
Datum zagovora: 6. 7. 2018

STUPAR, UROŠ
PRIPRAVA, RENATURACIJA IN KARAKTERIZACIJA ČLOVEŠKEGA REKOMBINANTNEGA PROTEINA GILT
Mentor: prof. ddr. Boris Turk
Datum zagovora: 10. 7. 2018

ČAMIČ, ŽIGA
SINTEZA IN KARAKTERIZACIJA KOORDINACIJSKIH SPOJIN BAKRA(II) IN KOBALTA(II) S TIOCIANATNIM LIGANDOM IN HIDROKSIPIRIDINSKIMI LIGANDI
Mentor: doc. dr. Nives Kitanovski
Datum zagovora: 10. 7. 2018

VOLAVŠEK, JANEZ
SINTEZA IN KARAKTERIZACIJA HIBRIDNIH ORGANSKO-ANORGANSKIH ELEKTROLITOV ZA SONČNE CELICE GRÄTZELOVEGA TIPA
Mentor: izr. prof. dr. Miha Lukšič
Somentor: doc. dr. Ivan Jerman
Datum zagovora: 11. 7. 2018

ORAŽEM, TILEN
DETEKCIJA NITROAROMATSKIH SPOJIN Z MODIFICIRANO ELEKTRODO IZ STEKLASTEGA OGLJIKA
Mentor: izr. prof. dr. Mitja Kolar
Datum zagovora: 11. 7. 2018

GRŠIČ, MARIJA
SINTEZA CILJNIH AMIDOV IN NJIHOVA AKTIVNOST NA HBCHE IN MACHE
Mentor: doc. dr. Uroš Grošelj
Datum zagovora: 11. 7. 2018

KLOFUTAR, DOMEN
KARAKTERIZACIJA MEHANIZMOV DELOVANJA NEKATERIH ALOSTERIČNIH REGULATORJEV IN HEPARINA NA KATEPSIN B
Mentor: izr. prof. dr. Marko Novinec
Datum zagovora: 11. 7. 2018

KERT, DOMINIK
PRETVORBA ŠARŽNEGA PROCESA Z DOHRANJEVANJEM V PERFUZIJSKI PROCES NA PRIMERU BIOPROCESA S SESALSKO CELIČNO KULTURO
Mentor: izr. prof. dr. Uroš Petrovič
Datum zagovora: 13. 7. 2018

LAVRENČIČ, JAKOB GAŠPER
KARAKTERIZACIJA STR-LOKUSA FH2054 PRI PSIH
Mentor: prof. dr. Peter Dovč
Somentor: Jernej Ogorevc
Datum zagovora: 13. 7. 2018

VIDMAR, VITA
VPLIV CISTEINSKIH OSTANKOV NA NEKROPTOTIČNO AKTIVNOST ČLOVEŠKEGA PROTEINA MLKL
Mentor: doc. dr. Gregor Gunčar
Datum zagovora: 21. 8. 2018

NAROBE, ROK
KLASIČNO IN FOTOKATALITSKO OKSIDATIVNO JODIRANJE ARENOV
Mentor: izr. prof. dr. Jernej Iskra
Datum zagovora: 24. 8. 2018

VAH, LUKA
NAČRTOVANJE, SINTEZA IN IN VITRO TESTIRANJE PIRAZOLNIH INHIBITORJEV DIHIDROOROTATA DEHIDROGENAZE PRI PLASMODIUM FALCIPARUM
Mentor: prof. dr. Jurij Svete
Datum zagovora: 24. 8. 2018

PLUT, EVA
KIRALNI SKVARAMIDNI IN (TIO)SEČNINSKI ORGANOKATALIZATORJI PRI ENANTIOSELEKTIVNI TVORBI OGLJIK–OGLJIK VEZI
Mentor: izr. prof. dr. Bogdan Štefane
Datum zagovora: 24. 8. 2018

IVANČIČ, ANŽE
UPORABA 5-SUBSTITUIRANIH PIROLONOV V REAKCIJAH, KATALIZIRANIH Z UVELJAVLJENIMI IN NOVIMI BIFUNKCIONALNIMI KATALIZATORJI S KAFRINIM SKELETOM
Mentor: doc. dr. Uroš Grošelj
Datum zagovora: 24. 8. 2018

KONČAN, LARA
SINTEZA SPOJIN ELEMENTOV PRVE VRSTE PREHODA S 4,6-DIHIDROKSIPIRIMIDINOM
Mentor: doc. dr. Bojan Kozlevčar
Datum zagovora: 29. 8. 2018

KOŠIČEK, MARTIN
OSMOZNI KOEFICIENTI NATRIJEVIH SOLI POLI(A-ALKILKARBOKSILNIH KISLIN)
Mentor: prof. dr. Ksenija Kogej
Datum zagovora: 29. 8. 2018

ZUPANC, ANŽE
SINTEZA NOVIH ENAMINONSKIH POLIMEROV
Mentor: prof. dr. Jurij Svete
Datum zagovora: 29. 8. 2018

BREČKO, ŽIVA
ČIŠČENJE R-FIKOERITRINA IZ RDEČIH MAKROALG V SISTEMU MIKROFLUIDNIH NAPRAV
Mentor: prof. dr. Polona Žnidaršič Plazl
Datum zagovora: 30. 8. 2018

STRAŠEK, NIKA
SINTEZA IN TESTIRANJE POTENCIALNIH INHIBITORJEV PLASMODIUM FALCIPARUM DIHIDROOROTAT DEHIDROGENAZE
Mentor: prof. dr. Jurij Svete
Datum zagovora: 31. 8. 2018

HOIVIK, ANDREJ
SINTEZA DVO- IN VEČVEZNIH LIGANDOV IZ SUBSTITUIRANIH BICIKLO[2. 2. 2]OKTENOV IN NJIHOVIH KOORDINACIJSKIH SPOJIN
Mentor: doc. dr. Krištof Kranjc
Datum zagovora: 31. 8. 2018

PUCIHAR, URH
FUNKCIONALIZACIJA KROMATOGRAFSKIH NOSILCEV Z IONSKO IZMENJEVALNIMI SKUPINAMI
Mentor: izr. prof. dr. Aleš Podgornik
Datum zagovora: 31. 8. 2018

HROVAT, SARA
VEČKRATNA KATALITSKA C–H FUNKCIONALIZACIJA DIHIDROPIRAZINSKEGA DERIVATA V VODI
Mentor: izr. prof. dr. Franc Požgan
Datum zagovora: 31. 8. 2018

ŠPINDLER, VIDA
NAČTOVANJE VELIKOSTNE PORAZDELITVE IN OBLIKE KRISTALOV Z OSCILACIJO TEMPERATURE SUSPENZIJE IN UPORABO MOKREGA MLETJA
Mentor: doc. dr. Blaž Likozar
Somentor: prof. dr. Igor Plazl
Datum zagovora: 4. 9. 2018

KOPAČ, TILEN
KINETIČNA ANALIZA TERMIČNEGA RAZPADA HIDRATIZIRANEGA TITANOVEGA DIOKSIDA
Mentor: izr. prof. dr. Marjan Marinšek
Datum zagovora: 4. 9. 2018

DLOUHY, MATJAŽ
REAKTIVNOST IN STABILNOST HIDROTRIOKSI RADIKALA
Mentor: prof. dr. Tomaž Urbič
Datum zagovora: 5. 9. 2018

SIMONČIČ, MATJAŽ
NASTANEK BIOKEMIJSKIH PREKURZORJEV V MEDZVEZDNEM PROSTORU
Mentor: prof. dr. Tomaž Urbič
Datum zagovora: 5. 9. 2018

KOBAL, TJAŽ
KINETIKA DIELS-ALDER REAKCIJE MED N-FENILMALEIMIDOM IN BENZOKSAZINOM NA OSNOVI FURANA V TALINI
Mentor: prof. dr. Urška Šebenik
Datum zagovora: 6. 9. 2018

NOSAN, MIHA
PRIMERJAVA HPLC IN REFLEKTOMETRIČNIH METOD ZA DOLOČANJE FORMALDEHIDA IN 5-(HIDROKSIMETIL) FURFURALA
Mentor: izr. prof. dr. Zdenko Časar
Somentor: prof. dr. Helena Prosen
Datum zagovora: 6. 9. 2018

GAČNIK, JAN
RAZVOJ IN OPTIMIZACIJA METOD DOLOČANJA 90SR V VODNIH VZORCIH
Mentor: doc. Marko Štrok
Somentor: prof. dr. Helena Prosen
Datum zagovora: 6. 9. 2018

GRIČAR, EMA
ELEKTROKEMIJSKE LASTNOSTI IN DOLOČANJE FEROCENSKIH DERIVATOV AMINOFOSFONATOV
Mentor: izr. prof. dr. Mitja Kolar
Datum zagovora: 6. 9. 2018

PALJK, TINA
ODLAGANJE FILMA LITIJEVEGA SULFIDA V RAZLIČNIH ELEKTROLITIH V LI-S AKUMULATORJIH
Mentor: izr. prof. dr. Robert Dominko
Datum zagovora: 6. 9. 2018

MENEGATTI, TADEJ
IMOBILIZACIJA BIOKATALIZATORJA V HIDROGELU IN NJEGOVA UPORABA V MIKROREAKTORJU
Mentor: prof. dr. Polona Žnidaršič Plazl
Datum zagovora: 7. 9. 2018

OBLAK, DOMEN
VPLIV DODANE SOLI NA KONFORMACIJSKE SPREMEMBE DNA ČLOVEŠKEGA TELOMERNEGA ZAPOREDJA 22GT
Mentor: prof. dr. Jurij Lah
Datum zagovora: 7. 9. 2018

HLADNIK, LUCIJA
SAMOCELJENJE BIO-OSNOVANIH BENZOKSAZINOV NA PRINCIPU SUPRAMOLEKULARNIH INTERAKCIJ
Mentor: prof. dr. Matjaž Krajnc
Datum zagovora: 7. 9. 2018

PAVLIN, ANŽE
TVORBA HALOGENSKIH VEZI V SOLEH DIATRIZOIČNE KISLINE
Mentor: izr. prof. dr. Franc Perdih
Datum zagovora: 7. 9. 2018

ŽOS, EVA
LUMINISCENČNE LASTNOSTI CINKOVIH KOORDINACIJSKIH SPOJIN S PIRIDIN-2,6-DIKARBOKSILNO KISLINO
Mentor: izr. prof. dr. Franc Perdih
Datum zagovora: 7. 9. 2018

ŽAGAR, TOMAŽ
KARAKTERIZACIJA OLIGOMERNIH STANJ PROTEINA EPCAM IN VIVO
Mentor: prof. dr. Brigita Lenarčič
Datum zagovora: 7. 9. 2018

MRAVLJAK, ROK
PRIPRAVA, FUNKCIONALIZACIJA IN KARAKTERIZACIJA GMA/EGDMA KOPOLIMERA IZ EMULZIJE Z VISOKO VSEBNOSTJO DISPERGIRANE FAZE
Mentor: izr. prof. dr. Aleš Podgornik
Datum zagovora: 7. 9. 2018

ŠTEMBERGER, ROK
PROFIL IZRAŽANJA MIŠIČNO-SPECIFIČNIH PROTEINOV V ČLOVEŠKI SKELETNI MIŠICI IN VITRO
Mentor: prof. dr. Tomaž Marš
Datum zagovora: 7. 9. 2018

HRIBAR, UROŠ
SINTEZA PEROVSKITNE KERAMIKE V SISTEMU NA0. 5BI0. 5TIO3-BATIO3-K0. 5NA0. 5NBO3 – MIKROSTRUKTURNE IN ELEKTRIČNE LASTNOSTI
Mentor: prof. dr. Danilo Suvorov
Datum zagovora: 10. 9. 2018

TAVČAR, PETRA
VPLIV AKTIVACIJE Z G-PROTEINI SKLOPLJENIH RECEPTORJEV NA BIOGENEZO LIPIDNIH KAPLJIC V ASTROCITIH V ORGANOTIPSKIH KULTURAH MOŽGANSKIH REZIN ODRASLIH PODGAN
Mentor: doc. dr. Nina Vardjan
Datum zagovora: 11. 9. 2018

CIGOJ, MATEJA
OPTIMIZACIJA METODE PRENOSA WESTERN ZA DOLOČANJE RECEPTORJEV ZA ESTROGEN IN RECEPTORJEV ZA ERITROPOETIN V CELIČNIH LINIJAH RAKA DOJKE
Mentor: izr. prof. dr. Nataša Debeljak
Datum zagovora: 11. 9. 2018

PAPEŽ, PETRA
HIDRATACIJA NIŽJIH ALKOHOLOV Z UPORABO TEORETIČNIH METOD
Mentor: prof. dr. Tomaž Urbič
Somentor: izr. prof. Franci Merzel
Datum zagovora: 11. 9. 2018

LORBER, KRISTIJAN
RAZVOJ FOTOKATALIZATORJA BIZMUT-TITANOV DIOKSID IN FOTOKATALITSKA REAKCIJA BISFENOLA A V ŠARŽNEM IN PRETOČNEM SISTEMU Z RECIKLOM
Mentor: prof. dr. Igor Plazl
Somentor: Petar Djinović
Datum zagovora: 12. 9. 2018

JUTERŠEK, MOJCA
PRIPRAVA IN PREVERJANJE UPORABNOSTI SINTEZNOBIOLOŠKEGA PLAZMIDA PMJC01 TER REPORTERSKEGA PROTEINA CISTATINA ZA DELO S CIANOBAKTERIJO SYNECHOCYSTIS SP. PCC 6803
Mentor: izr. prof. dr. Marko Dolinar
Datum zagovora: 12. 9. 2018

REBERC, MATEJ
KOVINSKO-ORGANSKI MATERIALI NA OSNOVI IMIDAZOLA IN TETRAHIDRIDOBORATOV LAHKIH KOVIN
Mentor: prof. dr. Anton Meden
Somentor: Jernej Stare
Datum zagovora: 13. 9. 2018

PODJED, NINA
ŠTUDIJ DIKETONATNIH LIGANDOV IN PRIPADAJOČIH KOVINSKIH KOMPLEKSOV
Mentor: prof. dr. Iztok Turel
Datum zagovora: 13. 9. 2018

PETRIČ, BOŠTJAN
PRIPRAVA FLUORESCENČNIH NANOTELES ZA DETEKCIJO KOFEINA
Mentor: doc. dr. Gregor Gunčar
Datum zagovora: 14. 9. 2018

ZALOKAR, MATEJA
AEROSOLI V KMETIJSKI DEJAVNOSTI
Mentor: prof. dr. Marija Bešter Rogač
Datum zagovora: 14. 9. 2018

PRELOŽNIK, SIMON
TVORBA HALOGENSKIH VEZI V SOLEH HALOGENIRANIH DERIVATOV BENZOJSKE KISLINE
Mentor: izr. prof. dr. Franc Perdih
Datum zagovora: 14. 9. 2018

SVETLIČIČ, MAJA
NAČRTOVANJE IN OVREDNOTENJE SISTEMOV SESALSKIH CELIC, KI OMOGOČAJO PRESKOK PREZGODNJIH TERMINACIJSKIH KODONOV
Mentor: znan. sod. dr. Iva Hafner Bratkovič
Somentor: doc. dr. Gregor Gunčar
Datum zagovora: 14. 9. 2018

POTOČNIK, KIM
STANDARDIZACIJA JEMANJA PERITONEALNIH VZORCEV PRI KONTROLNIH BOLNICAH ZA RAK JAJČNIKOV IN NORMALIZACIJA MERITEV KONCENTRACIJE TUMORSKEGA OZNAČEVALCA GLEDE NA KOLIČINO PROTEINOV
Mentor: Katarina Černe
Somentor: doc. dr. Borut Kobal
Datum zagovora: 14. 9. 2018

JAZBEC, VID
OPTIMIZACIJA IZRAŽANJA REKOMBINANTNEGA PROTEINA RANKL IN TESTIRANJE MOŽNIH INHIBITORJEV OLIGOMERIZACIJE
Mentor: izr. prof. dr. Marko Novinec
Datum zagovora: 14. 9. 2018

ZEKIČ, JURE
RAZVOJ METODE ZA DOLOČANJE ANTRAKINONA V KARTONU
Mentor: izr. prof. dr. Drago Kočar
Datum zagovora: 14. 9. 2018

TRATNIK, BLAŽ
UPORABA POLIMERNE IONSKE TEKOČINE V SODOBNIH BATERIJSKIH SISTEMIH
Mentor: prof. dr. Miran Gaberšček
Datum zagovora: 17. 9. 2018

BENSA, TJAŠA
VLOGA PREPISOVALNIH DEJAVNIKOV ICER PRI URAVNAVANJU CIRKADIANE URE
Mentor: prof. dr. Damjana Rozman
Datum zagovora: 17. 9. 2018

ČERNOŠA, TANJA
POŽARNA ODPORNOST VITKIH SOVPREŽNIH STEBROV
Mentor: izr. prof. dr. Simon Schnabl
Datum zagovora: 17. 9. 2018

KOSTANJEVEC, MOJCA
REKONSTITUCIJA PROTEINA EPCAM V FOSFOLIPIDNEM DVOSLOJU
Mentor: prof. dr. Brigita Lenarčič
Datum zagovora: 18. 9. 2018

ZGONC, ALJA
DOLOČANJE LOKUSOV KVANTITATIVNE LASTNOSTI POVEČANE VSEBNOSTI NEVTRALNIH LIPIDOV PRI KVASOVKI SACCHAROMYCES CEREVISIAE
Mentor: izr. prof. dr. Uroš Petrovič
Datum zagovora: 18. 9. 2018

BERKOPEC, KAJA
BIOLOŠKI VPLIV FLIKERJA
Mentor: prof. dr. Grega Bizjak
Datum zagovora: 18. 9. 2018

SVETELJ, JURE
PRIMERJAVA ŠARŽNE IN PRETOČNE PROIZVODNJE AKTIVNIH FARMACEVTSKIH UČINKOVIN
Mentor: prof. dr. Igor Plazl
Datum zagovora: 20. 9. 2018

VELIKONJA, MELITA
IZDELAVA EKSPERIMENTA IN E-UČNE ENOTE O ETERIČNIH OLJIH KRAŠKIH RASTLIN ZA POUK KEMIJE V GIMNAZIJI
Mentor: prof. dr. Bojana Boh Podgornik
Datum zagovora: 21. 9. 2018

CUZNAR, KRISTINA TADEJA
VPLIV KISLINSKEGA LUŽENJA NA POVRŠINO ŽELEZO-NIKELJ-KROMOVE ZLITINE
Mentor: doc. dr. Barbara Novosel
Datum zagovora: 21. 9. 2018

ŽUGELJ, LIDIJA
PREGLED 14. SKUPINE PERIODNEGA SISTEMA
Mentor: doc. dr. Nives Kitanovski
Datum zagovora: 21. 9. 2018

LAPANJA, TJAŠA
OPTIMIZACIJA METOD ZA AKTIVACIJO GENOV, VKLJUČENIH V DIFERENCIACIJO REGULATORNIH CELIC T (TREG), Z UPORABO NAČRTOVANIH TRANSKRIPCIJSKIH FAKTORJEV IN SISTEMA CRISPR/CAS9
Mentor: prof. dr. Simon Horvat
Datum zagovora: 24. 9. 2018

TRDIN, EVA
RAZVOJ METODE ZA DOLOČEVANJE RAZLIČNIH ZVRSTI OGLJIKA V SEDIMENTU
Mentor: prof. dr. Matevž Pompe
Datum zagovora: 24. 9. 2018

FRANTAR, ANJA
KATALITSKO HIDROAMINIRANJE ACETILENOV S PD-NHC KOMPLEKSOM
Mentor: prof. dr. Janez Košmrlj
Datum zagovora: 24. 9. 2018

AVBELJ, JUDITA
VLOGA STEFINA A PRI VNETJIH IN OKSIDATIVNEM STRESU
Mentor: Nataša Kopitar-Jerala
Somentor: prof. dr. Boris Turk
Datum zagovora: 24. 9. 2018

POTOKAR, KARIN
SINTEZA IN KARAKTERIZACIJA KOORDINACIJSKIH SPOJIN BAKRA(II) Z NIKOTINAMIDOM IN ANIONI DIKARBOKSILNIH KISLIN
Mentor: doc. dr. Bojan Kozlevčar
Datum zagovora: 24. 9. 2018

ČEBULJ, ANŽE
SINTEZA IN KARAKTERIZACIJA SPOJIN PREHODNIH ELEMENTOV Z ANIONOM 4-HIDROKSIBENZOJSKE KISLINE
Mentor: doc. dr. Bojan Kozlevčar
Datum zagovora: 25. 9. 2018

KOVAČIČ, MATIC
DOLOČANJE STRUKTUR G-KVADRUPLEKSOV STABILIZIRANIH S PIRENSKIMI SKUPINAMI
Mentor: prof. dr. Janez Plavec
Datum zagovora: 25. 9. 2018

JELENC, PETRA
ANALIZA EVAKUACIJE IZ VISOKIH STAVB
Mentor: izr. prof. dr. Simon Schnabl
Datum zagovora: 26. 9. 2018

KUHAR, TINA
DETEKCIJA PROTEINA MLKL V RAZLIČNIH CELIČNIH LINIJAH IN NEKROPTOZNA AKTIVNOST PROTEINSKEGA KONSTRUKTA MLKL N-154 D144K Z ZUNANJE STRANI CELIČNE MEMBRANE
Mentor: prof. dr. Peter Veranič
Somentor: doc. dr. Mojca Pavlin
Datum zagovora: 26. 9. 2018

STRAŽAR, PETRA
ELEKTROKEMIJSKO RAZTAPLJANJE RODIJA NA OGLJIKU V RAZREDČENI KISLINI Z UPORABO REAKTIVNIH PLINOV
Mentor: izr. prof. dr. Marjan Marinšek
Datum zagovora: 26. 9. 2018

ČRNIGOJ, TOMAŽ
DOLOČANJE EKSPLOZIJSKIH PARAMETROV HIBRIDNIH ZMESI
Mentor: doc. dr. Barbara Novosel
Datum zagovora: 26. 9. 2018

TEKAVEC, SIMONA
PRIPRAVA MINIATURNIH PRETOČNIH METAKRILATNIH MONOLITNIH SISTEMOV NA PLASTIČNIH NOSILCIH
Mentor: izr. prof. dr. Aleš Podgornik
Datum zagovora: 27. 9. 2018

ŽIŽEK, MATEJ
OCENJEVANJE VPLIVA VIBRACIJ CELEGA TELESA NA UPRAVLJALCA VILIČARJA V LOGISTIKI TRGOVSKE DEJAVNOSTI
Mentor: doc. dr. Mitja Robert Kožuh
Datum zagovora: 27. 9. 2018

KORPAR, TANJA
RAZPOREDITEV PROTEINOV MATRIKSA GOLGIJEVEGA APARATA V DEŽNIKASTIH CELICAH UROTELIJA SEČNEGA MEHURJA
Mentor: prof. dr. Rok Romih
Datum zagovora: 28. 9. 2018

BENČIČ, ALEKSANDER
PRIPRAVA SAMOSESTAVLJIVIH PROTEINSKIH KOMPLEKSOV Z UPORABO FUZIJSKEGA PROTEINA Z DIMERIZIRAJOČO IN TRIMERIZIRAJOČO DOMENO
Mentor: doc. dr. Gregor Gunčar
Datum zagovora: 5. 10. 2018

SMOLE, JANJA
VPLIV ORGANIZACIJSKIH, ČLOVEŠKIH IN KOMUNIKACIJSKIH DEJAVNIKOV NA VARNOST
Mentor: doc. dr. Mitja Robert Kožuh
Datum zagovora: 5. 10. 2018

GOGNJAVEC, TJAŠA
FOTOKEMIJSKE PRETVORBE SULFIDOV Z VODIKOVIM PEROKSIDOM V VODI
Mentor: izr. prof. dr. Marjan Jereb
Datum zagovora: 8. 10. 2018

ŠVAGELJ, MIHA
VZPOSTAVLJANJE ORIGINALNE PROSOJNOSTI MATERIALOV Z ZAPOLNJENJEM MIKRORAZPOK
Mentor: izr. prof. dr. Aleš Podgornik
Datum zagovora: 11. 10. 2018

ŽALIK, MIHA
UPORABA IN ZANESLJIVOST JAVLJALNIKOV CO TER EMISIJE CO PRI GORENJU KADIL
Mentor: izr. prof. dr. Simon Schnabl
Datum zagovora: 15. 10. 2018

BIRKELBACH, JOŽICA
PRENOS ROČNIH EKSTRAKCIJ V PRETOČNI SISTEM
Mentor: izr. prof. dr. Nataša Gros
Datum zagovora: 18. 10. 2018

PIRMAN, TOMAŽ
MIKROKINETIKA PARCIALNE FOTOKATALITSKE OKSIDACIJE GLICEROLA PREKO TIO2 KATALIZATORJA DO PRODUKTOV Z VIŠJO DODANO VREDNOSTJO
Mentor: izr. prof. dr. Aleš Podgornik
Somentor: doc. dr. Blaž Likozar
Datum zagovora: 19. 10. 2018

HODNIK, BLAŽ
RAZVOJ IN VALIDACIJA KROMATOGRAFSKE METODE ZA DOLOČANJE MIKROKRISTALINIČNE CELULOZE V TABLETAH
Mentor: izr. prof. dr. Drago Kočar
Datum zagovora: 25. 10. 2018

KUMAR, VANJA
VPLIV LINEARNE GOSTOTE NABOJA NA POLIIONU NA ENTALPIJE MEŠANJA RAZTOPIN POLIELEKTROLITOV Z RAZTOPINAMI ENOSTAVNIH SOLI
Mentor: izr. prof. dr. Janez Cerar
Datum zagovora: 26. 10. 2018

DEBELJAK, NATAŠA
IZRAŽANJE GLIKOZIDAZ IN NANOTELESA NA POVRŠINI KVASOVKE
Mentor: izr. prof. dr. Uroš Petrovič
Datum zagovora: 30. 10. 2018

VIDMAR, HELENA
OBIČAJNA IN POSEBNA DVIGALA ZA PREVOZ OSEB
Mentor: doc. dr. Boris Jerman
Datum zagovora: 12. 11. 2018

KOTNIK, ROBERT
SINTEZA AKRILATNIH NA PRITISK OBČUTLJIVIH LEPIL PO POSTOPKU RAZTOPINSKE POLIMERIZACIJE
Mentor: doc. dr. Jernej Kajtna
Somentor: doc. dr. Aleš Ručigaj
Datum zagovora: 13. 11. 2018

KISILAK, MARIJA
ŠTUDIJ VPLIVA NEKATERIH KOVINSKIH IONOV IN KOORDINACIJSKIH SPOJIN RUTENIJA NA AKTIVNOST KATEPSINA K
Mentor: prof. dr. Iztok Turel
Datum zagovora: 15. 11. 2018

CEROVIĆ, ROBERT
SINTEZA IN KARAKTERIZACIJA NOVIH KOVINSKO-ORGANSKIH HIBRIDNIH MATERIALOV
Mentor: viš. znan. sod. dr. Matjaž Mazaj
Somentor: prof. dr. Anton Meden
Datum zagovora: 19. 11. 2018

REGENT, LANA
SINTEZA IN KARAKTERIZACIJA NOVIH FLUORIDOOKSIDOVANADATOV
Mentor: prof. dr. Alojz Demšar
Somentor: doc. dr. Andrej Pevec
Datum zagovora: 28. 11. 2018

FURAR, URŠKA
DOLOČANJE AKTIVNOSTI IN KONCENTRACIJE TIMIDIN KINAZE V SERUMU BOLNIC Z RAKOM DOJKE
Mentor: prof. dr. Joško Osredkar
Datum zagovora: 30. 11. 2018

MIHOVEC, ROK
OKSIDACIJA ANTIBIOTIKA TIAMULIN FUMARATA Z OZONIRANJEM
Mentor: izr. prof. dr. Andreja Žgajnar Gotvajn
Datum zagovora: 4. 12. 2018

KONDA, MATEJA
UPORABA LIGNINOLITIČNIH ENCIMOV GLIVE DICHOMITUS SQUALENS ZA RAZGRADNJO ODPADNEGA MATERIALA
Mentor: doc. dr. Gabriela Kalčikova
Datum zagovora: 4. 12. 2018

KARADŽA, MATEJA
SINTEZA ELEKTROKATALIZATORJA ZA OKSIDACIJO VODE NA OSNOVI KOMPOZITA OGLJIKA IN Z DUŠIKOM DOPIRANEGA TITANOVEGA DIOKSIDA
Mentor: prof. dr. Miran Gaberšček
Datum zagovora: 17. 12. 2018

LAPORNIK, KATARINA
SPREMLJANJE DELOVANJA IN OPTIMIZACIJA MALE ČISTILNE NAPRAVE PLANINSKE KOČE VALVASORJEV DOM POD STOLOM
Mentor: izr. prof. dr. Andreja Žgajnar Gotvajn
Datum zagovora: 18. 12. 2018

SEDMINEK, ANJA
KOORDINACIJSKE SPOJINE NIKLJA S TIOSEMIKARBAZIDI IN TIOSEMIKARBAZONI
Mentor: doc. dr. Andrej Pevec
Datum zagovora: 18. 12. 2018

STRNAD, KATJA
VZORČENJE IN ANALIZA HLAPOV V ZRAKU
Mentor: prof. dr. Marija Bešter Rogač
Datum zagovora: 19. 12. 2018

LUKAN, TANJA
VPLIV POROZNOSTI IN POR KONVEKTIVNIH NOSILCEV NA HIDRODINAMSKE LASTNOSTI
Mentor: izr. prof. dr. Aleš Podgornik
Datum zagovora: 20. 12. 2018

ŠAVRIČ, ALEŠ
VLOGA AKTIVNEGA OGLJA IN NEČISTOČ PRI DEHIDROGENACIJI 5,6-DIFENIL-2,3-DIHIDROPIRAZINA
Mentor: doc. dr. Krištof Kranjc
Datum zagovora: 21. 12. 2018

DIPLOME – UNIVERZITETNI ŠTUDIJ

UNIVERZITETNI ŠTUDIJ – 1. STOPNJA

ŽIBERNA, KATARINA
SINTEZA PALADIJEVIH PRODUKTOV OKSIDATIVNE ADICIJE
Mentor: doc. dr. Martin Gazvoda
Datum zagovora: 6. 2. 2018

MIKUŽ, ALENKA
PROGNOSTIČNA VREDNOST CELOKUPNIH PROTEINOV V SERUMU IN ASCITESU Mentor: Katarina Černe
Datum zagovora: 13. 2. 2018

KRANJC, DOMEN
TITRACIJA Z AVTOMATSKIM TITRATORJEM
Mentor: izr. prof. dr. Nataša Gros
Datum zagovora:13. 2. 2018

AVGUŠTIN, NASTJA
PRIMERJAVA REAKTIVNOSTI ORGANSKIH SPOJIN PRI RAZLIČNIH POGOJIH
Mentor: izr. prof. dr. Marjan Jereb
Datum zagovora: 14. 2. 2018

JELŠEVAR, MARUŠA
FUNKCIONALIZACIJA SPOJIN PRI KLASIČNIH IN ALTERNATIVNIH POGOJIH
Mentor: izr. prof. dr. Marjan Jereb
Datum zagovora: 14. 2. 2018

POLES, PETER
GRAFENSKI MATERIALI ZA NAPREDNE TEKSTILNE MATERIALE
Mentor: doc. dr. Boštjan Genorio
Datum zagovora: 19. 2. 2018

MORAN, ANJA
MERITVE IN SANACIJA HRUPA V LESNI INDUSTRIJI
Mentor: doc. dr. Mitja Robert Kožuh
Datum zagovora: 28. 2. 2018

LONČAR, ANJA
SINTEZA IN KARAKTERIZACIJA KOMPLEKSA MANGANOVEGA(II) KLORIDA S PIRIDIN-2-ONOM
Mentor: doc. dr. Saša Petriček
Datum zagovora: 28. 2. 2018

UZAR, ALEKSANDRA
PRIPRAVA REKOMBINANTNIH ANTITOKSINOV IPF_1062 IN IPF_1067 CIANOBAKTERIJE MICROCYSTIS AERUGINOSA PCC 7806 V BAKTERIJI ESCHERICHIA COLI
Mentor: izr. prof. dr. Marko Dolinar
Datum zagovora: 1. 3. 2018

KRELJ, ŽIGA
KATALITSKA HIDRO(DEOKSI)GENACIJA LK IN GVL V REAKTORJU Z GOŠČO
Mentor: izr. prof. dr. Andreja Žgajnar Gotvajn
Datum zagovora:2. 3. 2018

TOMAN, ŽIGA
NOVI MATERIALI ZA VISOKOTEMPERATURNE GORIVNE CELICE S TRDNIM OKSIDNIM ELEKTROLITOM
Mentor: izr. prof. dr. Marjan Marinšek
Datum zagovora: 12. 3. 2018

KASTELIC, KRISTINA
PREPREČEVANJE NEZGOD PRI UPORABI NEVARNIH KEMIKALIJ
Mentor: doc. dr. Barbara Novosel
Datum zagovora: 20. 3. 2018

KUKOVIČIČ, KARMEN
UPORABA SAMODEJNE GASILNE AMPULE IN GRANATE BONPET PRI GAŠENJU ZAČETNIH POŽAROV
Mentor: izr. prof. dr. Simon Schnabl
Datum zagovora: 21. 3. 2018

BLAGOJEVIĆ, ALEKSANDAR
ALKALNO-KARBONATNA REAKCIJA V HIDRAVLIČNIH VEZIVIH
Mentor: izr. prof. dr. Marjan Marinšek
Datum zagovora: 26. 3. 2018

GAŠPERŠIČ, EMA
IZRAŽANJE IN KARAKTERIZACIJA MAKROFAGNE KOLONIJE STIMULIRAJOČEGA FAKTORJA (M-CSF)
Mentor: prof. dr. Boris Turk
Datum zagovora: 29. 3. 2018

GREGORC, JURE
SINTEZA METIL-4-OKSO-1-AZASPIRO[4. 4]NON-2-EN-3-KARBOKSILATA
Mentor: prof. dr. Jurij Svete
Datum zagovora: 11. 4. 2018

GOLTNIK, TJAŠA
NIZKOTEMPERATURNA SINTEZA IN SAMOČISTILNA UČINKOVITOST TANKIH PLASTI TIO2-ZRO2 NA STEKLENIH IN KOVINSKIH PODLAGAH
Mentor: prof. dr. Urška Lavrenčič Štangar
Datum zagovora: 20. 4. 2018

KOPAČ, URŠA
PARALELNE HETERODIMERNE OBVITE VIJAČNICE, NAČRTOVANE NA OSNOVI TROPOMIOZINA
Mentor: prof. dr. Simon Horvat
Datum zagovora: 24. 4. 2018

SUŠNIK, BLAŽ
ZDRAV ŽIVLJENJSKI SLOG ZAPOSLENIH NA OSNOVNI ŠOLI
Mentor: prof. dr. Marjan Bilban
Datum zagovora: 24. 4. 2018

ŽIGANTE, NIKA
UPORABA POLI(METIL METAKRILATA) V KOZMETIKI
Mentor: izr. prof. dr. Aleš Podgornik
Datum zagovora: 25. 4. 2018

CIRIKOVIĆ, DAVID
PROUČEVANJE ENTALPIJSKIH SPREMEMB PRI MEŠANJU RAZTOPIN MODELNIH ELEKTROLITOV S TEORIJO OZ/MSA
Mentor: izr. prof. dr. Miha Lukšič
Datum zagovora: 26. 4. 2018

TEKAVEC, SARA
VLOGA SIGNALNE POTI ERK PRI UČINKIH VLDL NA KARDIOMIOCITE
Mentor: doc. dr. Tadeja Režen
Datum zagovora: 26. 4. 2018

STRADOVNIK, ADISA
DIMERIZACIJA TERMINALNIH ACETILENOV
Mentor: doc. dr. Martin Gazvoda
Datum zagovora: 8. 5. 2018

ČERNE, ANA
VPLIV DETERGENTA NA OMOČENJE VLAKEN
Mentor: izr. prof. dr. Marko Hočevar
Datum zagovora: 15. 5. 2018

JOŠT, GAŠPER
VREDNOTENJE PORAZDELITVE ALKALNE ZALOGE V RAZKISLINJENIH KNJIGAH
Mentor: izr. prof. dr. Irena Kralj Cigić
Datum zagovora: 16. 5. 2018

ŽGANK, ANDREJ
DELNA PRIPRAVA AMINOMALEIMIDA KOT OSNOVNE MOLEKULE PRI PRIPRAVI RAZLIČNIH MALEIMIDOBENZOKSAZINOV
Mentor: doc. dr. Aleš Ručigaj
Datum zagovora: 28. 5. 2018

GEORGIEVSKI, ANA
TEMPERATURNO ODZIVNI POLIMERNI MATERIALI
Mentor: izr. prof. dr. Aleš Podgornik
Datum zagovora: 28. 5. 2018

SMRDELJ, BENJAMIN
MODELIRANJE KEMIJSKIH REAKCIJ Z UPORABO MREŽNE BOLTZMANNOVE METODE IN DISIPATIVNE DINAMIKE DELCEV
Mentor: prof. dr. Igor Plazl
Datum zagovora: 1. 6. 2018

JAKLIN, MATEJ
PREGLED PLASTOVITIH MATERIALOV IN NJIHOVA UPORABA
Mentor: doc. dr. Boštjan Genorio
Datum zagovora: 7. 6. 2018

ALEKSIČ, SIMON
VPLIV OKSIDACIJE GVANINA NA STRUKTURO IN ZVITJE TELOMERNIH G-KVADRUPLEKSOV
Mentor: prof. dr. Janez Plavec
Datum zagovora: 11. 6. 2018

RUS, AJDA
ZAMENJAVA IZOCIANATOV V DVOKOMPONENTNIH POLIURETANSKIH PREMAZIH
Mentor: prof. dr. Urška Šebenik
Datum zagovora: 15. 6. 2018

FAJS, ALENKA
UPORABA MALE VODNE LEČE ZA FITOREMEDIACIJO ODPADNIH VODA
Mentor: doc. dr. Gabriela Kalčikova
Datum zagovora: 19. 6. 2018

KEJŽAR, NEJC
STRUKTURNE ZNAČILNOSTI KLAVDINSKE OLIGOMERIZACIJE
Mentor: doc. dr. Miha Pavšič
Datum zagovora: 26. 6. 2018

BAKAČ, ALJOŠA
DOLOČEVANJE ŽELEZOVIH IONOV V TLEH Z MOLEKULSKO ABSORPCIJSKO SPEKTROMETRIJO
Mentor: prof. dr. Helena Prosen
Datum zagovora: 28. 6. 2018

COTMAN, KLEMEN
PIRIMIDINSKI DERIVATI KOT SUBSTRATI V REAKCIJAH C–H AKTIVACIJE
Mentor: izr. prof. dr. Franc Požgan
Datum zagovora: 2. 7. 2018

FERJAN, ŠPELA
FOTOKATALITIČNA PRODUKCIJA VODIKA Z CU/TIO2 KATALIZATORJEM
Mentor: prof. dr. Miran Gaberšček
Datum zagovora: 2. 7. 2018

RATAJ, JAN
ANALIZA TEKOČIH PRODUKTOV HIDROGENIRANJA LEVULINSKE KISLINE
Mentor: doc. dr. Aleš Ručigaj
Datum zagovora: 3. 7. 2018

KRIŽNIČ, KLARA
ŠKODLJIVI UČINKI HRUPA NA ZAPOSLENE V ODPRTIH PISARNAH
Mentor: doc. dr. Klementina Zupan
Datum zagovora: 4. 7. 2018

MARINIČ, DANA
VPLIV DIELS-ALDER ADUKTA NA ZAMREŽENE EPOKSIDNE SMOLE
Mentor: doc. dr. Aleš Ručigaj
Datum zagovora: 5. 7. 2018

ZALAR, ANŽE
SURFAKTANTI V ATMOSFERSKIH AEROSOLIH
Mentor: doc. dr. Bojan Šarac
Datum zagovora: 6. 7. 2018

HUDOVERNIK, ELA
SINTEZA SILILIRANEGA KISLINSKEGA DERIVATA SIMVASTATINA ZA PRIPRAVO BIOLOŠKO AKTIVNIH KOMPLEKSOV S CISPLATINOM
Mentor: prof. dr. Janez Košmrlj
Datum zagovora: 6. 7. 2018

PENKO, ANA
PRIMERNOST UPORABE METODE ELISA ZA UGOTAVLJANJE PRISOTNOSTI PROTEINOV V UMETNIŠKIH BARVAH
Mentor: izr. prof. dr. Irena Kralj Cigić
Datum zagovora: 10. 7. 2018

LAVRIHA, PIA
IZRAŽANJE IN IZOLACIJA NANOTELES PROTI MLKL N154 IN ANALIZA VEZAVE NANOTELESA 3MLK_84 NA MLKL N154
Mentor: doc. dr. Gregor Gunčar
Datum zagovora: 10. 7. 2018

AGREŽ, BARBARA
PEROVSKITNE SONČNE CELICE
Mentor: izr. prof. dr. Matija Tomšič
Datum zagovora: 10. 7. 2018

GAŠPARIČ, LEA
VPLIV VODIKOVE VEZI NA LASTNOSTI KEMIJSKIH IN BIOLOŠKIH SISTEMOV
Mentor: prof. dr. Andrej Jamnik
Datum zagovora: 10. 7. 2018

ANTONČIČ, TEJA
VREDNOTENJE UČINKOVITOSTI SISTEMA ZA PRIPRAVO PITNE VODE IZ POVRŠINSKEGA VIRA
Mentor: izr. prof. dr. Andreja Žgajnar Gotvajn
Datum zagovora: 11. 7. 2018

ŽIBERT, TAJA
VINIL ALKOHOL V MEDZVEZDNEM PROSTORU
Mentor: prof. dr. Tomaž Urbič
Datum zagovora: 11. 7. 2018

OSTANEK JURINA, LEON
Mentor: prof. dr. Polona Žnidaršič Plazl
Datum zagovora: 11. 7. 2018

RIJAVEC, MARŠA
Mentor: prof. dr. Urška Šebenik
Datum zagovora: 11. 7. 2018

PETROVIĆ, VITO
NESREČA V NUKLEARNI ELEKTRARNI ČERNOBIL: VZROKI IN POSLEDICE
Mentor: doc. dr. Mitja Robert Kožuh
Datum zagovora: 12. 7. 2018

ANTOLIĆ, MATEJ
INHALABILNOST KOVINSKIH DELCEV
Mentor: prof. dr. Marija Bešter Rogač
Datum zagovora: 12. 7. 2018

FERČEC, URBAN
IZRAŽANJE, IZOLACIJA IN KARAKTERIZACIJA HUMANIH KASPAZ-4 IN -5
Mentor: prof. dr. Boris Turk
Datum zagovora: 12. 7. 2018

ARH, NEJC
OBLIKOVANJE IN PRIPRAVA NANOTELES ZA SIMETRIČNO DIMERIZACIJO NA OSNOVI KOORDINACIJE KOVINSKIH IONOV
Mentor: doc. dr. Gregor Gunčar
Datum zagovora: 13. 7. 2018

KRIŽAJ, NINA
ENOSTAVNI ANALITIČNI MODEL VODE IN HIDROFOBNE HIDRATACIJE
Mentor: izr. prof. dr. Miha Lukšič
Datum zagovora: 13. 7. 2018

KLEMENČIČ, EVA
VPLIV AKTIVACIJE MAKROFAGOV NA IZRAŽANJE IN IZLOČANJE KATEPSINA C
Mentor: prof. ddr. Boris Turk
Datum zagovora: 13. 7. 2018

LUKŠIČ, TJAŠA
EVOLUCIJSKA DINAMIKA TRANSKRIPCIJSKIH FAKTORJEV PRI HOMINIDIH
Mentor: izr. prof. dr. Dušan Kordiš
Datum zagovora: 1. 8. 2018

MENCIGAR, MATEVŽ
BIOKATALITSKI PROCESI S CELICAMI V MINIATURIZIRANIH REAKTORJIH
Mentor: prof. dr. Polona Žnidaršič Plazl
Datum zagovora: 17. 8. 2018

KOVŠE, ALEN
RAZVOJ KOMPOZITNEGA MATERIALA ZAVORNIH PLOŠČIC
Mentor: izr. prof. dr. Marjan Marinšek
Datum zagovora: 22. 8. 2018

VEHAR, ANJA
VPLIV KAVITACIJSKEGA PREDČIŠČENJA ODPADNE VODE NA RAZBREMENITEV ULTRAFILTRACIJSKIH MODULOV
Mentor: izr. prof. dr. Andreja Žgajnar Gotvajn
Datum zagovora: 23. 8. 2018

PRIMOŽIČ, LUCIJA
RAZGRADNJA IN RAZBARVANJE ODPADNEGA PAPIRJA S POMOČJO GLIVE DICHOMITUS SQUALRNS
Mentor: doc. dr. Gabriela Kalčikova
Datum zagovora: 23. 8. 2018

HOČEVAR, JOŠT
VLOGA HIDROFOBNEGA ŽEPA EPCAM IN TROP2 PRI SIGNALIZIRANJU PREKO REGULIRANE INTRAMEMBRANSKE CEPITVE
Mentor: doc. dr. Miha Pavšič
Datum zagovora: 24. 8. 2018

HEINDLER, ANŽE
VARNO SKLADIŠČENJE IN UPORABA VODIKOVEGA KLORIDA
Mentor: doc. dr. Barbara Novosel
Datum zagovora: 29. 8. 2018

LIPOVŠEK, AGATA
SINTEZA PRIPOJENIH DERIVATOV 3-BENZOILAMINO-2H-PIRAN-2-ONA, 5-BENZOILNEGA ANALOGA IN NADALJNJE [4+2] CIKLOADICIJE Z MALEINANHIDRIDOM IN N-FENILMALEIMIDOM
Mentor: doc. dr. Krištof Kranjc
Datum zagovora: 30. 8. 2018

KAMIN, REBEKA
SINTEZA 6-SUBSTITUIRANIH 3-BENZOILAMINO-2H-PIRAN-2-ONSKIH DERIVATOV IN NJIHOVA UPORABA V DIELS–ALDERJEVIH REAKCIJAH Z MALEINANHIDRIDOM POD KLASIČNIMI IN MIKROVALOVNIMI POGOJI
Mentor: doc. dr. Krištof Kranjc
Datum zagovora: 30. 8. 2018

BERGLEZ, TILEN
SIPANJE SVETLOBE NA OKROGLIH STRUKTURAH: TOGA KROGLA, VOTLA KROGLA IN VEZIKLI
Mentor: prof. dr. Ksenija Kogej
Datum zagovora: 30. 8. 2018

FRIŠKOVEC VONČINA, ŠPELA
REAKCIJE BAKROVEGA(II) KLORIDA S PIRIDIN-2-ONOM IN PIRAZINOM
Mentor: doc. dr. Saša Petriček
Datum zagovora: 31. 8. 2018

MENART, SVIT
PRETVORBA KETONOV V SILILNE DERIVATE GEM-DIHIDROPEROKSIDOV
Mentor: izr. prof. dr. Jernej Iskra
Datum zagovora: 3. 9. 2018

SLABAJNA, BLAŽ
RENTGENSKA PRAŠKOVNA DIFRAKCIJA GEOLOŠKIH VZORCEV
Mentor: prof. dr. Anton Meden
Datum zagovora: 3. 9. 2018

ŠVIGELJ, NINA
VPLIV UČINKOVINE NA OSNOVI NUKLEINSKIH KISLIN NA RAZPAD TARČNIH PROTEINOV
Mentor: doc. dr. Aleš Ručigaj
Datum zagovora: 3. 9. 2018

KOTNIK, JAN
MATEMATIČNI OPIS SPROŠČANJA UČINKOVIN IZ POLIMERNIH HIDROGELOV
Mentor: doc. dr. Aleš Ručigaj
Datum zagovora: 3. 9. 2018

POGAČAR, ŽIGA
MODELI PRENOSA SNOVI V HIDROGELIH
Mentor: prof. dr. Matjaž Krajnc
Datum zagovora: 3. 9. 2018

PONIKVAR, ŽIGA
SINTEZA NEKATERIH 5,6-DISUBSTITUIRANIH 3-BENZOILAMINO-2H-PIRAN-2-ONOV IN NJIHOVA UPORABA V CIKLOADICIJAH Z MALEINANHIDRIDOM IN N-SUBSTITUIRANIM MALEIMIDOM
Mentor: doc. dr. Krištof Kranjc
Datum zagovora: 4. 9. 2018

DOLHAR, DAVID
SINTEZA IN LASTNOSTI t-BUTIL AZIDOFORMATA
Mentor: prof. dr. Janez Košmrlj
Datum zagovora: 4. 9. 2018

STIBILJ, KRISTJAN
IZOLACIJA IN IDENTIFIKACIJA GLIV IZ BAZENSKIH VODA TER VPLIV NATRIJEVEGA HIPOKLORITA NA RAST IZBRANIH GLIV
Mentor: prof. dr. Iztok Turel
Datum zagovora: 5. 9. 2018

BANFI, PRIMOŽ
STRUKTURA IN KARAKTERISTIKE SIDEROFOROV
Mentor: doc. dr. Črtomir Podlipnik
Datum zagovora: 5. 9. 2018

BRCAR, IDA
POSKUSI SONOGASHIROVEGA PRIPAJANJA Z ARIL KLORIDI
Mentor: prof. dr. Janez Košmrlj
Datum zagovora: 5. 9. 2018

CERNATIČ, FILIP
UPORABA METOD KEMOINFORMATIKE PRI RAZVOJU ANTIMALARIKOV
Mentor: doc. dr. Črtomir Podlipnik
Datum zagovora: 5. 9. 2018

BORŠIĆ, ELVIRA
SILILIRANJE KISLINSKEGA DERIVATA SIMVASTATINA
Mentor: prof. dr. Janez Košmrlj
Datum zagovora: 6. 9. 2018

ZUPANC, MAJA
URAVNAVANJE SIGNALIZACIJE TLR4/NF-?B/IL-6 V POVEZAVI S PRESNOVNO IN ENDOKRINO VLOGO SKELETNE MIŠICE
Mentor: prof. dr. Tomaž Marš
Datum zagovora: 6. 9. 2018

MALNARIČ, IRIS
EPOKSIDNI POLIMERI S SPOSOBNOSTJO SAMOCELJENJA
Mentor: doc. dr. Aleš Ručigaj
Datum zagovora: 6. 9. 2018

PRIVŠEK, PETRA
VPLIV RECIKLIRANJA NA REOLOŠKE IN TERMIČNE LASTNOSTI HDPE
Mentor: doc. dr. Lidija Slemenik Perše
Datum zagovora: 6. 9. 2018

KAPŠ, ŠPELA
SAMOCELJENJE POLIMERNIH MATERIALOV NA OSNOVI FOTOKEMIČNIH REAKCIJ
Mentor: doc. dr. Aleš Ručigaj
Datum zagovora: 6. 9. 2018

HERMAN, JOŠT
MORFOLOŠKE LASTNOSTI LIOFILIZIRANEGA GRAFEN OKSIDA IN GRAFENA
Mentor: doc. dr. Boštjan Genorio
Datum zagovora: 6. 9. 2018

ARNŠEK, MAŠA
UPORABA POLIMEROV Z OBLIKOVNIM SPOMINOM V BIOMEDICINI
Mentor: prof. dr. Urška Šebenik
Datum zagovora: 6. 9. 2018

ČUJEŠ, ANA
UPORABA NANOCELULOZE V BIOMEDICINI
Mentor: prof. dr. Urška Šebenik
Datum zagovora: 6. 9. 2018

BIZJAK, OŽBEJ
POLIHIPE
Mentor: izr. prof. dr. Aleš Podgornik
Datum zagovora: 6. 9. 2018

PELC, TIN
ADSORPCIJA BIOLOŠKIH MAKROMOLEKUL NA POVRŠINE
Mentor: izr. prof. dr. Aleš Podgornik
Datum zagovora: 6. 9. 2018

LEBAR, SERGEJA
UPORABA MEMBRANSKIH SUPRESORJEV ZA ODSTRANJEVANJE MOTEČIH IONOV
Mentor: prof. dr. Matevž Pompe
Datum zagovora: 6. 9. 2018

MOŽINA, JERNEJ
PAMETNE NAPRAVE NA OSNOVI POLIMEROV S SPOMINSKIM UČINKOM
Mentor: prof. dr. Urška Šebenik
Datum zagovora: 6. 9. 2018

KELHAR, NUŠA
IZBOLJŠANJE PROTOKOLA BLOKADE NEŽELENE VEZAVE PROTITELES PRI IMUNOOZNAČEVANJU PROTEINOV V TKIVNIH PREPARATIH
Mentor: prof. dr. Peter Veranič
Datum zagovora: 7. 9. 2018

PILPAH, TILEN
MIKROBIOREAKTORJI S TREMI FAZAMI
Mentor: prof. dr. Polona Žnidaršič Plazl
Datum zagovora: 7. 9. 2018

ŠADL, ALEN
SINTEZA IN DERIVATIZACIJA TIENIL KETONOV
Mentor: izr. prof. dr. Franc Požgan
Datum zagovora: 7. 9. 2018

ERHATIČ, JERNEJA
REAKCIJE BAKROVEGA(II) KLORIDA Z N-(2-PIRIDIL) PIRIDIN-2-TIOKARBOKSAMIDOM
Mentor: doc. dr. Andrej Pevec
Datum zagovora: 7. 9. 2018

ŽUNTAR, JAN
MODIFICIRANI SEPARATORJI V LITIJ-KOVINSKIH AKUMULATORJIH
Mentor: izr. prof. dr. Robert Dominko
Datum zagovora: 7. 9. 2018

KOZAMERNIK, MARK
FUNKCIONALIZACIJA GRAFENSKIH NANOTRAKOV ZA UPORABO V POLIMERNIH NANOKOMPOZITIH
Mentor: doc. dr. Boštjan Genorio
Datum zagovora: 7. 9. 2018

HRUP, MARTIN
INFRARDEČI SPEKTRI ALKOHOLAMINOV
Mentor: doc. dr. Barbara Modec
Datum zagovora: 7. 9. 2018

BAVČAR, MOJCA
ŠTUDIJ REAKCIJE ?-PINENA S HIDROKSILNIM RADIKALOM
Mentor: prof. dr. Matevž Pompe
Datum zagovora: 7. 9. 2018

RAJH, EVA
HISTOKEMIJSKA KAREKTERIZACIJA ORGANSKEGA MATRIKSA PRI RAKU PORCELLIO SCABER
Mentor: doc. dr. Nada Žnidaršič
Datum zagovora: 10. 9. 2018

ROGAN, MATIC
REAKTIVNOST ORGANSKIH SPOJIN PRI RAZLIČNIH POGOJIH
Mentor: izr. prof. dr. Marjan Jereb
Datum zagovora: 10. 9. 2018

HLEBŠ, TINA
OSEBNA VAROVALNA OPREMA GASILCA IN PRAKTIČNI PROBLEMI PRI NJENI UPORABI
Mentor: izr. prof. dr. Matija Tomšič
Datum zagovora: 10. 9. 2018

HRUŠEVAR, PETRA
IZOLACIJA IN KARAKTERIZACIJA BAKTERIJ ČLOVEŠKE RIBICE
Mentor: doc. dr. Martina Turk
Datum zagovora: 10. 9. 2018

GOSTENČNIK, ŽAN
SINTEZA LIGANDOV ZA ORGANOKOVINSKE KOMPLEKSE
Mentor: izr. prof. dr. Janez Cerkovnik
Datum zagovora: 10. 9. 2018

MAROLT, ŠPELA
OVREDNOTENJE VOLUMETRIČNIH OPERACIJ, IZVEDENIH S ČRPALKO NA OSNOVI BRIZGE
Mentor: izr. prof. dr. Nataša Gros
Datum zagovora: 10. 9. 2018

ŠMAJDEK, SVIT
REDOKS TITRACIJE Z ELEKTROKEMIJSKO DETEKCIJO KONČNE TOČKE
Mentor: izr. prof. dr. Nataša Gros
Datum zagovora: 10. 9. 2018

KRUŠIČ, JANA
ORGANOKATALIZIRANA SPIROCIKLIZACIJA METIL (5Z)-5-BENZILIDEN-1,2-DIMETIL-4-OKSO-4,5-DIHIDRO-1H-PIROL-3-KARBOKSILATA
Mentor: doc. dr. Uroš Grošelj
Datum zagovora: 11. 9. 2018

ČERNIČ, TINA
VPLIV ANTIBIOTIKOV NA MALO VODNO LEČO
Mentor: doc. dr. Gabriela Kalčikova
Datum zagovora: 11. 9. 2018

ZUPANČIČ, KLEMEN
ZMANJŠEVANJE EMISIJ PRAŠNIH DELCEV PM10
Mentor: izr. prof. dr. Andreja Žgajnar Gotvajn
Datum zagovora: 12. 9. 2018

KREJAN, EVA
PRIMERJAVA ORGANSKIH IN RUTENIJEVIH BARVIL V ELEKTROKEMIJSKIH SONČNIH CELICAH
Mentor: prof. dr. Urška Lavrenčič Štangar
Datum zagovora: 12. 9. 2018

ŠIMENC, JAKA
IZBIRA IN PRIPRAVA MATERIALA ZA TEHNOLOGIJO 3D TISKANJA
Mentor: doc. dr. Aleš Ručigaj
Datum zagovora: 12. 9. 2018

LIPOVŠEK, JAN
ANALIZA EVAKUACIJSKEGA ČASA V POSLOVNEM OBJEKTU S PROGRAMOM PATHFINDER
Mentor: izr. prof. dr. Simon Schnabl
Datum zagovora: 12. 9. 2018

SUŠNIK, MIHA
UKREPI ZA VARNO UPORABO ČISTIL
Mentor: doc. dr. Barbara Novosel
Datum zagovora: 12. 9. 2018

KOZOLE, MOJCA
ADSORPCIJA IZBRANIH KOVIN NA MIKROPLASTIKO
Mentor: doc. dr. Gabriela Kalčikova
Datum zagovora: 12. 9. 2018

PIRC, KARMEN
ADSORPCIJA MIKROPLASTIKE NA AKTIVNO BLATO IZ BIOLOŠKE ČISTILNE NAPRAVE
Mentor: doc. dr. Gabriela Kalčikova
Datum zagovora: 12. 9. 2018

BELLINA, NIKOL
ERGONOMSKO OBLIKOVANJE DELOVNEGA MESTA PRI IZDELAVI AVTOMOBILSKIH DELOV
Mentor: doc. dr. Klementina Zupan
Datum zagovora: 12. 9. 2018

ŽULA, MATEJ
ČIŠČENJE ODPADNIH VOD S KAVITACIJO
Mentor: izr. prof. dr. Andreja Žgajnar Gotvajn
Datum zagovora: 12. 9. 2018

BELINGAR, LUCIJA
PRIPRAVA IN KARAKTERIZACIJA BIOOGLJA IZ LIGNOCELULOZNE BIOMASE
Mentor: izr. prof. dr. Andreja Žgajnar Gotvajn
Datum zagovora: 12. 9. 2018

VIDRIH, ŽIGA
PRIPRAVA IN KARAKTERIZACIJA BIOOGLJA IZ LESNE BIOMASE
Mentor: izr. prof. dr. Andreja Žgajnar Gotvajn
Datum zagovora: 12. 9. 2018

BREZAR, TINA
INŠPEKCIJA DELA NA PODROCJU VARNOSTI IN ZDRAVJA PRI DELU
Mentor: Luka Tičar
Datum zagovora: 12. 9. 2018

LUKANČIČ, KATJA
OCENA ODSTRANJEVANJA CELOTNEGA FOSFORJA IZ ODPADNIH VOD NA CČN LJUBLJANA
Mentor: doc. dr. Gabriela Kalčikova
Datum zagovora: 12. 9. 2018

ZABRET, POLONA
POSINTEZNA MODIFIKACIJA TITANOVIH IN CIRKONIJEVIH KOVINSKO-ORGANSKIH MREŽ
Mentor: izr. prof. dr. Franc Perdih
Datum zagovora: 13. 9. 2018

TITOVŠEK, DAVID
Mentor: prof. dr. Kristina Djinović Carugo
Datum zagovora: 13. 9. 2018

SEME, TANJA
VPLIV KAVITACIJE NA RAZGRADJO BARVILA ZA TEKSTIL
Mentor: prof. dr. Matevž Dular
Datum zagovora: 13. 9. 2018

HALAS, JANEZ
PADEC TLAKA NA POROZNIH NOSILCIH
Mentor: izr. prof. dr. Aleš Podgornik
Datum zagovora: 13. 9. 2018

PERIC, TANJA
KARAKTERIZACIJA VPLIVA KOMPONENT PROTEINSKEGA KOMPLEKSA PERMES NA ACETILACIJO HISTONOV
Mentor: izr. prof. dr. Uroš Petrovič
Datum zagovora: 13. 9. 2018

ZORKO, DAVID
SPEKTROFOTOMETRIČNO DOLOČEVANJE MONOSAHARIDOV
Mentor: izr. prof. dr. Mitja Kolar
Datum zagovora: 13. 9. 2018

KORDEŽ, MAY
DOLOČANJE HLAPNIH SPOJIN V PIVU
Mentor: prof. dr. Helena Prosen
Datum zagovora: 13. 9. 2018

ŠPEGEL, MATEJA
DOLOČANJE KLORIRANIH TRIAZINSKIH PESTICIDOV V VODI Z GC-ECD
Mentor: prof. dr. Helena Prosen
Datum zagovora: 13. 9. 2018

VAN MIDDEN, KATARINA PETRA
PRIPRAVA VZORCEV ZA IDENTIIKACIJO INTERAKCIJSKIH PARTNERJEV PROTEINA FUS
Mentor: izr. prof. dr. Boris Rogelj
Datum zagovora: 14. 9. 2018

KAVČIČ, SANDI
STRUKTURA IN REAKTIVNOST PROSTIH RADIKALOV
Mentor: prof. dr. Tomaž Urbič
Datum zagovora: 14. 9. 2018

ŠTRANCAR, VIDA
OSNOVNA BIOKEMIJSKA KARAKTERIZACIJA METAKASPAZE TIPA 2 MODELNEGA ALGNEGA ORGANIZMA CHLAMYDOMONAS REINHARDTII
Mentor: izr. prof. dr. Marko Dolinar
Datum zagovora: 14. 9. 2018

KLANČNIK, BOR
SINTEZA IZOTIOCIANATNIH DERIVATOV ISATINA IN NJIHOVA UPORABA V ORGANOKATALIZIRANI KASKADNI REAKCIJI
Mentor: doc. dr. Uroš Grošelj
Datum zagovora: 14. 9. 2018

LOČNIŠKAR, JAN
OKSIDACIJA CIMETOVE IN FERULNE KISLINE V BENZALDEHID IN VANILIN
Mentor: izr. prof. dr. Jernej Iskra
Datum zagovora: 14. 9. 2018

VALETIČ, VASJA
Mentor: prof. dr. Iztok Turel
Datum zagovora: 14. 9. 2018

POGORELC, EVA
GOSTOTA IN VISKOZNOST VODNIH RAZTOPIN FUNKCIONALIZIRANIH KVARTERNIH OKTILAMONIJEVIH SURFAKTANTOV
Mentor: prof. dr. Marija Bešter Rogač
Datum zagovora: 14. 9. 2018

MLINAR, ŽIGA
DOLOČANJE RAZGRADNIH PRODUKTOV KOFEINA S TEKOČINSKO KROMATOGRAFIJO
Mentor: izr. prof. dr. Drago Kočar
Datum zagovora: 14. 9. 2018

GRIŽNIK, MOJCA
SINTEZA IN KARAKTERIZACIJA CINK-ALUMINIJEVIH PLASTOVITIH DVOJNIH HIDROKSIDOV
Mentor: izr. prof. dr. Romana Cerc Korošec
Datum zagovora: 14. 9. 2018

MASELJ, NIK
SINTEZA DIHALOJODATOV IN NJIHOVIH AMONIJEVIH SOLI
Mentor: izr. prof. dr. Jernej Iskra
Datum zagovora: 14. 9. 2018

VESEL, MATEJ
ERGONOMSKI PROBLEMI ZARADI PRETEŽNO SEDEČEGA DELA
Mentor: doc. dr. Klementina Zupan
Datum zagovora: 14. 9. 2018

BELAK VIVOD, MATIC
PRIPRAVA IN POMENE NAČRTOVANIH BIOLOŠKIH MOLEKUL
Mentor: prof. dr. Barbara Hribar Lee
Datum zagovora: 14. 9. 2018

ROČNIK, TINA
VPLIV VPELJAVE BIOTRANSFORMACIJ NA TRAJNOST KEMIJSKEGA PROCESA Mentor: prof. dr. Polona Žnidaršič Plazl
Datum zagovora: 14. 9. 2018

SINIČ, TADEJ
MATERIALI ZA SOLARNE CELICE
Mentor: izr. prof. dr. Marjan Marinšek
Datum zagovora: 17. 9. 2018

ŽIVIČ, ZALA
VPLIV AMINOKISLINSKEGA ZAPOREDJA NA TERMODINAMIKO INTERAKCIJE INTRINZIČNO NEUREJENIH PROTEINOV S TARČO
Mentor: prof. dr. Jurij Lah
Datum zagovora: 17. 9. 2018

SEDEJ, NELI
IDENTIFIKACIJA IN OPREDELITEV NARAVNIH VARIANT LANOSTEROL 14
-DEMETILAZE IN SILICO
Mentor: prof. dr. Damjana Rozman
Datum zagovora: 17. 9. 2018

HALUŽAN VASLE, ANA
VPLIV AKTIVACIJE ADRENERGIČNIH RECEPTORJEV NA ŠTEVILO IN VELIKOST LIPIDNIH KAPLJIC V PODGANJIH ASTROCITIH V KULTURI
Mentor: doc. dr. Nina Vardjan
Datum zagovora: 17. 9. 2018

SMERDU, MARK
GRAFEN OKSID KOT DODATEK PREMAZOM ZA SONČNE ABSORBERJE
Mentor: doc. dr. Boštjan Genorio
Datum zagovora:17. 9. 2018

MOTALN, KLEMEN
UVOD V NOVO ENCIMSKO KINETIKO
Mentor: prof. dr. Igor Plazl
Datum zagovora: 17. 9. 2018

KOLARIČ, MITJA
PRETVORBE ORGANSKIH SPOJIN S KISIKOVIMI FUNKCIONALNIMI SKUPINAMI
Mentor: izr. prof. dr. Marjan Jereb
Datum zagovora: 17. 9. 2018

MARINKO, ALJOŠA
IZOLACIJA CRISP IZ STRUPA MODRASA (VIPERA AMMODYTES AMMODYTES) IN NJIHOV VPLIV NA CELIČNO LINIJO RAKA DOJKE
Mentor: prof. dr. Igor Križaj
Datum zagovora: 17. 9. 2018

DIZDAREVIĆ, ŠEJLA
LITIJ-ŽVEPLOVE BATERIJE ZA KOMERCIALNO UPORABO
Mentor: prof. dr. Miran Gaberšček
Datum zagovora: 17. 9. 2018

RUPNIK, ALEN
IZDELAVA PRETOČNIH REAKTORSKIH SISTEMOV S TEHNOLOGIJO 3D TISKANJA
Mentor: doc. dr. Aleš Ručigaj
Datum zagovora: 17. 9. 2018

GREBENC, ANDREJ
PREGLED NAPREDNIH METOD ZA OPIS TRKOV V MREŽNI BOLTZMANNOVI METODI
Mentor: prof. dr. Igor Plazl
Datum zagovora: 17. 9. 2018

KAVČNIK, ANDREJA
ELEKTROKEMIJA V MIKROREAKTORJIH
Mentor: prof. dr. Igor Plazl
Datum zagovora: 17. 9. 2018

ŽIVIČ, SUZANA
REAKTIVNOST ORGANSKIH SPOJIN PRI KLASIČNIH IN ALTERNATIVNIH POGOJIH
Mentor: izr. prof. dr. Marjan Jereb
Datum zagovora: 17. 9. 2018

OCVIRK, MANCA
DOLOČEVANJE HLAPNIH SPOJIN V MEDU
Mentor: izr. prof. dr. Drago Kočar
Datum zagovora: 17. 9. 2018

REBERNIK, MIHAELA
SINTEZA IN KARAKTERIZACIJA TERNARNIH ORGANORUTENIJEVIH KOMPLEKSOV S PIRITIONOM IN FOSFINI
Mentor: doc. dr. Jakob Kljun
Datum zagovora: 17. 9. 2018

KORENČIČ, EVA
PRIMERJAVA ALKALNE ZALOGE V TESTNIH LISTIH IN KNJIGAH PO RAZKISLINJENJU
Mentor: izr. prof. dr. Irena Kralj Cigić
Datum zagovora:17. 9. 2018

KOLMAN, NEJC
REOLOŠKE LASTNOSTI VODNIH RAZTOPIN POLIETILEN GLIKOLA OB PRISOTNOSTI RAZLIČNIH SOLI
Mentor: izr. prof. dr. Janez Cerar
Datum zagovora: 17. 9. 2018

MUŠIČ, PETER
POŽARNA VARNOST PRI SKLADIŠČENJU GUM
Mentor: doc. dr. Domen Kušar
Datum zagovora:17. 9. 2018

KRAJNC, DOROTEJA
ZAMENJAVA TIO2 Z ZRO2 V BELIH PIGMENTNIH PREMAZIH
Mentor: izr. prof. dr. Marjan Marinšek
Datum zagovora: 17. 9. 2018

LESJAK, TINA
ERGONOMSKA ANALIZA DELOVNEGA MESTA PRI PROIZVODNJI ULITKOV V PODJETJU TALUM D. D. KIDRIČEVO
Mentor: doc. dr. Klementina Zupan
Datum zagovora: 17. 9. 2018

KRAGELJ, MIHA
VPLIV KAKOVOSTI SUROVINE NA LASTNOSTI ŽGANIH GLINENIH IZDELKOV
Mentor: izr. prof. dr. Marjan Marinšek
Datum zagovora: 17. 9. 2018

KOTNIK, LOVRO
OKSIDATIVNA ADICIJA 2-JODOETINILBENZENOVIH DERIVATOV NA PALADIJ
Mentor: prof. dr. Janez Košmrlj
Datum zagovora: 17. 9. 2018

ERHATIČ, KLEMEN
IZDELAVA IN RAZVOJ MIKROFLUIDNE NAPRAVE ZA SUHI REFORMING BIOPLINA
Mentor: prof. dr. Igor Plazl
Datum zagovora: 17. 9. 2018

ADAMEK, MAKSIMILJAN
VPLIVI GVAJAKOLA IN NEKATERIH NJEGOVIH DERIVATOV NA FIZIOLOGIJO RASTLIN
Mentor: izr. prof. dr. Marko Novinec
Datum zagovora: 17. 9. 2018

TOMC, ANŽE
POVEČEVALNI EFEKTI PROCESA OZONACIJE BIORAZGRADLJIVIH SNOVI V MIKROSISTEMIH
Mentor: prof. dr. Igor Plazl
Datum zagovora: 18. 9. 2018

GREGO, MARTIN
VPLIV SVETLOBE NA MELATONIN V ČLOVEKU
Mentor: prof. dr. Grega Bizjak
Datum zagovora: 18. 9. 2018

TRUDEN, ANJA
SINTEZA IZBRANIH 1,4-DIARIL-1,2,3-TRIAZOLOV
Mentor: prof. dr. Janez Košmrlj
Datum zagovora: 18. 9. 2018

LIPOVŠEK, MATEJ
VARNOST PRI PRIPRAVI PREMAZOV ZA PROIZVODNJO KARTONA
Mentor: doc. dr. Barbara Novosel
Datum zagovora: 18. 9. 2018

JANKOVIČ, DOMINIK
SINTEZA 1-ALKIL-4-ARIL-1,2,3-TRIAZOLOV
Mentor: doc. dr. Martin Gazvoda
Datum zagovora: 18. 9. 2018

SILJANOVSKA, ANA
PRIPRAVA STABILNIH DIAZOIJEVIH SOLI
Mentor: prof. dr. Janez Košmrlj
Datum zagovora: 18. 9. 2018

ŽNIDARIČ, MATEJA
4-METOKSIBENZIL AZID KOT REAGENT ZA PRIPRAVO TRIAZOLOV
Mentor: doc. dr. Martin Gazvoda
Datum zagovora: 18. 9. 2018

KLANČIŠAR, DAVID
PREPREČEVANJE ZASTRUPITEV Z OGLJIKOVIM OKSIDOM
Mentor: doc. dr. Barbara Novosel
Datum zagovora: 18. 9. 2018

NOVAK, VALENTINA
PRIPRAVA ČLOVEŠKIH PROTEINOV ANEKSINA A11 IN TRANSPORTINA 1 TER KARAKTERIZACIJA NJUNE VEZAVE
Mentor: doc. dr. Vera Župunski
Datum zagovora: 19. 9. 2018

VIDMAR, TIM
ANALIZA HIPOTETIČNEGA POŽARA NA KOLONSKO SKLADIŠČNEM PROSTORU V LESNO PREDELOVALNEM OBRATU
Mentor: izr. prof. dr. Simon Schnabl
Datum zagovora: 19. 9. 2018

ERZIN, ANJA
VIRUSI V ODPADNIH VODAH TER NJIHOVO ODSTRANJEVANJE
Mentor: izr. prof. dr. Andreja Žgajnar Gotvajn
Datum zagovora: 19. 9. 2018

BEMBIČ, PRIMOŽ
IDENTIFIKACIJA PROTEINSKIH TARČ MALOMOLEKULSKEGA LIGANDA Z AFINITETNO KROMATOGRAFIJO
Mentor:izr. prof. dr. Marko Novinec
Datum zagovora:19. 9. 2018

GERJOL, POLONA
VPLIV NANODELCEV NA OKOLJE
Mentor: prof. dr. Marija Bešter Rogač
Datum zagovora: 19. 9. 2018

KOS, JAKA
VPLIV NEKATERIH ARGININSKIH OSTANKOV NA VEZAVO HEPARINA NA KATEPSIN B
Mentor: izr. prof. dr. Marko Novinec
Datum zagovora: 19. 9. 2018

OJSTERŠEK, ADRIJANA
VLOGA BIOTRANSFORMACIJ V BIOTEHNOLOGIJI
Mentor: prof. dr. Polona Žnidaršič Plazl
Datum zagovora: 19. 9. 2018

HUDELJA, POLONA
VPLIV CELULOZNIH NANOVLAKEN NA TRIBOLOŠKE LASTNOSTI IN FAZNE SPREMEMBE KERAMIKE 3Y-TZP, V NAMEN PREVERJANJA PLAGIATORSTVA
Mentor: doc. dr. Bojan Kozlevčar
Datum zagovora: 21. 9. 2018

KRANJC PEČENKO, JAN
AVTOMATSKI PROTIPOŽARNI SISTEM PROTENG FM200
Mentor: izr. prof. dr. Simon Schnabl
Datum zagovora: 28. 9. 2018

MATEKOVIČ, JURE
ALKALNO-SILIKATNA REAKCIJA V BETONU
Mentor: izr. prof. dr. Marjan Marinšek
Datum zagovora: 1. 10. 2018

ŽIBERT, SARA
VPLIV VISKOELASTIČNIH LASTNOSTI POLTRDNIH SNOVI (KRUHA, TESTA) NA PROCES GNETENJA
Mentor: doc. dr. Lidija Slemenik Perše
Datum zagovora: 22. 11. 2018

FINK, ANJA
Mentor: prof. dr. Miran Gaberšček
Datum zagovora: 7. 12. 2018

IZAK, SARA ANA
SINTEZA IN DERIVATIZACIJA 3-PIRAZOLIDINONOV
Mentor: izr. prof. dr. Bogdan Štefane
Datum zagovora: 12. 12. 2018

KODERMAC, META ŠPELA
PALADIJ-KATALIZIRANO ARILIRANJE 4-HIDROKSIBENZIL AMINSKIH DERIVATOV
Mentor: izr. prof. dr. Bogdan Štefane
Datum zagovora: 12. 12. 2018

VRHUNEC, ENEJ
VPLIV PH NA MEHANSKO TRDNOST MELAMIN-FORMALDEHIDNIH MIKROKAPSUL
Mentor: izr. prof. dr. Marjan Marinšek
Datum zagovora: 14. 12. 2018

FIDEL, JAKA
POSREDOVANJE GASILCEV PRI POŽARIH VOZIL NA ALTERNATIVNE POGONE
Mentor: izr. prof. dr. Simon Schnabl
Datum zagovora: 19. 12. 2018

DIPLOME - VISOKOŠOLSKI STROKOVNI ŠTUDIJ

KEMIJSKA TEHNOLOGIJA – 1. STOPNJA

BAHOR, JERNEJA
BAKROVE SPOJINE Z ANIONOM AZELAINSKE KISLINE
Mentor: doc. dr. Bojan Kozlevčar
Datum zagovora: 12. 2. 2018

PROSEN, NIKA
PROGRAMI ZA AVTOMATSKO POIMENOVANJE KEMIJSKIH STRUKTUR
Mentor: doc. dr. Črtomir Podlipnik
Datum zagovora: 14. 2. 2018

ROTER, ANJA
INHALACIJSKA BIODOSTOPNOST POTENCIALNO STRUPENIH ELEMENTOV V OBCESTNIH SEDIMENTIH Z OBMOČJA IDRIJE
Mentor: doc. dr. Marija Zupančič
Datum zagovora: 16. 2. 2018

ZEC, SANDRA
ŠTUDIJA INHALACIJSKE BIODOSTOPNOSTI POTENCIALNO STRUPENIH ELEMENTOV V CESTNIH PRAHOVIH INDUSTRIJSKEGA OBMOČJA EMALAHLENI V JUŽNI AFRIKI
Mentor: doc. dr. Marija Zupančič
Datum zagovora: 16. 2. 2018

PEČJAK, SARA
ANALIZA NEKATERIH PREHRANSKIH DOPOLNIL Z RENTGENSKO PRAŠKOVNO DIFRAKCIJO
Mentor: prof. dr. Anton Meden
Datum zagovora: 16. 2. 2018

LULIĆ, ELVISA
FIZIKALNO-KEMIJSKE LASTNOSTI VZORCEV BIOOGLJA RAZLIČNIH IZVOROV
Mentor: doc. dr. Marija Zupančič
Datum zagovora: 26. 2. 2018

OBLAK, PETRA
NIKLJEVI(II) KOMPLEKSI S PIRIDIN-2-ONOM IN 3-HIDROKSIPIRIDIN-2-ONOM
Mentor: doc. dr. Saša Petriček
Datum zagovora: 28. 2. 2018

KRAGOLNIK, INES
KOORDINACIJSKE SPOJINE BAKRA(II) S KINALDINATOM IN 3-AMINO-1-PROPANOLOM
Mentor: doc. dr. Barbara Modec
Datum zagovora: 28. 2. 2018

ŽIVEC, NINA
PRIPRAVA PCP KLEŠČASTIH KOMPLEKSOV S KOVINA-OH VEZJO
Mentor: izr. prof. dr. Janez Cerkovnik
Datum zagovora: 1. 3. 2018

JANČAR, ANA
DOLOČITEV FLUORIDA V RAZLIČNIH VRSTAH VZORCEV S FLUORIDNO IONOSELEKTIVNO ELEKTRODO
Mentor: viš. pred. dr. Tatjana Zupančič
Datum zagovora: 8. 3. 2018

INTIHAR, KLARA
UPORABA GALVANSKIH ČLENOV V VSAKDANJEM ŽIVLJENJU
Mentor: prof. dr. Andrej Jamnik
Datum zagovora: 8. 3. 2018

MUHIČ, TEJA
SINTEZA (2E,5E)-BIS(DIMETILAMINOMETILIDEN) CIKLOHEKSAN-1,4-DIONA IN NJEGOVE PRETVORBE Z DIAMINI
Mentor: prof. dr. Jurij Svete
Datum zagovora: 13. 3. 2018

DOJČINOVIČ, ANA
SINTEZA IN PRETVORBA 5-(HIDROKSIMETIL) FURFURALA Z BIOTEHNOLOŠKIMI PROCESI
Mentor: prof. dr. Polona Žnidaršič Plazl
Datum zagovora: 14. 3. 2018

BORAK, GAŠPER
NAPOVEDNI MODELI ZA KLASIFIKACIJO LIGANDOV KINAZE B-RAF
Mentor: doc. dr. Črtomir Podlipnik
Datum zagovora: 19. 3. 2018

GRUBAR, KATJA
PRIPRAVA KLEŠČASTIH KOMPLEKSOV Z NEKATERIMI KOVINAMI PREHODA
Mentor: izr. prof. dr. Janez Cerkovnik
Datum zagovora: 26. 3. 2018

JAZBEC, BENJAMIN
SINTEZA IZBRANE 3-OKSOBUTANOJSKE KISLINE
Mentor: prof. dr. Janez Košmrlj
Datum zagovora: 27. 3. 2018

TOMAŽIN, MATEJA
ISKANJE ORGANOKATALIZATORJA ZA REAKCIJO 5-(3-(BENZILOKSI)-3-OKSOPROPIL)PIROLONA Z DERIVATOM ISATINIMINA
Mentor: doc. dr. Uroš Grošelj
Datum zagovora: 29. 3. 2018

KOVAČ, BLAŽ
OPTIMIZACIJA SINTEZ BAKROVIH IN KOBALTOVIH KOORDINACIJSKIH SPOJIN Z DIATRIZOATNIM LIGANDOM
Mentor: izr. prof. dr. Franc Perdih
Datum zagovora: 5. 4. 2018

GLIHA, ALEKSANDRA
SINTEZA RASTLINSKEGA HORMONA 2-(3,4-DIKLOROFENOL)TRIETILAMINA
Mentor: izr. prof. dr. Jernej Iskra
Datum zagovora: 12. 4. 2018

BALKOVEC, BARBARA
REGENERACIJA IN TESTIRANJE HPLC KOLON
Mentor: izr. prof. dr. Irena Kralj Cigić
Datum zagovora: 3. 5. 2018

CIGUT, ANA
TITRACIJSKE KRIVULJE KISLIN IN BAZ
Mentor: izr. prof. dr. Nataša Gros
Datum zagovora: 25. 5. 2018

ARNEŽ, KLEMEN
VPLIV UV SVETLOBE NA ABSORPCIJSK SPEKTER BARVILA 1,1-DIETIL-4,4 KARBOCIANIN JODID
Mentor: prof. dr. Barbara Hribar Lee
Datum zagovora: 4. 6. 2018

PFLAUM, MARGARETA
SREBROVE KOORDINACIJSKE SPOJINE Z B-DIKETONATO LIGANDI
Mentor: izr. prof. dr. Franc Perdih
Datum zagovora: 7. 6. 2018

VODA, EVA
TRDNE FAZE VODE
Mentor: izr. prof. dr. Miha Lukšič
Datum zagovora: 14. 6. 2018

GRABNAR, GAŠPER
REOLOŠKA KARAKTERIZACIJA NANOCELULOZNEGA HIDROGELA
Mentor: prof. dr. Urška Šebenik
Datum zagovora: 15. 6. 2018

PAVKOVIČ, VERONIKA
GOSTOTE ALKOHOLOV IN NJIHOVIH MEŠANIC
Mentor: prof. dr. Tomaž Urbič
Datum zagovora: 20. 6. 2018

ARHAR, SONJA
VPLIV HALS-OV NA UV STABILNOST ALKIDNEGA PREMAZA
Mentor: prof. dr. Urška Lavrenčič Štangar
Datum zagovora: 21. 6. 2018

KOLENC, MATEJ
VPLIV DIALIL FTALATA NA ZAMREŽEVANJE IN LASTNOSTI NENASIČENE POLIESTRSKE SMOLE
Mentor: viš. pred. dr. Branko Alič
Datum zagovora: 21. 6. 2018

GORŠEK, SIMONA
PRETVORBE KARBONILNIH SPOJIN
Mentor: izr. prof. dr. Marjan Jereb
Datum zagovora: 29. 6. 2018

KRŽIŠNIK, ZALA
GRADBENI MATERIALI ZA VARČEVANJE Z ENERGIJO
Mentor: doc. dr. Klementina Zupan
Datum zagovora: 5. 7. 2018

ĆOSIĆ, JANA
DOLOČEVANJE TEŽKIH KOVIN NA OBMOČJU RUDARSTVA Z METODAMA AAS IN MP-AES
Mentor: viš. pred. dr. Tatjana Zupančič
Datum zagovora: 10. 7. 2018

KORITNIK, IZTOK
PRIMERJAVA KVALITETE MIKOFENOLAT MOFETILA, SINTETIZIRANEGA IZ MIKOFENOLNE KISLINE RAZLIČNIH KVALITET
Mentor: izr. prof. dr. Janez Cerkovnik
Datum zagovora: 11. 7. 2018

STANKIĆ, ALEKSANDRA
SINTEZA NOVIH IMIDAZOLIDINONSKIH ORGANOKATALIZATORJEV NA OSNOVI FENILALANINA
Mentor: doc. dr. Uroš Grošelj
Datum zagovora: 12. 7. 2018

ZAFRAN, ANJA
VPLIV ŠTEVILA NANOSOV FOTOKATALITSKO AKTIVNIH TANKIH PLASTI TIO2 NA HITROST RAZGRADNJE BARVILA PLASMOCORINTH B
Mentor: izr. prof. dr. Romana Cerc Korošec
Datum zagovora: 13. 7. 2018

ROSIČ, NIVES
VPLIV PRETOKA KISIKA NA HITROST RAZGRADNJE BARVILA PLASMOCORINTHA B S FOTOKATALITSKO AKTIVNIMI TANKIMI PLASTMI TIO2
Mentor: izr. prof. dr. Romana Cerc Korošec
Datum zagovora: 13. 7. 2018

PIŠKUR, KRISTINA
DOLOČANJE ANORGANSKIH PIGMENTOV Z RENTGENSKO PRAŠKOVNO DIFRAKCIJO
Mentor: prof. dr. Anton Meden
Datum zagovora: 13. 7. 2018

RESNIK, SIMONA
HIDROFOBNI EFEKT
Mentor: izr. prof. dr. Miha Lukšič
Datum zagovora: 13. 7. 2018

MARKIČ, DANIJEL
POLIURETANSKI BARVNI PREMAZI NA VODNI OSNOVI
Mentor: izr. prof. dr. Marjan Marinšek
Datum zagovora: 22. 8. 2018

PORENTA, EMA
PRIMERJAVA PRIPRAVE IN FOTOKATALITSKE UČINKOVITOSTI PLASTI TIO2 PO SOL-GEL POSTOPKU IN S TEHNIKO NANAŠANJA PASTE
Mentor: izr. prof. dr. Romana Cerc Korošec
Datum zagovora: 22. 8. 2018

OBLAK, JURIJ
SINTEZA 2,3-DIARIL-SUBSTITUIRANIH PIRAZINSKIH DERIVATOV
Mentor: izr. prof. dr. Franc Požgan
Datum zagovora: 24. 8. 2018

PERŠOLJA, PETER
SINTEZA IN KARAKTERIZACIJA 1,4-DIHETEROARIL SUBSTITUIRANIH BENZENOV
Mentor: izr. prof. dr. Franc Požgan
Datum zagovora: 24. 8. 2018

SURINA, ROK
UPORABA PAMETNEGA TELEFONA KOT DETEKTORJA SVETLOBE V KEMIJI
Mentor: viš. pred. dr. Andrej Godec
Datum zagovora: 27. 8. 2018

TOLAR, KATARINA
ELEKTROKEMIČNA PRETVORBA IN HRANJENJE ELEKTRIČNE ENERGIJE V GALVANSKEM ČLENU
Mentor: izr. prof. dr. Matija Tomšič
Datum zagovora: 28. 8. 2018

KAVALIČ, TADEJ
KATALITSKO ARILIRANJE C-H VEZI 2-FENILPIRIMIDINA V VODI - PRIMERJAVA REAKTIVNOSTI ARIL BROMIDOV IN ARIL KLORIDOV
Mentor: izr. prof. dr. Franc Požgan
Datum zagovora: 29. 8. 2018

PRAH, NINA
VPLIV TEMPERATURE, ČASA IN PH MEDIJA NA TVORBO TANIN-PROTEIN KOMPLEKSA
Mentor: izr. prof. dr. Franc Požgan
Datum zagovora: 29. 8. 2018

ZAPLATAR, VALERIJA
ODVISNOST TERMIČNE STABILNOSTI DODEKAMERNE DVOVERIŽNE DNA OD ZAPOREDJA BAZNIH PAROV IN KONCENTRACIJE DNA
Mentor: prof. dr. Jurij Lah
Datum zagovora: 29. 8. 2018

GREGORC, LUCIJA
TERMIČNA ANALIZA MANGANOVEGA(II) IN NIKLJEVIH(II) KOMPLEKSOV S PIRIDIN-2-ONOM
Mentor: doc. dr. Saša Petriček
Datum zagovora: 29. 8. 2018

KOBE, TADEJ
ACETILPIRIDINI KOT KATIONI V HEKSAFLUORIDOSILIKATNIH SOLEH
Mentor: doc. dr. Andrej Pevec
Datum zagovora: 30. 8. 2018

BARTOLJ, IRENA
KARAKTERIZACIJA IN SINTEZA SPOJINE BAKROVEGA BENZOATA TRIHIDRATA
Mentor: doc. dr. Nives Kitanovski
Datum zagovora: 3. 9. 2018

PERKO, MARK
KARAKTERIZACIJA IN SINTEZA SPOJINE [MoBr3(C5H5N)3]
Mentor: doc. dr. Nives Kitanovski
Datum zagovora: 3. 9. 2018

BAVDEK, MAJA
KARAKTERIZACIJA IN SINTEZA SPOJINE trans-((C6H7N)2H)[Mo(NCS)4(C6H7N)2]
Mentor: doc. dr. Nives Kitanovski
Datum zagovora: 3. 9. 2018

GRACAR, KLAVDIJA
KARAKTERIZACIJA IN SINTEZA K[Cr(NCS)4py2]×4py
Mentor: doc. dr. Nives Kitanovski
Datum zagovora: 3. 9. 2018

LISJAK, ANA
VPLIV NEKATERIH KOVIN NA BARVO PAPIRJA PRI POSPEŠENEM TERMIČNEM STARANJU
Mentor: izr. prof. dr. Drago Kočar
Datum zagovora: 3. 9. 2018

MRGOLE, KRISTJAN
IZOLACIJA ELAGITANINOV IZ EKSTRAKTA KOSTANJEVEGA LESA IN ANALIZA NA HPLC-DAD
Mentor: viš. pred. dr. Tatjana Zupančič
Datum zagovora: 4. 9. 2018

RAJK, LUKA
PRIPRAVA FENIL SUBSTITUIRANIH KLEŠČASTIH KOMPLEKSOV Z NIKLJEM IN PALADIJEM
Mentor: izr. prof. dr. Janez Cerkovnik
Datum zagovora: 4. 9. 2018

PEČOVNIK, NINA
RAZVOJ METODE ZA DOLOČEVANJE TRIAZINSKIH PESTICIDOV V SADNIH SOKOVIH
Mentor: prof. dr. Helena Prosen
Datum zagovora: 5. 9. 2018

ZAFRAN, ANA
VPLIV PROCESNIH POGOJEV NA UV INICIRANO POLIMERIZACIJO AKRILAMIDA V RAZTOPINI
Mentor: viš. pred. dr. Branko Alič
Datum zagovora: 7. 9. 2018

LAZIĆ, VALERIJA
PRIMERJAVA ICP-OES IN ICP-MS ZA DOLOČANJE NIZKIH KONCENTRACIJ MANGANA
Mentor: izr. prof. dr. Drago Kočar
Datum zagovora: 7. 9. 2018

STRNAD, LIZA MARIJA
FAZNA ANALIZA RAZLIČNIH VZORCEV TAL S PODROČJA LJUBLJANE S PRAŠKOVNO DIFRAKCIJO
Mentor: izr. prof. dr. Amalija Golobič
Datum zagovora: 10. 9. 2018

TURK, MARKO
VPLIV RAZLIČNIH PARAMETROV NA UČINKOVITOST SONČNIH CELIC
Mentor: viš. pred. dr. Andrej Godec
Datum zagovora: 10. 9. 2018

POVŠIČ, LIDIJA
IZRAČUN FAZNEGA RAVNOTEŽJA TEKOČINA - PLIN V NEIDEALNIH MEŠANICAH VODE IN ETANOLA
Mentor: prof. dr. Jurij Reščič
Datum zagovora: 10. 9. 2018

BRULC, ANJA
VPLIV MAKROMOLEKUL NA STABILNOST PROTEINOV
Mentor: prof. dr. Jurij Reščič
Datum zagovora: 11. 9. 2018

ŽUPEVEC, NATALIJA
KEMIJSKA KINETIKA OZONA V STRATOSFERI
Mentor: viš. pred. dr. Andrej Godec
Datum zagovora: 11. 9. 2018

KEJŽAR, KATJA
OPTIMIZACIJA SINTEZE ANALOGOV LIGANDA SALEN NA OSNOVI O-VANILINA IN NJIHOVIH KOMPLEKSOV PREHODNIH KOVIN
Mentor: doc. dr. Jakob Kljun
Datum zagovora: 11. 9. 2018

BRATKOVIČ, MAŠA
BAKROVE KOORDINACIJSKE SPOJINE Z ANIONOM SUKCINSKE KISLINE
Mentor: doc. dr. Bojan Kozlevčar
Datum zagovora: 12. 9. 2018

MISLAJ, MATEJ
DOLOČITEV ŽELEZA V ZELENJAVI IN VEGETARIJANSKI PREHRANI
Mentor: viš. pred. dr. Tatjana Zupančič
Datum zagovora: 14. 9. 2018

LUŠTEK, KARMEN
DOLOČANJE PARACETAMOLA V TABLETAH LEKADOLA
Mentor: prof. dr. Barbara Hribar Lee
Datum zagovora: 14. 9. 2018

PLESNIK, KRISTINA
PRIPRAVA POLIENAMINONOV NA OSNOVI CIKLOHEKSAN-1,2-DIONA IN DIAMINOV
Mentor: prof. dr. Jurij Svete
Datum zagovora: 14. 9. 2018

MLAKAR, TINA
VPLIV AMINSKIH STABILIZATORJEV NA REOLOŠKE LASTNOSTI ALKIDNEGA PREMAZA
Mentor: prof. dr. Urška Lavrenčič Štangar
Datum zagovora: 17. 9. 2018

FILIPIČ, NIKA
KOROZIJSKA KARAKTERIZACIJA MEDENIN V STIKU S PITNO VODO
Mentor: izr. prof. dr. Marjan Marinšek
Datum zagovora: 17. 9. 2018

LEVC, ŽIVA
VPLIV ZAČETNE KONCENTRACIJE BARVILA PLASMOCORINTH B NA HITROST NJEGOVE RAZGRADNJE S FOTOKATALITSKO AKTIVNIMI TANKIMI PLASTMI TIO2
Mentor: izr. prof. dr. Romana Cerc Korošec
Datum zagovora: 17. 9. 2018

ŠTEPEC, MIHA
SINTEZA 1-ALKIL-N-BOC-ISATIN IMINOV
Mentor: prof. dr. Jurij Svete
Datum zagovora: 19. 9. 2018

TRELC, MAJA
FIZIKALNO-KEMIJSKI PROCESI OB VNOSU ZDRAVIL V TELO
Mentor: viš. pred. dr. Andrej Godec
Datum zagovora: 20. 9. 2018

KOZMUS, JASMINA
HALOGENIRANJE TERMINALNIH ACETILENOV
Mentor: doc. dr. Martin Gazvoda
Datum zagovora: 24. 9. 2018

SIMČIĆ, PATRIK
PRIPRAVA NEKATERIH HALOGENIH DERIVATOV
Mentor: izr. prof. dr. Marjan Jereb
Datum zagovora: 26. 9. 2018

PEZDIREC, MAJA
VPLIV TLAKA NA TRDNE FAZE VODE V LEDENIKIH
Mentor: viš. pred. dr. Andrej Godec
Datum zagovora: 27. 9. 2018

HROVAT, BLAŽ
PEROVSKITE SOLAR CELLS WITH MIXED HTMS
Mentor: prof. dr. Ksenija Kogej
Datum zagovora: 27. 9. 2018

MAL, SUZANA
IONOTERMALNA SINTEZA MIKROPOROZNEGA ALUMINOFOSFATA S KABAZITNIM STRUKTURNIM TIPOM
Mentor: izr. prof. dr. Amalija Golobič
Datum zagovora: 28. 9. 2018

URBIHA, ERIKA
ANALIZNE METODE ZA KARAKTERIZACIJO KROMOVEGA(III) OKSIDA
Mentor: izr. prof. dr. Mitja Kolar
Datum zagovora: 4. 10. 2018

EGART, MARJETA
POVRŠINSKO AKTIVNE SNOVI: UPORABA NA PODROČJU DOSTAVE ZDRAVILNIH UČINKOVIN
Mentor: prof. dr. Ksenija Kogej
Datum zagovora: 4. 10. 2018

PETEH, TOMAŽ
POLŠARŽNA POLIMERIZACIJA AKRILAMIDA IN ITAKONSKE KISLINE
Mentor: viš. pred. dr. Branko Alič
Datum zagovora: 22. 10. 2018

ŠIREC, JASNA
VPLIV INERTNIH SNOVI NA MINIMALNO VŽIGNO ENERGIJO GORLJIVIH PRAHOV
Mentor: doc. dr. Barbara Novosel
Datum zagovora: 30. 10. 2018

JONTEZ, URŠKA
REAKCIJE BAKROVEGA(II) KINALDINATA Z 1-AMINO-2-PROPANOLOM
Mentor: doc. dr. Barbara Modec
Datum zagovora: 8. 11. 2018

MIKLAVČIČ, CIRIL
SKLOPITEV DVODIMENZIONALNE KROMATOGRAFIJE Z MASNIM SPEKTROMETROM (2D-LCMS) – PRIKAZ PRINCIPA DELOVANJA SISTEMA NA UČINKOVINI KLOPIDOGREL HIDROGENSULFAT
Mentor: prof. dr. Matevž Pompe
Datum zagovora: 15. 11. 2018

BOLTES, TANJA
VPLIV TEMPERATURE NA MICELIZACIJO POVRŠINSKO AKTIVNIH SNOVI
Mentor: prof. dr. Marija Bešter Rogač
Datum zagovora: 29. 11. 2018

JANEŽIČ, BLAŽ
VLOGA IN UPORABA PROGRAMSKE OPREME ZA OBDELAVO KROMATOGRAFSKIH PODATKOV PRI HPLC ANALIZAH
Mentor: doc. dr. Bojan Šarac
Datum zagovora: 30. 11. 2018

POGORELC, PETRA
FOTOKATALITSKO UČINKOVITE PLASTI TIO2 ZA ČIŠČENJE STREŠNIH KRITIN
Mentor: izr. prof. dr. Romana Cerc Korošec
Datum zagovora: 14. 12. 2018

OKIĆ, EMA
KEMIJSKO LUŽENJE DUPLEKSNEGA NERJAVNEGA JEKA
Mentor: doc. dr. Bojan Šarac
Datum zagovora: 18. 12. 2018

UNIVERZA V MARIBORU
FAKULTETA ZA KEMIJO IN KEMIJSKO TEHNOLOGIJO

1. januar – 31. december 2018

DOKTORATI

DOKTORSKI ŠTUDIJ – 3. STOPNJA

HORVAT GABRIJELA
PRIPRAVA, KARAKTERIZACIJA IN APLIKACIJA POLISAHARIDNIH AEROGELOV
Mentor: red. prof. dr. ŽELJKO KNEZ, univ. dipl. inž. kem. tehnol.
Somentor: red. prof. dr. ZORAN NOVAK, univ. dipl. inž. kem. tehnol.
Datum zagovora: 23. 03. 2018

IVANOVIĆ MILENA
RAZVOJ ANALIZNIH METOD ZA SOČASNO IDENTIFIKACIJO IN DOLOČEVANJE FENOLNIH SPOJIN
Mentor: izr. prof. dr. MITJA KOLAR, univ. dipl. inž. kem.
Somentor: doc. dr. MAŠA ISLAMČEVIĆ RAZBORŠEK, prof. biol. in kem.
Datum zagovora: 30. 03. 2018

KORENAK JASMINA
BIOMIMETIČNE MEMBRANE ZA PROCES OSMOZE PRI OBDELAVI INDUSTRIJSKE ODPADNE VODE
Mentor: doc. dr. IRENA PETRINIĆ, univ. dipl. inž. kem. tehnol.
Somentor: izr . prof. dr. CLAUS HELIX NIELSEN
Datum zagovora: 06. 07. 2018

KRAVANJA GREGOR
NAČRTOVANJE VISOKOTLAČNIH PROCESOV ZA PREDELAVO POLIMEROV IN IZBOLJŠAVE PRENOSA TOPLOTE
Mentor: red. prof. dr. ŽELJKO KNEZ, univ. dipl. inž. kem. tehnol.
Somentor: doc. dr. MAŠA KNEZ HRNČIČ, univ. dipl. inž. kem. tehnol. , red. prof. dr. MOJCA ŠKERGET, univ. dipl. inž. kem. tehnol.
Datum zagovora: 15. 05. 2018

STAVBAR SEVERINA
PROCESI ODSTRANJEVANJA ANTIBIOTIKOV IZ BOLNIŠNIČNIH ODPADNIH VOD Mentor: red. prof. dr. SONJA ŠOSTAR TURK, univ. dipl. inž. tekst.
Somentor: doc. dr. MAŠA KNEZ HRNČIČ, univ. dipl. inž. kem. tehnol. , izr. prof. dr. MITJA KOLAR, univ. dipl. inž. kem.
Datum zagovora: 18. 04. 2018

MAGISTERIJI

MAGISTRSKI ŠTUDIJ – 2. STOPNJA

CMAGER NUŠA
KEMIJSKA MODIFIKACIJA POVRŠINE VINILBENZIL KLORIDNIH POLIHIPE MATERIALOV Z METODO RAFT GRAFTIRANJA
Mentor: red. prof. dr. PETER KRAJNC, univ. dipl. inž. kem.
Somentor: asist. dr. MUZAFERA PALJEVAC, prof. kem. in biol.
Datum zagovora: 21. 11. 2018

DEŽELAK BLAŽ
HIDROTERMIČNA Degradacija polietilena nizke gostote
Mentor: red. prof. dr. MOJCA ŠKERGET, univ. dipl. inž. kem. tehnol.
Somentor: red. prof. dr. ŽELJKO KNEZ, univ. dipl. inž. kem. tehnol.
Datum zagovora: 24. 10. 2018

DRETAR ROK
SINTEZA VELIKIH OMREŽIJ TOPLOTNIH PRENOSNIKOV
Mentor: red. prof. dr. ZDRAVKO KRAVANJA, univ. dipl. inž. kem. tehnol.
Somentor: doc. ddr. ANDREJA NEMET, univ. dipl. inž. kem. tehnol.
Datum zagovora: 24. 09. 2018

GOJZNIKAR MATEJA
POROZNI KOPOLIMERI IZ VINILESTROV IN TIOLOV KOT NOSILCI BIOLOŠKIH CELIC
Mentor: red. prof. dr. PETER KRAJNC, univ. dipl. inž. kem.
Somentor: asist. dr. MUZAFERA PALJEVAC, prof. kem. in biol.
Datum zagovora: 24. 09. 2018

GOVEJŠEK TAMARA
DOLOČANJE ARZENA V TITANOVEM DIOKSIDU
Mentor: doc. dr. MATJAŽ FINŠGAR, univ. dipl. kem.
ZUNANJI SOMENTOR
Datum zagovora: 29. 08. 2018

GRAČNAR MAJA
IZOLACIJA BIOLOŠKO AKTIVNIH KOMPONENT IZ PLODOV GOZDNIH BOROVNIC (Vaccinium Myrtillus L.)
Mentor: doc. dr. MAŠA KNEZ HRNČIČ, univ. dipl. inž. kem. tehnol.
Somentor: doc. dr. PETRA KOTNIK,univ. dipl. inž. kem. tehnol.
asis. DARIJA COR, , univ. dipl. inž. kem. tehnol.
dr. URŠKA ROZMAN
Datum zagovora: 11. 07. 2018

HERIC ANDREJA
PRIPRAVA EKSTRAKTOV ARONIJE ARONIA MELANOCARPA IN TESTIRANJE NJIHOVE BIOLOŠKE AKTIVNOSTI
Mentor: doc. dr. MAŠA KNEZ HRNČIČ, univ. dipl. inž. kem. tehnol.
Somentor: doc. dr. UROŠ MAVER, mag. farm.
doc. dr. PETRA KOTNIK,univ. dipl. inž. kem. tehnol
Datum zagovora: 24. 10. 2018

HREN MAŠA
VPLIV AGRESIVNEGA MEDIJA IN VNETNIH PROCESOV NA KOROZIJO BIOKOMPATIBILNIH KOVINSKIH IMPLANTATOV V UMETNI SLINI
Mentor: doc. dr. MOJCA SLEMNIK, univ. dipl. inž. kem. tehnol.
Somentor: doc. dr. IRENA BAN, univ. dipl. inž. kem. tehnol.
Datum zagovora: 12. 09. 2018

IVANOVSKI MAJA
FUNKCIONALIZIRANI KOPOLIMERI IZ MAKROLAKONOV Z ENCIMSKO POLIMERIZACIJO ODPIRANJA OBROČA
Mentor: red. prof. dr. PETER KRAJNC, univ. dipl. inž. kem.
ZUNANJI SOMENTOR
Datum zagovora: 24. 09. 2018

JEROMEL KAJA
DOLOČEVANJE ANTIMIKROBNEGA DELOVANJA ALOE VERE
Mentor: red. prof. dr. MAJA LEITGEB, univ. dipl. inž. kem. tehnol.
Somentor: doc. dr. MATEJA PRIMOŽIČ, univ. dipl. inž. kem. tehnol.
Datum zagovora: 24. 10. 2018

KEGL TINA
NOVI NANOMATERIALI ZA ADSORPCIJO REDKOZEMELJSKIH ELEMENTOV IZ VODNIH RAZTOPIN
Mentor: doc. dr. IRENA BAN, univ. dipl. inž. kem. tehnol.
ZUNANJI SOMENTOR
Datum zagovora: 04. 09. 2018

KERMC DOMEN
KARAKTERIZACIJA VISKIJEV Z GC-MS IN ICP-MS TER NJIHOVA KEMOMETRIJSKA KLASIFIKACIJA
Mentor: doc. dr. MAŠA ISLAMČEVIĆ RAZBORŠEK, prof. biol. in kem.
ZUNANJI SOMENTOR
Datum zagovora: 24. 09. 2018

KORES KATARINA
NAČRTOVANJE IN RAZVOJ NOVIH PROTIMIKROBNIH SPOJIN Z UPORABO ProBiS RAČUNALNIŠKIH PRISTOPOV
Mentor: izr. prof. dr. URBAN BREN, univ. dipl. kem.
ZUNANJI SOMENTOR
Datum zagovora: 25. 10. 2018

KUHAR DOROTEJA
ČIŠČENJE POVRŠINSKE VODE Z ULTRAFILTRACIJO
Mentor: izr. prof. dr. MARJANA SIMONIČ, univ. dipl. inž. kem. tehnol.
Somentor: doc. dr. IRENA PETRINIĆ, univ. dipl. inž. kem. tehnol.
Datum zagovora: 21. 03. 2018

LEDINEK NINA
OPTIMIZACIJA HPLC METODE ZA DOLOČANJE SORODNIH SUBSTANC PREDNISOLONA V UČINKOVINI
Mentor: red. prof. dr. ZORAN NOVAK, univ. dipl. inž. kem. tehnol.
Somentor: doc. dr. MATJAŽ FINŠGAR, univ. dipl. kem.
Datum zagovora: 17. 01. 2018

LJUBEC BARBARA
FORMULIRANJE FARMACEVTSKIH UČINKOVIN V POLIMERE S PLINI VISOKE GOSTOTE
Mentor: doc. dr. MAŠA KNEZ HRNČIČ, univ. dipl. inž. kem. tehnol.
Somentor: red. prof. dr. ZORAN NOVAK, univ. dipl. inž. kem. teh
asist. dr. DARIJA CÖR , univ. dipl. inž. kem. tehnol.
Datum zagovora: 04. 09. 2018

LUKAČ DAMJANA
RAZKROJ NEKATERIH ACETILACETONATOV PREHODNIH KOVIN S TERMIČNO IN ULTRAZVOČNO METODO
Mentor: izr. prof. dr. MATJAŽ KRISTL, univ. dipl. inž. kem. tehnol.
Somentor: doc. dr. IRENA BAN, univ. dipl. inž. kem. tehnol.
Datum zagovora: 11. 07. 2018

MATIS STAŠA
SINTEZA IN IZOLACIJA NANOCELULOZE IZ BAKTERIJE Gluconacetobacter xylinusd
Mentor: red. prof. dr. MAJA LEITGEB, univ. dipl. inž. kem. tehnol.
Somentor: doc. dr. MATEJA PRIMOŽIČ, univ. dipl. inž. kem. tehnol.
Datum zagovora: 11. 07. 2018

OHMAN MIHA
PROIZVODNJA TEKOČEGA OGLJIKOVEGA DIOKSIDA
Mentor: izr. prof. dr. DARKO GORIČANEC, univ. dipl. inž. kem. tehnol.
Somentor: doc. dr. DANIJELA URBANCL, univ. dipl. inž. kem. tehnol.
Datum zagovora: 21. 03. 2018

OSMIĆ AZRA
PRIPRAVA HIERARHIČNO POROZNIH MATERIALOV IZ MULTIPLIH ŠABLON
Mentor: red. prof. dr. PETER KRAJNC, univ. dipl. inž. kem.
Somentor: asist. dr. MUZAFERA PALJEVAC, prof. kem. in biol.
Datum zagovora: 24. 10. 2018

PETEK REGORŠEK VITA
Karakterizacija zeta potenciala votlo-vlaknastih membrand
Mentor: doc. dr. IRENA PETRINIĆ, univ. dipl. inž. kem. tehnol.
Zunanji somentor
Datum zagovora: 23. 05. 2018

POTRČ SANJA
PROIZVODNJA TRDNIH BIOGORIV S TOREFIKACIJO BIOMASE
Mentor: izr. prof. dr. DARKO GORIČANEC, univ. dipl. inž. kem. tehnol.
Somentor: doc. dr. DANIJELA URBANCL, univ. dipl. inž. kem. tehnol.
Datum zagovora: 24. 09. 2018

ROMANIĆ LUKA
FOTOKATALITSKI FILTER NA OSNOVI TiO2 ZA ČIŠČENJE ZRAKA
Mentor: doc. dr. MATJAŽ FINŠGAR, univ. dipl. kem.
Somentor: izr. prof. dr. REGINA FUCHS GODEC, univ. dipl. inž. kem. tehnol.
Datum zagovora: 12. 09. 2018

SEITL MAŠA
UČINKOVITOST RAZGRADNJE BISFENOLA A PO HIDROTERMIČNEM PROCESIRANJU ODPADNE VODE
Mentor: doc. dr. MAŠA KNEZ HRNČIČ, univ. dipl. inž. kem. tehnol.
Somentor: doc. dr. PETRA KOTNIK, univ. dipl. inž. kem. tehnol.
Datum zagovora: 11. 07. 2018

SIMONIČ TAJDA
IZBOLJŠANJE UČINKOVITOSTI VAKUUMSKEGA UPARJANJA TEKOČE FRAKCIJE DIGESTATA
Mentor: izr. prof. dr. MARJANA SIMONIČ, univ. dipl. inž. kem. tehnol.
Somentor: red. prof. dr. ZORKA NOVAK PINTARIČ, univ. dipl. inž. kem. tehnol.
Datum zagovora: 21. 02. 2018

ŠTIH VESNA
VODOTOPNE EMULZIJE KAROTENOIDOV
Mentor: red. prof. dr. MOJCA ŠKERGET, univ. dipl. inž. kem. tehnol.
ZUNANJI SOMENTOR
Datum zagovora: 11. 07. 2018

ŠTUMPF SARA
PROTIMIKROBNE LASTNOSTI TANINSKIH EKSTRAKTOV
Mentor: izr. prof. dr. URBAN BREN, univ. dipl. kem.
Somentor: red. prof. dr. MAJA LEITGEB, univ. dipl. inž. kem. tehnol
asist. dr. GREGOR HOSTNIK
Datum zagovora: 26. 09. 2018

TEVŽ NEJA
RAZVOJ KINETIČNEGA MODELA IN SPREMLJANJE RAZGRADNJE SPECIFIČNEGA ANTIBIOTIKA MED PROCESOM ODSTRANJEVANJA IZ ODPADNE VODE
Mentor: red. prof. dr. ANDREJA GORŠEK, univ. dipl. inž. kem. tehnol.
Somentor: doc. dr. DARJA PEČAR, univ. dipl. inž. kem. tehnol.
Datum zagovora: 21. 03. 2018

TOMPA SAŠA
MIKROBIOLOŠKA KINETIKA RASTI NARAVNE STARTER KULTURE V SIROTKI Mentor: doc. dr. DARJA PEČAR, univ. dipl. inž. kem. tehnol.
Somentor: red. prof. dr. ANDREJA GORŠEK, univ. dipl. inž. kem. tehnol.
Datum zagovora: 24. 09. 2018

VODOPIVEC KATJA
RAZVOJ IN VALIDACIJA MODIFICIRANE Bi-Sn ELEKTRODE
Mentor: doc. dr. MATJAŽ FINŠGAR, univ. dipl. kem.
Somentor: asist. BARBARA PETOVAR, mag. kem.
Datum zagovora: 04. 09. 2018

ŽALIG VALENTINA
SINTEZE IN KARAKTERIZACIJA NANODELCEV ZA UPORABO V OSMOTSKIH PROCESIH ČIŠČENJA ODPADNE VODE
Mentor: doc. dr. IRENA BAN, univ. dipl. inž. kem. tehnol.
Somentor: doc. dr. IRENA PETRINIĆ, univ. dipl. inž. kem. tehnol.
doc. dr. MOJCA SLEMNIK, univ. dipl. inž. kem. tehnol.
Datum zagovora: 04. 09. 2018

ŽITEK TAJA
VPLIV EKSTRAKTOV IZ NARAVNIH MATERIALOV NA METABOLNO AKTIVNOST ČLOVEŠKIH MELANOMSKIH CELIC (WM-266-4)
Mentor: doc. dr. MAŠA KNEZ HRNČIČ, univ. dipl. inž. kem. tehnol.
Somentor: red. prof. dr. MAJA LEITGEB, univ. dipl. inž. kem. teh.
Datum zagovora: 04. 09. 2018

DIPLOME – UNIVERZITETNI ŠTUDIJ

UNIVERZITETNI ŠTUDIJ – 1. STOPNJA

AMBROŽ ANA
PRIPRAVA OKOLJU PRIJAZNIH MIKROKAPSUL ZA KONTROLIRANO SPROŠČANJE HLAPNIH ORGANSKIH SPOJIN
Mentor: izr. prof. dr. MARJANA SIMONIČ, univ. dipl. inž. kem. tehnol.
Somentor: izr. prof. dr. JULIJA VOLMAJER VALH, univ. dipl. inž. kem. tehnol.
Datum zagovora: 12. 09. 2018

ARBEITER DAMJAN
PRIPRAVA IN ANALIZA NAPREDNIH PREVLEK NA OSNOVI HIDROKSICELULOZE NA KOVINSKIH SUBSTRATIH ZA BIOMEDICINSKE APLIKACIJE
Mentor: doc. dr. MATJAŽ FINŠGAR, univ. dipl. kem.
Somentor: doc. dr. UROŠ MAVER, mag. farm.
Datum zagovora: 27. 07. 2018

BANDUR PATRICIJA
ŠTUDIJA AKTIVNOSTI NEKATERIH ENCIMOV V GELU ALOE VERE
Mentor: red. prof. dr. MAJA LEITGEB, univ. dipl. inž. kem. tehnol.
Somentor: asist. KATJA VASIĆ, univ. dipl. inž. kem. tehnol.
Datum zagovora: 04. 09. 2018

DAMIJAN TJAŠA
ANTIOKSIDATIVNI POTENCIAL IN VSEBNOST TOTALNIH FENOLOV V EKSTRAKTU STEVIE REBAUDIANA BERT
Mentor: doc. dr. MAŠA KNEZ HRNČIČ, univ. dipl. inž. kem. tehnol.
Somentor: asist. dr. DARIJA CÖR , univ. dipl. inž. kem. tehnol.
Datum zagovora: 24. 09. 2018

DEGEN ALJAŽ
OPTIMIZACIJA SILIKATNE PREVLEKE NiCu NANODELCEV ZA APLIKACIJE V MEDICINI
Mentor: doc. dr. IRENA BAN, univ. dipl. inž. kem. tehnol.
Somentor: doc. dr. MOJCA SLEMNIK, univ. dipl. inž. kem. tehnol.
Datum zagovora: 04. 09. 2018

DOKL MONIKA
IZOLACIJA MIKRO IN NANOCELULOZE IZ RASTLINSKIH MATERIALOV
Mentor: red. prof. dr. MAJA LEITGEB, univ. dipl. inž. kem. tehnol.
Somentor: asist. KATJA VASIĆ, univ. dipl. inž. kem. tehnol.
Datum zagovora: 12. 09. 2018

DROBNIČ TEA
ANALIZA IN OPTIMIZACIJA PIGMENTNIH PAST ZA KOVINSKE PREMAZE NA VODNI OSNOVI
Mentor: doc. dr. MATJAŽ FINŠGAR, univ. dipl. kem.
ZUNANJI SOMENTOR
Datum zagovora: 04. 09. 2018

ERMENC TEJA
OPTIMIZACIJA PROCESIRANJA VZORCEV SLINE PRI RAKU GLAVE IN VRATU ZA ŠTUDIJE BIOLOŠKIH OZNAČEVALCEV
Mentor: prof. dr. UROŠ POTOČNIK, univ. dipl. kem.
Somentor: doc. dr. HELENA SABINA ČELEŠNIK, dipl. mikrobiolog
Datum zagovora: 12. 09. 2018

FLUCHER VIKTORIJA
VPLIV TEMPERATURE NA VOLUMETRIČNE LASTNOSTI BINARNIH MEŠANIC ALKOHOLOV
Mentor: izr. prof. dr. REGINA FUCHS GODEC, univ. dipl. inž. kem. tehnol.
Somentor: izr. prof. dr. URBAN BREN, univ. dipl. kem.
Datum zagovora: 11. 09. 2018

GIDER EVA
UVAJANJE DIGITALIZACIJE V LABORATORIJ Z UPORABO PROGRAMA sciNote®
Mentor: doc. dr. DUŠAN KLINAR, univ. dipl. inž. kem. tehnol.
Somentor: doc. dr. MILOŠ BOGATAJ, univ. dipl. inž. kem. tehnol.
Datum zagovora: 04. 09. 2018

GLAVAČ KAJA
SEPARACIJA AKTIVNIH KOMPONENT IZ LUPIN KAKAVOVCA
Mentor: red. prof. dr. MOJCA ŠKERGET, univ. dipl. inž. kem. tehnol.
Somentor: asist. MAJA ČOLNIK, univ. dipl. inž. kem. tehnol.
Datum zagovora: 24. 09. 2018

GYURKAČ MARCELL
SINTEZA IN KARAKTERIZACIJA MANGANOVIH KOORDINACIJSKIH SPOJIN Z AMINOPIRIDINI
Mentor: izr. prof. dr. MATJAŽ KRISTL, univ. dipl. inž. kem. tehnol.
Somentor: doc. dr. IRENA BAN, univ. dipl. inž. kem. tehnol.
Datum zagovora: 23. 05. 2018

ITERNIČKA BERNARD
PRIPRAVA POLI(GLICIDIL METAKRILATA) Z VEČ NIVOJSKO POROZNOSTJO
Mentor: red. prof. dr. PETER KRAJNC, univ. dipl. inž. kem.
Somentor: asist. dr. MUZAFERA PALJEVAC, prof. kem. in biol.
Datum zagovora: 12. 09. 2018

JANČIČ NATALIJA
BIOSORPCIJA Cr6+ IONOV NA IMOBILIZIRANI MEŠANICI ALG NA ALGINATNIH NOSILCIH
Mentor: izr. prof. dr. MARJANA SIMONIČ, univ. dipl. inž. kem. tehnol.
Somentor: red. prof. dr. ANDREJA GORŠEK, univ. dipl. inž. kem. tehnol.
Datum zagovora: 04. 09. 2018

KELC IRIS
EKSPRESIJSKI IN EPIGENETSKI VZORCI PRI BOLNIKIH S KRONIČNO VNETNO ČREVESNO BOLEZNIJO
Mentor: red. prof. dr. UROŠ POTOČNIK, univ. dipl. kem.
Somentor: doc. dr. HELENA SABINA ČELEŠNIK, dipl. mikrobiolog
Datum zagovora: 18. 04. 2018

KERŠIČ PIA
GENETSKA ANALIZA BOLNIKOV Z REVMATOIDNIM ARTRITISOM ZA POLIMORFIZME SNP V GENIH ZA VNETNE CITOKINE
Mentor: red. prof. dr. UROŠ POTOČNIK, univ. dipl. kem.
ZUNANJI SOMENTOR
Datum zagovora: 18. 04. 2018

KOCBEK SIMON
VPLIV MIKROVALOV NA ZVIJANJE â-PEPTIDA: RAČUNALNIŠKI PRISTOP
Mentor: izr. prof. dr. URBAN BREN, univ. dipl. kem.
Somentor: Martin Gladović, mag. kem.
Datum zagovora: 12. 09. 2018

KOGELNIK REBEKA
DOLOČEVANJE PRISOTNOSTI PROTEINOV IN AKTIVNOSTI NEKATERIH ENCIMOV V FIGAH
Mentor: red. prof. dr. MAJA LEITGEB, univ. dipl. inž. kem. tehnol.
Somentor: asist. KATJA VASIĆ, univ. dipl. inž. kem. tehnol.
doc. dr. MAŠA KNEZ HRNČIČ, univ. dipl. inž. kem. tehnol.
Datum zagovora: 04. 09. 2018

KORPIČ ŠPELA
EKSTRAKCIJE NARAVNIH PIGMENTOV IZ ALG
Mentor: red. prof. dr. MOJCA ŠKERGET, univ. dipl. inž. kem. tehnol.
ZUNANJI SOMENTOR
Datum zagovora: 11. 07. 2018

KOTNIK NUŠA
UGOTAVLJANJE UČINKOVITOSTI KLOROVEGA DIOKSIDA NA ESCHERICHIA COLI V PITNI VODI
Mentor: izr. prof. dr. MARJANA SIMONIČ, univ. dipl. inž. kem. tehnol.
ZUNANJI SOMENTOR
Datum zagovora: 24. 09. 2018

KOVŠE TJAŠA
HIDROTERMIČNA DEGRADACIJA PET EMBALAŽE
Mentor: red. prof. dr. MOJCA ŠKERGET, univ. dipl. inž. kem. tehnol.
Somentor: asist. MAJA ČOLNIK, univ. dipl. inž. kem. tehnol.
Datum zagovora: 04. 09. 2018

KRAVANJA KATJA ANDRINA
BIOLOŠKA AKTIVNOST KONVENCIONALNIH EKSTRAKTOV CEYLONSKEGA CIMETA (CINNAMOMUM ZEYLANICUM)
Mentor: doc. dr. MAŠA KNEZ HRNČIČ, univ. dipl. inž. kem. tehnol.
Somentor: dr. URŠKA ROZMAN
Datum zagovora: 04. 09. 2018

MAJER DAVID
VALIDACIJA METODE ZA ANALIZO Pb(II) Z UPORABO SPE SENZORJA
Mentor: doc. dr. MATJAŽ FINŠGAR, univ. dipl. kem.
Somentor: asist. BARBARA PETOVAR, mag. kem.
Datum zagovora: 29. 08. 2018

MALIĆ MARINA
ANTIKARCINOGENI POTENCIALI POLIFENOLNIH SPOJIN IZ SMILJA - RAČUNALNIŠKI PRISTOP
Mentor: izr. prof. dr. URBAN BREN, univ. dipl. kem.
Somentor: asist. VERONIKA FURLAN, mag. kem.
Datum zagovora: 12. 09. 2018

MARINČEK EVA
SINTEZA POROZNIH KOPOLIMERNIH POLIELEKTROLITOV NA OSNOVI 2-AKRILAMIDO-2-METILPROPANSULFONSKE KISLINE
Mentor: dr. SEBASTIJAN KOVAČIČ, prof. kem. in biol.
Datum zagovora: 04. 09. 2018

MERSLAVIČ MANCA
ZASNOVA IN ANALIZA NOVIH POLIMERNIH OBLOG Z VGRAJENIMI ZDRAVILNIMI UČINKOVINAMI NA ZLITINI TITAN/ALUMINIJ/VANADIJ
Mentor: doc. dr. MATJAŽ FINŠGAR, univ. dipl. kem
Somentor: doc. dr. UROŠ MAVER, mag. farm.
Datum zagovora: 12. 09. 2018

NAVODNIK ALEN
UPORABA PLAZEMSKIH REAKTORJEV ZA PRETVORBO METANA V VIŠJE OGLJIKOVODIKE IN SINTEZNI PLIN
Mentor: dr. BLAŽ LIKOZAR
Somentor: doc. dr. DARJA PEČAR, univ. dipl. inž. kem. tehnol.
Datum zagovora: 12. 09. 2018

OREL MATIC
UPORABA MIKROEMULZIJ ZA SINTEZO MAKROPOROZNIH POLISTIRENSKIH DERIVATOV
Mentor: red. prof. dr. PETER KRAJNC, univ. dipl. inž. kem.
Somentor: asist. dr. MUZAFERA PALJEVAC, prof. kem. in biol.
Datum zagovora: 12. 09. 2018

OSTROŠKO URŠKA
PREDOBDELAVA STUDENČNE VODE ZA PROCES REVERZNE OSMOZE
Mentor: doc. dr. IRENA PETRINIĆ, univ. dipl. inž. kem. tehnol.
Somentor: izr. prof. dr. MARJANA SIMONIČ, univ. dipl. inž. kem. tehnol.
Datum zagovora: 04. 09. 2018

PFEILER SEBASTIAN
DOLOČITEV OBRATOVALNIH KARAKTERISTIK ENO IN DVOSTOPENJSKE TOPLOTNE ČRPALKE
Mentor: izr. prof. dr. DARKO GORIČANEC, univ. dipl. inž. kem. tehnol.
Somentor: doc. dr. DANIJELA URBANCL, univ. dipl. inž. kem. tehnol.
Datum zagovora: 11. 07. 2018

PLAJNŠEK ALEN
DEAKTIVACIJA KATALIZATORJEV PRI POSTOPKU PROIZVODNJE METANOLA IZ OGLJIKOVEGA DIOKSIDA IN VODIKA
Mentor: dr. BLAŽ LIKOZAR
Somentor: doc. dr. LIDIJA ČUČEK, univ. dipl. inž. kem. tehnol.
Datum zagovora: 12. 09. 2018

PODRIČNIK MANCA
HITRA PRESOJA IN RAZVRŠČANJE VEČJIH NESREČ Z NEVARNIMI SNOVMI
Mentor: red. prof. dr. ZORKA NOVAK PINTARIČ, univ. dipl. inž. kem. tehnol.
Somentor: doc. ddr. ANDREJA NEMET, univ. dipl. inž. kem. tehnol.
Datum zagovora: 12. 09. 2018

PRELOG MIHA
PROIZVODNJA TRANSPORTNEGA GORIVA IZ BIOPLINA
Mentor: izr. prof. dr. DARKO GORIČANEC, univ. dipl. inž. kem. tehnol.
Somentor: asist. dr. PETER TROP, univ. dipl. inž. kem. tehnol.
Datum zagovora: 21. 03. 2018

PUHAR JAN
SIMULACIJA RAZPENJALNIKA S PROGRAMSKIMA ORODJEMA SCILAB IN GAMS Mentor: doc. dr. LIDIJA ČUČEK, univ. dipl. inž. kem. tehnol.
ZUNANJI SOMENTOR
Datum zagovora: 11. 09. 2018

ROŠKARIČ MATEVŽ
ZAŠČITNO DELOVANJE IZBRANIH POLIFENOLNIH SNOVI PROTI GENOTOKSIČNIM UČINKOM, KI JIH POVZROČA MIKOTOKSIN AFLATOKSIN B1 Mentor: izr. prof. dr. URBAN BREN, univ. dipl. kem.
ZUNANJI SOMENTOR
Datum zagovora: 12. 09. 2018

VERDNIK ALEKSANDRA
FAZNA RAVNOTEŽJA PRI POVIŠANIH TLAKIH ZA SISTEMA RESVERATROL/OGLJIKOV DIOKSID IN RESVERATROL/ETANOL/OGLJIKOV DIOKSID
Mentor: doc. dr. MAŠA KNEZ HRNČIČ, univ. dipl. inž. kem. tehnol.
Somentor: asist. dr. DARIJA CÖR , univ. dipl. inž. kem. tehnol.
Datum zagovora: 04. 09. 2018

VOGRINC MARKO
REGULACIJA PRETOČNEGA SISTEMA Z UPORABO PRETOČNEGA SENZORJA, AVTOMATSKEGA VENTILA IN POVRATNO-ZANČNEGA REGULACIJSKEGA SISTEMA
Mentor: doc. dr. MILOŠ BOGATAJ, univ. dipl. inž. kem. tehnol.
Somentor: doc. ddr. ANDREJA NEMET, univ. dipl. inž. kem. tehnol.
Datum zagovora: 24. 09. 2018

VOZLIČ ANA
KINETIKA PROIZVODNJE BIOPLINA MED ANAEROBNO FERMENTACIJO BIOLOŠKIH ODPADKOV PRECEPLJENIH Z GLIVAMA PLEUROTUS OSTREATUS IN TRAMETES VERSICOLOR
Mentor: doc. dr. DARJA PEČAR, univ. dipl. inž. kem. tehnol.
Somentor: red. prof. dr. ANDREJA GORŠEK, univ. dipl. inž. kem. tehnol.
Datum zagovora: 24. 09. 2018

DIPLOME – VISOKOŠOLSKI STROKOVNI ŠTUDIJ

KEMIJSKA TEHNOLOGIJA – 1. STOPNJA

BABIČ JERNEJA
INHIBITORNE LASTNOSTI BOROVNIC NA RAST MIKROBNIH CELIC
Mentor: red. prof. dr. MAJA LEITGEB, univ. dipl. inž. kem. tehnol.
Somentor: doc. dr. MATEJA PRIMOŽIČ, univ. dipl. inž. kem. tehnol.
doc. dr. MAŠA KNEZ HRNČIČ, univ. dipl. inž. kem. tehnol.
Datum zagovora: 11. 07. 2018

CIZL JASNA
BIOLOŠKA PREDOBDELAVA LIGNOCELULOZNIH MATERIALOV Z GLIVAMI BELE TROHNOBE
Mentor: doc. dr. LIDIJA ČUČEK, univ. dipl. inž. kem. tehnol.
Somentor: doc. dr. MAŠA ISLAMČEVIĆ RAZBORŠEK, prof. biol in kem.
Datum zagovora: 26. 09. 2018

GABERC JERNEJ
KOROZIJSKA HITROST BIOKOMPATIBILNIH KOVINSKIH MATERIALOV Z DODATKOM AGRESIVNIH IONOV V UMETNI SLINI
Mentor: doc. dr. MOJCA SLEMNIK, univ. dipl. inž. kem. tehnol.
Somentor: doc. dr. IRENA BAN, univ. dipl. inž. kem. tehnol.
Datum zagovora: 12. 09. 2018

GORENC PETRA
DOLOČANJE MAKROHRANIL V RAZLIČNIH DIGESTATIH IN UMETNIH GNOJILIH
Mentor: doc. dr. LIDIJA ČUČEK, univ. dipl. inž. kem. tehnol.
Somentor: doc. dr. MAŠA ISLAMČEVIĆ RAZBORŠEK, prof. biol in kem.
izr. prof. dr. MARJANA SIMONIČ, univ. dipl. inž. kem. tehnol.
Datum zagovora: 20. 08. 2018

KNECHTL IVAN
VPELJAVA TRAJNOSTNIH POSTOPKOV ZA LOČITEV BIO-OSNOVANIH GRADNIKOV IZ ODPADNE MORSKE BIOMASE ZA NAPREDNO UPORABO
Mentor: dr. BLAŽ LIKOZAR
Somentor: red. prof. dr. MOJCA ŠKERGET, univ. dipl. inž. kem. tehnol.
Datum zagovora: 24. 09. 2018

KOBALE TAMARA
DOLOČEVANJE AKTIVNOSTI NEKATERIH ENCIMOV V GRANATNEM JABOLKU
Mentor: red. prof. dr. MAJA LEITGEB, univ. dipl. inž. kem. tehnol.
Somentor: KATJA VASIĆ, univ. dipl. inž. kem. tehnol
doc. dr. MAŠA KNEZ HRNČIČ, univ. dipl. inž. kem. tehnol.
Datum zagovora: 12. 09. 2018

KRIVEC ROLANDO
PROIZVODNJA BIOPLINA Z ANAEROBNO DIGESTIJO BIOLOŠKIH ODPADKOV PRECEPLJENIH Z GLIVAMI NA SPECIFIČNEM SUBSTRATU
Mentor: red. prof. dr. ANDREJA GORŠEK, univ. dipl. inž. kem. tehnol.
Somentor: doc. dr. Darja Pečar, univ. dipl. inž. kem. tehnol.
Datum zagovora: 12. 09. 2018

KUZMAN NEJKA
RECIKLIRANJE ODPADNIH VODA ZDRAVILNE TERMALNE VODE, Z UPORABO RAZLIČNIH KOLON STEKLENIH SMOL
Mentor: doc. dr. IRENA PETRINIĆ, univ. dipl. inž. kem. tehnol.
Somentor: izr. prof. dr. MARJANA SIMONIČ, univ. dipl. inž. kem. tehnol.
Datum zagovora: 20. 06. 2018

MAKOVEC MAŠA
VPLIV PREDOBDELAVE PIŠČANČJE STELJE Z GLIVAMI NA PROIZVODNJO BIOPLINA
Mentor: doc. dr. LIDIJA ČUČEK, univ. dipl. inž. kem. tehnol.
Somentor: red. prof. dr. ZDRAVKO KRAVANJA, univ. dipl. inž. kem. tehnol.
Datum zagovora: 24. 09. 2018

MIKŠ NEŽA
MOŽNOST VRAČANJA DESTILATA PO ČIŠČENJU ODPADNE VODE V TEHNOLOŠKE PROCESE IZDELAVE Al ULITKOV
Mentor: izr. prof. dr. MARJANA SIMONIČ, univ. dipl. inž. kem. tehnol.
Somentor: doc. dr. IRENA PETRINIĆ, univ. dipl. inž. kem. tehnol.
Datum zagovora: 12. 09. 2018

MILOŠIČ LILIJANA
AKTIVNOST ENCIMOV V TEKOČIH IN TRDNIH PRALNIH SREDSTVIH
Mentor: red. prof. dr. MAJA LEITGEB, univ. dipl. inž. kem. tehnol.
Somentor: asist. MAJA ČOLNIK, univ. dipl. inž. kem. tehnol.
Datum zagovora: 24. 10. 2018

PALČNIK POLONA
Izolacija AKTIVNIH komponent iz semen chia z uporabo različnih tehnik ekstrakcije
Mentor: doc. dr. MAŠA KNEZ HRNČIČ, univ. dipl. inž. kem. tehnol.
Somentor: asist. dr. DARIJA CÖR , univ. dipl. inž. kem. tehnol.
Datum zagovora: 24. 10. 2018

SIHER ANJA
PRIPRAVA NANODELCEV Zn, Ni in Co TELURIDOV Z VISOKOTEMPERATURNO IN Z MEHANOKEMIJSKO METODO
Mentor: izr. prof. dr. MATJAŽ KRISTL, univ. dipl. inž. kem. tehnol.
Somentor: doc. dr. IRENA BAN, univ. dipl. inž. kem. tehnol.
Datum zagovora: 20. 08. 2018

STERNAD LEA
PROIZVODNJA BIOPLINA S PREDOBDELAVO LIGNOCELULOZE Z ORGANSKIM TOPILOM IN VROČO VODO
Mentor: doc. dr. LIDIJA ČUČEK, univ. dipl. inž. kem. tehnol.
Somentor: red. prof. dr. ZDRAVKO KRAVANJA, univ. dipl. inž. kem. tehnol.
Datum zagovora: 12. 09. 2018

ŠAŠEK ŽAN
OPTIMIZACIJA IN VALIDACIJA Cu MODIFICIRANE ELEKTRODE IZ STEKLASTEGA OGLJIKA ZA ANALIZO Pb(II)
Mentor: doc. dr. MATJAŽ FINŠGAR, univ. dipl. kem.
Somentor: asist. BARBARA PETOVAR, mag. kem.
Datum zagovora: 27. 07. 2018

ŠTUKOVNIK ZALA
EKSTRAKCIJA KOMPONENT IZ SEMEN NAVADNE AJDE (FAGOPYRUM ESCULENTUM)
Mentor: doc. dr. MAŠA KNEZ HRNČIČ, univ. dipl. inž. kem. tehnol.
Somentor: asist. dr. DARIJA CÖR , univ. dipl. inž. kem. tehnol.
Datum zagovora: 04. 09. 2018

TALJAN MIHAELA
AKTIVNOST LAKAZE IN CELULAZE V GLIVI PLEUROTUS OSTREATUS
Mentor: prof. dr. MAJA LEITGEB, univ. dipl. inž. kem. tehnol.
Somentor: asist. KATJA VASIĆ, univ. dipl. inž. kem. tehnol.
Datum zagovora: 11. 07. 2018

TRŽAN PRIMOŽ
VPLIV EKSTRAKCIJSKEGA POSTOPKA NA KVALITETO EKSTRAKTOV IZ LIOFILIZIRANIH HRUŠK (Pyrus communis)
Mentor: doc. dr. MAŠA KNEZ HRNČIČ, univ. dipl. inž. kem. tehnol.
Somentor: asist. dr. DARIJA CÖR , univ. dipl. inž. kem. tehnol.
Datum zagovora: 12. 09. 2018

TURK ANDREJA
EKSTRAKCIJA LUBJA KOSTANJA S SUBKRITIČNO VODO
Mentor: red. prof. dr. MOJCA ŠKERGET, univ. dipl. inž. kem. tehnol.
Somentor: asist. MAJA ČOLNIK, univ. dipl. inž. kem. tehnol.
Datum zagovora: 04. 09. 2018

VOLOVLEK ROK
ČISTILNO SREDSTVO ZA SOUPORABO S PRODUKTOM CAFÉLIER ZA ČIŠČENJE KAVNIH APARATOV
Mentor: doc. dr. ANITA KOVAČ KRALJ, univ. dipl. inž. kem.
Somentor: doc. ddr. ANDREJA NEMET, univ. dipl. inž. kem. tehnol.
Datum zagovora: 11. 07. 2018

ZUPANC TOMAŽ
MENJAVA METODE DOLOČANJA OPTIČNIH LASTNOSTI PIGMENTNEGA TITANOVEGA DIOKSIDA
Mentor: izr. prof. dr. MATJAŽ KRISTL, univ. dipl. inž. kem. tehnol.
Somentor: doc. dr. IRENA BAN, univ. dipl. inž. kem. tehnol.
Datum zagovora: 12. 09. 2018

FAKULTETA ZA ZNANOSTI O OKOLJU

1. januar – 31. december 2018

DOKTORATI

MOJCA ŽORŽ FURLAN
THE DETECTION AND STUDY OF BIOLOGICALLY ACTIVE COMPOUNDS IN ENVIRONMENTAL PROCESSES AND SAMPLES
Mentor: prof. dr. Mladen Franko
Datum zagovora: 31. 5. 2018

JOSÉ MANUEL CARITA GONÇALVES
DISTRIBUTION OF ENTERIC VIRUSES IN THE GULF OF TRIESTE AND THEIR INTERACTIONS WITH ENVIRONMENTALAND BIOLOGICAL PARAMETERS
Mentor: prof. dr. Valentina Turk
Somentor: dr. Jon Gutierrez Aguirre
Datum zagovora: 29. 6. 2018

BARBARA DEBELJAK
STRUCTURE AND FUNCTIONING OF THE HYPORHEIC ZONES IN THE GRAVEL-BEDS OF FIVE RIVERS IN RELATION TO CATCHMENT LAND USE
Mentor: prof. dr. Anton Brancelj
Datum zagovora: 29. 6. 2018

MAGISTERIJI

ŠTUDIJSKI PROGRAM OKOLJE – 2. STOPNJA

NIJAT RAHIMLI
EFFECTS OF POTENTIAL CLIMATE CHANGES ON THE BEHAVIOUR, FEEDING RATE AND REPRODUCTION OF SELECTED SOIL INVERTEBRATES
Mentor: doc. dr. Suzana Žižek
Datum zagovora: 9. feb. 18

ANA KARAT
OKOLJSKA OCENA TVEGANJA FUNGICIDA FOLPETA ZA TALNE EKOSISTEME Mentor: doc. dr. Suzana Žižek
Datum zagovora: 15. feb. 18

MOJCA VRČON MIHELJ
OPTOELEKTRONSKE IN FOTOKATALITSKE LASTNOSTI Z VANADIJEM DOPIRANEGA FE2TEO6
Mentor: prof. dr. Matjaž Valant
Datum zagovora: 18. maj. 18

LARA VALENTIĆ
ANALIZA MIKROPLASTIKE V IZBRANIH POVRŠINSKIH IN PODZEMELJSKIH KRAŠKIH VODAH
Mentor: izr. prof. dr. Tanja Pipan
Datum zagovora: 27. avg. 18

ŠPELA MAČEK
KOLIČINSKO IN KAKOVOSTNO OVREDNOTENJE VODNIH VIROV V RAZPOKLINSKEM IN KRAŠKEM VODONOSNIKU NA OBMOČJU OBČINE POSTOJNA
Mentor: izr. prof. dr. Metka Petrič
Datum zagovora: 10. sep. 18

DOROTEJA GOŠAR
ARSENIC IN NATURAL WATERS: HYDROGEOCHEMISTRY CHARACTERIZATION AND TOXICITY EFFECTS
Mentor: doc. dr. Martina Bergant Marušič
prof. dr. Maria do Rosario Melo da Costa
Datum zagovora: 25. sep. 18

TJAŠA BIRSA
DOLOČANJE ACETILHOLINESTERAZE V HUMANIH KRVNIH VZORCIH
Mentor: doc. dr. Martina Bergant Marušič
izr. prof. dr. Dorota Korte
Datum zagovora: 19. okt. 18

TJAŠA LOJPUR
VPLIV PROTEINOV APOBEC NA INFEKCIJO Z VIRUSI HPV
Mentor: doc. dr. Martina Bergant Marušič
Datum zagovora: 29. okt. 18

ANDREJ JERKIČ
DOLOČEVANJE AKTIVNOSTI ACHE ENCIMA V ČLOVEŠKEM SERUMU Z UPORABO FIA-TLS METODE
Mentor: prof. dr. Dorota Korte
Datum zagovora: 28. nov. 18

DIPLOME

ŠTUDIJSKI PROGRAM OKOLJE – 1. STOPNJA

TANJA BATKOVIČ
OS - EKOLOŠKO SPREJEMLJIVI PRETOK
Mentor: univ. dipl. inž. in kom. inž. Anja Potokar
Datum zagovora: 31. 5. 2018

ANŽE KURAJ
PRAKTIČNO USPOSABLJANJE NA KMETIJSKO GOZDARSKEM ZAVODU NOVA GORICA
Mentor: dr. Tjaša Jug
Datum zagovora: 14. 9. 2018

JAN DAVID
TRETIRANJE BALASTNIH VOD IN PROCESI CERTIFICIRANJA SISTEMOV
Mentor: Dr. Matej David
Datum zagovora: 9. 10. 2018

META KRIŽAJ
OBDELAVA PODATKOV S PODROČJA KAKOVOSTI ZRAKA V RAZLIČNIH TEKOČIH PROJEKTIH
Mentor: dr. David Kocman
Datum zagovora: 9. 10. 2018

MOJCA ZOTLER
KOMPOZIT IZ DIGESTATA IZ ANAEROBNE RAZGRADNJE MEŠANIH KOMUNALNIH ODPADKOV, GLINE IN PEPELA KOT ALTERNATIVEN GRADBENI MATERIAL
Mentor: doc. Dr. Ana Mladenovič
Somentor: dr. Primož Oprčkal
dr. Vesna Zalar Serjun
Datum zagovora: 9. 10. 2018

KOLEDAR VAŽNEJŠIH ZNANSTVENIH SREČANJ S PODROČJA KEMIJE IN KEMIJSKE TEHNOLOGIJE

SCIENTIFIC MEETINGS – CHEMISTRY AND CHEMICAL ENGINEERING

June 2019

2 – 6	14TH INTERNATIONAL SYMPOSIUM ON MACROCYCLIC AND SUPRAMOLECULAR CHEMISTRY Lecce, Italy
Information:	https://ismsc2019.eu/
16 – 19	LOSS PREVENTION 2019 Delft, The Netherlands
Information:	http://lossprevention2019.org/
16 – 19	29TH EUROPEAN SYMPOSIUM ON COMPUTER-AIDED PROCESS ENGINEERING Eindhoven, The Netherlands
Information:	https://escape29.nl/
19 – 21	IBERO-AMERICAN CONGRESS OF CHEMICAL ENGINEERING (CIBIQ) Santander, Spain
Information:	https://anque-icce2019.com/es/
16 – 20	17TH INTERNATIONAL CONFERENCE ON CHEMISTRY AND THE ENVIRONMENT – ICCE2019 Thessaloniki, Greece
Information:	http://www.euchems.eu/events/17th-international-conference-chemistry-environment-icce2019/
16 – 20	12TH IWA INTERNATIONAL CONFERENCE ON WATER RECLAMATION AND REUSE Berlin, Germany
Information:	http://efce.info/IWA+Conference+2019.html
26 – 28	THERMODYNAMICS 2019 Huelva, Spain
Information:	http://efce.info/Thermodynamics+2019.html
26 – 30	6TH EUROPEAN CONFERENCE ON ENVIRONMENTAL APPLICATIONS OF ADVANCED OXIDATION PROCESSES – EAAOP-6 Ljubljana, Slovenia
Information:	http://eaaop6.ki.si/

July 2019

1 – 3	CONGRESS ON NUMERICAL METHODS IN ENGINEERING Guimarães, Portugal
Information:	www.cmn2019.pt
3 – 6	8TH INTERNATIONAL CONFERENCE ON EXPERIMENTS / PROCESS / SYSTEM MODELING / SIMULATION / OPTIMIZATION Athens, Greece
Information:	http://www.epsmso.gr/

5 – 12	IUPAC 2019 Paris, France
Information:	https://www.iupac2019.org/
10 – 11	10TH WORLD CONGRESS ON GREEN CHEMISTRY AND TECHNOLOGY Paris, France
Information:	https://greenchemistry.chemistryconferences.org/
17 – 19	8TH EUROPEAN VARIETY IN UNIVERSITY CHEMISTRY EDUCATION Tuscany, Italy
Information:	https://www.monash.edu/eurovariety-2019/_nocache
17 – 19	INTERNATIONAL CONFERENCE ON MATERIALS AND NANOMATERIALS Paris, France
Information:	https://mns-19.com/
21 – 26	THE 18TH INTERNATIONAL SYMPOSIUM ON NOVEL AROMATIC COMPOUNDS (ISNA-18) Sapporo City, Japan
Information:	https://iupac.org/event/18th-international-symposium-novel-aromatic-compounds-isna-18/
22 – 24	5TH INTERNATIONAL CONGRESS ON WATER, WASTE AND ENERGY MANAGEMENT Paris, France
Information:	https://waterwaste-19.com/
30 – Aug. 1	8TH INTERNATIONAL CONFERENCE FOR NETWORK FOR INTER-ASIAN CHEMISTRY EDUCATORS (NICE) Taipei, Taiwan
Information:	https://iupac.org/event/8th-international-conference-network-inter-asian-chemistry-educators/

August 2019

4 – 8	36TH INTERNATIONAL CONFERENCE ON SOLUTION CHEMISTRY (ICSC) Xining, China
Information:	http://icsc2019.csp.escience.cn/dct/page/1

September 2019

8 – 13	33ND CONFERENCE OF EUROPEAN COLLOID AND INTERFACE SOCIETY (ECIS) Leuven, Belgium
Information:	https://kuleuvencongres.be/ecis2019/
9 – 13	EUROPEAN CORROSION CONGRESS Seville, Spain
Information:	https://eurocorr.org/EUROCORR+2019.html
11 – 14	7TH INTERNATIONAL CONFERENCE ON SEMICONDUCTOR PHOTOCHEMISTRY – SP7 Milano, Italy
Information:	https://www.sp7.unimi.it/
15 – 19	11TH EUROPEAN CONGRESS OF CHEMICAL ENGINEERING – ECCE11 & 4TH EUROPEAN CONGRESS OF APPLIED BIOTECHNOLOGY – ECAB5 Florence, Italy
Information:	http://efce.info/ECCE12_ECAB5-p-112545.html
25 – 27	SLOVENIAN CHEMICAL SOCIETY ANNUAL MEETING 2019 Portorož, Slovenia
Information:	http://chem-soc.si/slovenian-chemical-society-annual-meeting-2019

October 2019

1 – 6	14TH CONFERENCE ON SUSTAINABLE DEVELOPMENT OF ENERGY, WATER AND ENVIRONMENT SYSTEMS (SDEWES) Dubrovnik, Croatia
Information:	http://www.dubrovnik2019.sdewes.org/
17 – 18	2019 WATER DAYS, INTERNATIONAL SYMPOSIUM – CONNECTED TO WATER FOR 25 YEARS Bernardin Congress Centre, Portorož, Slovenia
Information:	https://sdzv-drustvo.si/en/water-days-2019/
21 – 24	24RD INTERNATIONAL CONGRESS OF CHEMICAL AND PROCESS ENGINEERING CHISA 2019 Seč, Czech Republic
Information:	http://2019.chisa.cz/

November 2019

27 – 29	EAPRIL Tartu, Estonia
Information:	https://eapril.org/eapril-2019

Acta Chimica Slovenica

Author Guidelines

Submissions

Submission to ACSi is made with the implicit understanding that neither the manuscript nor the essence of its content has been published in whole or in part and that it is not being considered for publication elsewhere. All the listed authors should have agreed on the content and the corresponding (submitting) author is responsible for having ensured that this agreement has been reached. The acceptance of an article is based entirely on its scientific merit, as judged by peer review. There are no page charges for publishing articles in ACSi. The authors are asked to read the Author Guidelines carefully to gain an overview and assess if their manuscript is suitable for ACSi.

Additional information

- Citing spectral and analytical data
- Depositing X-ray data

Submission material

Typical submission consists of:

- full manuscript (PDF file, with title, authors, abstract, keywords, figures and tables embedded, and references)
- supplementary files
  - ***Full manuscript*** (original Word file)
  - ***Statement of novelty*** (Word file)
  - ***List of suggested reviewers*** (Word file)
  - ***ZIP file containing graphics*** (figures, illustrations, images, photographs)
  - ***Graphical abstract*** (single graphics file)
  - ***Proposed cover picture*** (optional, single graphics file)
  - ***Appendices*** (optional, Word files, graphics files)

Incomplete or not properly prepared submissions will be rejected.

Submission process

Before submission, authors should go through the checklist at the bottom of the page and prepare for submission.

Submission process consists of 5 steps.

Step 1: Starting the submission

- Choose one of the journal sections.
- Confirm all the requirements of the ***checklist.***
- Additional plain text comments for the editor can be provided in the relevant text field.

Step 2: Upload submission

- Upload full manuscript in the form of a Word file (with title, authors, abstract, keywords, figures and tables embedded, and references).

Step 3: Enter metadata

- First name, last name, contact email and affiliation for all authors, in relevant order, must be provided. Corresponding author has to be selected. Full postal address and phone number of the corresponding author has to be provided.
- ***Title and abstract*** must be provided in plain text.
- Keywords must be provided (max. 6, separated by semicolons).
- Data about contributors and supporting agencies may be entered.
- ***References*** in plain text must be provided in the relevant text filed.

Step 4: Upload supplementary files

- Original Word file (original of the PDF uploaded in the step 2)
- ***Statement of novelty*** in a Word file must be uploaded
- All ***graphics*** have to be uploaded in a single ZIP file. Graphics should be named Figure 1.jpg, Figure 2.eps, etc.
- ***Graphical abstract image*** must be uploaded separately
- ***Proposed cover picture*** (optional) should be uploaded separately.
- Any additional ***appendices*** (optional) to the paper may be uploaded. Appendices may be published as a supplementary material to the paper, if accepted.
- For each uploaded file the author is asked for additional metadata which may be provided. Depending of the type of the file please provide the relevant title (Statement of novelty, List of suggested reviewers, Figures, Graphical abstract, Proposed cover picture, Appendix).

Step 5: Confirmation

- Final confirmation is required.

Article Types

Feature Articles are contributions that are written on editor's invitation. They should be clear and concise summaries of the most recent activity of the author and his/her research group written with the broad scope of ACSi in mind. They are intended to be general overviews of the authors' subfield of research but should be written in a way that engages and informs scientists in other areas. They should contain the following (see also general directions for article structure in ACSi below): (1) an introduction that acquaints readers with the authors' research field and outlines the important questions to which answers are being sought; (2) interesting, new, and recent contributions of the author(s) to the field; and (3) a summary that presents possible future directions. Manuscripts normally should not exceed 40 pages of one column format (letter size 12, 33 lines per page). Generally, experts in a field who have made important contribution to a specific topic in recent years will be invited by an editor to contribute such an **Invited Feature Article**. Individuals may, however, send a proposal (one-page maximum) for an Invited Feature Article to the Editor-in-Chief for consideration.

Scientific articles should report significant and innovative achievements in chemistry and related sciences and should exhibit a high level of originality. They

should have the following structure:

1. Title (max. 150 characters),
2. Authors and affiliations,
3. Abstract (max. 1000 characters),
4. Keywords (max. 6),
5. Introduction,
6. Experimental,
7. Results and Discussion,
8. Conclusions,
9. Acknowledgements,
10. References.

The sections should be arranged in the sequence generally accepted for publications in the respective fields and should be successively numbered.

Short communications generally follow the same order of sections as Scientific articles, but should be short (max. 2500 words) and report a significant aspect of research work meriting separate publication. Editors may decide that a Scientific paper is categorized as a Short Communication if its length is short.

Technical articles report applications of an already described innovation. Typically, technical articles are not based on new experiments.

Preparation of Submissions

Text of the submitted articles must be prepared with Microsoft Word. Normal style set to single column, 1.5 line spacing, and 12 pt Times New Roman font is recommended. Line numbering (continuous, for the whole document) must be enabled to simplify the reviewing process. For any other format, please consult the editor. Articles should be written in English. Correct spelling and grammar are the sole responsibility of the author(s). Papers should be written in a concise and succinct manner. The authors shall respect the ISO 80000 standard [1], and IUPAC Green Book [2] rules on the names and symbols of quantities and units. The Système International d'Unités (SI) must be used for all dimensional quantities.

Graphics (figures, graphs, illustrations, digital images, photographs) should be inserted in the text where appropriate. The captions should be self-explanatory. Lettering should be readable (suggested 8 point Arial font) with equal size in all figures. Use common programs such as MS Excel or similar to prepare figures (graphs) and ChemDraw to prepare structures in their final size. Width of graphs in the manuscript should be 8 cm. Only in special cases (in case of numerous data, visibility issues) graphs can be 17 cm wide. All graphs in the manuscript should be inserted in relevant places and **aligned left**. The same graphs should be provided separately as images of appropriate resolution (see below) and submitted together in a ZIP file (Graphics ZIP). Please do not submit figures as a Word file. In **graphs**, only the graph area determined by both axes should be in the frame, while a frame around the whole graph should be omitted. The graph area should be white. The legend should be inside the graph area. The style of all graphs should be the same. **Figures and illustrations** should be of sufficient quality for the printed version, i.e. 300 dpi minimum. **Digital images and photographs** should be of high quality (minimum 250 dpi resolution). On submission, figures should be of good enough resolution to be assessed by the referees, ideally as JPEGs. High-resolution figures (in JPEG, TIFF, or EPS format) might be required if the paper is accepted for publication.

Tables should be prepared in the Word file of the paper as usual Word tables. The captions should appear above the table and should be self-explanatory.

References should be numbered and ordered sequentially as they appear in the text, likewise methods, tables, figure captions. When cited in the text, reference numbers should be superscripted, following punctuation marks. It is the sole responsibility of authors to cite articles that have been submitted to a journal or were in print at the time of submission to ACSi. Formatting of references to published work should follow the journal style; please also consult a recent issue:

1. J. W. Smith, A. G. White, *Acta Chim. Slov.* **2008**, *55*, 1055–1059.
2. M. F. Kemmere, T. F. Keurentjes, in: S. P. Nunes, K. V. Peinemann (Ed.): Membrane Technology in the Chemical Industry, Wiley-VCH, Weinheim, Germany, **2008**, pp. 229–255.
3. J. Levec, Arrangement and process for oxidizing an aqueous medium, US Patent Number 5,928,521, date of patent July 27, **1999**.
4. L. A. Bursill, J. M. Thomas, in: R. Sersale, C. Collela, R. Aiello (Eds.), Recent Progress Report and Discussions: 5th International Zeolite Conference, Naples, Italy, 1980, Gianini, Naples, **1981**, pp. 25–30.
5. J. Szegezdi, F. Csizmadia, Prediction of dissociation constant using microconstants, http://www. chemaxon.com/conf/Prediction_of_dissociation _constant_using_microco nstants.pdf, (assessed: March 31, 2008)

Titles of journals should be abbreviated according to Chemical Abstracts Service Source Index (CASSI).

Special Notes

- Complete characterization, **including crystal structure**, should be given when the synthesis of new compounds in crystal form is reported.
- Numerical **data should be reported with the number of significant digits corresponding to the magnitude** of experimental uncertainty.
- **The SI system of units and IUPAC recommendations** for nomenclature, symbols and abbreviations should be followed closely. Additionally, the authors should follow the general guidelines when citing spectral and analytical data, and depositing crystallographic data.
- **Characters** should be correctly represented throughout the manuscript: for example, 1 (one) and l (ell), 0 (zero) and O (oh), x (ex), D7 (times sign), B0 (degree sign). Use Symbol font for all Greek letters and mathematical symbols.
- The rules and recommendations of the **IUBMB** and the **International Union of Pure and Applied Chemistry (IUPAC)** should be used for abbreviation of chemical names, nomenclature of chemical compounds, enzyme nomenclature, isotopic compounds, optically active isomers, and spectroscopic data.
- **A conflict of interest** occurs when an individual (author, reviewer, editor) or its organization is involved in multiple interests, one of which could possibly corrupt the motivation for an act in the

other. Financial relationships are the most easily identifiable conflicts of interest, while conflicts can occur also as personal relationships, academic competition, etc. **The Editors** will make effort to ensure that conflicts of interest will not compromise the evaluation process; potential editors and reviewers will be asked to exempt themselves from review process when such conflict of interest exists. When the manuscript is submitted for publication, **the authors** are expected to disclose any relationships that might pose potential conflict of interest with respect to results reported in that manuscript. In the Acknowledgement section the source of funding support should be mentioned. The statement of disclosure must be provided as Comments to Editor during the submission process.

- **Published statement of Informed Consent.** Research described in papers submitted to ACSi must adhere to the principles of the Declaration of Helsinki (***http://www.wma.net/e/policy/b3.htm***). These studies must be approved by an appropriate institutional review board or committee, and informed consent must be obtained from subjects. The Methods section of the paper must include: 1) a statement of protocol approval from an institutional review board or committee and 2), a statement that informed consent was obtained from the human subjects or their representatives.
- **Published Statement of Human and Animal Rights.**When reporting experiments on human subjects, authors should indicate whether the procedures followed were in accordance with the ethical standards of the responsible committee on human experimentation (institutional and national) and with the Helsinki Declaration of 1975, as revised in 2008. If doubt exists whether the research was conducted in accordance with the Helsinki Declaration, the authors must explain the rationale for their approach and demonstrate that the institutional review body explicitly approved the doubtful aspects of the study. When reporting experiments on animals, authors should indicate whether the institutional and national guide for the care and use of laboratory animals was followed.
- To avoid conflict of interest between authors and referees we expect that not more than one referee is from the same country as the corresponding author(s), however, not from the same institution.
- Contributions authored by **Slovenian scientists** are evaluated by non-Slovenian referees.
- Papers describing **microwave-assisted reactions** performed in domestic microwave ovens are not considered for publication in *Acta Chimica Slovenica.*
- *Manuscripts that are **not prepared and submitted** in accord with the instructions for authors are not considered for publication.*

Appendices

Authors are encouraged to make use of supporting information for publication, which is supplementary material (appendices) that is submitted at the same time as the manuscript. It is made available on the Journal's web site and is linked to the article in the Journal's Web edition. The use of supporting information is particularly appropriate for presenting additional graphs, spectra, tables and discussion and is more likely to be of interest to specialists than to general readers. When preparing supporting information, authors should keep in mind that the supporting information files will not be edited by the editorial staff. In addition, the files should be not too large (upper limit 10 MB) and should be provided in common widely known file formats to be accessible to readers without difficulty. All files of supplementary materials are loaded separately during the submission process as supplementary files.

Proposed Cover Picture and Graphical Abstract Image

Graphical content: an ideally full-colour illustration of resolution 300 dpi from the manuscript must be proposed with the submission. Graphical abstract pictures are printed in size 6.5 x 4 cm (hence minimal resolution of 770 x 470 pixels). Cover picture is printed in size 11 x 9.5 cm (hence minimal resolution of 1300 x 1130 pixels)

Authors are encouraged to submit illustrations as candidates for the journal Cover Picture*. The illustration must be related to the subject matter of the paper. Usually both proposed cover picture and graphical abstract are the same, but authors may provide different pictures as well.

* The authors will be asked to contribute to the costs of the cover picture production.

Statement of novelty

Statement of novelty is provided in a Word file and submitted as a supplementary file in step 4 of submission process. Authors should in no more than 100 words emphasize the scientific novelty of the presented research. Do not repeat for this purpose the content of your abstract.

List of suggested reviewers

List of suggested reviewers is a Word file submitted as a supplementary file in step 4 of submission process. Authors should propose the names, full affiliation (department, institution, city and country) and e-mail addresses of three potential referees. Field of expertise and at least two references relevant to the scientific field of the submitted manuscript must be provided for each of the suggested reviewers. The referees should be knowledgeable about the subject but have no close connection with any of the authors. In addition, referees should be from institutions other than (and preferably countries other than) those of any of the authors.

How to Submit

Users registered in the role of author can start submission by choosing USER HOME link on the top of the page, then choosing the role of the Author and follow the relevant link for starting the submission process.

Prior to submission we strongly recommend that you familiarize yourself with the ACSi style by browsing the journal, particularly if you have not submitted to the ACSi before or recently.

Correspondence

All correspondence with the ACSi editor regarding the paper goes through this web site and emails. Emails are sent and recorded in the web site database. In the correspondence with the editorial office please provide ID number of your manuscript. All emails you receive from the system contain relevant links. **Please do not answer the emails directly but use the embedded links in the emails for carrying out relevant actions.** Alternatively, you can carry out all the actions and correspondence through the online system by logging in and selecting relevant options.

Proofs

Proofs will be dispatched via e-mail and corrections should be returned to the editor by e-mail as quickly as possible, normally within 48 hours of receipt. Typing errors should be corrected; other changes of contents will be treated as new submissions.

Submission Preparation Checklist

As part of the submission process, authors are required to check off their submission's compliance with all of the following items, and submissions may be returned to authors that do not adhere to these guidelines.

1. The submission has not been previously published, nor is it under consideration for publication in any other journal (or an explanation has been provided in Comments to the Editor).
2. All the listed authors have agreed on the content and the corresponding (submitting) author is responsible for having ensured that this agreement has been reached.
3. The submission files are in the correct format: manuscript is created in MS Word but will be **submitted in PDF** (for reviewers) as well as in original MS Word format (as a supplementary file for technical editing); diagrams and graphs are created in Excel and saved in one of the file formats: TIFF, EPS or JPG; illustrations are also saved in one of these formats. The preferred position of graphic files in a document is to embed them close to the place where they are mentioned in the text (See ***Author guidelines*** for details).
4. The manuscript has been examined for spelling and grammar (spell checked).
5. The ***title*** (maximum 150 characters) briefly explains the contents of the manuscript.
6. Full names (first and last) of all authors together with the affiliation address are provided. Name of author(s) denoted as the corresponding author(s), together with their e-mail address, full postal address and telephone/fax numbers are given.
7. The ***abstract*** states the objective and conclusions of the research concisely in no more than 150 words.
8. Keywords (minimum three, maximum six) are provided.
9. ***Statement of novelty*** (maximum 100 words) clearly explaining new findings reported in the manuscript should be prepared as a separate Word file.
10. The text adheres to the stylistic and bibliographic requirements outlined in the ***Author guidelines***.
11. Text in normal style is set to single column, 1.5 line spacing, and 12 pt. Times New Roman font is recommended. All tables, figures and illustrations have appropriate captions and are placed within the text at the appropriate points.
12. Mathematical and chemical equations are provided in separate lines and numbered (Arabic numbers) consecutively in parenthesis at the end of the line. All equation numbers are (if necessary) appropriately included in the text. Corresponding numbers are checked.
13. Tables, Figures, illustrations, are prepared in correct format and resolution (see ***Author guidelines***).
14. The lettering used in the figures and graphs do not vary greatly in size. The recommended lettering size is 8 point Arial.
15. Separate files for each figure and illustration are prepared. The names (numbers) of the separate files are the same as they appear in the text. All the figure files are packed for uploading in a single ZIP file.
16. Authors have read ***special notes*** and have accordingly prepared their manuscript (if necessary).
17. References in the text and in the References are correctly cited. (see ***Author guidelines***). All references mentioned in the Reference list are cited in the text, and vice versa.
18. Permission has been obtained for use of copyrighted material from other sources (including the Web).
19. The names, full affiliation (department, institution, city and country), e-mail addresses and references of three potential referees from institutions other than (and preferably countries other than) those of any of the authors are prepared in the word file. At least two relevant references (important papers with high impact factor, head positions of departments, labs, research groups, etc.) for each suggested reviewer must be provided.
20. Full-colour illustration or graph from the manuscript is proposed for graphical abstract.
21. ***Appendices*** (if appropriate) as supplementary material are prepared and will be submitted at the same time as the manuscript.

Privacy Statement

The names and email addresses entered in this journal site will be used exclusively for the stated purposes of this journal and will not be made available for any other purpose or to any other party.

ISSN: 1580-3155

Koristni naslovi

Slovensko kemijsko društvo
www.chem-soc.si
e-mail: chem.soc@ki.si

Wessex Institute of Technology
www.wessex.ac.uk

SETAC
www.setac.org

European Water Association
http://www.ewa-online.eu/

European Science Foundation
www.esf.org

European Federation of Chemical Engineering
https://efce.info/

International Union of Pure and Applied Chemistry
https://iupac.org/

Novice europske zveze kemijskih društev (EuCheMS) najdete na:

EuCheMS: Brussels News Updates
http://www.euchems.eu/newsletters/

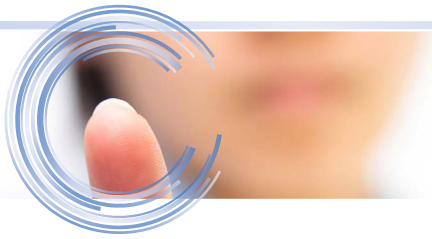

DONAU LAB Ljubljana
Member of LPPgroup

Donau Lab d.o.o., Ljubljana
Tbilisijska 85
SI-1000 Ljubljana
www.donaulab.si
office-si@donaulab.com

ZASTOPAMO:

B BRAUN

VSE NA ENEM MESTU:

PRODAJA

SERVIS

REZERVNI DELI

POTROŠNI MATERIAL

Razvoj in inovacije za globalno uspešnost

Znanje, kreativnost zaposlenih in inovacije so ključnega pomena v okolju, kjer nastajajo Heliosovi pametni premazi. Z rešitvami, ki zadostijo široki paleti potreb, kontinuiranim razvojem ter s kakovostnimi produkti Helios predstavlja evropski center za inovacije, know-how in poslovni razvoj skupine Kansai Paint.

www.helios-group.eu

HELIOS

Designing Excellence

BODITE **NEUSTAVLJIVI**

MAGNEZIJ Krka 300

edinstvena kombinacija
Mg+B_2

Granulat za pripravo napitka vsebuje **magnezijev citrat** in **vitamin B_2**.

Magnezij in vitamin B_2 prispevata k zmanjševanju utrujenosti in izčrpanosti ter normalnemu delovanju živčnega sistema.

Magnezij prispeva tudi k delovanju mišic.

www.magnezijkrka.si

- Okus po pomaranči in limeti.
- Brez konzervansov.
- Brez umetnih barvil, arom in sladil.
- Ena vrečka na dan.

Prehransko dopolnilo ni nadomestilo za uravnoteženo in raznovrstno prehrano. Skrbite tudi za zdrav življenjski slog.

NOVO

KRKA

Acta Chimica Slovenica

Year 2019, Vol. 66, No. 2

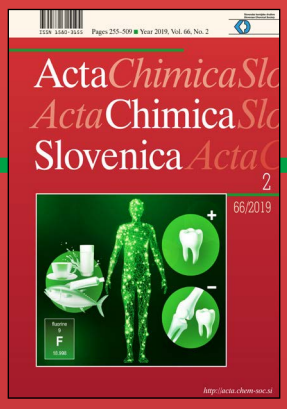

It appears that, in our current state of knowledge, fluoride illustrates surprisingly well the classical medical concept that the effect of a substance depends on the dosage regimen. As Paracelsus (1493–1541) said: "All substances are poisons; there is none which is not a poison. The right dose differentiates a poison and a remedy" (page 255).